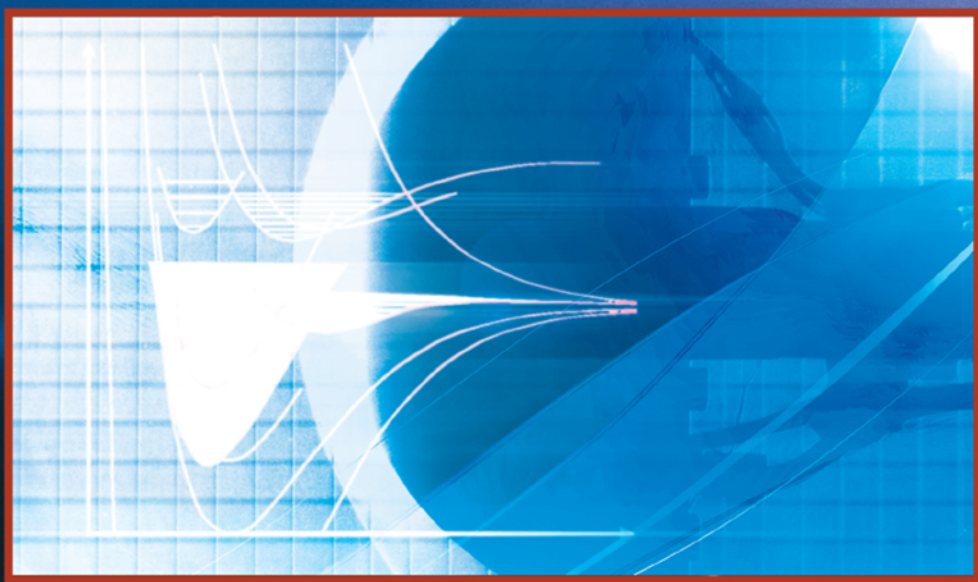


Hypersonic Nonequilibrium Flows: Fundamentals and Recent Advances

Edited by
Eswar Josyula



PROGRESS IN ASTRONAUTICS AND AERONAUTICS

Timothy C. Lieuwen, Editor-in-Chief
Volume 247

Hypersonic Nonequilibrium Flows: Fundamentals and Recent Advances

Hypersonic Nonequilibrium Flows: Fundamentals and Recent Advances

EDITED BY

Eswar Josyula

*U.S. Air Force Research Laboratory
Wright-Patterson Air Force Base, Ohio*



Volume 247
Progress in Astronautics and Aeronautics

Timothy C. Lieuwen, Editor-in-Chief

*Georgia Institute of Technology
Atlanta, Georgia*

Published by
American Institute of Aeronautics and Astronautics, Inc.
1801 Alexander Bell Drive, Reston, VA 20191-4344



American Institute of Aeronautics and Astronautics, Inc., Reston, Virginia

1 2 3 4 5

Copyright © 2015 by the American Institute of Aeronautics and Astronautics, Inc. All rights reserved. Reproduction or translation of any part of this work beyond that permitted by Sections 107 and 108 of the U.S. Copyright Law without the permission of the copyright owner is unlawful. The code following this statement indicates the copyright owner's consent that copies of articles in this volume may be made for personal or internal use, on condition that the copier pay the per copy fee (\$2.50) plus the per-page fee (\$0.50) through the Copyright Clearance Center, Inc., 222 Rosewood Drive, Danvers, Massachusetts 01923. This consent does not extend to other kinds of copying, for which permission requests should be addressed to the publisher. Users should employ the following code when reporting copying from the volume to the Copyright Clearance Center:

978-1-62410-328-5/15 \$2.50 + .50

Data and information appearing in this book are for informational purposes only. AIAA is not responsible for any injury or damage resulting from use or reliance, nor does AIAA warrant that use or reliance will be free from privately owned rights.

ISBN 978-1-62410-328-5



PROGRESS IN ASTRONAUTICS AND AERONAUTICS

EDITOR-IN-CHIEF

Timothy C. Lieuwen

Georgia Institute of Technology

EDITORIAL BOARD

Paul M. Bevilaqua

Lockheed Martin (Ret.)

Steven A. Brandt

U.S. Air Force Academy

José A. Camberos

U.S. Air Force Research Laboratory

Richard Curran

Delft University of Technology

Jonathan How

Massachusetts Institute of Technology

Christopher H. M. Jenkins

Montana State University

Eswar Josyula

U.S. Air Force Research Laboratory

Mark J. Lewis

University of Maryland

Richard C. Lind

University of Florida

Dimitri N. Mavris

Georgia Institute of Technology

Daniel McCleese

Jet Propulsion Laboratory

Alexander J. Smits

Princeton University

Sun Xiaofeng

Beijing University of Aeronautics & Astronautics

Oleg A. Yakimenko

U.S. Naval Postgraduate School

TABLE OF CONTENTS

Preface	xii
----------------	-------	------------

Chapter 1 Fundamental Fluid Transport Equations for Hypersonic Nonequilibrium Flows

*Eswar Josyula, U.S. Air Force Research Laboratory, Wright-Patterson AFB, Ohio,
Prakash Vedula, University of Oklahoma Norman, Oklahoma*

I.	Introduction	1
II.	Kinetic Theory: The Boltzmann Equation	10
III.	Macroscopic Transport Equations Coupled to Master Equation	22
IV.	Macroscopic Nonequilibrium Transport Equations With Simplified Energy Exchange Models	32
V.	Summary and Concluding Remarks	37
	Acknowledgment	37
	References	38

Chapter 2 Computation of Hypersonic Nonequilibrium Flows using the Direct Simulation Monte Carlo Method

Iain D. Boyd, University of Michigan, Ann Arbor, Michigan

I.	Introduction	45
II.	Basic Algorithm of the DSMC Technique	48
III.	Physical Models of the DSMC Technique	50
IV.	DSMC Analysis of Hypersonic Flows	67
V.	Hybrid DSMC-Continuum Methods	79
VI.	Summary	93
	Acknowledgments	95
	References	95

Chapter 3 First Principles Calculation of Heavy Particle Rate Coefficients

Richard L. Jaffe and David W. Schwenke, NASA Ames Research Center, Moffett Field, California, Marco Panesi, University of Illinois at Urbana Champaign, Urbana, Illinois

I.	Introduction	103
II.	Calculation of Potential Energy Surfaces	107
III.	Collisional Calculations to State-to-State Rate Coefficients	119
IV.	Phenomenological Rate Coefficients from a Detailed Master Equation Model	139

V. Coarse-Grained Model	150
VI. Concluding Remarks	154
Acknowledgments	154
References	155

Chapter 4 Radiation from Hypersonic Bodies—A Window on Non-Equilibrium Processes 159

Deborah A. Levin, *University of Illinois at Urbana-Champaign, Urbana, Illinois*

I. Introduction	159
II. Brief History of Radiation Models	161
III. Elements of the Theory of a Radiation Model in the Ultraviolet Spectral Region	163
IV. Application of Radiation Modeling to Three Cases of Hypersonic Flows	174
V. Future Challenges	193
Acknowledgment	195
References	195

Chapter 5 CFD Methods for Hypersonic Flows and Aerothermodynamics 203

Graham V. Candler, Pramod K. Subbareddy and Ioannis Nompelis,
University of Minnesota, Minneapolis, Minnesota

I. Introduction	204
II. Upwind Numerical Flux Functions	206
III. Low-dissipation Numerical Flux	219
IV. Implicit Time Integration	224
V. Test Case: Double-cone Flow	227
VI. Simulation of an Ablating Thermal Protection System	231
VII. Future Prospects	233
VIII. Conclusions	233
Acknowledgments	234
References	234

Chapter 6 Surface Chemistry in Non-Equilibrium Flows 239

Jochen Marschall, *Molecular Physics Program, SRI International, Menlo Park, California*, Matthew MacLean, *Aerosciences Sector, CUBRC, Inc., Buffalo, New York*, Paul E. Norman and Thomas E. Schwartzentruber, *Aerospace Engineering & Mechanics, University of Minnesota, Minneapolis, Minnesota*

I. Introduction	241
II. Background	242

III.	A Finite–Rate Surface Chemistry Model	245
IV.	Computational Chemistry Approaches for Surface Chemistry Modeling	265
V.	Computational Examples	285
VI.	Future Directions	308
VII.	Summary/Conclusion	315
	Acknowledgments	316
	References	317

Chapter 7 High-Enthalpy Facilities and Plasma Wind Tunnels for Aerothermodynamics Ground Testing 329

Olivier Chazot and Francesco Panerai, *Von Karman Institute for Fluid Dynamics, Rhode St-Genèse, Belgium*

I.	Introduction	329
II.	Aerothermodynamic Ground Testing	330
III.	High-Enthalpy Facilities	334
IV.	Plasma Wind Tunnels	338
V.	Conclusion	339
	References	341

Chapter 8 Molecular-Based Optical Diagnostics for Hypersonic Nonequilibrium Flows 343

Paul M. Danehy and Brett F. Bathel, *NASA Langley Research Center, Hampton, Virginia*, Craig T. Johansen, *University of Calgary, Calgary, Canada*, Michael Winter, *University of Kentucky, Lexington, Kentucky*, Sean O’Byrne, *University of New South Wales Canberra, Canberra, Australia*, Andrew D. Cutler, *The George Washington University, Newport News, Virginia*

I.	Introduction	343
II.	Equipment Used for Molecular-based Optical Measurement	348
III.	Optical Emission Spectroscopy	352
IV.	Absorption Spectroscopy	373
V.	Laser-induced Fluorescence (LIF)	391
VI.	Rayleigh and Raman Scattering	418
VII.	Coherent Anti-stokes Raman Spectroscopy	431
VIII.	Other Molecular-based Measurement Techniques	444
IX.	Conclusions	448
	Acknowledgments	450
	References	450

Appendix High-Enthalpy Facilities and Plasma Wind Tunnels for Aerothermodynamics Ground Testing	471
Olivier Chazot and Francesco Panerai, <i>Von Karman Institute for Fluid Dynamics, Rhode St-Genèse, Belgium</i>	
Index	523
Supporting Materials	541

PREFACE

Creation of the present volume has been motivated by recent unprecedented scientific advances in the field of nonequilibrium processes for aerospace applications; these advances have primarily been driven by interest in space access and exploration or in developing military technologies involving hypersonic flight regimes.

The high-temperature environment poses an unusual challenge in the understanding of the basic physics, and a lack of such understanding can lead to risks and uncertainties in the design of aerospace vehicles. A recent illustrative failure is that of the Hypersonic Technology Vehicle 2 (HTV-2), an unmanned technology demonstration vehicle conceived by DARPA. During a demonstration flight in the summer of 2011, an HTV-2 maintained stable flight for about three minutes at 13,000 mph over the Pacific Ocean before its safety system plunged it in the ocean. The accident investigation pointed to the existence of shock waves associated with peeling skin that were 100 times stronger than the vehicle was designed to withstand. The failure, attributed to extreme heat and speed, reveals the challenges involved in modeling complex, high-speed flows involving a wide range of length scales.

In the modeling of hypersonic flows, the last decade has witnessed a revisit of fundamental principles of kinetic theory and quantum chemistry to describe the kinetic and thermal states, respectively, of the individual gas particles. Modern aerospace programs where nonequilibrium energy transfer processes play a major role may be broadly categorized as exo- and endo-atmospheric. The exo-atmospheric flight programs consist of Earth and planetary reentry programs, as well as access to space programs for applications that include space exploration, flight experiments and demonstrations, missile defense, and the nascent space tourism industry. The endo-atmospheric flight programs are primarily motivated by hypersonic military applications requiring high-precision engagement for tactical and strategic defense, as well as applications involving intelligence, surveillance, and reconnaissance.

The nonequilibrium processes considered in this volume are generally associated with flight Mach numbers between 7 and 25, where the shock-layer temperatures range from 3000 to 25,000 K. Flights at Mach 7 to 10 primarily involve thermal excitation and dissociation, surface catalytic effects and, in some cases, radiative emission and absorption. Phenomena expected at a Mach number of 25 include significant gas phase radiation, dissociation, and ionization in the reactive mixture. Translational and rotational nonequilibrium, although primarily associated with high altitude (e.g. above 80 km) conditions, can play a significant role for geometries with small length scales at lower altitudes.

Over the past several decades, continual advances in modeling approaches and computational resources have dramatically influenced the efficacy of numerical simulation in the design of hypersonic vehicles. As numerical analysis of

hypersonic aerothermal phenomena has become a progressively more important element in vehicle design, established models have repeatedly been superseded by newer models following identification of model limitations or deficiencies. The 1960s saw applications of the simple Lighthill dissociation model, the Landau–Teller vibrational relaxation model, the Fay and Riddel model for heat transfer, and bridging functions for rarefied gas flows. The computational fluid dynamics (CFD) requirements in the 1980s for solving high Mach number flows for reentry applications prompted development of simplified models, such as the Park two-temperature model for determining the rate controlling temperature in dissociation flows and the Larsen–Borgnakke model for implementing internal energy relaxation in rarefied flow analysis. The Park model was pervasive in CFD for over three decades owing to its simplicity. However, a long-held false sense of maturity in the field is partly attributable to the popularity of this model, due to both in its oversimplification in representing the physics and the lack of rigorous experiments to establish its presumed validity. Although deficiencies of the Park model were recognized and acknowledged in the 1990s, there was not a concerted effort to develop more general and accurate alternative models until recent years.

Over the last four decades, the lack of adequate ground test facilities for representing the hypersonic environment has made CFD tools a mainstay of the aerospace design cycle. The excessive reliance and rapid turnaround requirements on CFD has put immense pressure on the aerospace community to develop simple mathematical models to represent complex physical phenomena, thus contributing to delays in development of proper modeling and understanding of the flow physics. It is only in the recent years that we see resurgence in fundamental non-equilibrium flow modeling, thus bringing into focus the real challenges in accurate prediction of hypersonic flows by CFD methods. This book is thus timely; it provides a rigorous groundwork for alternate models in addition to a survey of facilities and measurement techniques, with the expectation that improvements in model accuracy will change the nature of computational tools for future aerospace development.

The fundamental governing equation describing a flow of nonequilibrium gas is the Boltzmann equation for the case of a monatomic gas and the generalized Boltzmann equation for a gas with internal degrees of freedom. In the continuum flight regime, however, source terms in the Navier–Stokes equations may be used to account for the deviation from equilibrium in the distribution of internal energy states for the gas molecules. Proper modeling of internal energy distributions is, in turn, governed by the master equation that accounts for state-specific populations in the various energy modes. The related computational chemistry research consists of developing potential energy surfaces for the reactions of interest, and conducting trajectory calculations for prediction of state-to-state kinetic rates and cross sections of the internal energy modes.

One of the major challenges in the modeling of the flowfield is the effective use of so-called high-performance computers with a large number of processors. The

large-scale parallel analysis of complex hypersonic flow problems to aid our understanding of the physics is a necessary step in development of reduced order models for routine CFD use during the vehicle design cycle. This step requires the associated algorithm development and validation with ground and/or flight tests.

The challenges described form the basis for the material presented in this volume. In addition to the fundamental equations with applications in both continuum and rarefied flight regimes, the present volume covers the state of the art experimental facilities and diagnostic techniques relevant to nonequilibrium flow physics. The presentation in this volume of the nonequilibrium approach to testing of some of the most advanced facilities worldwide is, to our knowledge, not found elsewhere. This volume does not cover the related extensions to plasmas, uncertainty quantification and sensitivity analysis, CFD method development, and flight tests.

Chapter 1 presents the fundamental governing equations of nonequilibrium fluid transport, and Chapter 2 provides an overview of the direct simulation Monte Carlo method for rarefied gas flow analysis. Chapter 3 presents the computational chemistry approach to calculating the rates and cross sections in the quantized energy states, and Chapter 4 is focused on radiative heat transfer as a nonequilibrium process. Chapter 5 presents a CFD perspective and Chapter 6 describes nonequilibrium surface chemistry. Chapter 7 presents the high enthalpy experimental facilities and Chapter 8 gives an overview of diagnostic techniques.

We are thankful to the anonymous reviewers for their valuable feedback and to David Arthur, the acquisitions editor at AIAA, who has been a pleasure to work with.

Eswar Josyula

May 2015

Fundamental Fluid Transport Equations for Hypersonic Nonequilibrium Flows

Eswar Josyula*

U.S. Air Force Research Laboratory, Wright-Patterson AFB, Ohio

Prakash Vedula[†]

University of Oklahoma Norman, Oklahoma

I. INTRODUCTION

The classification of hypersonic flow applies to flight speeds far greater than the speed of sound. The characteristic hypersonic features [1, 2] may broadly be divided into those of a hydrodynamic nature that arise because the flight Mach number is large and those of a physical or chemical nature because the kinetic energy of the freestream flow is large. For hypersonic flows around bodies, the front of the body facing the flow is enveloped by a shock wave extending all the way downstream of the body as a flare; the flowfield domain of interest includes the shock layer, which is the region between the shock and body. Far downstream, the shock wave becomes weak, and a wake is observed directly downstream of the body. Within the shock layer, the temperature and pressure are much greater than in the freestream. Furthermore, if the temperature of the body is of the order of the temperature of the freestream, a considerable heat transfer takes place from the gas to the body.

Fundamental understanding and modeling of hypersonic flows are important for a number of aerospace applications in space exploration and military technologies [3, 4]. Hypersonic flows relevant to such applications often exhibit complex multiphysics phenomena at high temperatures in the rarefied, continuum, and transition flight regimes. In particular, these flows exhibit deviations from thermodynamic equilibrium at high altitudes in the rarefied regime where the nonequilibrium occurs in the translational energy mode and further nonequilibrium owing to internal degrees of excitation. At the high temperatures expected through much of the shock layer the flows could be in a state of thermochemical nonequilibrium with the presence of chemical reactions, ionization, and radiation.

*Senior Research Aerospace Engineer.

[†]Associate Professor.

Deviations from equilibrium associated with these physical and chemical mechanisms affect the predictions of vehicle stability and control, the aerodynamic thrust, drag, and surface heating. These design parameters require accurate predictions of surface temperatures, gas-surface interactions, chemical compositions, boundary layer transition, and shock-boundary layer interaction. As the characteristic time scales associated with some of these physical and chemical mechanisms are sometimes comparable to one another and also comparable to the characteristic time scales of the flow, it is important to consider mathematical formulations that account for interactions among various processes.

The dimensionless quantity Knudsen number (Kn) is quite often the criterion that distinguishes the continuum and rarefied flight regimes, where the Knudsen number is defined as follows:

$$Kn = \frac{1}{\nu t_f} \quad (1)$$

where ν represents the intermolecular collision rate and t_f the characteristic flow time. Alternatively, letting \bar{c} be the mean molecular speed, λ the mean free path (the average distance traveled by a molecule before encountering a collision), and L represent a characteristic length scale, the above equation becomes

$$Kn = \frac{1}{\nu t_f} = \frac{1}{(\bar{c}/\lambda)(L/\bar{c})} = \frac{\lambda}{L} \quad (2)$$

However, the choice of characteristic length scale may be somewhat ambiguous. Choosing a length scale based upon the geometry over which the flow is considered results in a parameter which may describe globally how well the continuum equations apply, however, it does not address the properties of the local flow physics. A better choice is to consider a local length scale related to the physical characteristics of the flowfield. This may be a quantity such as shock thickness, boundary layer thickness, or some other length associated with the local flow physics. The mean free path is in turn defined as the average distance—typically in a reference frame which moves with the flow—that a molecule travels before colliding with another molecule. When the Kn is less than 0.01 the gas is assumed to be in a state of continuum and can be described by the continuum gas dynamic equations. For $Kn > 0.01$, the gas is said to be rarefied. Rarefied gas flows are primarily classified in three flow regimes:

- $0.01 < Kn < 0.1$ Slip flow regime
- $0.1 < Kn < 10$ Transitional regime
- $Kn > 10$ Free molecular regime

Applications in slip flow regime manifest mainly near the boundaries of vehicles in high-speed flight, as the so-called velocity slip and temperature jump phenomena, which are treated by special boundary conditions. For the

rest of the flowfield, the continuum gas dynamics equations are mostly valid. For the other extreme of the free molecular regime where Kn is high, the gas is very rarefied. In the free molecular regime, where the mean free path is much larger than the characteristic dimension of the body, the collisions occur infrequently even after the particles hitting the surface reflect away. In the transitional regime ($0.1 < Kn < 10$), both the collisions between particles and with the surface assume importance, hence this is an area of rarefied gas dynamics with considerable body of research.

The Boltzmann transport equation is the fundamental governing equation for nonequilibrium flow systems. It describes the statistical behavior of a system that is in a state of thermodynamic nonequilibrium [5]. It is an integro-differential equation to describe the evolution of the velocity distribution function for a dilute gas in space and time. Other assumptions under which the Boltzmann equation is valid are: 1) collisions are considered to be binary; 2) the distribution function does not change significantly on a time scale of the order of the duration of a collision, or on a length scale on the order of the intermolecular forces; 3) the pre-collision velocities of colliding molecules are uncorrelated (the assumption of molecular chaos). The Boltzmann equation has found many applications in modern physics, such as the electron transport in plasma, neutron transport in reactors and in aerospace applications, in particular the field of rarefied gas dynamics. Owing to the difficulties in obtaining exact solutions of the Boltzmann equation, engineers and physicists have sought specific solutions with particular initial and boundary values of interest. However, the numerical solutions of the Boltzmann equation have gained popularity in the last century. See for example the monograph by Aristov [6]. The conservation equations for macroscopic physical quantities are obtained as the velocity moments of the Boltzmann equation. The zeroth and first-order approximations of the Chapman–Enskog approximation lead to the Euler and Navier–Stokes equations that are commonly used to simulate the continuum flows. The Navier–Stokes equations are derived assuming only small deviations from equilibrium as characterized by a Maxwellian distribution function. In the equilibrium state of a gas, the distribution of molecular energy states does not vary with time. Similarly, if the gas were to undergo a reaction, the equilibrium state would imply that the rate at which the forward reaction progresses is exactly equal to the rate at which the reverse reaction progresses, such that the composition of the gas does not vary over time. On the other hand, a state of nonequilibrium is a departure from the equilibrium state.

The last decade has seen a resurgence of direct methods in the numerical solution of the Boltzmann equation. Historically, however, one can count only a handful of successful attempts at the solution of the full Boltzmann equation and mention is made here of Tcheremissine's method [7] as one such successful attempt. Tcheremissine's method consists of a fast evaluation of the collision integral based on a uniform discrete ordinate velocity discretization. In this approach the collision integral is written in the form of an eight-fold integral—six velocity and two spatial integrals—using Dirac delta-function formalism. Conservation of

mass, momentum, and energy is achieved by using a special interpolation of the velocity distribution function at the off-grid values of post-collision velocities. A quasi-stochastic Korobov integration is used for efficient evaluation of the multi-dimensional integral. Tcheremissines approach was successfully applied to simulations of the Boltzmann equation for a multi-species nonreactive gas mixture, [8] with internal energy excitation [9] and in more than one spatial dimension [10]. On the other hand, not being a fully deterministic method, its accuracy is not easy to evaluate. See Alexkseenko and Josyula [11] for a brief survey and recent advances made in the numerical formulation of the Boltzmann equation.

In flowfields that have mixed continuum and rarefied regions, it is often desirable to use hybrid computational approaches based on identification of regions where equilibrium-based macroscopic transport theories are applicable. In these hybrid approaches, the computationally efficient macroscopic transport equations in continuum regions are used in conjunction with kinetic-theory-based formulations in rarefied regions. In simulations of complex flows with rarefied and continuum regions, a measure of the local flow Knudsen number is used to switch between full kinetic solvers (based on the Boltzmann equation) in high Knudsen number regions, and in regions where Knudsen number is small, solvers used based on equilibrium-based macroscopic transport equations. Flow computations in continuum regions can be efficiently accomplished for solution of simple model kinetic equations, such as the Bhatnagar–Gross–Krook (BGK) approximation of the collision operator or by solving the continuum Euler/Navier–Stokes equations. (See Xu et al. [12] for a numerical method using the BGK gas kinetic scheme.) These solutions can be dynamically coupled with direct Boltzmann solvers in the non-continuum, transitional flow regimes. Kolobov et al. [13] have shown that coupling of a direct Boltzmann solver for description of non-continuum regions coupled with a BGK model kinetic equation for description of continuum regions, based on an adaptive mesh mesh and algorithm refinement results in accurate and stable solutions for a class of rarefied-continuum flows.

In the context of the hybrid approaches, additional challenges appear owing to the nature of information exchange between continuum solvers and rarefied flow solvers not directly based on the Boltzmann equation. Along domain boundaries separating the continuum and rarefied flow regions, information based on macroscopic quantities obtained by solving the macroscopic transport equations needs to be used to update the distribution function across the boundaries. This involves the use of some sort of a model/reconstruction procedure to determine the information needed to update the distribution functions based on macroscopic moments. Errors associated with such models/reconstructions, along with errors associated with classification of regions near equilibrium and far from equilibrium, need to be carefully quantified for effective use of high fidelity hybrid solvers. In this work we refer to the direct simulation Monte Carlo (DSMC) method (see Bird [14]) as an example of a rarefied flow simulation scheme not directly based on the Boltzmann equation. The DSMC method is a rarefied gas simulation approach, whereby a large population of particles is

used to represent atoms or molecules throughout the simulated flowfield, and collision operations are considered on a probabilistic basis to simulate the underlying physics in the flow. The DSMC method is widely used to model rarefied gas flows and in conjunction with Navier-Stokes solvers has found use in hybrid rarefied-continuum flow problems. The DSMC method is the subject of Chapter 2 of this volume.

As a representative problem of a hybrid continuum-rarefied flow, consider a typical blunt body in hypersonic flow. The physics involved with the associated structure of the strong shocks invalidate the continuum equations due to the presence of translational nonequilibrium inside the shock wave. Aft of the shock the continuum equations may hold and close to the body, strong gradients exist across the boundary layer. In the post-shock region and the shock layer, the gas is in a state of thermal nonequilibrium owing to the excitation of the internal energy modes of the particles. Further downstream, the flow may expand around the body to the point at which the density is too low for the continuum equations to hold. Such a mixed flowfield exemplifies why a hybrid method is desirable and illustrates the importance of understanding where the continuum equations are valid, and further emphasizes the need for a good understanding of nonequilibrium phenomena. In the past, several parameters have been examined in an attempt to quantify continuum breakdown. For obvious reasons, many of the initial investigations considered parameters in the form of a Knudsen number based upon the local flow physics. This approach is based on the observation that if flow variables change over relatively small distances in comparison to the local mean free path, it is unlikely that enough collisions are experienced for the gas to reach equilibrium at the new conditions. Bird [14] was one of the first to examine the validity of such a parameter using DSMC. He did so in the context of nonequilibrium resulting from expansions of the gas. In doing so, he suggested the following parameter as a means of quantifying equilibrium breakdown.

$$P = \frac{1}{\nu} \left| \frac{D(\ln \rho)}{Dt} \right| \quad (3)$$

where ρ is the density of the gas and ν the viscosity. In the case of one-dimensional steady flow, this becomes

$$P = \frac{u}{\rho v} \left| \frac{d\rho}{dx} \right| = M \sqrt{\frac{\pi \gamma}{8}} \lambda \left| \frac{d\rho}{dx} \right| \quad (4)$$

where u is the bulk gas velocity and M is the Mach number in the gas. Bird found that a value of P greater than 0.02 tended to predict the onset of nonequilibrium well.

Although this parameter seems to indicate continuum breakdown well in the specific case of gaseous expansions, it does not predict nonequilibrium well in regions of low velocity. As seen in the above equation, the Mach number dependence will drive P to zero in regions of low velocity no matter what the degree of

nonequilibrium. Improvements were made based upon a gradient local length by Boyd et al. [15] further refined by Wang et al. [16]. Unfortunately, although such parameters are relatively easy to compute, they do not necessarily have a firm theoretical grounding. They could be understood qualitatively that many forms of nonequilibrium are invoked by the presence of strong gradients in the macroscopic flow variables. Such parameters are similar to our limited understanding of a Knudsen number restriction on the continuum equations. However, given that multiple parameters need to be computed suggests that the continuum breakdown criterion is problem dependent at this stage of development.

Thermal nonequilibrium among the internal modes of motion of the molecular species in supersonic and hypersonic flows has major influences on flowfield temperatures, radiation signatures, and aerodynamic heating. Prediction of such flowfields by computer modeling techniques requires a detailed knowledge of the rates and mechanism of energy storage and transfer among the internal modes of molecular motion. Among the large body of literature, we mention a few: Anderson [2], Capitelli [17], Chernyi et al. [18, 19], Rich et al. [20], and Adamovich et al. [21]. The various modes of motion for diatomic gas molecules which are of interest in aerothermodynamics are translation, rotation, vibration, electronic, and the mutual interaction of these modes. In addition, molecules can dissociate and ionize. The relative magnitude of the relaxation times may be stated as follows:

$$\tau_0 \approx \tau_T < \tau_R \ll \tau_V < \tau_d \quad (5)$$

where τ_0 is the mean collision time and τ_T , τ_R , τ_V , and τ_d are, respectively, the relaxation times for translational, rotational, vibrational energy modes, and dissociation. For our purposes of engineering interest, translational motion can be described by classical mechanics. However, to quantify the degree of nonequilibrium in the internal energy modes one would have to consider the internal energy modes of rotation, vibration, and electronic excitation, all of which are quantized. When the gas is in a state of thermal equilibrium, the distribution of internal energy among the various modes is said to be governed by a Maxwell-Boltzmann distribution.

Another parameter of interest in reacting flows is the Damköhler number (Da). The Da is a dimensionless number to relate the reaction timescale (reaction rate) to the transport phenomena rate occurring in a system. The use of Da has been found in both numerical algorithm development of the nonequilibrium reacting flow systems as well as in the understanding the physics of nonequilibrium flow systems. The role of Da in CFD algorithm development by Eppard and Godfrey [22] related to dissipation is described by Pandolfi et al. [23] In a strongly coupled system of continuum flow equations with the chemical equations, the temperature values are highly sensitive to variations in species concentration (owing to the high formation energies). This sensitivity feeds back in the fluid transport, the Da representing the stiffness of this coupling. High values of Da denote flows close to local equilibrium and low values refer to

near frozen conditions. In both of the extreme cases, there is no dissipation related to the chemical effects. In the intermediate range of the Da, we expect a typical nonequilibrium phenomenon and the occurring of the related dissipation. Its role as a scaling parameter in nonequilibrium flows is presented by Inger [24] and for blunt body shock standoff distance predictions in Reference [25].

In delineating the role of thermal nonequilibrium for aeroheating in the continuum flight regime, the study of chemical kinetics involves examining the vibrational relaxation process in a reacting gas. The state-to-state (STS) kinetic models of vibrational relaxation give the state specific mass concentrations and mean vibrational energy of molecules as a function of time for chemically reacting gas. The primary assumption of these models is that the characteristic time of vibrational relaxation is much greater than the translational and rotational relaxation, but is comparable with the characteristic time of chemical reaction. In the upper levels of the vibrational manifold, the vibrational-translational (VT) processes dominate the energy transfer. The reactive process of dissociation has an activation energy typically more than an order of magnitude greater than the energy associated with the VT exchange. The non-reactive and reactive processes have contrasting effects on the state of nonequilibrium. Non-reactive kinetic processes tend to bring about an equilibrium distribution in the vibrational manifold, whereas the dissociation process perturbs it [26]. Figure 1 shows a schematic of various energy transfer mechanisms used to describe thermochemical nonequilibrium.

The semiclassical approach to diatom-diatom and atom-diatom collision problem gives a fast and reliable calculation of a large number of rate constants if the potential energy surface is provided. Using this calculation approach, Billing [27–29] advanced the theory to calculate the STS rates of single-quantum vibration-vibration (V-V) and vibration-translation (V-T) transfers for nitrogen collisions. Capitelli et al. consider single quantum transitions and empirically

determine the VT rates from semiclassical calculations verified by experiments [30, 31]. The forced harmonic oscillator (FHO) theory, an approximation of Billing's method, was adopted by Macheret and Adamovich [32] for developing a theory of dissociation of diatomic molecules based on the anharmonicity-corrected and energy-symmetrized FHO quantum scaling [33] in conjunction with free-rotation or impulsive energy-transfer

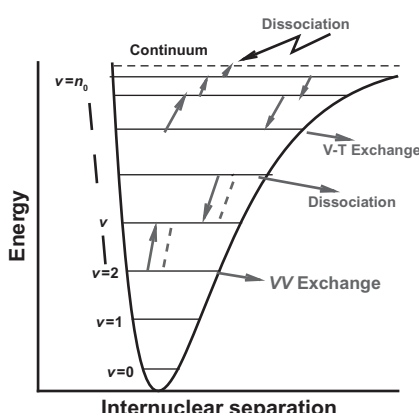


Fig. 1 Schematic diagram showing various rates processes in the vibrational states.

models. The model predicts state specific dissociation rates for N₂-N₂ collisions by accounting for molecular rotation and three-dimensional collisions and is computationally tractable without any adjustable parameters. The FHO model was used in modeling STS kinetic vibrational relaxation by Boyd and Josyula [34] and dissociation in hypersonic flows by Josyula et al. [35]. More recently, a first principles approach was attempted by Galina et al. [36] for the N-N₂ collisions for calculating STS dissociation rate constants with the ultimate goal of assessing heating rates on hypersonic vehicles.

Other recent studies address some of the deficiencies in the current semiempirical approaches and suggest improvements. Da Silva et al. [37] constructed a database of kinetic rates for nitrogen for high temperatures (up to 100,000 K) nonequilibrium dissociation processes for use in flowfield simulations of vehicles at atmospheric entries. This modification to the FHO model consists of energies of 59 bound vibrational levels of the nitrogen molecule, an increase from the earlier work (see for example Reference [32]) of 48 vibrational quantum levels for dissociation. The work of Shui et al. [38] demonstrates the contribution of the N₂A³Σ metastable electronic state, which were used in modeling of the nonequilibrium distributions in hypersonic flows past solid bodies by Armenise et al. [39] and in a nozzle flow by Colonna and Capitelli [40]. Reduced-order models from state kinetic rates were presented by different researchers [41–45] and the efforts ongoing. Attempts at applying the kinetic rates are presented by Armenise et al. [46] who use the quasiclassical molecular dynamic calculations (QCT) of vibrationally and rotationally state selected dissociation cross-sections for nitrogen atom-molecule collisions and used them to evaluate dissociation-recombination kinetics in hypersonic boundary layer flows. Recently the quasiclassical trajectory calculations by Esposito and Capitelli [47] report complete set of V-T rates in the temperature range of 500 K–4000 K for the N₂(v) + N → N₂(v') + N. The work by Armenise et al. [48, 49] models the kinetic processes and heterogenous surface processes in the boundary layer of reentry vehicles and demonstrate the highly nonequilibrium vibrational distributions and the non-Arrhenius behavior of dissociation constants. Armenise et al. [48] demonstrated the recombination assisted dissociation process resulting in non-Arrhenius behavior of the dissociation constant affecting the surface heat transfer. However, the validity of these rates depends on the availability of experimental data and/or ab initio rates. The computational chemistry approach to determining the ab initio rates is the subject of Chapter 3 of this volume.

Thermal radiation has an effect on surface heat transfer and temperature distribution on a solid surface immersed in a high-temperature flows where there is a strong coupling between physicochemical and radiative mechanisms. To accurately account for the nonequilibrium behavior of such flows, rigorous kinetic-theory-based formalisms may be used, that account for a combined treatment of absorption/emission/scattering of photons along with translational and internal energy exchanges among molecules including rotational/vibrational relaxation, exchange reactions, dissociation, and recombination. In particular,

the kinetic equation describing the evolution of the distribution function of molecules, also known as material particles is coupled to the kinetic equation for evolution of photons via the underlying collision operators. In many flows, it has been found that the characteristic time scales associated with emission/absorption of photons is comparable with those associated with vibrational/electronic/chemical energy transfer and macroscopic flow time scale, whereas the characteristic timescales for translation and rotation are significantly smaller in comparison. This separation of timescales allows for treatment of slow and fast processes (where the fast processes are assumed to have reached a state of equilibrium) for use in asymptotic analysis (e.g. using the Chapman–Enskog method) and in the derivation of macroscopic fluid transport equations [50, 51]. Radiation as a nonequilibrium process in hypersonic flows is the subject of Chapter 4 of this volume.

Detailed computational predictions of such nonequilibrium effects in gas transport are possible, in principle, by solution of the underlying Wang–Chang–Uhlenbeck (WCU) equation that accounts for STS kinetics. However, the information on the distribution functions may not be necessary in the continuum flight regimes, and simplified set of continuum governing equations suffice. Hence the detailed simulations based on the WCU equation can serve as benchmark solutions for developing accurate reduced-order models for routine CFD use in aerospace vehicle design. A detailed treatment of the fundamental nonequilibrium gas transport equations can be found in the work of Ferziger and Kaper [52]. Further extensions in deriving transport coefficients with state kinetic dependence in the nonequilibrium processes are given by Nagnibeda and Kustova [53], Kustova [54], and Chikhaoui et al. [55]. The basic governing equations in the flight regime of the aero-assisted orbital transfer vehicles with reduced-order models using simplified approximations of the nonequilibrium energy transfer processes were given by Lee [50] and for weakly ionized hypersonic flows by Josyula and Bailey [56]. The conservation equations for a nonequilibrium plasma by Appleton and Bray [57], and plasma chemical physics by Capitelli and co-workers [58]. A collection of articles on the physical and chemical phenomena relating to the high temperature phenomena in shock waves are presented by Brun [59].

A hierarchy of equations suitable for gases with thermochemical nonequilibrium with extensions to radiation and weakly ionized gas is presented in this chapter, cast into a working set of equations. Sample solutions are presented for different levels of approximations. The hierarchical structure of the gas transport equations is shown starting in Sec. II with the generalized Boltzmann equation and the Chapman–Enskog expansion for deriving the macroscopic Euler/Navier–Stokes equations with the associated transport coefficients. Section III presents the coupling of the macroscopic transport equations to the master equation with extensions to multiquantum transitions. Owing to the practical limitation of solving the generalized Boltzmann equation and the state kinetic formulations for engineering applications, a simplified set of energy exchange models coupled to

the macroscopic nonequilibrium transport equations are presented in Sec. IV that form the basis of today's hypersonic CFD solvers.

II. KINETIC THEORY: THE BOLTZMANN EQUATION

The Boltzmann equation expresses the behavior of many-particle kinetic system in terms of the evolution equation for the single particle gas distribution function. The Boltzmann equation is written as

$$\frac{\partial f}{\partial t} + \xi \frac{\partial f}{\partial \mathbf{x}} = I(\xi) \quad (6)$$

where f , the distribution function, gives the number density at position \mathbf{x} and velocity ξ at time t . The left-hand side of the above equation represents the free streaming of molecules in space, and the right side denotes the collision term, which can be expressed as

$$I(\xi) = \int [f(\xi')f^*(\xi'^*) - f(\xi)f^*(\xi^*)] \mathcal{B}(\xi, \xi^*, \Omega) d\Omega d\xi^* \quad (7)$$

where the primes denote post-collision quantities, \mathcal{B} denotes the collision kernel and Ω denotes a vector on the unit sphere S^2 . If the distribution function f is known, macroscopic variables of the mass, momentum, energy and stress can be obtained by integration.

A. SEMI-CLASSICAL DESCRIPTION: THE GENERALIZED BOLTZMANN EQUATION

In this section, we provide a semi-classical description of kinetic-theory-based on the generalized Boltzmann equation, specifically the WCU equation [60, 61]. In the molecular description of a gas, the kinetic theory is based on the hypothesis that the gas is composed of molecules. Translational energy is treated classically and the internal energy quantized.

Consider a multispecies gas-mixture, where the distribution function characterizing an internal state i , corresponding to species α (at the quantized energy level i) is represented as: $f_i^\alpha \equiv f_i^\alpha(\mathbf{x}, \xi, t)$, where \mathbf{x} , ξ , and t denote the physical (position) space, (microscopic) velocity space and time variables, respectively. The particle velocity, spatial location, and the time evolution are given by ξ , \mathbf{x} , and t , respectively. Similar to the monoatomic Boltzmann equation, the moments of f_i^α in the WCU equation yield the macroscopic thermo-fluid quantities of interest. In addition to the usual definitions of density, flow velocity, and pressure tensor, when forming moments for integrating, we now sum over the internal states. The various dynamic modes of diatomic gas molecules which are of interest in aerothermodynamics are translation, rotation, vibration, and electronic. In addition, we assume that molecules can dissociate and ionize. For our purposes of engineering interest, translational motion is described by

classical mechanics, but the internal energy modes are quantized. When the gas is in a state of thermal equilibrium, the distribution of internal energy among the various modes is governed by a Maxwell–Boltzmann distribution, which can be written as the fractional number of molecules n_i/N in the i th internal energy state as [62]:

$$\frac{n_i}{N} = \frac{g_i}{Q_{\text{int}}} \exp\left(-\frac{E_{i,\text{int}}}{kT}\right) \quad (8)$$

where the internal partition function Q_{int} is given by

$$Q_{\text{int}} = \sum_i g_i \exp\left(-\frac{E_{i,\text{int}}}{kT}\right) \quad (9)$$

where $N = \sum_i n_i$ is the total number of molecules and g_i is the statistical weight of the i th internal energy state, k is the Boltzmann constant, and T is the kinetic temperature of the gas.

The distribution function, f_i^α , can be used to obtain the macroscopic density ρ_α , macroscopic velocity \mathbf{v}_α and macroscopic energy E_α of any given species α , as

$$\rho_\alpha = \sum_i \int m_\alpha f_i^\alpha(\boldsymbol{\xi}) d\boldsymbol{\xi} \quad (10)$$

$$\rho_\alpha \mathbf{v}_\alpha = \sum_i \int m_\alpha \boldsymbol{\xi} f_i^\alpha(\boldsymbol{\xi}) d\boldsymbol{\xi} \quad (11)$$

$$\rho_\alpha E_\alpha = \sum_i \int m_\alpha \left(\epsilon_i^\alpha + \frac{1}{2} \|\boldsymbol{\xi}\|^2 \right) f_i^\alpha(\boldsymbol{\xi}) d\boldsymbol{\xi} \quad (12)$$

where $m_\alpha \epsilon_i^\alpha$ corresponds to the energy associated with the i th quantized energy level for species α and m_α is the molecular (or atomic) mass of species α . The macroscopic properties of the underlying mixture can be obtained via a summation of each of the above equations over index α . The evolution of the underlying distribution function for a gas mixture is given by the WCU equation, expressed as,

$$\partial_t f_i^\alpha + \boldsymbol{\xi} \cdot \partial_{\mathbf{x}} f_i^\alpha + \mathbf{F}_i^\alpha \cdot \partial_{\boldsymbol{\xi}} f_i^\alpha = \sum_{j,k,l,\alpha^*} Q_{(i,j) \rightarrow (k,l)}^{\alpha,\alpha^*} + J_v^{\text{rad}} \quad (13)$$

where the collision operator $Q_{(i,j) \rightarrow (k,l)}^{\alpha,\alpha^*}$ is given by

$$Q_{(i,j) \rightarrow (k,l)}^{\alpha,\alpha^*} = \int \left[\frac{q_i^\alpha q_j^{\alpha^*}}{q_k^\alpha q_l^{\alpha^*}} f_i^\alpha(\boldsymbol{\xi}') f_j^{\alpha^*}(\boldsymbol{\xi}'') - f_i^\alpha(\boldsymbol{\xi}) f_j^{\alpha^*}(\boldsymbol{\xi}'') \right] \mathcal{B}_{(i,j) \rightarrow (k,l)}^{\alpha,\alpha^*}(\boldsymbol{\xi}, \boldsymbol{\xi}^*, \Omega) d\Omega d\boldsymbol{\xi}'' \quad (14)$$

where F_i^α represents the external force per unit mass. As an example of a successful method, the collision integral can be evaluated on a uniform grid

following the method of Tcheremissine [7]. In the above equation, the degeneracy associated by the i th quantum energy level for species α is denoted with q_i^α and primed quantities represent the post-collision physical quantities. Ω is a vector on the unit sphere S^2 . Considering information on quantized vibrational energy levels v , rotational energy levels r and electronic states s (for each species α), we can associate the index i with the triplet (v, r, s) , as $i \equiv (v, r, s)$ and the evolution of the underlying distribution functions f_i^α can be obtained based on the above equation (Eq. (14)). Expression for J_v^{rad} are given in Kustova and co-workers [63, 64]. The evolution of this distribution function, F_i^α , involving material particles is coupled to the evolution of the distribution function for photons $f_v(\mathbf{x}, \mathbf{p}, t)$ (where \mathbf{p} denotes the momentum coordinate) as

$$\partial_t f_v + c \boldsymbol{\Omega}_v \cdot \partial_{\mathbf{x}} f_v = J_v \quad (15)$$

where $\boldsymbol{\Omega}_v$ denotes the direction of photon propagation, c denotes the speed of light, and v is the frequency. Note that the term, J_v^{rad} , appearing in Eq. (13) depends on the distribution function, F_i^α , of material particles and the evolution of the distribution function of photons, f_v is given in Eq. (15). This formulation not only allows for elastic and inelastic collisions—including rotation–translation, vibration–translation, vibration–vibration, and vibraton–electonic energy exchanges, chemical exchange reactions and dissociation–recombination—but also accounts for radiative transitions corresponding to absorption and induced emission processes and spontaneous emission.

The conservation equations for momentum and total energy at the microscopic level, neglecting the effects of radiation, are given by

$$m_\alpha \boldsymbol{\xi} + m_{\alpha^*} \boldsymbol{\xi}^* = m_\alpha \boldsymbol{\xi}' + m_{\alpha^*} \boldsymbol{\xi}'^* \quad (16)$$

and

$$\begin{aligned} \frac{1}{2} m_\alpha \|\boldsymbol{\xi}\|^2 + m_\alpha \boldsymbol{\epsilon}_i^\alpha + \frac{1}{2} m_{\alpha^*} \|\boldsymbol{\xi}^*\|^2 + m_{\alpha^*} \boldsymbol{\epsilon}_j^{\alpha^*} \\ = \frac{1}{2} m_\alpha \|\boldsymbol{\xi}'\|^2 + m_\alpha \boldsymbol{\epsilon}_k^\alpha + \frac{1}{2} m_{\alpha^*} \|\boldsymbol{\xi}'^*\|^2 + m_{\alpha^*} \boldsymbol{\epsilon}_l^{\alpha^*} \end{aligned} \quad (17)$$

and can be used to relate the pre-collision and post-collision velocities through the following relation:

$$\boldsymbol{\xi}' = \boldsymbol{\xi}_{\text{cm}} + \Omega \frac{\sqrt{2} \mu_{\alpha, \alpha^*}}{m_\alpha} \sqrt{\frac{1}{2} \|\boldsymbol{\xi}_{\text{rel}}\|^2 + \Delta \boldsymbol{\epsilon}_{(i,j) \rightarrow (k,l)}^{\alpha, \alpha^*}} \quad (18)$$

$$\boldsymbol{\xi}'^* = \boldsymbol{\xi}_{\text{cm}} - \Omega \frac{\sqrt{2} \mu_{\alpha, \alpha^*}}{m_{\alpha^*}} \sqrt{\frac{1}{2} \|\boldsymbol{\xi}_{\text{rel}}\|^2 + \Delta \boldsymbol{\epsilon}_{(i,j) \rightarrow (k,l)}^{\alpha, \alpha^*}} \quad (19)$$

where the center of mass velocity ξ_{cm} vector and the relative velocity ξ_{rel} vector are given by

$$\xi_{\text{cm}} = \frac{m_\alpha \xi + m_{\alpha^*} \xi^*}{m_\alpha + m_{\alpha^*}} \quad (20)$$

$$\xi_{\text{rel}} = \xi - \xi^* \quad (21)$$

and the reduced mass given by, $\mu_{\alpha,\alpha^*} = m_\alpha m_{\alpha^*} / (m_\alpha + m_{\alpha^*})$. Note that the term accounting for the change of internal energy during a transition is given by

$$\Delta \epsilon_{(i,j) \rightarrow (k,l)}^{\alpha,\alpha^*} = \frac{m_\alpha}{\mu_{\alpha,\alpha^*}} (\epsilon_i^\alpha - \epsilon_k^\alpha) + \frac{m_{\alpha^*}}{\mu_{\alpha,\alpha^*}} (\epsilon_j^{\alpha^*} - \epsilon_l^{\alpha^*}) \quad (22)$$

The collision kernel is given by the following positive function:

$$\mathcal{B}_{(i,j) \rightarrow (k,l)}^{\alpha,\alpha^*} = \|\xi - \xi^*\| \sigma_{(i,j) \rightarrow (k,l)}^{\alpha,\alpha^*}(\xi, \xi^*, \Omega), \quad (23)$$

where the microscopic cross-section $\sigma_{(i,j) \rightarrow (k,l)}^{\alpha,\alpha^*}$ of the collision $(\xi, i), (\xi^*, j) \rightarrow (\xi', k), (\xi', l)$ satisfies the following detailed balance relation obtained from Fermi's golden rule:

$$\begin{aligned} q_i^\alpha q_j^{\alpha^*} \sigma_{(i,j) \rightarrow (k,l)}^{\alpha,\alpha^*}(\xi, \xi^*, \Omega) \|\xi - \xi^*\| d\xi d\xi^* d\Omega \\ = q_k^\alpha q_l^{\alpha^*} \sigma_{(k,l) \rightarrow (i,j)}^{\alpha,\alpha^*}(\xi', \xi^{*\prime}, \Omega') \|\xi' - \xi^{*\prime}\| d\xi' d\xi^{*\prime} d\Omega' \end{aligned} \quad (24)$$

In the above, the microscopic cross-section $\sigma_{(i,j) \rightarrow (k,l)}^{\alpha,\alpha^*}$ of the collision needs to be obtained for the specific (state transition or reaction) system under consideration. To illustrate a model of cross-sections that satisfy the above relation, we mention the model proposed by Anderson et al. [65], as

$$\sigma_{(i,j) \rightarrow (k,l)}^{\alpha,\alpha^*}(\xi, \xi^*, \Omega) = \sigma_0^{\alpha,\alpha^*} p_{(i,j) \rightarrow (k,l)}^{\alpha,\alpha^*}(\xi, \xi^*) \quad (25)$$

where atoms are globally considered as hard spheres with cross-section $\sigma_0^{\alpha,\alpha^*} \equiv \pi(r_\alpha + r_{\alpha^*})^2$. The conditional transition probability from the quantum state $(i, j) \rightarrow (k, l)$ for species α and α^* as a function of microscopic velocities ξ and ξ^* is given by

$$p_{(i,j) \rightarrow (k,l)}^{\alpha,\alpha^*}(\xi, \xi^*) = \frac{q_k^\alpha q_l^{\alpha^*} \left(\frac{1}{2} \|\xi_{\text{rel}}\|^2 + \Delta \epsilon_{(i,j) \rightarrow (k,l)}^{\alpha,\alpha^*} \right)}{\sum_{\oplus m,n} q_m^\alpha q_n^{\alpha^*} \left(\frac{1}{2} \|\xi_{\text{rel}}\|^2 + \Delta \epsilon_{(i,j) \rightarrow (m,n)}^{\alpha,\alpha^*} \right)} \quad (26)$$

where the symbol \oplus in the denominator denotes summation over terms that are positive. The forbidden transitions, i.e. $p_{(i,j) \rightarrow (k,l)}^{\alpha,\alpha^*}(\xi, \xi^*) = 0$, corresponds to the case when $\frac{1}{2} \|\xi_{\text{rel}}\|^2 + \Delta \epsilon_{(i,j) \rightarrow (k,l)}^{\alpha,\alpha^*} \leq 0$. In the Eq. (26), the degenerate states are considered to be individual states.

Direct numerical solution of the WCU equation for aerospace applications can be obtained in principle using direct integration solvers, as shown for the above formulation in the work of Josyula et al. [9]. However, the high computational cost and the availability of realistic collision cross-sections have hindered the progress. Hence, whenever possible we seek approximate solutions of the WCU equation that can accurately predict macroscopic behavior in selected flow regimes (e.g. when Knudsen number is not a small parameter) at a significantly lower computational cost. Macroscopic behavior can be obtained for instance using the Chapman–Enskog approach, in which the true distribution is represented in terms of an equilibrium and a disturbance about the equilibrium. As discussed earlier, traditional continuum gas dynamics models tend to break down owing to gradient transport assumptions for diffusion terms in continuum equations of mass, momentum, and energy conservation and thus the transport coefficients dependent on the STS kinetics is necessary for flows that are in translational equilibrium but their internal energies are in thermochemical nonequilibrium. Sample solutions of the Boltzmann equation are presented next.

B. NUMERICAL SOLUTIONS

Figure 2 shows a qualitative comparison of the distribution function, $f(x, \xi_1, \xi_2)$ of the Tcheremissine's method [7] of solving the Boltzmann equation for a Mach 3 shock wave. (See the work of Josyula et al. [66] for additional details). The Mach 3 shock thickness is approximately fifteen mean free paths. The Mach number reduces from the upstream to downstream across the shock by a factor of 5.74. One can see from the figure that there are relatively small deviations from the asymptotic distribution in the upstream and downstream locations Figs. 2a and 2d. For the locations inside the shock front, Figs. 2b and 2c, reduction of the mean velocity and the shock heating lead to non-Maxwellian distributions. Figure 3 shows variations of macroscopic variables of velocity, density, temperature, xx-component of viscous stress, and the streamwise component of the heat flux along the shock wave structure.

The distribution function for the flow with two levels of internal energy states is shown in Fig. 4. See the work of Josyula et al. [9] for more details. Downstream from the middle of the shock wave at $X/\lambda = 0.8$, Fig. 4, one can see a bimodal distribution with two distinct peaks for the elastic collisions (Fig. 4a), whereas the velocity distribution function (VDF) in ground state shows a bimodal distribution with one peak more prominent than the other (Fig. 4b) and the VDF in the first excited state shows a distribution (Fig. 4c) closer to that of the elastic cross-section. It is noted that for the Mach 5 shock wave, the VDF of the first excited state is similar to that of the elastic only case and the VDF in the ground state appears to be more non-Maxwellian than in the first excited state.

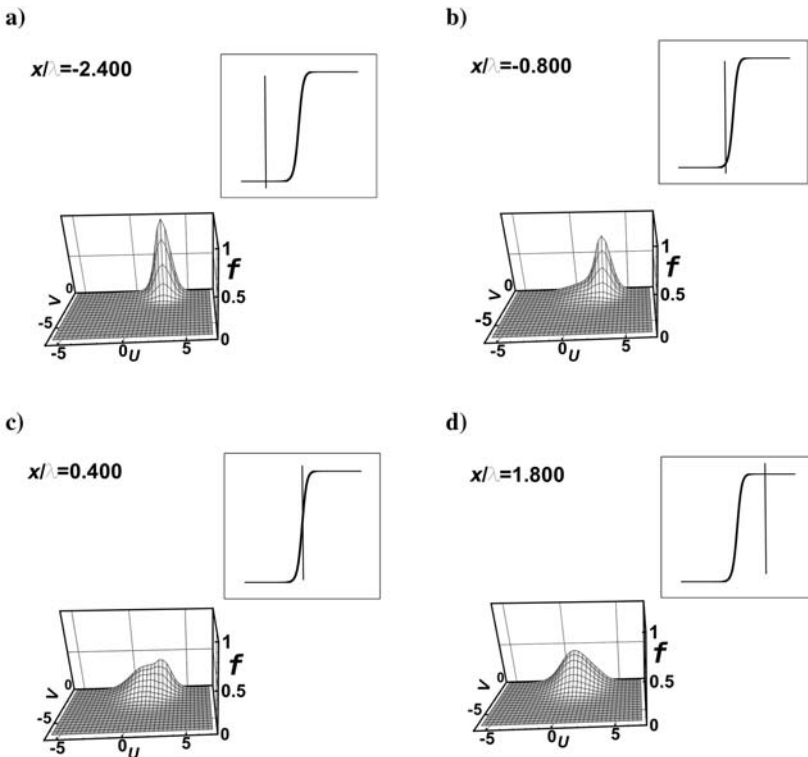


Fig. 2 Distribution function in Mach 3 shock wave with hard sphere collision model:
a) $x/\lambda = -2.4$, b) $x/\lambda = -0.8$, c) $x/\lambda = 0.4$, d) $x/\lambda = 1.8$.

Figure 5 shows the comparisons of macroscopic variables for the Mach 5 shock wave for a case with elastic collisions (only) with a case of elastic plus inelastic collisions for a two-level internal energy system of energy gap of 2. From the density variation, Fig. 5a, one can see that the inelastic collisions contribute to a faster equilibration to a different equilibrium state at the downstream. The T_x , T_y components in Figs. 5b and 5c show an earlier temperature rise due to inelastic collisions and a lower temperature beyond the middle of the shock wave.

C. DERIVATION OF MACROSCOPIC TRANSPORT EQUATIONS USING CHAPMAN-ENSKOG APPROACH

The Chapman-Enskog expansion [67] is referred to in this chapter for its use in the derivation of the Navier-Stokes equation and its transport coefficients from

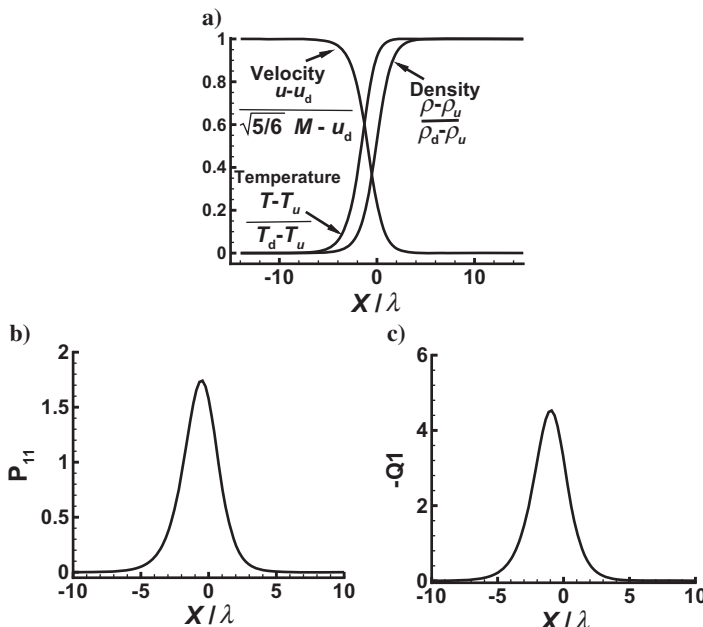


Fig. 3 Macroscopic parameters for a Mach 3 shock wave with hard sphere collision model:
a) u -velocity, b) viscous stress xx -component, c) heat flux x -component.

the Boltzmann equation. To illustrate the derivation of macroscopic transport equations based on the Chapman–Enskog approach, we consider a multispecies, reacting gas mixture, whose underlying distribution functions corresponding to each species c , quantized vibrational energy level i and (quantized) rotational energy level j are represented as $f_{cij}(\mathbf{x}, \mathbf{u}_c, t)$, where \mathbf{x} , \mathbf{u}_c and t denote the spatial coordinate, (microscopic) velocity and time instance, respectively. In this section we ignore the effects of excited electronic states and radiation. The evolution of these distribution functions, based on kinetic theory, can be expressed as [52, 54, 55, 68, 69]

$$\partial_t f_{cij} + \mathbf{u}_c \cdot \partial_{\mathbf{x}} f_{cij} = J_{cij} \quad (27)$$

where J_{cij} denotes the full collision operator that accounts for interactions not only owing to elastic collisions but also due to rotational and vibrational energy exchanges and chemical reactions. Although each of these mechanisms can be associated with a characteristic time scale, it was found from experimental data under typical reentry conditions that there exists a separation of time scales according to the relation $\tau_{\text{el}} < \tau_{\text{rot}} \ll \tau_{\text{vib}} < \tau_{\text{react}} \sim \theta$, where, τ_{vib} , τ_{react} and θ correspond to mean times characterizing collisions resulting in translational,

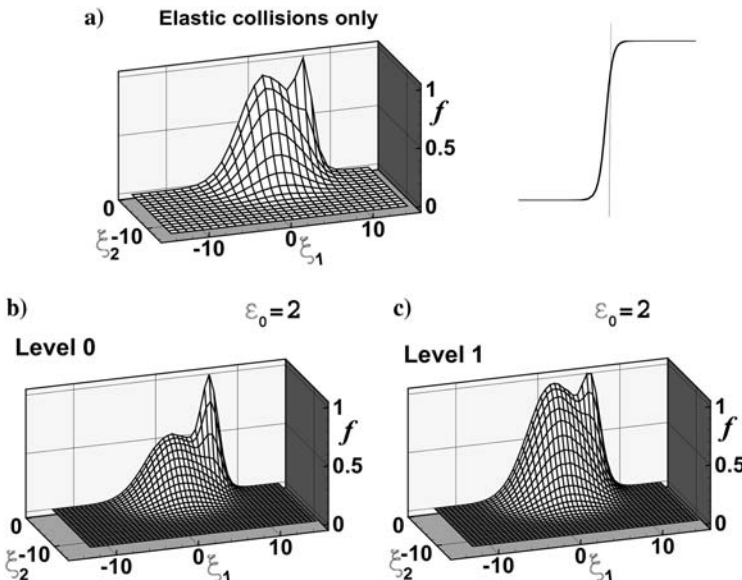


Fig. 4 Velocity distribution functions (VDFs) for Mach 5 shock wave structure: solutions of Boltzmann equation (elastic collisions only) and WCU equation (elastic plus inelastic collisions with two-level internal energy modes, $X/\lambda = 0.8$. Each VDF normalized to 1: a) elastic collisions only, b) elastic plus inelastic collisions, energy gap, $\epsilon_0 = 2$, ground state distribution, c) elastic plus inelastic collisions, energy gap, $\epsilon_0 = 2$, first excited state distribution.

rotational, vibrational energy transfer, chemical reactions, and macroscopic time scale, respectively. In other words, as translational and rotational energy modes tend to equilibrate much faster in comparison with other modes, the collision operator on the right-hand side of Eq. (27) can be expressed as $J_{cij} = \frac{1}{\epsilon} J_{cij}^{\text{rapid}} + J_{cij}^{\text{slow}}$, where $J_{cij}^{\text{rapid}} \equiv J_{cij}^{\text{el}} + J_{cij}^{\text{rot}}$ and $J_{cij}^{\text{slow}} \equiv J_{cij}^{\text{vib}} + J_{cij}^{\text{react}}$ correspond to collision operators of rapid and slow processes and ϵ is a small parameter denoting the ratio of timescales of fast and slow (collisional) processes. Note that the collision operators J_{cij}^{el} , J_{cij}^{rot} , J_{cij}^{vib} , and J_{cij}^{react} correspond to elastic collisions, rotational energy exchanges, vibrational energy exchanges and chemical reactions, respectively. While a direct solution of Eq. (27) can be very computationally expensive, the generalized Chapman-Enskog method can be used to obtain approximate solutions. In this approach, the distribution functions f_{cij} are expressed in a power series involving the (small) parameter ϵ . The zeroth-order solution $f_{cij}^{(0)}$ satisfies the relation $J_{cij}^{\text{el}}(f_{cij}^{(0)}, f_{cij}^{(0)}) + J_{cij}^{\text{rot}}(f_{cij}^{(0)}, f_{cij}^{(0)}) = 0$. Consideration of collision invariants leads to the following form for the

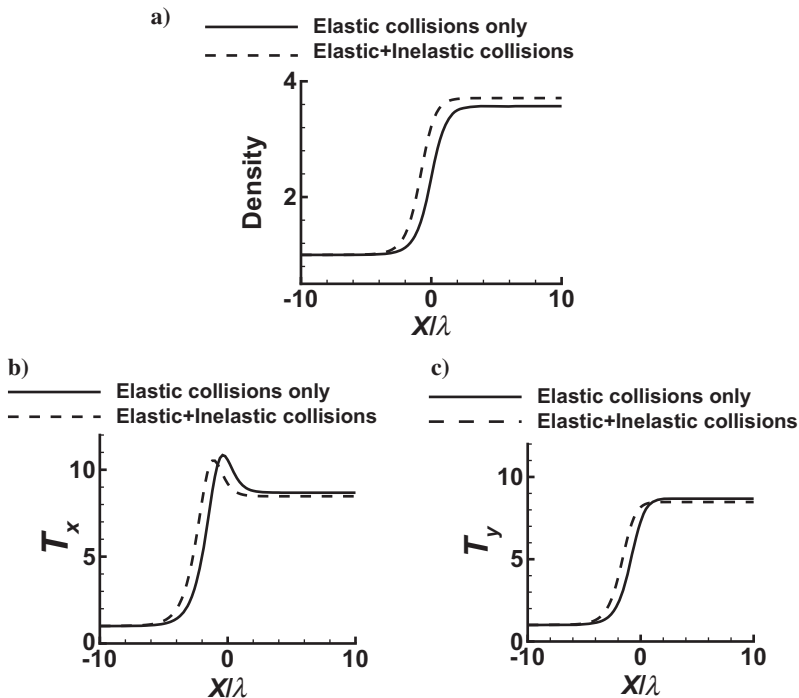


Fig. 5 Comparison of macroscopic variables in Mach 5 shock wave structure for solutions of Boltzmann equation (elastic collisions only) and WCU equation (elastic plus inelastic collisions) with two-level internal energy modes with energy gap, $\epsilon_0 = 2$: a) density, b) parallel component of temperatures, T_x , c) perpendicular component of temperature, T_y .

zeroth-order distribution function:

$$f_{cij}^{(0)} = \left(\frac{m_c}{2\pi kT} \right)^{3/2} s_j^{ci} \frac{n_{ci}}{Z_{ci}^{\text{rot}}(T)} \exp \left(-\frac{m_c c_c^2}{2kT} - \frac{\epsilon_j^{ci}}{kT} \right) \quad (28)$$

where n_{ci} is the number density of molecules of species c with molecular mass m_c in vibrational level i , s_j^{ci} denotes the statistical weight, k is the Boltzmann constant, T is the temperature, $\mathbf{c}_c \equiv \mathbf{u}_c - \mathbf{v}$ is the peculiar velocity, \mathbf{v} is the macroscopic gas velocity and Z_{ci}^{rot} is the rotational partition function. The macroscopic parameters $n_{ci}(x, t)$, $\mathbf{v}(x, t)$ and $T(x, t)$ are defined in terms of the distribution function and satisfy the following relations:

$$n_{ci} = \sum_j \int f_{cij} \, d\mathbf{u}_c = \sum_j \int f_{cij}^{(0)} \, d\mathbf{u}_c \quad (29)$$

$$\rho \mathbf{v} = \sum_{cij} m_c \int \mathbf{u}_c f_{cij} d\mathbf{u}_c = \sum_{cij} m_c \int \mathbf{u}_c f_{cij}^{(0)} d\mathbf{u}_c \quad (30)$$

$$\rho U = \sum_{cij} \int \left(\frac{1}{2} m_c c_c^2 + \epsilon_i^c + \epsilon_j^{ci} + \epsilon^c \right) f_{cij} d\mathbf{u}_c \quad (31)$$

$$= \sum_{cij} \int \left(\frac{1}{2} m_c c_c^2 + \epsilon_i^c + \epsilon_j^{ci} + \epsilon^c \right) f_{cij}^{(0)} d\mathbf{u}_c \quad (32)$$

Note that U denotes the total internal energy per unit mass defined such that $\rho U \equiv \frac{3}{2} nkT + \rho E_r + \rho E_v + \rho E_f$. For each species c and vibrational level i , the corresponding (mass) density is defined as $\rho_{ci} = m_c n_{ci}$, the vibrational energy of the molecule is given by ϵ_i^c (based on reference minimum of its potential curve, $\epsilon^c = -D_c$, where D_c is the energy of dissociation of the molecular species c). The components of total energy per unit volume due to rotation, vibration and dissociation are given by $\rho E_r = \sum_{cij} \int \epsilon_j^{ci} f_{cij} d\mathbf{u}_c$, $\rho E_v = \sum_{ci} \epsilon_i^c n_{ci}$, and $\rho E_f = \sum_c \epsilon^c n_c$, respectively. Also note that the number density of species c is given by $n_c = \sum_i n_{ci}$, the total number of particles is given by $n = \sum_{ci} n_{ci}$ and the density of the gas mixture is given by $\rho = \sum_c m_c \sum_i n_{ci}$.

Based on Eqs. (27–32), macroscopic equations governing the evolution of $n_{ci}(\mathbf{x}, t)$, $\mathbf{v}(\mathbf{x}, t)$, and $T(\mathbf{x}, t)$ for a multicomponent reacting gas mixture in vibrational and chemical nonequilibrium can be obtained as

$$\frac{dn_{ci}}{dt} + n_{ci} \nabla \cdot \mathbf{v} + \nabla \cdot (n_{ci} \mathbf{V}_{ci}) = R_{ci} \quad (33)$$

$$\rho \frac{d\mathbf{v}}{dt} + \nabla \cdot \mathbf{P} = 0 \quad (34)$$

$$\rho \frac{dU}{dt} + \nabla \cdot \mathbf{q} + \mathbf{P} : \nabla \mathbf{v} = 0 \quad (35)$$

where the production terms are given by $R_{ci} \equiv \sum_j J_{cij}^{\text{slow}} d\mathbf{u}_c$, the diffusion velocity of \mathbf{V}_{ci} of the chemical species c at vibrational level i is given by $n_{ci} \mathbf{V}_{ci} \equiv \sum_j \int \mathbf{c}_c f_{cij} d\mathbf{u}_c$, the pressure tensor is given by $\mathbf{P} \equiv \sum_{cij} \int m_c \mathbf{c}_c \mathbf{c}_c f_{cij} d\mathbf{u}_c$ and the heat flux vector is given by $\mathbf{q} \equiv \sum_{cij} \int (m_c c_c^2 / 2 + \epsilon_j^{ci} + \epsilon_i^c + \epsilon^c) \mathbf{c}_c f_{cij} d\mathbf{u}_c$. Based on the zeroth-order distribution function, the corresponding approximations for the diffusion velocity, pressure tensor and heat flux vector can be obtained as $\mathbf{V}_{ci}^{(0)} = 0$, $\mathbf{P}^{(0)} = p\mathbf{I}$, and $\mathbf{q}^{(0)} = 0$, where p denotes the pressure and \mathbf{I} denotes the unit tensor. First-order corrections to these approximations can be obtained from linear integral equations for the first-order distribution functions $f_{cij}^{(1)} \equiv f_{cij}^{(0)} \phi_{cij}$. These linear integral equations result in the following form

of the first-order distribution function:

$$f_{cij}^{(1)} = \frac{f_{cij}^{(0)}}{n} \left(-\mathbf{A}_{cij} \cdot \nabla \ln T - \sum_{dk} \mathbf{D}_{cij}^{dk} \cdot \mathbf{d}_{dk} - \mathbf{B}_{cij} : \nabla \mathbf{v} - F_{cij} \nabla \cdot \mathbf{v} - \mathbf{G}_{cij} \right) \quad (36)$$

The functions \mathbf{A}_{cij} , \mathbf{B}_{cij} , \mathbf{D}_{cij}^{dk} , F_{cij} , and \mathbf{G}_{cij} , which depend on microscopic velocities \mathbf{u}_c and macroscopic parameters $n_{ci}(\mathbf{x}, t)$, $\mathbf{v}(\mathbf{x}, t)$, and $T(\mathbf{x}, t)$ can be identified as coefficients of the underlying gradient terms in the linear integral equations. Note that the diffusion driving forces for each chemical species c at vibrational level i is given by $\mathbf{d}_{ci} = \nabla(n_{ci}/n) + \{(n_{ci}/n) - (\rho_{ci}/\rho)\}\nabla \ln p$. The detailed procedure for the calculation of above unknown functions in Eq. (36) is described in Kustova and Nagnibeda [69]. Expanding these functions into the double series of Sonine and Waldmann-Trübenbacher polynomials in velocity and rotational energy allows reducing the integral equations to transport linear systems including as coefficients bracket integrals over cross-sections of elastic collisions and rotational energy exchange. Simplifying the bracket integrals [54] we can express them in terms of collision integrals $\Omega_{cd}^{(l,r)}$ and rotational relaxation times. Integrals $\Omega_{cd}^{(l,r)}$ are calculated [67] on the basis of the Lennard-Jones potential for temperatures lower than 1000 K, and repulsive Born-Meyer potential for higher temperatures. The rotational relaxation time is calculated using the Parker formula [70].

The first-order distribution functions (36) can be used to obtain expressions for the diffusion velocity, pressure tensor and total heat flux vector as:

$$\mathbf{V}_{ci} = - \sum_{dk} D_{cidk} \mathbf{d}_{dk} - D_{Tci} \nabla \ln T \quad (37)$$

$$\mathbf{P} = (p - p_{\text{rel}} - \eta \nabla \cdot \mathbf{v}) \mathbf{I} - 2\mu \mathbf{S} \quad (38)$$

$$\mathbf{q} = -\lambda' \nabla T - p \sum_{ci} D_{Tci} \mathbf{d}_{ci} + \sum_{ci} \left(\frac{5}{2} kT + \langle \epsilon_j^c \rangle_r + \epsilon_i^c + \epsilon^c \right) n_{ci} \mathbf{V}_{ci} \quad (39)$$

Here D_{cidk} and D_{Tci} denote the diffusion coefficient and thermal diffusion coefficient for each chemical and vibrational species, given in terms of bracket integrals as $D_{cidk} = \frac{1}{3n} [\mathbf{D}^{ci}, \mathbf{D}^{dk}]$ and $D_{Tci} = \frac{1}{3n} [\mathbf{D}^{ci}, \mathbf{A}]$. Note that the pressure tensor (based on the first-order approximation) depends on the strain rate tensor S , the shear viscosity coefficient $\mu = \frac{kT}{10} [\mathbf{B}, \mathbf{B}]$, the bulk viscosity coefficient $\eta = kT[F, F]$ and the relaxation pressure $p_{\text{rel}} = kT[F, G]$. As a result of inelastic translational and rotational energy transfers in collisions between molecules of different vibrational and chemical species, additional terms appear in the pressure tensor in the form of relaxation pressure and bulk viscosity. The coefficient of thermal conductivity $\lambda' = \frac{k}{3} [\mathbf{A}, \mathbf{A}]$ appearing in the total heat flux vector also depends on the elastic and inelastic exchanges between translational and

rotational modes. The transport coefficients corresponding to shear viscosity, thermal conductivity, mass diffusion, and thermal diffusion coefficients can be obtained using Sonine and Waldmann-Trübenbacher orthogonal polynomials. An important aspect of this approach for obtaining the transport coefficients is that detailed interactions owing to vibrational energy transfers and chemical kinetics are carefully considered and could result in more accurate expressions for diffusion velocity, stress tensor, and heat flux vector in the presence of thermochemical nonequilibrium.

D. PARAMETRIC STUDY OF STATE KINETIC TRANSPORT COEFFICIENTS

A series of calculations were performed in Josyula et al. [71] to conduct a parametric study for assessment of the effect of the following parameters on the magnitude of the state-specific diffusion coefficients: 1) widely different population distributions, 2) atomic mass concentration, and 3) binary atomic to molecular diffusion coefficient ratio. Following Kustova [54] the diffusion coefficients—both binary and self—are expressed in terms of mass fractions of the relevant species. The system under consideration is a mixture of molecular nitrogen and atomic nitrogen. A state specific approach is adopted with the relevant molecular states being the vibrational states. Only a single atomic state is considered. The molecular mass fraction for a given molecular state is recast into a fractional vibrational population form and the diffusion coefficients simplified. The fractional population is displayed in Fig. 6a as a function of the vibrational states.

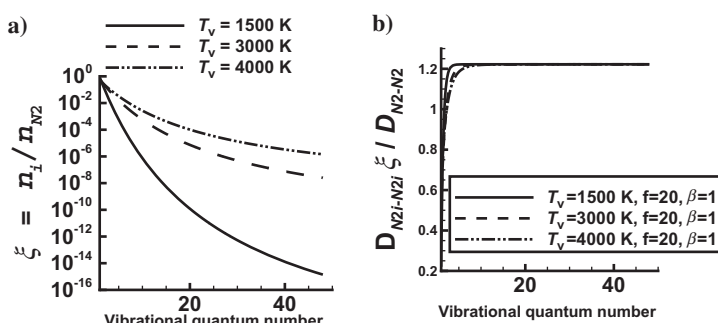


Fig. 6 Parametric study in a mixture of molecular and atomic nitrogen: a) molecular mass fraction cast as fractional population distribution in vibrational energy states from 1500 K to 4000 K to study the effect of this distribution on self-diffusion coefficient, b) self-diffusion coefficient from 1500 K to 4000 K, $f = 20$, $\beta = 1$. Here, nitrogen mass fraction is given as $1/f$; $D_{N2i-N2}/D_{N2-N2}^{\xi}$ is β ; vibrational state concentrations is represented as fractional population ξ . Note that the asymptotic value is insensitive to vibrational temperature and population departures from Boltzmann form.

The vibrational temperature, $T_v = -\Delta/\ln[n_2/n_1]$, ranges from 1500 to 3000 K with Δ set to $[0.3 \times 11,600 \text{ K}]$. An artificially enhanced population in the high vibrational states is introduced (shown in Eq. (40) below) to simulate effects owing to anharmonic pumping and biased recombination.

$$n_i/n_{N2} = \exp [-0.3 \times i / ((T_v/11,600) \times (1 + 0.0431 \times i))] \quad i = 0, 1, 2, 3 \dots 48 \quad (40)$$

The original form of the self-diffusion coefficient in Reference [54] given below (Eq. (41)) is cast in a functional form that permits

$$\mathcal{D}_{N_{2i},N_{2i}} = \frac{\left(\frac{C_N}{\mathcal{D}_{N_2}} + \frac{2(-1 - C_N + 1/C_{N_{2i}})}{\mathcal{D}_{NN_2}} \right) \mathcal{D}_{NN_2} m_N^2 n^2}{\left(\frac{C_{N_2}}{2\mathcal{D}_{N_2}} + \frac{C_N}{\mathcal{D}_{NN_2}} \right) \rho^2} \quad i = 0, 1, 2, 3 \dots \quad (41)$$

This form is achieved by expressing the atomic nitrogen mass fraction as $1/f$, the ratio of the binary, atomic nitrogen-molecular nitrogen diffusion coefficients $\mathcal{D}_{NN_2}/\mathcal{D}_{N_2}$ as β and the vibrational state concentrations, ξ , in terms of the fractional populations. The resulting equation,

$$\mathcal{D}_{N_{2i},N_{2i}} = \mathcal{D}_{N_2} \frac{(1+f)^2 \beta [2f^2(-1+\xi) + \xi(-2+\beta) - f\xi\beta]}{2(-1+f)f^2\xi[2+(-1+f)\beta]} \quad (42)$$

asymptotically depends inversely on the fractional population. This is made obvious in Fig. 6b by plotting the product of the state concentration and the state-specific self-diffusion coefficient. For this and the future comparisons, we have normalized the diffusion coefficients to the molecular nitrogen self-diffusion coefficient, \mathcal{D}_{N_2} . Note that the asymptotic value is insensitive to vibrational temperature and population departures from Boltzmann form.

III. MACROSCOPIC TRANSPORT EQUATIONS COUPLED TO MASTER EQUATION

In this section, we present the continuum gas dynamic equations with appropriate treatment of nonequilibrium processes at the microscopic level to account for the excitation of internal energy states. Considering a multicomponent, reacting and radiative gas mixture, the macroscopic equations, governing the evolution of the number density $n_{ci}(\mathbf{x}, t)$ (corresponding to state i and species c), velocity of the mixture $\mathbf{v}(\mathbf{x}, t)$ and total internal energy per unit mass $U(\mathbf{x}, t)$, can be expressed as [63, 72]

$$\frac{dn_{ci}}{dt} + n_{ci} \nabla \cdot \mathbf{v} + \nabla \cdot (n_{ci} \mathbf{V}_{ci}) = R_{ci} \quad (43)$$

$$\rho \frac{d\mathbf{v}}{dt} + \nabla \cdot \mathbf{P} = 0 \quad (44)$$

$$\rho \frac{dU}{dt} + \frac{\partial E_{\text{rad}}}{\partial t} + \nabla \cdot \mathbf{q} + \nabla \cdot \mathbf{q}_{\text{rad}} + \mathbf{P} : \nabla \mathbf{v} = 0 \quad (45)$$

$$\frac{1}{c} \frac{\partial I_v}{\partial t} + \boldsymbol{\Omega}_v \frac{\partial I_v}{\partial \mathbf{x}} = \frac{h^4 v^3}{c^3} J_v^{\text{rad}} \quad (46)$$

where I_v is the specific intensity of the radiation field, $E_{\text{rad}} \equiv \frac{1}{c} \int_0^\infty \int_{4\pi} I_v d\Omega_v dv$ denotes the radiation energy and $\mathbf{q}_{\text{rad}} \equiv \int_0^\infty \int_{4\pi} I_v \boldsymbol{\Omega}_v d\Omega_v dv$ denotes the radiative heat flux vector.

A. SIMPLIFICATIONS IN THE TRANSPORT EQUATIONS FOR A STEP-BY-STEP TREATMENT

For the purpose of the simplifications presented here, the equations are written considering the nitrogen molecule. Effect of radiation is neglected in the following analysis. Similar treatment is possible for other diatomic molecules of interest. Although STS transport coefficients can be obtained in principle from the knowledge of collision integrals, the number of independent diffusion coefficients is large. The latter number can be reduced further under the assumption that the collision cross-sections for elastic collisions do not depend on the vibrational states [54]. This assumption was validated by Bruno et al. [73], where the effect of a variable oscillator diameter on the transport coefficients was found to be small. Based on this assumption, the independent diffusion coefficients for the $N_2 - N$ system can be reduced to (a) thermal diffusion coefficient, $D_{Tci} = D_{Tc}$ for all i , (b) multicomponent diffusion coefficients of different chemical species, $D_{cidk} = D_{cd}$ for all i, j and $c \neq d$, (c) self diffusion coefficient, $D_{cici} = D_{cc}$ and (d) diffusion coefficients of the same chemical species at different vibrational levels, $D_{cicj} = \tilde{D}_{cc}$ if $i \neq j$. Hence, simplified expressions for diffusion velocity and heat flux can be written as:

$$\mathbf{V}_{ci} = -D_{cici} \mathbf{d}_{ci} - \tilde{D}_{cc} \sum_{k \neq i} \mathbf{d}_{ck} - \sum_{d \neq c} D_{cd} \mathbf{d}_d - D_{Tc} \nabla \ln T \quad (47)$$

$$\mathbf{q} = -\lambda' \nabla T - p \sum_c D_{Tc} \mathbf{d}_c + \sum_{ci} \left(\frac{5}{2} kT + \langle \epsilon_j^{ci} \rangle_r + \epsilon_i^c + \epsilon^c \right) n_{ci} \mathbf{V}_{ci} \quad (48)$$

where

$$\mathbf{d}_c \equiv \sum_i \mathbf{d}_{ci} = \nabla \left(\frac{n_c}{n} \right) + \left(\frac{n_c}{n} - \frac{\rho_c}{\rho} \right) \nabla \ln p \quad (49)$$

In spite of these simplifications, the inclusion of the resulting STS transport coefficients that are based on rigorous kinetic theory into CFD codes would often result in prohibitively expensive simulations.

It is important to compare and quantify the performance of model predictions based on rigorous kinetic theory with a simplified state kinetic model in the

context of diffusion and heat transfer. In the latter case, terms associated with diffusion due to temperature and pressure gradients are neglected, which could be a source of model errors. In this simplified model, the diffusion velocity is assumed to be given by Fick's law rather than the detailed description discussed earlier. Further, the Lewis number is assumed to be constant in the simplified model.

An explicit expression for the vibrational heat flux $\mathbf{q}_{\text{vib}_c}$ is assumed based on Fick's law and the diffusion or mean peculiar velocity $\tilde{\mathbf{V}}_{ci}$ relative to species mass-average velocity for species c , level i is given as

$$\rho_{ci} \tilde{\mathbf{V}}_{ci} = -\rho_c D_{11} \nabla(\rho_{ci}/\rho_c) \quad (50)$$

where D_{11} is the self-diffusion coefficient which can be obtained from kinetic theory as $D_{11} = \eta' \mu / \rho$, where η' is 1.2 for hard sphere molecules, is 1.43 for Maxwell molecules and is somewhere in between these two values based on experimental results [67]. The species diffusion velocity $\mathbf{V}_c \equiv \tilde{\mathbf{C}}_c - \mathbf{v}$ defined as the species mass-averaged velocity $\tilde{\mathbf{C}}_c \equiv \frac{1}{\rho_c} \sum_{i,j} m_c \int \mathbf{u}_c f_{cij} d\mathbf{u}_c$ relative to the mixture mass-averaged velocity \mathbf{v} , can also be approximated by Fick's law as

$$\rho_c \mathbf{V}_c = -\rho D_{12} \nabla(\rho_c/\rho) \quad (51)$$

where the binary diffusion coefficient D_{12} is obtained by assuming a constant Lewis number. (See the work of Kustova and Nagnibeda [69] for a rigorous kinetic theory algorithm for the calculation of the STS transport coefficients.) In a STS description of the internal energy states, the conservation of mass equation takes the form given below representing each of the energy states in a given internal energy mode.

$$\partial_t \rho_{ci} + \nabla \cdot [\rho_{ci} (\mathbf{v} + \mathbf{V}_c + \mathbf{V}_{ci})] = \dot{\omega}_{ci} \quad (52)$$

The conservation Eq. (52) is used in the STS kinetics code, written for mass density in quantum level i for diatomic nitrogen. The source term $\dot{\omega}_{ci}$ derived from the vibrational master equations is made up of the relevant energy exchange processes consisting of the V-T and V-V energy exchange mechanisms, shown below for a nitrogen and oxygen gas mixture.

$$\begin{aligned} \dot{\omega}_{ci} = & (\dot{\rho}_{N_2-N_2})^{V-T} + (\dot{\rho}_{N_2-N_2})^{V-V} + (\dot{\rho}_{N_2-O_2})^{V-T} + (\dot{\rho}_{N_2-O})^{V-T} \\ & + (\dot{\rho}_{N_2-N})^{\text{diss}} \end{aligned} \quad (53)$$

The density of molecular nitrogen is the sum of population densities in the various vibrational levels, $\rho_{N_2} = \sum_{i=0,1,\dots} \rho_i$. For diatomic nitrogen in the STS kinetics formulation, a separate vibrational conservation equation is not necessary as the vibrational energy is calculated at each quantum level.

The kinetics of the particle exchanges among the quantum states of N_2 can be simulated by the vibrational master equations, the population distributions

calculated by [74]:

$$\dot{\omega}_i = \frac{1}{M} \left\{ \sum_{i'} [k_{VT}(i' \rightarrow i) \rho_{i'} \rho - k_{VT}(i \rightarrow i') \rho_i \rho] + \sum_w [k_{VV}(i', w' \rightarrow i, w) \rho_{i'} \rho_{w'} - k_{VV}(i, w \rightarrow i', w') \rho_i \rho_w] \right\} \quad (54)$$

Considering single quantum transitions, the equations governing the V-T reactions responsible for the variation of the particles distributed in the i th vibrational level of diatomic nitrogen are:



where M represents O_2 , O , N_2 . The equations governing the V-V processes in N_2 giving the reactions responsible for the variation of the particles distributed in the w th vibrational level are:



For the kinetics of diatomic nitrogen, a set of V-T and V-V excitation and de-excitation rates will enable calculation of the energy exchanges in the vibrational manifold. The vibrational energy of the N_2 molecule is given in terms of the quantum level energies by

$$e_{vib_{N_2}} = \sum_{i=1,2,\dots} \frac{\rho_i}{\rho_{N_2}} \epsilon_i \quad (57)$$

where the index i is used to denote the quantum level. In this equation, $\frac{\rho_i}{\rho_{N_2}}$ is the fractional population of the i th vibrational level and ϵ_i the quantum level energy given by the third-order approximating formula:

$$\frac{\epsilon_i}{hc} = \omega_e \left(i - \frac{1}{2} \right) - \omega_e x_e \left(i - \frac{1}{2} \right)^2 + \omega_e y_e \left(i - \frac{1}{2} \right)^3 \quad i = 1, 2, \dots l+1 \quad (58)$$

The above equation represents anharmonic-oscillator behavior of the N_2 molecule, where h is Planck's constant and c is the speed of light. The spectroscopic constants are given by $\omega_e = 2358.57 \text{ cm}^{-1}$, $\omega_e x_e = 14.324 \text{ cm}^{-1}$, and $\omega_e y_e = -0.00226 \text{ cm}^{-1}$ [75]. When $i = 45$, the value of energy exceeds the N_2 dissociation energy, 9.62 eV. These simplified approximations in the treatment of the transport coefficients and the terms in the master equation can be used in conjunction with the global conservation equations as:

$$\partial_t \rho_{ci} + \nabla \cdot [\rho_{ci} (\mathbf{v} + \mathbf{V}_c + \mathbf{V}_{ci})] = \dot{\omega}_{ci} \quad (59)$$

$$\partial_t \rho_c + \nabla \cdot [\rho_c (\mathbf{v} + \mathbf{V}_c)] = \dot{\omega}_c \quad (60)$$

$$\partial_t (\rho \mathbf{v}) + \nabla \cdot (\rho \mathbf{v} \mathbf{v} + \tilde{\boldsymbol{\tau}}) = 0 \quad (61)$$

$$\partial_t(\rho e_{\text{vib}}) + \nabla \cdot [\rho e_{\text{vib}}(\mathbf{v} + \mathbf{V}_c) + \dot{\mathbf{q}}_{\text{trans}} + \dot{\mathbf{q}}_{\text{vib}}] = \rho \dot{\omega}_{\text{vib}} \quad (62)$$

$$\partial_t(\rho e) + \nabla \cdot \left[\rho(e + p/\rho)\mathbf{v} - \sum \dot{\mathbf{q}}_{\text{vib}} + \sum (\rho_c h_c \mathbf{V}_c) - \mathbf{v} \cdot \boldsymbol{\tau} \right] = 0 \quad (63)$$

The mass conservation of species is represented by Eq. (60). The production of small amounts of atoms due to dissociation of molecules is included in the source term, $\dot{\omega}_c$. The mixture density, ρ is the sum of the partial species densities in partially dissociated air, which may be written as,

$$\rho = \rho_{N_2} + \rho_{O_2} + \rho_O + \rho_{NO} + \rho_N \quad (64)$$

Equation (61) gives the conservation of total momentum. Equation (62) also includes terms for the conduction and diffusion of vibrational energy. The conservation of total energy is given by Eq. (63) with heat conduction and species diffusion terms.

The master equation methodology presented above uses STS kinetic transition rates obtained from non-ab initio approaches, meant to understand the underlying physics of nonequilibrium in the internal energy states. It is noted that in the master equation approach, the use of ab initio rates and to understand new reaction rates and reaction paths is an active research area that will have a significant impact on the future CFD predictions involving nonequilibrium processes; see for example a more recent work of Panesi et al. [76]. A solution procedure for the resulting mass conservation equation with stiff source terms are described next.

B. NUMERICAL SOLUTION METHODOLOGY

To describe the numerical solution of the underlying macroscopic transport equations with stiff source terms, we consider a convenient representation of these equations as,

$$\partial_t \mathbf{U} + \nabla \cdot \mathbf{F} = \mathbf{H} \quad (65)$$

where the vector \mathbf{U} is given by $[\rho_0 \quad \rho_1 \quad \dots \quad \rho_N \quad \rho u \quad \rho v \quad \rho e]^T$. Similarly \mathbf{F} and \mathbf{H} can also be written out from Eq. (70–72). Explicit and/or implicit methods could be used to obtain numerical solutions of these equations, depending on preferences for accuracy, ease of implementation and numerical stability. As explicit approaches are commonly used due to their ease of implementation, we describe some explicit approaches that are commonly used in solution of macroscopic transport equations. Numerical solutions of the transport equations in strong coupling form have been obtained by Josyula et al. [77] via an explicit, predictor–corrector method with second-order accuracy in space and time. In these implementations, the Roe approximate Riemann solver is used to determine the inviscid fluxes. Formal second-order accuracy is obtained using the MUSCL

approach in conjunction with the minmod limiter to degenerate the solution to first-order accuracy in the vicinity of strong waves [77, 78].

Numerical solution of the underlying governing equations can be quite challenging especially due to high computational costs, arising not only due to many degrees of freedom but also due to inherent stiffness of the governing differential equations. Numerical implementations involving a strong coupling of convection processes with STS transitions (via master equations) often lead to stiff systems that are difficult to solve. For time dependent problems, this difficulty can lead to the use of a needless and unreasonably small time step for both transport and kinetics. To alleviate this difficulty, operator splitting methods can be used where the solution is split into separate integrations for i) physical transport and ii) STS kinetics [79]. Such operator splitting methods allow for separate time steps can be used for each of these two integration stages. Numerical integration of physical transport operator is performed using a standard second-order Runge–Kutta scheme, whereas the STS kinetics are handled using a stiff solver for ordinary differential equations (such as DLSODA). Such operator splitting approaches (e.g. Strang splitting) [80–84] have been widely used in computational combustion, where the complete evolution operator is split into for physical transport and stiff chemistry. It can be shown that operator splitting introduces an error which can be alleviated with a proper ordering of the operators.

To better describe the operator splitting approach, we denote the evolution operator accounting for both transport and collisions (via Master equation) over time step Δt as $\Phi^{\Delta t}$ corresponding to Eq. (65). Based on this evolution operator, the state vector \mathbf{U} at time $t + \Delta t$ (denoted at $\mathbf{U}^{t+\Delta t}$) can be expressed as

$$\mathbf{U}^{t+\Delta t} = \Phi^{\Delta t} \mathbf{U}^t \quad (66)$$

Instead of directly seeking numerical approximations of the operator Φ which accounts for the effects of both transport and collision operators, one could use an operator split formalism where the state vector at \mathbf{U} at time $t + \Delta t$ can be expressed as

$$\mathbf{U}^{t+\Delta t} = \Phi_C^{\Delta t/2} \Phi_T^{\Delta t} \Phi_C^{\Delta t/2} \mathbf{U}^t \quad (67)$$

where Φ_T and Φ_C denote evolution operators due to pure transport and pure collision processes (master equation) corresponding to the following system of equations.

$$\Phi_T: \quad \partial_t \mathbf{U} + \nabla \cdot \mathbf{F} = 0 \quad (68)$$

$$\Phi_C: \quad \partial_t \mathbf{U} = \mathbf{H} \quad (69)$$

This operator split formalism, consistent with original formulation by Strang [83], can be shown to be second-order accurate in time. Based on the above operator split formalism, we further approximate the operators Φ_T and Φ_C . The former

is treated numerically similar to the non-split case (except that source term $\mathbf{H} = 0$ for the pure transport step) discussed earlier, where a second-order accurate predictor–corrector method with Roe upwind difference scheme is used. While the evolution operator for collisions Φ_C (given by the master equation) is treated via a stiff ordinary differential equation (ODE) integration solver. Some recent studies in this context used the DLSODA stiff ODE integration package [85].

Recent advancements in a CFD method for hypersonic flow and aerothermodynamics is presented in Chapter 5 of this volume.

C. NUMERICAL SOLUTIONS

The effect of using a state to state kinetic thermochemical nonequilibrium model on flow past a hemisphere cylinder is shown in Figs. 7 and 8. Comparison of heat transfer to the surface in Fig. 7 shows the heat transfer prediction within 5%. The discrepancies primarily in the stagnation region can be attributed to nitrogen dissociation and nitric oxide formation included only with the Landau–Teller model, not with the state to state kinetics model. Figure 8 shows the nitrogen vibrational population distribution at the stagnation point. Here the viscous effects decrease the state density for the Mach 11.18 case. The inviscid case shows a Boltzmann behavior for the population distribution as expected, whereas the viscous cases of Mach 8.6 and 11.18 both show non-Boltzmann population distributions: for the Mach 8.6 case, seen as a lowering of the population in the tail of the distribution, whereas for the Mach 11.18 case, there is an increase in population starting at $i = 7$ with elevated population in the intermediate and upper energy states.

The effects of radiation in a Mach 19.83 N_2 gas flow behind a shock using a model based on the STS approach by considering vibration-translation and vibration-electronic jumps and dissociation by Aliat et al. [86]

In particular, in the context of the flow set-up, the importance of coupling between physico-chemical and radiative processes was identified in this work (as shown in Fig. 9). It was found that the lack of coupling tends to overestimate the emitted radiation and the

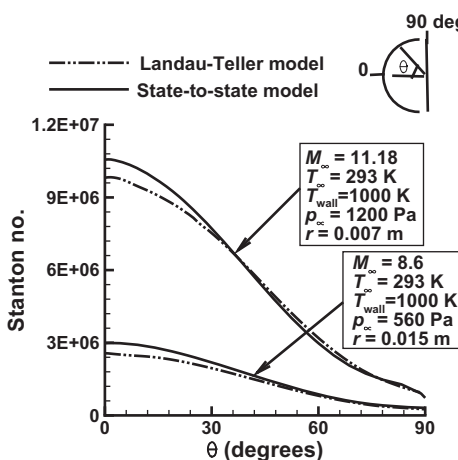


Fig. 7 Stanton number along surface for flow past a hemisphere cylinder, Medium = Air.

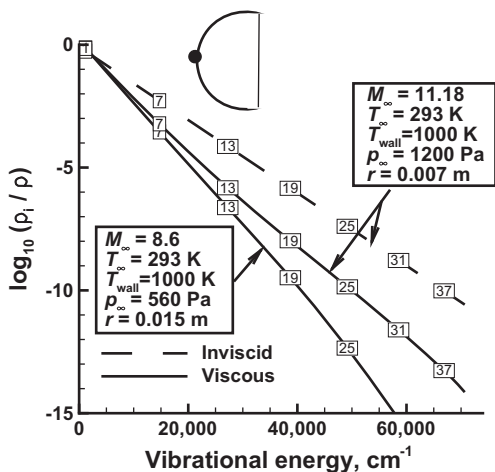


Fig. 8 N_2 vibrational population distribution at stagnation point for flow past a hemisphere cylinder, Medium = Air.

discrepancy increases with the intensity of emitted radiation. Small discrepancies between predictions of intensities obtained from STS, one-temperature (OT) and two-temperature (TT) models were also observed.

D. INVISCID FLUID TRANSPORT EQUATIONS COUPLED TO MASTER EQUATION WITH MULTIQUANTUM TRANSITIONS

Solving the inviscid gas transport equations numerically is a convenient way to study the effect of thermal nonequilibrium in high temperature gas flows. The effects of multiquantum transitions were recently investigated by Josyula et al. [87] using global conservation equations in mass-averaged velocity form to

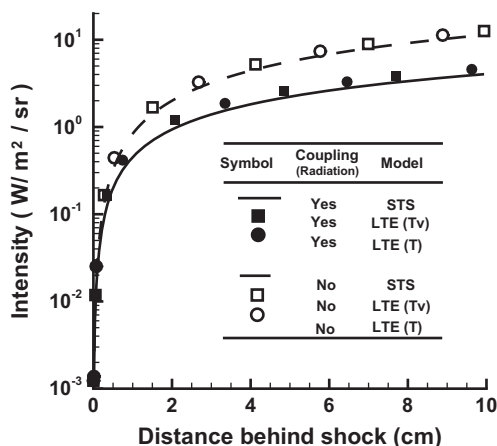


Fig. 9 Illustration of effects of coupling between physicochemical and radiative processes on radiation intensities behind the shock for different Mach numbers, $M = 19.83$ (unfilled symbols) and $M = 25$ (filled symbols), based on STS and LTE (T_v and T) approaches.

simulate hypersonic flow are presented in this section. The models used to simulate the V-T and V-V processes are then discussed.

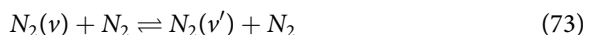
$$\frac{\partial}{\partial t}(\rho_v) + \nabla \cdot (\rho_n \vec{u}) = \dot{\omega}_v \quad v = 0, 1, \dots \quad (70)$$

$$\frac{\partial}{\partial t}(\rho \vec{u}) + \nabla \cdot (\rho \vec{u} \vec{u} - p \vec{\delta}) = 0 \quad (71)$$

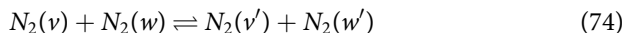
$$\frac{\partial}{\partial t}(\rho e) + \nabla \cdot [\rho(e + p/\rho) \vec{u}] = 0 \quad (72)$$

Equations (70) to (72) describe the conservation of mass, momentum, and energy in the flowfields of interest. A microscopic kinetic approach was taken by treating the molecule as anharmonic oscillator, calculating the state populations using the master equations. In the treatment of vibrational energy for the diatomic species in the master equation approach, a separate vibrational conservation equation is not necessary as the vibrational energy can be calculated for each quantum level.

The symbolic equations governing the V-T transitions responsible for the variation of the particles distributed in the v th vibrational level in a flow of non-reacting nitrogen are given by,



the equations governing the V-V process are:



E. NUMERICAL SOLUTIONS

A reduced-order model developed by Josyula and Bailey [56, 88] considered vibrational population depletion due to dissociation, to account for the internal energy mode relaxation in dissociating flows. This model was employed, with various V-T and V-V transition rates, to study the effect of dissociation from the last level on the population depletion in the vibrational states. More recently, a higher fidelity model, for which dissociation can proceed from any quantum vibrational level, was implemented by Josyula et al. [35]. The population distribution for a Mach 20 blunt body flow with dissociation was calculated using this model, and is shown in Fig. 10. At the two locations presented in the figure – one a small distance downstream of the shock ($T = 9479$ K) and the other near the stagnation point ($T = 21,426$ K) – it is seen that the population distributions are highly non-Boltzmann. In particular, a greatly reduced population is found with increasing vibrational quantum levels due to the partial heating of the vibrational manifold. Additionally in high temperature flows, effects of multiquantum transitions can be important and the relaxation of a N_2 gas flow

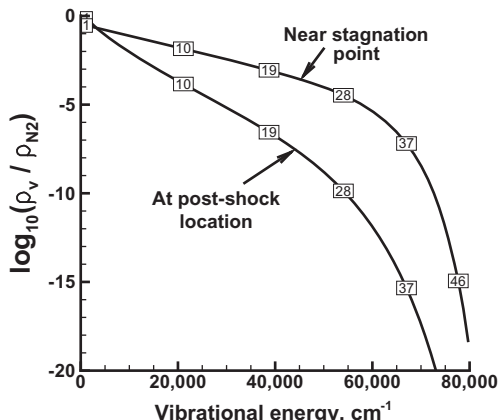


Fig. 10 Population distribution in the vibrational levels at two locations in the shock layer, for a blunt-body Mach 19.83 flow with dissociation from all vibrational quantum levels. Note: Numbers in boxes on the curves denote vibrational quantum number.

to 12-quantum transitions are shown in Fig. 11. One can see a higher translational temperature immediately behind the shock wave in the forebody region for the case of single-quantum transitions, as shown in Fig. 11, where the density is the highest.

Effects of single-, up to 2-quantum, and up to 12-quantum jumps at the immediately post-shock wave and mid-shock layer locations are shown in Fig. 12. It is seen that in the immediate post-shock location where the temperature is the highest and the nonequilibrium is the greatest, there is a greater effect of multiquantum transitions than further downstream in the shock layer. The effect of mass density on the vibrational population distribution for the various multiquantum jumps is apparent. See the work of Josyula et al. [87] for additional details on this case.

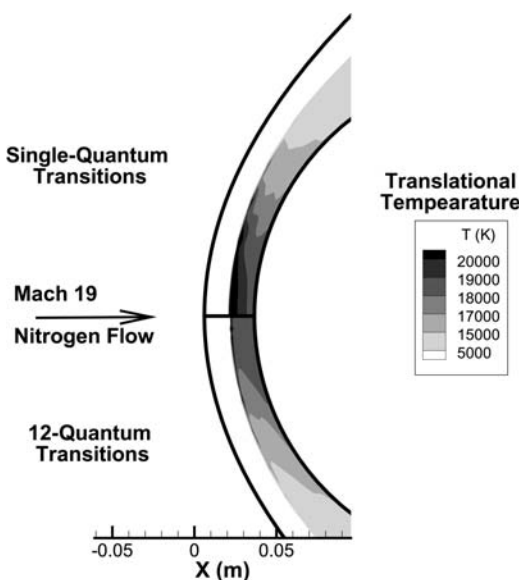


Fig. 11 Translational temperature contours, $M_\infty = 19.82$, $T_\infty = 300$ K, $p_\infty = 27$ Pa, $r = 0.1524$ m.

behind a shock wave are treated in Aliat et al. [89] and for state specific dissociation modeling in Reference [90].

Comparisons of the translational contours of single and up

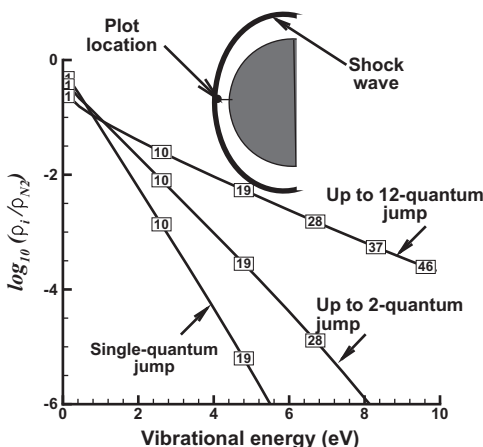


Fig. 12 Population distribution at post-shock using single- and multiquantum VT rates for nitrogen flow past blunt body, $M_\infty = 19.82$, $T_\infty = 300$ K, $p_\infty = 27$ Pa, $r = 0.1524$ m.

IV. MACROSCOPIC NONEQUILIBRIUM TRANSPORT EQUATIONS WITH SIMPLIFIED ENERGY EXCHANGE MODELS

The governing equations presented in the above sections are based on the generalized Boltzmann equation and the state kinetic approach of treating the internal energy excitation. These above mentioned approaches are currently active research areas in the areas of development of realistic collision cross-sections and physics-based reduced-order models, needing to reach a level of technology maturation that is required for use in routine CFD use in aerospace vehicle design. Therefore we present in this section, macroscopic transport equations with simplified energy exchange models for a high temperature weakly ionized gas consisting of multicomponent air mixture for the purpose of demonstrating the scope of the hypersonic flow problem that needs to be addressed with physics-based formulations given in the above sections.

First we provide a few definitions pertaining to a weakly ionized gas. An ideal plasma is a quasi-neutral collection of charged particles exhibiting collective behavior. For a plasma to be ideal, the physical scale of the system, L , must be greater than the Debye length, λ_D and the observational or characteristic time scale, τ , must be greater than $1/\omega_{pe}$, the inverse of the plasma frequency. In a plasma environment, macroscopic neutrality is maintained because of the mutual compensation of the space charge of the positive ions and electrons. This compensation, however, takes place in terms of spatial and temporal averages for sufficiently large volumes and sufficiently long time. Accounting for these spatial and temporal restrictions, a plasma is said to be a quasi-neutral medium. The spatial scale length associated with quasi-neutrality is the Debye

length, λ_D , where

$$\lambda_D \equiv \sqrt{\frac{\epsilon_0 k T}{N_\infty e^2}} \quad (75)$$

The corresponding temporal scale length is the inverse of the electron plasma frequency, ω_{pe} .

$$\omega_{pe}^{-1} = \lambda_{D_e} \sqrt{\frac{k T_e}{M_e}} \quad (76)$$

This “time” represents the time for the average particle (electron) to traverse the Debye length.

The governing equations for a weakly ionized, thermochemical nonequilibrium flow over a hypersonic vehicle were developed by Lee [50]. The flow is modeled as a multicomponent gas mixture that is characterized by separate vibrational temperatures for each diatomic species and an electron temperature. The governing equations include [50, 51]:

$$\partial_t \rho_c + \nabla \cdot [\rho_c (\mathbf{U} + \mathbf{u}_c)] = \dot{w}_c \quad (77)$$

Mixture momentum conservation:

$$\partial_t (\rho \mathbf{U}) + \nabla \cdot (\rho \mathbf{U} \mathbf{U} + p \mathbf{I} - \boldsymbol{\tau}) = \rho_e \mathbf{E} + (\mathbf{J} \times \mathbf{B}) \quad (78)$$

Vibrational energy equation for each diatomic species:

$$\partial_t (\rho_c e_{cv}) + \nabla \cdot [\rho_c (\mathbf{U} + \mathbf{u}_c) e_{cv} + q_{cv}] = e_{cv} \dot{w}_c + Q_{v,\Sigma} \quad (79)$$

Electron energy equation:

$$\begin{aligned} \partial_t (\rho_e e_e) + \nabla \cdot [\rho_c (\mathbf{U} + \mathbf{u}_c) e_e + \mathbf{U} \cdot p_e \mathbf{I} + q_e] \\ = e_e \dot{w}_c + \mathbf{E} \cdot \mathbf{J} + [\rho_c \mathbf{E} + (\mathbf{J} \times \mathbf{B})] \cdot (\mathbf{U} + \mathbf{u}_c) + Q_{e,\Sigma} \end{aligned} \quad (80)$$

Total energy equation:

$$\begin{aligned} \partial_t (\rho e) + \nabla \cdot [\rho e \mathbf{U} - \kappa \nabla T + \sigma \rho_c u_c h_c + q_{\text{rad}} + \mathbf{U} \cdot p \mathbf{I} + \mathbf{U} \cdot \boldsymbol{\tau}] \\ + Q_{vt} - Q_{et} = 0, \end{aligned} \quad (81)$$

Where \mathbf{J} , the current density of the partially ionized gas is given by

$$\mathbf{J} = e[-d_c \nabla n_c + d_e \nabla n_e + (n_c \mu_c + n_e \mu_e) \mathbf{E}] \quad (82)$$

in which the drift velocity and the diffusion velocity of both ions and electrons are included. The contributions due to both induced and applied electric and magnetic field intensities are included in the definitions of the vector fields

E and **J**. The total energy is defined as

$$\begin{aligned} \rho e = & \sum_c \rho_c \left(c_{v,c} T + \frac{1}{2} \mathbf{U} \cdot \mathbf{U} \right) + \sum_c \rho_c e_{cv} \\ & + \sum_c \rho_c h_c^0 + \rho_e \left(c_{v,e} T_e + \frac{1}{2} \mathbf{u}_e \cdot \mathbf{u}_e \right) \end{aligned} \quad (83)$$

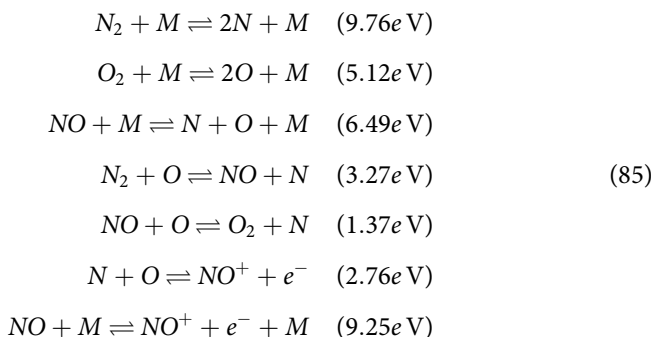
and the translational-rotational temperature can be obtained from this relation, assuming that the translational energy modes and the rotational energy modes are in equilibrium. Various models for net energy transfers (Q_{vp} , Q_{et} , $Q_{v,\Sigma}$, and $Q_{e,\Sigma}$) between translational, vibrational and electronic excitations have been discussed in the literature (see for example Reference [50]).

The total radiation heat flux is obtained by considering the governing equation of spectral intensity for radiation, as

$$\Omega \frac{\partial \mathbf{J}_\omega(\mathbf{r}, \Omega)}{\partial \mathbf{r}} + \kappa_\omega(\mathbf{r}) \mathbf{J}_\omega(\mathbf{r}, \Omega) = j_\omega(\mathbf{r}) \quad (84)$$

where $J_\omega(\Omega)$, $\kappa_\omega(\mathbf{r})$, and $j_\omega(\mathbf{r})$ denote the spectral intensity of heat radiation, the spectral absorption coefficient and the spectral emission coefficient, respectively. The latter can be obtained from Kirchoff law, under the assumption of local thermodynamic equilibrium, as $j_\omega(\mathbf{r}) = \kappa_\omega(\mathbf{r}) J_{b,\omega}(\mathbf{r})$. Note that the total energy equation and the radiative energy transfer equation are coupled via the radiation heat flux \mathbf{q}_{rad} term, which can be obtained via integration of the spectral intensity of heat radiation over the full spectrum ω and the solid angle Ω .

Contributions to $\dot{\omega}_c$ arise from such sources and sinks as, dissociation, ionization, recombination, and attachment. As a simple example of the application of this set of equations in a weakly ionized flow, we consider a study of plasma generation at high Mach numbers arising from the associative-ionization reaction. The primary species of air considered in the present study are O_2 , O , N_2 , N , NO , NO^+ , and e^- . The significant reactive collisions constituting sources and sinks in the continuity equations are [62, 91]:



where the reaction threshold for the forward (dissociation or ionization) process is given in the parenthesis. The first three reactions are dissociation–recombination and the fourth and fifth are exchange reactions. The sixth reaction equation is the associative–ionization and its inverse the dissociative–recombination reaction. The net energy (2.76 eV) that must be supplied for the associative–ionization reaction of N and O is considerably less than the full ionization potential (9.25 eV) for the $NO + M \rightleftharpoons NO^+ + e^- + M$ reaction [62]. From the studies of Lin et al. [91] and Wilson [92] for the case of air, this associative–ionization mechanism is dominant for shock speeds below 9 km/s. Above this velocity, electron-impact [92] ionization dominates. At high temperatures, additional mechanisms lead to the creation of O_2^+ , O^+ , N_2^+ , however, these mechanisms are not relevant in the present study addressing the lower temperature regime. Readers may consult References [9] and [93] for details on these kinetic processes.

The dissociation rates were calculated using the following functional form of the Arrhenius equation:

$$k_f(T_{\text{eff}}) = C_f T_{\text{eff}}^\eta \exp(\theta_d/T_{\text{eff}}) \quad (86)$$

The recombination rates were calculated from the equilibrium curve fits.

$$k_b(T_{\text{eff}}) = \frac{k_f(T_{\text{eff}})}{K_{\text{eq}}(T_{\text{eff}})} \quad (87)$$

The reaction rates and equilibrium constants are presented in Park [95] for the first five reactions and from Wray [96] for the sixth reaction. More recent studies on reaction rates in air are available from the work of Park [97, 98] for components of air and Bose and Candler [99] for the nitric oxide formation reaction. The species-conservation equation (Eq. (77)) is solved for each species, O_2 , O , N_2 , N , NO , NO^+ , and e .

A. ELECTRIC FIELD MODELS

The Poisson equation links the space charge of the plasma to the electrostatic potential, ϕ . In the electrostatic approximation, the electric field (\vec{E}) is given by the negative of the gradient of ϕ . As $\nabla \cdot \vec{E} = \zeta/\epsilon_0$, the Poisson equation is stated as,

$$\nabla^2 \phi = -\frac{\zeta}{\epsilon_0} \quad (88)$$

where ζ is the total charge density given by

$$\zeta = \sum_s q_s N_s \quad (89)$$

Here ϵ_0 is the permittivity of free space given by 8.8542×10^{-12} F/m, q_s is the charge and N_s is the number density of the species, s . If the individual species

are analyzed separately, the total charge density may be accumulated and the electric field, accounting for the boundary conditions, can be established self-consistently through a solution of Poisson's equation. The solution, however, may be computationally expensive and introduce stringent time steps and grid requirements. Often, instead, approximate forms are introduced which do not require solution of Poisson's equation.

In many circumstances of interest the pressure gradient and the electric field term in Eq. (78) dominate the momentum balance. This enables an approximate evaluation of the field:

$$E^i = -\frac{1}{N_e \epsilon} \frac{\partial p_e}{\partial x^i} \quad (90)$$

where ϵ is the elementary electronic charge and the subscript e denotes values for the electron. In this approximation, the electron pressure gradient balances the forces arising from space charge or impressed fields. This approximation is convenient and often appropriate for specifying the field without resorting to a solution of the Poisson's equation. For a spatially homogeneous electron temperature, this form states that the electrons achieve a Boltzmann equilibrium with the field.

When considering current flow to an insulated surface, the electric field may be evaluated using ambipolar diffusion theory. Owing to the significant disparity in the transport coefficients (diffusion and mobility) of electrons and ions, a positive space charge develops at an insulating boundary, limiting the electron flux to the surface and enhancing the flux of ions. Current continuity demands that the net current to the surface be zero. Equality of the electrons and ion fluxes defines this ambipolar condition (denoted below by the subscript a).

$$\Gamma_e = \Gamma_I = \Gamma = D_a \nabla N \quad (91)$$

where Γ denotes the electron (e) or ion (I) flux density and

$$D_a \approx D_I \left(1 + \frac{T_e}{T_I} \right) \quad (92)$$

It follows that the ambipolar diffusion coefficient is much less than the electron free diffusion coefficient and greater than the ion free diffusion coefficient:

$$D_I < D_a \ll D_e \quad (93)$$

Now, $D_a = D_I$ for $T_e \ll T_I$. For isothermal plasmas, when $T_e = T_I$, Eq. (92) approximates to $D_a \approx 2D_I$. For an ambipolar assumption the flux of electrons and ions in any region must be equal such that charge does not build up. The electric field, in this approximation, is given by,

$$E^i = \frac{D_I - D_e}{\mu_I + \mu_e} \frac{\nabla N}{N} \quad (94)$$

The simplified energy exchange models presented above in this section and their variants were used in several studies; among them we mention a few: Josyula et al. [56], Candler and MacCormack [100], and Grasso and Capano [101]. These studies exemplify the simplified approaches for the calculation of the electron density distribution along surface, which has flight-test data of the RAM-C II vehicle.

V. SUMMARY AND CONCLUDING REMARKS

In this chapter, a generalized set of transport equations has been presented for the numerical modeling of the hypersonic flowfields about aerospace vehicles. Starting with the generalized Boltzmann equation of the WCU form, the collision terms were written for high temperature aerodynamic simulations. Using the Chapman–Enskog expansion, the simplified governing fluid dynamic equations for continuum flight regime are presented. The thermochemical nonequilibrium effects are modeled using a master equation approach that accounts for the population in the internal energy states of the various internal energy modes. We also consider the dependence of state kinetics on the transport coefficients in the nonequilibrium gas. Numerical methods are briefly discussed along with sample solutions.

One may note that in the field of nonequilibrium hypersonic flow research, there has been a continuous trend in the past four decades to create simplified models without establishing the limits of validity. In particular, many phenomenological or semi-empirical models for nonequilibrium flow processes have been developed with the general goal of predicting flowfield characteristics while avoiding excessive computational cost. Historically efforts have been focused on the use of increases in computing power to gain a better understanding of the physics. However, in the absence of experiments and first principles calculations there has remained a lack of fundamental understanding of the physics on which reliable models could be based. Investigations into the fundamental physics as described by the Boltzmann equation, the WCU equation, the master equation and other governing equations presented here should ideally set a standard against which future models can be evaluated. More generally, it is hoped that the more rigorous nonequilibrium models presented in this chapter will help in gaining a better understanding of the hypersonic flow physics.

ACKNOWLEDGMENT

The authors would like to thank Jonathan Burt for the review of the article and for the many suggestions and helpful discussions.

REFERENCES

- [1] Hayes, W., and Probstein, R., *Hypersonic Flow Theory*, Vol. I., Academic Press, New York, 1959.
- [2] Anderson, J. D. Jr., *Hypersonic and High Temperature Gas Dynamics*, AIAA Education Series, AIAA, Reston, VA, 2006.
- [3] Hirschel, E. H., “Basics of Aero-thermodynamics,” *Progress in Astronautics and Aeronautics*, Vol. 206, 2004, DOI: 10.2514/4.476914.
- [4] Weiland, C., and Hirschel, E. H., “Selected Aero-thermodynamic Design Problems of Hypersonic Flight Vehicles,” *Progress in Astronautics and Aeronautics*, Berlin, 2009, DOI: 10.2514/4.479908.
- [5] Cercignani, C., *Boltzmann Equation and its Applications*. Springer-Verlag, New York, 1988.
- [6] Aristov, V. V., *Direct Methods for Solving the Boltzmann Equation and Study of Non-Equilibrium Flows Phenomena*, Kluwer Academic Publishers, Dordrecht, 2001.
- [7] Tcheremissine, F. G., “Solution of the Boltzmann Kinetic Equation for High-Speed Flows,” *Computational Mathematics and Mathematical Physics*, Vol. 46, No. 2, 2006, pp. 315–329.
- [8] Josyula, E., Vedula, P., Bailey, W. F., and Suchyta, C. J. III, “Kinetic Solution of the Structure of a Shock Wave in a Nonreactive Gas Mixture,” *Physics of Fluids*, Vol. 23(017101), No. 1, 2011, pp. 017101-1–017101-9.
- [9] Josyula, E., Suchyta, C. J. III, Boyd, I. D., and Vedula, P., “Internal Energy Relaxation in Shock Wave Structure,” *Physics of Fluids*, Vol. 25(126102), No. 12, 2013, pp. 126102-1–126102-19.
- [10] Kolobov, V. I., Arslanbekov, R. R., Aristov, V. V., Frolova, A. A., and Zabelok, S. A., “Unified Flow Solver for Rarefied and Continuum Flows with Adaptive Mesh and Algorithm Refinement,” *Journal of Computational Physics*, Vol. 223, No. 2, 2007, pp. 589–608.
- [11] Alekseenko, A., and Josyula, E., “Deterministic Solution of the Spatially Homogeneous Boltzmann Equation Using Discontinuous Galerkin Discretizations in the Velocity Space,” *Journal of Computational Physics*, Vol. 272, 2014, pp. 170–188.
- [12] Xu, K., Tang, Lei, and Mao, Meilang, “A Multidimensional Gas-Kinetic Scheme for Hypersonic Viscous Flow,” *Journal of Computational Physics*, Vol. 203, No. 2, 2005, pp. 405–421.
- [13] Kolobov, V. I., Bayyuk, S. A., Arslanbekov, R. R., Aristov, V. V., Frolova, A. A., and Zabelok, S. A., “Construction of a Unified Continuum/Kinetic Solver for Aerodynamic Problems,” *Journal of Spacecrafts and Rockets*, Vol. 42, No. 4, July–August 2005, pp. 598–606.
- [14] Bird, G. A., “Breakdown of Translational and Rotational Equilibrium in Gaseous Expansions,” *AIAA Journal*, Vol. 8, No. 11, 1970, p. 1997.
- [15] Boyd, I. D., Chen, G., and Candler, G., “Predicting the Failure of the Continuum Fluid Equations in Transitional Hypersonic Flows,” *Physics of Fluids*, Vol. 7, 1995, pp. 210–221.
- [16] Wang, W. L., Sun, Q., and Boyd, I. D., “Towards Development of a Hybrid DSMC-CFD Method for Simulating Hypersonic Interacting Flows,” AIAA Paper 2002-3099, 2002.

- [17] Capitelli, M. (ed.), *Nonequilibrium Chemical Kinetics*, Springer-Verlag, Berlin, 1986.
- [18] Chernyi, G. G., Losev, S. A., Macheret, S. O., and Potapkin, B. V., "Physical and Chemical Processes in Gas Dynamics: Cross Sections and Rate Constants for Physical and Chemical Processes, Volume I," *Progress in Astronautics and Aeronautics*, Vol. 196, 2002.
- [19] Chernyi, G. G., Losev, S. A., Macheret, S. O., and Potapkin, B. V., "Physical and Chemical Processes in Gas Dynamics: Physical and Chemical Kinetics and Thermodynamics, Volume II," *Progress in Astronautics and Aeronautics*, Vol. 197, 2004.
- [20] Rich, J. W., Macheret, S. O., and Adamovich, I. V., "Aerothermodynamics of vibrationally excited gases," *Experimental Thermal and Fluid Science*, Vol. 13, No. 1, 1996, pp. 1–10.
- [21] Adamovich, I. V., Macheret, S. O., Rich, J. W., and Treanor, C. E., "Vibrational Relaxation and Dissociation Behind Shock Waves Part 1: Kinetic Rate Models," *AIAA Journal*, Vol. 33, No. 6, 1995, pp. 1064–1069.
- [22] Eppard, W. M., and Godfrey, A. G., "Damköhler Limiting of Chemical Time Scales," *AIAA Paper 2005-1400*, 2005.
- [23] Pandolfi, M., Arina, R., and Botta, N., "Nonequilibrium Hypersonic Flows over Corners," *AIAA Journal*, Vol. 29, No. 2, February 1991, pp. 235–241.
- [24] Inger, G. R., "Scaling Nonequilibrium-Reacting Flows: The Legacy of Gerhard Damköhler," *Journal of Spacecraft and Rockets*, Vol. 38, No. 2, March–April 2001, pp. 185–190.
- [25] Inger, G. R., Higgins, C., and Morgan, R., "Shock Standoff on Hypersonic Blunt Bodies in Nonequilibrium Gas Flows," *AIAA Paper 2001-0812*, 2001.
- [26] Osipov, A. I., and Stupochenko, E. V., "Kinetics of the Thermal Dissociation of Diatomic Molecules I. Small Impurity of Diatomic Molecules in a Monoatomic Inert Gas," *Combustion, Explosion and Shock Waves, Translated from Fizika Gorenija i Vzryva*, Vol. 10, No. 3, 1974, pp. 303–313.
- [27] Billing, G. D., "Rate Constants and Cross Sections for Vibrational Transitions in Atom–Diatom and Diatom–Diatom Collisions," *Computer Physics Communications*, Vol. 32, No. 1, 1984, pp. 45–62.
- [28] Billing, G. D., "Rate Constants for Vibrational Transitions in Diatom–Diatom Collisions," *Computer Physics Communications*, Vol. 44, No. 3, 1987, pp. 121–136.
- [29] Billing, G. D., "Vibration–Vibration and Vibration–Translation Energy Transfer, Including Multiquantum Transitions in Atom–Diatom and Diatom–Diatom Collisions," *Topics in Current Physics*, edited by M. Capitelli, Springer-Verlag, Berlin/New York/Heidelberg, 1986, pp. 85–111.
- [30] Capitelli, M., Gorse, C., and Billing, G. D., "V–V Pumping Up in Nonequilibrium Nitrogen: Effects on the Dissociation Rate," *Chemical Physics*, Vol. 52, No. 3, 1980, pp. 299–304.
- [31] Billing, G. D., and Fisher, E. R., "VV and VT Rate Coefficients in Diatomic Nitrogen by a Quantum Classical Model," *Chemical Physics*, Vol. 43, No. 3, 1979, pp. 395–401.
- [32] Macheret, S. O., and Adamovich, I. V., "Semiclassical Modeling of State-Specific Dissociation Rates in Diatomic Gases," *Journal of Chemical Physics*, Vol. 113, No. 17, Nov. 2000, pp. 7351–7361.

- [33] Adamovich, I. V., and Rich, J. W., "Three-dimensional Nonperturbative Analytic Model of Vibrational Energy Transfer in Atom–Molecule Collisions," *Journal of Chemical Physics*, Vol. 109, No. 18, Nov. 1998, pp. 7711–7724.
- [34] Boyd, I. D., and Josyula, E., "State Resolved Vibrational Relaxation Modeling for Strongly Nonequilibrium Flows," *Physics of Fluids*, Vol. 23(017101), No. 5, 2011, pp. 057101-1–057101-9.
- [35] Josyula, E., Bailey, W. F., and Suchyta, C. J., III, "Dissociation Modeling in Hypersonic Flows Using State-to-State Kinetics," *Journal of Thermophysics and Heat Transfer*, Vol. 25, No. 1, Jan.–March 2011.
- [36] Galina, C., Jaffe, R., Schwenke, D. W., and Huo, W. "Dissociation Cross-Sections and Rate Coefficients for Nitrogen from Accurate Theoretical Calculations," AIAA Paper 2008-1209, Jan. 2008.
- [37] da Silva, M. L., Guerra, V., and Loureiro, J., "Nonequilibrium Dissociation Processes in Hyperbolic Atmospheric Entries," *Journal of Thermophysics and Heat Transfer*, Vol. 21, No. 2, April–June 2007, pp. 303–310.
- [38] Shui, V. H., Appleton, J. P., and Keck, J. C., "Three-Body Recombination and Dissociation of Nitrogen: A Comparison between Theory and Experiment," *Journal of Chemical Physics*, Vol. 53, No. 7, 1970, pp. 2547–2558.
- [39] Armenise, I., Capitelli, M., Colonna, G., Koudriavtsev, N., and Smetanin, V., "Nonequilibrium Vibrational Kinetics during Hypersonic Flow of Solid Bodies in Nitrogen and its Influence on the Surface Heat Flux," *Plasma Chemistry and Plasma Processing*, Vol. 15, No. 3, 1995, pp. 501–528.
- [40] Colonna, G., and Capitelli, M., "The Influence of Atomic and Molecular Metastable States in High-Enthalpy Nozzle Expansion Nitrogen Flows," *Journal of Physics D: Applied Physics*, Vol. 34, No. 2, pp. 1812–1818, Oct. 2001.
- [41] Josyula, E., "Effect of Oxygen Atoms' on Vibrational Relaxation of Nitrogen in Blunt-Body Flows," *Journal of Thermophysics and Heat Transfer*, Vol. 15, No. 1, Jan–Mar 2001, pp. 106–115.
- [42] Josyula, E., and Bailey, W. F., "Vibrational Population Enhancement in Nonequilibrium Dissociating Hypersonic Nozzle Flows," *Journal of Thermophysics and Heat Transfer*, Vol. 18, No. 4, 2004, pp. 550–553.
- [43] Colonna, G., Armenise, I., Bruno, D., and Capitelli, M., "Reduction of State-to-State Kinetics to Macroscopic Models in Hypersonic Flows," *Journal of Thermophysics and Heat Transfer*, Vol. 20, No. 3, July–September 2006, pp. 477–486.
- [44] Doraiswamy, S., Kelley, J. D., and Candler, G. V., "Energy Bin Modeling for High-Enthalpy Flows Using Prior Recombination Distribution," *Journal of Thermophysics and Heat Transfer*, Vol. 26, No. 4, Oct.–Dec. 2012, pp. 545–558.
- [45] Guy, A., Bourdon, A., and Perrin, M.-Y., "Consistent Multi-Internal-Temperature Models for Nonequilibrium," *Chemical Physics*, Vol. 420, 2013, pp. 15–24.
- [46] Armenise, I., Esposito, F., and Capitelli, M., "Dissociation–Recombination Models in Hypersonic Boundary Layers," *Chemical Physics*, Vol. 336, 2007, pp. 83–90.
- [47] Esposito, F., and Capitelli, M., "QCT Calculations for the Process $\text{N}_2(v) + \text{N} \rightarrow \text{N}_2(v') + \text{N}$," *Chemical Physics Letters*, Vol. 418, No. 4–6, 2006, pp. 581–585.
- [48] Armenise, I., Capitelli, M., and Gorse, C., "Nitrogen Nonequilibrium Vibrational Distributions and Non-Arrhenius Dissociation Constants in Hypersonic Boundary Layers," *Journal of Thermophysics and Heat Transfer*, Vol. 12, No. 1, Jan.–March 1998, pp. 45–51.

- [49] Armenise, I., and Capitelli, M., "State to State Vibrational Kinetics in the Boundary Layer of an Entering Body in Earth Atmosphere: Particle Distributions and Chemical Kinetics," *Plasma Sources Science and Technology*, Vol. 14, No. 2, May 2005, pp. S9–S17.
- [50] Lee, J. H., "Basic Governing Equations for the Flight Regimes of Aeroassisted Orbital Transfer Vehicles," *Progress in Astronautics and Aeronautics: Thermal Design of Aeroassisted Orbital Transfer Vehicles*, Vol. 96, 1985, pp. 3–53.
- [51] Shang, J. S., and Surzhikov, S. T., "Simulating Stardust Earth Reentry with Radiation Heat Transfer," *Journal of Spacecraft and Rockets*, Vol. 48, No. 3, May–June 2011, pp. 385–396.
- [52] Ferziger, J. H., and Kaper, H. G., *Mathematical Theory of Transport Processes in Gases*, North Holland Publishing Company, New York, 1972.
- [53] Nagnibeda, E., and Kustova, E., *Non-Equilibrium Reacting Gas Flows*, Springer-Verlag, 2009.
- [54] Kustova, E. V., "On the Simplified State-to-State Transport Coefficients," *Chemical Physics*, Vol. 270, No. 1, 2001, pp. 177–195.
- [55] Chikhaoui, A., Dudon, J. P., Kustova, E. V., and Nagnibeda, E. A., "Transport Properties in Reacting Mixture of Polyatomic Gases," *Physica A*, Vol. 247, No. 1–4, 1997, pp. 526–552.
- [56] Josyula, E., and Bailey, W. F., "Governing Equations for Weakly Ionized Plasma Flowfields of Aerospace Vehicles," *Journal of Spacecraft and Rockets*, Vol. 40, No. 6, Nov.–Dec. 2003, pp. 845–857.
- [57] Appleton, J. P., and Bray, K. N. C., "The Conservation Equations for a Nonequilibrium Plasma," *Journal of Fluid Mechanics*, Vol. 20, No. 4, 1964, pp. 659–672.
- [58] Capitelli, M., Bruno, D., and Laricchiuta, A., *Fundamental Aspects of Plasma Chemical Physics*, Springer-Verlag, Berlin/New York/Heidelberg, 2013.
- [59] Brun, R., *High Temperature Phenomena in Shock Waves* Springer-Verlag, Berlin/New York/Heidelberg, 2012.
- [60] Dellacherie, S., "On the Wang–Chang–Uhlenbeck Equation," *Discrete and Continuous Dynamical Systems-Series B*, Vol. 3, No. 2, 2003, pp. 229–253.
- [61] Dellacherie, S., "Coupling the Wang–Chang–Uhlenbeck Equations with the Multispecies Euler System," *Journal of Computational Physics*, Vol. 189, No. 1, 2003, pp. 239–276.
- [62] Vincenti, W. G., and Kruger, C. H., Jr., *Introduction to Physical Gas Dynamics*. Wiley, New York, 1967.
- [63] Kustova, E. V., and Chikhaoui, A., "Kinetic Modelling of Radiative Reacting Gas Flow Under Strong Nonequilibrium Conditions," *Chemical Physics*, Vol. 255 2000, pp. 59–71.
- [64] Kustova, E. V., Aliat, A., and Chikhaoui, A., "Vibration–Electronic and Chemical Kinetics of Non-Equilibrium Radiative Diatomic Gas Flows," *Chemical Physics Letters*, Vol. 344, No. 5–6, 2001, pp. 638–646.
- [65] Anderson, J. B., Foch, J. D., Stern, R. C., and Wu, B. J., "Statistical Theory of Electronic Energy Relaxation," *Rarefied Gas Dynamics: 15th International Symposium*, Ed: Vinkio Botti, and B.G. Carlo Cercignani Teubner, Stuttgart, 1986.
- [66] Josyula, E., Xu, K., Suchyta, C. J., III, and Bailey, W. F., Kinetic Methods for Solving the Internal Structure of Shock Waves. AIAA Paper 2009–3841, June 2009.

- [67] Chapman, S., and Cowling, T. G., *The Mathematical Theory of Non-Uniform Gases*. Cambridge University Press, New York, 1990.
- [68] Kustova, E. V., and Nagnibeda, E. A., “Strong Nonequilibrium Effects on Specific Heats and Thermal Conductivity of Diatomic Gas,” *Chemical Physics*, Vol. 208, 1996, pp. 313–329.
- [69] Kustova, E. V., and Nagnibeda, E. A., “Transport Properties of a Reacting Gas Mixture with Strong Vibrational and Chemical Nonequilibrium,” *Chemical Physics*, Vol. 233, No. 1, 1998, pp. 57–75.
- [70] Parker, J. G., “Rotational and Vibrational Relaxation in Diatomic Gases,” *Physics of Fluids*, Vol. 2, No. 4, 1959, pp. 449–462.
- [71] Josyula, E., Burt, J. M., Bailey, W. F., and Vedula, P., “Role of State-to-State Kinetics in Determining Transport Coefficients for Hypersonic Flow Simulations,” *The Open Plasma Physics Journal*, Vol. 7(Suppl 1:M11), 2014, pp. 173–180.
- [72] Aliat, A., Chikhaoui, A., and Kustova, E. V., “Nonequilibrium Kinetics of a Radiative CO Flow Behind a Shock Wave,” *Physical Review E*, Vol. 68(056306), No. 5, 2003, pp. 056306-1–056306-11.
- [73] Bruno, D., Capitelli, M., Kustova, E., and Nagnibeda, E., “Non-equilibrium Vibrational Distributions and Dransport Coefficients of N₂(v)-N Mixtures,” *Chemical Physics Letters*, Vol. 308, No. 5–6, 1999, pp. 463–472.
- [74] Josyula, E. “Computational Study of vibrationally Relaxing Gas Past Blunt Body in Hypersonic Flows,” *Journal of Thermophysics and Heat Transfer*, Vol. 14, No. 1, Jan. 2000, pp. 18–26.
- [75] Huber, K. P., and Herzberg, G., *Constants of Diatomic Molecules*, Van Nostrand Reinhold Company, New York, 1979, pp. 420–421
- [76] Panesi, M., Jaffe, R. L., Schwenke, D. W., and Magin, T. E., “Rovibrational Internal Energy Transfer and Dissociation of N₂(¹Σ_g⁺) – N(⁴S_u),” *The Journal of Chemical Physics*, Vol. 138(044312), No. 4, 2013, pp. 044312-1–044312-16.
- [77] Josyula, E., Gaitonde, D., and Shang, J. S., “Hypersonic Nonequilibrium Flow Computations Using the Roe Flux-Difference Split Scheme,” *AIAA Journal*, Vol. 31, No. 5, 1993 pp. 812–813.
- [78] Walters, R. W., Cinnella, P., and Slack, D. C., “Characteristic-Based Algorithms for Flows in Thermochemical Non-equilibrium,” *AIAA Journal*, Vol. 30, No. 5, 1992, pp. 1304–1313.
- [79] Vedula, P., and Josyula, E. “Numerical Simulation of Hypersonic Blunt Body and Nozzle Flows using Master Equation,” *AIAA Paper 2010-4331*, 2010.
- [80] Knio, O. M., Najm, H. N., and Wyckoff, P. S., “A Semi-Implicit Numerical Scheme for Reacting Flow II. Stiff, Operator-split Formulation,” *Journal of Computational Physics*, Vol. 154, No. 2, 1999, pp. 428–467.
- [81] Ren, Z., and Pope, S. B. “Second-order Splitting Schemes for a Class of Reactive Systems,” *Journal of Computational Physics*, Vol. 227, No. 17, 2008, pp. 8165–8176.
- [82] Singer, M. A., Pope, S. B., and Najm, H. N., “Operator-splitting with ISAT to Model Reacting Flow with Detailed Chemistry,” *Combustion Theory and Modelling*, Vol. 10, No. 2, 2006, pp. 199–217.
- [83] Strang, G., “On the Construction and Comparison of Difference Schemes,” *SIAM Journal of Numerical Analysis*, Vol. 5, No. 3, 1968, pp. 506–517.

- [84] Kim, J., and Cho, S. Y., "Computation Accuracy of Time-splitting Method in Solving Atmospheric Transport/Chemistry Equations," *Atmospheric Environment*, Vol. 31, No. 15, 1997, pp. 2215–2224.
- [85] Harten, A., Lax, P. D., and van Leer, B., "Upstream Differencing and Godunov-type Schemes for Hyperbolic Conservation Laws," *SIAM Review*, Vol. 25, No. 1, 1983, pp. 35–61.
- [86] Aliat, A., Vedula, P., and Josyula, E., "State-to-State Modeling of Radiation Coupled to Vibrational–Translational Relaxation and Dissociation in Nonequilibrium Gas Flow," *Physical Review E*, Vol. 83(067302), No. 6, 2011, pp. 067302-1–067302-4.
- [87] Josyula, E., Aliat, P., and Vedula, A., "Multiquantum State-to-State Transitions in Hypersonic Blunt Body Flows," AIAA Paper 2011-532, 2011.
- [88] Josyula, E., and Bailey, W. F., "Vibration–Dissociation Coupling using Master Equations in Nonequilibrium Hypersonic Blunt-Body Flow," *Journal of Thermophysics and Heat Transfer*, Vol. 15, No. 2, April–June 2001, pp. 157–167.
- [89] Aliat, A., Vedula, P., and Josyula, E., "Simple Model for Vibration–Translation Exchange at High Temperatures: Effects of Multiquantum Transitions on the Relaxation of a N₂ Gas Flow Behind a Shock," *Physical Review E*, Vol. 83(026308), No. 2, 2011, pp. 026308-1–026308-11.
- [90] Aliat, A., Vedula, P., and Josyula, E., "State-Specific Dissociation Modeling with Multiquantum Vibration–Translation Transitions," *Physical Review E*, Vol. 83(037301), No. 3, 2011, pp. 037301-1–037301-4.
- [91] Lin, S.-C., and Teare, J. D., "Rate of Ionization Behind Shock Waves in Air. II. Theoretical Interpretations," *Physics of Fluids*, Vol. 6, No. 3, March 1963, pp. 355–375.
- [92] Wilson, J., "Ionization Rate of Air behind High-Speed Shock Waves," *Physics of Fluids*, Vol. 9, No. 10, Oct. 1066, pp. 1913–1921.
- [93] Park, C., *Nonequilibrium Hypersonic Aerothermodynamics*, Wiley, New York, 1990.
- [94] Gupta, R. N., Lee, K. P., Thompson, R. A., and Yos, J. M., "A Review of Reaction Rates and Transport Properties for an 11-Species Air Model for Chemical and Thermal Nonequilibrium Calculations to 30000 K," Technical Report NASA TM 85820, NASA Langley Research Center, Hampton, VA, 1990.
- [95] Park, C., "On Convergence of Computation of Chemically Reacting Flows," AIAA Paper 85-0247, January 1985.
- [96] Wray, K. L., "Chemical Kinetics of High Temperature Air," *ARS Progress in Astronautics and Rocketry; Hypersonic Flow Research*, edited by F. R. Riddell, Vol. 7, Academic Press, New York, 1962, pp. 181–204.
- [97] Park, C., and Yoon, S., "A Fully-Coupled Implicit Method for Thermo-Chemical Nonequilibrium Air at Sub-Orbital Flight Speeds," AIAA Paper 89-1974, 1989.
- [98] Park, C., "Calculation of Real-Gas Effects on Blunt-Body Trim Angles," *AIAA Journal*, Vol. 30, No. 4, April 1992, pp. 999–1006.
- [99] Bose, D., and Candler, G. Z., "Advanced Model of Nitric Oxide Formation in Hypersonic Flows," *Journal of Thermophysics and Heat Transfer*, Vol. 12, No. 2, April–June 1998, pp. 214–222.
- [100] Candler, G. V., and MacCormack, R. W., "Computation of Weakly Ionized Hypersonic Flows in Thermochemical Nonequilibrium," *Journal of Thermophysics and Heat Transfer*, Vol. 5, No. 3, July 1991, pp. 266–273.
- [101] Grasso, G., and Capano, G., "Modeling of Ionizing Hypersonic Flows in Nonequilibrium," *Journal of Spacecraft and Rockets*, Vol. 32, No. 2, 1995, pp. 217–224.

Computation of Hypersonic Nonequilibrium Flows using the Direct Simulation Monte Carlo Method

Iain D. Boyd*

University of Michigan, Ann Arbor, Michigan

I. INTRODUCTION

The analysis of dilute gas flows at all Knudsen numbers can be derived from the Boltzmann equation that describes the evolution of the molecular Velocity Distribution Function (VDF) [1]. In the absence of a body force, the Boltzmann equation is written:

$$\frac{\partial}{\partial t}(nf) + \bar{C} \cdot \frac{\partial}{\partial \bar{r}}(nf) = \Delta(f) \quad (1)$$

where f is the VDF, n is the number density, \bar{C} is the particle velocity vector, \bar{r} is the particle position vector, t is time, and $\Delta(f)$ represents the rate of change in the VDF owing to collision processes. Here, “particle” refers to an atom or molecule. The equilibrium solution of the Boltzmann equation is the Maxwellian VDF:

$$f(\bar{C})d\bar{C} = \left(\frac{m}{2\pi kT}\right)^{3/2} \exp\left(-\frac{mC^2}{2kT}\right)d\bar{C} \quad (2)$$

where m is the mass of a particle, k is Boltzmann’s constant, and T is the temperature. The left-hand side of Eq. (2) represents the probability of finding a particle within the finite region of velocity space between \bar{C} and $\bar{C} + d\bar{C}$. The physical mechanism that maintains the VDF in equilibrium is inter-molecular collisions, and so a gas falls into a nonequilibrium state under conditions where there are not a large enough number of collisions occurring to maintain equilibrium. The two main physical flow conditions that lead to nonequilibrium are low density and small length scales. A low density leads to a reduced collision rate while a small length scale reduces the size of a fluid element. The

*James E. Knott Professor of Engineering

usual metric for determining whether a particular gas flow is in a state of nonequilibrium is the Knudsen number defined as follows:

$$Kn = \frac{\lambda}{L} \quad (3)$$

where λ is the mean free path of the gas and L is the characteristic length scale. The mean free path is the average distance traveled by each particle between collisions and is given for a hard sphere by

$$\lambda = \frac{1}{\sqrt{2n\sigma}} \quad (4)$$

where n is again the number density, and σ is the hard sphere collision cross section. Thus, at low density, the mean free path (and therefore Kn) becomes large. Similarly, for small length scales, L becomes small and again Kn becomes large. As a guiding rule, it is generally accepted that kinetic nonequilibrium effects become important when $Kn > 0.01$.

At a Knudsen number near zero, the velocity distribution function everywhere in a flow field has the Maxwellian form, there are no molecular transport processes, such as viscosity and thermal conductivity, and the flow may be modeled using the Euler equations. Indeed, the Euler equations of fluid flow can be derived by taking moments of the Boltzmann equation and evaluating them using the Maxwellian VDF. As the Knudsen number increases up to values below 0.01, the velocity distribution function in the flow field may be represented as a small perturbation from the equilibrium Maxwellian form that is known as the Chapman–Enskog distribution [1]. Evaluation of moments of the Boltzmann equation using the Chapman–Enskog VDF leads to the Navier–Stokes equations in which shear stress and heat flux depend linearly on the spatial gradients of velocity and temperature, respectively. As the Knudsen number rises above 0.01, these linear transport relations are unable to accurately describe the strong nonequilibrium processes. It is then necessary to develop higher order sets of partial differential equations (such as the Burnett equations) or to solve the Boltzmann equation. Although there has been some success achieved in formulating and solving the Burnett equations, there remain issues with boundary conditions, and it is not clear that the amount of additional Knudsen number range provided is worth the significant additional effort in numerical analysis. Unfortunately, development of robust and general numerical solution schemes for the Boltzmann equation has also proved a significant challenge, particularly for high speed flows. Again, some progress has been made, but there is still much work to be done to be able to simulate all of the flow physics of interest in hypersonic flows.

The direct simulation Monte Carlo (DSMC) method was first introduced by Graeme Bird in 1961 [2] specifically to analyze high Knudsen number flows. Since that time, books have been written on the method [3, 4] and

thousands of research papers have been published that report on development and application of the technique. The significance of the DSMC technique has been its ability over 40 years of development to fill the void described above in gas analysis methodology for high Knudsen number flows. The DSMC technique emulates the same physics as the Boltzmann equation without providing a direct solution. The DSMC method follows a representative set of particles as they collide and move in physical space. It has been demonstrated that DSMC converges to solution of the Boltzmann equation in the limit of a very large number of particles [4].

High Knudsen number conditions arise in many areas of science and technology including space and atmospheric science, vapor processing of materials, spacecraft propulsion systems, and micro-scale gas flows. As illustrated in Fig. 1, hypersonic flow conditions may fall into the kinetic nonequilibrium regime at sufficiently low density (that occurs at high altitude in the Earth's atmosphere) and for very small hypersonic objects (e.g. meteoroids that have a diameter on the order of a centimeter [5]). In addition, situations arise where localized regions of a flow may contain low density (e.g. the wake behind a capsule) or small length scales (e.g. sharp leading edges on a vehicle, or shock waves and boundary layers that may have very steep spatial gradients in flow field properties).

For hypersonic flows, it is an important question to ask whether high Knudsen number phenomena lead to effects that are of practical significance. Detailed studies [6–8] have compared DSMC and CFD computations of hypersonic flows over cylinders and wedges for global Knudsen numbers ranging from continuum ($Kn = 0.002$) to rarefied ($Kn = 0.25$). The focus of the studies was the effect of any nonequilibrium flow phenomena on surface properties such as drag and heat transfer. It was found at $Kn = 0.002$ that DSMC and CFD gave identical results for all surface properties including drag force and peak heat transfer. However, as Kn was increased, the differences between

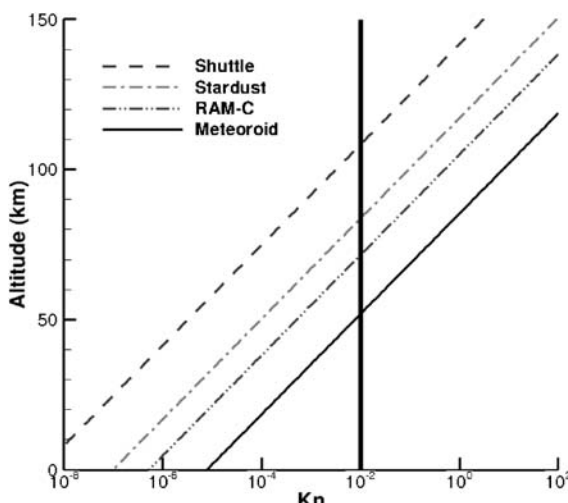


Fig. 1 Knudsen number profiles in the Earth's atmosphere for several hypersonic entry bodies.

DSMC and CFD surface results also grew larger. For example, in Mach 25 flow of nitrogen over a cylinder at the highest Knudsen number of 0.25, in comparison to CFD, DSMC predicted a 23% lower drag force and a 29% lower peak heat flux. These differences are clearly significant and indicate that accurate determination of surface properties in high Knudsen number flows does require a non-continuum, kinetic approach, such as DSMC.

An important part of the success of the DSMC technique in analyzing high Knudsen number hypersonic flows, has been the ability to include in the technique models that are effective in simulating high temperature, real gas effects. Such effects include mixtures of chemical species, relaxation of internal energy modes, chemical reactions such as dissociation and ionization, radiation, and gas–surface interaction. In this article, the fundamental aspects of the DSMC technique are described with an emphasis on physical modeling issues related to its application to hypersonic problems and the simulation of the associated real gas effects. Examples are provided that illustrate the current capabilities of these models and areas where further work is needed are identified. The application of the DSMC technique to the analysis of hypersonic flows is then discussed.

II. BASIC ALGORITHM OF THE DSMC TECHNIQUE

The DSMC technique emulates the physics of the Boltzmann equation by following the motions and collisions of a large number of model particles. Each particle possesses molecular level information including a position vector, a velocity vector, and physical information such as mass and size. Particle motion and collisions are decoupled over a time step Δt that is smaller than the local mean free time. During the movement of particles, boundary conditions such as reflection from solid surfaces are applied. The physical domain to be simulated in a DSMC computation is covered by a mesh of cells. These cells are used to collect together particles that may collide. There are a number of DSMC schemes for simulating collisions and all of them achieve a faster numerical performance than the molecular dynamics (MD) method [9]. The enhanced numerical performance obtained by DSMC is a result of several aspects including the statistical rather than deterministic selection of colliding particles, and allowing each DSMC particle to represent a large number of real molecules. The DSMC collision selection approach requires that the size of each cell be less than the local mean free path of the flow. Bird's No Time Counter (NTC) scheme [4] is the most widely used collision scheme in which a number of particle pairs in a cell are formed that is given by:

$$N_c = \frac{1}{2} n \bar{N} (\sigma g)_{\max} \Delta t \quad (5)$$

where n is the number density, \bar{N} is the average number of particles in the cell, σ is the collision cross section, and g is the relative velocity. Each of the N_c pairs of

particles is formed at random regardless of position in the cell, and then a probability of collision for each pair is evaluated using:

$$P_c = \frac{\sigma g}{(\sigma g)_{\max}} \quad (6)$$

This procedure reproduces the expected equilibrium collision rate under conditions of equilibrium. It is determined whether the particle pair actually collides by comparing the collision probability, P_c , to a random number. When a collision occurs, post-collision velocities are calculated using conservation of momentum and energy.

The cells employed for simulating collisions are also often used for the sampling of macroscopic flow properties such as density, velocity, and temperature. There is no necessity to have the collision and sampling cells be identical, however, and sometimes a coarser mesh is used for sampling.

The basic steps in each iteration of the DSMC method are: (1) move particles over the time step Δt ; (2) apply boundary conditions such as introducing new particles at inflow boundaries, removing particles at outflow boundaries, and processing reflections at solid boundaries; (3) sort particles into cells and calculate collisions; and (4) sample average particle information. As an example of how sampled particle information is employed to determine a macroscopic flow property, the average mass density in a computational cell of volume V is given by

$$\rho = \frac{\sum_{i=1}^{N_p} m_i}{V \times N_t} \quad (7)$$

where m_i is the mass of particle i , N_p is the total number of particles that have occupied this cell over N_t iterations of the computation. Also, as an illustration of the determination of surface properties, for a surface element of area A , the average shear stress is given by

$$\tau_w = \frac{\sum_j m_j (u_t^i - u_t^r)_j}{A \times N_t \times \Delta t} \quad (8)$$

where u_t^i and u_t^r are the incident and reflected velocity components tangent to the surface element of each particle j to hit the element during N_t iterations of the computation.

A simulation begins from some initial condition, and a finite number of iterations must elapse in order for the flow to reach a steady state. Generally, steady state is detected as a leveling off of the total number of particles in the simulation. After steady state is reached, sampling of flow field and surface properties begins and the simulation is continued a further number of iterations in order to reduce the statistical noise in the sampled information to an acceptable level. A typical DSMC computation may employ one million particles, reach steady state after

50,000 iterations, and continue sampling for a further 50,000 iterations. On a modern desktop computer, such a simulation should take about 3 h.

The DSMC method uses a mesh to collect together particles that should be considered for collision and for the output of averaged information. A variety of approaches to grid handling has been considered from the use of multi-level Cartesian cells with cut-cells employed at surfaces, to body-fitted, solution-adapted unstructured meshes.

The DSMC algorithm allows a simulation to evolve in time, and so it is certainly possible to use the method to analyze unsteady flows. The main challenge is in the significant statistical fluctuations that will arise through evaluation of flow properties over a single iteration. Such fluctuations may be reduced by averaging flow properties over small but finite numbers of iterations, and/or by performing ensemble averaging where the entire simulation is repeated several times.

While the ideas behind the DSMC technique are simple, implementation in an algorithm takes on many different forms. Specific DSMC algorithms have been developed for vector computers [10] and parallel computers [11, 12]. Bird has focused work on customizing the algorithm to achieve efficient performance on single processor machines [13]. In addition, a number of more elaborate DSMC procedures have been proposed to improve the handling of specific situations. Examples include: sub-cells, to improve localization of colliding particles; spatially varying time steps: to reduce the cost of flows containing a very broad range of time scales, such as nozzles and plumes; and, weighting schemes, to allow resolution of trace species.

Having provided a general overview of the basic elements of the DSMC method, in the following sections some of the physical models are described that are most critical to the application of the DSMC technique to analyze hypersonic flows.

III. PHYSICAL MODELS OF THE DSMC TECHNIQUE

In this section, the most commonly employed physical models are reviewed for DSMC computation of hypersonic flows. The basic ideas are described for simulation of a number of physical phenomena including momentum exchange, internal energy relaxation, chemical reactions, and gas-surface interactions. Where possible, examples are provided of efforts to validate these models using laboratory data.

A. ELASTIC MOMENTUM EXCHANGE

In the absence of internal energy exchange and chemical reactions, an elastic collision between two particles leads only to changes in their velocity (or momentum) components. The frequency of such interactions is determined by the collision cross section for which a number of models have been developed

for DSMC. The most widely used forms are the Variable Hard Sphere (VHS) [14] and the Variable Soft Sphere (VSS) [15]. For hypersonic flow, the VHS model is usually considered sufficiently accurate, for which the cross section is given as:

$$\sigma = \sigma_{\text{ref}} \left(\frac{g}{g_{\text{ref}}} \right)^{-2\omega} \quad (9)$$

where σ_{ref} and g_{ref} are reference values, and ω is related to the viscosity temperature exponent. Specifically, it is assumed that the gas viscosity is described by a simple temperature relation:

$$\mu = \mu_{\text{ref}} \left(\frac{T}{T_{\text{ref}}} \right)^{0.5+\omega} \quad (10)$$

and the relationship between the reference parameters is provided by Bird [4]. Values of these reference parameters for many common species are listed in Bird [4] and these are generally obtained by comparison with measured or computed viscosity data. For the VHS model, isotropic scattering is assumed in which the unit vector of the post-collision relative velocity is assigned at random on the unit sphere. The VSS model represents an improvement over VHS in that it allows collision parameters to be determined through comparison with both viscosity and diffusivity data. For example, the VSS cross-section scattering angle is given by:

$$\chi = 2\cos^{-1} \left\{ \left(\frac{b}{d} \right)^{1/\alpha} \right\} \quad (11)$$

where α is determined from diffusivity data, b is the distance of closest approach and d is the collision diameter. Again, values of α for common gases are provided by Bird [4]. Note that $\alpha = 1$ corresponds to the VHS model.

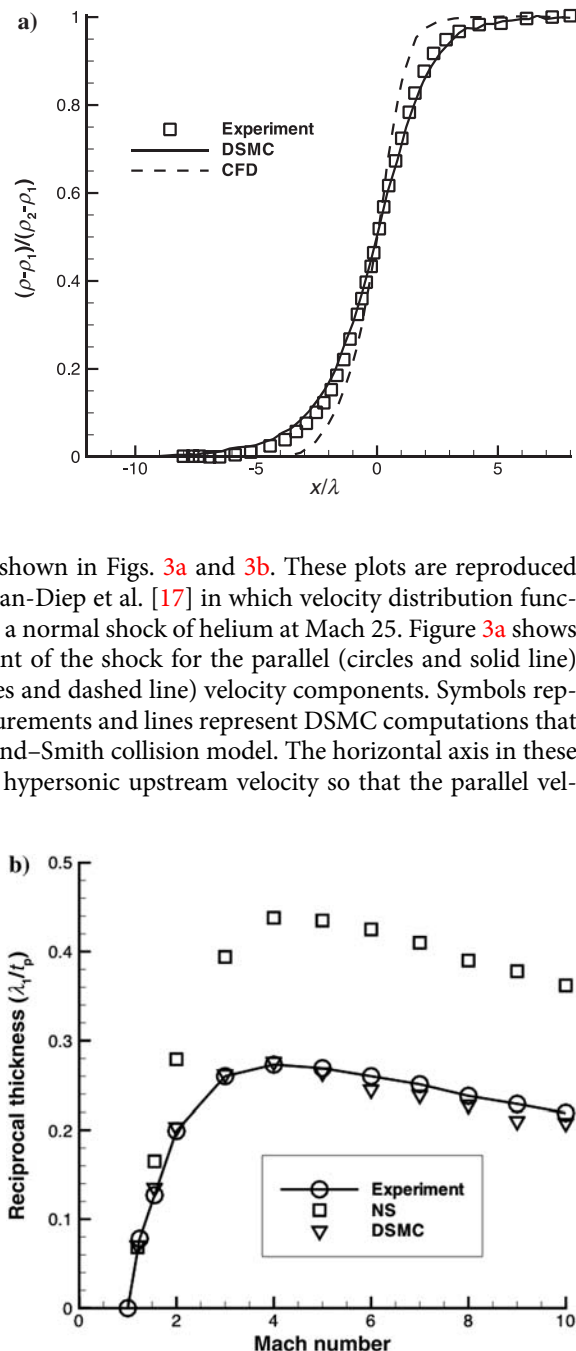
One of the most common test cases for evaluation of the DSMC technique in simulating nonequilibrium flows involving only elastic momentum exchange are normal shock waves of noble gases. Figure 2a shows the density profile through a normal shock wave at Mach 9 for argon. Detailed measurements were obtained using an electron beam technique by Alsmeyer at a number of different Mach numbers in both argon and nitrogen [16]. Included in Fig. 2a are both DSMC and CFD results. The DSMC computations used the VHS model while the CFD results solved the Navier-Stokes equations with the viscosity given by the same VHS parameters used in DSMC. The comparison shows that the DSMC technique is able to reproduce the measured data very accurately, whereas CFD predicts a shock wave that is too thin. Figure 2b shows the reciprocal shock thickness (a measure of the density gradient at $x/\lambda = 0$) for all the argon shock waves investigated by Alsmeyer [16]. Once again, it is clear that DSMC provides excellent agreement with the measurements for all conditions considered. CFD

Fig. 2a Profiles of normalized density through a Mach 9 normal shock wave of argon: measurements from [16].

consistently predicts an inverse shock thickness that is too large (that is, shocks that are too thin) for all Mach numbers above about 1.50. Another compelling validation of the capability of DSMC in simulating nonequilibrium hypersonic flows is pro-

vided by the comparisons shown in Figs. 3a and 3b. These plots are reproduced from the study by Pham-Van-Diep et al. [17] in which velocity distribution functions were examined inside a normal shock of helium at Mach 25. Figure 3a shows the distributions in the front of the shock for the parallel (circles and solid line) and perpendicular (triangles and dashed line) velocity components. Symbols represent electron beam measurements and lines represent DSMC computations that employed a detailed Maitland-Smith collision model. The horizontal axis in these plots is normalized by the hypersonic upstream velocity so that the parallel velocity distribution has its peak centered around 1.0 towards the right of the figure. The parallel velocity distribution shows a strong nonequilibrium profile with the higher velocity, lower temperature peak on the right, and a higher temperature, lower velocity peak towards the middle.

Fig. 2b Reciprocal shock thickness for normal shock waves of argon: measurements from [16].



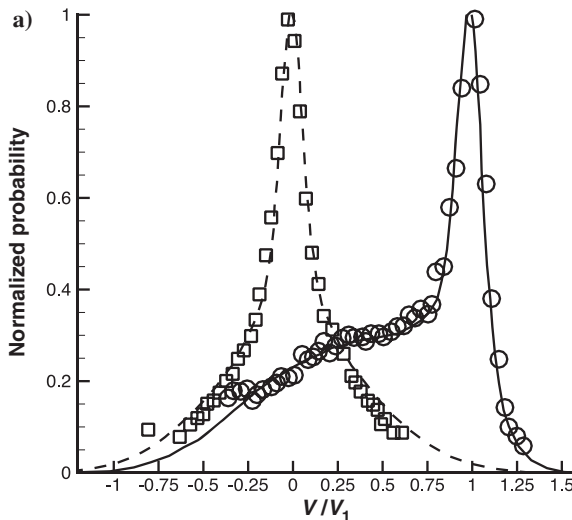


Fig. 3a Velocity distribution functions in the front a Mach 25 normal shock of helium: symbols = experiments; lines = DSMC [17].

profiles in Fig. 3b are obtained further downstream towards the middle of the shock and continue to show strongly nonequilibrium behavior. Clearly, the Navier-Stokes equations, that are based on a small perturbation from equilibrium, are not able to accurately model such phenomena. The excellent agreement with measured data shown in these plots is one of the strongest illustrations of the ability of the DSMC technique to reproduce nonequilibrium flow at the level of the distribution functions.

The main limitation of the VHS/VSS collision

The distribution of the perpendicular component is centered on zero and also consists of two distinct populations from the low temperature freestream and the high temperature post-shock regions. The pro-

models is their reliance on the need to model viscosity and diffusivity using a simple temperature exponent. Even for the common gases for which VHS/VSS parameters are provided by Bird [4], the viscosity dependence on temperature may change over a

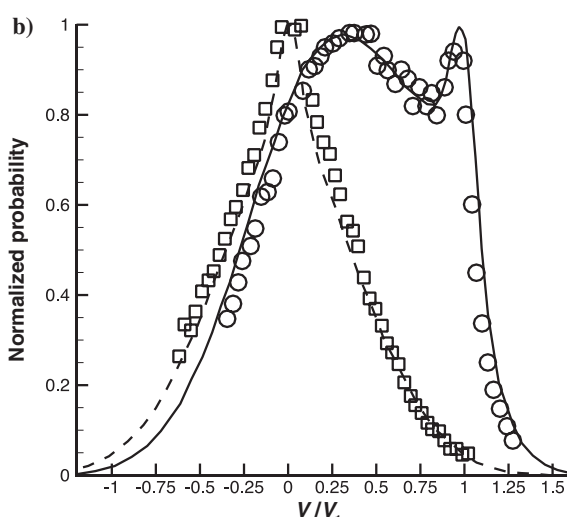
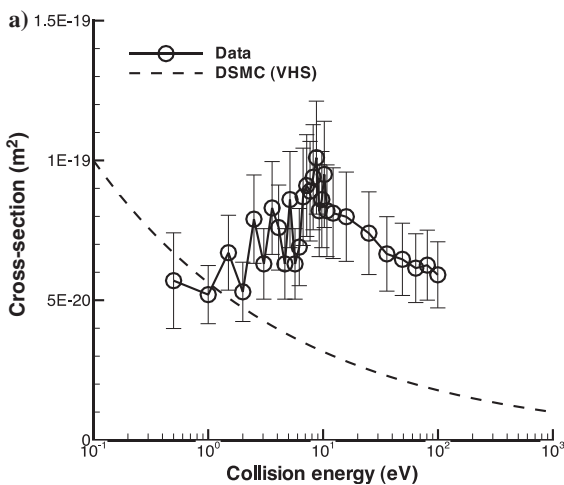


Fig. 3b Velocity distribution functions in the middle of a Mach 25 normal shock of helium: symbols = experiments; lines = DSMC [17].

Fig. 4a Electron-oxygen atom collision cross sections [18].

sufficiently wide temperature range. As an illustration of the types of problems encountered with the VHS/VSS models, Figs. 4a and 4b show collision cross sections as a function of collision energy for two different collisions involving electrons [18]. For such interactions, direct measurements of cross sections are available in the literature. Development of more general and detailed collision cross-section models for use in DSMC computations is an area where further work is required.

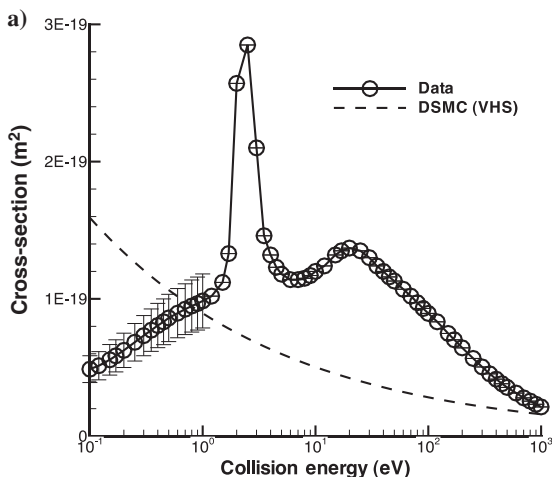


B. ROTATIONAL ENERGY EXCHANGE

The DSMC technique usually simulates the internal energy modes of molecules and atoms by assigning rotational, vibrational, and electronic energies to each particle. In hypersonic flows, generally the electronic modes are ignored, as is the case for CFD studies. Analysis of jet flows including electronic energy is described for example in [19]. We focus here on rotational and vibrational energy exchange.

The rotational mode is usually simulated using a classical physics approach in which the rotational

Fig. 4b Electron-nitrogen molecule collision cross sections [18].



energy, ε_r , is assumed continuously distributed at equilibrium according to a Boltzmann distribution:

$$f(\varepsilon_r) d\varepsilon_r = \frac{1}{\Gamma(\zeta/2)} \left(\frac{\varepsilon_r}{kT} \right)^{\zeta/2-1} \exp\left(-\frac{\varepsilon_r}{kT}\right) d\left(\frac{\varepsilon_r}{kT}\right) \quad (12)$$

where ζ is the number of rotational degrees of freedom ($=2$ for a diatomic molecule; $=3$ for a polyatomic molecule), k is Boltzmann's constant, and T is the temperature.

When a particle representing a molecule is injected into a DSMC computation, it is given an initial rotational energy sampled from Eq. (12). The rotational energy of the particle can change through collisions with other particles and through collisions with a solid surface (see Section III.G). In a continuum analysis of rotational energy exchange, the rotational relaxation equation of Jeans is usually employed:

$$\frac{de_r}{dt} = \frac{e_r^* - e_r}{\tau_r} \quad (13)$$

where e_r is the specific rotational energy, e_r^* is the equilibrium value at temperature T , and τ_r is the rotational relaxation time. The equivalent DSMC procedure involves evaluating a probability of rotational energy exchange for each collision followed by appropriate energy exchange mechanics for those collisions that lead to rotational relaxation. The average probability of rotational energy exchange is:

$$\langle P_{\text{rot}} \rangle = \frac{1}{Z_{\text{rot}}} = \frac{\tau_t}{\tau_r} = \frac{1}{\tau_r \nu} \quad (14)$$

where Z_{rot} is the rotational collision number, τ_t is the translational relaxation time that is equal to the inverse of the collision frequency, ν . Boyd [20] developed the following instantaneous rotational energy exchange probability based on Parker's model [21] for the rotational collision number and the VHS collision model:

$$P_{\text{rot}} = \frac{1}{(Z_{\text{rot}})_\infty} \left(1 + \frac{\Gamma(\zeta+2-\omega)}{\Gamma(\zeta+3/2-\omega)} \left(\frac{kT^*}{\varepsilon_{\text{tot}}} \right)^{\frac{1}{2}} \frac{\pi^{\frac{3}{2}}}{2} + \frac{\Gamma(\zeta+2-\omega)}{\Gamma(\zeta+1-\omega)} \left(\frac{kT^*}{\varepsilon_{\text{tot}}} \right) \left(\frac{\pi^2}{4} + \pi \right) \right) \quad (15)$$

where ε_{tot} is the total collision energy (the sum of the translational collision energy and the rotational energy), T^* is the characteristic temperature of the intermolecular potential, and $(Z_{\text{rot}})_\infty$ is the limiting value. After evaluation of the rotational energy exchange probability, a random number is used to decide whether the collision leads to energy exchange. For those collisions involving rotational energy exchange, the Borgnakke–Larsen (BL) model [22] is employed to assign new post-collision rotational energies. The BL model

assumes local thermodynamic equilibrium to sample the fraction of the total collision energy due to rotation, $\varepsilon_{\text{rot}}/\varepsilon_{\text{tot}}$, from the following expression:

$$\frac{P}{P_{\text{max}}} = \left(\frac{\zeta + 1 - \omega}{2 - \omega} \left(1 - \frac{\varepsilon_{\text{rot}}}{\varepsilon_{\text{tot}}} \right) \right)^{2-\omega} \left(\frac{\zeta + 1 - \omega}{\zeta - 1} \left(\frac{\varepsilon_{\text{rot}}}{\varepsilon_{\text{tot}}} \right) \right)^{\zeta-1} \quad (16)$$

Once the new rotational energy is assigned, the remaining energy is the new translational energy and hence determines the new post-collision relative velocity. The regular DSMC collision mechanics is then performed to calculate the velocities of the colliding particles.

Lumpkin et al. [23] noted that an additional correction must be applied to any DSMC rotational energy exchange probability in order to make BL exchange mechanics consistent with the continuum rotational relaxation equation, Eq. (13). The form of the correction is:

$$P_{\text{particle}} = P_{\text{continuum}} \left(1 + \frac{2\zeta}{4 - 2\omega} \right) \quad (17)$$

that is usually close to a factor of two.

While the rotational energy is usually simulated in the classical limit, a quantum mechanical approach for DSMC has also been developed by Boyd [24].

A detailed set of experimental measurements of hypersonic normal shock waves in nitrogen was collected by Robben and Talbot [25]. Again, an optical diagnostic technique was employed to measure both the density and the rotational energy distribution function through the shock wave for a number of different Mach numbers. Figure 5a compares DSMC simulations [24] with the measurements of the density and rotational temperature profiles at a Mach number of 12.9. Clearly, very good agreement between simulation and measurement is obtained.

Figure 5b shows rotational energy distribution functions measured at two different locations in this same shock wave. Once again, the excellent agreement obtained between DSMC and experiment at the level of the distribution function

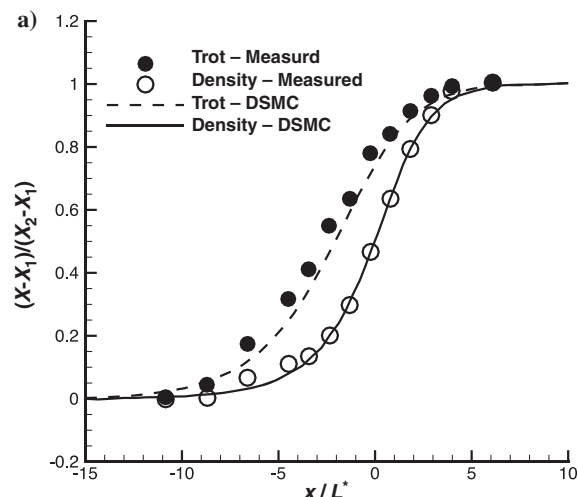


Fig. 5a Profiles of density and rotational temperature in a Mach 12.9 normal shock of N_2 [24].

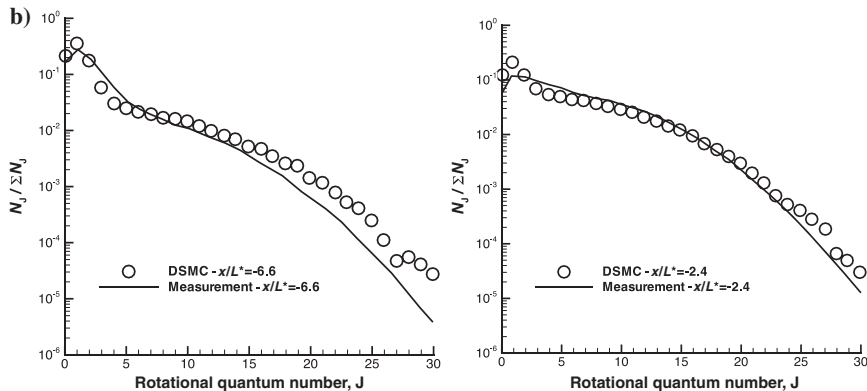


Fig. 5b Rotational energy distribution functions at two different locations in a Mach 12.9 normal shock of N_2 [24].

is one of the strongest illustrations of the ability of the technique to accurately simulate nonequilibrium phenomena. The main limitation of the Robben and Talbot data is that it was collected for a flow with a total temperature of just 300 K. There is a strong requirement for additional, detailed measured data sets for true high-temperature hypersonic conditions that can be used to evaluate DSMC rotational relaxation models.

C. VIBRATIONAL ENERGY EXCHANGE

The simulation of vibrational relaxation follows a similar procedure to that for rotation. The average probability of vibrational energy exchange is typically evaluated using the vibrational relaxation time used in hypersonic CFD models owing to Millikan and White [26] with the Park high-temperature correction [27]:

$$\tau_{\text{vib}} = \tau_{\text{MW}} + \tau_{\text{Park}} \quad (18)$$

To accurately reproduce this vibrational relaxation time in a DSMC computation, due to its complex temperature dependence, it is necessary to evaluate a collision averaged vibrational exchange probability [28]. Unlike rotational relaxation, a quantum mechanical approach is almost always employed for simulation of vibrational energy relaxation in hypersonic flows. A quantized vibrational energy exchange model corresponding to the classical BL approach was formulated by Bergemann and Boyd [29]. It involves first determining the maximum vibrational quantum level available based on the total collision energy:

$$\nu_{\max} = \left\lfloor \frac{\varepsilon_{\text{tot}}}{k\theta_v} \right\rfloor \quad (19)$$

where ε_{tot} is the total collision energy (the sum of the translational collision energy and the vibrational energy), $\lfloor \cdot \rfloor$ means truncation, and θ_v is the characteristic temperature for vibration of the molecule. Then, the post-collision vibrational quantum number, v , is sampled from:

$$\frac{P}{P_{\max}} = \left(1 - \frac{\nu k \theta_v}{\varepsilon_{\text{tot}}}\right)^{1-\omega} \quad (20)$$

The Lumpkin et al. [23] correction factor must also be applied to the vibrational exchange probability.

More detailed vibrational relaxation models for DSMC have also been developed and applied to hypersonic flows. For example, in [30], the basis for a new, high-fidelity DSMC model is the basic transition probability of the Forced Harmonic Oscillator (FHO) model described by Adamovich et al. [31]. Specifically, in a molecule-molecule collision, the probability of transition from initial vibrational levels (i_1, i_2) to final vibrational levels (f_1, f_2) is given by:

$$P_{\text{VVT}}(i_1, i_2 \rightarrow f_1, f_2, \varepsilon, \rho) = \left| \sum_{r=0}^n C_{r+1, i_2+1}^{i_1+i_2} C_{r+1, f_2+1}^{f_1+f_2} \exp[-i(f_1 + f_2 - r)\rho] P_{\text{VT}}^{1/2} \times (i_1 + i_2 - r \rightarrow f_1 + f_2 - r, 2\varepsilon) \right|^2 \quad (21)$$

where

$$P_{\text{VT}}(i \rightarrow f, \varepsilon) = i! f! \varepsilon^{i+f} \exp(-\varepsilon) \left| \frac{(-1)^r}{r!(i-r)!(f-r)!} \frac{1}{\varepsilon^r} \right|^2 \quad (22)$$

and

$$\varepsilon = S_{\text{VT}} \frac{4\pi^3 \omega (\tilde{m}^2 / \mu) \gamma^2}{\alpha^2 h} \sinh^{-2} \left(\frac{\pi \omega}{\alpha \bar{v}} \right) \quad (23)$$

$$\rho = \left(S_{\text{VV}} \frac{\alpha^2 \bar{v}^2}{\omega_1 \omega_2} \right)^{1/2} \quad (24)$$

In these equations: $C_{a,b}^c$ are transformation matrices defined in Reference [31], S_{VT} and S_{VV} are steric factors, ω is the oscillator frequency, \tilde{m} is the collision reduced mass, μ is the oscillator reduced mass, γ is oscillator mass ratio, α characterizes the intermolecular potential, h is Planck's constant, and \bar{v} is the symmetrized relative velocity. Further definitions and numerical values of the key parameters are provided in Reference [31].

There are no measurements in the literature of vibrational energy distribution functions in hypersonic flows of air that can be used to validate the DSMC vibrational relaxation models. A rare example of this type of experimental data was obtained for carbon monoxide by Meolans and Brun [32] in a shock-tube facility. Using spectroscopy, the population of CO molecules in the fourth

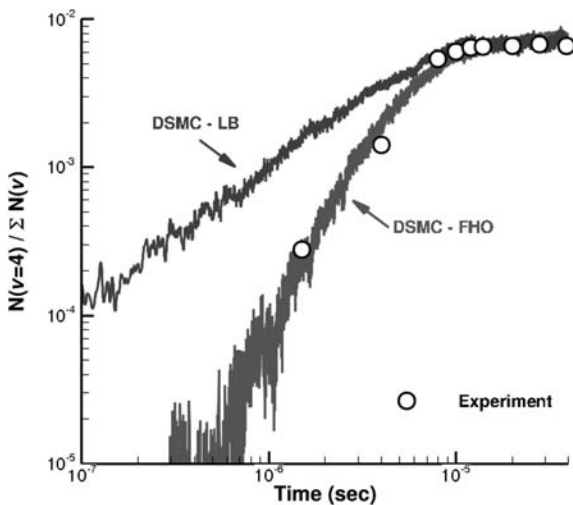


Fig. 6 Profiles of the relative population in the fourth vibrational state for a Mach 7 normal shock wave of carbon monoxide [30].

Larsen approach (BL) and the implementation of the FHO model [30]. The standard BL model populates the fourth excited state much too rapidly, whereas the FHO model provides very good agreement with the measurements. Further detailed experiments of this kind are required to validate the DSMC simulation approach for vibrational relaxation of air molecules.

D. CHEMICAL REACTIONS

The most commonly used DSMC chemistry model is the Total Collision Energy (TCE) model of Bird [4]. This model is based on a modified Arrhenius rate coefficient of the form:

$$C = aT^b \exp\left(-\frac{\varepsilon_{\text{act}}}{kT}\right) \quad (25)$$

where a and b are constants, and ε_{act} is the activation energy of the reaction. By integrating over the equilibrium distribution function for the total collision energy, it may be shown that the form of the reaction probability consistent with Eq. (22) for the VHS collision model is given by:

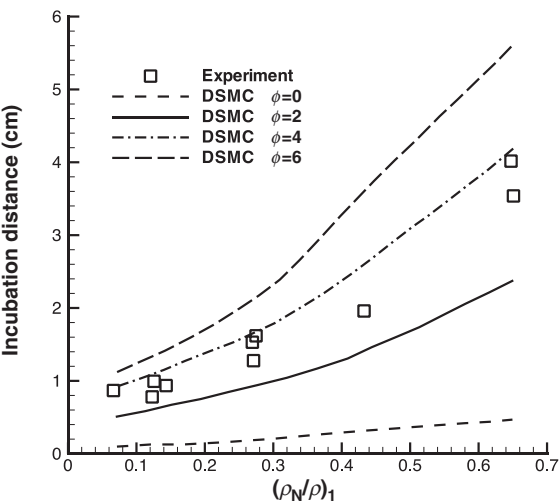
$$P_{\text{TCE}} = A \frac{(\varepsilon_{\text{tot}} - \varepsilon_{\text{act}})^{b+\zeta+\frac{1}{2}}}{(\varepsilon_{\text{tot}})^{\zeta+1-\omega}} \quad (26)$$

where ε_{tot} is the total collision energy of all modes of both particles participating in the collision, and constant A depends on the Arrhenius parameters and molecular constants. The TCE model was extended to include the

vibrational state relative to the ground state was measured behind a Mach 7 shock wave [32]. The measured profiles are compared in Fig. 6 with results obtained with two different DSMC vibrational relaxation models: the standard Borgnakke-

Fig. 7 Dissociation incubation distance as a function of atom mass fraction [33].

important physical phenomenon of vibration-dissociation coupling by Haas and Boyd [33] in the Vibrationally Favored Dissociation (VFD) model. The VFD model makes it possible to increase the dissociation probability of particles having large vibrational energy:



$$P_{\text{VFD}} = A \frac{(\varepsilon_{\text{tot}} - \varepsilon_{\text{act}})^{b+\zeta+\frac{1}{2}}}{(\varepsilon_{\text{tot}})^{\zeta+1-\omega}} (\varepsilon_{\text{vib}})^{\phi} \quad (27)$$

Values of the VFD parameter ϕ for air molecules have been determined through comparison with experimental data. For example, Fig. 7 shows comparisons [33] for dissociation incubation distances between DSMC predictions and data measured by Hornung [34] in hypersonic flows of N₂. The DSMC results show a strong sensitivity to the level of vibrational favoring included in the model with the incubation distance growing significantly as the model parameter ϕ is increased. Based on these comparisons, a value of $\phi = 3$ is generally employed for nitrogen dissociation.

Ideally, the reaction cross sections for use in DSMC would be determined directly rather than through indirect means such as measuring incubation distance as employed in Fig. 7. Measurements of reaction cross sections of interest in hypersonic air flows are not generally available, except for some reactions involving electrons. As ab initio computational chemistry techniques mature, there is the hope in the future that detailed computed data bases can be used to help develop more accurate DSMC chemistry models. One example of such a database was constructed using a Quasi-Classical Trajectory (QCT) method by Bose and Candler [35] for the Zeldovich exchange reaction:



This QCT database was employed [36] to perform a detailed evaluation of the TCE model for this particular reaction. Figure 8a shows reaction cross-sections as

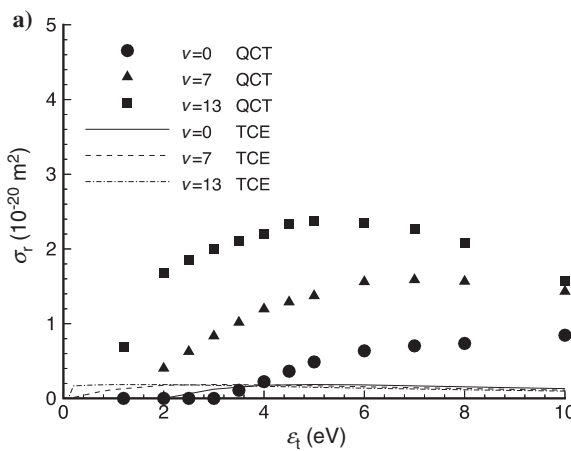


Fig. 8a Reaction cross-sections at $J = 64$ for nitric oxide formation [36].

a function of translational collision energy, at a particular rotational energy level ($J = 64$) of the reactant, N_2 , for three different reactant vibrational levels ($v = 0, 7, 13$). Clearly, the TCE model is not at all accurate for this reaction in terms of collision

cross section. This poor comparison motivated the development of a new DSMC chemistry model that allows favoring from each of the translational, rotational and vibrational energy modes. Termed the Generalized Collision Energy (GCE) model, the reaction probability is given by [36]:

$$P_{\text{GCE}} = A \frac{(\epsilon_{\text{tot}} - \epsilon_{\text{act}})^{b+\zeta+\frac{1}{2}}}{(\epsilon_{\text{tot}})^{\zeta+1-\omega}} (\epsilon_{\text{vib}})^\phi (\epsilon_{\text{tra}})^\alpha (1 - \epsilon_{\text{rot}}/\epsilon_{\text{tot}})^\beta \quad (29)$$

Figure 8b provides comparisons between the QCT data and the GCE reaction cross sections. While the comparisons are far from perfect, they represent a significant improvement over the TCE model. For this particular reaction, the

GCE model parameter values were: $\alpha = 0.2$, $\beta = -0.5$, $\phi = 0.3$.

The detailed QCT database makes it possible to evaluate several aspects of DSMC chemistry modeling. The second aspect concerns the energy distribution of the particles selected

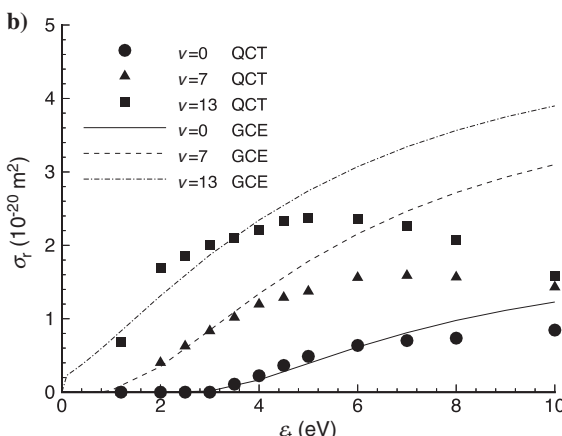


Fig. 8b Reaction cross-sections at $J = 64$ for nitric oxide formation [36].

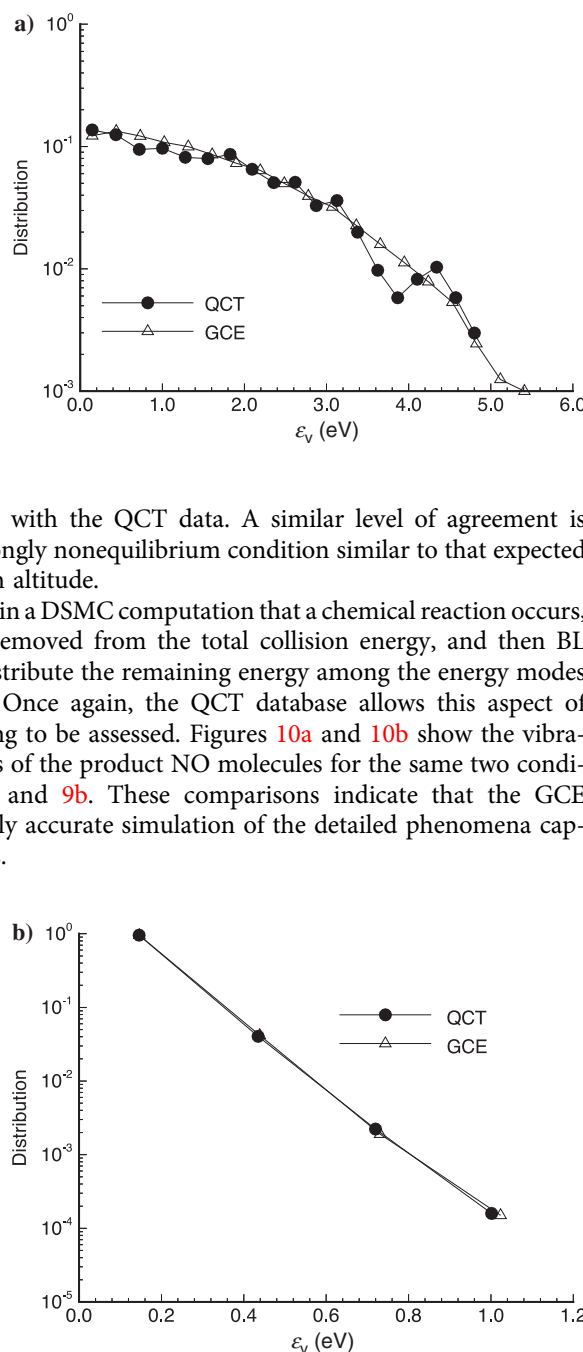
Fig. 9a Vibrational energy distribution function of reactants in nitric oxide formation: $T_t = T_r = T_v = 5000$ K [36].

for reaction. Figure 9a shows the vibrational energy distribution function of the reacting N_2 molecules under a thermal equilibrium condition where all mode temperatures are at 5000 K. Clearly, the GCE model provides almost perfect agreement with the QCT data. A similar level of agreement is shown in Fig. 9b for a strongly nonequilibrium condition similar to that expected in hypersonic flow at high altitude.

When it is determined in a DSMC computation that a chemical reaction occurs, the activation energy is removed from the total collision energy, and then BL procedures are used to distribute the remaining energy among the energy modes of the product particles. Once again, the QCT database allows this aspect of DSMC chemistry modeling to be assessed. Figures 10a and 10b show the vibrational energy distributions of the product NO molecules for the same two conditions shown in Figs. 9a and 9b. These comparisons indicate that the GCE model provides remarkably accurate simulation of the detailed phenomena captured by the QCT analysis.

Details of simulating backward chemical rate processes with the DSMC technique have been discussed by Boyd [37]. An important issue here is that the TCE model, and its derivatives such as

Fig. 9b Vibrational energy distribution function of reactants in nitric oxide formation: $T_t = 14,000$ K, $T_r = 5000$ K, $T_v = 1000$ K [36].



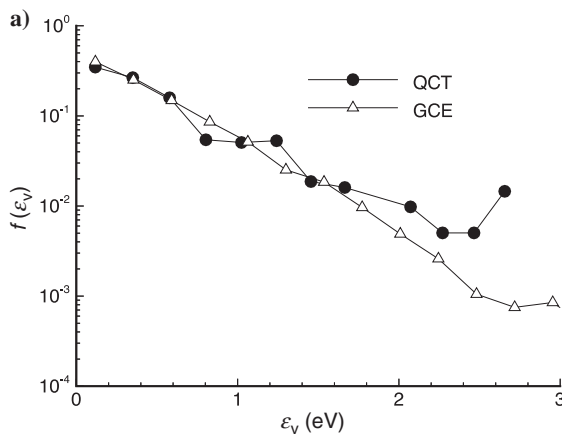


Fig. 10a Vibrational energy distribution function of products in nitric oxide formation: $T_t = T_r = T_v = 5000$ K [36].

and the equilibrium constant that is usually a highly complex function of temperature. Thus, it is not generally possible to express the backward rate coefficient in the simple Arrhenius form. This problem is either addressed by performing a best-fit of the true backward rate coefficient to an Arrhenius form over a temperature range of interest, or by calculating the temperature in each cell of the DSMC computation in order to evaluate the equilibrium constant exactly [37].

While the DSMC method is based on the premise of a dilute gas for which three body collisions are ignored, it is sometimes important to include recombination in DSMC calculations and models for such reactions are presented in References [4] and [28].

Several other DSMC chemistry models relevant to hypersonic flows have been developed including the maximum entropy model [38], the weak vibrational bias model [39], the threshold line model [40], and the Quantum Kinetic (QK) model of Bird [41]. Many of the models are reviewed and evaluated in [42] and [43].

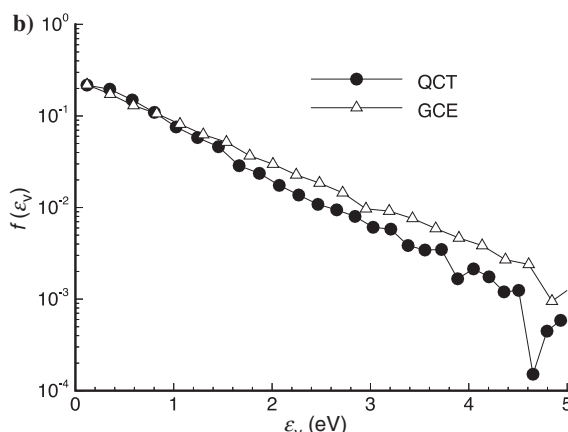


Fig. 10b Vibrational energy distribution function of products in nitric oxide formation: $T_t = 14,000$ K, $T_r = 5000$ K, $T_v = 1000$ K [36].

VFD and GCE, all depend on the use of a rate coefficient expressed in Arrhenius form. Backward rate coefficients are generally evaluated as the quotient of the forward rate coefficient

E. CHARGED SPECIES

Ions and electrons are formed in sufficiently energetic hypersonic flows first through associative ionization and then through electron impact ionization. Although these reactions can be simulated using the TCE chemistry model with DSMC, the presence of electrons in a DSMC computation presents some special challenges. Specifically, due to their very low mass relative to other species: (1) the thermal velocity of an electron is orders of magnitude higher than for other species; and so (2) the collision frequency of electrons is orders of magnitude higher than for other species. If an electron was not charged, then the first problem would simply require use of a much smaller time step Δt than would be required otherwise. However, electrostatic attraction means that electrons and ions interact with one another such that electron diffusion is reduced and ion diffusion is slightly increased. A common model to describe this behavior is ambi-polar diffusion in which it is assumed that ions and electrons diffuse at the same rate. Bird [44] first introduced a DSMC model for ambi-polar diffusion in which every electron particle was tied directly to the ion it was born with. These pairs of charged particles then move throughout the flow domain based on the velocity components of the ion particle. This method is reasonably successful, but it is difficult to implement and has poor performance at high ionization levels. Carlson and Hassan [45] introduced a scheme in which electric fields are evaluated based on averaged charged particle properties. The charged particles are moved in these fields with the electrons processed at a significantly smaller time step than the ions. An alternate approach was proposed by Boyd [46] in which electron particles are moved throughout the domain based on cell-averaged ion velocities. The electron and ion particles are no longer tied together explicitly making the method much easier to implement and the approach is found to be generally more robust than Bird's technique. Using either of the Bird [44] or Boyd [46] approaches means that electron particles are moved at the time scale of the heavier species and so there is no need to reduce the simulation time step.

The second issue faced in simulating electrons, related to their significantly higher collision frequency, must also be addressed. The obvious choices are as follows: (1) reduce the global time step; (2) allow electron particles to collide more than once over each iteration; or (3) perform subcycling of collisions. Subcycling involves calling the collision subroutine several times over each movement iteration so that the number of collision pairs to be tested is evaluated several times using a subcycling time step Δt_c that is smaller than the global time step Δt , usually by a factor of about 100.

F. RADIATION

Radiation is of interest in hypersonic flows in terms of the emission signature and at very high speeds for the radiative component of vehicle heating. Emission signatures are usually simulated decoupled from the flow field, and examples are

discussed of such analysis later in this article. There have been several DSMC studies on emission signatures where the excited states of interest were simulated directly as additional chemical species [47, 48]. A key issue here is the availability, or lack of it, of accurate excitation rate coefficients. For estimation of radiative heating, Bird first included thermal radiation effects in DSMC for analysis of an aero-assist orbital transfer vehicle [44, 49] and his ideas were extended by Carlson and Hassan [50]. These models essentially represent an extension of the rotational and vibrational relaxation models using BL energy disposal. As a phenomenological approach, these models performed reasonably well, but this is another area where further research is warranted.

G. GAS-SURFACE INTERACTION

The most important outcome from most DSMC analyses of hypersonic flows is the determination of the properties at the vehicle surface and in particular the aerodynamic forces and moments, and the convective heat transfer. The surface properties are of course very sensitive to the model assumed in DSMC for gas-surface interaction. The most common gas-surface interaction model used in DSMC is fully diffuse reflection in which a particle reflects from the surface with new velocity components that are sampled from Maxwellian distributions characterized by the wall temperature (note that the velocity component normal to the surface is sampled from a biased Maxwellian distribution). In the diffuse model, the particle's internal energies are also sampled from the appropriate equilibrium distribution, such as Eq. (12) for rotation, using the wall temperature. The opposite limit to diffuse reflection is specular reflection in which the only change to the particle's properties is its velocity component normal to the surface that is simply reversed in sign. Many DSMC computations use an accommodation coefficient, α , to simulate a combination of diffuse and specular reflections such that $\alpha = 1$ is fully diffuse, and $\alpha = 0$ is fully specular, and this approach is sometimes referred to as the Maxwell model for gas-surface interaction. Real engineering surfaces generally require a value in the range of $\alpha = 0.8\text{--}0.9$.

Figure 11 shows a comparison of measured [51] and computed distributions of argon atoms reflecting from a platinum surface. Clearly, the measured pattern is not reproduced by either of the specular or diffuse reflection models (and indeed cannot be reproduced by any combination of the two models). This type of comparison led to the development of more sophisticated gas-surface interaction models for DSMC, for example the Cercignani-Lampis-Lord (CLL) model [52]. Such models tend to have a stronger theoretical basis, such as using a reciprocity relation, and offer more control through use of additional parameters. Figure 12a shows DSMC computed particle reflection distributions for Mach 10 flow of N_2 over a flat plate [53] for a variety of different gas-surface interaction models. Fully diffuse reflection (Maxwell, $\alpha = 1.0$) gives the cosine distribution. Fully specular reflection (Maxwell, $\alpha = 0$) gives a distribution that is almost tangent to the surface. Through variation of the accommodation

Fig. 11 Distributions of argon scattering from platinum: measurements from [51].

coefficient σ_T (a parameter in the CLL model), a wide range of reflected distributions can be generated that lie between the ideal limits of diffuse and specular reflection. Figure 12b compares profiles of the velocity component parallel to the flat plate measured by Cecil and McDaniel [54] using Planar Laser Induced Fluorescence (PLIF) and a number of DSMC computations using the Maxwell and the CLL reflection models with a range of model parameters. Note, at the surface, that both measurements and computations show a significant level of velocity slip. Such comparisons allow identification of appropriate parameter values for use in the CLL model. However, the use of such models is relatively limited due to the lack of this type of basic information to

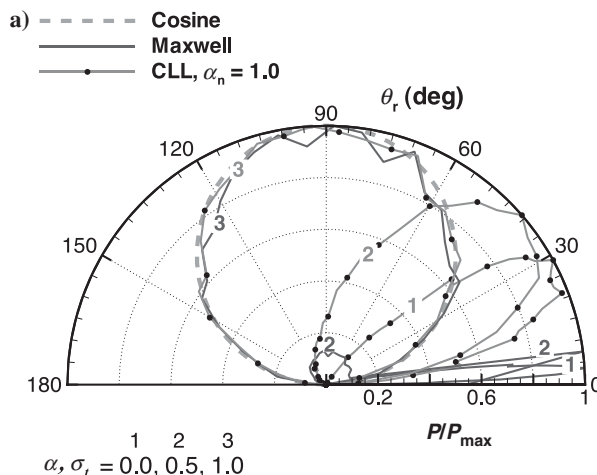
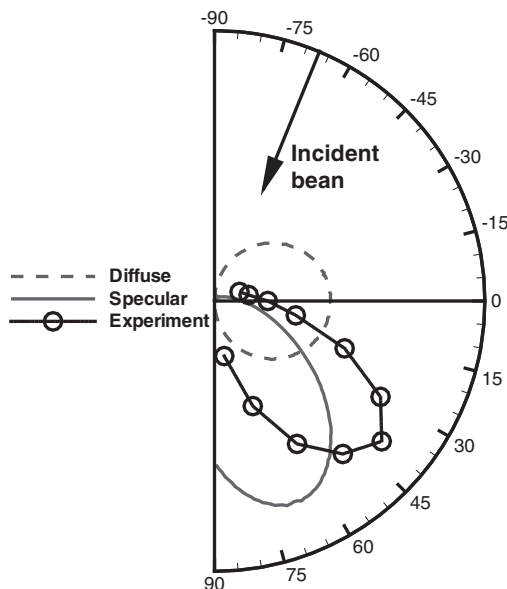


Fig. 12a Computed scattering distributions from a DSMC simulation of hypersonic flow of N₂ over a flat plate [53].

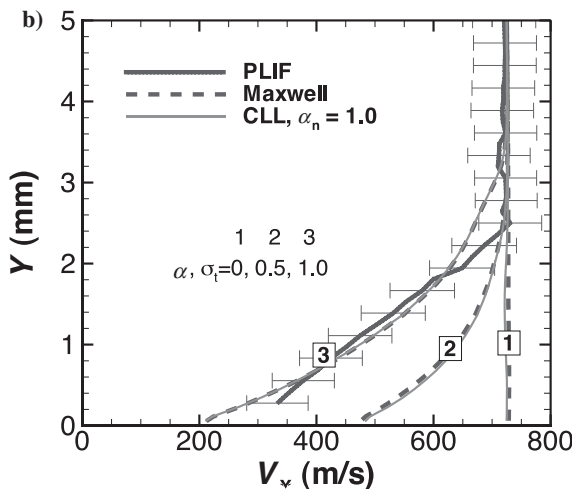


Fig. 12b Velocity profiles for hypersonic flow of N_2 over a flat plate [53].

identify parameter values for real systems of interest. This is another area where computational chemistry simulations using molecular dynamics can provide data bases that can be used to build more advanced DSMC physical models.

There are two important phenomena arising

from gas–surface interaction under high Knudsen number conditions: velocity slip and temperature jump. The relatively low number of collisions experienced by a gas at high Kn means that the average velocity at the wall has a finite value, even for a surface with fully diffuse reflection. This phenomenon reduces shear stress and may affect separation. Similarly, owing to the low collision rate, the temperature of the gas at the wall is not equilibrated with the surface. In a hypersonic flow where the wall temperature is cooler than the gas, this phenomenon leads to a reduction in heat transfer. These effects are naturally included in a DSMC simulation using the diffuse reflection and CLL models whereas the usual approach for CFD is to assume no slip and no temperature jump at a wall. The omission of these high Knudsen number surface phenomena in CFD partially explains some of the differences noted in the detailed comparisons under hypersonic flow conditions of DSMC and CFD reported in [6, 7]. One approach to try and extend the usefulness of CFD into the high Knudsen number range is to employ velocity slip and temperature jump models, see for example [7]. However, although some of these models do improve the agreement between CFD and DSMC results for surface quantities, it is not always achieved with a corresponding improvement in the comparisons of the flow properties. This situation again illustrates the need to perform non-continuum computations of high Knudsen number flows using kinetic methods such as the DSMC technique.

IV. DSMC ANALYSIS OF HYPERSONIC FLOWS

In the following sections, a review is provided of the status of the application of the DSMC technique to hypersonic, nonequilibrium flows. We first consider the

application of DSMC to analyze hypersonic experiments conducted in ground-based facilities. Next, use of DSMC to analyze hypersonic flows in Earth's atmosphere is divided into slender and blunt body vehicle configurations. Finally, a summary of the use of DSMC for analysis of hypersonic flow in planetary atmospheres is provided.

A. DSMC ANALYSES OF HYPERSONIC LABORATORY EXPERIMENTS

Generation of rarefied, hypersonic flows in ground-based facilities presents a technical challenge, and very few data sets exist that enable a detailed assessment of DSMC codes. One notable code validation activity resulted from a NATO-AGARD working group on hypersonics. A planetary probe geometry was tested under rarefied, hypersonic flow conditions in several different experimental facilities and a number of research groups generated DSMC results for comparison. Many articles have been published on these studies and details of the experiments and numerical results are summarized in [55]. Examples of results obtained using the MONACO DSMC code are provided in Figs. 13a through 13c. Figure 13a shows the unstructured mesh that has been adapted to the local mean free path for the experiment conducted in the SR3 wind-tunnel in nitrogen at a Mach number of 20 and a Knudsen number of 0.03 [56]. Despite the high Mach number, this was a low-enthalpy facility with a total temperature of 1100 K. Thus, neither vibrational relaxation nor chemistry occurs in these flows. While such experiments provide the opportunity to assess the collision cross sections (VHS, VSS) and rotational relaxation models [20], they provide no insight on the DSMC models for vibrational relaxation [28], and chemistry [33]. An electron beam diagnostic was employed in the SR3 wind-tunnel to measure the density field around the capsule geometry and Fig. 13b

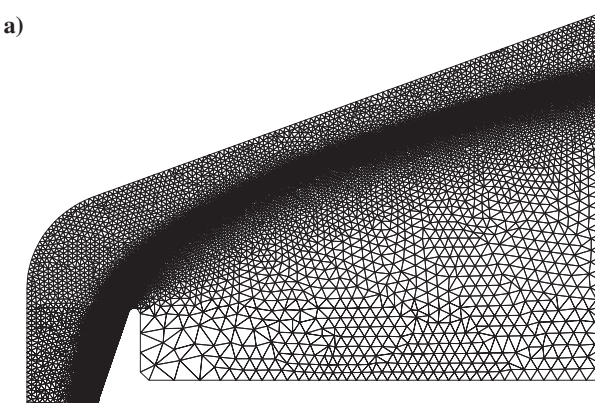


Fig. 13a Adapted mesh for Mach 20, $\text{Kn} = 0.03$ flow over a planetary probe.

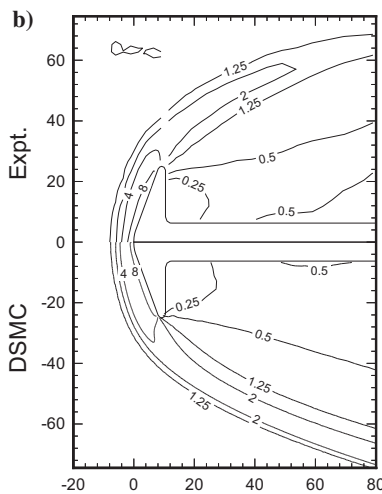


Fig. 13b Contours of ρ/ρ_∞ for Mach 20, $Kn = 0.03$ flow over a planetary probe [11].

shows the excellent agreement obtained between DSMC and the measured data. Another experiment was conducted using the same geometry in the LENS facility again in nitrogen at a Mach number of 15.6 and a Knudsen number of 0.002 [57]. This higher enthalpy experiment had a total temperature of 4350 K so that vibration was activated but there was still no chemistry. Figure 13c shows comparisons between measurements from LENS and DSMC computation for the heat flux along the surface of the probe. Again, excellent agreement is obtained. While studies of this type indicate that the DSMC method is an accurate simulation method, the flows are not energetic enough to permit detailed assessment of DSMC thermochemical models.

Another code validation exercise (for both DSMC and CFD) was focused on hypersonic viscous interactions that can be generated on slender body configurations. A series of experiments was performed in the LENS facility for a number of configurations including double cones, and cylinder-flares [58].

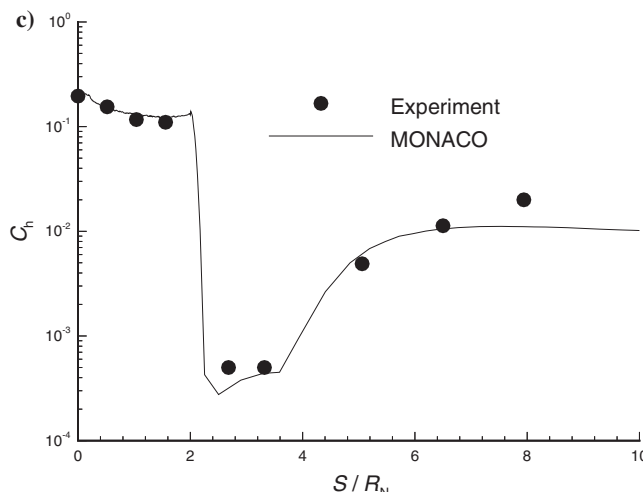


Fig. 13c Heat flux coefficient on a planetary probe at Mach 15.6, $Kn = 0.002$ [11].

Fig. 14a Pressure along the surface of a double cone tested at Mach 15.6, $Kn = 0.002$ [59].

While several groups performed DSMC analyses of some of these cases, Moss and Bird [59] provide the most comprehensive comparisons with the measured data. Figures 14a and 14b show comparisons for surface pressure and heat flux for a Mach 15.6, $Kn = 0.001$ flow of nitrogen over a double cone configuration.

DSMC results from two different codes (DS2V and SMILE) are provided and clearly give excellent agreement with the measurements. Similar levels of agreement between DS2V DSMC computations and measurements of pressure and heat flux are also shown in [59] for a Mach 12.4, $Kn = 0.0004$ flow of nitrogen over a cylinder flare configuration. Similar to the planetary probe case, while vibrational energy of nitrogen was barely activated, there was no chemistry present in these flows.

There are very few comprehensive data sets measured under rarefied conditions involving three-dimensional (3-D) flows. An interesting example concerns data obtained in a low density, hypersonic wind-tunnel in the 1960s as part of the Apollo program [60–63]. A variety of very small models were tested that included cones as well as capsules such as Apollo, Gemini, and Mercury. The MONACO DSMC code was applied to

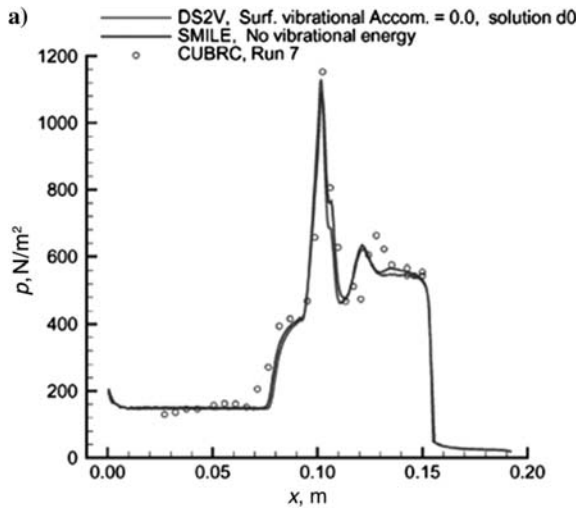
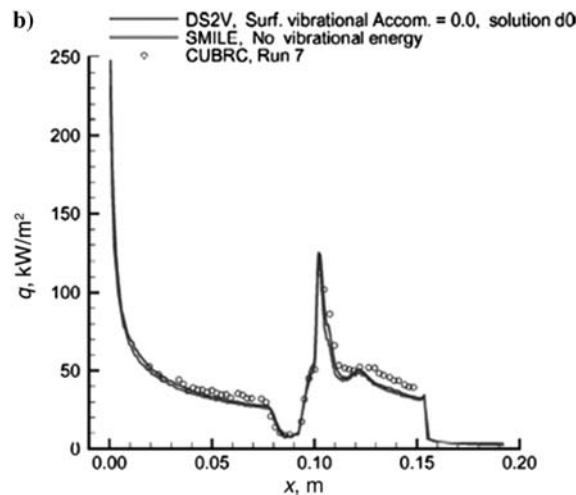


Fig. 14b Heat flux along the surface of a double cone tested at Mach 15.6, $Kn = 0.002$ [59].



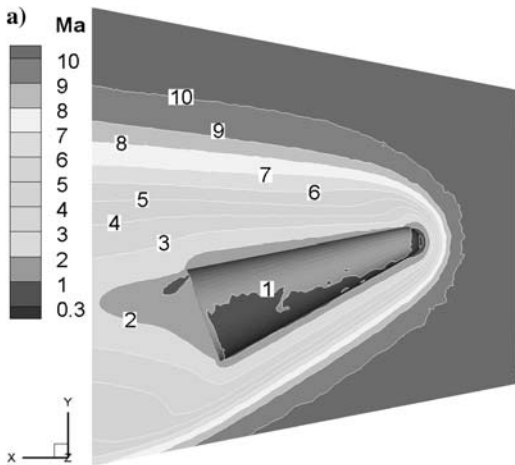


Fig. 15a Contours of Mach number about a cone at angle of attack [64].

"FMF" shows results obtained from free molecular theory, and "MN" indicates modified Newtonian theory. For both the drag and the pitching moment, the 3-D DSMC computations are in excellent agreement with the measured data. The comparisons also show that neither the free molecular theory nor the Newtonian theory provide any useful results for this condition indicating that the more computationally expensive DSMC approach is required. Figures 16a, 16b, and 16c show the corresponding results for Mach 10 flow of nitrogen over a model of the Apollo Command Module capsule at a Knudsen number of 0.067 conducted in the exact same facility as the cone studies. In this case, significant differences between simulation and measurement are found for the drag force. Similarly, there is relatively poor agreement between the MONACO DSMC solutions for pitching moment coefficient and the measured values, as shown in Fig. 16c. For example, DSMC predicts a trim angle that is about 15 deg. different from the experiments. Independent DSMC computations of the same flows were performed using the DS3V DSMC code, and the results show excellent agreement with the MONACO DSMC profiles.

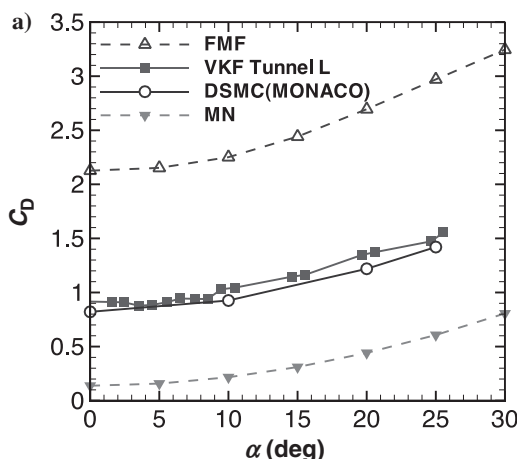


Fig. 15b Drag coefficient for a cone at angle of attack [64].

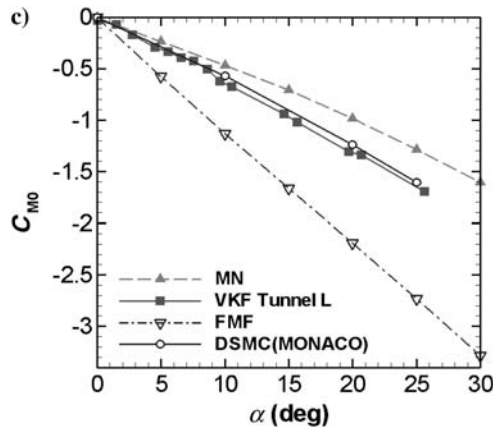
simulate the tests on the cones that were conducted in a Mach 10 flow of nitrogen at a global Knudsen number of 0.065 [64]. Figure 15a shows contours of Mach number computed for an angle of attack of 20 deg. Figures 15b and 15c show comparisons for aerodynamic properties between measurement and simulation. In these figures,

Downloaded by 80.82.77.83 on February 21, 2018 | http://arc.aiaa.org | DOI: 10.2514/4.103292

Fig. 15c Pitching moment for a cone at angle of attack [64].

The fact that good agreement between measurement and simulation is obtained in one case and not in another for two tests performed in the same experimental facility illustrates the difficulties involved in validating the DSMC approach using the limited amounts of laboratory data. This situation clearly calls out for additional experiments to be carried out carefully under hypersonic, rarefied flow conditions.

Despite the lack of detailed validation using laboratory data, the DSMC technique has been applied to analyze the aerodynamics and aerothermodynamics of many different spacecraft entering the atmospheres of Earth and of planets in the Solar System. In the following sections, we provide a review of prior DSMC studies of hypersonic flight that is divided into three parts: (1) slender bodies in Earth's atmosphere; (2) blunt bodies in Earth's atmosphere; and (3) flight in planetary atmospheres.



B. DSMC ANALYSES OF FLIGHT IN EARTH'S ATMOSPHERE

The review of previous DSMC analyses of hypersonic flows in the atmosphere of the Earth is divided into those related to defense applications and those related to return of payloads from space. These two classes of missions involve very different trajectories and vehicle configurations.

1. SLENDER BODY CONFIGURATIONS

Very high speed delivery of military payloads is achieved using slender vehicle geometries. The Bow-Shock Ultra-Violet-2 (BSUV-2) hypersonic flight experiment represents an example of such a vehicle that was flown in 1991 [65]. The vehicle geometry

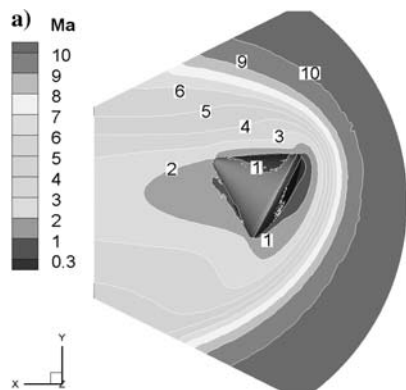


Fig. 16a Contours of Mach number about a capsule at angle of attack [64].

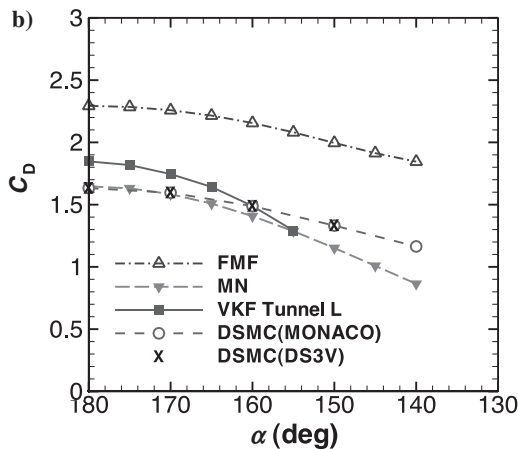


Fig. 16b Drag coefficient for a capsule at angle of attack [64].

on-board instrumentation. Calculation of the radiative emission was performed in a decoupled approach. The chemically reacting flow field was computed using both continuum (CFD) [66–68] and direct simulation Monte Carlo (DSMC) methods [36]. Then, the emission was predicted from the flow field solutions using the NASA nonequilibrium radiation code NEQAIR [69]. Initial comparisons between DSMC-based results and measurement produced poor agreement at high altitude. This led to significant activity in the study of the oxygen dissociation and nitric oxide formation chemistry models used in the DSMC computations [36, 70]. The final results obtained for nitric oxide radiance as a function of altitude are shown in Fig. 17a [71]. Note that the BSUV-2 Knudsen number ranged from 0.008 at 71 km to 0.215 at 90 km. In addition to obtaining very good agreement with radiance, the spectral features

consisted of a spherically capped 15 deg. cone with a nose radius of about 10 cm. BSUV-2 reentered the atmosphere at 5.1 km/s and provided data in the altitude range from 110 to 60 km. Measurements of the ultra-violet emission owing to nitric oxide and vacuum-ultra-violet emission due to atomic oxygen resonance transitions were obtained by

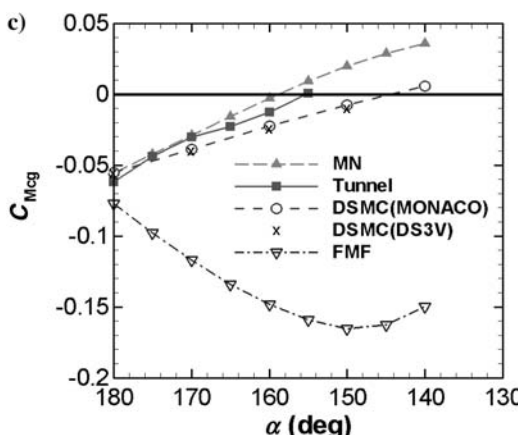


Fig. 16c Pitching moment for a capsule at angle of attack [64].

Fig. 17a NO emission as a function of altitude for the BSUV-2 hypersonic flight [71].

coefficient, α_t . The BSUV-2 studies clearly illustrated that access to detailed experimental measurements are needed in order to make significant advances in thermochemical modeling using the DSMC technique.

The Radio Attenuation Measurement (RAM) experiments involved a series of hypersonic flights designed to study communications blackout. This is an important operational issue for all hypersonic vehicles in which the plasma formed at very high speed interferes with radio waves sent to and from the vehicle. The vehicle of interest here (RAM-C II), consisted of a cone with a spherical nose cap of radius 0.1524 m, a cone angle of 9 deg., and a total length of about 1.3 m. While entering at orbital velocity (7.8 km/s), the RAM-C II experiment made measurements from about 90 km to 60 km altitude. Electron number density was measured using two different diagnostics at several locations in the plasma layer surrounding the vehicle [72, 73]. A series of reflectometers was used to measure the maximum plasma density along lines normal to the vehicle surface in four different locations. A rake of Langmuir probes measured variation in the plasma density across the plasma layer near the rear of the vehicle. DSMC analysis of the RAM-C experiment at 81 km was performed by Boyd [74] in order to make assessment of DSMC procedures for simulating charged species (electrons, ions) in trace amounts. The DSMC results were compared directly with the measurements of plasma

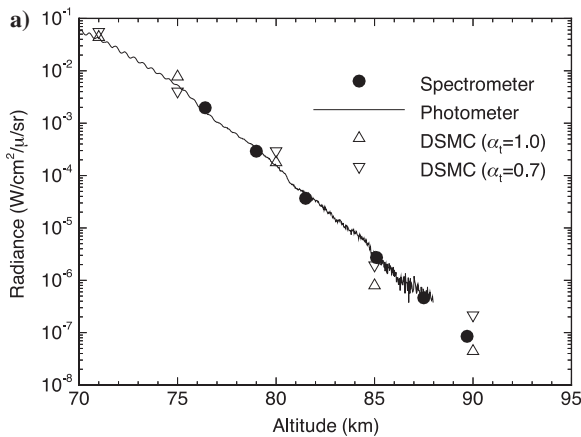
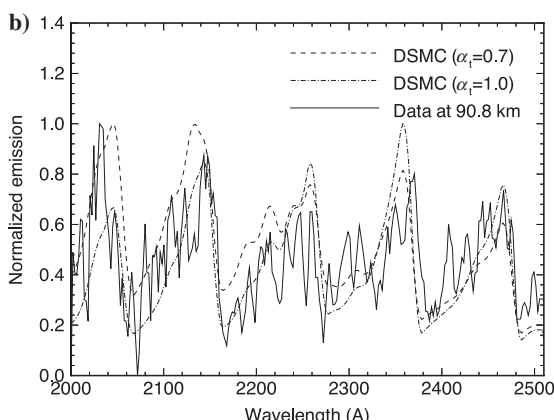


Fig. 17b Normalized NO spectra at an altitude of 90 km for the BSUV-2 flight [71].



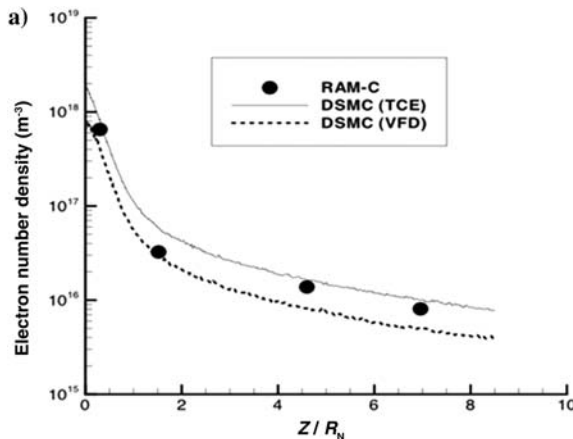


Fig. 18a Peak plasma density as a function of axial location along the RAM-C vehicle [74].

density taken on the RAM-C II flight and these are shown in Figs. 18a and 18b. In each case, the sensitivity of the DSMC results to the model (TCE or VFD) employed for dissociation chemistry is investigated.

Clearly, very good agreement is obtained between simulation and measurement that provided validation of the new DSMC procedures.

2. BLUNT BODY CONFIGURATIONS

The successful return of payloads (including people) from space requires use of blunt vehicle geometries to provide reduced levels of deceleration and heat load. One of the first applications of the DSMC technique to analyze the entry aerodynamics of a full-scale vehicle was performed by Rault [75] who simulated the aerodynamics of the Space Shuttle Orbiter at altitudes from 170 to 100 km where the Knudsen number ranged from about 2 to 0.005. Performed around 1993, these 3-D computations were extremely expensive for the time.

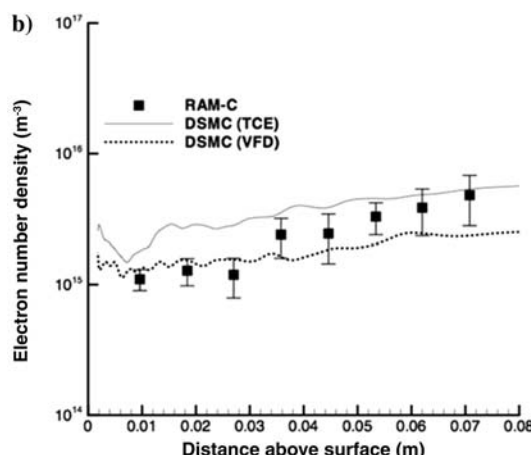


Fig. 18b Plasma density as a function of radial distance from the RAM-C surface [74].

Significant discrepancies were, however, found both for the normal force coefficient and for the pitching moment.

Ivanov et al. [76] describe DSMC analysis using SMILE of the aerodynamics of a Russian entry capsule over the altitude range from 130 to 85 km. Comparisons made between the DSMC results and free flight experimental measurements for the axial and normal force and pitching moment coefficients revealed excellent agreement. The SMILE code was also applied by Markelov et al. [77] to help in the analysis of de-orbiting the Russian space station Mir. The highly complex, 3-D geometry was analyzed using DSMC over the altitude range from 200 to 110 km for which the effective Knudsen number varies from about 20 to 0.05. It was found that aerodynamic coefficients do not change significantly until about 120 km and that the vehicle is statically stable throughout this altitude range.

Moss [78] applied the DS2V DSMC code to analyze the aerothermodynamics of a proposed ballute deceleration system for Earth entry at velocities from 14 to 7 km/s and altitudes from 200 to 100 km. A number of interesting and important conclusions were drawn from the analyses including the observation of unsteady flow phenomena for certain capsule-ballute configurations, and that the highest heat fluxes were experienced on the ballute tether.

NASA's Stardust Sample Return Capsule (SRC) entered the Earth's atmosphere at a velocity of about 12.8 km/s making it the most energetic man-made vehicle to undergo hypersonic entry. The SRC geometry is shown in Fig. 20a. The DSMC codes G2 (an earlier form of Bird's DS2V code) and DAC were used by Wilmoth et al. [79] prior to the flight in 1998 in order to analyze the entry aerodynamics. Focused on aerodynamics, those early Stardust DSMC computations omitted ionization and employed simple thermochemical models. During the SRC entry in 2006, a suite of spectroscopic instruments measured the radiation emitted from the very strong bow shock wave formed around the vehicle [80]. With the availability of detailed experimental measurements, several further DSMC studies

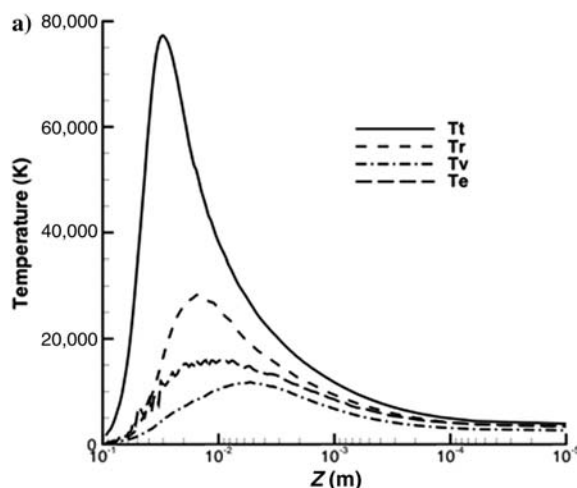


Fig. 19a Temperature profiles along the Stardust SRC stagnation streamline at 81 km [82].

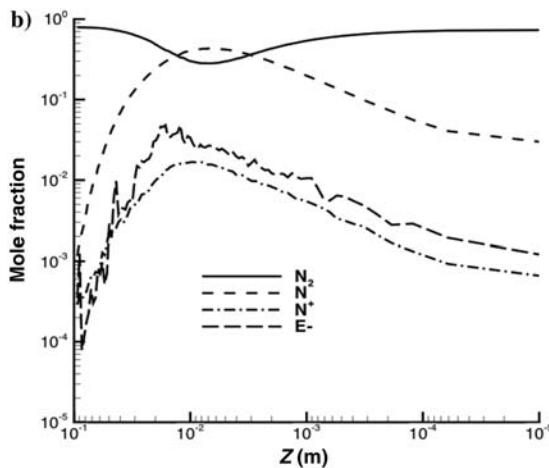


Fig. 19b Mole fraction profiles along the Stardust SRC stagnation streamline at 81 km [82].

along the stagnation streamline of the SRC at an altitude of 81 km are shown in Fig. 19a. The separation among these profiles illustrates the strong degree of thermal nonequilibrium of the gas under these extreme conditions. Profiles along the stagnation streamline of the mole fractions of selected chemical species are shown in Fig. 19b illustrating the high degree of chemical activity present in the flow. The NEQAIR radiation code [69] was again employed to estimate the radiation spectra based on the DSMC flow field results. An example of a direct comparison between the computed and measured

of the SRC entry have been performed recently that employed state-of-the-art thermochemistry modeling including ionization [81–83]. Profiles of the temperatures from the various energy modes (T_t = translation; T_r = rotational; T_v = vibrational; T_e = electron) predicted

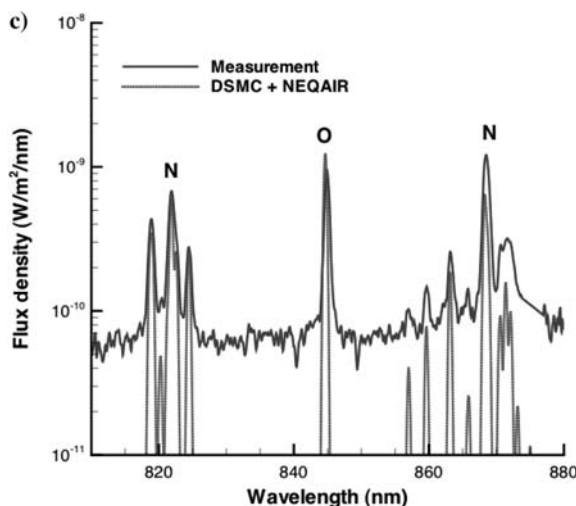


Fig. 19c Comparison of measured and computed spectra for Stardust at 81 km [83].

spectra at an altitude of 81 km is shown in Fig. 19c. Generally, it is found that air plasma atomic line features are quite well predicted by the combination of DSMC and NEQAIR.

C. DSMC ANALYSES OF FLIGHT IN PLANETARY ATMOSPHERES

Several DSMC studies have been performed of the aerodynamics and heating of vehicles entering the Mars atmosphere that consists of 95.4% of CO₂ and 4.6% of N₂. Direct comparisons between DSMC predictions obtained using DAC and flight measurements taken during the Viking-1 entry for the ratio of normal to axial aerodynamic force yielded excellent agreement [84]. Similar comparisons for the drag coefficient indicated that the DSMC results were not inconsistent with the measurements although the flight data were only taken in the continuum regime so direct comparison with DSMC was not possible. An extensive aerodynamics database was constructed using G2 and DAC for the Mars Pathfinder mission by Moss et al. [85]. The DSMC analyses traversed a Knudsen number range from 100 to 0.027 and angle of attack variation from 0 to 35 deg. The database was used for Martian atmosphere density reconstruction and spacecraft attitude determination based on in-flight accelerometer data. DAC was again used by Wilmoth et al. [86] to analyze the aerothermodynamics of the Mars Global Surveyor (MGS). The data generated were employed for spacecraft design, mission planning, flight operations, and atmospheric reconstruction. MGS was the first planetary entry mission designed to use aerobraking to customize its orbit by gradually descending into the Mars atmosphere over a period of several months. The Knudsen number during the aerobraking process varied from about 10 down to 0.05 placing the flows firmly in the transition regime. The DSMC generated aerothermodynamic database played a key role in the successful completion of the aerobraking maneuver. Finally, the DAC and G2 DSMC codes were applied by Moss et al. [87] to generate an aerothermodynamic database for Mars Microprobes. Aerodynamics characteristics and surface heat flux were determined over a Knudsen number range from 80 to 0.002.

DSMC analyses have been performed on the interaction of the Magellan spacecraft with the atmosphere of Venus. The composition of the Venusian atmosphere is 76% CO₂, 9% CO, 9% Ar, and 6% N₂. Near the end of its mission, the Magellan spacecraft for the first time successfully performed an aero-brake maneuver in the atmosphere to circularize its orbit. Rault [88] applied a 3-D DSMC code to compute the aerodynamic characteristics of the complex spacecraft geometry at an altitude of 140 km as part of the assessment of whether to perform the aero-brake maneuver. The flow had a freestream Knudsen number of about 10 and the DSMC results indeed showed only minor departures from free molecular analysis. A similar analysis was reported by Haas and Schmitt [89] using a different 3-D DSMC code. They found relatively small differences of 5–10% between DSMC and free molecular theory for forces, moments, and heating. In a related

study, Haas and Feiereisen [90] used DSMC to analyze the heating to the Magellan spacecraft during proposed aero-pass maneuvers.

DSMC analysis of the rarefied portion of the entry of the Galileo probe into the atmosphere of Jupiter was performed by Haas and Milos [91]. The Jovian atmosphere consists of 89% H₂ and 11% He. Seven points along the entry trajectory were investigated with the freestream Knudsen number ranging from 400 to 0.07 and all at zero angle of attack. The purpose of the analysis was to accurately compute the drag coefficient that was needed to infer atmospheric density from an accelerometer experiment. A unique aspect of this study was the coupling of the convective heating predictions from DSMC to a thermal response code in order to estimate out-gassing rates of pyrolyzed gas originating in the thermal protection system of the probe. The predicted flux of pyrolysis products was as much as an order of magnitude higher than the freestream flux and had a significant effect on the probe aerodynamics, for example reducing the drag coefficient by 15%.

V. HYBRID DSMC-CONTINUUM METHODS

A. INTRODUCTION

Often, rarefied flows of interest in hypersonic applications are embedded within largely continuum flow fields. Neither continuum nor kinetic methods provide both physically accurate and numerically efficient techniques to simulate the entire flow field. Instead, multi-scale methods can provide the capability of achieving the efficiency of continuum methods in regions where the degree of collisional nonequilibrium is small, while maintaining the physical accuracy of kinetic methods in rarefied portions of the flow. This section begins with an outline of typical hypersonic flows that may require a multi-scale analysis in order to make accurate and efficient predictions. It then provides an overview of the research performed in developing hybrid methods for partially rarefied, hypersonic gas flows. Finally, some results derived from current state of the art hybrid codes are presented and emerging developments are described.

B. EXAMPLES OF MULTI-SCALE HYPERSONIC FLOWS

At moderately high altitudes, some regions of the flow about blunted, hypersonic vehicles can be rarefied due to very small length scales, within a mostly continuum flow field. For example, Fig. 20 shows a Schlieren image of typical flow over a blunted, hypersonic vehicle. In general, the flow length scales within the thin bow shock and boundary layer are small and the collision length scales in the wake are sufficiently large such that a microscopic analysis of these regions is required to maintain the physical accuracy of the simulation. As the vehicle spends a larger portion of its time in these partially-rarefied flows with recently proposed trajectory maneuvers [92], the ability to maintain physically accurate

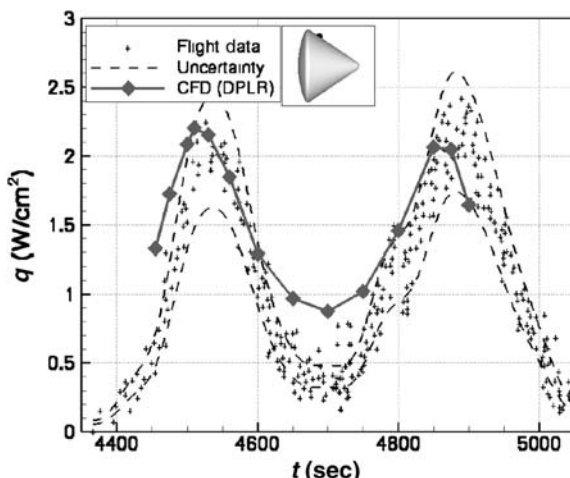
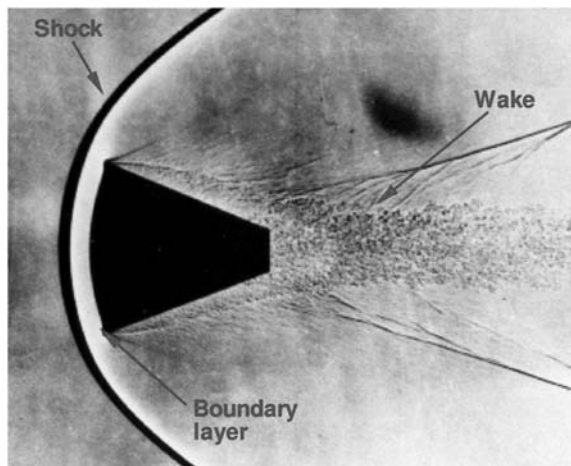
Fig. 20 Schematic of a multi-scale hypersonic flow over a blunted body with regions that typically exhibit non-continuum effects.

predictions becomes even more important to minimize the predictive uncertainty and increase vehicle reliability.

The AS-202 flight case from the Apollo program is one of the few flight tests that used a skip trajectory. Wright et al. [93] performed detailed simulations of the entire flight trajectory using a continuum description of the flow. In general, they found that agreement between available heat transfer measurements from the flight tests and numerical predictions was good over most of the trajectory. However, at the crest of the skip portion of the trajectory, the simulation results over-predict the measured data across most of the lee side of the aft-body. For example, Fig. 21 compares heat transfer predictions and flight measurements from a calorimeter located on the top of the lee side. During the skip portion, the CFD simulation method over-predicts the measurements by over a factor of two.

The corresponding Knudsen number of the vehicle at this point on the trajectory is about 0.001, and it is therefore possible that

Fig. 21 Heat transfer predictions made by macroscopic methods (CFD) on the after-body of the AS-202 flight capsule and comparison with experimental flight data [93].



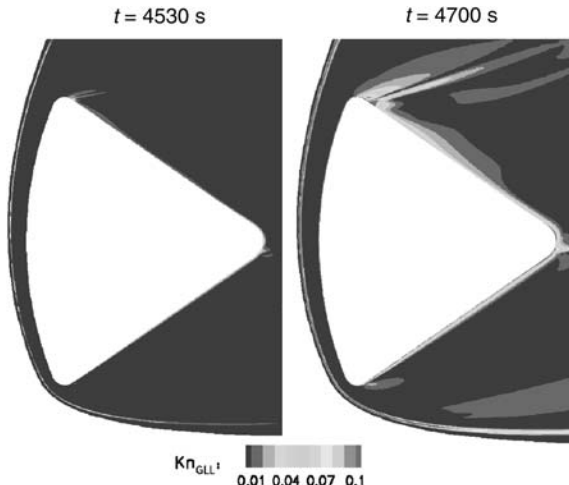


Fig. 22 Variation of the gradient-length Knudsen number for flow over the AS-202 capsule at two different trajectory points [93] (see color section).

the flow around the vehicle has transitioned from being fully continuum to partially rarefied. This idea is supported by contours of local Knudsen number shown in Fig. 22 that indicate localized nonequilibrium regions at the higher altitude, $t = 4700$ s trajectory point. Because of this, Wright et al. concluded that the over-prediction of heat transfer may be due to the inability of the continuum methods used in that work to capture the important microscopic effects. However, for this particular flow, application of kinetic methods to the entire flow would be computationally expensive. Instead, a multi-scale approach that only uses the expensive, microscopic description in required regions, while using the continuum description throughout the rest of the flow field, is more suitable to examine any rarefied flow effects.

Simulation of other multi-scale, hypersonic flows is of particular importance for developing technologies that will enable potential high-mass, Mars missions. Compared to the Earth's atmosphere, Mars' relatively thin atmosphere causes entry vehicles to decelerate at much lower altitudes. Depending on the mass, size, and shape of a vehicle, it may never reach a subsonic terminal velocity. This necessitates additional technology to slow the vehicle so that it can reach subsonic speeds with sufficient time to prepare for landing. Many of these new technologies require successful prediction of multi-scale interaction flows to ensure reliability. In order to increase the frontal area of the vehicle, an inflatable aerodynamic decelerator (IAD), often called a ballute, may be used to slow the vehicle down at higher altitudes [94]. The dynamic fluid structure interaction at deployment will most certainly occur in the rarefied regime [95] and will require a detailed fluid structure interaction with accurate prediction of surface properties throughout the entire trajectory. In addition, the flow field around the deployed ballute in the upper atmosphere will include both large regions of continuum flow, owing to the very

large body, and small nonequilibrium interactions around tethers, connections, and the low density wake which may require kinetic analysis. Another possible option that will enable high-mass, Mars missions is supersonic retro-propulsion [96], where a jet is aimed out the front of the aeroshell displacing the shock and increasing the total axial force on the vehicle. At high altitudes, these flows may include a very dense, continuum region within the core of the jet, while much of the flow may be rarefied. Multi-scale methods that can accurately simulate these flow fields will be an indispensable tool in development of these new technologies that enable future scientific and exploration missions [94].

Hypersonic viscous interaction flows involve the interactions between shock waves and boundary layers, producing complex and highly non-linear flow fields. Shock-boundary layer interactions occur in inlets of supersonic and hypersonic propulsion devices and in the vicinity of control surfaces on hypersonic vehicles. In such flows, shock-shock interactions often produce reflected shock waves that impinge on the surface of the vehicle. The interaction between a strong shock wave and a boundary layer often causes the flow to separate and form a region of high-pressure, recirculating gas next to the surface. High-speed flow hitting such a separation region significantly alters shock structures and interaction regions, which, in turn, affect the extent of flow separation. Peak aerothermal loads are observed at the location of shock impingement on the vehicle surface and therefore accurate prediction of this phenomenon is important in the design of a hypersonic vehicle. In addition, the heating and frictional loads generated within a separated region are drastically different than when the flow is purely attached. Such differences may reduce the effectiveness of a control surface and thus accurately predicting the extent of any flow separation is also a very important aspect in the design of hypersonic vehicles.

An example of a viscous interaction flow is shown in Fig. 23 that was part of a blind validation study with experimental measurements taken in the Large Energy National Shock (LENS) facility at the Calspan - University of Buffalo Research Center (CUBRC) [97]. For Run 11, which had a global Knudsen number of 0.0008, it has been found that solutions to the Navier-Stokes equations predict a separation bubble that forms along the surface that is significantly larger than experimental measurements. In general, DSMC predictions of the same case have better agreement with the experimental measurements in this leading edge region, but require a large computational expense to accurately resolve the shock impingement downstream of the flare junction [97, 98]. Instead, if a multi-scale method can apply a continuum solver in regions where the mean free path is small, and the Navier-Stokes equations are valid, the computational requirements of obtaining a physically accurate solution may be reduced.

C. HYBRID PARTICLE-CONTINUUM FRAMEWORK

This section provides an overview of typical challenges associated with the development of hybrid particle-continuum simulation techniques along with

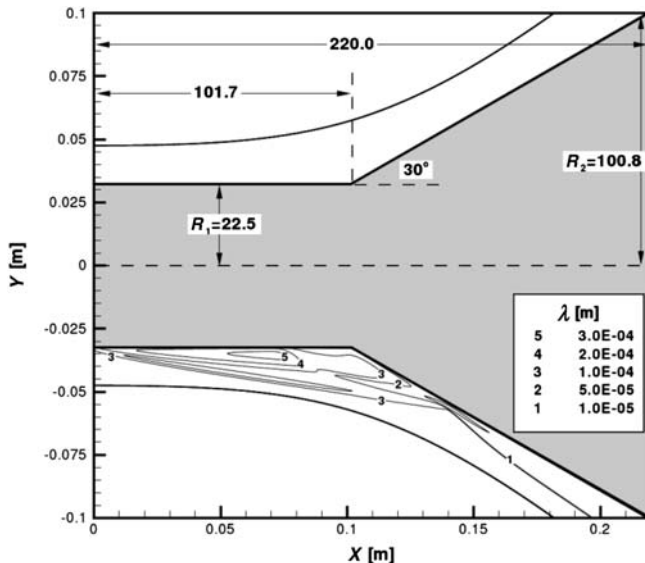


Fig. 23 Geometry and variation in mean free path for a hypersonic shock-boundary layer interaction test case [116].

published solutions. First, an overview of methods to compute the demarcation between continuum and rarefied regions of the flow is provided. Then, typical coupling procedures used to transfer information between flow modules is outlined.

1. CONTINUUM BREAKDOWN

Both the accuracy and efficiency of a hybrid DSMC-CFD method depend strongly on proper placement of the interface location. For physical accuracy, the interface must be located within regions that can be considered in collisional equilibrium, where the velocity distribution is only slightly perturbed from equilibrium, and the Navier-Stokes equations are valid. To maximize efficiency, a hybrid method requires the interface between CFD and DSMC to be located near the edge of the collisional equilibrium region. Empirical breakdown parameters have been used both as switching criteria for hybrid rarefied-continuum methods and also in analysis of continuum predictions to ensure that the Navier-Stokes equations are valid throughout the flow field.

Boyd et al. [99, 100] have proposed a gradient-length Knudsen number, shown in Eq. (30) where λ is the local mean free path and Q is some macroscopic

flow quantity of interest, such as density, flow speed, or temperature.

$$Kn_{GL-Q} = \lambda \left| \frac{\nabla Q}{Q} \right| \quad (30)$$

The local mean free path used in the gradient-length Knudsen number is calculated using Eq. (31) where n is the number density, T_{TRA} is the translational temperature, ω is the macroscopic viscosity temperature exponent, and T_{ref} is the temperature that the reference cross section, σ_{ref} , is calculated at, which is consistent with the variable hard sphere collision model [4] used in the DSMC simulation and the corresponding temperature viscosity relation used within the CFD module. The reference cross section can be calculated using Eq. (32) where k is the Boltzmann constant and μ_{ref} is the coefficient of viscosity at T_{ref} .

$$\lambda = \frac{1}{\sqrt{2}n\sigma_{ref}} \left(\frac{T_{TRA}}{T_{ref}} \right)^{\omega-1/2} \quad (31)$$

$$\sigma_{ref} = \frac{15\sqrt{\pi mkT_{ref}}}{2(5-2\omega)(7-2\omega)\mu_{ref}} \quad (32)$$

The gradient-length Knudsen numbers are directly related to the Chapman-Enskog expansion terms for mass, momentum, and energy molecular diffusion. Through detailed comparison of kinetic and continuum simulations of planar shock waves, spherically blunted bodies, and interaction flows, Boyd et al. found that in regions where the maximum gradient-length Knudsen number exceeded 0.05, the difference between full DSMC and full CFD exceeds 5%. Therefore, a conservative breakdown parameter of 0.05, such that DSMC is used when the maximum >0.05 and CFD is used elsewhere, should not introduce more than 5% error within a hybrid method. Recent results [101, 102] with a hybrid DSMC-CFD method have shown that relaxing the breakdown parameter to a value of 0.1 still produces hybrid predictions that remain in excellent agreement with full DSMC simulation results.

Development of continuum breakdown parameters has been studied extensively, with alternative approaches considering the shear stress and heat flux terms in the Chapman-Enskog expansion, entropy production, and direct comparisons of velocity distribution functions. This remains an area of active research in the development of hybrid DSMC-CFD methods.

In addition to collisional nonequilibrium, a hybrid method must ensure that DSMC is used in other regions of the flow where certain physical processes, such as rotational relaxation, are important but are ignored in the continuum module. For example, if the continuum module assumes that translational and rotational modes are in equilibrium, then the hybrid method should ensure that regions that can be considered in collisional equilibrium, such that the velocity distribution function can be described by a Chapman-Enskog velocity distribution function,

but where the rotational mode is not in equilibrium with the translational mode be assigned to the DSMC module. For near equilibrium flows over blunt bodies, which are of interest for hybrid methods, almost the entire region behind the strong expansion displays significant nonequilibrium between the rotational and translational energy modes. This would greatly increase the size of the region simulated with the DSMC module in a hybrid simulation and have a serious adverse effect on the numerical efficiency. Schwartzentruber et al. [101, 103, 104] found that only the strong thermal relaxation behind a strong bow shock had a large adverse effect on the physical accuracy of the hybrid method and proposed an additional breakdown parameter shown in Eq. (33) with a switching parameter of 0.01 so that regions where the translational temperature exceeds the rotational temperature by more than 1% are simulated with the DSMC method.

$$Kn_{ROT-NEQ} = \frac{(T_{TRA} - T_{ROT})}{T_{ROT}} \quad (33)$$

In addition to the strong bow shock, this additional breakdown parameter has been found to increase the size of the DSMC region behind the recompression wave in the wake of blunt body flows [105]. This has an adverse effect on the efficiency of a hybrid method, but is required to maintain sufficient physical accuracy. By inclusion of a separate rotational energy equation in the continuum module, nearly the entire region that displays rotational nonequilibrium with near translational equilibrium can be instead simulated within the continuum module with little physical error.

However, even if a separate rotational energy equation is included in the continuum module, the additional breakdown parameter is still needed to ensure the rotational energy probability density function is near equilibrium in the continuum region, but the breakdown value can be relaxed to 0.1 such that DSMC is used in all regions where the rotational temperature deviates from the translational temperature by more than 10%.

For example, Fig. 24 shows a comparison of translational temperature prediction of a hybrid method with (top) and without (bottom) the rotational nonequilibrium switch activated along with full DSMC simulation results. Without the nonequilibrium switch, the interface location between the CFD and DSMC modules is located very near the shock. Since CFD does not contain the physical accuracy required to model this portion of the rotational relaxation process as the rotational energy distribution function is highly non-Boltzmann in this region, the post shock temperatures are over predicted compared to full DSMC. With a rotational nonequilibrium cutoff parameter of 0.1, such that DSMC is used in regions where the difference between the translational and rotational temperatures exceeds 10% of the rotational temperature, the portion of the flow field modeled with the continuum solver is slightly decreased to only regions where

Fig. 24 Comparison of translational temperatures predicted by the MPC method with (top) and without (bottom) the rotational nonequilibrium breakdown parameter compared with full DSMC of Mach 12 flow over a cylinder with a global Knudsen number of 0.01.

the continuum solver is physically valid and agreement between the hybrid method and full DSMC results is greatly improved.

In addition, velocity and rotational energy distribution functions are sampled from the full DSMC solution at locations at the edge of the interface location predicted by each of the hybrid simulations denoted as A and B in Fig. 24. Figures 25a and 25b, respectively, compare the velocity distribution functions and rotational energy distribution function sampled at point A from DSMC with equilibrium theory. Although the velocity probability density functions are in excellent agreement with equilibrium theory,

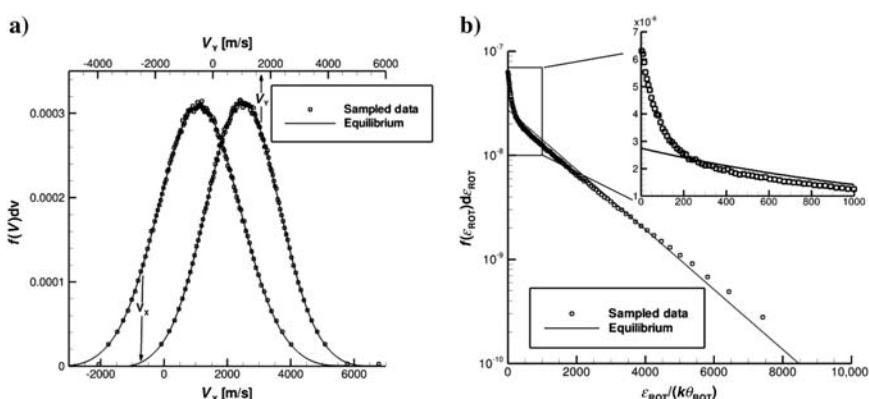
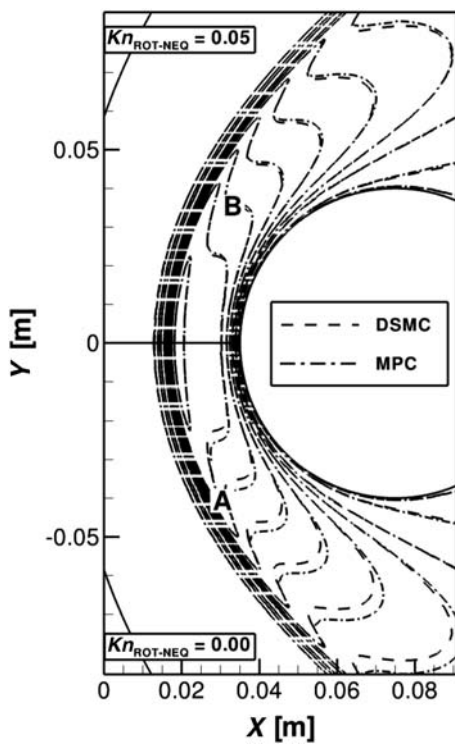


Fig. 25 Comparison of probability density functions predicted by DSMC and equilibrium theory at point A shown in Fig. 24: a) velocity; b) rotational energy.

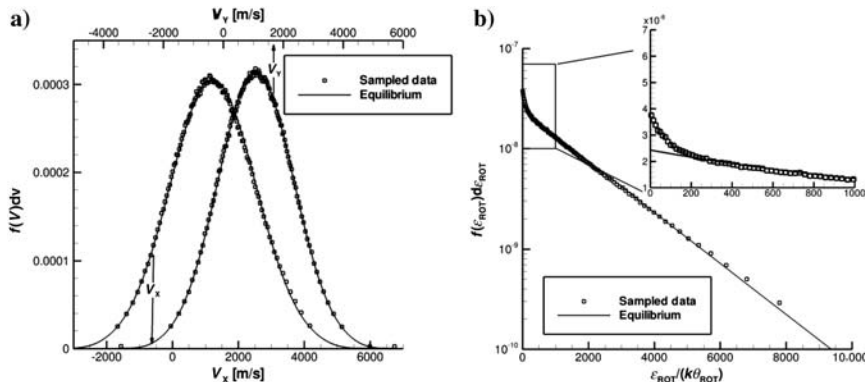


Fig. 26 Comparison of probability density functions predicted by DSMC and equilibrium theory at point B shown in Fig. 24: a) velocity; b) rotational energy.

the rotational energy distribution function differs significantly from equilibrium. The peak in the rotational energy probability density function at low rotational energies signifies that there is still a large number of particles that have not experienced a rotationally inelastic collision at the post shock temperature and still maintain the slope of an equilibrium probability density function at the free stream temperature. In contrast, Figs. 26a and 26b compare the velocity and rotational energy distribution functions, respectively, at the continuum interface location computed with the added breakdown parameter at point B. At this point in the flow, both the velocity and rotational energy probability density functions are in much better agreement with the equilibrium description and the models used in the continuum solver are valid. Since the equilibrium rotational energy distribution function is calculated based on the average rotational energy, comparison of higher order moments, such as the variance, calculated from sampled data and the equilibrium distribution can be used as a measure of degree of rotational nonequilibrium. At point A, the sampled variance differs by nearly 25% from equilibrium, while the sampled variance differs by less than 10% from the equilibrium value at point B.

D. COUPLING PROCEDURES

In hypersonic flows, the continuum breakdown surfaces may occur in regions of both subsonic and supersonic flow. Therefore, hybrid methods for such flows must be able to account for full two-way coupling between the DSMC and CFD algorithms. The method of information transfer between particle and continuum methods can typically be split into two categories: coupling by maintaining consistent fluxes or coupling by maintaining consistent state properties in reservoir cells. Figure 27 provides a visual comparison of the two coupling methods. A

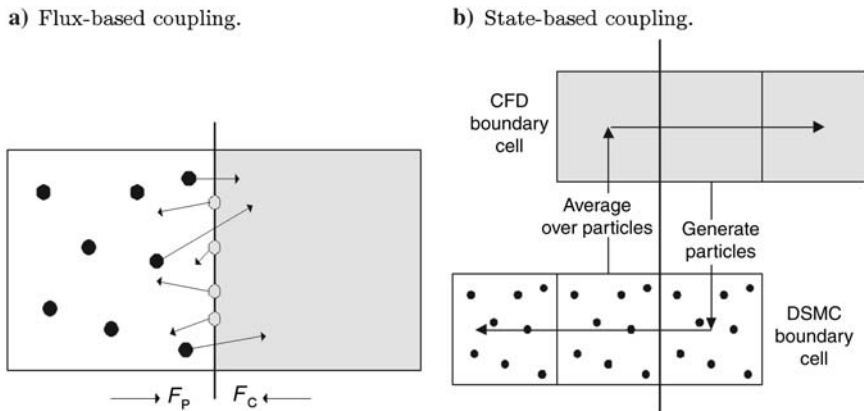


Fig. 27 Schematic of typical hybrid coupling procedures.

flux-based, coupling method, which is depicted in Fig. 27a, involves calculating fluxes of conserved variables at the interface location according to particle cell, F_p , and according to the continuum cell, F_c . The particle flux can be directly calculated by tracking the number of particles that cross the interface, but the continuum flux must be extrapolated using macroscopic cell-averaged state quantities and their gradients. In general, the estimated fluxes are not the same and are often modified to ensure that mass, momentum, and energy are conserved within the simulation. This modified flux is applied as a boundary condition to both simulation techniques and is used to update the continuum solution and to estimate the probability density functions that are sampled to assign DSMC particle information.

With state-based coupling, shown in Fig. 27b, transfer of information between simulation methods is performed by one method providing a Dirichlet boundary condition to the other simulation technique. Each method can then update its respective regions using algorithms internal to the corresponding simulation method. For coupling from the particle to the continuum method, these values are calculated by performing an averaging procedure to sample state quantities of interest, such as average density, velocity, and energy in DSMC cells along the edge of the interface location. These values are assigned to continuum ghost cells that are used to calculate inviscid and viscous fluxes to update the solution within the continuum domain. For coupling from the continuum to the particle method, average state and gradient information is used to estimate the probability density functions in DSMC boundary cells. Before each particle iteration, all simulators in these boundary cells are deleted and new particles are generated consistent with the estimated probability density functions constructed from the continuum data. Then, simulators in reservoir cells are allowed to move throughout the domain using the internal DSMC move algorithm.

For both coupling procedures, techniques to reduce the statistical scatter are often employed to ensure that the continuum method remains stable. For many flows that involve strong two-way coupling, the efficiency of the hybrid method is determined by how often information is passed between flow modules. Unfortunately, the statistical scatter of averaged DSMC data over very few time-steps can have large variations at the continuum-rarefied boundary that could create numerical instabilities in the continuum module. Many techniques to reduce this statistical scatter have been proposed for different hybrid methods and will be reviewed in the following subsection.

Often, an overlap region between the continuum and particle boundary cells is also used, where the particle region is extended into the continuum domain and both simulation methods calculate the solution. These overlap cells can be used to filter the physical inaccuracies from an incorrect initial solution or to compare simulation predictions to ensure that the interface location is located in a near continuum region, where the Navier–Stokes equations are appropriate.

E. HYBRID CODES AND THEIR APPLICATION

Over the past two decades, many studies of hybrid particle-continuum techniques have been performed that have continuously expanded the state of the art capabilities.

Hash and Hassan also coupled particle and continuum codes using a flux-based procedure to simulate Couette flow [106] and near equilibrium, hypersonic flow over a sting-mounted blunted sphere-cone [107]. Bird's DSMC method that took into account internal excitation and finite rate chemistry was used as the DSMC module while the modified Navier–Stokes equations were solved on a structured grid in the continuum module. Both the Marshak condition and property interpolation technique were employed to transfer information at the interface. Along much of the rarefied-continuum interface location for the hypersonic flow case, the normal Mach number was small which greatly increased the statistical scatter associated with particle fluxes at the boundary. The statistical scatter was reduced using a smoothing operator over highly sampled data for the property extrapolation before imposing the flux boundary condition. Although these smoothing procedures reduced the scatter for bulk properties, oscillations of properties with large gradients along the boundary could produce unphysical, negative values of density. In addition, the statistical scatter of gradients were still appreciable with low order smoothing operators so a fourth-order smoothing procedure with a 7-point stencil had to be used in certain regions. To maintain consistency at the interface, the researchers also found that sampling particle velocities from the Chapman-Enskog velocity probability density function was necessary in regions that displayed significant momentum or energy transfer [106].

Schwartzentruber and Boyd [108] have proposed a Modular Particle-Continuum (MPC) method to simulate partially rarefied, steady-state flow over

hypersonic vehicles. This method couples existing DSMC and CFD modules that remain nearly unmodified. State-based coupling is performed with particle velocities assigned by sampling of the Chapman–Enskog velocity distribution function using the algorithm of Garcia and Alder [109], while the statistical scatter of particle samples is reduced by use of a an exponential moving average, Sun and Boyd [110], which is shown in Eq. (34) where Q is a quantity of interest, j is the current iteration, and ϕ is the subrelaxation parameter. Typically a subrelaxation parameter value of 0.001 is used.

$$\langle Q \rangle_j = (1 - \phi)\langle Q \rangle_{j-1} + \phi Q_j \quad (34)$$

The MPC method does not call the continuum solver until the interface has stopped moving to ensure that the continuum method is applied only in regions where the Navier–Stokes equations are valid. This is vital for the proper simulation of the shock layers over hypersonic, blunt bodies to correctly predict the post-shock condition and shock standoff distance. The method has been successfully applied to reproduce full DSMC predictions for planar shock waves [108], two-dimensional (2-D) blunt body flows [111, 103], and axi-symmetric blunt body [101] and viscous interaction flows [116].

Recently, extensions of the MPC method have allowed for simulation of rotational [105] and vibrational nonequilibrium [113] throughout the entire flow domain, and the method has been parallelized [114] for distributed memory systems using dynamic domain decomposition routines. The computational speed-up of the MPC method over full DSMC has ranged from about 1.5 for

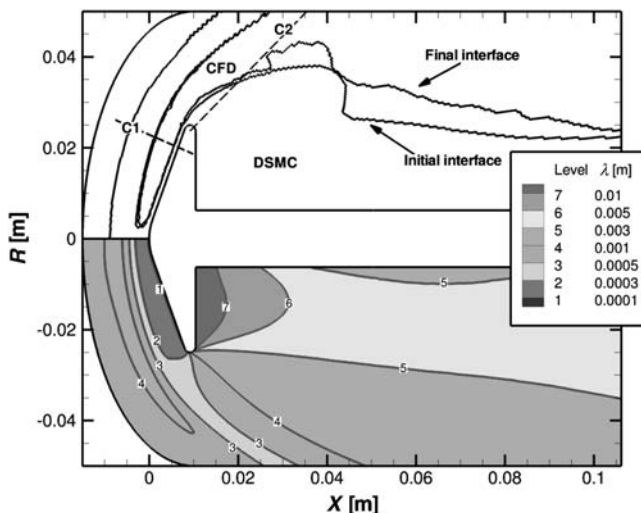


Fig. 28 Interface location and variation of mean free path around a hypersonic probe.

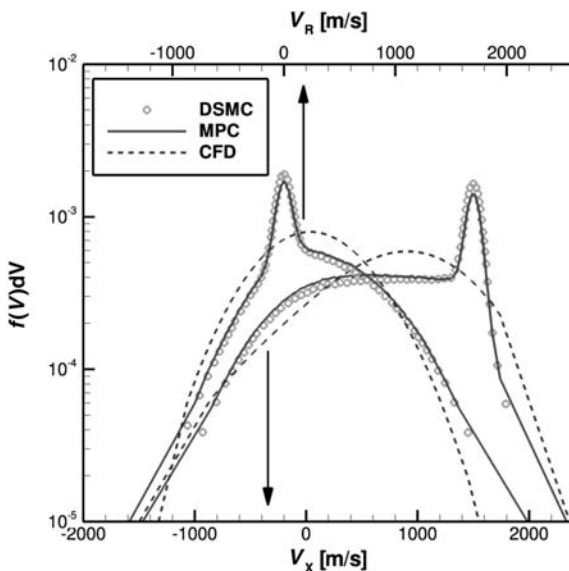


Fig. 29 Comparison of velocity distribution functions predicted by DSMC, CFD, and the MPC method within the bow shock.

flows that are nearly entirely rarefied to over a factor of 30 for near equilibrium flows.

An example of results obtained by the MPC method for Mach 20 flow over a sting-mounted planetary probe with a global Knudsen number of 0.01 is shown in Figs. 28–31. This flow condition corresponds to a low-density experiment performed at the CNRS facility in France [115–117]. Owing to the very low free stream densities associated with this expansion tunnel, the vibrational energy is assumed frozen at room temperature for all flow conditions. The variation in mean free path around the probe and initial and final rarefied-continuum interface locations are shown in Fig. 28.

Figures 29 and 30, respectively, compare velocity and rotational energy probability density functions predicted by full DSMC, full CFD, and the MPC method at a point in the bow shock. Owing to the high degree of collisional

Downloaded by 80.82.77.83 on February 21, 2018 | http://arc.aiaa.org | DOI: 10.2514/4.103292

flow condition corresponds to a low-density experiment performed at the CNRS facility in France [115–117]. Owing to the very low free stream densities associated with this expansion tunnel, the vibrational energy is assumed frozen at room temperature for all flow conditions. The variation in mean free path around the probe and initial and final rarefied-continuum interface locations are shown in Fig. 28.

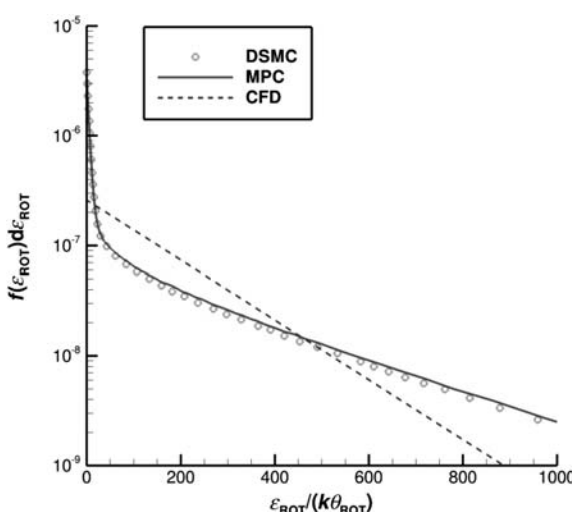


Fig. 30 Comparison of rotational energy distribution functions predicted by DSMC, CFD, and the MPC method within the bow shock.

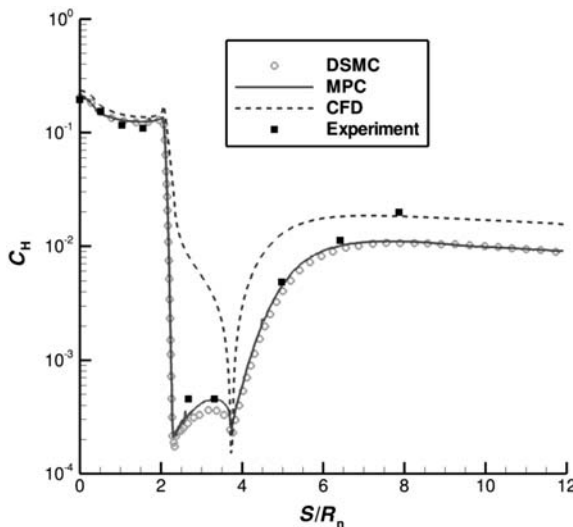


Fig. 31 Surface heat transfer along the planetary probe.

nonequilibrium within the shock, the CFD velocity distribution function, which is generated from gradients and the first order Chapman-Enskog expansion, does not contain sufficient information to correctly generate the velocity distribution function predicted by full DSMC. In contrast, the MPC method is able to remain in very good agreement with DSMC throughout the entire velocity space. Despite the macroscopic rotational temperature predicted by CFD being within 5% of the full DSMC result, the rotational energy distribution function predicted by full CFD is in poor agreement with the DSMC result throughout the entire rotational energy space. Similar to the velocity distribution function, the MPC method remains in excellent agreement with full DSMC results for the rotational energy probability density function.

Figure 31 compares the surface coefficient of heat flux, defined in Eq. (35), predicted by full DSMC, full CFD, and the MPC method with available experimental measurements.

$$C_H = \frac{q}{\frac{1}{2} \rho_\infty U_\infty^3} \quad (35)$$

Along the fore body where the flow is highly collisional, all three methods are in good agreement with each other and the experimental measurements. Despite this highly collisional flow, CFD still slightly over predicts DSMC and MPC results. This is due to the inability to correctly model the Knudsen layer within the CFD solver. As the flow expands around the corner, full CFD over predicts both DSMC and experimental measurements by over an order of

magnitude. In contrast, the MPC method remains in good agreement with both the experimental measurements and the full DSMC results. Similarly, the MPC method remains in excellent agreement with full DSMC and experimental measurements along the sting mount, while full CFD over predicts full DSMC along the entire sting mount.

F. REMAINING CHALLENGES

Despite the sophisticated capabilities of hybrid particle-continuum simulation techniques, additional advancements of the technology can still be achieved. One area is further study of a predictor of continuum breakdown. Many of the switching parameter values have been found by comparison of predictions of fully continuum and kinetic simulation techniques. However, in all flows of interest for application of hybrid particle-continuum methods, the continuum regions are dependent on accurate prediction of nearby rarefied regions. Therefore, full simulations of these flows with a continuum method can shift the results in regions that are truly continuum. Additional study of the rarefied-continuum breakdown and switching parameter using a hybrid particle-continuum simulation technique may result in a more appropriate switching parameter that reduces the computational cost of hybrid techniques while maintaining the same level of physical accuracy.

Further development of the hybrid methods to simulate full 3-D flows may have the largest computational savings over fully kinetic methods. However, very few hybrid particle-continuum methods have demonstrated the capability of simulating these flows over complicated 3-D geometries. Further work in this area to mature the technology is still required.

As seen with the inclusion of rotational and vibrational energy nonequilibrium within the MPC method, the use of additional physical models within a hybrid particle-continuum code may require extra considerations to maintain a high level of physical accuracy. Very few studies of the effect of dissociation [8, 118] and ionization on continuum breakdown have been performed. Among other unknown difficulties, the mitigation of the statistical scatter associated with trace species may be necessary.

VI. SUMMARY

The direct simulation Monte Carlo method (DSMC) has evolved over more than 50 years into a powerful analysis tool for computation of kinetic nonequilibrium hypersonic flows. The heart of the technique is its detailed treatment of collisional phenomena including momentum exchange, relaxation of internal energy modes, chemistry, radiation, and gas–surface interaction. In this article, the current status of DSMC models for simulating these physical phenomena has been reviewed. It was demonstrated that the DSMC technique is able to simulate accurately highly

nonequilibrium velocity distribution functions generated inside strong shock waves of noble gases. However, there is still a need for development of collision cross-section models for large temperature ranges and for specific species interactions. Detailed validation of rotational energy relaxation models was also demonstrated at the level of rotational energy distribution functions measured inside a strong shock wave. However, there are no corresponding measurements of such phenomena at the high temperature conditions of hypersonic flows with the result that DSMC models of such phenomena are not yet validated. Both phenomenological and detailed, quantum transition DSMC models for vibrational relaxation were discussed. Similar to the situation for rotational relaxation, measurements of vibrational energy distributions in hypersonic flows are required to allow evaluation of the DSMC models. Several different DSMC chemistry models were described and two of them evaluated using detailed information obtained from ab initio computational chemistry analysis. In the absence of detailed measurements of reaction cross sections, such analyses appear very promising to help in the construction and evaluation of detailed DSMC thermochemistry models. Descriptions were also provided of the present status for DSMC computation of charged species (ions, electrons), and radiation. These are also areas where further work is required. The status for DSMC computation of gas–surface interaction was reviewed. It was shown that the idealized Maxwell models employing a combination of diffuse and specular reflection is not able to accurately reproduce reflections measured under hypersonic conditions. While more sophisticated gas–surface interaction models have been developed, their use is limited due to the difficulty in determining parameters in the models. Again, this is an area where ab initio computational analysis using molecular dynamics may be useful for building improved DSMC modeling capabilities.

In terms of application to hypersonic flows, assessment of the DSMC technique using ground-based experimental measurements has been largely successful for surface properties (heat flux, pressure) and overall aerodynamics (drag, pitching moment). However, all of these studies are limited to conditions without chemistry due to the technical challenges of generating high-energy, rarefied flows. The DSMC method has been evaluated using flight data for slender body vehicles (BSUV-2, RAM-C) based on measurements of radiation emission and plasma density. The DSMC technique has also been applied to analyze the entry into Earth's atmosphere of several different blunt body configurations including comparisons with flight measurements for the Space Shuttle, space station Mir, and Stardust. The DSMC technique generally provides excellent comparisons with most of the measured data sets. The confidence obtained in the physical accuracy of the DSMC method has led to its application to analyze the aerothermodynamic performance of proposed vehicles such as balloons and to aid in the design of entry flight experiments. The DSMC technique has played a key role in the design and flight analysis of several NASA Mars entry missions including the entry of Pathfinder and the aerobraking of Mars Global Surveyor. Further notable applications of the DSMC technique

to planetary entries include analysis of the aero-braking maneuver of the Magellan spacecraft in the atmosphere of Venus, and entry into Jupiter of the Galileo probe.

Hybrid DSMC-continuum simulation techniques have evolved over the past two decades as a powerful analysis tool for computation of hypersonic flows that cannot be simulated with either continuum or kinetic methods and still maintain both physical accuracy and numerical efficiency. Typical multi-scale flows that may require application of a hybrid particle-continuum method were described. A review of demarcation and coupling procedures used to construct hybrid methods has been provided. A detailed example of hybrid simulation results was presented that illustrate the benefits provided by this approach.

ACKNOWLEDGMENTS

The author gratefully acknowledges contributions by Tim Deschenes, Erin Farbar, and Jose Padilla to this article. In addition, funding was provided to support this work by the NASA Constellation University Institutes Program (Grant NCC3-989) and the Air Force Office of Scientific Research (Grant FA-9550-11-1-0309).

REFERENCES

- [1] Vincenti, W. G., and Kruger, C. H., *Introduction to Physical Gas Dynamics*, Wiley, New York, 1965.
- [2] Bird, G. A., "Approach to Translational Equilibrium in a Rigid Sphere Gas," *Physics of Fluids*, Vol. 6, 1963, pp. 1518–1519.
- [3] Bird, G. A., *Molecular Gas Dynamics and the Direct Simulation of Gas Flows*, Oxford University Press, Oxford, 1994.
- [4] Bird, G. A., *The DSMC Method*, <https://www.createspace.com/3689652>, 2013.
- [5] Boyd, I. D., "Computation of Atmospheric Entry Flow About a Leonid Meteoroid," *Earth, Moon, and Planets*, Vol. 82, 2000, pp. 93–108.
- [6] Lofthouse, A. J., Boyd, I. D., and Wright, M. J., "Effects of Continuum Breakdown on Hypersonic Aerothermodynamics," *Physics of Fluids*, Vol. 19, 2007, Article 027105.
- [7] Lofthouse, A. J., Scalabrin, L. C., and Boyd, I. D., "Velocity Slip and Temperature Jump in Hypersonic Aerothermodynamics," *Journal of Thermophysics and Heat Transfer*, Vol. 22, 2008, pp. 38–49.
- [8] Holman, T. D., and Boyd, I. D., "Effects of Continuum Breakdown on Hypersonic Aerothermodynamics for Reacting Flow," *Physics of Fluids*, Vol. 23, 2011, Article 027101.
- [9] Alder, B. J., and Wainwright, T. E., "Studies in Molecular Dynamics," *Journal of Chemical Physics*, Vol. 27, 1957, pp. 1208–1209.
- [10] Boyd, I. D., "Vectorization of a Monte Carlo Simulation Scheme for Nonequilibrium Gas Dynamics," *Journal of Computational Physics*, Vol. 96, 1991, pp. 411–427.

- [11] Dietrich, S., and Boyd, I. D., "Scalar and Parallel Optimized Implementation of the Direct Simulation Monte Carlo Method," *Journal of Computational Physics*, Vol. 126, 1996, pp. 328–342.
- [12] LeBeau, G. J., "A Parallel Implementation of the Direct Simulation Monte Carlo Method," *Computer Methods in Applied Mechanics and Engineering*, Vol. 174, 1999, pp. 319–337.
- [13] Bird, G. A., "Sophisticated Versus Simple DSMC," *Proceedings of the 25th International Symposium on Rarefied Gas Dynamics*, St. Petersburg, Russia, July 2006.
- [14] Bird, G. A., "Monte Carlo Simulation in an Engineering Context," *Progress in Astronautics and Aeronautics*, Vol. 74, AIAA, New York, 1981, pp. 239–255.
- [15] Koura, K., and Matsumoto, H., "Variable Soft Sphere Molecular Model for Air Species," *Physics of Fluids A*, Vol. 4, 1992, pp. 1083–1085.
- [16] Alsmeyer, H., "Density Profiles in Argon and Nitrogen Shock Waves Measured by the Absorption of an Electron Beam," *Journal of Fluid Mechanics*, Vol. 74, 1976, pp. 497–513.
- [17] Pham-Van-Diep, G., Erwin, D., and Muntz, E. P., "Nonequilibrium Molecular Motion in a Hypersonic Shock Wave," *Science*, Vol. 245, 1989, pp. 624–626.
- [18] Farbar, E. D., and Boyd, I. D., "Simulation of FIRE II Reentry Flow Using the Direct Simulation Monte Carlo Method," AIAA Paper 2008-4103, June 2008.
- [19] Balakrishnan, J., Boyd, I. D., and Braun, D. G., "Monte Carlo Simulation of Vapor Transport in Physical Vapor Deposition of Titanium," *Journal of Vacuum Science & Technology A*, Vol. 18, 2000, pp. 907–916.
- [20] Boyd, I. D., "Analysis of Rotational Nonequilibrium in Standing Shock Waves of Nitrogen," *AIAA Journal*, Vol. 28, 1990, pp. 1997–1999.
- [21] Parker, J. G., "Rotational and Vibrational Relaxation in Diatomic Gases," *Physics of Fluids*, Vol. 2, 1959, pp. 449–462.
- [22] Borgnakke, C., and Larsen, P. S., "Statistical Collision Model for Monte Carlo Simulation of Polyatomic Gas Mixture," *Journal of Computational Physics*, Vol. 18, 1975, pp. 405–420.
- [23] Lumpkin, F. E., Haas, B. L., and Boyd, I. D., "Resolution of Differences Between Collision Number Definitions in Particle and Continuum Simulations," *Physics of Fluids A*, Vol. 3, 1991, pp. 2282–2284.
- [24] Boyd, I. D., "Relaxation of Discrete Rotational Energy Distributions Using a Monte Carlo Method," *Physics of Fluids A*, Vol. 5, 1993, pp. 2278–2286.
- [25] Robben, R., and Talbot, L., "Experimental Study of the Rotational Distribution Function of Nitrogen in a Shock Wave," *Physics of Fluids*, Vol. 9, 1966, pp. 653–662.
- [26] Millikan, R. C., and White, D. R., "Systematics of Vibrational Relaxation," *Journal of Chemical Physics*, Vol. 39, 1963, pp. 3209–3213.
- [27] Park, C., *Nonequilibrium Hypersonic Aerothermodynamics*, Wiley, New York, 1990.
- [28] Boyd, I. D., "Analysis of Vibration-Dissociation-Recombination Processes Behind Strong Shock Waves of Nitrogen," *Physics of Fluids A*, Vol. 4 (1), 1992, pp. 178–185.
- [29] Bergemann, F., and Boyd, I. D., "New Discrete Vibrational Energy Method for the Direct Simulation Monte Carlo Method," *Rarefied Gas Dynamics*, Progress in Astronautics and Aeronautics, AIAA, Washington, Vol. 158, 1994, p. 174.

- [30] Boyd, I. D., and Josyula, E., "State Resolved Vibrational Relaxation Modeling for Strongly Nonequilibrium Flows," *Physics of Fluids*, Vol. 23, 2011, Article 057101.
- [31] Adamovich, I. V., Macheret, S. O., Rich, J. W., and Treanor, C. E., "Vibrational Energy Transfer Rates Using a Forced Harmonic Oscillator Model," *Journal of Thermophysics and Heat Transfer* Vol. 12, 1998, pp. 57–65.
- [32] Meolans, J. G., and Brun, R., "Nonequilibrium Vibrational Population Behind Shock Waves: Comparison Theory–Experiments," *Proceedings of the 15th International Symposium on Rarefied Gas Dynamics*, Teubner, Stuttgart, 1986, p. 345.
- [33] Haas, B. L., and Boyd, I. D., "Models for Direct Monte Carlo Simulation of Coupled Vibration-Dissociation," *Physics of Fluids A*, Vol. 5, 1993, pp. 478–489.
- [34] Hornung, H. G., "Induction Time for Nitrogen Dissociation," *Journal of Chemical Physics*, Vol. 56, 1972, pp. 3172–3174.
- [35] Bose, D., and Candler, G. V., "Thermal rate Constants of the $\text{N}_2 + \text{O} \rightarrow \text{NO} + \text{N}$ Reaction Using Ab Initio 3A" and 3A' Potential Energy Surfaces," *Journal of Chemical Physics*, Vol. 104, 1996, pp. 2825–2834.
- [36] Boyd, I. D., Bose, D., and Candler, G. V., "Monte Carlo Modeling of Nitric Oxide Formation Based on Quasi-Classical Trajectory Calculations," *Physics of Fluids*, Vol. 9, 1997, pp. 1162–1170.
- [37] Boyd, I. D., "Modeling Backward Chemical Rate Processes in the Direct Simulation Monte Carlo Method," *Physics of Fluids*, Vol. 19, 2007, Article 126103.
- [38] Gallis, M. A., and Harvey, J. K., "Maximum Entropy Analysis of Chemical Reaction Energy Dependence," *Journal of Thermophysics and Heat Transfer*, Vol. 10, 1996, pp. 217–223.
- [39] Koura, K., "A Set of Model Cross-sections for the Monte Carlo Simulation of Rarefied Real Gases: Atom-Diatom Collisions," *Physics of Fluids*, Vol. 6, 1994, pp. 3473–3486.
- [40] Boyd, I. D., "A Threshold Line Dissociation Model for the Direct Simulation Monte Carlo Method," *Physics of Fluids*, Vol. 8, 1996, pp. 1293–1300.
- [41] Bird, G. A., "The Q-K Model for Gas-Phase Chemical Reaction Rates," *Physics of Fluids*, Vol. 23, 2011, Article 106101.
- [42] Boyd, I. D., "Nonequilibrium Chemistry Modeling in Rarefied Hypersonic Flows," *Chemical Dynamics in Extreme Environments*, edited by R. A. Dressler, World Scientific Press, Singapore, 2001, pp. 81–137.
- [43] Wysong, I. J., Dressler, R. A., Chiu, Y. H., and Boyd, I. D., "Direct Simulation Monte Carlo Dissociation Model Evaluation: Comparison to Measured Cross-sections," *Journal of Thermophysics and Heat Transfer*, Vol. 16, 2002, pp. 83–93.
- [44] Bird, G. A., "Nonequilibrium Radiation During Re-entry at 10 km/s," AIAA Paper 87-1543, June 1987.
- [45] Carlson, A. B., and Hassan, H. A., "Direct Simulation of Re-entry Flows With Ionization," *Journal of Thermophysics and Heat Transfer*, Vol. 6, 1992, pp. 400–404.
- [46] Boyd, I. D., "Monte Carlo Simulation of Nonequilibrium Flow in Low Power Hydrogen Arcjets," *Physics of Fluids*, Vol. 9, 1997, pp. 3086–3095.
- [47] Gallis, M. A., and Harvey, J. K., "Atomic Species Radiation from Air Modeled Using the Direct Simulation Monte Carlo Method," *Journal of Thermophysics and Heat Transfer*, Vol. 9, 1995, pp. 456–463.

- [48] Kossi, K. K., Boyd, I. D., and Levin, D. A., "Direct Simulation of High Altitude Ultra-Violet Emission From the Hydroxyl Radical," *Journal of Thermophysics and Heat Transfer*, Vol. 12, 1998, pp. 223–229.
- [49] Bird, G. A., "Direct Simulation of Typical AOTV Entry Flows," AIAA Paper 86-1310, June 1986.
- [50] Carlson, A. B., and Hassan, H. A., "Radiation Modeling With Direct Simulation Monte Carlo," *Journal of Thermophysics and Heat Transfer*, Vol. 6, 1992, pp. 631–636.
- [51] Hinchen, J. J., and Foley, W. M., "Scattering of Molecular Beams by Metallic Surfaces," *Rarefied Gas Dynamics*, edited by J. H. de Leeuw, Academic Press, New York, 1966, Vol. 2, p. 505.
- [52] Lord, R. G., "Some Extensions to the Cercignani-Lampis Gas Scattering Kernel," *Physics of Fluids A*, Vol. 3, 1991, pp. 706–710.
- [53] Padilla, J. F., and Boyd, I. D., "Assessment of Gas-Surface Interaction Models for Computation of Rarefied Hypersonic Flow," *Journal of Thermophysics and Heat Transfer*, Vol. 23, 2009, pp. 96–105.
- [54] Cecil, D. E., and McDaniel, J. C., "Planar Velocity and Temperature Measurements in Rarefied Hypersonic Flow Using Iodine LIF," AIAA Paper 2005-4695, June 2005.
- [55] Moss, J. N., and Price, J. M., "Survey of Blunt Body Flows Including Wakes at Hypersonic Low-Density Conditions," *Journal of Thermophysics and Heat Transfer*, Vol. 11, 1997, pp. 321–329.
- [56] Allegre, J., and Birsch, D., "Blunted Cone at Rarefied Hypersonic Conditions—Experimental Density Flowfields, Heating Rates, and Aerodynamic Forces," CNRS Report, RC 95-2, 1995.
- [57] Holden, M., Kolly, J., and Chadwick, K., "Calibration, Validation, and Evaluation Studies in the LENS Facility," AIAA Paper 95-0291, 1995.
- [58] Holden, M. S., and Wadham, T. P., "Code Validation Study of Laminar Shock/Boundary layer and Shock/Shock Interactions in Hypersonic Flow. Part A: Experimental Measurements," AIAA Paper 2001-1031, January 2001.
- [59] Moss, J. N., and Bird, G. A., "Direct Simulation Monte Carlo Simulations of Hypersonic Flows With Shock Interactions," *AIAA Journal*, Vol. 43, 2005, pp. 2565–2573.
- [60] Boylan, D. E., and Potter, J. L., "Aerodynamics of Typical Lifting Bodies under Conditions Simulating Very High Altitudes," *AIAA Journal*, Vol. 5, 1967, pp. 226–232.
- [61] Griffith, B. J., "Comparison of Aerodynamic Data from the Gemini Flights and AEDC-VKF Wind Tunnels," *Journal of Spacecraft*, Vol. 4, No. 7, 1967, pp. 919–924.
- [62] Griffith, B. J., and Boylan, D. E., "Reynolds and Mach Number Simulation of Apollo and Gemini Re-entry and Comparison with Flight," *Specialists' Meeting on Hypersonic Boundary Layers and Flow Fields of the Fluid Dynamics Panel of AGARD*, North Atlantic Treaty Organization, Paris, 1968, pp. 8-1–8-21.
- [63] Boylan, D. E., and Griffith, B. J., "Simulation of the Apollo Command Module Aerodynamics at Re-entry Altitudes," *Proceedings of the 3rd National Conference on Aerospace Meteorology*, American Meteorological Society, Boston, 1968, pp. 370–378.

- [64] Padilla, J. F., and Boyd, I. D., "Assessment of Rarefied Hypersonic Aerodynamics Modeling and Windtunnel Data," AIAA Paper 2006-3390, June 2006.
- [65] Erdman, P. W., Zipf, E. C., Espy, P., Howlett, L. C., Levin, D. A., Collins, R. J., and Candler, G. V., "Measurements of Ultraviolet Radiation From a 5-km/sec Bow Shock," *Journal of Thermophysics and Heat Transfer*, Vol. 8, 1994, pp. 441–446.
- [66] Levin, D. A., Candler, G. V., Collins, R. J., Erdman, P. W., Zipf, E., and Howlett, L. C., "Examination of Ultraviolet Radiation Theory for Bow Shock Rocket Experiments-I," *Journal of Thermophysics and Heat Transfer*, Vol. 8, 1994, pp. 447–453.
- [67] Levin, D. A., Candler, G. V., Howlett, L. C., and Whiting, E. E., "Comparison of Theory With Atomic Oxygen 130.4 nm Radiation Data From the Bow Shock Ultraviolet 2 Rocket Flight," *Journal of Thermophysics and Heat Transfer*, Vol. 9, 1995, pp. 629–635.
- [68] Candler, G. V., Boyd, I. D., and Levin, D. A., "Continuum and DSMC Analysis of Bow Shock Flight Experiments," AAA Paper 93-0275, January 1993.
- [69] Whiting, E. E., Park, C., Liu, Y., Arnold, J. O., and Paterson, J. A., "NEQAIR96, Nonequilibrium and Equilibrium Radiative Transport and Spectra Program: User's Manual," *NASA Reference Publication 1389*, December 1996.
- [70] Boyd, I. D., Candler, G. V., and Levin, D. A., "Dissociation Modeling in Low Density Hypersonic Flows of Air," *Physics of Fluids*, Vol. 7, 1995, pp. 1757–1763.
- [71] Boyd, I. D., Phillips, W. D., and Levin, D. A., "Sensitivity Studies for Prediction of Ultra-Violet Radiation in Nonequilibrium Hypersonic Bow-Shock Waves," *Journal of Thermophysics and Heat Transfer*, Vol. 12, 1998, pp. 38–44.
- [72] Grantham, W. L., "Flight Results of a 25000 Foot Per Second Reentry Experiment Using Microwave Reflectometers to Measure Plasma Electron Density and Standoff Distance," *NASA Technical Note D-6062*, 1970.
- [73] Linwood-Jones, W., and Cross, A. E., "Electrostatic Probe Measurements of Plasma Parameters for Two Reentry Flight Experiments at 25000 Feet Per Second," *NASA Technical Note D-6617*, 1972.
- [74] Boyd, I. D., "Modeling of Associative Ionization Reactions in Hypersonic Rarefied Flows," *Physics of Fluids*, Vol. 19, 2007, Article 096102.
- [75] Rault, D. F. G., "Aerodynamics of the Shuttle Orbiter at High Altitudes," *Journal of Spacecraft and Rockets*, Vol. 31, 1994, pp. 944–952.
- [76] Ivanov, M. S., Markelov, G. N., Gimelshein, S. F., Mishina, L. V., Krylov, A. N., and Grechko, N. V., "High-Altitude Capsule Aerodynamics With Real Gas Effects," *Journal of Spacecraft and Rockets*, Vol. 35, 1998, pp. 16–22.
- [77] Markelov, G. N., Kashkovsky, A. V., and Ivanov, M. S., "Space Station Mir Aerodynamics Along the Descent Trajectory," *Journal of Spacecraft and Rockets*, Vol. 38, 2001, pp. 43–50.
- [78] Moss, J. N., "Direct Simulation Monte Carlo Simulations of Ballute Aerothermodynamics Under Hypersonic Rarefied Conditions," *Journal of Spacecraft and Rockets*, Vol. 44, 2007, pp. 289–298.
- [79] Wilmoth, R. G., Mitcheltree, R. A., and Moss, J. N., "Low-Density Aerodynamics of the Stardust Sample Return Capsule," *Journal of Spacecraft and Rockets*, Vol. 36, 1999, pp. 436–441.

- [80] Jenniskens, P., "Observations of the STARDUST Sample Return Capsule Entry with a Slit-Less Echelle Spectrograph," AIAA Paper 2008-1210, January 2008.
- [81] Ozawa, T., Zhong, J., Levin, D. A., Boger, D., and Wright, M. J., "Modeling of the Stardust Reentry Flows With Ionization in DSMC," AIAA Paper 2007-0611, January 2007.
- [82] Boyd, I. D., Trumble, K. A., and Wright, M. J., "Modeling of Stardust Entry at High Altitude, Part 1: Flowfield Analysis," *Journal of Spacecraft and Rockets*, Vol. 47, 2010, pp. 708–717.
- [83] Boyd, I. D., and Jenniskens, P., "Modeling of Stardust Entry at High Altitude, Part 2: Radiation Analysis," *Journal of Spacecraft and Rockets*, Vol. 47, 2010, pp. 901–909.
- [84] Blanchard, R. C., Wilmouth, R. G., and Moss, J. N., "Aerodynamic Flight Measurements and Rarefied-Flow Simulations of Mars Entry Vehicles," *Journal of Spacecraft and Rockets*, Vol. 34, 1997, pp. 687–690.
- [85] Moss, J. N., Blanchard, R. C., Wilmouth, R. G., and Braun, R. D., "Mars Pathfinder Rarefied Aerodynamics: Computations and Measurements," *Journal of Spacecraft and Rockets*, Vol. 36, 1999, pp. 330–339.
- [86] Wilmouth, R. G., Rault, D. F. G., Cheatwood, F. M., Engelund, W. C., and Shane, R. W., "Rarefied Aerothermodynamic Predictions for Mars Global Surveyor," *Journal of Spacecraft and Rockets*, Vol. 36, 1999, pp. 314–322.
- [87] Moss, J. N., Wilmouth, R. G., and Price, J. M., "Direct Simulation Monte Carlo Calculations of Aerothermodynamics for Mars Microprobe Capsules," *Journal of Spacecraft and Rockets*, Vol. 36, 1999, pp. 399–404.
- [88] Rault, D. F. G., "Aerodynamic Characteristics of the Magellan Spacecraft in the Venus Upper Atmosphere," *Journal of Spacecraft and Rockets*, Vol. 31, 1994, pp. 537–542.
- [89] Haas, B. L., and Schmitt, D. A., "Simulated Rarefied Aerodynamics of the Magellan Spacecraft During Aerobraking," *Journal of Spacecraft and Rockets*, Vol. 31, 1994, pp. 980–985.
- [90] Haas, B. L., and Feiereisen, W. J., "Particle Simulation of Rarefied Aeropass Maneuvers of the Magellan Spacecraft," *Journal of Spacecraft and Rockets*, Vol. 31, 1994, pp. 17–24.
- [91] Haas, B. L., and Milos, F. S., "Simulated Rarefied Entry of the Galileo Probe into the Jovian Atmosphere," *Journal of Spacecraft and Rockets*, Vol. 32, 1995, pp. 398–403.
- [92] Putnam, Z. R., Bairstow, S. H., Braun, R. D., and Barton, G. H., "Improving Lunar Return Entry Range Capability Using Enhanced Skip Trajectory Guidance," *Journal of Spacecraft and Rockets*, Vol. 45, 2008, pp. 309–315.
- [93] Wright, M. J., Prabhu, D. K., and Martinez, E. R., "Analysis of Apollo Command Module Afterbody Heating Part I: AS-202," *Journal of Thermophysics and Heat Transfer*, Vol. 20, 2006, pp. 16–30.
- [94] Cianciolo, A. M. D., Davis, J. L., Komar, D. R., Munk, M. M., Samareh, J. A., Williams-Byrd, J. A., Zang, T. A., Powell, R. W., Shidner, J. D., Stanley, D. O., Wilhite, A. W., Kinney, D. J., McGuire, M. K., Arnold, J. O., Howard, A. R., Sostaric, R. R., Studak, J. W., Zumwalt, C. H., Llama, E. G., Casoliva, J., Ivanov, M. C., Clark, I., and Sengupta, A., "Entry, Descent, and Landing Systems Analysis Study: Phase 1 Report," NASA/TM-2010-216720, July 2010.

- [95] Clark, I. G., Hutchings, A. L., Tanner, C. L., and Braun, R. D., "Supersonic Inflatable Aerodynamic Decelerators for Use on Future Robotic Missions to Mars," *Journal of Spacecraft and Rockets*, Vol. 46, 2009, pp. 340–352.
- [96] Korzun, A. M., Braun, R. D., and Cruz, J. R., "Survey of Supersonic Retropropulsion Technology for Mars Entry, Descent, and Landing," *Journal of Spacecraft and Rockets*, Vol. 46, 2009, pp. 929–937.
- [97] Harvey, J. K., Holden, M. S., and Wadhams, T. P., "Code Validation Study of Laminar Shock/Boundary Layer and Shock/Shock Interactions in Hypersonic Flows Part B: Comparison with Navier–Stokes and DSMC Solutions," AIAA Paper 2001-1031, January 2001.
- [98] Moss, J. N., and Bird, G. A., "Direct Simulation Monte Carlo Simulations of Hypersonic Flows with Shock Interactions," *AIAA Journal*, Vol. 43, 2006, pp. 2565–2573.
- [99] Boyd, I. D., Chen, G., and Candler, G. V., "Predicting failure of the continuum fluid equations in transitional hypersonic flows," *Physics of Fluids*, Vol. 9, 1995, pp. 210–219.
- [100] Wang, W.-L., and Boyd, I. D., "Predicting Continuum Breakdown in Hypersonic Viscous Flows," *Physics of Fluids*, Vol. 15, 2003, pp. 91–100.
- [101] Schwartzenruber, T. E., Scalabrin, L. C., and Boyd, I. D., "Multiscale Particle-Continuum Simulations of Low Knudsen Number Hypersonic Flow Over a Planetary Probe," *Journal of Spacecraft and Rockets*, Vol. 45, 2008, pp. 1196–1206.
- [102] Deschenes, T. R., and Boyd, I. D., "Application of a Modular Particle-Continuum Method to Partially Rarefied, Hypersonic Flow," *Proceedings of the 27th International Symposium on Rarefied Gas Dynamics*, AIP, Melville, 2011, p. 539.
- [103] Schwartzenruber, T. E., Scalabrin, L. C., and Boyd, I. D., "Hybrid Particle-continuum Simulations of Nonequilibrium Hypersonic Blunt-body Flowfields," *Journal of Thermophysics and Heat Transfer*, Vol. 22, 2008, pp. 29–37.
- [104] Schwartzenruber, T. E., Scalabrin, L. C., and Boyd, I. D., "Investigation of Continuum Breakdown in Hypersonic Flows using a Hybrid Particle-Continuum Algorithm," AIAA Paper 2008-4108, June 2008.
- [105] Deschenes, T. R., Holman, T. D., and Boyd, I. D., "Effects of Rotational Energy Relaxation in a Modular Particle-Continuum Method," *Journal of Thermophysics and Heat Transfer*, Vol. 25, 2011, pp. 218–227.
- [106] Hash, D. B., and Hassan, H. A., "Assessment of Schemes for Coupling Monte Carlo and Navier–Stokes Solution Methods," *Journal of Thermophysics and Heat Transfer*, Vol. 10, 1996, pp. 242–249.
- [107] Hash, D. B., and Hassan, H. A., "Two-Dimensional Coupling Issues of Hybrid DSMC/Navier–Stokes Solvers," AIAA Paper 1997-2507, June 1997.
- [108] Schwartzenruber, T. E., and Boyd, I. D., "A Hybrid Particle-continuum Method Applied to Shock Waves," *Journal of Computational Physics*, Vol. 215, 2006, pp. 402–416.
- [109] Garcia, A. L., and Alder, B. J., "Generation of the Chapman-Enskog Distribution," *Journal of Computational Physics*, Vol. 140, 1998, pp. 66–70.
- [110] Sun, Q., and Boyd, I. D., "Evaluation of Macroscopic Properties in the Direct Simulation Method," *Journal of Thermophysics and Heat Transfer*, Vol. 19, 2005, pp. 329–335.

- [111] Schwartzenruber, T. E., Scalabrin, L. C., and Boyd, I. D., "A Modular Particle-continuum Numerical Method for Hypersonic Non-equilibrium Gas Flows," *Journal of Computational Physics*, Vol. 225, 2007, pp. 1159–1174.
- [112] Schwartzenruber, T. E., Scalabrin, L. C., and Boyd, I. D., "Hybrid Particle-Continuum Simulations of Hypersonic Flow over a Hollow-Cylinder-Flare Geometry," *AIAA Journal*, Vol. 46, 2008, pp. 2086–2095.
- [113] Deschenes, T. R., and Boyd, I. D., "Extension of a Modular Particle-Continuum Method to vibrationally excited, Hypersonic Flows," *AIAA Journal*, Vol. 49, 2011, pp. 1951–1959.
- [114] Deschenes, T. R., and Boyd, I. D., "Parallelization of Modular Particle-Continuum Method for Hypersonic," Near Equilibrium Flows," AIAA Paper 2010-0808, January 2010.
- [115] Allegre, J., Bisch, D., and Lengrand, J.C., "Experimental Rarefied Aerodynamic Forces at Hypersonic Conditions over 70-Degree Blunted Cone," *Journal of Spacecraft and Rockets*, Vol. 34, 1997, pp. 719–723.
- [116] Allegre, J., Bisch, D., and Lengrand, J.C., "Experimental Rarefied Density Flowfields at Hypersonic Conditions over 70-Degree Blunted Cone," *Journal of Spacecraft and Rockets*, Vol. 34, 1997, pp. 714–718.
- [117] Allegre, J., Bisch, D., and Lengrand, J. C., "Experimental Rarefied Heat Transfer at Hypersonic Conditions over 70-Degree Blunted Cone," *Journal of Spacecraft and Rockets*, Vol. 34, 1997, pp. 724–728.
- [118] Holman, T. D., and Boyd, I. D., "Effects of Continuum Breakdown on the Surface Properties of a Hypersonic Sphere," *Journal of Thermophysics and Heat Transfer*, Vol. 23, 2009, pp. 660–673.

First Principles Calculation of Heavy Particle Rate Coefficients

Richard L. Jaffe*

NASA Ames Research Center, Moffett Field, California

David W. Schwenke†

NASA Ames Research Center, Moffett Field, California

Marco Panesi‡

University of Illinois at Urbana Champaign, Urbana, Illinois

I. INTRODUCTION

One important goal of aerothermodynamics research has been understanding the physics and chemistry of shock heated air formed around a space vehicle or object traveling at hypersonic speed through the upper reaches of Earth's atmosphere. The high postshock temperatures induce chemical changes in the atmospheric gases, e.g. dissociation and ionization, and the low gas density means there are often insufficient collisions between the atomic and molecular species to maintain a state of thermodynamic equilibrium. Thus, there is a time interval after the shock before the internal energy modes are equilibrated with the gas kinetic temperature. One consequence of this nonequilibrium condition is an extra amount of photonic emission from the shock layer gas that increases the heat flux impinging on the vehicle [1]. For lunar or mars return missions, the entry velocity will exceed 10 km/s, the shock-layer gases will be mostly dissociated and radiative heating can be a significant contributor to the heat load experienced by the spacecraft. Ground-based shock tube experiments, ballistic range tests and flight tests carried out in the 1960s during development of the Apollo return capsule identified this phenomenon, but could not quantify the extent of this contribution to the total heat flux [2]. Further work in the 1980s to define the requirements for the thermal protection system (TPS) of spacecraft like the Galileo probe and the Aeroassisted Orbital Transfer Vehicle (AOTV) capsule led to a better understanding of nonequilibrium effects [2, 3]. As computer capabilities increased, NASA began to rely more heavily on Computational Fluid Dynamics (CFD) simulations for space mission design and undertook the development of reacting

*Research Scientist.

†Research Scientist.

‡Assistant Professor.

gas models for CFD to describe re-entry phenomena. The chemical kinetic and multi-temperature models used today by NASA were developed during that time by Chul Park [4, 5]. For that model Park assumed that a single translational or kinetic temperature (T) could describe the velocity distribution of all the atoms and molecules and that the vibrational-level population of the molecules is described by a Boltzmann distribution at a different temperature (T^V), called the vibrational temperature. Furthermore, it is assumed that vibration and rotation levels are separable and that the rotational level population is described by a rotational temperature (T^R) with $T^R = T$ (i.e., the rotational and translational modes are equilibrated). The excited electronic state populations are usually described by a Boltzmann distribution using T^V . For the simplified case of a common vibrational-electronic state temperature for all molecules, this is the well-known two-temperature (2-T) model that has been used for non-equilibrium CFD simulations for the last 25 years [6, 7].

In the 2-T model, the translational temperature T is determined from the overall mass, energy and momentum conservation relationships and T^V is determined from a first-order relaxation equation based on the Landau-Teller equation for the equilibration of a harmonic oscillator [8, 9]:

$$\frac{dE_{\text{vib}}(T^V)}{dt} = \frac{E_{\text{vib}}(T) - E_{\text{vib}}(T^V)}{\tau_{\text{vib}}}, \quad (1)$$

where τ_{vib} is the vibrational relaxation time, which is related to the vibrational relaxation rate coefficient ($k(1 \rightarrow 0)$) and $T^V(t)$ is determined by inverting the Boltzmann expression for the thermal vibrational energy:

$$E_{\text{vib}} = \frac{\sum_v E_{\text{vib}}(v) \exp(-E_{\text{vib}}(v)/k_B T^V)}{\sum_v \exp(-E_{\text{vib}}(v)/k_B T^V)},$$

where $E_{\text{vib}}(v)$ is the energy of the v th vibrational level and k_B is Boltzmann's constant. The rationale for assuming $T^R = T$ and $T^V < T$ is that, at moderate temperatures (generally < 5000 K), the rotational level populations in a gas are equilibrated after a small number of collisions ($\lesssim 10$), whereas equilibration of the vibration populations require $\approx 10^3$ collisions. Data for parameterizing rotational and vibrational relaxation times have generally come from shock-tube experiments at temperatures of 5000–10,000 K, and usually are extrapolated to 20,000 K or even higher. However, at temperatures greater than 10,000 K vibration and rotation relaxation times are comparable and a coupled rotation-vibration relaxation model is a more accurate description. For a harmonic oscillator (i.e., the original Landau-Teller model), collisions can only change the vibrational quantum number by $\Delta v = \pm 1$, so the equilibration occurs by a series of small steps. In reality, however, owing to effects of anharmonicity and chemical reactions, larger Δv 's are likely. Park also defined an average temperature,

$$T_{\text{ave}} = T^p \times T^{V(1-p)} \quad (3)$$

(originally $p = 0.5$ was used so T_{ave} was given by $\sqrt{T \times T^V}$) and modified the familiar Arrhenius expression for the collisional dissociation reaction rate coefficient by using T_{ave} instead of T

$$k^D(T_{\text{ave}}) = AT_{\text{ave}}^n \exp(-T_d/T_{\text{ave}}) \quad (4)$$

where A is the pre-exponential constant, n is the temperature coefficient and T_d is the dissociation temperature ($D_0/(N_{\text{av}}k_B)$). D_0 is the dissociation energy and N_{av} is Avogadro's number (6.0225×10^{23} atoms or molecules per mole). Usually T_d is fixed at the experimental value, whereas A and n are treated as adjustable parameters.

The treatment of vibrational relaxation and the use of T_{ave} in the 2-T chemistry model create a time delay for dissociation that approximates the induction time observed in shock tube experiments, while still allowing for some rapid atom production behind the shock. In shock tube experiments for gas mixtures that include N_2 , the initial radiation pulse is attributable to the N_2 1st positive transition. The Arrhenius pre-exponential factor A and the temperature coefficient n were adjusted so the computed non equilibrium emission matched the observed experimental quantity. A more detailed discussion of the collisional physical and chemical processes and the implementation of the 2-T model is given in Park's textbook "Non equilibrium Hypersonic Aerothermodynamics" [1]. The framework of the 2-T model is essentially empirical, because the ad hoc definition of T_{ave} and some of the individual reaction rate coefficient parameters were adjusted so the CFD calculations of the flow behind a shock could reproduce a set of experimental observations. As newer experimental data became available, more empirical adjustments have been made [10, 11].

A full characterization of the nonequilibrium gas requires detailed accounting of the distribution of rotation-vibration levels and electronic states for each of the air species. When the 2-T model was being developed, such an undertaking was completely impractical. With current computational resources that is no longer the case and a group of scientists at NASA Ames Research Center has begun the task of formulating a detailed collisional model for hypersonic flows. This new high-fidelity air chemistry model is based on first principles theoretical calculations that will be suitable for Earth entry at velocities of 10–15 km/s and Mars entries at velocities up to 8 km/s. It has long been realized that computational chemistry modeling can be used to determine the dissociation and energy transfer rates for high-temperature air under these conditions. The atomistic simulation methods for studying these collisional processes are based on classical mechanics, but require knowledge of the inter-atomic forces acting between the collision partners, which can be obtained from the change in the total potential energy during a collision. The potential energy surface (PES) is the representation of the total potential energy of the system at all geometric arrangements of these collision partners and the inter-atomic forces are the negatives of the derivatives of PES with respect to the geometric coordinates. Originally, empirical PESs, with

parameters that had been adjusted to reproduce available experimental data [12], were used for the PES. For example, Billing [13], Laganà [14, 15] and Esposito et al. [16] and their coworkers have used this approach, coupled with classical or semi-classical scattering calculations for computation of collision cross sections and dissociation rate coefficients for $N_2 + N$ collisions. However, with current computer resources, it is possible use ab initio quantum chemistry methods to compute the potential energy of the atoms and molecules involved in the collision for a large number of geometric arrangements. An analytical representation of the resulting PES can be combined with a classical scattering method called quasi-classical trajectory (QCT) for the simulation of large numbers of collisions to obtain collision cross sections and reaction rate coefficients. As part of our work, we have computed complete sets of cross sections and state-specific rate coefficients for rotation-vibration energy transfer and dissociation in collisions of $N_2 + M$, where $M = N$ or N_2 . For $N_2 + N$ these data have been used to evaluate the relaxation and excitation rates for all rotation-vibration energy levels of N_2 to enable us to fully characterize the shock layer for air under hypersonic conditions. The goal of this project is to construct a hypersonic chemistry model for non-equilibrium flows that is free from assumptions about temperatures. This project was started with support of the NASA/ARMD Fundamental Aerodynamics Program and is currently sponsored by the Entry Systems Modeling project in the NASA Space Technology Mission Directorate (STMD).

In this chapter we illustrate the computational methods used for computing detailed energy transfer and dissociation rate coefficients for $N_2 + N$ and $N_2 + N_2$ collisions. In Sec. II we describe the methods used for quantum mechanical calculation of PESs and the analytical representation of the PES used in the quasi-classical trajectory calculations and in Sec. III we describe the QCT method and present some of the rate coefficients that we obtained from of those calculations. In Sec. IV we describe a master equation model that uses the detailed rate coefficients to determine phenomenological reaction rates at conditions appropriate to hypersonic flows and a coarse-grained model to generate a reduced set of rate coefficients that can be used for CFD simulations. Our goal for this chapter is to demonstrate some of the approximations and tradeoffs that must be made to make this endeavor feasible with current computer resources.

Before starting to describe the specific methods we have been using, we provide justification for our hybrid quantum/classical approach. The determination of the state-to-state cross sections and microscopic rate coefficients required to describe the dissociation/excitation/relaxation processes via first principles requires the description of the behavior of three or four nitrogen nuclei and 21 or 28 electrons for $N_2 + N$ and $N_2 + N_2$ collisional processes, respectively. This is a very complicated problem, and approximations are required to make progress. Fortunately, over the last many decades, procedures that yield reliable results have been developed.

One problem is that, in contrast to our macroscopic world, the world of atoms and molecules is very different. This is primarily due to their relative sizes.

Calculations of atomic and molecular properties are most conveniently carried out in atomic units, and in the system of units we use, Hartree atomic units, the unit of length is the Bohr radius a_o , the unit of mass is the electron mass m_e , the unit of charge is the electron charge e , and Planck's constant \hbar is taken to be equal to 2π , or rather $\hbar = h/2\pi = 1$. In more customary units, $1 a_o \approx 0.53 \times 10^{-10} \text{ m}$, $1 m_e \approx 9.1 \times 10^{-31} \text{ kg}$, $1 e \approx 1.6 \times 10^{19} \text{ C}$, and $h \approx 6.6 \times 10^{-34} \text{ J-sec}$. Planck's constant governs the degree of quantum behavior via the dimensionless ratio of the De Broglie wavelength $\frac{\hbar}{p}$ to characteristic size of the system, where the momentum p is most conveniently expressed in terms of the energy: $E = p^2/2m$, where m is the mass of the system. If we are considering an electron near a nitrogen nucleus, taking E to be the ionization potential, 14.5 eV, so that $p \approx 1$ atomic unit, and the characteristic size to be the equilibrium bond length of the ground state of N₂ divided by 2, i.e., $2.06 a_o/2 \approx 1 a_o$, this ratio is equal to 2π . If we are considering a nitrogen nucleus, $m \approx 2.5 \times 10^3 m_e$ and if we take $E = k_B T$, where k_B is Boltzmann's constant (in Hartree atomic units $k_B \approx 3.2 \times 10^{-6}$), then at $T = 10,000 \text{ K}$ we find $p = 40 \text{ a.u.}$ Taking the characteristic length $b \approx 10 a_o$ gives us a dimensionless ratio of 1.6×10^{-2} . In comparison, a macroscopic object like a baseball traveling at 94 mph (42 m/s), such as a fast ball thrown by a major league pitcher, has $p = 3.0 \times 10^{24} \text{ a.u.}$ Taking the characteristic length to be 1 m, the dimensionless ratio is 1.1×10^{-34} . Thus for an electron, a nitrogen atom and a baseball the De Broglie wavelengths are approximately $6.3, 10^{-2}$ and 10^{-34} , respectively.

It is thus seen that although an electron is very clearly quantum mechanical in nature and a baseball is very clearly governed by classical mechanics, the motion of an atom or small molecule is somewhat intermediate in nature. There are many aspects of nuclear motion that are well described by classical mechanics, whereas others, such as subthreshold tunneling and predissociation, as well as nuclear spin symmetry, arise purely from quantum effects. The set of approximations that we use is to formulate the problem in terms of quantum mechanics, but then substitute classical mechanics where it is applicable. To simulate some phenomena, we must resort to "semi-classical" or "old quantum mechanics" treatments, and this will be discussed in detail below.

II. CALCULATION OF POTENTIAL ENERGY SURFACES

In quantum mechanics, the interactions between the particles (e.g., atomic nuclei and electrons) is given by the time-dependent Schrödinger equation:

$$i\hbar \frac{d}{dt} \Psi(x, t) = \left[-\frac{\hbar^2}{2m} \nabla^2 + V(x) \right] \Psi(x, t) = H(x) \Psi(x, t) \quad (5)$$

where Ψ is the wave function, m is the particle mass and H is the Hamiltonian operator that governs the total energy (i.e., kinetic plus potential energy V). For conservative systems, H and V only depend on the position coordinates, x , and

the wave function can be factored into time-dependent and time-independent components, $[\exp(-iEt/\hbar)]$ and $[\psi(x)]$, respectively. The resulting time-independent Schrödinger equation,

$$H(x)\psi(x) = E\psi(x) \quad (6)$$

is used to compute the state energy of the particles in a stationary state.

The first approximation we make to enable a practical solution is to invoke the Born-Oppenheimer approximation [17] to separate the electronic and nuclear motion. We justify this by the low density of electronic states and very large mass difference between an electron and a nitrogen nucleus—as mentioned above that ratio is about 2.5×10^3 . The low density of states means that we can just consider one electronic state, and the mass ratio means we can neglect the action of nuclear momentum operators on the electronic wave function. Under these conditions, the equations of motion for the nuclei are equivalent to the classical motion of three or four nitrogen atoms on a potential energy hyper-surface (PES) in 9 or 12 dimensions, and the height of this surface is given by the sum of the electronic energy and nuclear potential energy calculated at a given geometry of the nitrogen nuclei.

At this point, it is worth discussing the coordinates that are used in this work. The motion of the electrons is very strongly coupled to the positions of the nuclei, and as the nuclei are taken to move slowly compared to the electrons, we use Cartesian coordinates for the electrons, and the origin of this coordinate system will be the center of mass of the nuclei.

For the nuclei, we will use a variety of coordinate sets. For N_3 , starting from the $3 \times 3 = 9$ Cartesian coordinates of the atoms, we can transform to a set of relative coordinates whereby $3 \times 2 = 6$ coordinates specify the nuclear positions relative to the nuclear center of mass, and three coordinates specify the center of mass. We will consider two sets of relative coordinates. This first set is called Jacobi coordinates, and they consist of the vector \mathbf{r}_a that goes from the position of N_a to the center of mass of N_bN_c , and the vector \mathbf{R}_a that goes from the position of N_b to the position of N_c . The spherical polar form of these vectors are particularly useful in describing situations where N_a is far from N_bN_c . We define in a cyclic fashion the vectors \mathbf{r}_b , \mathbf{R}_b and \mathbf{r}_c , \mathbf{R}_c . Thus we see that for the case of the reaction $N_a + N_bN_c \rightarrow N_b + N_cN_a$, we would want to start out using \mathbf{r}_a and \mathbf{R}_a and end up using \mathbf{r}_b and \mathbf{R}_b . This is indeed what one does if quantum calculations are carried out. However, in the classical calculations, it is not at all convenient to change coordinates during the course of a trajectory. Although in principle, one could use say \mathbf{r}_a and \mathbf{R}_a for the reactive collision, but after the reaction, both vectors would become large as the products separate from each other, and one could have numerical problems converting into the more physical coordinates. Thus, when we carry out our classical trajectories, we use Cartesian coordinates for the first two atoms, and determine the coordinates for the third atom by requiring that the center of mass be at the origin [18, 19].

The Jacobi coordinates can be converted from Cartesian to spherical polar coordinates: i.e., \mathbf{r}_a can be parameterized by r_a , θ_a , and φ_a , etc. Another useful parameterization is to transform to a rotating coordinate system whereby the Jacobi coordinates take the form

$$(\mathbf{r}_a \mathbf{R}_a) = \begin{pmatrix} 0 & R_a \sin \chi_a \\ 0 & 0 \\ r_a & R_a \cos \chi_a \end{pmatrix} \quad (7)$$

Then the complete set of coordinates are r_a , R_a , χ_a , α_a^{LB} , β_a^{LB} , and γ_a^{LB} , where the last three angles are the Euler angles that transform the rotating system to the nonrotating system [20, 21].

When representing potential energy hyper-surfaces for 3- and 4-atom systems, like N_3 and N_4 , it is convenient to use the three or six atom–atom distances R_{ij} , respectively. These coordinates, however, are not suitable for dynamics calculations, because they are not all independent, i.e.,

$$R_{ab} \leq R_{ac} + R_{bc} \quad (8)$$

However, it is quite easy to use them with the law of cosines to generate the other internal coordinates.

The potential energy hyper-surface is a function of $3n-6$ geometric coordinates and represents the potential energy for all geometric arrangements of the n atoms comprising the colliding species. Note that, in this treatment, the position of the center of mass of the system and its orientation with respect to the center of mass are considered stationary. For atom-diatom collisions (e.g., $\text{N}_2 + \text{N}$), $n = 3$ and the PES is a function of three positional variables. For collisions between two diatomic molecules, $n = 4$ and the PES is a 6-D hyper-surface. We obtain the PES by solving the time-independent Schrödinger equation for the energy of the electrons with the nuclei fixed at some geometric arrangement. The quantum Hamiltonian operator H consists of a electron kinetic energy term and coulomb potential terms for electron-electron and electron-nuclei interactions. The resulting electronic energy E is the value of the potential energy of atoms at that geometry. The wave-function ψ contains information about the probability density distribution of the electrons in the presence of the nuclei. For all but the simplest cases, the electronic Schrödinger equation is solved by a series of numerical expansions. First, the wave function is taken to be a linear combination of atomic orbitals, each expressed as a sum of Gaussian functions centered on each nucleus (called the one-particle basis set). Then the electron-electron coulomb potential is simplified so each electron experiences only the average potential of the remaining electrons (the so-called Hartree Fock approximation) and the Schrödinger equation is solved variationally to minimize the energy E . The resulting coefficients for the basis transform the atomic orbitals into molecular orbitals that are delocalized over all the nuclei. To go beyond the Hartree Fock approximation, electron correlation effects are

considered whereby each electron feels the instantaneous potential of the other electrons. Electron correlation is usually introduced by mixing in a series of arrangements of electrons in the molecular orbitals (a second expansion over molecular orbitals) and solving the resulting eigenvalue problem. It is generally not possible to obtain the exact solution of the electron correlation contribution to the total energy for a given atomic orbital basis, because the number of arrangements in the molecular orbitals grows factorially with the number of electrons. Thus, numerical methods have been devised to obtain the bulk of the electron correlation energy in the most economical fashion.

For $N_2(X^1\Sigma_g^+) + N(^4S)$ collisions, we need to compute the ground electronic state energy for N_3 , which has quartet electronic spin multiplicity and A'' symmetry (denoted ${}^4A''$). If the three N atoms are labeled N_a , N_b and N_c , the PES describes the N_aN_b , N_aN_c and N_bN_c nitrogen molecules, separated atoms ($N_a + N_b + N_c$) and a possible triatomic complex ($N_aN_bN_c$ and its permutations). If we consider the collision between $N_a - N_b$ (v , j) and N_c , the possible outcomes are $N_a - N_b(v', j') + N_c$, $N_a - N_c(v', j') + N_b$, $N_b - N_c(v', j') + N_a$, and $N_a + N_b + N_c$. The first outcome is a nonreactive, but inelastic, collision resulting in the N_2 molecule having a different internal energy level and the last is dissociation of the initial N_2 molecule. The other two outcomes represent products of an exchange reaction where the atoms comprising the final N_2 molecule are different from the initial molecule. This PES is a function of three geometric variables (the atoms form a triangle defined by the three N-N inter-nuclear distances or two N-N inter-nuclear distances and one angle). For a 4-atom system such as N_2-N_2 , the situation is considerably more complicated. Six geometric variables are required to define the arrangement of the atoms and there are three different pairs of N_2 molecules that can be formed.

Many computer codes are available to carry out ab initio electronic structure calculations. We use a modified version of MOLPRO [22]. Most codes use the same basic numerical methods for solving the electronic Schrödinger equation. In our opinion, MOLPRO is a very efficient code for calculating the sophisticated electronic wave functions and energies required for the determination of a complete PES for a three- or four-atom system. For this work, we use the augmented-correlation consistent polarized valence triple zeta (aug-cc-pVTZ) one-particle basis set of Kendall [23]. The correlation consistent polarized valence basis sets are a family of basis sets that systematically improve the accuracy of the expansion. The double zeta set has 3 s-type, 2 p-type and 1 d-type functions centered on each nitrogen atom. Triple zeta as has 4 s-type, 3 p-type, 3 d-type and 1 f-type functions, and so on. These sets can be augmented by adding more diffuse basis functions for more flexibility in describing the electron distribution around the nuclei when the bonds are stretched. The aug-cc-pVTZ basis set consists of 5 s-type functions, 4 p-type functions, 3 d-type functions, and 2 f-type functions centered on each nitrogen nuclei. There are a total of 138 basis functions, and this represents a compromise between the “good” correlation consistent

valence triple zeta one-particle basis set of Dunning [24] and the “better” correlation consistent valence quadrupole zeta one-particle basis set of Dunning [24]. The Dunning basis sets are the current de facto standard for this type of electronic structure calculations.

An earlier version of the N₃ PES was published in 2003 [25] in which we were mainly concerned about the potential energy hyper-surface in the vicinity of the reaction path for the nitrogen exchange reaction, i.e., the most important region for the process N_a + N_bN_c → N_b + N_cN_a. To study the dissociation reaction as well, we decided to recompute the entire PES using a different approach for solving the electron correlation problem. This newer PES is described in References [26–28]. Galvao and Varandas [29] have also computed the N₃ (⁴A'') PES using a similar approach. Our N₄ PES has been described in Reference [30]. All of these PES calculations utilized the same aug-cc-pVTZ one-particle basis set, but the details of the methods used to compute the electronic energies are somewhat different.

More recently, Paukku et al. [31, 32] carried out calculations on the N₄ system, and they also used a one electron basis set based on the cc-pVTZ basis, except that they augmented the basis only with diffuse *s* and *p* type functions, whereas in the aug-cc-pVTZ basis, diffuse *d* and *f* functions are also added. In our work, we used the full set of diffuse functions for several reasons. First of all, convergence tests [33] show that the rate of convergence of the fully augmented basis sets is superior to the unaugmented ones, and just including *s* and *p* functions would reduce the convergence rate to be the same as the unaugmented basis sets. Secondly, one of the purposes of augmenting the basis with diffuse functions is to gain a better description of the outer reaches of the molecular orbitals. This is important, for the asymptotic dependence of the molecular orbital on radial distance is a decaying exponential, whereas the basis functions have a Gaussian form which decays much faster. Thus we expect that as the diatom dissociates, there will be intermediate regions where the potential energy is transitioning from the noninteracting region to the strongly interacting region where the results might be quite sensitive to the outer reaches of the basis. This is an effect that might change the shape of the potential energy hyper-surface and hence impact the dissociation rate, but not have significant effect on the properties near the equilibrium bond length and the dissociation energy. There is no particular reason to suppose that this effect is limited to only *s* and *p* symmetries. The third reason is nitrogen is a rather odd atom. Specifically, it has no bound anion states, yet in the presence of other atoms, it tends to play roles that indicate it has an electron affinity. For example, the dipole moment of NH₃ is substantial and the CN group is a notorious electron withdrawing group in organic compounds. Another role of the diffuse functions is to help with the description of anionic character in the wave function. This dichotomy, coupled with the fact that the exponential parameters in the basis sets are optimized solely for the ground electronic state of the atom, tends to bias the calculations towards further soft pedaling of any ionic character. See

Reference [34] for an indication of this. Thus we believe our choice of basis is superior to that of Paukku et al.

For our initial calculations [25], we determined the MOs via the spin-restricted Hartree-Fock (RHF) approximation, and then determined the electronic energy using the spin-unrestricted coupled-cluster single-doubles (UCCSD) approach with the (T) correction. In these calculations, the 1s-like MOs were always kept doubly occupied, and we computed the electronic wave functions for the lowest energy quartet A'' state. This is the spin-space symmetry that includes the ground state of $N_2(X^1\Sigma_g^+) + N(^4S)$.

Although the RHF UCCSD(T) calculations are an efficient way of computing good approximations for the electronic energy in the vicinity of the reaction path for the nitrogen exchange reaction, the assumptions explicit in the method break down when an collision results in dissociation, and nonphysical energies would be obtained.

Thus, in order to be able to accurately treat dissociative collisions, we need to go to more sophisticated methods. This is because although the electronic wave function for $N_2X^1\Sigma_g^+$ near its minimum energy geometry is reasonably well described by a zero-order function that only includes closed shells, i.e., where all MOs are doubly occupied, at the dissociation limit, the electronic wave function requires a zeroth-order function that includes at minimum six open shells, i.e., half-filled molecular orbitals. But the RHF method requires a fixed number of open and closed shells, so cannot make a smooth transition from closed to open shells.

The methods required to smoothly treat variable number of open shells all start with the multi-configuration Hartree–Fock (MCHF) method to determine the MOs. In the MCHF calculations, the number of occupied orbitals are increased compared to the RHF method, and in the determination of the MOs, we also simultaneously determine configuration mixing coefficients. In the RHF calculations, there is no configuration mixing. This makes the MCHF calculations much more expensive, but it also makes them much more robust in being able to reasonably describe a multiplicity of bonding possibilities.

Once we have the MOs from the MCHF calculations, we consider two ways to compute the electronic energy. In the first method, the internally contracted Multi-Reference-Configuration-Interaction (icMRCI) method, we diagonalize the electronic Hamiltonian in a very large basis (upwards of tens of millions of functions) of configuration state functions. The icMRCI method is a very general method, capable of giving very good energies and wave functions for very general situations, but at the cost of being significantly more expensive than the UCCSD method. In the second method, we used the internally contracted Average-Coupled-Pair-Functional (icACPF) method. This method is of very similar cost to the icMRCI method, but improves the treatment of electron rich systems. The tradeoff, however, is one can only get results for the lowest spin-symmetry state, and one only gets an energy but not a wave function. The icMRCI energies can also be simply improved somewhat by using the Davidson

quadrupoles correction (+Q), and we will do so in our calculations. Which energy, ACPF or icMRCI+Q, is better is a matter of debate.

In our original plan of attack, we were going to augment our previously determined RHF UCCSD(T) energies at 4306 geometries with MCHF icMRCI+Q energies computed in the dissociation regime. Thus we carried out MCHF icMRCI+Q calculations at 56 geometries. In these calculations, we also used the aug-cc-pVTZ one particle basis, whereas in the MCHF calculations, we included three doubly occupied MOs for the 1s electrons and 15 electrons in 12 active MOs, and optimized the MOs and configuration mixing coefficients by minimizing the energy of the lowest quartet A'' state. In the icMRCI+Q calculations, we kept the 3 N 1s-like MOs doubly occupied, but correlated the remaining 15 electrons, again going after the lowest quartet A'' state. These calculations were very expensive, and as it turned out, not useful. This is because as N_2 dissociates, the configuration mixing coefficients lead to the 2s-like MOs being only doubly occupied. This then means that the MCHF energy becomes only very weakly dependent on mixing between the 1s-like MOs and the 2s-like MOs. Then as the 1s and 2s-like MOs are not treated the same in the icMRCI calculations, erratic results were seen in the final energies. The resolution of this problem that we used was to change to a MCHF calculation where we included six doubly occupied MOs and nine electrons in nine active MOs. However, we still correlated the 2s-like MOs in the icMRCI+Q calculations. This made the energies much more reliable and also reduced the cost somewhat. However, these calculations were still quite arduous not only because of the large number of variables that must be optimized, but also because the variation of the number of open-shells from three to nine severely tested the numerical schemes in MOLPRO. Thus we also investigated the effect of not correlating the 2s-like MOs in the icMRCI calculations.

As a test of this approximation compared to the icMRCI+Q calculations correlating 15 electrons, we carried out the analogous calculations on the $X^1\Sigma_g^+$ state of the N_2 molecule. The results are shown in Fig. 1. For N_2 , the analog of the RHF UCCSD(T) calculations are the HF CCSD(T) calculations, the analog of the 15e icMRCI+Q calculations are the 10e icMRCI+Q calculations, and finally the analog of the 9e ACPF calculations are the 6e icACPF calculations. We also show the results using the aug-cc-pVTZ basis and 6e CASPT2 energies, which is the equivalent to the calculations of Paukku et al. [31] as well as the accurate experimentally determined curve of Le Roy et al. [35]. All curves are shifted to have the zero of energy at the equilibrium bond length. At the level of resolution of this figure, energies from the icMRCI, icMRCI+Q, and ACPF methods are indistinguishable. We see that near the minimum, all three curves are indistinguishable, with the HF CCSD(T) results diverging from the 10e icMRCI+Q results starting about $3 \text{ } a_0$, and the 6e icACPF tracking the 10e icMRCI+Q results very well out to the dissociation limit. The principle difference between the 6e and 10e calculations are the 6e results give a little larger dissociation energy, and this in fact greatly improves the agreement with Le Roy's potential.

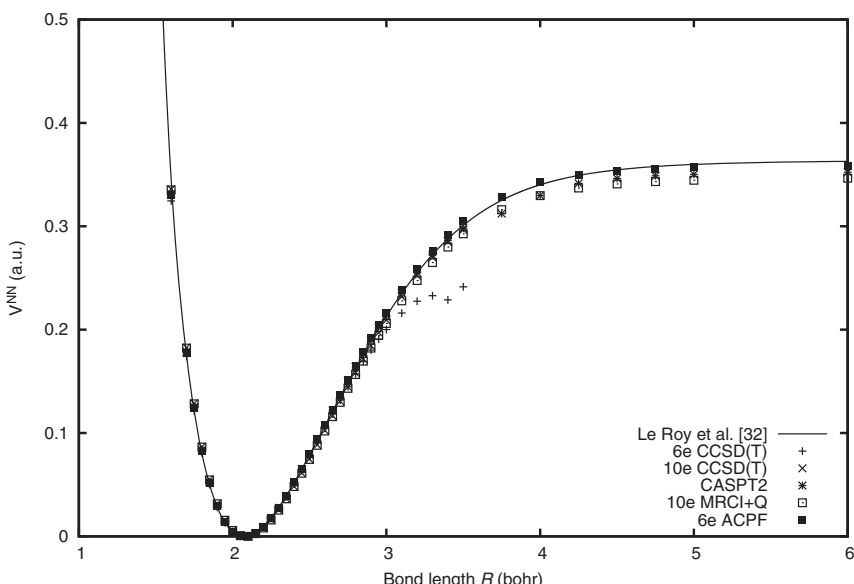


Fig. 1 Potential energy curves for N_2 . V^{NN} has atomic units (i.e., au or Hartree).

This is of course attributable to fortuitous cancellation of error, but it appears that either calculation does a pretty good job of prediction the potential curve. The 6e icCASPT2 results track the 6e icMRCI+Q results quite well until about 3.5 \AA , after which they behave in somewhat an erratic manner.

It is interesting to consider what sort of calculation is required to do a better job on the N_2 potential curve. In Fig. 2, we show the results of a sequence of three calculations of V^{NN} compared to the Le Roy potential. In these calculations, we determined the MOs using six electrons in the active space, but then when we determined the energies, we correlated all the electrons. The three calculations differ in they used the $spdf$, $spdfg$, and $spdfgh$ core-valence basis sets recommended by Schwenke [34]. One can see these calculations are nicely converging to a dissociation energy very close to that given by Le Roy's empirical potential. Owing to the larger one-electron basis sets used, and the fact that all electrons are correlated, calculations at the $spdfgh$ level are currently not feasible for the N_3 potential energy hyper-surface. Thus in the icMRCI+Q calculations for N_3 , we will only correlate nine electrons.

When we attempted to construct an analytic representation based on the composite RHF UCCSD(T) and MCHF icMRCI+Q energies, we did not obtain very reasonable results. More icMRCI+Q data were added, eventually up to 421 geometries, and high energy RHF UCCSD(T) energies were deleted, all to no avail. Finally this was eventually traced back to erratic behavior of the

RHF UCCSD(T) energies, probably owing to the RHF calculations converging to local minima rather than the global minimum. After multiple failed attempts to correct this situation, we decided to discard the RHF UCCSD(T) energies and carry out new calculations.

The most consistent approach would have been to carry out additional icMRCI+Q calculations. However, due to a variety of reasons, we instead used the 9e icACPF method for the replacement points. Using this method, we computed energies at 923 different geometries. These geometries were a mixture of densely spaced points near the transition state geometry for the exchange reaction as well as a uniform grid in R_{ab} , θ_{abc} , and R_{bc} . Altogether, the icMRCI+Q calculations were based on a grid having $\theta_{abc} = 70, 90, 120, 150$, and 175 deg, $R_{ab} \leq R_{bc}$ with values taken from 3, 3.25, 3.5, 3.75, 4, 4.5, 5, 5.5, 6, 7, 8, 9, and 10 bohr. In the ACPF calculations, we augmented the θ_{abc} values listed above with 70, 80, 100, 110, 116.5, 130, and 165 deg, and used $R_{ab} \leq R_{bc}$ with R_{ab} taken from 1.6, 1.7, 1.8, 1.9, 2, 2.15, 2.3, 2.5, 2.8, and 3 bohr, and R_{bc} sampling those as well as 3.5, 4, 5, 6, 8, and 10 bohr.

Now we cannot directly mix the 9e MCHF icACPF and 9e MCHF icMRCI+Q energies, because although the change in the method of computing the energies does not significantly alter the shape of the potential energy hyper-surface,

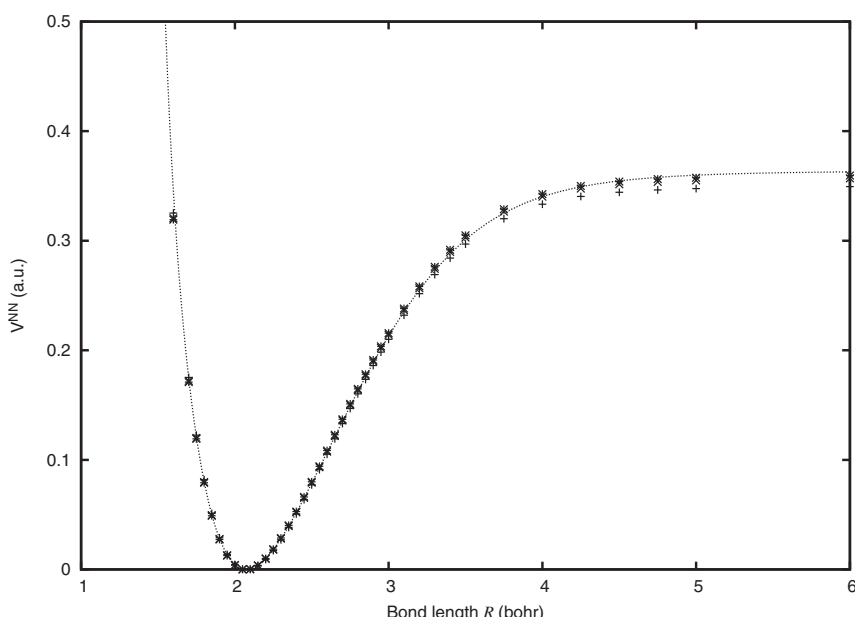


Fig. 2 Potential curves for N_2 correlating all electrons: line Le Roy potential, + spdf basis, x spdfg basis, and * spdfgh basis.

it does change the height of the potential energy hyper-surface. Before we carried out the determination of the parameters in the analytic representation, we corrected the energies to make them compatible. Specifically, we took the PES to take the form

$$V = V^{\text{NN}}(R_{ab}) + V^{\text{NN}}(R_{bc}) + V^{\text{NN}}(R_{ac}) + V^{\text{3-body}}(R_{ab}, R_{bc}, R_{ac}) \quad (9)$$

where R_{ij} is the distance between nuclei i and j and V^{NN} is the asymptotic $\text{N}_2(X^1\Sigma_g^+)$ potential curve, and then we assumed that although V and V^{NN} will be different for the 9e MCHF icACPF and 9e MCHF icMRCI+Q calculations, $V^{\text{3-body}}$ will be the same, apart from a constant. We will address this assumption later.

Thus in the course of this work we determined three different $\text{N}_2(X^1\Sigma_g^+)$ potential curves. The first is a fit to 6e MCHF icACPF data, shifted to match the asymptotic 9e MCHF icACPF data, the second is a fit to the 6e MCHF icMRCI+Q data, shifted to match the asymptotic 9e MCHF icMRCI+Q data, and the final one is based on a fit to extensive experimental data [35]. The first two V^{NN} functions were only used in the fit to determine the parameters in $V^{\text{3-body}}$, whereas the third V^{NN} function was used only in the final PES.

In preliminary calculations, we directly used the Le Roy V^{NN} as the third function. However, it soon became apparent that in some regions, our potential had nonphysical energies. Part of these were traced to nonphysical behavior of the Le Roy potential curve: the short-range repulsive part of the potential was much too strong. That this occurred is perhaps not to surprising, for the experimental data used to refine that function is not sensitive to that part of the potential. Thus we re-fit the Le Roy potential with the same functional form as we used for the ab initio data, but only used points generated from the Le Roy potential below the dissociation limit.

The functional forms used were as follows: we write V^{NN} as the sum of a long-range term, a repulsive term, and a short-range term. The long-range term takes the form

$$-\frac{C_6}{R^6 + \delta^6} - \frac{C_8}{(R^4 + \delta^4)^2} - \frac{C_{10}}{(R^2 + \delta^2)^5} \quad (10)$$

the repulsive term being

$$49 \exp(-\alpha_r R) / R \quad (11)$$

and the short-range term being

$$R^6 \exp(-\alpha_s R) \sum_j C_j (R - R_e)^j \quad (12)$$

The values of C_n in the long-range term were taken from [36], the sum over j in the short-range term running over $j = 0 - 7$, the exponent 6 was chosen by

trial and error, and the C_j , α_r , α_s , and δ were determined by a nonlinear least squares fit.

Now we further decompose $V^{3\text{-body}}$ into long-range and short-range interactions:

$$\begin{aligned} V^{3\text{-body}} = & V^{LR}(R_c, r_c, \theta_c) + V^{LR}(R_a, r_a, \theta_a) + V^{LR}(R_b, r_b, \theta_b) \\ & + V^{SR}(R_{ab}, R_{ac}, R_{bc}) \end{aligned} \quad (13)$$

where \mathbf{r}_c is vector from N_c to the average of the N_a and N_b positions, \mathbf{R}_c is the vector from N_a to N_b , r_c is the length of \mathbf{r}_c , R_c is the length of \mathbf{R}_c , and θ_c is the angle between \mathbf{r}_c and \mathbf{R}_c etc. For the long interaction we use [36]

$$V^{LR} = -C_6 P_2(\cos \theta) \exp[-a^{LR}(R - R^{LR})]/(r^6 + r_d^6) \quad (14)$$

where P_l is a Legendre polynomial, and the parameters C_6 , a^{LR} , R^{LR} , and r_d are determined from previous work on $N_2 + N$ transport properties [36].

The short-range term is given by

$$V^{SR} = \sum_{\alpha} \exp(-b_1 r_{\alpha}^2 - b_2 R_{\alpha}^2) \sum_{ijk} C_{ijk} r_{\alpha}^i R_{\alpha}^j P_k(\cos \theta_{\alpha}) \quad (15)$$

where $\alpha = a, b$, or c , and the parameters being optimized by fitting to the ab initio data were b_1 , b_2 , and the C_{ijk} .

We experimented with several choices for the limits on the ijk sum, and settled on the terms with k even and $0 < i + j + k \leq 7$, excluding the terms with $ijk = 000, 100, 010, 200$, and 020 . This lead to 52 terms.

We optimized the fitting parameters via weighted nonlinear least squares. The weights w were taken to be

$$w = 1 + a_w \sum_{\alpha} \exp[-a_R(R_{\alpha} - R_{ts})^2 - a_{\theta}(\cos \chi_{\alpha} - \cos \chi_{ts})^2 - a(\tilde{R}_{\alpha} - \tilde{R}_{ts})^2] \quad (16)$$

where $\tilde{R}_a = R_{ab}$, χ_a is the abc angle, with cyclic permutations defining the other quantities. The variables subscripted ts are those corresponding to our estimate of the transition state geometry for the exchange reaction. This term ensures that our analytic representation faithfully represents the region of the transition state, for $a_w = 25$.

Despite all our efforts to use only reliable input ab initio data in the determination of the analytic representation, bad points can occur. This might be attributable to the MCHF calculations not converging to the global minimum, or it might be due to an excited electronic state crossing the state we are interested in. At any rate, it is important to be able to identify these points and not include them in the final determination of the fitting parameters. We did this as follows. We started out using the weights given above, and performed a

nonlinear least squares fit. Then we computed the percentiles of the error distribution. If the error at a given geometry was over 5 times the 90th percentile, or more negative than 5 times the error of the 10th percentile, then the weight for that point was zeroed, and the parameters were re-fit. We then iterated this until no more points were eliminated. In our final fit, 28 points of the 1344 total had their weights set to zero.

Using this function we then looked at the properties of the exchange reaction transition state region of the PES. This region is characterized by a local energy minimum for equal $N_a - N_b$ and $N_b - N_c$ bond lengths and an $N_a - N_b - N_c$ bond angle of $\approx 120^\circ$ and energy barriers for dissociation of the N_3 complex into $N_a - N_b + N_c$ and $N_a + N_b - N_c$. The energy minimum has traditionally been dubbed “Lake Eyring,” in honor of Henry Eyring who formulated the first practical theory of chemical reaction rates. First of all, we consider our purely ab initio PES, i.e., we use for V^{NN} the fit to the 6e icACPF data. The predicted barrier energy is 55.3 kcal/mol, and the predicted Lake Eyring minimum is 52.9 kcal/mol above the energy of separated N_2 and N. This is about 10 kcal/mol higher than our previous predictions [25]. Now if replace the ab initio V^{NN} with the one based on Le Roy’s potential [35], the transition state energy is now predicted to be 45.5 kcal/mol and Lake Eyring minimum to be at 43.5 kcal/mol. This is in quite good agreement with our previous calculations correlating 15 electrons. The N-N bond lengths and bond angle for the barrier geometry are 1.18 and 1.46 Å (2.23 and 2.75 bohr, respectively) and 120° . For Lake Eyeing the bond length is 1.26 Å (2.38 bohr) and the bond angle is 119° . Galvao and Varandas [29] report similar geometries and energies for their N_3 PES. Our PES is shown in Fig. 3. The internal lines in the figure represent equal energy contours. The closed loops under the label $N_a N_b N_c$ is Lake Eyring, the dark blue regions represent the reactants and products of the exchange reaction and the plateau with the label $N_a + N_b + N_c$ represents the dissociation products.

It is worthwhile comparing some of the details used in the present work to that used by Paukku et al. [31] to determine the N_4 potential. In their calculations, the “spectator” diatom was restricted to have only three different bond lengths: $R_e \pm 0.38 a_o$, and the dissociating diatom had a bond length going from 1.5–11 a_o . The dissociating diatom bond lengths are similar to what is used in the present work. For our N_4 potential, not described here, we used a 9 by 9 grid of bond lengths ranging from 1.8–3.1 a_o calculated using the CCSD(T) method, correlating 20 electrons. This was augmented by dissociation calculations using the icACPF method, correlating 12 electrons. The number of orientations Paukku et al. consider is only 8 for the $N_2 + N_2$ geometries, which is much less than we use here. Unless one uses a very good model for the interpolating function, these will probably not be a sufficient number of angles. In our N_4 PES, we consider nine orientations for $N_2 + N_2$, but only consider three orientations for dissociating geometries. This, combined with a carefully chosen functional form, is expected to do a good job of representing the complete potential energy hyper-surface.

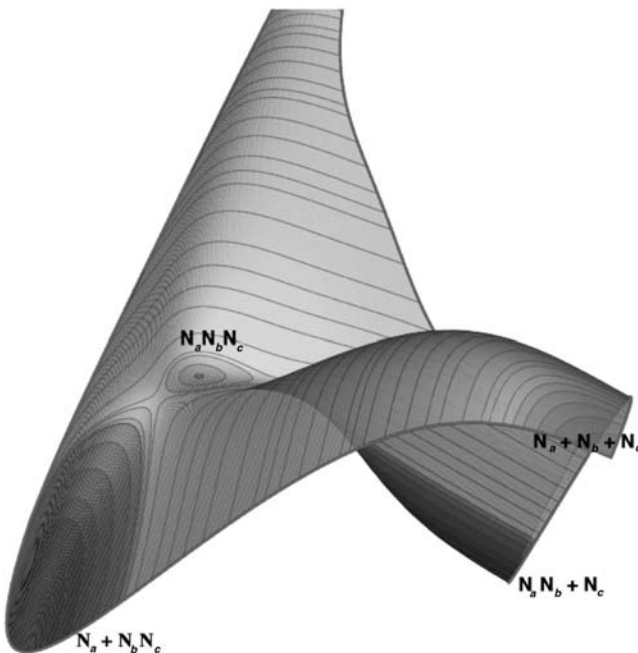


Fig. 3 Analytical representation of the potential energy surface for N_3 (with the atoms labeled N_a , N_b and N_c) in terms of $R(\text{N}_a\text{N}_b)$ and $R(\text{N}_b\text{N}_c)$ with the angle $\angle \text{N}_a\text{N}_b\text{N}_c$ fixed at 115 deg. Blue regions are lowest in energy and red are highest (see color section).

III. COLLISIONAL CALCULATIONS TO STATE-TO-STATE RATE COEFFICIENTS

A. QUANTUM MECHANICAL THEORY

From statistical mechanics, the microscopic state-to-state rate coefficients are given by the following expression [37]

$$k_{if}(T) = \frac{1}{3} (2k_B T)^{\frac{3}{2}} (\mu \pi)^{-\frac{1}{2}} \int_0^{\infty} \sigma_{if}(E_i) E_i \exp\left(-\frac{E_i}{k_B T}\right) dE_i \quad (17)$$

where i specifies the initial (v, j) state, f the final (v, j) state, k_B is Boltzmann's constant, T is the translational temperature, μ is the reduced mass for the reactants, equal to $2m_N/3$ for $\text{N}_2 + \text{N}$ and m_N for $\text{N}_2 + \text{N}_2$, m_N the mass of a nitrogen nucleus, and σ_{if} is the integral cross section for transitions from i to f for initial state translational energy E_i . This expression applies to all bimolecular collision processes, including elastic, inelastic, exchange, and dissociative ones.

The integral cross section computed using quantum mechanics takes the form [38]

$$\sigma_{\text{if}} = \frac{\pi}{g_i k_i^2} \sum_{\text{nl}} |S_{\text{in fl}}(E) - \delta_{\text{if}} \delta_{\text{nl}}|^2 \quad (18)$$

where g_i is the degeneracy of state specified by i , k_i is the initial state wave vector given by $k_i^2 = 2\mu E_i/\hbar^2$, $E_i = E - \varepsilon(v, j)_i$, with E the total energy, ε_i the energy of the (v, j) state specified by i , and $S_{\text{in fl}}$ is the scattering matrix element giving the outgoing wave amplitude from entrance channel specified by (v, j) state i and other quantum numbers n , to exit channel specified by (v, j) state f and other quantum numbers l . The other quantum numbers would specify the “arrangement” of the nitrogen atoms, i.e., $N_a + N_b N_c$, $N_b + N_c N_a$, $N_c + N_a N_b$, or $N_a + N_b + N_c$, and the angular momentum quantum numbers related to the three-body system. The quantity δ_{ab} is a Kronecker delta, and is unity if $a = b$ and zero otherwise, and $|a|^2$ means $a^* a$, where a^* is the complex conjugate of a . This is required because the scattering matrix is a complex symmetric unitary matrix.

For connection between quantum and classical mechanics, it is worth elucidating what is meant by the angular momentum quantum numbers related to the three-body system. Several choices are possible, with the most simplistic being m_j , the projection of the diatom rotation on the space fixed z axis (sfz) divided by \hbar , ℓ , the orbital angular momentum of the atom divided by \hbar , and m_ℓ , the projection of the atomic orbital angular momentum on the sfz divided by \hbar . This is called the uncoupled representation. Another useful choice is to form total angular momentum eigenfunctions, in which case the angular momentum quantum numbers are ℓ, J , the total angular momentum quantum number, and M , the projection of the total angular momentum on the sfz divided by \hbar . A final choice is to use J, M , and K , where K is the projection of the total angular momentum on the body fixed z axis divided by \hbar (see Eq. (7) for the definition of the body fixed z axis). The scattering matrices in one representation can be analytically transformed into the other representations, and the computed cross section will be independent of the choice of the representation. The advantage of the total angular momentum representations in quantum calculations is that there is no dependence of the scattering matrix on M , and there is no coupling between different values of J .

The interpretation of the integral cross section is as follows: it has units of area (think “target size”), and one can clearly see the factor π/k_i^2 is the formula for the area of the circle of radius $1/k_i$. The astute reader will notice that $1/k_i$ is essentially the De Broglie wave length defined earlier. The factor of 2π difference between $1/k_i$ and the De Broglie wave length arises from the convention of measuring frequency in terms of radians per unit time rather than cycles per unit time, and thus has no physical significance. If $i \neq f$, the rest of the expression for the integral cross section represents the probability of going from i to f , summed over all

irrelevant quantities of f and averaged over all irrelevant quantities of i . For elastic scattering, $I = f$ and we have to include the term δ_{nl} , which is a purely quantum mechanical interference term.

Now let us consider not the transition from i to f but rather the transition from f to i . Assume that both i and i are for bound states of N_2 . From statistical mechanics we know that

$$\frac{k_{if}}{k_{fi}} = \frac{Q_f}{Q_i} = \frac{g_f}{g_i} \exp\left(-\frac{\varepsilon_f - \varepsilon_i}{k_B T}\right) \quad (19)$$

where Q_i is the partition function of level i , and similarly for f . Now let us derive this expression from Eqs. (17) and (18). The scattering matrix is symmetric, i.e., for a given total energy $E = E_i + \varepsilon_i = E_f + \varepsilon_f$, $S_{in\ fl} = S_{fl\ in}$, thus we see that

$$\sigma_{if}(E_i) = \sigma_{fi}(E_f) \frac{g_f k_f^2}{g_i k_i^2} = \sigma_{fi}(E_f) \frac{g_f E_f}{g_i E_i} \quad (20)$$

Substituting this into Eq. (17) then yields Eq. (19). It should be noted that Eq. (19) is commonly referred to as detailed balance, whereas Eq. (20) is commonly referred to as microscopic reversibility, and these in turn follow from the symmetry of the scattering matrix, and that is due to time reversal symmetry [38].

Before we move on to the classical treatment that we actually used in this work, it is valuable to motivate the use of that approximation by describing how one would go about carrying out a quantum mechanical calculation. The goal of quantum mechanics is to determine the wave function Ψ^{in} that solves the Schrödinger equation:

$$i\hbar \frac{\partial}{\partial t} \Psi^{in} = H \Psi^{in} \quad (21)$$

subject to the boundary conditions specified by the initial state specified by superscript in. In this equation, $i = \sqrt{-1}$, t is time and the object H is the Hamiltonian operator, which, in the Born–Oppenheimer approximation, is made up of the nuclear kinetic energy operator and the potential energy hyper-surface. We also require that Ψ^{in} be regular, i.e., there are no regions of space where the average value of $|\Psi^{in}|^2 d\tau$ is not finite, where $d\tau$ is the volume element. Now H has no time dependence, so we can write

$$\Psi^{in} = \exp(-iEt/\hbar)\psi^{in} \quad (22)$$

with ψ^{in} having no time dependence. The physical interpretation of E is it is the total energy of the system. Then ψ^{in} can be seen to satisfy

$$H\psi^{in} = E\psi^{in} \quad (23)$$

Now we can solve this equation a wide variety of ways, but all start by making an expansion in terms of basis functions:

$$\psi^{\text{in}} = \sum_x \chi_x f_x^{\text{in}}(\rho_x, E) \quad (24)$$

where ρ_x is the “scattering coordinate” for basis function x , f_x^{in} is an unknown function, and χ_x is a known basis function that includes the dependence on all other coordinates. It is usual that included in the sum over x are all the terms f_l occurring in Eq. (18), although for accurate results, the sum over x cannot just consist of the f_l .

Now we must find the f_x^{in} subject to the boundary conditions specified by state i . If i and f_l refer to bound states of N_2 , then $\rho_{f_l} = r_l$, (see the discussion at the start of this chapter for the definition of r_a), so [38]

$$\lim_{r_l \rightarrow \infty} f_{fl}^{\text{in}}(r_l, E) = \frac{1}{r_l} k_f^{-\frac{1}{2}} [\delta_{if} \delta_{nl} \exp(-ik_f r_l) - \exp(ik_f r_l) S_{in fl}(E)] \quad (25)$$

The physical interpretation of this equation is there is an incoming wave (the $-ikr$ term) with unit amplitude along with a scattered wave (the $+ikr$ term) modulated by the complex coefficient $S_{in fl}$. As $E \rightarrow \infty$ or $\ell, J \rightarrow \infty$, there is no interaction, thus $S_{in fl} \rightarrow \delta_{if} \delta_{nl}$.

Now one way to solve for the f_{fl}^{in} is to expand them in terms of known functions [39]. Then the unknowns become coefficients rather than functions. For sake of argument, say that we need \mathcal{N} functions per f_x^{in} to obtain accurate results. Then the determination of the unknowns for a single i requires the solution $\mathcal{N} \times N_x$ coupled linear equations, where N_x is the number of basis functions x . Now using our V^{NN} , the N_2 molecule has about $10^4(v, j)$ states, so the f part of f_l in x is $\approx 10^4$. The l part of N_x depends on what one uses for basis functions. In the total angular momentum representation, which is the basis that allows for maximum decoupling, the l functions fall into blocks of maximum size $j+1$, where j runs from 0 to 100 or more. Thus the number of coupled linear equations could easily exceed 10^6 to 10^7 , depending on N . This then, becomes a very, very formidable task.

Another possibility is not to solve for the f_{fl}^{in} , but rather use perturbation theory to solve directly for the scattering matrix. In perturbation theory, we partition the Hamiltonian operator H into a part H^0 and the rest: $\Delta H = H - H^0$, and we assume that we can determine the Green’s function for H^0 . Then we can write [40]

$$S_{in fl} \approx S_{in fl}^0 + \Delta S_{in fl}^{\text{DWBA}} \quad (26)$$

with $S_{in fl}^0$ the scattering matrix for the zero-order problem and

$$\Delta S_{in fl}^{\text{DWBA}} = \frac{2\pi}{\hbar^2} \sum_{xy} \int f_x^{0\text{in}} \chi_x^* \Delta H \chi_y f_y^{0\text{fl}} \quad (27)$$

where DWBA stands for distorted wave Born approximation, and $f_x^{0\text{in}}$ is the radial function for the zero-order problem. The integral is over all space.

We can make H^0 such that the $f_x^{0\text{in}}$ is nonzero only for $x = \text{in}$, and similarly for fl , so this sort of calculation is feasible; however, the reliability is another question. This route might be the only practical route for predicting low probability events, for in that case $f_x^{0\text{in}}$ and $f_y^{0\text{fl}}$ can be expected to provide a good description of the true case.

Another problem of a quantum treatment occurs when we have energy large enough to dissociate the N_2 molecule. Then the boundary conditions of Eq. (25) do not apply. In fact, the specific form of the boundary conditions still alludes researchers, and until recently, attempts to actually compute the dissociation cross section were limited to model problems. A very significant step forward occurred when McCurdy et al. [41] realized that by adding a complex absorbing potential to H in Eq. (23), they could ensure that all flux heading to the double dissociation limit would be absorbed without affecting any of the other scattered flux. Then the computed scattering matrix would no longer satisfy the unitarity relation:

$$\sum_{\text{fl}} |S_{\text{in fl}}^{\text{ap}}|^2 \neq 1 \quad (28)$$

so that the dissociation integral cross section could be computed as

$$\sigma_{\text{id}} = \frac{\pi}{g_i k_i^2} \sum_n \left(1 - \sum_{\text{fl}} |S_{\text{in fl}}^{\text{ap}}|^2 \right) \quad (29)$$

where the superscript ap on the scattering matrix means it is computed in the presence of an absorbing potential.

The microscopic dissociation rate coefficient is determined essentially by Eq. (17) using the dissociation cross section. To determine the microscopic recombination rate coefficient, we utilize the dissociation rate coefficient and statistical mechanics: e.g.,

$$k_{\text{di}}/k_{\text{id}} = Q_i/Q_N^2 \quad (30)$$

where Q_N is the atomic partition function and Q_i is the partition function for N_2 level i .

B. CLASSICAL MECHANICAL TREATMENT OF COLLISION

Let us now turn to the classical simulation of the integral cross sections. The rough outline is we start with some initial conditions specified by $i = vj$ as well as some uninteresting initial conditions, then we integrate forward in time until the projectile is now flying away from the target and is in some new state f , and other uninteresting final conditions. We will do this many times for different values of the uninteresting initial conditions and average over them. An important

difference right off the bat between the classical and quantum calculations is that in the classical calculations, a given set of initial conditions produces only one final condition, whereas in quantum calculations, a single initial quantum state gives rise to all possible final states. This is a very important feature that will motivate how we do the averaging. This is discussed further below.

Now to implement this in practice, we need to know how to specify the initial condition i and analyze for the final condition f . This requires that we know how the quantum numbers (v, j) relate to the motion of the N_2 molecule. The way to do this has its birth in the Einstein–Brillouin–Keller (EBK) quantization condition [42–44], and formally it requires a transformation to “good action-angle variables”. Let us explain this. The classical description of particles is most conveniently given by the solution of Hamilton’s equations [45]:

$$\dot{x} = \frac{\partial H}{\partial p} \quad (31)$$

$$\dot{p} = -\frac{\partial H}{\partial x} \quad (32)$$

where x is some coordinate, dot means time derivative, p is the momentum conjugate to x , and H is the sum of the classical kinetic energy and the potential energy (V). If x is a Cartesian coordinate, then $p = m\dot{x}$ with m the mass for x , and $H = p^2/2m + V(x)$. Then Hamilton’s equations reduce to $-\partial V/\partial x = m\ddot{x}$, or Newton’s second law, force is mass times acceleration. The real beauty of Hamilton’s equations is not revealed until complex coordinate and momentum transformations are made. In particular, suppose by some operation one could transform to a new variable θ and conjugate momentum I such that $H = f(I)$, where f is some function. Then Hamilton’s equations tell us that

$$\dot{\theta} = \frac{\partial f(I)}{\partial I} = f'(I) \quad (33)$$

and

$$\dot{I} = -\frac{\partial f(I)}{\partial \theta} = 0 \quad (34)$$

We can integrate these equations by inspection: $I(t) = I(t_o)$ and $\theta(t) = \theta(t_o) + f'(I)(t - t_o)$, where t_o is the initial time. In this situation it is said that we have found good action-angle variables, and the momentum I is the action variable and the coordinate θ is the angle variable. Then the EBK quantization condition is that the action I can only take on the values $I = \hbar(n + \frac{1}{2})$, where n is a nonnegative integer.

Let us illustrate this by an example. Suppose $V = \frac{1}{2}m\omega^2x^2$, i.e., the potential for a harmonic oscillator. As time goes forward, we know that x oscillates back and forth between the turning points, and that p also oscillates back and forth

with p zero at the turning points and maximum when $x = 0$. Thus it does not seem unreasonable to try

$$x(t) = a \sin bt \quad (35)$$

Then we see

$$\dot{x} = ab \cos bt = \frac{p}{m} \quad (36)$$

thus

$$p = mab \cos bt \quad (37)$$

and

$$\dot{p} = -mab^2 \sin bt = -m\omega^2 x = -m\omega^2 a \sin bt \quad (38)$$

We then see that $b^2 = \omega^2$ and $H = (m/2)a^2\omega^2$ is independent of time. This then suggests that if we take $\theta = bt$, we can write H without θ and have found our good action-angle variables. To define the action variable I , we note that $\dot{\theta} = f'(I) = \omega$, which then implies that $H = I\omega$, or $I = (m/2)a^2\omega$. Then the EBK quantization condition for the energy becomes $H = \hbar\omega(n + \frac{1}{2})$, which we recognize as being identical to the quantum mechanical result.

So in analogy to the quantum mechanical situation where we have the interesting quantum numbers (v, j) and the uninteresting ones specified by n , in the classical treatment the interesting labels are the action variables for vibration and rotation, and the uninteresting ones include the angle variables for vibration and rotation.

Now the harmonic oscillator problem is very simple, and we must deal with real world examples that are not nearly so simple. To do this properly, one has to deal with the diatomic Hamiltonian

$$H = \frac{p_R^2}{2m} + \frac{p_\chi^2}{2mR^2} + V^{NN}(R) \quad (39)$$

where p_R is the momentum conjugate to the diatomic bond length R and p_χ is the momentum conjugate to the rotation angle χ . We take the diatom to lie in the xz plane and χ to be the angle rotating the z axis to the diatom bond axis. Because V^{NN} is a complicated function and because H couples R and χ , the determination of good action-angle variables must be done numerically. Eaker [46] has shown how to do this by choosing a set of initial conditions for R , p_R , χ , and p_χ , numerically integrating the equations of motion forward in time for a suitability long period of time, then carrying out a Fourier transformation to express the coordinates and momenta in the frequency domain rather than the time domain. The Fourier coefficients are then analyzed to find the peak heights and peak spacing. From these one can determine the actions and express the R , p_R , χ , and p_χ as a function of the angle variables. This is a rather complicated

process, for example, the length of time one integrates the trajectories prior to applying the Fourier transformation determines the resolution in the frequency domain spectrum, thus variable amounts of time will be required depending on the initial conditions. Thus we use a simplified approach.

In our approach, we take advantage of the fact that for a 1-D problem, the integral $\oint pdq$ is independent of the choice of coordinates, where \oint means the integral over one period of oscillation. This integral is easily evaluated in action-angle variables: it equals $2\pi I$. Then if we take $p_\chi = \hbar(j + \frac{1}{2})$, to solve the vibrational problem we need to find the energy ε_{vj} that satisfies the EBK quantization condition, i.e.,

$$\oint pdq = 2 \int_{R_-}^{R_+} \sqrt{2m \left[\varepsilon_{vj} - V^{NN} - \frac{\hbar^2 \left(j + \frac{1}{2} \right)^2}{2mR^2} \right]} dR = h \left(v + \frac{1}{2} \right) \quad (40)$$

where $R \pm$ are the classical turning points and the quantity under the radical is p_R found by inverting Eq. (39). We can evaluate the integral accurately using the appropriate Gaussian quadrature, making this is just a nonlinear root finding problem [18].

This provides ε_{vj} for the initial state, but not R , χ , \dot{R} , and $\dot{\chi}$ that are required to actually set up the initial conditions for the molecule. To do this, we must specify the angle variables, but we do not know the relation between the angle variables and the physical variables. But we do know that the angle variable and time are linearly related, so if τ_{vj} is the period of oscillation for state (v, j) , then if θ_0 is the angle variable we want to start from, we can just as well set $R = R_+$ and $p_R = 0$, and the integrate the equations of motion for R and p_R (Hamiltonian's equations generated from Eq. (39)) forward in time the amount $\tau_{vj}\theta_0/2\pi$. Then R and p_R at time $\tau_{vj}\theta_0/2\pi$ are the quantities we require. This is easy to do once we have τ_{vj} and, fortunately, τ_{vj} is found easily by

$$\oint (\dot{R})^{-1} dR = \tau, \quad (41)$$

where $\dot{R} = p_R/2m$ from Eqs. (31) and (39).

We are left with the specification of χ . This is a much harder nut to crack, and to do things properly, one could follow a procedure such as that described by Eaker [46]. The problem is although χ runs from 0 to 2π , it does not do so linearly in time, for there is the $1/R^2$ factor in $\dot{\chi}$, and R also depends on time. Nonetheless we will assume that reasonable results can be had by sampling χ uniformly. As an assessment of the error caused by this, we show in Fig. 4 χ as a function of time for selected values of (v, j) . In this figure, the arrows mark the vibrational period, and the curves repeat themselves for each vibrational period. The rotational periods are several times the vibrational periods, so an accurate calculation would first select the vibrational angle variable, which would then tell one

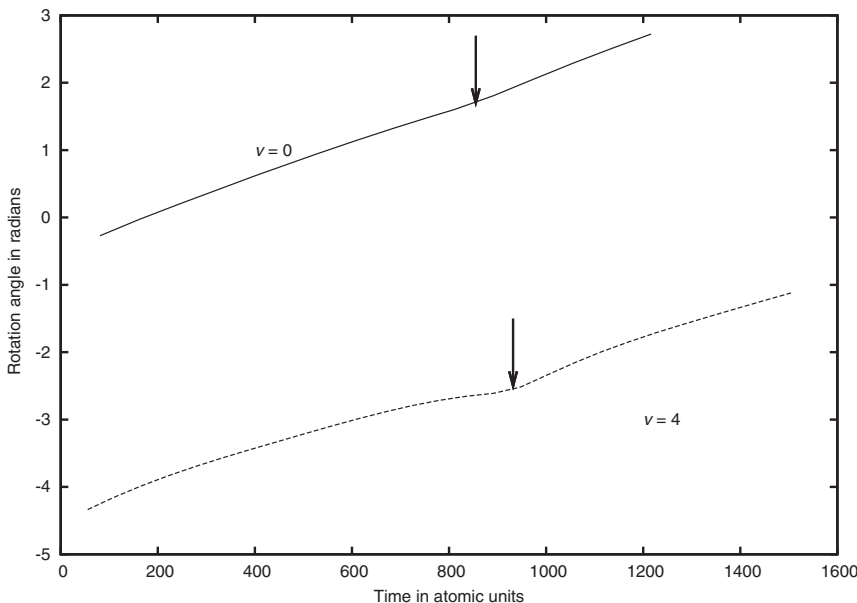


Fig. 4 Rotation angle as a function of time for $j = 100$.

where to start on the curve, then one would select the rotational angle variable, and that would tell you how far to move along the curve to get the starting value of χ . In any case, the departure from linearity does not seem to be large enough to cause concern.

Now consider the analysis of the final condition of a trajectory. From the final diatom positions and velocities, we can compute the angular momentum of the diatom: p_χ . Then we can compute the angular momentum quantum number as $j = (p_\chi/\hbar) - \frac{1}{2}$. Next we compute the vibrational quantum number v by evaluating Eq. (40) with the final internal energy of the diatom. Now we have v and j , but in general, they will not be integers. The simplest way to proceed is to now make them integers by replacing them with the closest nonzero integer. This is basically what we do. If the collision is nonreactive, then we have a further restriction that Δj must not be odd, as N_2 is a homo-nuclear diatom. In this case, we find the closest integer to $j - \delta/2$, where δ is the remainder when the initial j is divided by 2, and then set j to twice this integer plus δ .

It is immediately clear from the determination of the final conditions that there is an inherent asymmetry between computing $i \rightarrow f$ and $f \rightarrow i$: the initial (v, j) are integral whereas the final (v, j) are not. Thus, when computing cross sections from classical mechanics, the relation of Eq. (20) will not be satisfied, and to ensure proper equilibrium, we must force Eq. (20) to be satisfied. We believe that one of σ_{fi} or σ_{if} will be computed more accurately than the other, and so we will

discard the less accurate one and instead compute it from the more accurate one and Eq. (20). We assume that the more accurate one will be the cross section computed in the exothermic direction, i.e., the direction where the final state has lower energy than the initial state.

Now it turns out with classical mechanics we can compute the square of the S matrix element, directly compute the cross section without computing the S matrix elements, or directly compute the microscopic rate coefficient without computing the cross section. To understand this, let us first consider the calculation of the square of the S matrix in the uncoupled representation.

In the uncoupled representation, $i = vj$ and $n = m_j, \ell, m_\ell$. We have described how we can get $R, \dot{R}, \chi, \dot{\chi}$ specified by $i = vj$ and θ_v and θ_χ . To orient the diatom angular momentum vector in space, we need to make the z component m_j , but we are still free to choose the x and y components: we do this by specifying the variable θ_j . We will place the center of mass of the diatom at the origin. Similarly, we need to choose initial conditions for the atom such that the orbital angular momentum has magnitude $\ell\hbar$ and z axis component $m_\ell\hbar$. Again, the x and y components are unspecified, so we fix them by specifying the variable θ_ℓ . We will place the atom a distance d from the origin. Now we can run the trajectory until an atom-atom distance is greater than d_f , with $d_f > d$. At this point we can analyze the final state of the diatom.

That is one trajectory. To get the square of the scattering matrix element, the probability of going from in to fl, we need to average over $\theta_v, \theta_\chi, \theta_j$, and θ_ℓ . As these are continuous variables, the average takes the form of a four-dimensional integral, with the integrand the measure of whether or not those θ s led from in to fl: this measure is either zero or one. The important thing to note is the integrand is not at all smooth, and no derivatives exist. Thus classical quadrature schemes will give very poor results if they are used to evaluate these integrals. Really the only way to evaluate these integrals is to use the Monte-Carlo method. Here we randomly choose the values of $\theta_v, \theta_\chi, \theta_j$, and $\theta_\ell N$ times, and the value of the integral apart from prefactors is $N_{\text{in fl}}/N$, where $N_{\text{in fl}}$ is the number of trajectories that started with initial condition in and ended with final condition fl. An important by-product of the Monte-Carlo method is the estimate of the error in the integral. It is proportional to $1/\sqrt{N}$. This error estimate is a two edged sword: on one hand the convergence is rather slow: to halve the error, one would have to run four times as many trajectories. But on the other hand, the error estimate is independent of the number of dimensions in the integral. This last observation has huge consequences. Rather than individually computing the hundreds or thousands of terms entering into the cross sections, if we change the sums over n and l into integrals, with the same number of trajectories we can compute the cross sections with an accuracy 10–30 times better.

Similarly, if the ultimate goal is the microscopic rate coefficient, rather than computing the cross section as a function of energy, and then evaluating Eq. (17), we can throw the E_i integration into the Monte-Carlo procedure as well and get better results with fewer trajectories.

Now consider how we change the sum over ℓ and m_ℓ into integrals. Now m_ℓ is the projection of ℓ onto the space-fixed axis system. But we do not have to carry out the trajectories in the space-fixed axis system, rather we will carry out the trajectories in the body-fixed axis system. Recall that in the body-fixed axis system, we require the center of mass of the system to be stationary at the origin. However, it is useful to set up the initial conditions with the atom in the xy plane and the diatom center of mass stationary at the origin. Then the initial coordinates and momentum of the atom are $(b, d, 0)$ and $(p_i, 0, 0)$, where $p_i = -\sqrt{2\mu E_i}$. The quantity b is called the impact parameter, and is the distance of closest approach of the atom to the center of mass of the diatom if there was no interaction. Then the initial orbital angular momentum is $(0, 0, -p_i b)$. So the first observation we make is that our body-fixed axis system is chosen in such a way to be independent of m_ℓ . Thus we can analytically perform the sum over m_ℓ , and the result is $2\ell + 1$. We need to evaluate the sum $\sum_\ell (2\ell + 1)P(\ell)$. To do this, it is convenient to change variables from ℓ to b : they are related by $\ell\hbar = p_i b$. Now let us consider for a moment the likely sizes of ℓ . At the start of this section we mentioned that at $T = 10,000$ K, a nitrogen atom would have $p \approx 40$ a.u. Then if we assume that $\tilde{P}(b) = P(p_i b / \hbar)$ is independent of b until the impact parameter reaches some maximum value, say b_{\max} , and taking $b_{\max} = R_e/2 \approx 1$ a.u., we see that ℓ will run from 0 to 40, and $\sum_\ell (2\ell + 1)P(\ell) = 41^2 P(0) = 1681 P(0)$. If instead we replaced $2\ell + 1$ with 2ℓ , the sum would be $1640 P(0)$, for an error of only 2.4%. This is an acceptable error, so henceforth we use 2ℓ instead of $2\ell + 1$. Now the way to turn the sum over ℓ into an integral is the Euler-MacLaurin summation formula, i.e.,

$$\sum_\ell 2\ell P(\ell) \approx \int_0^{b_{\max}} 2\ell P(\ell) d\ell \quad (42)$$

where we have used the fact that the lower limit and upper limits give no contribution to the integral. Then, changing variables from ℓ to b gives us

$$\frac{2p_i^2}{\hbar^2} \int_0^{b_{\max}} \tilde{P}(b) b db. \quad (43)$$

If $\tilde{P}(b)$ is independent of b , then the integral can be evaluated analytically, and we obtain $\tilde{P}(0) p^2 b_{\max}^2 / \hbar^2$, so that the cross section becomes

$$\sigma_{\text{if}} = \tilde{P}(0) \frac{\pi b_{\max}^2}{g_i}, \quad (44)$$

i.e., the area of the circle of radius b_{\max} times the probability of going from i to f divided by the degeneracy factor.

Now in actuality, $\tilde{P}(b)$ is not independent of b , and we actually must compute the integral. To do this by Monte-Carlo methods, we need to change variables to

achieve a constant volume element and integration range 0 to 1, and this is done by the substitution $\theta = (b/b_{\max})^2$, so that

$$\int_0^{b_{\max}} f(b) b db = \frac{2}{b_{\max}^2} \int_0^1 f(\sqrt{\theta} b_{\max}) d\theta \quad (45)$$

The problem with using this form for the integral is uniformly sampling on θ will tend to more likely sample b near b_{\max} than near $b = 0$, and as b_{\max} is chosen so that $\tilde{P}(b_{\max}) = 0$, this means the Monte-Carlo method will give even slower convergence. Instead, we use a stratified sampling technique [47]. Here we choose a sequence of b_{\max} values so we can concentrate b to small values for low probability events as well as allow for larger values for high probability events. The sequence we use is $b_{\max} = 0.25, 0.5, 1, 3, 5$, and $8 a_o$.

Now let us consider elastic scattering for a moment: the case where $f = i$. In quantum mechanics, this is where the $-\delta_{if} \delta_{nl}$ term comes into play and the cross section is finite. In classical mechanics, for the limit $b \rightarrow \infty$, the probability of going from i to $f = i$ becomes unity. Thus in classical mechanics the elastic cross section is infinite and it is not possible to compute the elastic cross section from classical calculations. Fortunately for our purposes, the elastic cross section plays no role in our kinetics calculations.

For direct simulation Monte Carlo (DSMC) flow calculations, it would be nice to compute transport properties during the simulations. To do this, one requires not the integral elastic cross section, which cannot be computed from classical mechanics, but rather the integral of the elastic differential cross section $d\sigma/d\Omega$ times the weighting function $1 - \cos^l \theta$, with $l = 1, 2$ or 3 . In quantum mechanics, the $\delta_{if} \delta_{nl}$ term serves two purposes: firstly it ensures the integral cross section is finite, and it causes the differential cross section to be a highly oscillatory. In classical mechanics, the integral cross section diverges because the differential cross section at zero θ becomes infinite. However the factor $1 - \cos^l \theta$ should remove this singularity so that finite integrals can be computed. Also, this oscillatory behavior of the quantum results will not be present in classical simulations, but as the important collision integrals include factors that are not strong functions of angle for θ significant different from zero, the classical calculations should be able to give reasonable results.

Now let us discuss the selection of the initial relative translational energies. In Figs. 5 and 6 we show the Boltzmann distribution for several temperatures. In these figures the maximum probability is not normalized to aid the reader. We see that at low temperature, say 300 K, the energy distribution is very sharply peaked. In contrast, at high temperature, say 20,000 K, the energy distribution is very broad. Now if one is considering a range of temperatures, as is the case in the present work, one has two choices to select the relative translational energies. In the first case, we compute the cross sections at specific representative energies, and in the figure we indicate with arrows what those energies might be. A second choice is to assume a translational temperature and sample the energy from the Boltzmann distribution at that temperature. We then will bin the

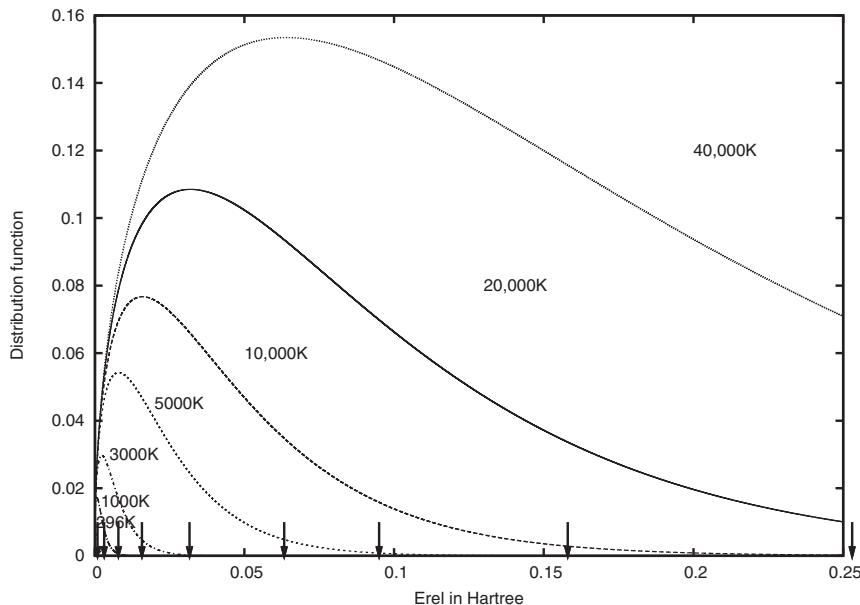


Fig. 5 Unnormalized relative translational energy distributions (linear energy axis).

energies, and compute a cross-section representative for this bin. In the later choice, energies that are unlikely will not be sampled often, and thus efficiency is gained. This choice will only be usable when the Boltzmann distribution is not that different for all translational temperatures of interest. In our work, we sampled the translational energy from a 60,000 K Boltzmann distribution. Thus we can reliably predict state-to-state rate coefficients only down to about 5000 K. This should not be a limitation for the type of simulations we are currently interested in doing.

We have thus described the calculation of cross sections and rate coefficients for transitions between bound states. Now we need to extend the discussion to include quasi-bound states and dissociated states.

First consider quasi-bound states. These are states for which one can find good action-angle variables in classical mechanics, but in quantum mechanics these states can decay to atoms via tunneling through the centrifugal barrier (the $p_\chi^2/2mR^2$ term in Eq. (39)). These states are called different things in different fields of study: in spectroscopy they are called predissociated states, and in quantum scattering theory they are called resonant states [38]. The properties of these states has been studied intensely via formal scattering theory, and the salient result is they are very much like true bound states, except rather than having quantized energies on the real energy axis, they have quantized energies in the complex energy plane: call this energy $E_{vj} - i\Gamma_{vj}/2$ with E_{vj} and Γ_{vj} real.

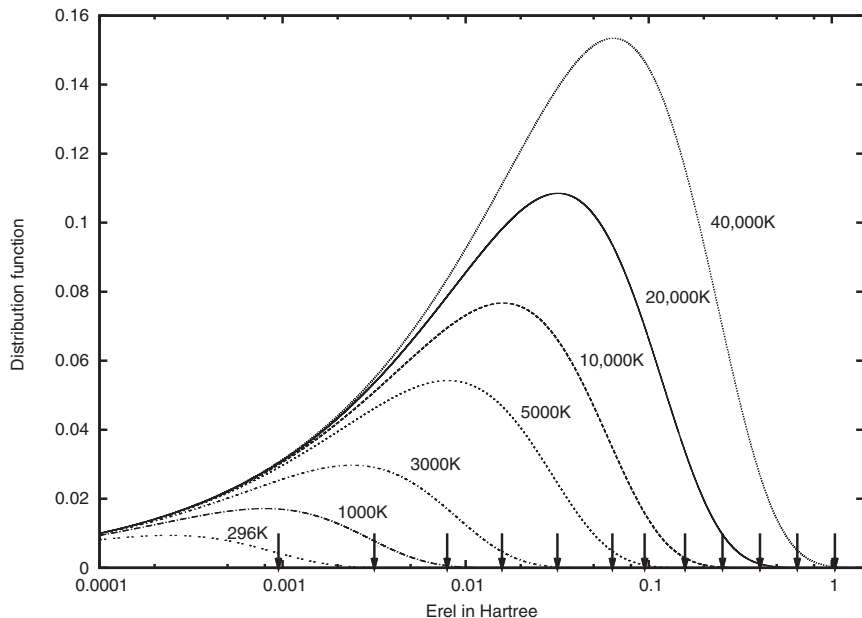


Fig. 6 Unnormalized relative translational energy distributions (logarithmic energy axis).

Of course, the physical energy axis is the real energy axis, thus the imaginary part of the quantized energy, Γ_{vj} is observed only indirectly. Commonly Γ_{vj} is called the width of resonance (v, j), for a feature in the optical spectra involving this state looks like a Lorentzian with full width at half max equal to Γ_{vj} if the resonance is isolated. Furthermore, the uni-molecular decay rate of this state given by \hbar / Γ_{vj} . Thus the computation of Γ_{vj} will be important for our simulations.

In classical mechanics, there is no way to compute the width Γ_α , for in classical mechanics this state α is actually bound. What we do is use what is called a semi-classical procedure. Rather than start with classical mechanics and quantizing the actions, as described above, one can also start with quantum mechanics and assume a particular form for the wave function and expand in powers of \hbar . The simplest form, the primitive WKB method, gives exactly the same result as above for the vibrational energy levels. Then the next level, called the uniform semi-classical method, yields a correction to Eq. (40) as well as a nonzero result for Γ_{vj} . In our work, we neglect the correction to Eq. (40) for ε_{vj} , but we use the uniform semi-classical result for the width:

$$\tau_{vj} \Gamma_{vj} = \hbar \exp \left\{ - \int_{R+}^{R_0} \sqrt{2m \left[V^{NN} + \frac{\hbar^2 \left(j + \frac{1}{2} \right)^2}{2mR^2} - \varepsilon_{vj} \right]} dR / \hbar \right\} \quad (46)$$

where R_o is smallest distance greater than R_+ for which the radial in the integrand is zero.

So by these means we can easily compute ε_{vj} , τ_{vj} , and Γ_{vj} . Now for initial conditions, we follow the procedure described above for bound states, except we now do not just use the initial energy ε_{vj} , but rather sample from a gaussian distribution with center ε_{vj} and width Γ_{vj} .

C. RESULTS OF THE QUASI-CLASSICAL TRAJECTORY CALCULATIONS

In the previous section we discussed how collision cross sections σ_{if} and state-to-state rate coefficients $k_{if}(T)$ can be simulated using the classical equations of motion with all the necessary parameters selected by Monte Carlo sampling schemes. Now we show how thermal rate coefficients for $N_2 + N$ and $N_2 + N_2$ collisions are obtained from the state-to-state rate coefficients. The thermal rate coefficient is defined through the chemical kinetics rate equation for the process $N_2 + N \rightarrow \text{products}$:

$$\frac{dn_{N_2}}{dt} = k(T)n_{N_2}n_N \quad (47)$$

where n_X is the gas density of species X in molecules/cm³ and t is time in seconds. Thus the rate coefficient has units of cm³ molecule⁻¹ second⁻¹. Sometimes rate coefficients are expressed in molar units by multiplying k by Avogadro's number. The thermal rate coefficient is obtained as the summation of the state-to-state cross sections multiplied by the Boltzmann weighting of each rovibrational level.

First we need to enumerate the rovibrational levels that are obtained by using the modified Le Roy potential for the N_2 molecule with the addition of a centrifugal term due to rotation and solving the Schrödinger equation for the nuclear motion. The potential (V_j) for a rotating and vibrating diatomic molecule is

$$V_j(R) = V_{j=0} + j(j+1)\frac{\hbar^2}{2\mu R^2} \quad (48)$$

$V_j = 0$ is the rotationless potential, in this case the modified Le Roy et al. [35] expression, j is the rotation quantum number, μ is the reduced mass of the diatomic molecule, $m_N/2$ for N_2 , where m_N is the mass of the nitrogen nucleus, and R is the distance between the atoms in the molecule. We use the semi-classical WKB approximation to obtain the rovibrational energy levels and vibrational wave functions. The addition of the centrifugal term produces an energy barrier in the diatomic potential for $j > 0$. Energy levels that lie above the dissociation energy (D_e and below this barrier have finite lifetimes and are labelled as quasi bound. For N_2 , most of these quasi bound levels have lifetimes considerably longer than the time between collisions and should be considered in the

calculation of state-to-state rate coefficients. The rotating potential for N_2 , based on the Le Roy expression is shown in Fig. 7 for various values of J .

For the Le Roy N_2 potential with $j = 0$ there are 61 vibrational levels ($v = 0, 1, \dots, 60$) and for $j \neq 0$, there is at least one bound vibrational level for values of j up to 279 [27, 28]. Figure 7 shows the potentials for 8 values of J including $j = 0$ and 279. For larger values of j the potential does not exhibit a minimum for finite R . In all there are 9390 bound and quasi bound rovibrational levels of N_2 as expressed by the modified Le Roy potential. Of these 7421 are bound and 1969 are quasi-bound. Most of the levels lie within 20 kcal/mol of the N_2 dissociation energy, which is 224.93 kcal/mol (D_0). The energy of the highest rovibrational level ($v = 0, j = 279$) is 344.09 kcal/mol. For increasing j the effective dissociation energy (the difference between the centrifugal barrier and the energy of the $(0, j)$ level) drops from D_0 to near zero. For $j = 136$ it is 140.61 kcal/mol and for $j = 230$ it is 36.27. In addition, the vibrational spacing,

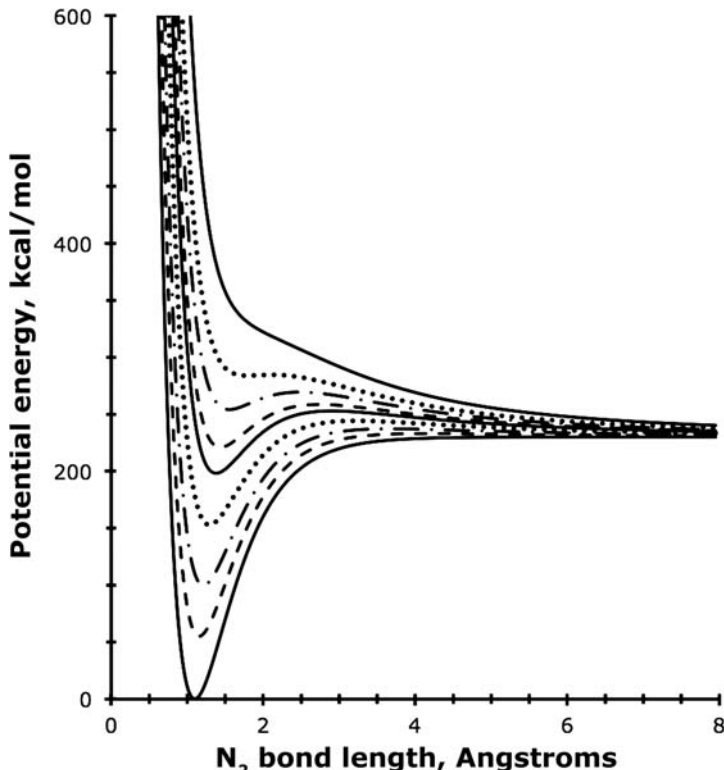
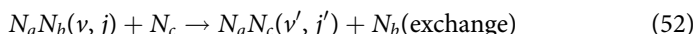
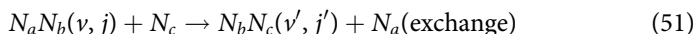
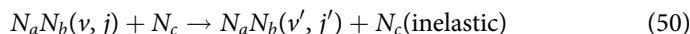
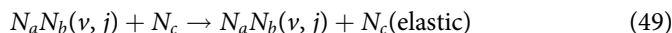


Fig. 7 Potential energy curves for N_2 . V^{NN} has units of kcal/mol and the bond length R is in Angstroms. The curve with the lowest minimum energy is for $j = 0$. The other curves, in vertical order, have $j = 100, 136, 170, 200, 212, 230$ and 279.

$E(1, j) - E(0, j)$, is 2329 cm^{-1} for $j = 0$ and 1327.8 cm^{-1} for $j = 230$. Similarly, the rotational spacing (defined as $E(0, j+1) - E(0, j)$) is 4.0 cm^{-1} for $j = 0$ and 641.2 cm^{-1} for $j = 230$. The dependence of these values on j is a manifestation of the strong coupling between rotation and vibration [48].

We have computed state-to-state rate coefficients for $\text{N}_2 + \text{N}$ pairs for each of these levels using the Quasi-Classical Trajectory method. The translation energy was sampled from a 20,000 K thermal distribution using a discrete set of 64 energies between 6.5 and 1160 kcal/mol with a thermal weighting factor of $0.5E_{\text{rel}} \exp(-E_{\text{rel}}/k_B T)$. A batch of 6000 trajectories was run for each $\text{N}_2(v, j)$ level. The individual trajectories in each set can be re-weighted for a different temperature so that cross sections and rate coefficients can be computed at other temperatures as well. With the range of E_{rel} values used in these calculations, we can compute energy transfer rate coefficients for a range of temperatures from ≈ 7500 to 40,000 K. With the random sampling scheme used for initial conditions of each trajectory, the statistical error associated with each computed cross section is inversely proportional to the square root of the sample size. In our work the most of the individual state-to-state cross-section values have statistical errors of 20% or less. Other sources of error are difficult to quantify; these include the accuracy of the quantum chemical potential and the fidelity of the analytic fit of the PES. The final states of these trajectories depend on whether the collision is elastic (no translation to internal energy transfer), inelastic or an exchange reaction (with translation to internal energy transfer), or dissociating:



All of these outcomes are possible. However, as discussed previously, our sampling of initial conditions for the classical trajectories is not designed to yield an accurate determination of the elastic scattering cross section and corresponding rate coefficient. Figure 8 displays all the state-to-state inelastic (above the diagonal) and exchange rate coefficients (below the diagonal) for $T = 10,000$ K. Both kinds of processes have the largest rate coefficients clustered near the diagonal, which means that smaller amounts of energy transfer are more probable. However, the distribution of exchange rate coefficients shows greater width, indicative of larger amounts of energy transfer. The yellow region on the plot shows rate coefficients that are $\approx 10^3$ times smaller than those near the diagonal. Thus, the red region of the plot represents the important energy transfer processes at 10,000 K. Note that these rate coefficients extend through the energy range of the quasi-bound rovibrational energy levels (rovibrational greater than 9.75 eV). The dark blue areas in the figure represent E_i and E_j where rate coefficients were not determined and are assigned a value of zero.

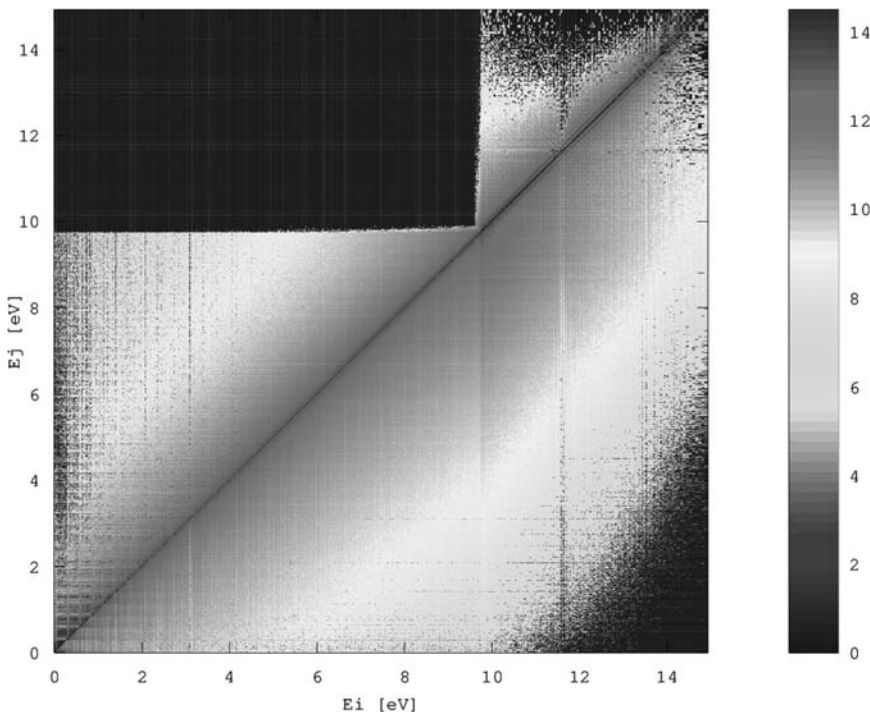


Fig. 8 Molar rate coefficients in $\text{cm}^3 \text{mole}^{-1} \text{second}^{-1}$ for inelastic and exchange processes at $T = 10,000 \text{ K}$. $\log(k_{ij})$ is plotted for rovibrational energies E_i and E_j with i and j referring to initial and final $\text{N}_2(v, j)$, respectively. The diagonal starting at the origin represents the elastic channel. Inelastic rate coefficients are plotted above the diagonal and exchange rate coefficients are plotted below. The color key is given on the right. Dark blue areas correspond to the rate coefficients with value zero (see color section).

A similar illustration for the dissociation rate coefficients for $\text{N}_2(v, j)$ is shown in Fig. 9. The largest dissociation rate coefficients are for (v, j) with rotation quantum number near the maximum value for each vibration quantum number. All the levels with J greater than ≈ 215 are in the quasi bound region. The light blue through red region of the plot represent rate coefficients that are important contributors to overall dissociation reaction.

The full set of rate coefficients shown in Figs. 8 and 9 are used to determine phenomenological rate coefficient that are discussed in the next section. It is of interest, however, to see how the thermal dissociation rate coefficient obtained from the state-specific dissociation rate coefficients agrees with the published results of shock tube experiments probing the dissociation of N_2 , in N_2/Ar mixtures, during the 1960s and 70s. These are the work of Cary [49] for the

temperature range 6000–10,000 K, Byron [50] for 6000–9000 K, Appleton et al. [49] for the 8000–15,000 K and Hanson and Baganoff [52] for 6000–12,000 K. In these papers Arrhenius fits to the dissociation rate coefficient are given for $\text{N}_2 + \text{N}_2$, $\text{N}_2 + \text{N}$ and $\text{N}_2 + \text{Ar}$. These rate coefficients are ≈ 5 times smaller than the results of the other shock tube experiments. In general, it is found that the $\text{N}_2 + \text{N}$ reaction is 3–8 times faster than $\text{N}_2 + \text{N}_2$. Park [4, 5] chose to use Appleton's values [51] for the $\text{N}_2 + \text{N}$ and $\text{N}_2 + \text{N}_2$ dissociation rate coefficients for his 2-T model, because the experimental data extend to higher temperatures. However he increased the pre-exponential factor to obtain better agreement of his 2-T model with experimental data. Our thermal rate coefficient for $\text{N}_2 + \text{N}$ is compared with the result of Appleton in Fig. 10. The agreement between the QCT (asterisks) and Appleton (solid line) results is quite good, but the two determinations have somewhat different slopes. This is attributable to the QCT rate coefficient being well described by a two-parameter Arrhenius expression,

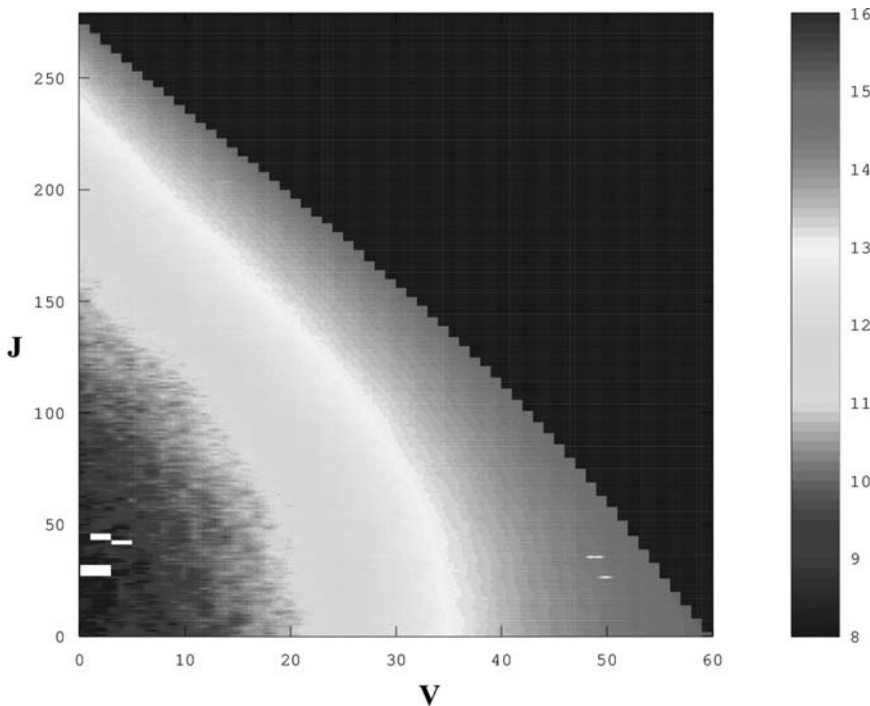


Fig. 9 Molar rate coefficients in cm^3 per mole per second for dissociation processes at $T = 10,000$ K. $\log(k_{ij})$ is plotted for each value of vibration and rotation quantum numbers. The jagged red-orange line represents the highest value of J for each v . The color key is given on the right. Dark blue areas correspond to the rate coefficients with value zero (see color section).

whereas the Appleton result is fit to a three-parameter one. Also shown are the rate coefficients used by Park in the 2-T model [4–7] (dashed line) and the QCT rate coefficients computed by Esposito et al. [16, 53, 54] (dot-dashed line). Those calculations were based on an empirical PES and were only carried out for $T < 10,000$ K. In that temperature range the rate coefficients are about $5 \times$ larger than our QCT values.

We have also obtained thermal rate coefficients for the $\text{N}_2 + \text{N}_2$ dissociation reaction using the QCT method and the N_4 PES. This rate coefficient is compared with experimental determinations in Fig. 11. The QCT rate coefficients (asterisks) are in very good agreement with Appleton's [51] (solid line) and Byron's [50] (dot-dashed line) measurements. On the other hand, Hanson's determination [52] (dotted line) has a markedly different variation with temperature. The

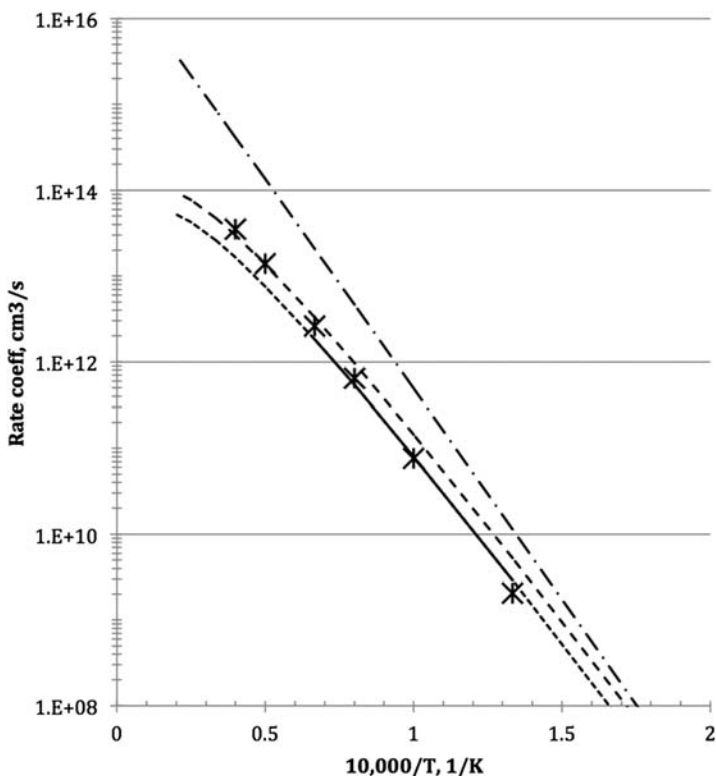


Fig. 10 Thermal rate coefficients for N_2 dissociation due to collision with N atoms. The asterisks are the QCT results. The solid line is the rate coefficient determined by Appleton [51] as a fit to shock tube data, with the solid portion representing the measured temperature range and the dotted portions extrapolation of Appleton's Arrhenius expression. The dashed line represents the rate coefficient selected by Park for the 2-T model and the dot-dashed line is the QCT rate coefficient computed by Esposito et al. [54].

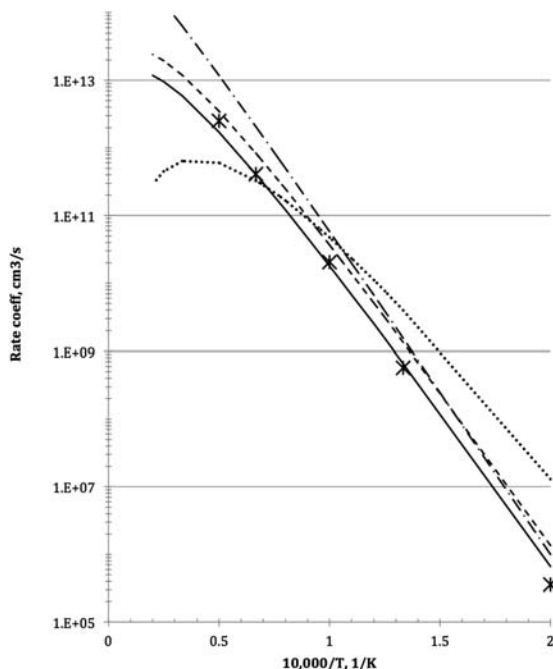


Fig. 11 Thermal rate coefficients for N_2 dissociation resulting from $N_2 + N_2$ collisions. The QCT results (asterisks) are compared with the rate coefficients determined from shock tube experiments: Byron (Reference [50]) dot-dashed line, Appleton (Reference [51]) solid line, and Hanson (Reference [52]) dotted line. The dashed line represents the rate coefficient in the Park model (References [4, 5]).

Park (dashed line) and Appleton rate coefficients also exhibit more Arrhenius curvature than does the QCT result. In general, one can conclude that the QCT method using the PES's described in this chapter yield thermal rate coefficients that are within a factor of two of the best shock tube determinations for N_2 dissociation. Also, the QCT rate coefficients and Appleton data exhibit a similar ratio between dissociation rate coefficients for $N_2 + N$ and $N_2 + N_2$. Appleton [51] reported $\frac{k_{N_2+N}}{k_{N_2+N_2}} = 4.3$ and the QCT rate coefficients give values of 3.76 and 5.50 at 10,000 K and 20,000 K, respectively.

IV. PHENOMENOLOGICAL RATE COEFFICIENTS FROM A DETAILED MASTER EQUATION MODEL

It is not practical to use the full set of state-to-state rate coefficients in flow-field calculations. However, we can use these rate coefficients to develop a new

rovibrational collisional model free of any assumptions about the rovibrational temperature. Instead, we track the populations of all the rovibrational energy levels as the system relaxes to equilibrium. We have carried out this analysis for a zero-dimensional chemical reactor and a 1-D shock wave. The zero-dimensional analysis aims at unraveling the main features of state-to-state kinetics in a controlled environment free of the complications introduced by the flow chemistry coupling [55]. The system examined is a mixture of molecular nitrogen and a small amount of atomic nitrogen. This mixture, initially at room temperature, is heated by several thousands of degrees Kelvin, driving the system toward a strong nonequilibrium condition. The evolution of the population densities of each individual rovibrational level is explicitly determined via the numerical solution of the master equation for temperatures ranging from 5000 to 50,000 K. The shock wave analysis aims at investigating the coupling of the detailed kinetics with the flow. The master equation is coupled with a 1-D flow solver. The system of equations is solved for conditions expected for reentry into Earth's atmosphere at 10 km/s. Although extremely accurate, the rovibrational state-to-state approaches can only be applied to zero and 1-D problems owing to their large computational cost. Thus, in order to extend their applicability to multi-dimensional flow conditions, reduced-order model must be constructed. To this aim, a coarse-grained model is proposed by lumping the rovibrational energy levels into a smaller number of bins. The results obtained by means of the full rovibrational collisional model are compared to those obtained by means of a vibrational collisional model.

A. KINETIC PROCESSES INCLUDED IN THE MODELS

The NASA Ames database [26, 28, 30, 56], that includes the rate coefficients described in Sec. I, comprises a complete and self-consistent set of thermodynamic and kinetic data needed to describe the elementary state-to-state kinetics of N₂-N and N₂-N₂ interactions. Although the analysis carried out in this work is restricted to the study of N₂-N relaxation, an ongoing effort addresses the study of dynamics of the N₂-N₂ system.

The database includes 9390 rovibrational energy levels N₂(ν, j) for the electronic ground-state of nitrogen. These levels can also be sorted by increasing energy and denoted by means of a global index i . The relation between the i and (ν, j) notations is expressed as

$$i = i(\nu, j), \quad \nu = 0, \dots, \nu_{\max}, \quad j = 0, \dots, j_{\max}(\nu)$$

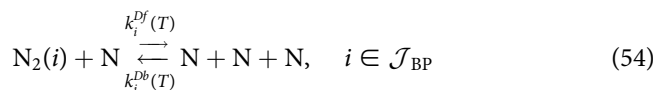
and conversely by the relations

$$\nu = \nu(i), \quad j = j(i), \quad i \in \mathcal{J}_{\text{BP}}$$

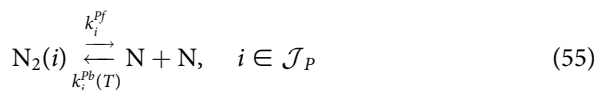
where \mathcal{J}_{BP} is the set of global indices for the nitrogen energy levels. This set of energy levels includes the quasibound (or predissociated) levels as well as the bound levels. The bound energy levels are denoted by the set \mathcal{J}_B , and the predissociated energy levels, by the set \mathcal{J}_P , with $\mathcal{J}_B \cup \mathcal{J}_P = \mathcal{J}_{\text{BP}}$ and

$\mathcal{J}_B \cap \mathcal{J}_P = \emptyset$. The total wave function for the nitrogen molecule must be symmetric with respect to exchanging the nuclei (Bose-Einstein statistics), the degeneracy of the energy levels is given by the expression $g_i = (2J(i) + 1)g_i^{NS}$, $i \in \mathcal{J}_{BP}$, where the nuclear spin degeneracy is $g_i^{NS} = 6$ for even $J(i)$ and $g_i^{NS} = 3$ for odd $J(i)$.

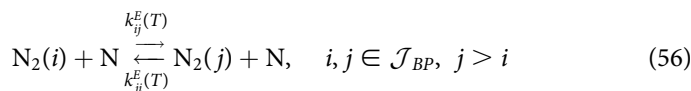
The database for the $N_2 + N$ system comprises more than 20 million reactions in total for three types of processes: collisional dissociation of bound states and predissociated states,



predissociation, or tunneling, of predissociated states,



and collisional excitation between all states,



The collisional excitation processes include the contribution of both inelastic (nonreactive) and exchange processes

$$k_{ij}^E(T) = k_{ij}^{IE}(T) + k_{ij}^{EE}(T) \quad (57)$$

The first term $k_{ij}^{IE}(T)$ accounts for the contribution owing to inelastic processes, where kinetic energy is transferred into internal energy during the collision. The second term $k_{ij}^{EE}(T)$ accounts for exchange processes and the transfer between kinetic and internal energies occurs via substitution of one bounded atom of the molecule with the colliding partner. The importance of this elementary process on the kinetics of dissociation is discussed later in this section.

The direct reaction rate coefficients $k_i^{Df}(T)$, $k_i^{pf}(T)$, and $k_{ij}^E(T)$, $j > i$, used in the present work, have been computed, as described in the previous section, using the QCT method for nine values of the gas translational temperature T between 7500 and 50,000 K [26, 56]. Reverse rate coefficients result from micro-reversibility of the processes among the energy levels E_i , $i \in \mathcal{J}_{BP}$, yielding the following expressions for the equilibrium constants for collisional dissociation of truly bound states and predissociated states,

$$K_i^D(T) = \frac{k_i^{Df}(T)}{k_i^{Df}(T)} = \frac{[g_N Q_N^t(T)]^2}{g_i Q_{N_2}^t(T)} \exp\left(\frac{-(2E_N - E_i)}{k_B T}\right), \quad i \in \mathcal{J}_{BP} \quad (58)$$

predissociation, or tunneling, of predissociated states,

$$K_i^P(T) = \frac{k_i^{Pf}(T)}{k_i^{Pb}(T)} = \frac{[g_N Q_N^t(T)]^2}{g_i Q_{N_2}^t(T)} \exp\left(\frac{-(2E_N - E_i)}{k_B T}\right), \quad i \in \mathcal{J}_P \quad (59)$$

and collisional excitation between all states,

$$K_{ij}^E(T) = \frac{k_{ij}^E(T)}{k_{ji}^E(T)} = \frac{g_j}{g_i} \exp\left[\frac{-(E_j - E_i)}{k_B T}\right], \quad i, j \in \mathcal{J}_{BP}, \quad j > i. \quad (60)$$

The translational partition functions are defined as

$$Q_{N_2}^t(T) = \left(\frac{2\pi k_B m_{N_2} T}{h^2}\right)^{3/2}, \quad Q_N^t(T) = \left(\frac{2\pi k_B m_N T}{h^2}\right)^{3/2}. \quad (61)$$

The nitrogen atom degeneracy is $g_N = 12$ (nuclear and electronic spin contributions).

The total number of possible combinations for collisional excitation exceeds 44 million processes and the number of nonzero rate coefficients in the database exceeds 19 million. The remaining transitions have very small probabilities, because they are transitions with large activation energy (i.e., $E_j \gg E_i$) or are forbidden by quantum mechanical arguments (inelastic transitions for which ΔJ is odd). Notice that both endothermic (excitation) and exothermic (de-excitation) processes are found in the database. The number of exothermic processes with nonzero rate coefficient, (13.5 million), is larger than the number of endothermic processes (7.1 million). A small number of transitions (about 1.5 million) have rate coefficients for both types of processes in the database. In this case, the exothermic rate coefficients are preferentially used, as the QCT method should give more reliable results in this direction. In general, we have observed that the endothermic rate coefficients agree within 70% of the quantities computed by means of the exothermic rate coefficients using micro-reversibility. These discrepancies are due to differences in the statistical sampling errors of the QCT calculations between direct and reverse processes. We have found the results of the master equation calculations to be insensitive to the rate coefficients selected when data from both processes are available.

B. MASTER EQUATIONS

We wish to investigate the behavior of nitrogen molecules in their electronic ground state undergoing dissociation, when subjected to sudden heating in an ideal chemical reactor. We make the following assumptions.

- The reactor is plunged into a thermal bath maintained at constant temperature T .

- The initial number density of the gas inside of the reactor is set to $n = 2.4 \times 10^{24} [\text{m}^{-3}]$. For this value, the translational energy mode of the atoms and molecules is assumed to follow a Maxwell–Boltzmann distribution at the temperature T of the thermal bath. This is equivalent to an initial pressure of 10,000 [Pa].
- At the beginning of the numerical experiment, the population of the rovibrational energy levels is assumed to follow a Maxwell–Boltzmann distribution at the internal temperature $T_0^I = 300 \text{ K}$.
- The volume of the chemical reactor is kept constant during the experiment and the thermodynamic system is closed (no mass exchange with surrounding environment).
- The electronic excitation and ionization processes are neglected. Dissociation and excitation processes by molecular nitrogen impact are assumed to be negligible with respect to the processes induced by atomic nitrogen impact. This assumption is justified given the initial concentration of atomic nitrogen equal to the nonequilibrium molar fraction value $x_N = 5\%$.

The rotation and vibration of molecules of a gas can be described by means of a kinetic approach. The temporal evolution of the populations of molecules in a particular rovibrational energy level (ν, j) is then obtained by solving a system of master equations. It comprises the following species continuity equations for the nitrogen atom and the rovibrational energy levels of molecular nitrogen

$$\frac{d}{dt} n_N = 2 \sum_{i \in \mathcal{J}_{\text{BP}}} \dot{\omega}_i^D + 2 \sum_{i \in \mathcal{J}_P} \dot{\omega}_i^P \quad (62)$$

$$\frac{d}{dt} n_i = -\dot{\omega}_i^D + \dot{\omega}_i^E, \quad i \in \mathcal{J}_B \quad (63)$$

$$\frac{d}{dt} n_i = -\dot{\omega}_i^D - \dot{\omega}_i^P + \dot{\omega}_i^E, \quad i \in \mathcal{J}_P \quad (64)$$

where quantity n_N is the atomic nitrogen number density, and n_i , the number density of level i . The chemical production rates for the processes of collisional dissociation, $\dot{\omega}_i^D$, predissociation, $\dot{\omega}_i^P$, and collisional excitation, $\dot{\omega}_i^E$, are given by the expressions

$$\dot{\omega}_i^D = n_N k_i^{Df}(T) \left[n_i - \frac{1}{K_i^D(T)} (n_N)^2 \right], \quad i \in \mathcal{J}_{\text{BP}} \quad (65)$$

$$\dot{\omega}_i^P = k_i^{Pf}(T) \left[n_i - \frac{1}{K_i^P(T)} (n_N)^2 \right], \quad i \in \mathcal{J}_P \quad (66)$$

$$\begin{aligned}\dot{\omega}_i^E = & -n_N \sum_{\substack{j \in \mathcal{J}_{BP} \\ j < i}} k_{ji}^E(T) \left[\frac{1}{K_{ij}^E(T)} n_i - n_j \right] \\ & - n_N \sum_{\substack{j \in \mathcal{J}_{BP} \\ j > i}} k_{ij}^E(T) \left[n_i - \frac{1}{K_{ij}^E(T)} n_j \right], \quad i \in \mathcal{J}_{BP}\end{aligned}\quad (67)$$

The master equations allow for the simulation of an isochoric reactor plunged into a thermal bath. The initial n_i populations follow a Maxwell-Boltzmann distribution at the internal temperature $T_0^I = 300$ K. Owing to its stiffness, the system of coupled ordinary differential Eqs. (62–64) is solved using the backward differentiation method [57] implemented in the LSODE package [58]. Notice that the pressure can be calculated at any time by means of the relation $p = nk_B T$, with the mixture number density $n = n_{N_2} + n_N$.

C. RESULTS: ENERGY TRANSFER AND DISSOCIATION KINETICS

In this section, the rovibrational collisional model, describing the detailed kinetics in the isothermal and isochoric reactor, is used to the study of energy transfer and dissociation processes for a wide range of conditions. Three observables are calculated and discussed: internal relaxation times, a global dissociation rate, and the coupling of dissociation and internal energy excitation.

Insights in the dynamics of the relaxation can be obtained by the analysis of the time-evolution of the rotational and vibrational temperatures, shown in Fig. 12a. The behavior of the excitation process is sensitive to the temperature of the heat bath, T . At low temperature (e.g., $T = 5000$ – $10,000$ K), the time response of the rotational energy modes appears to be significantly faster than vibration. This behavior is not surprising and the differences in the time-response of the rotational manifold at low temperature are well documented in literature. The internal temperature sits in between the two other temperatures, thus yielding an inadequate description of the internal excitation of the internal manifold. The relaxation of the gas at higher temperatures (e.g., $T = 30,000$ K) is profoundly different. Vibrational and rotational temperatures relax at the same rate, thus implying the existence of a unique internal temperature. The situation described here is often encountered in the post relaxation region behind a strong shock during high speed atmospheric entry. In this situation, conventional physical models assume a fast equilibration of rotation and translational temperature, whereas the vibrational temperature is assumed to relax at much lower rate. The results here presented clearly demonstrate that this assumption is not valid. At intermediate temperatures (e.g., $T = 15,000$ to $20,000$ K), relaxation of

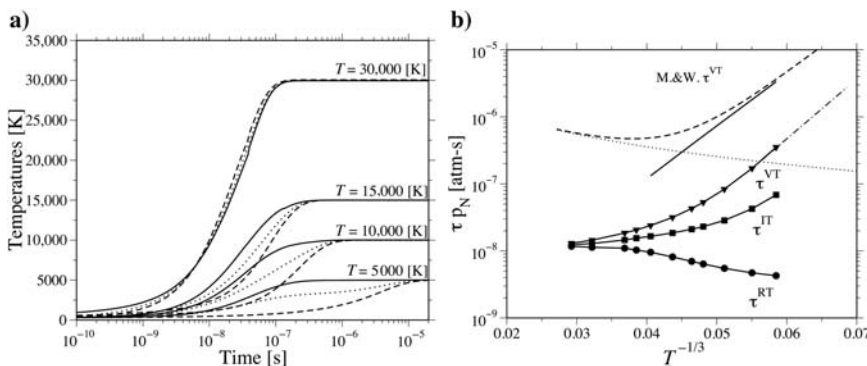


Fig. 12 a) Thermal relaxation studies for constant temperature heat-bath for different kinetic temperatures. Rotational temperatures are represented by unbroken lines, whereas the vibrational temperatures are indicated with broken lines. The internal temperatures are represented by dotted lines. Dissociation processes are not considered. b) Comparison of the ab initio relaxation time τ_{VT} against the Millikan–White correlation formula [59]. The dotted line is the limiting high temperature correction proposed by Park. In the same figure, τ_{RT} and τ_{IT} are shown as a function of the kinetic temperature. Dissociation processes are not considered.

rotation is to some extent faster than vibration, with the internal temperature being a fairly good indicator of the process.

The analysis of the time evolution of the various temperatures suggests the possibility of describing the relaxation processes by using the simple linear relaxation model proposed by Landau and Teller [8, 9]. The characteristic relaxation times extracted from the time evolution of the ensemble are shown in Fig. 12b. To the best of our knowledge, there is no experimental data on the relaxation of N₂-N systems. Most of the experiments available in literature focus on the vibrational relaxation of nitrogen molecules with non-reacting collision partners (e.g., N₂, Ar, O₂ ...) [59]. In the 1960s, Millikan and White [59] generated empirical correlation formulas to describe the behavior of the relaxation times as a function of the heat bath temperature. These formulas are often applied to the description of the relaxation of diatomic molecules for which experimental data are not available. In Fig. (12b), we compare the relaxation times for vibrational, rotational and internal relaxation with the correlation formula introduced by Millikan and White [59]. At high temperatures, the Millikan and White relaxation time has been corrected to account for the limiting of the excitation rates, as suggested by Park [6]. The direct comparison of the vibrational relaxation (τ^{VT}) shows similar temperature dependence $T^{-1/3}$, although the absolute value of the relaxation time seems to be shorter at least by one order of magnitude. At low temperatures ($T < 15,000$ K), the characteristic relaxation

times for rotation are significantly lower than the vibrational and internal relaxation times. The large disparity in relaxation times observed at low temperatures disappears at the higher temperatures as all the relaxation times converge to a common asymptote.

The evolution of the rovibrational energy populations of the nitrogen molecule are depicted in Fig. 13 as a function of the level energy at various times of the relaxation. In the early stages of the numerical simulation, the bulk of the nitrogen molecules occupy the lower rovibrational energy levels. Over 99% of the molecules are found in the ground vibrational state and only the low lying rotational levels ($J < 25$) are significantly populated. With time, the random motion of molecules and atoms brings about collisions, thus enabling the transfer of kinetic energy into rotational and vibrational energy. Initially, the population of the internal levels strongly depart from equilibrium condition and the dynamics of each level is governed by its own kinetics. The low lying levels are at frozen at T_0^I and the population of higher levels steadily increases, displaying a characteristic “banana shape”. By 10^{-8} s, the high-lying levels are nearly at T, even if the distribution is still fairly broad. The experimental results of Robben and Talbot [60] confirmed a similar behavior for the relaxation of pure nitrogen gas behind a strong shock wave. Robben and Talbot “found that it was possible to represent their results approximately by the merging of

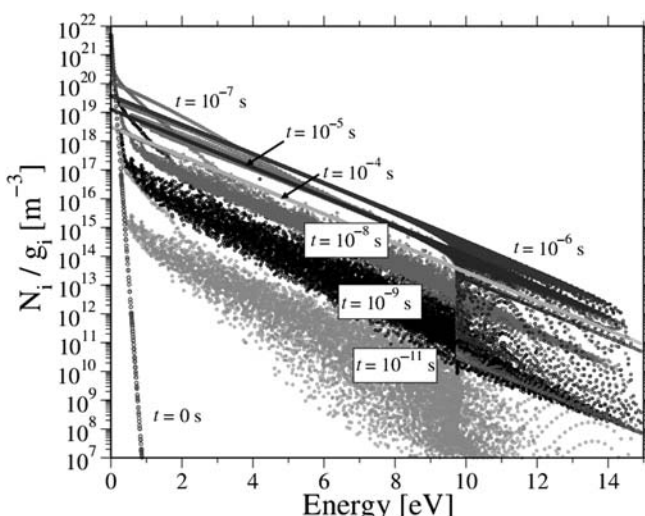


Fig. 13 Normalized population distribution function (N_i/g_i) for different times in the relaxation: $t = 0$ in violet; $t = 10^{-11}$ s in brown; $t = 10^{-9}$ s in black; 10^{-8} s in green; 10^{-7} s in red; 10^{-6} s in blue; 10^{-5} s in maroon; 10^{-4} s in orange. The heat bath temperature is 10,000 K (see color section).

two rotational distribution function corresponding to the temperatures upstream and downstream of the shock wave." As the relaxation proceeds further, e.g., $t = 10^{-7}$, part of the gas reaches a state of partial equilibrium (shown in red symbols), during which the population is dissected into separate strands for each low-lying v , whereas the high-lying levels have already thermalized at the heat bath temperature, T . This is a manifestation of the faster equilibration of rotation at lower temperatures. The entire relaxation process takes up to 1 μs . At this time, the population of the internal levels has relaxed to the final Maxwell-Boltzmann distribution at heat bath temperature, $T = 10,000 \text{ K}$ (shown in blue).

In the early times of the simulation, the dynamics of the populations of the bound states and part of the quasi-bound is not influenced by dissociation. Thus, close to 1 μs , when the dissociation becomes significant (blue symbols), the distribution is already very close to equilibrium. This behavior is characteristic of low temperature relaxation: at these conditions, dissociation and relaxation are two distinct processes and the energy transfer process is almost completed before the onset of dissociation. Departures from the Maxwell-Boltzmann distribution are limited the high lying states close to the dissociation and the quasi-bound states. During the incubation period, part of the quasi-bound levels are already depleted, owing to their short lifetime.

At higher temperatures ($T > 10,000\text{--}15,000 \text{ K}$), dissociation occurs while the internal structure of the gas is not completely relaxed to the heat bath temperature. At 30,000 K significant dissociation occurs only after 0.01 μs , when a bit less than half of the equilibration energy has been transferred to the rotational and vibrational energy modes.

The global dissociation rate coefficient, k^D , defined as

$$\sum_{i \in \mathcal{J}_{BP}} \omega_i^D = k^D(T) n_{N_2} n_N \quad (68)$$

changes with time throughout the relaxation, as shown in Fig. 14a. This is attributable to the fact that the state specific rate coefficients of each rovibrational level differ and the distribution of the molecules in the rovibrational levels change with time. Only when the system reaches the QSS condition is it possible to define a meaningful global rate coefficient, because the relative populations do not change appreciably. Thus, the plateau in the time evolution of k^D is used to define the reaction rate coefficient. This method was firstly proposed by Bourdon and Vervish [61] for the estimation of the ionization rate coefficient of nitrogen atoms. At low temperature the time required to establish a QSS distribution is shorter than the time needed for the onset of dissociation. As the temperature increases, the QSS distribution is established only when a significant fraction of molecules have dissociated. This is clearly shown in Fig. 14b. At 30,000 K, the population reaches the QSS condition and over 50% of the nitrogen molecules are already completely dissociated. In this case the k^D cannot be

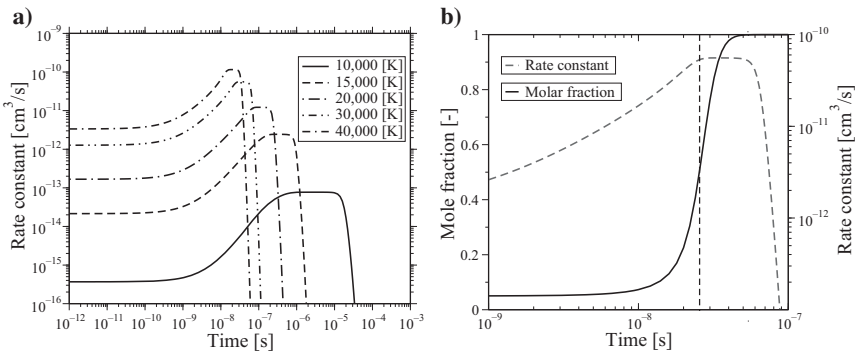


Fig. 14 a) Estimation of the instantaneous global rate coefficient for dissociation as function of the kinetic temperature. **b)** Atomic nitrogen mole fraction (unbroken line) and instantaneous rate coefficient (dashed lines) as a function of time for a heat bath temperature of 30,000 K.

used to describe the global dissociation of nitrogen molecules, thus losing its meaning.

In Fig. 15a, the dissociation rate k^D as a function of temperature is compared against the experimental data by Appleton et al. [51]. The agreement between predicted and experimental data is excellent. In the same figure, we have included the rate coefficients obtained by averaging the state specific rates with a Maxwell–Boltzmann distribution, k^{D*} , referred to as the thermal rate coefficient in the following. As expected the assumption of equilibrium leads to an overestimation of the dissociation rate coefficient, as the thermal rates does not account for the distortion in the tail of the distribution due to dissociation. The influence of predissociation on the rate coefficient appears negligible, whereas the exchange processes significantly affect the global dissociation reaction rate. If exchange processes are neglected, the dissociation rate is underestimated by a factor 2–3.

More insight into the dynamics of dissociation can be revealed from the analysis of the dissociation probability density function (PDF) and the cumulative distribution function (CDF). The PDF is defined as

$$p(E_i) = \frac{k_i^{Df}(T)n_i n_N}{k^D(T)}, \quad (69)$$

and the CDF is defined as the cumulative sum (or integral in the continuous case) of the PDF. Thus, the value of the CDF accounts for the contribution (in percentage) of the energy levels with energy lower and equal to a given energy level, to the total dissociation rate coefficient. The dissociation PDFs and CDFs, in

Fig. 15b, show a small number of low-lying levels with a large PDF value. Given their reduced number, these levels do not contribute significantly to the dissociation rate coefficient (levels <5 eV contributes less than 10% at 30,000 K), thus demonstrating the existence of preferential mechanism in dissociation. According to this mechanism the dissociation of molecular species is favored by the rovibrational excitation. Thus, the molecules in the higher rovibrational levels are assumed to be preferentially dissociated. This phenomenon has been extensively studied in literature without any clear conclusion. The dissociation probabilities for 10,000 and 30,000 K clearly show that the most of the dissociation comes from the high lying vibrational, internal and rotational energy levels. Some differences can be observed when comparing the low and high temperature heat baths. In the lower temperature case, about 80% of dissociation comes from the bound levels in the energy range 8–10 eV. At the higher temperature, the distribution is more uniform and the contribution from the same levels is only about 40–50%. About 30% of the dissociation comes from the lower levels and the rest from the quasi-bound levels. Given the important contribution to the dissociation coming from the upper part of the distribution, the correct prediction of

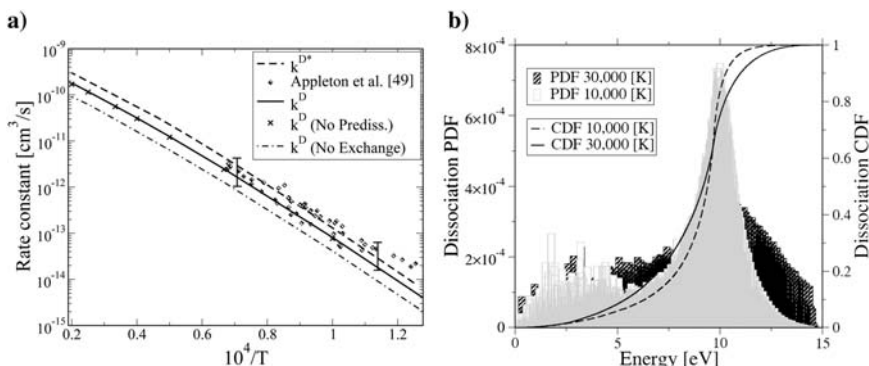


Fig. 15 a) Comparison of the global rate coefficient for dissociation with experimental value from Appleton et al. [51]. In the same figure: the thermal rate k^{D^*} is presented in broken line; Diamonds symbols refer to the experimental data; The remaining curves were obtained by the solution of the master equations: the unbroken line curve includes all the processes. The cross symbols do not include the predissociation processes, while the dash-dotted line includes all the processes with the exception of exchange reactions. b) Dissociation probabilities (PDFs) as a function of the energy level in the midst of the QSS regions. The empty bars refer to the low temperature case (10,000 K) at $t = 8 \times 10^{-6}$. The filled bars refer to the high temperature case (30,000 K) at $t = 3 \times 10^{-8}$. The cumulative distribution functions (CDFs) for the low- and high-temperature cases are represented by the dashed and solid lines, respectively.

the population of the high-lying states become important for the correct modeling of the dissociation process.

The analysis of the results, obtained through the solution of the master equation, demonstrates the differences in the dynamics of low lying, intermediate and high-lying (bound and quasi-bound) levels. The population of the low lying vibrational levels can be approximated by a series of Maxwell–Boltzmann distributions at a rotational temperature $T^R(v)$, where the temperature of each vibrational level monotonically increases with the vibrational quantum number [55]. The population of the intermediate and high lying bound levels quickly thermalize at the common temperature close to the heat-bath kinetic temperature, thanks, in large part, to the contribution of the exchange processes. Substantially different is the behavior of quasi-bound levels that can be further classified in long and short lived, depending on their widths, k_i^{pf} . Long lived levels constitute significant part of quasi-bound levels and due to their small widths, have a nonnegligible influence on the relaxation process. During the entire relaxation, their population distribution strongly departs from a thermal distribution, owing to the large dissociation rate coefficients, k_i^{Df} . The short lived quasi-bound states are strongly depleted due to their large widths and can be safely neglected, as they play a very small role in the relaxation.

The dynamics of relaxation strongly varies with the kinetic temperature of the heat-bath: At low temperature, the rotational relaxation is very fast and the rotational and translational energy modes quickly equilibrates, whereas vibration lags behind. At high temperature, rotational and vibrational temperatures relax at the same rate, thus justifying the existence of a common internal temperature. Thus, the assumption of fast thermalization of the rotational manifold at the heat bath temperature ($T = T^R$) appears questionable in strong nonequilibrium conditions. Across all the temperature range, rotational and vibrational relaxation can be well approximated by a simple Landau–Teller formula, provided that the phenomenological relaxation times are fitted using the solution of the full master equation.

V. COARSE-GRAINED MODEL

The unprecedented level of physical realism achieved by the ab initio computations in the characterization of the interaction of colliding particles allows for the complete description of the nonequilibrium state of the gas by tracking the individual rotational and vibrational states.

In practice, however, the determination of the population of each internal state of every particle in the flow is unfeasible, given the extremely large number of excited states and excitation pathways in the gas. The study of the rovibrational kinetics quickly becomes intractable even in 0-D simulations! The huge amount of information provided by ab initio calculations has great value, but it must be tailored and synthesized to fulfill the needs of practical hypersonic flow problems. Thus, it is imperative that reduced-order models be developed.

A. THEORY

Substantial reduction of the computational effort can be obtained by using a coarse-grained model to represent the kinetics of the internal states of atoms and molecules. The approach consists of three steps:

1. grouping of the internal energy levels
2. reconstruction of the level population of each internal energy mode and derivation of the group averaged quantities, e.g., reaction rate coefficients.
3. solution of the master equation

1. ENERGY GROUPING

The large number of internal levels of atoms and molecules requires the knowledge of a huge number of kinetic parameters, describing the elementary processes occurring in a reacting gas. Often, however, the calculation of these parameters is unfeasible (e.g., N₂-N₂) or extremely time consuming. Furthermore, the description of the dynamics of each individual level of atoms and molecules in the gas is not required, as often times is the description of macroscopic processes (e.g., energy transfer) that matters or at most a coarse description of the internal distribution function. A major reduction in the computational complexity of the problem can be obtained by grouping the internal levels of similar energy into groups (or bins), thus filtering out dynamically irrelevant degrees of freedom. The grouping is obtained by partitioning the internal energy space into multiple regions, similar to the grid cells or elements used in the physical space in CFD. However, the subdivision here is more flexible. It can be based on the values of energy levels, or vibrational and rotational quantum numbers.

2. POPULATION RECONSTRUCTION

The population of the rovibrational energy levels grouped in these energy bins can be easily obtained, once the bin distribution is specified. In this work, it is assumed that the population of the energy levels within each bin follows a Boltzmann distribution at the local translational temperature T :

$$\frac{n_i}{\tilde{n}_k} = \frac{g_i}{\tilde{Q}_k(T)} \exp\left(-\frac{\Delta \tilde{E}_k(i)}{k_B T}\right), \quad i \in I_k, \quad k \in K_{\text{BP}} \quad (70)$$

where the number density \tilde{n}_k and the partition function $\tilde{Q}_k(T)$ of the energy bin k in Eq. (70) are defined as:

$$\tilde{n}_k = \sum_{i \in I_k} n_i \quad (71)$$

$$\tilde{Q}_k(T) = \sum_{i \in I_k} g_i \exp\left(-\frac{\Delta \tilde{E}_k(i)}{k_B T}\right), \quad k \in K_{\text{BP}} \quad (72)$$

The assumption of local equilibrium of the internal levels within each bin is justified by the large reaction rate coefficients for excitation and de-excitation which characterize groups of levels with similar internal energy. This assumption is found to work quite well in the condition of interest to this work as shown in Sec. V.B. Furthermore, increasing the number of energy bins can easily extend the range of validity of this model to stronger non equilibrium conditions.

3. SOLUTION OF THE MASTER EQUATION

The group densities \tilde{n}_k in Eq. (72) constitute the unknowns of the mathematical problem to be solved. The governing equations are obtained by summing the master equations of the full or ungrouped system over the states within each group. Thus, the system of equations can be expressed as follows:

$$\begin{aligned} \sum_{i \in \mathcal{J}_k} \frac{d}{dt} n_i &= \frac{d}{dt} \tilde{n}_k = \overbrace{\sum_h \sum_{i \in \mathcal{J}_k} \sum_{j \in \mathcal{J}_h} (-k_{ij} n_i n_N + k_{ji} n_j n_N)}^{\text{Chemical source term}} + \dots \\ &= \sum_h -\tilde{k}_{kh} \tilde{n}_k n_N + \tilde{k}_{hk} \tilde{n}_h n_N \end{aligned} \quad (73)$$

where the generic k and h groups are indicated with \mathcal{J}_k and \mathcal{J}_h . The state-specific reaction rate coefficients are indicated with k_{ij} , and the group-averaged rate coefficients with \tilde{k}_{kh} . The Eq. (73) constitute a system of nonlinear ODE and can be solved numerically.

B. SHOCK TUBE HEATED FLOWS

In this section, we apply this coarse-grained model to the simulation of thermochemical relaxation behind a strong shock wave. The nonequilibrium flow behind a normal shock wave is computed under the following assumptions: 1) the flow is steady and 1-D; 2) the flow is inviscid; and 3) the shock wave moves at constant speed.

The flow problem is conveniently studied in the shock reference frame. The shock front is treated as a mathematical discontinuity, in that the flow quantities experience a discrete jump, when crossing the shock. The governing equations for the problem under investigation are the steady, 1-D Euler equations. The flow-field behind the shock is obtained by solving numerically the governing equation. The solution initial value is obtained by means of the Rankine-Hugoniot jump relations (with the assumption of frozen dissociation and excitation within the shock). The population of the rovibrational levels immediately behind the shock is assumed to follow a Maxwell-Boltzmann distribution.

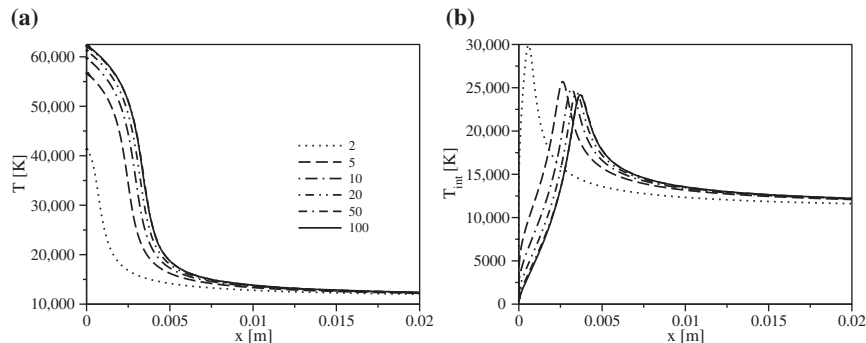


Fig. 16 Bin number convergence study on: a) the translational temperature b) the internal temperature. Spatial evolution behind the shock wave. See (a) for definition of the various lines.

A detailed description of the governing equations for the inviscid shock test-case are given in literature [62, 63].

Figures 16 and 17 show the evolution of the temperatures and the N atom mole fraction behind the shock wave for different number of energy bins. The numerical solution obtained when using two and five bins tends to overestimate the dissociation rate, implying that a larger number of groups should be used. It should be mentioned that this behavior could be partly due to the lower value of the postshock temperature (especially for the two energy bins case). The accuracy improves, as expected, when the number of energy bins is increased. For the calculations shown in Figs. 16 and 17, the differences between the 50 and 100 energy bin solutions are barely noticeable. A further increase of the number of energy bins does not induce appreciable changes in the solution. The dissociation dynamics is already well captured with only 20 energy bins. A

larger number of bins would certainly allow for a more accurate description of the dynamics of the elementary levels at the cost of a more expensive calculation and a more complex physical model. It is worth mentioning

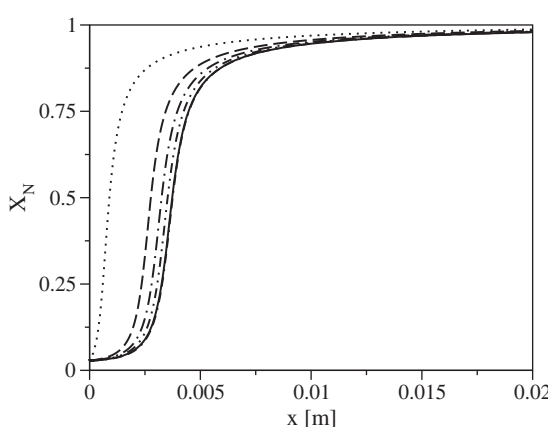


Fig. 17 Bin number convergence study on mole fraction evolution behind the shock wave. See Fig. 16(a) for definition of the lines.

that the cost of the numerical simulation scales with the square of the number of pseudospecies included in the model.

VI. CONCLUDING REMARKS

In this chapter we make a very detailed discussion of nonequilibrium effects that are important for hypersonic earth entry. We start from first principles, solving the quantum mechanical equations of motion for electrons and nuclei. We show how the separation of electronic and nuclear motion is achieved, and give practical procedures for obtaining accurate analytic representations of the PESs. We discuss in detail the issues involved in solving for the nuclear motion and the tradeoffs one must make to move forward.

Now in the universe that consists of two particles, N and N_2 or $N_2 + N_2$, the observable quantity is the cross section for a transition from initial state i to final state f , and this can be straightforwardly computed using the steps described above. In the macroscopic world, however, where there are many, many particles (recall there are 6.0×10^{23} particles in a mole), and the time evolution of a population distribution is governed, in 0-D, by the Master equation. This requires the cross sections for all possible initial and final states. For the N_2 molecule, there are 9390 possible v, j levels. This makes solving the Master equation a very arduous task, and in order to accurately couple nonequilibrium effects to CFD or DSMC calculations, one needs a reliable, vastly simplified model.

We have used our comprehensive database of cross sections for the $N + N_2$ system to carry out a series of benchmark calculations of the nonequilibrium effect in 0-D or 1-D by solving the full Master equation. We have then carefully analyzed the results as a function of propagation time, not only for Macroscopic quantities like the internal temperature, but for individual state populations. This is led us to develop and test new models for accurately reproducing the results of the full Master equation but at a very small fraction of the cost. We find that a fairly small number of bins can well reproduce the results of the full 9390 coupled state problem. This is a very encouraging result, for this is such a simple approximation. We fully expect that more sophisticated models can be developed that will improve the situation even further.

ACKNOWLEDGEMENTS

R. J. and D. S. acknowledge support from the NASA Space Technology Mission Directorate, Entry Systems Modeling Project (formerly Hypersonic Entry Descent and Landing Project). M. P. acknowledges support from a University of Illinois starting grant. We are grateful to Christopher Henze of the Computational Technologies Branch at NASA Ames Research Center for preparing the PES plot shown in Figure 3 and Alessandro Munafò and Winifred Huo for carefully reading the manuscript.

REFERENCES

- [1] Park, C., *Nonequilibrium Hypersonic Aerothermodynamics*, J. Wiley, New York, 1990.
- [2] Park, C., "Radiation Enhancement by Nonequilibrium in Earth's Atmosphere," *J. Spacecraft and Rockets*, Vol. 22, 1985, pp. 27–36.
- [3] Park, C., "A Review of Reaction Rates in High Temperature Air," AIAA Paper AIAA-89-1740, 1989.
- [4] Park, C., "Assessment of a Two-Temperature Kinetic Model for Dissociating and Weakly Ionizing Nitrogen," *J. Thermophys. Heat Trans.*, Vol. 2, 1988, pp. 8–16.
- [5] Park, C., "Assessment of a Two-Temperature Kinetic Model for Ionizing Air," *J. Thermophys. Heat Trans.*, Vol. 3, 1989, pp. 233–244.
- [6] Park, C., Howe, J., Jaffe, R., and Candler, G., "Review of Chemical-Kinetic Problems of Future NASA Missions, II: Mars Entries," *J. Thermophys. Heat Trans.*, Vol. 7, 1993, pp. 385–398.
- [7] Park, C., Jaffe, R., and Partridge, H., "Chemical-Kinetic Parameters of Hyperbolic Earth Entry," *J. Thermophys. Heat Trans.*, Vol. 15, 2001, pp. 76–90.
- [8] Landau, L., and Teller, E., "Theory of sound dispersion," *Phys. Z. Sowjet.*, Vol. 10, 1936, pp. 34–40.
- [9] Landau, L., and Teller, E., *Physik. Z. Sowjetunion*, Vol. 11, 1937, pp. 18.
- [10] Johnston, C., Brandis, A., and Sutton, K., "Shock Layer Radiation Modeling and Uncertainty for Mars Entry," AIAA Paper AIAA-2012-2866, 2012.
- [11] Brandis, A., Johnston, C., Cruden, B., and Prabhu, D., "Investigation of Nonequilibrium Radiation for Mars Entry," AIAA Paper AIAA-2013-1055, 2013.
- [12] Laganà, A., Garcia, E., and Ciccarelli, L., "Deactivation of vibrationally excited Nitrogen Molecules by Collision with Nitrogen Atoms," *J. Phys. Chem.*, Vol. 91, No. 2, 1987, pp. 312–314.
- [13] Billing, G. D., "The Semiclassical Treatment of Molecular Roto/Vibrational Energy Transfer," *Computer Physics Reports*, Vol. 1, 1984, pp. 237–296.
- [14] Laganà, A., and Garcia, E., "Temperature Dependence of N + N₂ Rate Coefficients," *J. Phys. Chem.*, Vol. 98, 1994, pp. 502–507.
- [15] Longo, N. F., Laganà, A., Garcia, E., and Gimenez, X., "Thermal Rate Coefficients for the N + N₂ Reaction: Quasiclassical, Semiclassical and Quantum Calculations," CCSA 2005, LNCS, Vol. 3480, Springer Verlag, Berlin, 2005, pp. 1083–1092.
- [16] Esposito, F., Capitelli, M., and Gorse, C., *Chem. Phys.*, Vol. 257, No. 23, 2000, pp. 193–202.
- [17] Born, M., and Oppenheimer, R., "On the Quantum Theory of Molecules," *Ann. Phys. (Leipzig)*, Vol. 84, 1927, pp. 457.
- [18] Schwenke, D., "Calculations of rate constants for the three-body recombination of H₂ in the presence of H₂," *J. Chem. Phys.*, Vol. 89, 1988, pp. 2076.
- [19] Bunker, D. L., and Blais, N. C., *J. Chem. Phys.*, Vol. 41, 1964, pp. 2377–2386.
- [20] Schwenke, D., "Variational calculations of rovibrational energy levels and transition intensities for tetratomic molecules," *J. Phys. Chem.*, Vol. 100, 1996, pp. 2867–2884.

- [21] Schwenke, D., "Errata for Variational calculations of rovibrational energy levels and transition intensities for tetratomic molecules," *J. Phys. Chem.*, Vol. 100, 1996, pp. 18884.
- [22] Werner, H.-J., and Knowles, P. J., www.molpro.net.
- [23] Kendall, R. A., Dunning, T. H., and Harrison, R. J., *J. Chem. Phys.*, Vol. 96, 1992, pp. 6796.
- [24] Dunning, T. H., *J. Chem. Phys.*, Vol. 90, 1989, pp. 1007–1023.
- [25] Wang, D., Stallcop, J., Huo, W., Dateo, C., Schwenke, D., and Partridge, H., "Quantal study of the exchange reaction for N + N₂ using an *ab initio* potential energy surface," *J. Chem. Phys.*, Vol. 118, 2003, pp. 2186–2189.
- [26] Chaban, G., Jaffe, R., Schwenke, D., and Huo, W., "Dissociation Cross Sections and Rate Coefficients for Nitrogen from Accurate Theoretical Calculations," AIAA Paper AIAA-2008-1209, 2008.
- [27] Jaffe, R., Schwenke, D., and Chaban, G., "Vibrational and Rotational Excitation and Relaxation of Nitrogen from Accurate Theoretical Calculations," AIAA Paper AIAA-2008-1208, 2008.
- [28] Jaffe, R., Schwenke, D., and Chaban, G., "Theoretical Analysis of N₂ Collisional Dissociation and Rotation-Vibration Energy Transfer," AIAA Paper AIAA-2009-1569, 2009.
- [29] Galvao, B. R. L., and Varandas, A. J. C., "Accurate Double Many-Body Expansion Potential Energy Surface for N₃ (⁴A") from Correlation Scaled *ab Initio* Energies with Extrapolation to the Complete Basis Set Limit," *J. Phys. Chem. A*, Vol. 113, 2009, pp. 14424–14430.
- [30] Jaffe, R., Schwenke, D., and Chaban, G., "Vibrational and Rotational Excitation and Dissociation in N₂-N₂ Collisions from Accurate Theoretical Calculations," AIAA Paper AIAA-2010-4517, 2010.
- [31] Paukku, Y., Yang, K., Varga, Z., and Truhlar, D., "Global *ab Initio* ground-state potential energy surface of N₄," *J. Chem. Phys.*, Vol. 130, 2013, pp. 044309–1:8.
- [32] Paukku, Y., Yang, K., Varga, Z., and Truhlar, D., "Global *ab Initio* ground-state potential energy surface of N₄: Erratum," *J. Chem. Phys.*, Vol. 140, 2014, pp. 019903.
- [33] Schwenke, D. W., "The extrapolation of one electron basis sets in electronic structure calculations: how it should work and how it can be made to work," *J. Chem. Phys.*, Vol. 122, 2004, pp. 14107.
- [34] Schwenke, D. W., "A new paradigm for determining one electron basis sets: core-valence basis sets for C, N and O," *Mol. Phys.*, Vol. 108, 2010, pp. 2751.
- [35] Le Roy, R., Huang, Y., and Jary, C., "An accurate analytic potential function for ground-state N₂ from a direct-potential-fit analysis of spectroscopic data," *J. Chem. Phys.*, Vol. 125, No. 16, Oct. 2006, pp. 164310.
- [36] Stallcop, J., Partridge, H., and Levin, E., "Effective Potential Energies and transport coefficients for atom-molecule interactions of nitrogen and oxygen," *Phys. Rev. A*, Vol. 64, 2001, pp. 042722.
- [37] Karplus, M., and Sharma, R. D., "Exchange reactions with activation energy. I. Simple barrier potential for (H, H₂)," *J. Chem. Phys.*, Vol. 43, 1965, pp. 3259–3287.
- [38] Taylor, H. S., *Scattering Theory: The Quantum Theory of Nonrelativistic Collisions*, Rober E. Krieger, Malabar, 1983.

- [39] Schwenke, D., Haug, K., Truhlar, D. J., Sun, Y., Zhang, J., and Kouri, D., "Variational basis-set calculations of accurate quantum mechanical reaction probabilities," *J. Phys. Chem.*, Vol. 91, 1987, pp. 6080.
- [40] Schwenke, D., Haug, K., Zhao, M., Truhlar, D., Sun, Y., J.Z.H. Z., and Kouri, D., "Quantum Mechanical Algebraic Variational Methods for Inelastic and Reactive Molecular Collisions," *J. Phys. Chem.*, Vol. 92, 1988, pp. 3202–3216.
- [41] McCurdy, C., Baertschy, M., and Rescigno, T., "Solving the three-body Coulomb breakup problem using exterior complex scaling," *J. Phys. B: At. Mol. Opt. Phys.*, Vol. 37, 2004, pp. R137.
- [42] Einstein, A., *Ver. Deut. Phys.*, Vol. 19, 1917, pp. 82.
- [43] Brillouin, L., *J. Phys.*, Vol. 7, 1926, pp. 353.
- [44] Keller, J., *Ann. Phys.*, Vol. 4, 1958, pp. 180.
- [45] Goldstein, H., *Classical Mechanics*, Addison-Wesley Publishing Company, Reading, 1980, 2nd edition.
- [46] Eaker, C. W., "A Fast Fourier Transform Method For Quasiclassical Selection Of Initila Coordinates And Momenta For Rotating Diatoms," *J. Chem. Phys.*, Vol. 90, 1989, pp. 105–111.
- [47] Blais, N. C., and Truhlar, D. G., *J. Chem. Phys.*, Vol. 65, 1976, pp. 5335.
- [48] Jaffe, R., "The Calculation of High-Temperature Equilibrium and Nonequilibrium Specific Heat Data for N₂, O₂ and NO," AIAA Paper AIAA-1987-1633, 1987.
- [49] Cary, B., "Shock-Tube Measurements of the Rate of Dissociation of Nitrogen," *Phys. Fluids*, Vol. 8, 1975, pp. 26–35.
- [50] Byron, S., "Shock-Tube Measurements of the Rate of Dissociation of Nitrogen," *J. Chem. Phys.*, Vol. 44, 1966, pp. 1378–1388.
- [51] Appleton, M. S., and Liquornik, D., "Shock-Tube Study of Nitrogen Dissociation Using Vacuum-Ultraviolet Light Absorption," *J. Chem. Phys.*, Vol. 48, 1968, pp. 599–608.
- [52] Hanson, R., "Shock-Tube Study of Nitrogen Dissociation Rates Using Pressure Measurements," *AIAA J.*, Vol. 10, 1972, pp. 211–215.
- [53] Capitelli, M., Colonna, G., and Esposito, F., "On the Coupling of Vibrational Relaxation with the Dissociation Recombination Kinetics: From Dynamics to Aerospace Applications," *J. Phys. Chem. A*, Vol. 108, No. 41, 2004, pp. 8930–8934.
- [54] Esposito, F., Armenise, I., and Capitelli, M., *Chem. Phys.*, Vol. 331, 2006, pp. 1–8.
- [55] Panesi, M., Jaffe, R. L., Schwenke, D., and Magin, E. T., "Rovibrational internal energy transfer and dissociation of N(⁴S_u) + N₂(¹Σ_g⁺) system in hypersonic flows," *Journal of Chemical Physics*, Vol. 138, 2013, pp. 044312.
- [56] Schwenke, D. W., "Dissociation cross-sections and rates for nitrogen." *VKI LS 2008, Non-equilibrium Gas Dynamics*, Rhode-Saint-Genése, Belgium, 2008.
- [57] Gear, C. W., *Numerical Initial-Value Problems in Ordinary Differential Equations*, Prentice Hall PTR, Upper Saddle River, NJ, USA, 1971.
- [58] Hindmarsh, A. C., "LSODE and LSODI, two new initial value ordinary differential equation solvers," *SIGNUM Newslett.*, Vol. 15, No. 4, Dec. 1980, pp. 10–11.
- [59] Millikan, R. C., and White, D. R., "Systematics of Vibrational Relaxation," *J. Chem. Phys.*, Vol. 39, 1963, pp. 3209–3213.
- [60] Robben, F., and Talbot, L., "Measurement of Shock Wave Thickness by the Electron Beam Fluorescence Method," *Phys. Fluids*, Vol. 9, 1966, pp. 633.

- [61] Bourdon, A., and Vervish, P., "Three body recombination rates of atomic nitrogen in low pressure plasma flows," *Phys. Rev. E*, Vol. 54, 1996, pp. 1888–1898.
- [62] Panesi, M., Munafò, A., Jaffe, R. L., and Magin, T. E., "Nonequilibrium shock-heated nitrogen flow using a rovibrational state-to-state method," *Phys. Rev. E*, Vol. 90, 2014, pp. 013009.
- [63] Munafò, A., Panesi, M., and Magin, T. E., "Boltzmann rovibrational collisional coarse-grained model for internal energy excitation and dissociation in hypersonic flows," *Phys. Rev. E*, Vol. 89, No. 2, 2014, pp. 023001.

Radiation from Hypersonic Bodies—A Window on Non-Equilibrium Processes

Deborah A. Levin*

University of Illinois at Urbana-Champaign, Urbana, Illinois

I. INTRODUCTION

The modeling of radiative heat loads resulting from high-temperature plasmas has been an area of significant research over the past 50 years with the NASA operational goal of developing spacecraft TPS that can withstand these severe flow conditions. Similar operational requirements also exist for many DoD and Air Force missions and in addition, radiation modeling is an important component in national surveillance missions. Research has progressed in the development of accurate numerical methods for modeling coupled aerodynamics and chemistry to predict reactions in high-temperature gas dynamics, which in turn, enables high-temperature radiation modeling. An undertaking to review all of the developments in radiation theory and modeling pertinent to hypersonic flows is daunting and some boundaries must be drawn. The main objective of this article is to focus on the aspects of radiation modeling that are special to the hypersonic, thermochemical nonequilibrium environment. As will be discussed, this means that the collision rate is sufficiently low that the gas translational-internal temperatures may not be equilibrated for either atomic or molecular systems, the distribution of excited electronic states can be non-Boltzmann, coupling between the flow and radiation may occur, and the ability to treat wide ranges of opacities is required. As a very large portion of the radiative heat transfer for NASA missions occurs in the vacuum ultra-violet (VUV) spectral region and the ultraviolet to visible spectral regions provide important diagnostics about the fundamental thermochemical gas-dynamic modeling this review considers primarily these spectral regions. Clearly there are missions and diagnostic value in infrared radiation in terms of providing information about molecular vibrational and rotational temperatures, but, the research related to modeling these spectral regions will mostly not be discussed here. Radiation from expanding flows, such as propulsion plumes [1] for chemical and electric propulsion systems

*Professor

is also an important aspect of the space environment. The study of such radiation provides important surveillance information to space-based sensors as well as insight into spacecraft contamination. However, because the radiation modeling of these flows is strongly related to combustion science, a phenomenology sufficiently different from that caused by hypersonic bodies in-flight, it too is considered outside the scope of this review. Finally, this review focusses on single phase, gaseous flows. Only radiation from noncarbonaceous air species is considered, but, in doing so a large important class of radiation-ablator processes are not addressed. It will be seen that the verification of the radiation models for pure air-derived flows is still incomplete, even without this additional challenge, however, a summary of the important challenges of modeling the radiation from ablating flows will be briefly discussed.

The outline of this paper is as follows. In the next section we provide a brief chronology of the development of radiation models. Two general themes characterize the history of development—(1) inclusion of models to account for non-Boltzmann distributions of radiating states and (2) progressions from band to line-by-line to efficient line-by-line models. In Sec. III the basic relationships of VUV/UV/Vis radiation by atomic and molecular species is outlined along with the quasi-steady-state (QSS) theory of determining the radiating state populations. Once the local emission is known it must be transported to other regions in the flow, subject to the spatial distribution of the gas absorbtivity. Two of the many types of radiative transport approaches, the tangent-slab (TS) approximation, and the more general, but, computationally expensive, photon Monte Carlo (PMC) approaches are presented. In addition, corrections for the non-local absorption behavior on the upper electronic state populations for optically thick flows is discussed. Three examples of how these radiation models are used is discussed in Sec. IV. Because hypersonic radiation is dependent on the flow species and temperatures and due to the author's expertise, the three cases are all modeled using the direct simulation Monte Carlo (DSMC) kinetic-particle based approach. This gas dynamic technique readily provides species dependent temperatures as well and although more computationally expensive than CFD/NS approaches provides the highest fidelity of thermochemical nonequilibrium. As will be shown, improvements in cheap computing and the scalability of the approach to large number of computer clusters does allow this gas dynamic technique to be applied to peak heating conditions. To that end the first case discussed is that of the Stardust, extreme Mach number reentry flow in Sec. IV.A. In this flow the radiation is optically thick, highly coupled with the gas dynamics, and non-local. The second example is for a moderate Mach number wherein molecular radiators are now present. The fidelity of modeling the molecular translational to vibrational temperature relaxation is considered and surprisingly the existence of distinct molecular internal temperatures can be observed in simulated UV spectra. In the third example, related to gas-surface interactions in low earth orbit (LEO), spacecraft glow, is considered. A simple gas-surface model is proposed and shown to capture the source of the glow, the weak interaction region

in the RAM direction of the spacecraft, and the features of both measured and simulated UV and IR glow spectra are discussed. Finally in Sec. V we present the many remaining challenges in this field.

II. BRIEF HISTORY OF RADIATION MODELS

In the early work of Zhigulev et al. [2] a systematic examination of the effect of radiation from a high-temperature gas flow past a vehicle was analyzed and it was verified that radiation contributed to the change of the characteristics of hypersonic flows around the vehicle—especially at the temperature and the species concentration of the radiating gas flow. The influence of radiation to convective heating was studied by Goulard [3] using approximate inviscid flowfields with transparent or gray-gas radiation, estimating that the flowfield temperature decreased and the convective heat transfer was also reduced as a result of radiative cooling effects. Viscous flowfields coupled with equilibrium gas radiation were studied to examine the effect of radiation cooling and contribution of the convective and radiative heating to an ablating body [4]. In that work, only the absorption coefficients of continuum radiation were employed for atomic radiation and the smeared band model was used for evaluating the molecular line absorption coefficients.

In the 1970s, non-gray equilibrium radiation models were adopted to the radiative heating problem for the entry into Earth and other planetary atmospheres. Moss [5] performed radiative viscous shock layer calculations with a coupled ablation injection model used in Earth reentry equilibrium flowfields surrounding axisymmetric blunt bodies. A non-gray radiation model including atomic line and continuum transitions was used in that work. The investigation of stagnation region radiative heating for Venus entry was carried out using coupled viscous shock layer equations with a non-gray radiation model by Page and Woodward. [6] and Sutton and Falanga. [7] Sutton applied a coupled inviscid and boundary layer approach with an equilibrium line-by-line radiation model for Venusian entry [8] and outer planet entry [9]. He showed that the radiative heat flux toward the body was attenuated in the boundary layer of the downstream regions of the body as well as at the stagnation point, and the attenuation of radiation by the boundary layer reduced the radiative heating to the body by 10–20% for the Venusian entry conditions.

Perhaps the most of significant development of nonequilibrium radiation in air [10, 11] and thermo-chemical nonequilibrium kinetics models [12–15] was made by Park in the 1980 and 1990s. A formulation was developed to account for many important aspects of nonequilibrium radiation, such as, non-Boltzmann distribution of electronic states of radiating species, multiple flow temperatures, radiation entrapment, line-by-line radiative transport, and the presence of thermochemical nonequilibrium in the flow. Two temperature kinetic model has been widely used to calculate chemical reactions in Navier–Stokes flow solvers

[16, 17]. This model, however, does not directly consider the electron temperature, which was assumed to be identical to the vibrational temperature. As the electron temperature is an important parameter for both equilibrium and non-equilibrium high-Mach number radiation calculations this assumption is problematic.

More recently, atomic and molecular radiation models have been improved by the development of sophisticated spectroscopic databases and the prediction of excited state populations for electronic, rotational and vibrational energy modes [18–22]. Hypersonic nonequilibrium flowfield and radiation modeling have been performed for the analysis of Stardust [23–28] and Fire II [29] vehicles, using established radiation models such as the Langley Optimized Radiative Nonequilibrium (LORAN) code [18] and the Nonequilibrium Air Radiation (NEQAIR) code [19]. In addition, coupled flowfield-radiation interactions have been also performed for the Huygens probe for conditions close to peak heating for reentry into Titan atmosphere, Saturn's largest moon [30]. In that study, the viscous shock layer (VSL) technique for the calculation of the stagnation region of the flow and a modified smeared-rotational band model for the radiation calculation were combined to reduce CPU time rather than solving the full Navier–Stokes equations and a line-by-line radiation model such as LORAN and NEQAIR. The approach provided frequency-integrated heat flux values within 5% of a line-by-line calculation over a range of conditions for Huygens entry.

Recently, closely coupled radiation calculations with advanced hypersonic continuum fluid dynamics (CFD) tools such as DPLR [17] and LAURA [31] and a newly developed efficient line-by-line radiation database based on NEQAIR [32] have been performed for the Stardust and Fire II reentry conditions [33, 34]. A one-dimensional (1-D) TS method to solve the radiative transfer equation (RTE), using the exact analytical solutions based on exponential integrals [35] was used. The coupled CFD-radiation studies assumed the governing electronic temperature to be equal to the heavy particle translational temperature (in the case of DPLR) or the vibrational temperature (LAURA).

The LORAN code [18] and the NEQAIR code [19] have been used extensively in many atmospheric entry radiative simulations. NEQAIR includes atomic bound-bound, bound-free, free-free transition and line-by-line models for molecular bands. The LORAN model is similar to NEQAIR, and was developed to lower the computational cost of NEQAIR by using a smeared rotational band model for the molecular species. Both NEQAIR and LORAN use the QSS assumption to determine the electronic state population. More recently, Johnston developed a radiation model known as HARA (High-temperature Aerothermodynamic RAdiation) that applied up-to-date atomic and molecular data for both the non-Boltzmann modeling of the radiating state and spectral distributions [36, 37]. In his model, an approximate atomic collisional radiative model was developed to calculate the electronic state populations of atomic species. For molecular radiation a simplified non-Boltzmann model for the molecular electronic

state populations was developed by assuming that the contribution of electron-impact dissociation and heavy particle induced excitation processes may be neglected. The smeared rotational band model was chosen to reduce the computational cost for molecular radiation. In nonequilibrium flows, the radiation field may also affect the population of electronic states to the extent that a coupled radiative transport solution is required for an exact solution. Therefore, it is crucial to determine emission and absorption coefficients in an efficient manner such that a large number of solutions of the radiative transfer equation (RTE) may be performed.

The NEQAIR and HARA codes are under continual development and improvement to include more recent QSS models, line information and continuum radiation cross sections. For example, McCorkle et al. [38, 39] have updated NEQAIR96 to include bound–bound transition probabilities of C, N, and O from the NIST ATomic Spectra data base, Stark broadening expressions that include correlations and temperature dependence, cross sections for bound–free transitions from the Opacity Project’s TOP base and additional transitions bands for N₂ and was used to simulate conditions in the NASA/Ames Electric Arc Shock Tube (EAST) Facility [38, 39]. In addition the Structured Package for RADIAtion ANalysis (SPARADIAN) has been developed jointly by the Korea Advanced Institute of Science and Technology (KAIST) and JAXA and has many physical models similar to NEQAIR [40]. Finally, research ongoing between the von Karmen Institute for Fluids Dynamics and Ecole Central Paris has been involved in a number of radiation studies and the development and improvement of the Specair code [41, 42].

III. ELEMENTS OF THE THEORY OF A RADIATION MODEL IN THE ULTRAVIOLET SPECTRAL REGION

A. BASIC RELATIONS OF RADIATION BY ATOMIC SPECIES

There are three radiative mechanisms in a radiating nonscattering medium: spontaneous emission, stimulated emission, and absorption. The spontaneous spectral emission coefficient is defined as [19]

$$\varepsilon_\lambda = g_U N_U A_{UL} h c \phi_\lambda \frac{1}{\lambda} \frac{1}{4\pi} \quad (1)$$

Stimulated emission and absorption, unlike spontaneous emission, are caused by the presence of photons in the vicinity of the emitting or absorbing species. The effective volumetric absorption coefficient is obtained in terms of the stimulated emission and absorption coefficients, as given by [19]

$$\kappa_\lambda = (g_L N_L B_{LU} - g_U N_U B_{UL}) \frac{h}{\lambda} \phi_\lambda \quad (2)$$

Using detailed balance [15, 19] $g_L B_{LU} = g_U B_{UL}$, the absorption coefficient expression can be reduced to

$$\kappa_\lambda = (N_L - N_U) g_U B_{UL} \frac{h}{\lambda} \phi_\lambda \quad (3)$$

Normalized emission and absorption coefficients can be defined by dividing Eqs. (1) and (3) by the number density of the radiating species, n_a , giving,

$$\varepsilon_\lambda^* = \frac{\varepsilon_\lambda}{n_a} = \varepsilon_\lambda^c \left(\frac{N_U}{n_a} \right) \phi_\lambda \quad (4)$$

$$\kappa_\lambda^* = \frac{\kappa_\lambda}{n_a} = \kappa_\lambda^c \left(\frac{N_L}{n_a} - \frac{N_U}{n_a} \right) \phi_\lambda \quad (5)$$

where ε_λ^c and κ_λ^c are defined as

$$\varepsilon_\lambda^c = g_U A_{UL} h \frac{c}{\lambda} \frac{1}{4\pi} \quad (6)$$

$$\kappa_\lambda^c = g_U B_{UL} \frac{h}{\lambda} \quad (7)$$

and

$$B_{UL} = \frac{\lambda^5}{8\pi hc} A_{UL} \quad (8)$$

for all bound–bound transitions at the specific line-center wavelength [15, 19, 35].

There are two other transition mechanisms, which lead to a change of energy level by emission or absorption of a photon. Transitions from a bound to a dissociated state, known as bound–free transitions and the reverse transitions, called free–bound transitions are two such mechanisms. Also transitions between two continuum states, called free–free transitions, are possible mechanisms caused by photon–atom interactions. For atomic radiation, the bound–bound transitions are the largest contributions to the radiation compared to bound–free and free–free transitions. The bound–free radiation occurs when the upper state is in the ionized, or continuum state. In that case, the wavelength of the transition is determined by the kinetic energy of the free electron, E_k , or,

$$\lambda = \frac{1}{\Delta E} = \frac{1}{E_\infty - E_i + E_k} \quad (9)$$

where E_∞ is the ionization potential of the atom and E_i is the energy of the i th bound level. As the electron kinetic energy, E_k , is continuously distributed according to a Maxwellian distribution, radiation from bound–free transitions is spectrally continuous. The bound–free absorption cross section, σ_λ^{bf} , is defined in

terms of the ionization cross section of the hydrogen atom, $\sigma_{\lambda H}$, multiplied by a correction factor known as the Gaunt factor [43]. The hydrogenic cross sections are defined by Kramer's formula [44] as

$$\sigma_{\lambda H} = 7.9 \times 10^{-18} n \left(\frac{\lambda}{\lambda_n} \right)^3 \quad (10)$$

where the value of λ_n is given as $\lambda_n = n^2 10^8 / I_H$, I_H is the ionization potential of atomic hydrogen, $109,679 \text{ cm}^{-1}$ and n is the principal quantum number. The Gaunt factor, GF_λ , is defined as

$$GF_{\lambda,i} = \frac{\sigma_{\lambda,i}^{\text{bf}}}{\sigma_{\lambda H}} \quad (11)$$

The Gaunt factor is determined by comparing the cross sections with those of Peach [43]. Note that for a specific electronic state $\sigma_\lambda^{\text{bf}}$ is only a function of wavelength. Finally, the bound-free absorption coefficient for each energy level is obtained by the bound-free cross section multiplied by the electronic state population as

$$\kappa_\lambda^{\text{bf}} = \sum_{i=1}^l (\sigma_{\lambda,i}^{\text{bf}} N_i) \quad (12)$$

where l stands for the number of electronic states modeled in the NEQAIR database. For atomic O and N, there are $l = 15$ out of the total 19 states and 14 out of 22, respectively. The remaining levels do not contribute to the sum because they are assumed to be quasi-nonbound or existing in the continuum. The bound-free emission is calculated from Eq. (12) using relations given by [19],

$$\varepsilon_\lambda^{\text{bf}} = \sum_{i=1}^l \left(\sigma_{\lambda,i}^{\text{bf}} N_i \frac{2hc^2}{\lambda^5 (N_i/N_U - 1)} \right) \quad (13)$$

where N_U is chosen as the population at the ionization limit given by,

$$N_U = 2.07 \times 10^{-16} \frac{n_+ n_e}{Q_e^e T_e^{1.5}} \exp \left(-\frac{hc E_\infty}{k_B T_e} \right) \quad (14)$$

The value of 2.07×10^{-16} is calculated from the expression of $(h^2 / (2\pi m_e k_B))^3/2 / 2$ given by Reference [19]. A free-free transition occurs when an electron in the vicinity of an ion or an atom is decelerated and emits radiation to conserve energy. The free-free absorption coefficient divided by the atomic number density, employing the hydrogenic free-free cross section, $\sigma_{\lambda H}^{\text{ff}}$, is calculated as [19]

$$\frac{\kappa_\lambda^{\text{ff}}}{n_a} = \frac{n_+ n_e}{n_a} \sigma_{\lambda H}^{\text{ff}} (1 + d_{\text{ff}}) \quad (15)$$

where d_{ff} is a correction factor for the free-free cross section of nonhydrogenic atomic species [43]. Finally, the free-free emission is calculated using the black-body function given by [19],

$$\varepsilon_{\lambda}^{\text{ff}} = \kappa_{\lambda}^{\text{ff}} \frac{2hc^2}{\lambda^5 [\exp(hc/\lambda k_B T_e) - 1]} \quad (16)$$

B. BASIC RELATIONS OF RADIATION BY DIATOMIC SPECIES

Modeling of molecular radiation is more complex than for atomic species because in addition to electronic transitions, rotational and vibrational transitions must also be considered. The large number of rotational lines in a diatomic band system makes the task of determining the Einstein coefficients for each line complicated. The expression for the Einstein A coefficient, A_{UL} , is given by [19]

$$A_{UL} = \left(\frac{64\pi^4 \tilde{\nu}_{UL}^3}{3h} \right) (ea_0)^2 \text{Re}^2 q_{V_U V_L} S_{J_U J_L} / (2J_U + 1) \quad (17)$$

where

$$\tilde{\nu}_{UL} = \frac{1}{\lambda_c} = T_{eU} - T_{eL} + [G(V_U) - G(V_L)] + [F(J_U) - F(J_L)] \quad (18)$$

By using Eqs. (1) and (17), the spontaneous emission coefficient can be written as [45]

$$\varepsilon_{\lambda} = \frac{16\pi^3 \tilde{\nu}_{UL}^4 c}{3(2J_U + 1)} (ea_0)^2 N_U g_U \text{Re}^2 q_{V_U V_L} S_{J_U J_L} \phi_{\lambda} \quad (19)$$

where ϕ_{λ} is again the line shape function and N_U is the upper state population in a given vibrational rotational state.

As an electronic transition in a molecule takes place much more rapidly than a vibrational transition, in a vibronic transition, the nuclei have very nearly the same position and velocity before and after the transition [46]. A transition moment between two vibrational quantum numbers, V_U and V_L of different electronic states can, therefore, be approximated by [46]

$$R_{V_U V_L} = \text{Re} \int \Psi_{V_U} \Psi_{V_L} dr_c \quad (20)$$

where Re is an averaged value of the electronic transition moment. The transition probability is directly proportional to $R_{V_U V_L}^2$ or $|\int \Psi_{V_U} \Psi_{V_L} dr_c|^2$, where the vibrational overlap integral, $q_{V_U V_L} = |\int \Psi_{V_U} \Psi_{V_L} dr_c|^2$, is called the Franck-Condon factor and does not depend on species concentrations or temperatures [46]. The line strength factor, $S_{J_U J_L}$, depends on the type of electronic transition and the spin multiplicity as well as rotational quantum number. Using standard

spectroscopic relationships it can be shown that the upper state population, N_U , is given by:

$$N_U = \frac{N_U^e}{(Q_{VR})_U} (2J_U + 1) \exp \left[-\frac{hc}{k_B} \left(\frac{G(V_U)}{T_{vib}} + \frac{F(J_U)}{T_{rot}} \right) \right] \quad (21)$$

where N_U^e and $(Q_{VR})_U$ are the electronic upper state population and upper state total partition function respectively. Using the above relationships, the population ratio, N_L/N_U , is given by

$$\frac{N_L}{N_U} = \frac{N_L^e}{N_U^e} \frac{(Q_{VR})_U}{(Q_{VR})_L} \left(\frac{2J_L + 1}{2J_U + 1} \right) \exp \left[\frac{hc}{k_B} \left(\frac{G(V_U) - G(V_L)}{T_{vib}} + \frac{F(J_U) - F(J_L)}{T_{rot}} \right) \right] \quad (22)$$

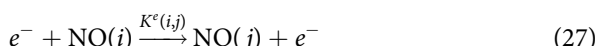
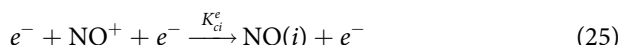
where the upper state total partition function, Q_{VR} , is given as [45]

$$(Q_{VR})_U = \sum_{V_U=0}^{\max} \left[\left(\sum_{J_U=0}^{\max} (2J_U + 1) \exp \left(-B_{V_U} J_U (J_U + 1) \frac{hc}{k_B T_{rot}} \right) \right) \times \exp \left(-G(V_U) \frac{hc}{k_B T_{vib}} \right) \right] \quad (23)$$

C. DETERMINATION OF POPULATIONS IN RADIATING STATES

To calculate the radiation from a gaseous species the populations in the upper electronic state, N_U , must be determined. As there are not enough collisions to assume a Boltzmann distribution of the electronic states a set of excitation and deexcitation mechanisms must be proposed. These processes occur quickly compared to typical gas dynamic time constants and so the QSS solution may be used to determine the upper electronic state populations. The process is illustrated for the case of molecular radiation for the NO molecule for a moderate Mach number flow such as will be discussed in Sec. IV.B. In particular, we are interested in radiation from the NO gamma band that is initiated from the electronically excited NO $A^2\Sigma^+$ state.

The baseline excitation/de-excitation processes for NO are modeled as



where M and e^- represent a third heavy particle and an electron, respectively. The third heavy body species modeled for a moderate Mach number flow are N_2 , O , O_2 , and NO . In terms of rate coefficients, $A(i, j)$ is the Einstein coefficient for spontaneous emission from electronic state i to state j , $K^e(i, j)$ and $K(i, j)$ are the electron-impact and neutral-impact excitation rate coefficients between two electronic states, i, j , of NO , respectively, and K_{Mi} and K_{ci}^e represent the recombination rate coefficients due to heavy particle collision and electron impact, respectively. Note that when $i < j$, $K(i, j)$ represents an excitation rate and if $i > j$ it represents a de-excitation rate, as is also true for $K^e(i, j)$ type terms. Also, the reversal of indices such as, “ Mi ” to “ iM ” changes the rate coefficient from recombination to collisionally induced dissociation. Although only the forward direction is shown for Eqs. (24–27), the reverse mechanisms also occur and the forwards and backwards rates are interrelated assuming microscopic reversibility. Here process (28) is written to occur only in the forwards direction because molecular absorption is too low to significantly affect the population in excited electronic levels. In Sec. III.E we extend Eqs. (24–28) to account for the effect of re-adsorption due to strong atomic emissions on the electronic state population in extreme Mach number cases.

The time rate of change of the nonequilibrium population of NO in the i th electronic state, N_i , is given by the difference between the incoming rates and outgoing rates in the master equation [15],

$$\begin{aligned} \frac{\partial N_i}{\partial t} = & - \left[\sum_{j=1}^{l_m} [K^e(i, j)n_e + K(i, j)n_M + A(i, j)] + K_{ic}^e n_e + K_{iM} n_M \right] N_i \\ & + \sum_{j=1}^{l_m} [K^e(j, i)n_e + K(j, i)n_M + A(j, i)] N_j + [K_{ci}^e n_e^2 n_{NO^+} + K_{Mi} n_N n_{ON} n_M] \end{aligned} \quad (29)$$

in which n_e , n_M , n_N , n_O , and n_{NO^+} are the number density of electrons, heavy particles, atomic nitrogen, atomic oxygen and NO^+ , respectively, and the summations imply $i \neq j$. The number of electronic energy levels, l_m , considered in the QSS model for NO excitation currently is three for the NO ground and the A and B electronically excited states.

Under the QSS condition, the left-hand side (LHS) is set to zero and the system of differential equations becomes a matrix equation of the form,

$$M\bar{N} = \bar{C} \quad (30)$$

where the diagonal element of matrix M is written as

$$M(i, i) = \sum_{j=1}^{l_m} [K^e(i, j)n_e + K(i, j)n_M + A(i, j)] + K_{ic}^e n_e + K_{iM} n_M \quad (31)$$

and the off-diagonal elements of the matrix M are

$$M(i, j) = - \sum_{j=1}^{l_m} [K^e(j, i)n_e + K(j, i)n_M + A(j, i)] \quad (32)$$

and the component of vector, \bar{C} , can be expressed as

$$C(i) = K_{ci}^e n_e^2 n_{NO^+} + K_{Mi} n_n n_{O_2} n_M \quad (33)$$

The electronic state populations, N_p , are finally determined by an $l_m \times l_m$ matrix inversion.

D. RADIATIVE TRANSPORT

1. THE ONE-DIMENSIONAL TANGENT SLAB APPROXIMATION, A METHOD FOR RADIATIVE TRANSPORT

The radiative intensity, I_λ , is defined as the radiative energy flow per unit solid angle and unit area normal to an intensity ray. This intensity can be attenuated and augmented through emitting and absorbing media and can be described in differential form by the 1-D equation of radiative transfer as given as

$$\frac{dI_\lambda(\theta)}{dx} = -\kappa_\lambda I_\lambda(\theta) + \varepsilon_\lambda \quad (34)$$

where ε_λ and κ_λ are the emission and absorption coefficients, respectively. The TS approximation is one of the basic methods to solve the RTE for a 1-D gas media. The spectral radiative heat flux, $q_R(\tau_\lambda)$, which is of interest for heat transfer applications, is written as [35]

$$q_R(\tau_\lambda) = \int_0^{2\pi} \int_0^\pi I_\lambda(\theta) \cos \theta \sin \theta d\theta d\psi \quad (35)$$

where $\tau_\lambda = \int_0^l \kappa_\lambda ds$ is the optical thickness. The final form to obtain $q_R(\tau_\lambda)$ may be written in terms of the second- and third-order exponential integrals as,

$$q_R(\tau_\lambda) = 2\pi [I_{b1} E_3(\tau_\lambda) - I_{b2} E_3(\tau_{\lambda L} - \tau_\lambda)] + 2\pi \left[\int_0^{\tau_\lambda} S_c(\tau'_\lambda) E_2(\tau_\lambda - \tau'_\lambda) d\tau'_\lambda - \int_{\tau_\lambda}^{\tau_{\lambda L}} S_c(\tau'_\lambda) E_2(\tau'_\lambda - \tau_\lambda) d\tau'_\lambda \right] \quad (36)$$

where I_{b1} and I_{b2} are the blackbody intensities at the two wall boundaries. Detailed derivations to solve the radiative heat flux (q_R) and the incident radiative intensity ($G_\lambda = \int_{4\pi} I_\lambda d\Omega$) for the parallel plate media are discussed in

Reference [35]. In equilibrium conditions without scattering the source term, S_c , is defined as the blackbody function. However, for nonequilibrium conditions, local emission and absorption coefficients must be calculated individually for each cell condition, leading to $S_{c\lambda} = \varepsilon_\lambda/\kappa_\lambda$. The radiative energy change in a cell is then calculated by

$$\nabla \cdot q_R(\tau_\lambda) = \frac{\Delta q_R(\tau_\lambda)}{\Delta x} \quad (37)$$

where Δx is the cell thickness.

2. THE PHOTON MONTE CARLO RAY TRACING SCHEME, A SECOND METHOD FOR RADIATIVE TRANSPORT

Although the TS approximation is a useful approximation that can be frequently used in the stagnation region, there are geometric situations where full three-dimensional (3-D) radiative transport must be used. One general method is known as the PMC approach which although time consuming, particularly when the flow and radiation are coupled, provides complete generality. Regardless of whether the PMC method is to be used with a CFD or a DSMC method many of the elements are the same. When the conditions in the cell are determined by quantities such as temperature we refer to the PMC as a finite-volume (FV) approach, as was initially developed to use a CFD body-fitted structured grid system [47]. Alternatively when a particle method such as DSMC is used, it is possible to use a particle based PMC approach, pPMC [48]; however, such an approach was not found to be easy to extend to closely coupled DSMC-radiation simulations. Instead a two-dimensional (2-D) axisymmetric finite-volume based PMC (FV-PMC) code was developed using the same macroparameter grid structure of the DSMC code and the same physical model and principles as in the PMC 3-D model. As the example to be shown in Sec. IV.A was calculated using a DSMC code which uses a Cartesian based grid system we outline the general PMC approach for a structured-square type cell that uses the DSMC macroparameters such as temperature. The concepts readily transfer for other grid types, although, we note that the formulae for calculating the distance that a photon bundle has to travel through the cell as well as the searching procedures for finding the cell face intersected by the photon bundle are simpler in the Cartesian system than in a body-fitted grid system.

The FV-PMC method simulates radiation by tracing photon bundles from an emission point to a termination location. The locations and directions of the emitting photon bundles in each cell are determined using random number relations. The direction of each ray is selected randomly by,

$$\psi = 2\pi R_\psi \quad (38)$$

$$\theta = \cos^{-1}(1 - 2R_\theta) \quad (39)$$

where R_ψ and R_θ are uniformly distributed random numbers from 0 to 1.

The finite-volume-based PMC (FV-PMC) tracing scheme uses the energy partitioning method [47], which traces a photon bundle and calculates the fraction of energy absorbed by each cell that the bundle passes through. To accomplish this, the distance (S_d) which the bundle travels as it passes through the cell and to the particular cell face with which it intersects has to be determined. That distance is used to calculate the quantity of energy absorbed, and the intersection coordinates on the cell face of the photon bundle become the new initial location of the ray tracing in the next cell.

As the photon travels through the computational domain, the energy associated with the photon bundle is decreased due to the absorptivity of the traversed cell. The optical length traveled through the cell can be calculated as,

$$\alpha = 1 - e^{-\kappa_\lambda S_d} \quad (40)$$

where κ_λ denotes the cell absorption coefficient. The amount of energy absorbed by the cell, E_{abs} , and the energy carried by the photon bundle, E_{trans} , can be calculated as,

$$E_{\text{abs}} = \alpha E_{\text{bundle}} \quad (41)$$

$$E_{\text{trans}} = E_{\text{bundle}} - E_{\text{abs}} \quad (42)$$

The absorbed energy (E_{abs}) is calculated by tracing a large number of bundles using the random number relations (Eqs. (38–39)). Therefore, as the number of photon bundles increases the standard deviation in each cell is reduced. For a non-gray medium, a ray is randomly assigned a wavelength using an emission random number database (ERND) for the cell species.

Finally, the divergence of the radiative heat flux ($\nabla \cdot q_R$) term is calculated as the difference between the emission and absorption energy for each cell by,

$$(\nabla \cdot q_R)_{ij} = \left(\frac{E_{\text{emis}} - E_{\text{abs}}}{V_{\text{cell}}} \right)_{ij} \quad (43)$$

where i and j are cell indices and V_{cell} denotes a cell volume. Additional information may be found in Reference [49]

E. THE EFFECT OF NON-LOCAL VUV RADIATION ON A HYPERSONIC NON-EQUILIBRIUM FLOW

As mentioned earlier, in nonequilibrium flow conditions, radiative transitions also have an important role in determining the electronic state of neutral species. The time rate of change of the number density of an electronically excited state, N_i , is given by the difference between the sum of the rates of all collisional and radiative transitions that populate and depopulate state i . The form for the rate equation of a specified transition from upper state i to lower state j that includes loss and gain

of population due to radiation processes can be written as,

$$\begin{aligned} \left(\frac{\partial N_i}{\partial t} \right) &= -K^e(i, j)N_i n_e + K^e(j, i)N_j n_e - \left(\frac{\partial N_i}{\partial t} \right)_{ij}^{\text{rad}} + \left(\frac{\partial N_i}{\partial t} \right)_{ji}^{\text{rad}} \\ &\quad + K(c, i)n_+n_e^2 - K(i, c)N_i n_e + A(c, i)n_+n_e - A(i, c)N_i \end{aligned} \quad (44)$$

where the degree of ionization is so high we neglect neutral collisions. The change of radiative energy per unit time, per unit area, distance and per unit solid angle is [35]

$$h \frac{c}{\lambda} \frac{d}{d\Omega} \left(\frac{\partial N_i}{\partial t} \right)_{ij}^{\text{rad}} = (N_j B(j, i) - N_i B(i, j)) \frac{h}{\lambda} I_\lambda \quad (45)$$

As the radiative transition occurs across a wavelength interval, Eq. (45) becomes

$$\frac{d}{d\Omega} \left(\frac{\partial N_i}{\partial t} \right)_{ji}^{\text{rad}} = \int_{\lambda_1}^{\lambda_2} \frac{(N_j B(j, i) - N_i B(i, j))(h/\lambda) \phi_\lambda I_\lambda}{hc/\lambda} d\lambda \quad (46)$$

$$= \int_{\lambda_1}^{\lambda_2} \frac{\kappa_\lambda I_\lambda}{hc/\lambda} d\lambda \quad (47)$$

where κ_λ is the absorption coefficient and I_λ and ϕ_λ are the incident radiative intensity and the line broadening function, respectively. By integrating Eq. (47) over all directions, the fourth term in Eq. (44) is expressed as

$$\begin{aligned} \left(\frac{\partial N_i}{\partial t} \right)_{ji}^{\text{rad}} &= \int_{\lambda_1}^{\lambda_2} \frac{\kappa_\lambda \int_{4\pi} I_\lambda d\Omega}{hc/\lambda} d\lambda \\ &= \int_{\lambda_1}^{\lambda_2} \frac{\kappa_\lambda G_\lambda}{hc/\lambda} d\lambda \end{aligned} \quad (48)$$

where $G_\lambda = \int_{4\pi} I_\lambda d\Omega$ is the integrated incident radiative intensity from over all directions. The final form of the rate equation can be written as,

$$\begin{aligned} \left(\frac{\partial N_i}{\partial t} \right) &= -K^e(i, j)N_i n_e + K^e(j, i)N_j n_e - A(i, j)N_i + \int_{\lambda_1}^{\lambda_2} \frac{\kappa_\lambda G_\lambda}{hc/\lambda} d\lambda \\ &\quad + K(c, i)n_+n_e^2 - K(i, c)N_i n_e + A(c, i)n_+n_e - A(i, c)N_i \end{aligned} \quad (49)$$

where the third term on the right-hand side (RHS) comes from the standard definition of the Einstein transition coefficient for spontaneous emission. The fourth term in Eq. (49) represents the number of transitions from a lower to an upper

electronic state owing to the absorption of incoming radiative intensity where G_λ is defined as the spectral incoming intensity transferred from every other points in the flowfield. It is this term which makes the radiation non-local in character and potentially difficult to calculate. In Eq. (48), the fraction of the incoming intensity that contributes to the absorption from a lower to a higher electronic state may be obtained by multiplying the incoming intensity by an absorption coefficient κ_λ . The escape factor, ρ_{ij} , the ratio of the number of transitions from a lower to an upper electronic state to the number of transitions leaving the upper electronic state due to spontaneous emission is determined by subtracting this ratio from unity, i.e.,

$$\rho_{ij} = 1 - \frac{\int_{\lambda_1}^{\lambda_2} \frac{\kappa_\lambda G_\lambda}{hc/\lambda} d\lambda}{A(i, j)N_i} \quad (50)$$

This form is consistent with earlier formulations in the literature [30, 50]. When Eq. (50) is substituted into Eq. (44), we obtain,

$$\begin{aligned} \left(\frac{\partial N_i}{\partial t} \right) &= -K^e(i, j)N_i n_e + K^e(j, i)N_j n_e - \rho_{ij}A(i, j)N_i \\ &\quad + K(c, i)n_+n_e^2 - K(i, c)N_i n_e + A(c, i)n_+n_e - A(i, c)N_i \end{aligned} \quad (51)$$

Finally, in the QSS assumption the LHS of Eq. (51) is set to be zero because electronic transitions in the VUV occur at a much faster time scale than the gas dynamic residence time in hypersonic shocks. As the escape factor goes to unity, which means that the flow is optically thin, the emitted photons from a specific upper electronic state all escape from the vicinity and, as can be seen from Eq. (51), the population of the upper electronic state decreases. However, when the escape factor approaches zero, indicating that the flow is optically thick, the emitted photons are re-absorbed during the transition from a lower to an upper electronic state and the corresponding upper electronic state density is re-populated. In high density flows, the collision rate is much greater than the radiative transition rate and the distribution of electronic state populations becomes close to the Boltzmann distribution regardless of the value of the escape factor. Thus, the escape factor is insignificant in such collision-dominated flows. In the rarefied, nonequilibrium gas regime, however, the contribution of collisional transitions to excitation/de-excitation processes is low. Thus, the radiative transition rates associated with the escape factor are important in determining the population densities of electronic states for highly nonequilibrium conditions.

The escape factor for a specific transition given in Eq. (50) is not known a priori and must be calculated by solving the RTE to obtain the non-local incoming intensity over all directions G_λ . Either the TS approximation [33, 35] or the PMC method [47, 49] can be used to calculate the incoming intensity and then be

iteratively coupled with the collisional-radiative population modeling to obtain the converged distribution of electronic state populations [30, 50]. To calculate the initial distribution of electronic state populations and the corresponding spectral emission and absorption coefficients, the initial value of the escape factor is assumed to be one (optically thin). In the next iteration, the new escape factor is calculated by solving the RTE with the PMC method (or TS) and is then substituted into the QSS model again to obtain the new electronic state populations. The escape factor corresponding to the new distribution of electronic state population is then re-calculated. This procedure was found to work well and converged electronic state populations were obtained typically after 3–4 iterations.

To avoid the complexity of the non-local escape factor, an approximate local escape factor approach has been suggested [19]. This approximate method assumes that the photon escaping phenomena occurs in a small spherical homogeneous radiating gas medium that is governed by the local source function [51, 52]. In other words, the absorption of the radiative energy carried by photons due to the incident radiative intensity from other gas cells can be neglected. The approximate form of escape factor introduced in Reference [51] is identical to the form used in NEQAIR [19] expressed as,

$$\rho_{ij} = \frac{\int_{\lambda_1}^{\lambda_2} \varepsilon_\lambda \exp(-\kappa_\lambda D) d\lambda}{\int_{\lambda_1}^{\lambda_2} \varepsilon_\lambda d\lambda} \quad (52)$$

where D is the distance that a photon travels through a homogeneous gas before being re-absorbed. Note that there is no established criteria for selecting this value, but, in NEQAIR, a value of $D = 1.0$ cm is recommended for calculating the local escape factor given by Eq. (52). This approximation will be compared with the exact non-local value in the Sec. IV.A.

IV. APPLICATION OF RADIATION MODELING TO THREE CASES OF HYPERSONIC FLOWS

In this section three applications of radiation modeling are selected to illustrate the important coupled physics of thermochemical nonequilibrium flows with radiation modeling. The first considers an extreme Mach number NASA-type reentry into Earth's atmosphere where the radiative heat load can approach 25% and the nature of the modeling of optical thickness for these extreme cases is important [53]. A coupled particle-state-of-the-art radiative transfer approach will be used to model transitional to fully continuum flow conditions. Of the three cases to be considered here, this one is most complex from the radiation point of view. In the second example, slower speeds closer to DoD missions spectroscopic data obtained and modeled are discussed. Here the radiative heat loads are

sufficiently low that the radiation modeling can be de-coupled from the flow models, although the fidelity of the former is naturally strongly dependent on the latter. Finally, the third example considers a very high altitude application where moderate Mach number “flows” (low earth orbital velocities) still cause chemical reactions to occur in the RAM direction of a spacecraft (regardless of its material). For this case, gas–surface reactions dictate fractional surface coverage of bow–“shock” generated species, and radiation in the visible spectral region (orange) is observed from emission from gas–surface metastable species.

A. STARDUST, A NASA EARTH REENTRY MISSION

We first consider the effect of radiation on the flowfield and then the importance of radiative coupling on the heat fluxes at conditions corresponding to peak heating. Figure 1 shows a comparison of distributions of the translational, rotational, vibrational, and electron temperatures along the stagnation streamline between cases without and with (final iteration) radiation cooling at 61.8 km altitude. Iterations of the DSMC-PMC calculations were performed until both the flow macro-parameters and radiation are converged within a 5% criterion, which at this altitude occurred after three iterations. Along the stagnation streamline, the radiation peak is located near $X = -0.015$ m, and the effect of radiative cooling on the flow along the stagnation streamline can be seen between $X = -0.015$ m and the surface in the figure. Translational and internal temperatures decreased by a maximum of approximately 2000 and 1500 K, respectively, owing to the high radiative energy in this region after one iteration of DSMC-PMC coupling. At this altitude, after the first iteration, the temperature profiles did not change significantly when additional coupling calculations were performed [49].

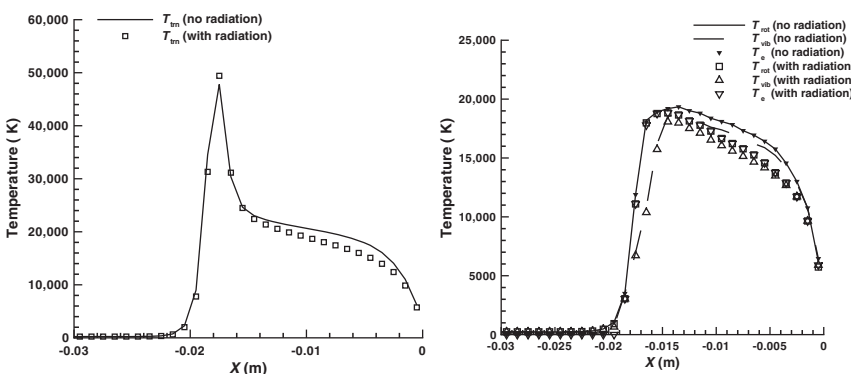


Fig. 1 Comparison of distributions of the translational (top) and rotational, vibrational, and electron temperatures (bottom) along the stagnation streamline between cases with and without radiation at 61.8 km altitude.

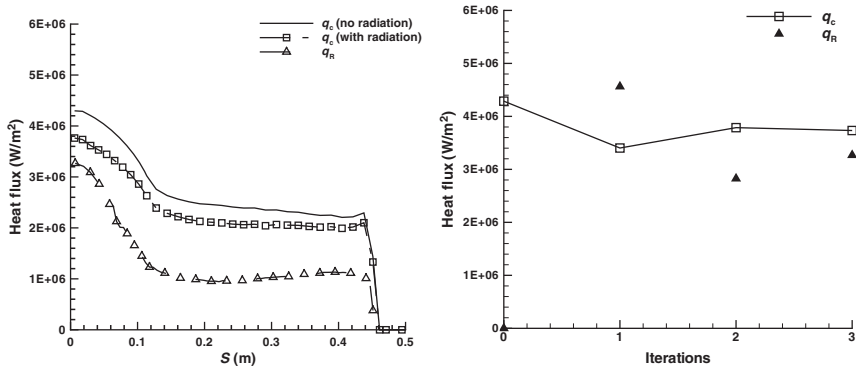


Fig. 2 Comparison of heat fluxes along the forebody surface for cases with and without radiation (LHS) and heat flux at the stagnation point as a function of DSMC-PMC coupling iterations (RHS) for the Stardust body at 61.8 km altitude.

The convective and radiative heat fluxes to the vehicle surface were also calculated and compared in Fig. 2 for cases with and without radiation coupling. The radiative heat flux spatial dependence is consistent with the electron number density and temperature contours at this altitude where both have maximum values in the stagnation region only. It is also observed that the convective heat flux along the surface is reduced by the effect of radiation cooling. Figure 2 (RHS) presents the convective and radiative heat flux to the stagnation point with respect to the coupling iterations. The figure shows that both the convective and radiative heat fluxes are nearly converged after the first iteration. It can be seen that that surface convective heat flux after the first coupling iteration decreases by 21% due to radiation. However, with additional iterations, the convective heat flux obtained from the third iteration is not significantly different from the second iteration result, and finally, the convective heat flux after three iterations is reduced by 13%. The behavior in the change of the convective heat flux as a function of iteration at the stagnation point is also consistent with the small change in the translational temperature profiles shown in the LHS portion of Fig. 1. The contribution of the radiative heat flux to the total heat flux is approximately 46% at this altitude. As a noncatalytic surface condition was used in these calculations, there is no additional heat at the surface due to atomic recombination so that the convective heating rate to the surface is not much higher than the radiative heating [49].

Next a comparison of the stagnation-point convective and radiative heat fluxes for the Stardust vehicle along the reentry trajectory was obtained from the coupled DSMC/FV-PMC method discussed in Sec. III.B. Figure 3 (LHS) shows a comparison of convective heat flux to the stagnation point with and without radiation coupling as a function of the product of the square root of the freestream mass density and the freestream velocity raised to the cubic

power. The selection of the abscissa is based on the correlation of convective heat flux with freestream conditions suggested by Sutton [54] and is discussed further in Anderson [55]. Also shown is a comparison of our DSMC results with the previous CFD calculations performed by Olynick et al. [23]. First it can be seen that both CFD and DSMC predict a linear dependence of convective heat flux with the freestream correlation. It can also be seen that the DSMC-PMC coupled convective fluxes have a very similar dependence with altitude to the DSMC without radiation values. The difference in magnitudes between these two cases is small, but some decrease in the convective heat flux occurs when radiative cooling is taken into account. The difference in the DSMC convective heat flux results with those of Olynick et al. [23] is a factor of two to three owing to the use of a fully catalytic surface boundary condition in the CFD simulations. Additional DSMC simulations performed with a catalytic surface boundary condition confirmed this conclusion. Comparison of the four sets of results shows that the effect of radiation coupling on the convective heat flux is much smaller than the gas–surface interaction model. Given the very different numerical approaches, the CFD and DSMC convective heat flux dependence with freestream conditions are in good agreement and comparing the open and closed triangles of the LHS part of Fig. 3, it can be seen that the difference is within 20%.

The radiative heat flux to the stagnation point at the same four altitudes is shown in Fig. 3 (RHS). In this figure, two PMC radiation results, which use Doppler and Voigt line shapes, are compared to Olynick's results and the radiative heat flux correlation suggested by Tauber and Sutton [56]. The correlation of Tauber and Sutton [56] for stagnation-point radiative heating relations for Earth and Mars entries is based on an equilibrium radiation model coupled with an inviscid flowfield code that assumed thermo-chemical equilibrium conditions. Their relationship [56] used tabulated radiative heating velocity functions

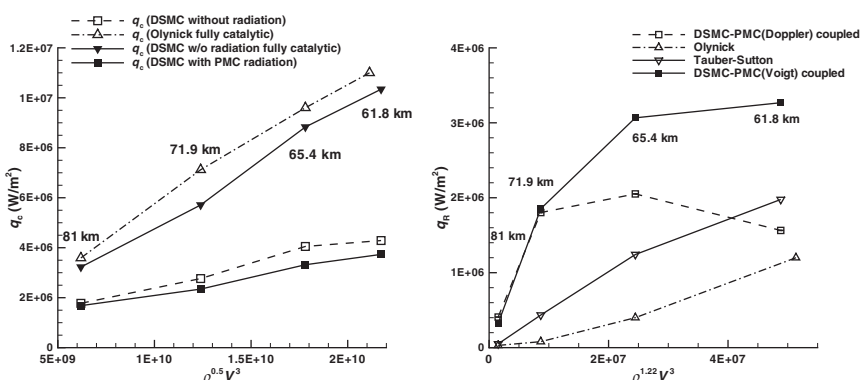


Fig. 3 Comparison of the stagnation-point convective heat flux (LHS) and radiative heat flux (RHS) vs free stream correlation during the Stardust reentry trajectory.

and a linear interpolation to calculate the stagnation-point radiative heating rate. We obtained a correlation of $\rho_{\infty}^{1.22} V_{\infty}^3$ as our independent variable on the X-axis of Fig. 3 by trial and error. The power of the freestream number density is given by the Tauber and Sutton correlation, but, the freestream velocity power dependence was selected such that the radiative heat flux should vary linearly with it.

Two important conclusions can be drawn from Fig. 3 (RHS) for the radiative heating, i.e., the DSMC, CFD, and Tauber–Sutton correlation have different magnitudes and altitude dependence. The agreement, however, between the CFD and the correlation is not better than the DSMC-CFD agreement because the flow and radiation model used in the correlation are different from Olynick's CFD calculation. In Tauber and Sutton's work, thermo-chemical equilibrium and nonablative are assumed throughout. The differences in flow modeling between the two continuum approaches also have a large influence on the radiative heating and has been shown by Hash et al. [31], even when different continuum flow models predict similar convective heating, the radiative heating rates can be significantly different.

With respect to the DSMC-PMC coupled simulations we see that using the Doppler line shape predicts a different freestream dependence compared to that obtained using the Voigt line shape. In addition, the stagnation-point radiative heating calculated from the DSMC-PMC with the Doppler line shape is not linearly related to the freestream correlation. As Doppler line broadening is only dependent on the translational temperature, the wings of narrow atomic lines are not sufficiently broadened compared to the Voigt line shape so that the net radiatively transferred energy is almost re-absorbed near the line-center wavelength. However, for the high electron concentration flows discussed here, electron collisions are an important mechanism for line broadening. By using the Voigt line shape, the combination of Gaussian and Lorentzian line broadening components, the wings of a line extend further from the line-center allowing the transport of strong spectral radiative flux in the line wings. When the Voigt line shape is used in DSMC-PMC coupling calculations, the peak radiative heating occurs near 61.8 km altitude and the stagnation-point radiative heating rate is proportional to the freestream correlation, similar to the CFD results.

In addition, the question remains why the DSMC-PMC simulations that use the Voigt line-shape predict a radiative heat flux about a factor of two higher than the CFD results of Olynick. In Olynick's calculations the NOVAR radiation model, which was developed from the LORAN code was used. This model calculates atomic line and continuum and molecular radiation using a 1-D TS approximation. However, differences in the radiation approaches used in the DSMC and CFD results presented here are not assessed to be the main reason for the discrepancies in the radiative heat flux. Our previous comparisons with CFD simulations for Stardust as well as the DSMC simulations of others find that the electron temperature in DSMC is predicted to be nearly twice as high as the internal temperatures in continuum flow models [57, 58]. As the population of the upper electronic levels for strong atomic emitters is strongly dependent on

the electron temperature, this discrepancy between the CFD and DSMC simulations has a significant impact on the radiative heat flux. This discrepancy could probably be reduced by using similar thermo-chemical models in the two different gas dynamic approaches [31] and should be strongly considered for reentry flows into highly nonequilibrium atmospheric conditions.

The above discussion illustrates that radiative transport can now be applied to calculating operational factors as important as radiative heat transfer using high fidelity simulations tools such as line-by-line transport, QSS electronic state population models, and photon Monte Carlo radiative transport. However a number of key fundamental questions still remain. For example, in all of the aforementioned results we use the commonly accepted, perhaps universally accepted, concept that the distribution of electronic states can be characterized by a single *electronic* temperature. Whether this is true or not was examined in Li and Levin [59] where the actual, DSMC-derived distribution function to calculate excitation and ionization rates was used. The well known relationship between the excitation (or ionization) cross section and the corresponding rate, K , is given by,

$$K = \int \sigma w f dw \quad (53)$$

where f is the electron velocity distribution function, σ is the excitation (or ionization) cross section, and w is the electron velocity. Without any additional specific information about the electron velocity distribution function, we usually assume that it is Maxwellian, as is done NEQAIR [19], and all radiation models. Using the DSMC derived electron distribution functions at different points in the flow, electron collisional excitation rates of atomic nitrogen, $K(1, 2)$ and $K(1, 3)$, were calculated using Eq. (53). The electron excitation cross sections for atomic nitrogen were taken from the work of Huo [60], originally from Stone and Zipf [61]. Figure 4a shows the comparison of electron impact excitation rates from the calculation using the actual distribution functions with those obtained assuming a Maxwellian distribution (designated as NEQAIR in the figure). The rates calculated using the DSMC-derived distribution functions are within an order of magnitude from those that are obtained assuming a Maxwellian distribution. In addition, the rates from the DSMC-derived distribution functions are generally smaller, and this explains why the DSMC excited populations are smaller at those locations. The new rates obtained using the DSMC-derived distribution functions were then used to obtain the QSS solution and compared with the original baseline (indicated as NEQAIR). Figure 4b shows the comparison of the two electronically excited state populations obtained using the DSMC-derived vs the Maxwellian distribution functions in the QSS equations as well as the excited state populations obtained directly from DSMC [62]. It can be seen that regardless of the method used, the population of the second state is higher than that of the third, as expected. Generally, the populations obtained using the DSMC-derived distribution function and those from DSMC directly

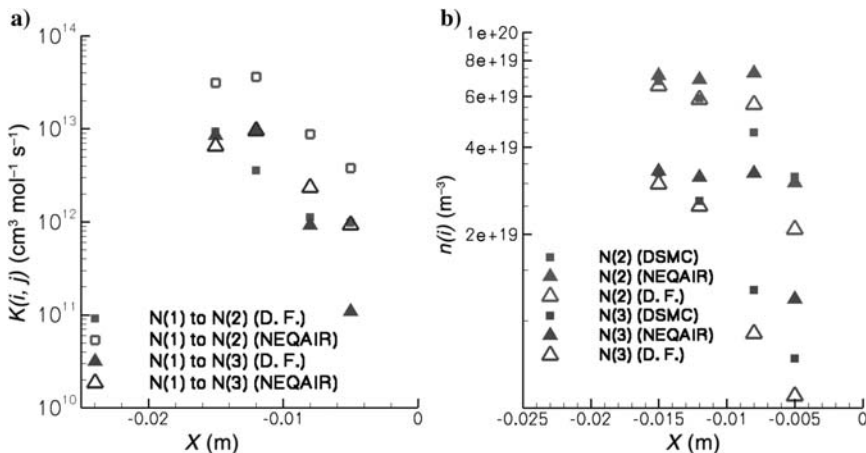


Fig. 4 Li et al. Comparison of QSS using Maxwellian vs. DSMC derived distribution functions: a) shows the excitation rates and b) shows the excitation state populations. The symbols designated “DSMC” are the full, electronic state-specific DSMC simulations performed in Reference [62].

agree better than the QSS values computed assuming that the distribution function is Maxwellian (NEQAIR). Finally, the latter approach always is higher than the two exact approaches.

The cost of the 2-D finite-volume–photon Monte Carlo method (FV-PMC) compared to the 1-D tangent-slab radiative transport is not insignificant, particularly when one needs to reduce the statistical uncertainty leading to large number of simulated photon rays. The spatial distribution of the 2-D radiative heat flux contours about the Stardust SRC body is shown in the top portion of Fig. 5 using a 2-D axisymmetric FV-PMC simulation and assuming an escape factor of unity [63]. Both the bound–bound electronic transitions from atomic N and O and the corresponding electron impact continuum transitions were considered in the PMC modeling. Five hundred million photon rays were traced to obtain the averaged divergence of radiative heat flux ($\nabla \cdot q_R$) with a total volumetric standard deviation of less than 5% using 16 processors. It can be clearly seen that the TS result is predicted to be close to the PMC in the forebody region, as expected, because the gradient of flow properties along the normal direction to the surface is much greater than along the tangential direction to the surface. For the downstream region beyond the shoulder, the species concentrations and temperature significantly decrease so that the gradients from one line-of-sight to the next are too large for the TS method to be used to solve 2-D radiative transport. The bottom portion of the figure shows that there is a greater than a 50% difference of $\nabla \cdot q_R$ in the afterbody flow region (green region beyond

$x \sim 0.2$ m). In this region, the radiative transport must be considered as 3-D and the PMC method is thus required to calculate the radiative heat source and absorbed radiative energy regardless of the escape factor value.

Finally, in all of the results that were discussed in this section we have assumed an escape factor of unity. As discussed in Sec. III.E, the escape factor plays an important role in rarefied, nonequilibrium gases and potentially can significantly deviate from one. Figure 6 shows the distributions of the escape factor for the strongest transitions for atomic N and O around the Stardust SRC body. It is seen that the escape factor for the atomic N transition from the 4th to the ground state (LHS) is less than 0.2 for the entire domain. This low value of the escape factor for the strongest atomic transition in VUV spectrum causes the re-population of the 4th electronic state population and the corresponding radiative energy from the 4th energy level for the entire flowfield around the vehicle body. The escape factor for the strongest atomic O transition from the 5th to the ground state is found to be less than 0.2 for the region of the forebody shock layer and the expanding flow as shown in the RHS portion of Fig. 6. Similar to the atomic N transition, the density of the 5th electronic energy level and the

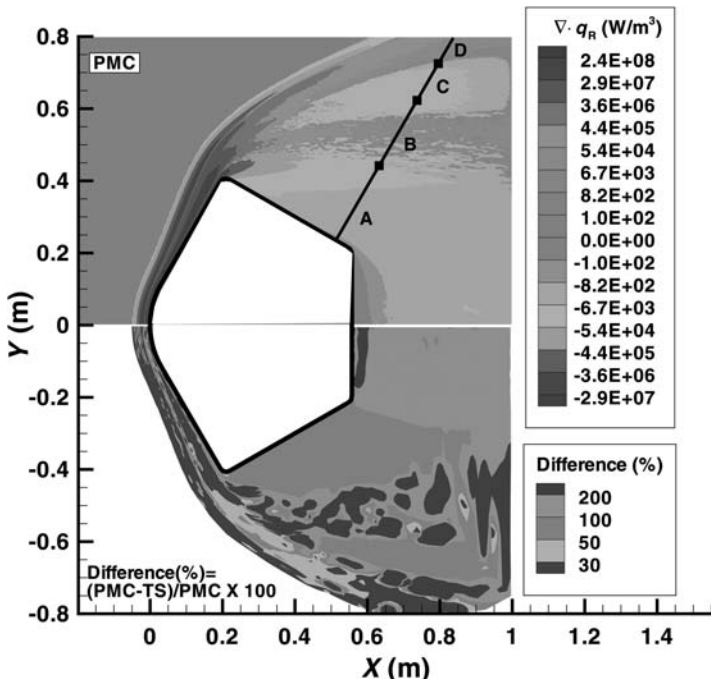


Fig. 5 Divergence of radiative heat flux ($\nabla \cdot q_R$) calculated by PMC (Top) and difference of $\nabla \cdot q_R$ between PMC and TS method (bottom) at an altitude of 81 km (see color section).

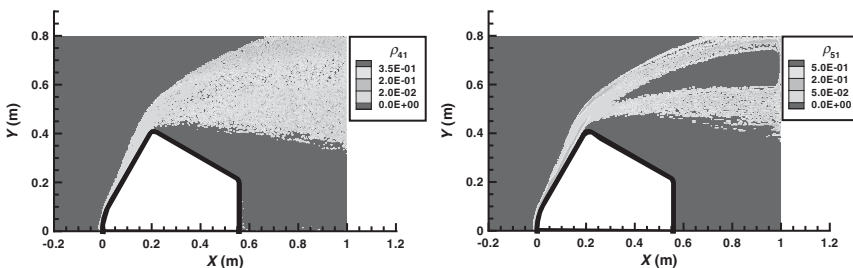


Fig. 6 Distribution of escape factor of atomic N 4th to ground state transition ($^4P_{5/2,3/2,1/2} \rightarrow ^4S_{3/2}$) (LHS) and O 5th to ground state transition ($^3S_1 \rightarrow ^3P_{2,1,0}$) (RHS) around the Stardust SRC body at 81 km (see color section).

corresponding emissive energy of atomic O increases due to the fact that the escape factor is small.

B. ENDO-ATMOSPHERIC RADIATION FROM HYPERSONIC VEHICLES

For Air Force/DoD missions, radiation is small compared to convective heat loads (even at 7–8 km/s) and so it serves as a diagnostic about flow. The Bow Shock Ultraviolet flight experiments I and II were sounding rocket experiments that illustrated this role by collecting spectral radiation data in the 1990s. The first flight experiment was launched on April 25, 1990 from Wallops Island, VA, flying a Terrier Malemute stack up [64]. The payload reached a velocity of approximately 3.5 km/s at an altitude of 37 km. Data were obtained between approximately 39 km (when the nose cone deployed) to approximately 70 km altitude. The second Bow Shock flight [65] was launched from Barking Sands, Kawaii, Hawaii. This flight was more complex, obtaining bow shock data at a speed of approximately 5.1 km/s upon reentry and other measurements on a solid rocket motor plume were obtained during the second and third Antares II and Star-27 stages [66]. Reentry spectra were obtained from approximately 110 km down to burn up of about 66-km altitude. Figures 7 and 8 show examples of radiometer and spectra that were obtained during these flights. The radiometric data shown in Fig. 7 is at a center wavelength of 230 ± 2.5 nm and covers the main portion of the NO γ and β band system. Note the five orders of magnitude difference between pre-flight estimates and the state-of-the-art (at that time) predictions. The radiometer gave good altitude resolution and overlaps with a portion of the onboard spectral data to check consistency. Figure 8 shows examples of spectra that were obtained during the two flights. The rapid scanning spectrometers [65] covered the 190–400-nm wavelength range in a 1.0 and 0.25-s per scan for BSUV2 and 1, respectively. The spectrometer instrument is known as a modified Fastie–Ebert design of 150-mm focal length and had a 10-deg (total angle) field of view (FOV) centered on the vehicle centerline. The spectral range between the

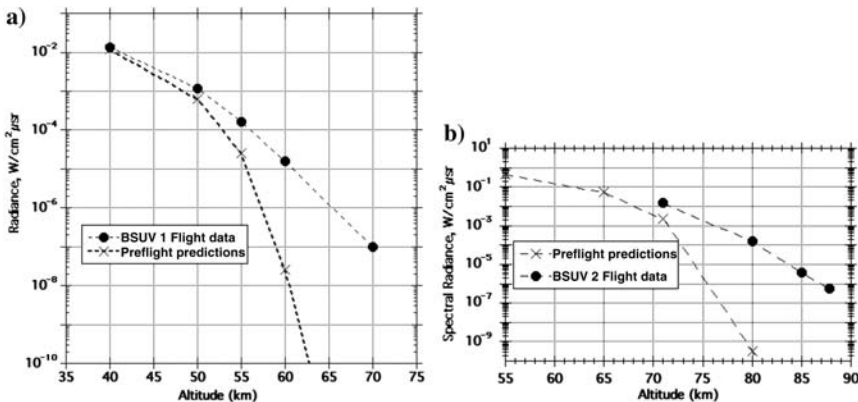


Fig. 7 Forward viewing radiometer intensities as a function of altitude for the first (LHS) and second (RHS) bow-shock flights.

short wavelength cutoff of quartz at 190 and 400 nm was covered by two separate detectors with different photocathodes, CsTe and Bialkali. The accuracy of the spectrometer absolute radiance measurements was generally within 20%.

The data shown in Figs. 7 and 8 were analyzed by a large number of researchers, attesting to the importance of the data to the hypersonic aerothermodynamics community. No attempt is made here to list all of the relevant papers. Comparison of pre-flight simulations with data showed that the greater the degree of thermochemical nonequilibrium in the flow, the worse the agreement with data. In fact, as free stream density decreased the errors between theory and experiment grew to

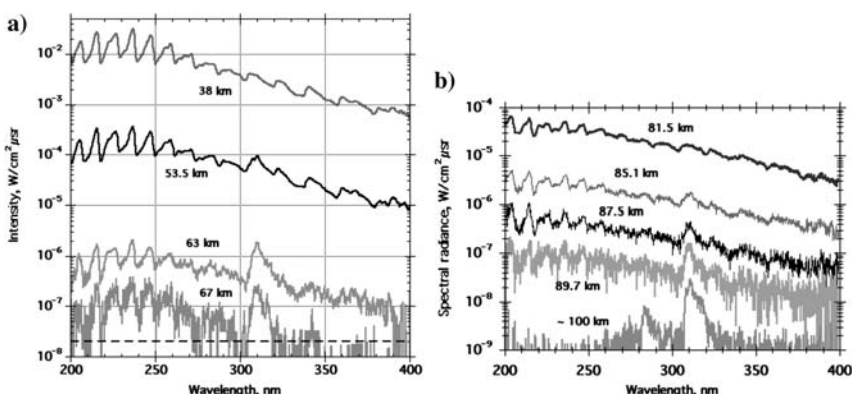


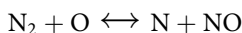
Fig. 8 Spectra as a function of altitude for the first (LHS) and second (RHS) bow-shock flights.

five orders of magnitude [67–69]. This serious discrepancy was due to inadequacies in the thermochemical rates as well as the failure to incorporate all electronic excitation mechanisms that could populate upper electronic excited states that radiate in the UV. Analyses of the spectra also identified other species which radiate, such as the hydroxyl radical [70, 71]. Although OH is not a major radiator, it is an indicator of the degree of thermal nonequilibrium in the flow as its internal temperatures were found to be different from the bulk species.

There have also been a number of fundamental advances in particle as well as continuum models to capture thermochemical nonequilibrium in shocks, which in turn, affects the modeling of radiation. These include molecular dynamics quasi-classical trajectory methods, state-specific particle approaches, development of nitrogen state specific vibrational models, and electronic state specificity. For many of these reasons an AFOSR MURI entitled “Fundamental Processes in High-temperature Hypersonic Flows” has focused on nonequilibrium flows and understanding the modeling of radiation from such flows.

As part of that work we have been using the DSMC approach to study the internal energy distributions of species created by chemical reactions, such as NO, in the shock and then using the steady state temperatures and number densities we have simulated spectra [72]. When Ro-vibronic spectra are measured they provide important information about the radiating species internal modes. Generally when such spectra are simulated it is assumed that the collision rate between the radiating species (in this case NO) is sufficiently high so that its temperature is the same as that of the bulk flow species. However, if the flow is sufficiently rarefied this assumption may fail and the spectral radiation will reflect the nascent distribution of the radiating species. For this reason we compare the bulk (primarily N₂) temperatures with those of the NO molecule for free stream conditions of 7 km/s at 81 km, to understand why they are different, and then illustrate how the different temperatures would be reflected in the molecular spectra.

Figure 9 (LHS) shows a comparison of the translational temperatures of NO molecules and the overall gas species along the stagnation streamline. It is seen that the species-averaged translational temperature in the freestream is 185 K, as specified, and increases until the peak of species-averaged temperature occurs at X = -0.014 m. However, the NO translation temperature is different from the bulk averaged one. The NO translational temperature is nearly coincident with the species-averaged value from the wall to the temperature overshoot region. Upstream of the temperature overshoot region, the NO translational temperature increases up to about 100,000 K in the freestream region. Because NO molecules are produced primarily from the exchange chemical process within the shocklayer by the reaction,



they are formed continually and their concentration finally increases to be nearly equal to the N₂ and O₂ concentrations near the surface. As NO molecules

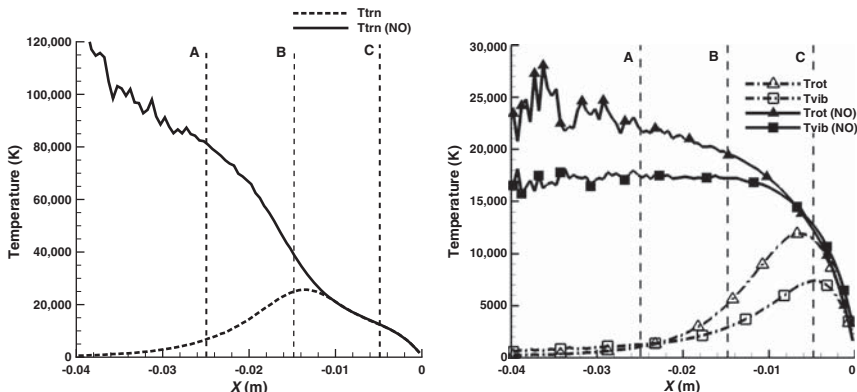


Fig. 9 Comparison of bulk vs NO translational (LHS) and internal (RHS) temperatures.

produced from chemical reactions within the shock layer diffuse to the freestream and the production rate of NO through the above exchange chemical process is quite small in the region outside of the shock layer, the thermal velocity of the diffused NO molecules to the freestream direction is high enough to reach such a high translational temperature of about 100,000 K. This phenomenon can be explained by comparing the velocity distribution of NO with that of N₂, as is shown in Reference [72].

With respect to internal energy modes, the flow residence time in a hypersonic shock is sufficiently short such that the lack of internal mode thermal relaxation is also quite apparent. Figure 9 (RHS) shows a comparison of the rotational and vibrational temperature of NO molecules with those of the overall gas species along the stagnation streamline. It is seen that the species-averaged rotational and vibrational temperatures in the freestream is 185 K and increases until the peaks of species-averaged temperature approximately occurs at location C. Similar to the NO translation temperature shown in Fig. 9 (LHS), the NO rotational temperature is nearly coincident with the species-averaged one from the wall to the location C where the maximum vibrational temperature occurs. From location C to the freestream, the NO rotational temperature increases up to about 23,000 K in the free stream region. As discussed previously, NO molecules produced from chemical reactions within the shock layer diffuse to the freestream and the production rate of NO through the two exchange chemical processes is quite small in the region outside of the shock layer. Similarly, the rotational energy of the diffused NO molecules to the freestream direction is high enough to reach such a high rotational temperature of about 23,000 K. The profile of vibrational temperature of NO molecules is, however, quite different from that of the species-averaged one. It is seen that the vibrational temperature of NO molecules is higher

than the averaged-vibrational temperature over all species along the whole stagnation streamline and it reaches finally about 18,000 K at the freestream region. This different behavior of rotational and vibrational temperature of NO molecules can be explained through the rotational and vibrational energy distribution of NO molecules [72].

Finally, we consider the influence that the different T-V and chemistry models may have on the cumulative spectral radiance integrated along the stagnation streamline. At each point along the stagnation streamline the local spontaneous emission, ε , is given as,

$$\varepsilon \propto \frac{16\pi^3 c \bar{v}^4}{3(2J_U + 1)} N_U \{ |R_e|^2 q_{V_U V_L} \} \{ S_{J_U J_L} \}$$

where the three terms in the {} brackets are spectroscopic and molecular constants related to transitions between the vibrational and rotational levels of the $X \rightarrow A$ state transitions (see Eq. (19)) and the term N_U is the population of molecules in a specific vibrational and rotational state of the A state. The dependence of the upper electronic state, N_U , on the NO vibrational and rotational temperatures, assumed here to be the same for both electronic states, is what causes the spectral radiation to provide important information about the multiple gas temperatures. This is the only way, albeit indirect, that we can validate shocklayer flow gas temperatures. Figure 10 shows four self-normalized spectra, integrated along the stagnation streamline, computed in the ultraviolet spectral region with 1 nm spectral resolution. The NO gamma band spectra are computed using the two T-V/chemistry models, LB-TCE and FHO-QCT, using either the bulk flow or the NO-specific vibrational and rotational temperatures. Also indicated are the locations of the vibrational transitions from the upper to lower electronic states. For each peak, several vibrational transitions are actually included, but the strongest vibrational transition (i.e., the transition with the highest Franck-Condon value) is displayed. The sensitivity of the spectral shape to the internal temperatures is very strong because the relative peak heights are governed by the vibrational temperature, and the peak widths are related to the rotational temperature. Examination of the spectra shows that there is more similarity in spectral structure when the NO vs the bulk species flow temperatures are used. For both the FHO-QCT and LB-TCE cases the higher peak heights for the $V_U \rightarrow V_L$ of $8 \rightarrow 3$, $7 \rightarrow 3$, $4 \rightarrow 1$ transitions are a result of the higher NO internal temperatures. Although the use of the FHO model does change the bulk vibrational temperature, the change in the spectra is small. When the NO-specific temperature is used in computing the NO spectra, it can be seen that the structure dramatically changes for these highly nonequilibrium conditions.

We are in the process of applying similar approaches to modeling ground based hypersonic experiments that have obtained radiation measurements under the present MURI effort. Tables 1 and 2 summarize some of the key ground

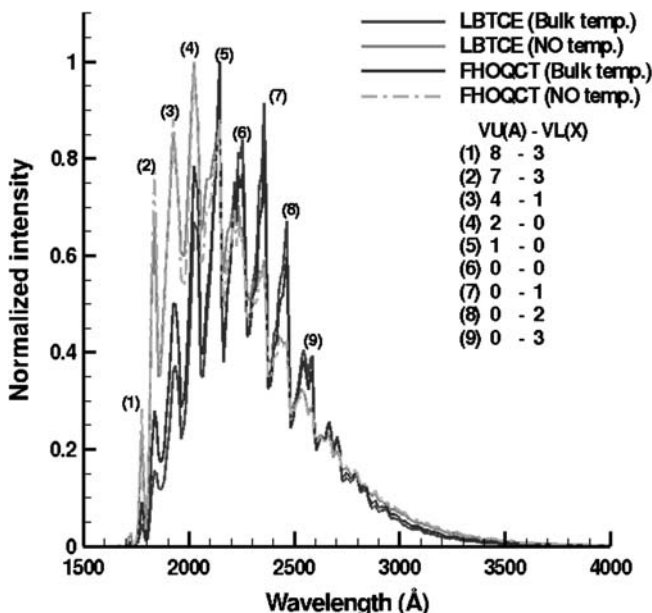


Fig. 10 Effect of T-V relaxation rates, chemistry models, and temperatures on NO vibronic spectra (see color section).

measurements in the moderate Mach number range. Modeling of the radiation measured in many of the facilities will allow us to test our improved thermochemical nonequilibrium models until such time as onboard flights can be employed again.

C. SPACECRAFT GLOW

Spacecraft glow is radiation in the visible spectral region seen surrounding spacecraft in low earth orbits. The understanding and prediction of the phenomena are important for scientific and operational reasons. Any spacecraft making optical measurements, scientific, or business (remote sensing) will measure the spacecraft glow signal as well as the desired source. The spacecraft glow signal represents a background noise signal or equivalently, optical contamination. Figure 11 shows a comparison of the Atmospheric Explorer (AE) measurements of Yee and Abreu [78] from a nonthrusting satellite with that of the space shuttle. Direct comparison of the AE and Shuttle data is ambiguous. These observations and others led to fundamental questions about spacecraft glow in terms of understanding its source, whether it is due to outgassing or can occur from a “clean” body, or both, does it depend on the body shape or size, and whether it is sensitive to the spacecraft material. Before 1997, most modeling of spacecraft glow was phenomenological—

TABLE 1 EXPERIMENTAL MEASUREMENTS OF NORMAL SHOCK FLOW FIELDS

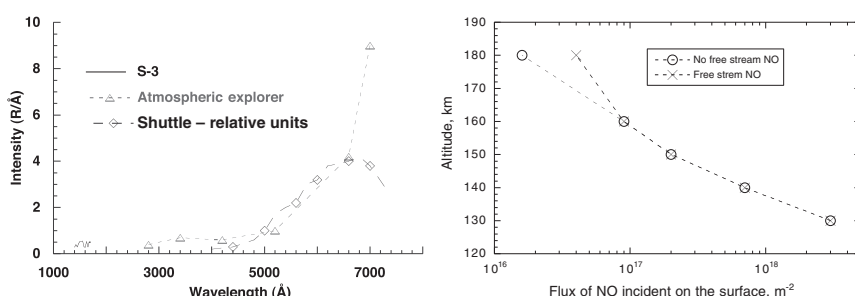
Researcher	Gas Components	Speed (km/s)	Pressure (Torr)	Altitude (km)	Direct Measurements	Calculated Parameters
Kewley and Hornung [73]	N ₂	4~10	2~42		ρ/ρ_∞	
Sharma and Gillsepie [74]	N ₂	6.2	1			$T_r \ T_v \ t^a \ P_\infty$
Treanor and Williams [75]	N ₂ and O ₂	3~4	1; 2.25; 4	46; 40; 36		
Gorelov et al. [76]	Air	5~9	0.1			
Fujita et al. [77]	Air	7~16	0.1; 2.0			
	N ₂	11.9	0.3			$T_r \ T_v$

^a Lab air typically contains a large fraction of a percent of water.

TABLE 2 EXPERIMENTAL MEASUREMENTS OF RADIATION FROM NORMAL SHOCKS

Researcher	Gas Components	Radiating Species	Spectral Region	Spectral Resolution (nm)	Note
Sharma and Gillsepie [74]	N ₂	N ₂ ⁺ , N ₂	UV	0.03; 0.054	
Treanor and Williams [75]	N ₂ and O ₂	NO	IR		Time history
Gorelov et al. [76]	Air	NO; N ₂ ⁺	UV		Peak value
Fujita et al. [77]	Air	N; N ₂ ⁺ , N ₂	UV, Visible	0.69; 016	
	N ₂	N; N ₂ ⁺ , N ₂	UV, Visible	0.69	

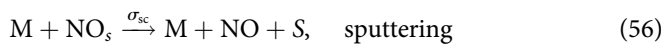
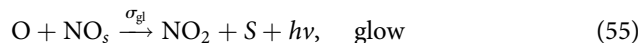
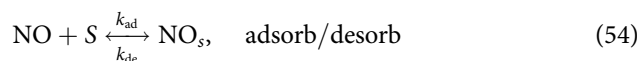
i.e., no unified, quantitative approach. As AE is a “clean” body, we sought to model its glow before considering the shuttle which clearly had on orbit firings. A plot of the measured AE radiance in the 732 ± 2 nm photometric band as a function of altitude is not smooth but rather has a “kink” in it (see Fig. 1 of Reference [78]). Because spacecraft glow processes occur at high altitudes, traditional computational fluid dynamics approaches fail and methods of rarefied gas dynamics must be used. The DSMC computational tool SMILE was used in simulations with different gas phase and the gas–surface models to predict the NO flux levels as a function of altitude that correspond to the elliptical orbit of AE. The RHS of Fig. 11 shows a comparison of the predicted NO flux levels to the spacecraft RAM surface as a function of altitude and a slight bend in the flux profile can be discerned at an altitude close to the experimental “kink”. From this type of comparison it was concluded that NO is the precursor to the AE spacecraft glow [79, 80]. Furthermore, comparison of computed NO flux levels vs altitude with and without consideration of free stream NO shows that for altitudes

**Fig. 11 Introductory concepts of spacecraft glow.**

<160 km the dominant source of NO is due to chemical reactions created in the very diffuse reaction zone in front of the spacecraft. Even at 180 km, the inclusion of free stream NO only increases the NO surface flux only by a factor of ~ 2 . The DSMC simulations also showed that if all of the NO formed in the gas phase reacted at the RAM spacecraft surface, the predicted radiance would be much greater than observations. Thus to determine the efficiency of surface radiation processes one must postulate a surface model.

The gas-surface model that we developed was relatively simple with the following assumptions. The satellite surface is a metal oxide, i.e., any bare metal in LEO will rapidly become oxidized. The oxygen that is chemisorbed or strongly bonded to the spacecraft is *not* available to react with the RAM gas flux. Of the three gases impacting the surface, N₂, O, and NO, only NO will form a weakly chemisorbed, physisorbed, bond with the spacecraft oxide surface.

The gas-surface processes are:



where S represents a spacecraft surface site available for absorption, NO_s represents nitric oxide adsorbed on the surface, and M represents another gas species, e.g., N₂, O, or NO and Eqs. (55–56) are in the forward direction only. The scrubbing processes, Eq. (56), are the nonreactive removal of adsorbed NO from the spacecraft surface. Note that Eq. (55) represents the sum of two distinct processes,



where NO₂^{*} is an electronically excited state of the NO₂ molecule. The two processes are assumed to occur so quickly that they can be combined as one mechanism. The forward and reverse rate coefficients, $k_{\text{ad,de}}$ are given by

$$k_{\text{ad}} = S_o / n_T \quad (59)$$

$$k_{\text{de}} = \frac{k_B \theta_D}{h} \exp\left(-\frac{H_{\text{os}}}{k_B T}\right) \quad (60)$$

$$= \tau_o^{-1} \exp\left(-\frac{H_{\text{os}}}{k_B T}\right) \quad (61)$$

where S_o is the sticking coefficient which has a typical value of 0.5 for spacecraft materials, θ_D is the Debye temperature of 400 K, T is the spacecraft surface temperature, assumed here to be 300 K, n_T is the total number of surface sites, H_{os} is the

heat of adsorption of NO bonded to a metal oxide surface, and τ_o is the surface residence time $\sim 1.2 \times 10^{-13}$ s, which is typical of contamination residence times.

The glow radiation can be modeled exactly in DSMC, i.e., collisions leading to photon production described by Eq. (55), or, the radiation can be approximated by the tangent slab model. If the tangent slab approximation of radiation is used it can be shown that the glow radiation is

$$I = \frac{\sigma_{\text{gl}} n_{\text{NO}_s}^{\text{ss}} f_O}{2} \quad (62)$$

where NO_s^{ss} designates the steady state value of the number of NO molecules adsorbed to the surface and is obtained from the steady state solution of Eqs. (54–56) and f_O is the flux of oxygen atoms to the surface in molec·m $^{-2}$ s $^{-1}$. Note that this expression does not depend on the lifetime of the metastable NO_2^* , a quantity which is uncertain and possibly material dependent. Examination of two sets of DSMC simulations [81], presented in Fig. 12, shows that the DSMC simulation of the radiance (labelled “full simulation”) and the tangent slab (labelled “analytic approach”) are quite close, although there is a slight difference in the slope between 150 and 160 km.

As Fig. 12 shows, the radiation is dependent on the surface model parameters such as, σ_{gl} , σ_{sc} , and most importantly H_{os} which has a range of values from 10–20 Kcal/mole. It can be shown that for $H_{\text{os}} < 10$ Kcal/mole, the surface concentration of NO_s is too low to predict the magnitude of the measured glow radiation and values of $H_{\text{os}} > 20$ Kcal/mole cannot be justified from basic chemical — surface bonding concepts. As the figure shows, the slope of the normalized radiance radiance for set 2 is much closer to the measurements than surface set 1 and is due to change in the surface scrubbing cross sections, σ_{sc} . For the range of values considered here, the heat of adsorption variation only changes the magnitude of the radiance vs altitude dependence and not the slope. More details may be found in References [81] and [82].

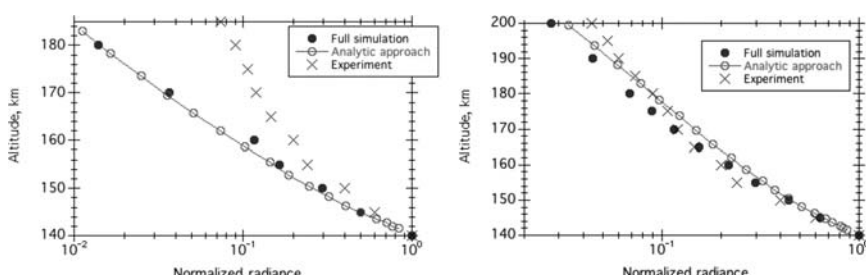
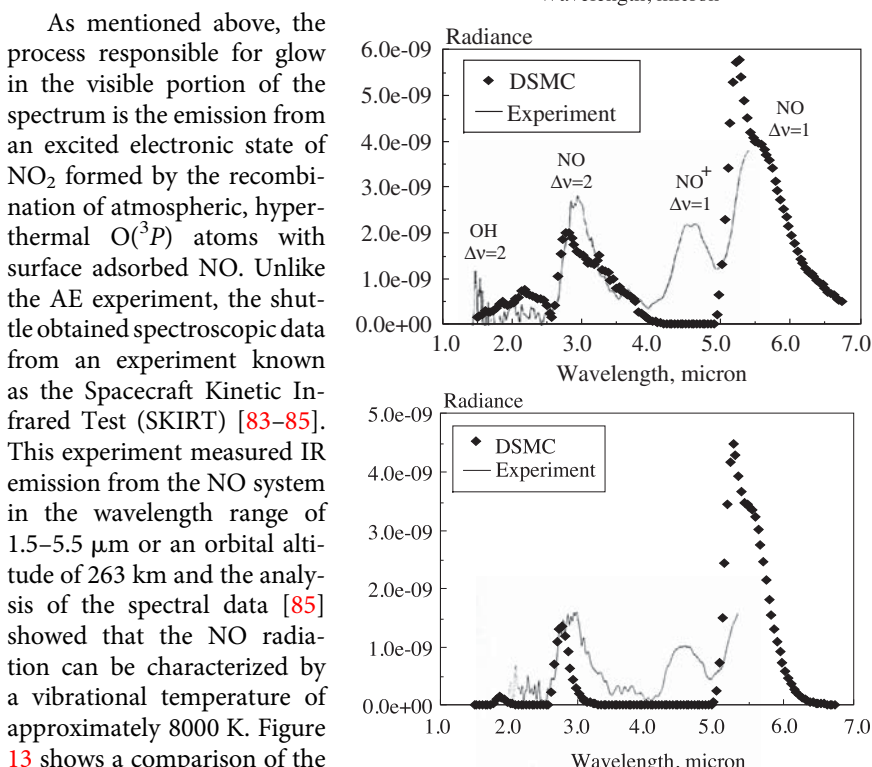


Fig. 12 Comparison of altitude dependence for predicted (set 1, LHS) and (set 2, RHS) surface properties and measured radiances.

Fig. 13 Comparison of measured SKIRT and simulated radiance ($\text{W}/\text{cm}^2 \mu\text{-sr}$), top = zero angle of attack and thermal accommodation coefficient = 1, middle = zero angle of attack and thermal accommodation coefficient = 0.8, and bottom = 45-deg angle of attack and thermal accommodation coefficient = 0.8.



As mentioned above, the process responsible for glow in the visible portion of the spectrum is the emission from an excited electronic state of NO_2 formed by the recombination of atmospheric, hyperthermal $\text{O}({}^3P)$ atoms with surface adsorbed NO. Unlike the AE experiment, the shuttle obtained spectroscopic data from an experiment known as the Spacecraft Kinetic Infrared Test (SKIRT) [83–85]. This experiment measured IR emission from the NO system in the wavelength range of 1.5–5.5 μm or an orbital altitude of 263 km and the analysis of the spectral data [85] showed that the NO radiation can be characterized by a vibrational temperature of approximately 8000 K. Figure 13 shows a comparison of the radiance measured and predicted for three angles of attack. Our calculations did not include OH or NO^+ as potential IR sources and although NO_2 radiates in this spectral region, it is consistently not observed in the IR glow data. Consistent with the data, the predicted level of radiation decreases

for higher angle of attack. For the 0 deg angle of attack, there is a considerable difference observed in the widths of the predicted and experimental data for the $\Delta\nu = 2$ spectral region for a translational energy accommodation coefficient, $\alpha_t = 1$ (Fig. 13 top). The results of $\alpha_t = 1$ under predict the data, whereas the calculation with $\alpha_t = 0.8$ overpredicts it (Fig. 13 middle). However, (Fig. 13 middle) shows that the calculated width of the NO $\Delta\nu = 2$ peak is in closer agreement to the experiment if a value of $\alpha_t = 0.8$ is assumed. Use of a vibrational temperature based on the upper levels for $\alpha_t = 0.8$ was found to be close to 8000 K similar to that obtained in Reference [85]. The location of the calculated peak in Fig. 13 (top and middle) is also different, 2.8 μm vs the value of 3.0 μm observed in the experiment. As shown in Fig. 13 (bottom), the agreement is better for the angle of attack of 45 deg when $\alpha_t = 0.8$ is used. Generally, the experimental shape and absolute value is reproduced well if a value of α_t between 0.8 and 1.0 is used.

V. FUTURE CHALLENGES

Although the last several years have witnessed significant advanced in our ability to model radiation from complex nonequilibrium flows a number of important challenges remain. The ability to model radiation from two-phase gas mixtures due to charring ablators with the same rigor as noncarbonaceous air species will be nontrivial. Although the primary mechanisms of charring ablators are to lower the *convective* heat transfer to the body, the increase or decrease of the radiative heating load will strongly depend on the optical properties of the pyrolysis gases and their complex interaction with the boundary layer. The gaseous species could consist of C₃, CO, C, HCN, CN, and H and arcjet experiments have shown that CN is a primary radiating species [86]. The significant effects of ablation and radiation coupling to the flow have been demonstrated by Johnston et al. [87] for different wall boundary conditions and flight missions. They note that although ablation products tend to absorb the shock layer radiation in the VUV region, re-emission can occur in longer wavelength spectral regions leading to the change in radiative heat transfer to the vehicle. Recently a number of groups have embarked on ground-based measurement campaigns to quantify the VUV/UV spectral radiation from ablation products [88–90]. In addition to these efforts, the continuing development of radiation codes such as HyperRad [91] which is being compared with NASA/Ames EAST data and the present radiation codes, HARA and NEQAIR will further expand the capabilities of radiation modeling for NASA missions.

With respect to moderate Mach number flows, such as would be encountered in Air Force missions, the necessity to model highly complex charring ablators spectra is not applicable and understanding the coupling between the flow and radiative heat transfer is less of an issue. The flight regime is such that both neutral and electron excitation cross sections among the different electronic states of molecular as well as atomic species are important in establishing the

population of radiating electronic states. The cross sections for electron impact are fairly well known, but, there are essentially no direct calculations of neutral excitation cross sections and they are inferred from primarily quenching rates from electronically excited states to the ground state by assuming microscopic reversibility. This is a serious problem complicated by the difficulty of calculating accurate quantum mechanical potential energy surfaces of electronically excited diatomic and small polyatomic species. For example, the actual mechanism for formation of NO in its first electronically excited state, $A^2\Sigma^+$, in a shock, is simply unknown. Is it formed by direct collisional excitation from its ground electronic state by N₂ or O or is there energy pooling in the dark (nonradiating) N₂ (A) state?

As useful as the data has been from the BSUV flights, there are important deficiencies that should be corrected either through new flight experiments or ground based measurements. These limitations include the fact that there is no spectral data from the UV through IR at any free stream velocity, thereby, missing independent measurements of vibrational and rotational temperatures, especially for species that do not strongly radiate in the UV. The UV spectra have a spectral resolution of only 1 nm, a choice dictated by instrument type, anticipated S/N, and measurement time. This spectral resolution is adequate for modeling of electronic and vibrational temperatures averaged over the shock-layer, but, does not provide enough sensitivity to validate flow rotational temperatures. Furthermore, measurements were taken at fixed views of the shocklayer and do not provide any estimate of range resolution along the line of sight to the vehicle. VUV photoionization cells obtained integrated measurements of the optically thick atomic oxygen radiation, but, the lack of corresponding spectra for the visible atomic transitions remains a concern in the interpretation of the photoionization cell data. At speeds higher than 5 km/s, the importance of this data will increase even more. By design, the BSUV data was taken for “clean”, non-ablating flows, but, for Air Force reusable vehicle concepts the creation of ablating species and their role in modifying the shock layer thermochemical nonequilibrium is important. The PAET Experiment [92] suggests that importance of ionization for Earth reentry flows occurs even at 6 km/s, but, the true velocity threshold is simply not known. Finally, fifteen years later we still do not have UV spectral data taken under flight conditions that would confirm the major thermochemical and radiation mechanisms for speeds on the order of 7 km/s! Yet it is at this upper end of the Mach number flight space that the Air Force will encounter the harshest environment from a TPS material view point.

Although spectral radiation measurements are being performed in ground based facilities, there have been no flight experiments with onboard spectrometer since BSUV. While it is true that the NASA and Air Force flight regimes overlap for the former at its lowest Mach number of interest, there has unfortunately been little to no scientific and technical cooperation on a future flight. This is unfortunate because the most recent NASA reentry spectrometer flight data harkens back to the Apollo era and even that spectral data has been reconstructed from a

scanning spectrometer whose reverse scanning capability malfunctioned. Yet these data continue to be the bench mark for essentially every new flow and radiation in our discipline. The velocity region of 6–8 km/s is important because it represents the onset of sufficient ionization in the bow shock to create radiation from strong molecular ionic species. It is this author's strong opinion that, although obtaining spectral data from remote targets of opportunity is relatively inexpensive compared to a dedicated flight, the value of such data is severely compromised by the large spatial averaging that occurs. The promise of relatively low cost, robust, flight-tested spectrometers has been established on the harsh environment of sounding rocket experiments. The transference of these low cost, COT instruments can be implemented on small cube satellite experiments if in-flight data collection through existing low earth orbit satellites can be established.

Finally, it has been assumed in the simple gas–surface interaction model discussed in Sec. IV.C that the principal process for surface glow is an EleyRideal mechanism [93] with NO_2^* formed by collisions of O with surface-physisorbed NO. The formation of NO_2^* could potentially occur via a Langmuir Hinshelwood mechanism involving the reaction of both surface adsorbed NO and O, but this mechanism was not considered, based on the range of heat of adsorption values that are reasonable for a surface glow model. Gasser [93] provides an estimate of the number of surface sites a surface adsorbed species can visit based on its heat of adsorption. A low value of about four site hops and that the fractional coverage of surface adsorbed O will be shown to be very low make the EleyRideal mechanism a more realistic choice. However, for other materials or contaminants other than hydrazine and its fragments (new ionic liquid propellants, ion-sputtered species, etc.) reaction forcefield—molecular dynamics approaches should provide better estimates of the key surface parameters.

ACKNOWLEDGMENT

This research performed at the Pennsylvania State University was supported by Grant No. NNX10AP97G.

REFERENCES

- [1] Simmons, F. S., *Rocket Exhaust Plume Phenomenology*, Aerospace Corporation, El Segundo, CA, 2000, ISBN 1-884989-08-X.
- [2] Zhigulev, V. N., Romishevskii, Y. A., and Vertushkin, V. K., “Role of Radiation in Modern Gasdynamics,” *AIAA Journal*, Vol. 1, 1963, pp. 1473–1485.
- [3] Goulard, R., “The Coupling of Radiation and Convection in Datedash Shock Layers,” *Journal of Quantitative Spectroscopy and Radiative Transfer*, Vol. 1, 1961, pp. 249–257.

- [4] Hoshizaki, H., and Lasher, L. E., "Convective and Radiative Heat Transfer to an Ablating Body," *AIAA Journal*, Vol. 6, 1968, pp. 1441–1449.
- [5] Moss, J. N., "Radiative Viscous-Shock-Layer Solutions with Coupled Ablation Injection," *AIAA Journal*, Vol. 9, 1976, pp. 1311–1317.
- [6] Page, W. A., and Woodward, H. T., "Radiative and Convective Heating during Venus Entry," *AIAA Journal*, Vol. 10, 1972, pp. 1379–1381.
- [7] Sutton, K., and Falanga, R. A., "Stagnation Region Radiative Heating with Steady-State Ablation during Venus Entry," *AIAA Journal*, Vol. 10, 1973, pp. 155–157.
- [8] Sutton, K., "Coupled Nongray Radiating Flow about Ablating Planetary Entry Bodies," *AIAA Journal*, Vol. 12, 1974, pp. 1099–1105.
- [9] Sutton, K., "Radiative Heating about Outer Planet Entry Probes," *Journal of Spacecraft and Rockets*, Vol. 13, 1976, pp. 294–300.
- [10] Park, C., "Calculation of Nonequilibrium Radiation in the Flight Regimes of Aeroassisted Orbital Transfer Vehicles," AIAA Paper 1984-0306, 22nd Aerospace Sciences Meeting, Reno, Nevada, Jan. 1984.
- [11] Park, C., "Radiation Enhancement by Nonequilibrium in Earth's Atmosphere," *Journal of Spacecraft and Rockets*, Vol. 22, 1985, pp. 27–36.
- [12] Park, C., "Problems of Rate Chemistry in the Flight Regimes of Aeroassisted Orbital Transfer Vehicles," AIAA Paper 1984-1730, *19th Thermophysics Conference*, Snowmass, Colorado, June 1984.
- [13] Park, C., "Assessment of a Two-Temperature Kinetic Model for Dissociating and Weakly Ionizing Nitrogen," *Journal of Thermophysics and Heat Transfer*, Vol. 2, 1988, pp. 8–16.
- [14] Park, C., "Assessment of Two-Temperature Kinetic Model for Ionizing Air," *Journal of Thermophysics and Heat Transfer*, Vol. 3, 1989, pp. 233–244.
- [15] Park, C., *Nonequilibrium Hypersonic Aerothermodynamics*, Wiley, New York, 1990.
- [16] Gnoffo, P. A., "Upwind-Biased Point-Implicit Relaxation Strategies for Viscous Hypersonic Flows," AIAA Paper 1989-1972, *9th AIAA Computational Fluid Dynamics Conference*, Buffalo, New York, June 1989.
- [17] Wright, M., Candler, G. V., and Bose, D., "Data-Parallel Line Relaxation Method for the Navier-Stokes Equations," *AIAA Journal*, Vol. 36, No. 9, 1998, pp. 1603–1609.
- [18] Hartung, L. C., "Development of a Nonequilibrium Radiative Heating Prediction Method for Coupled Flowfield Solutions," *Journal of Thermophysics and Heat Transfer*, Vol. 6, 1992, pp. 618–625.
- [19] Whiting, E. E., Park, C., Liu, Y., Arnold, J. O., and Paterson, J. A., "NEQAIR 96 User Manual," Tech. Rept., NASA Ames Research Center, Moffett Field, CA, 1996.
- [20] Johnston, C. O., "Nonequilibrium Shock-Layer Radiative Heating for Earth and Titan Entry," Ph.D. Thesis, Department of Aerospace Engineering, Virginia Polytechnic Institute and State University, Virginia, 2006.
- [21] Hyun, S. Y., "Radiation Code SPRADIAN07 and Its Applications," Ph.D. Thesis, Division of Aerospace Engineering, Korea Advanced Institute of Science and Technology, Daejun, Korea, 2009.
- [22] Feldick, A., "Coupled Nonequilibrium Flow, Energy, and Radiation Transport for Hypersonic Planetary Entry", Ph.D. Thesis, The Pennsylvania State University, 2013.

- [23] Olynick, D., Chen, Y. K., and Tauber, M. E., "Aerothermodynamics of the Stardust Sample Return Capsule," *Journal of Spacecraft and Rockets*, Vol. 36, No. 3, 1999, pp. 442–462.
- [24] Gupta, R. N., "Aerothermodynamic Analysis of Stardust Sample Return Capsule with Coupled Radiation and Ablation," *Journal of Spacecraft and Rockets*, Vol. 37, No. 4, 2000, pp. 507–514.
- [25] Suzuki, T., Furudate, M., and Sawada, K., "Trajectory-Based Heating Analysis for the Stardust Sample Return Capsule," AIAA Paper 2002-0908, 40th AIAA Aerospace Sciences Meeting and Exhibit, Reno, Nevada, Jan. 2002.
- [26] Park, C., "Calculation of Stagnation-Point Heating Rates Associated with Stardust Vehicle," *Journal of Spacecraft and Rockets*, Vol. 44, 2007, pp. 24–32.
- [27] Liu, Y., Prabhu, D., Trumble, K., Saunders, D., and Jenniskens, P., "Radiation Modeling for the Reentry of the Stardust Sample Return Capsule," AIAA Paper 2008-1213, 46th AIAA Aerospace Sciences Meeting and Exhibit, Reno, Nevada, Jan. 2008.
- [28] Beerman, A. F., Lewis, M. J., Starkey, R. P., and Cybik, B. Z., "Significance of Nonequilibrium Surface Interactions in Stardust Return Capsule Ablation Modeling," *Journal of Thermophysics and Heat Transfer*, Vol. 23, 2009, pp. 425–432.
- [29] Olynick, D. R., Henline, W. D., Hartung, C. L., and Candler, G. V., "Comparison of Coupled Radiative Flow Solutions with Project Fire II flight Data," *Journal of Thermophysics and Heat Transfer*, Vol. 9, No. 4, 1995, pp. 586–594.
- [30] Johnston, C. O., and Hollis, B. R., "Radiative Heating Methodology for the Huygens Probe," *Journal of Spacecraft and Rockets*, Vol. 44, No. 5, 2007, pp. 993–1002.
- [31] Hash, D., Olejniczak, J., Wright, M., Prabhu, D., Pulsonetti, M., Hollis, B., Gnoffo, P., Barnhardt, M., Nompelis, I., and Candler, G., "Fire II Calculations for Hypersonic Nonequilibrium Aerothermodynamics Code Verification: DPLR, LAURA and US3D," AIAA Paper 2007-605, 45th AIAA Aerospace Sciences Meeting Exhibit, Reno, Nevada, Jan. 2007.
- [32] Sohn, I., Bansal, A., Levin, D. A., and Modest, M. F., "Advanced Radiation Calculations of Hypersonic Reentry Flows Using Efficient Databasing Schemes," *Journal of Thermophysics and Heat Transfer*, Vol. 24, No. 3, July–Sept 2010.
- [33] Feldick, A. M., Modest, M. F., and Levin, D. A., "Closely Coupled Flowfield-Radiation Interactions For Flowfields Created during Hypersonic Reentry," AIAA Paper 2008-4104, 40th Thermophysics Conference, Seattle, Washington, June 2008.
- [34] Feldick, A. M., Modest, M. F., Levin, D. A., Gnoffo, P., and Johnston, C. O., "Examination of Coupled Continuum Fluid Dynamics and Radiation in Hypersonic Simulations," AIAA Paper 2009-475, 47th AIAA Aerospace Sciences Meeting including the New Horizon Forum and Aerospace Exposition, Orlando, Florida, Jan. 2009.
- [35] Modest, M. F., *Radiative Heat Transfer*, 2nd ed., Academic Press, New York, 2003.
- [36] Johnston, C. O., Hollis, B. R., and Sutton, K., "Spectrum Modeling for Air Shock-Layer Radiation at Lunar-Return Conditions," *Journal of Spacecraft and Rockets*, Vol. 45, No. 5, 2008, pp. 865–878.
- [37] Johnston, C. O., Hollis, B. R., and Sutton, K., "Non-Boltzmann Modeling for Air Shock-Layer Radiation at Lunar-Return Conditions," *Journal of Spacecraft and Rockets*, Vol. 45, No. 5, 2008, pp. 879–890.

- [38] McCorkle, E., Bose, D., Hash, D., and Hassan, H., "Improved Modeling of Shock Layer Radiation in Air," AIAA 2009-1028, *47th AIAA Aerospace Sciences Meeting Including The New Horizons Forum and Aerospace Exposition*, 5–8 January 2009, Orlando, Florida.
- [39] McCorkle, E., and Hassan, H., "Examination of EAST Data Using Updated NEQAIR: Shock Tube Flow," AIAA 2009-3921, *41st AIAA Thermophysics Conference*, 22–25 June 2009, San Antonio, Texas.
- [40] Fujita, K., and Abe, T., "SPRADIAN, Structured Package for Radiation Analysis: Theory and Application," technical Report 669, Inst. of Space and Astronautical Science, Tokyo, Japan, 1997.
- [41] Laux, C., "Optical Diagnostics and Collisional-Radiative Models," *VKI Course on Hypersonic Entry and Cruise Vehicles*, Stanford University, June 30 July 3, 2008.
- [42] "Specair User Manual, Version 3.0," www.specair-radiation.net/Specair%20manual.pdf, 2012.
- [43] Peach, G., "Continuous Absorption Coefficient for Non-Hydrogenic Atoms," *Memoirs of the Royal Astronomical Society*, Vol. 73, 1970, pp. 1–123.
- [44] Zel'dovich, Y. B., and Raizer, Y. P., *Physics of Shock Waves and High-Temperature Hydrodynamic Phenomena*, Vol. 1. Translated by Scripta Technica, Inc., Academic Press, London, 1966.
- [45] Arnold, J. O., Whiting, E. E., and Lyle, G. C., "Line by Line Calculation of Spectra from Diatomic Molecules and Atoms assuming A Voigt Line Profile," *Journal of Quantitative Spectroscopy and Radiative Transfer*, Vol. 9, No. 6, 1969, pp. 775–798.
- [46] Herzberg, G., *Molecular Spectra and Molecular Structure 1. Spectra of Diatomic Molecules*, D. Van Nostrand Company, New York, 1950.
- [47] Feldick, A. M., Giegel, J., and Modest, M. F., "A Spectrally Accurate Tightly-Coupled 2-D Axisym- metric Photon Monte-Carlo RTE Solver For Hypersonic Entry Flows," HT2009-88241, *ASME Summer Heat Transfer Conference*, San Francisco, California, July 2009.
- [48] Ozawa, T., Wang, A., Levin, D., and Modest, M., "Development of Coupled Particle Hypersonic Flowfield—Photon Monte Carlo Radiation Methods," *Journal of Thermophysics and Heat Transfer*, Vol. 24, No. 3, July–Sept. 2010.
- [49] Sohn, I., Li, Z., Levin, D. A., and Modest, M. F., "Coupled DSMC-Photon Monte Carlo Radiation Simulations of a Hypersonic Reentry," *Journal of Thermophysics and Heat Transfer*, Vol. 26, No. 1, January–March 2012.
- [50] Bose, D., Wright, M. J., Bogdanoff, D. W., Raiche, G. A., and Allen, G. A., "Modeling and Experimental Validation of CN Radiation Behind a Strong Shock Wave," AIAA Paper 2005-768, 43rd AIAA Aerospace Sciences Meeting and Exhibit, Reno, Nevada, Jan. 2005.
- [51] Salzmann, D., *Atomic Physics in Hot Plasmas*, Oxford University Press, New York, 1998.
- [52] Salzmann, D., "Escape Factors in Spherically Symmetric Plasmas," *Journal of Quantitative Spectroscopy and Radiative Transfer*, Vol. 107, No. 1, 2007, pp. 47–60.
- [53] John, D., and Anderson, J., *Fundamentals of Aerodynamics*, 3rd ed., McGraw-Hill, 2001.
- [54] Sutton, K., "Air Radiation Revisited," AIAA Paper 84-1733, 19th AIAA Thermophysics Conference, Snowmass, Colorado, June 1984.

- [55] Anderson, J. D., *Hypersonic and High-Temperature Gas Dynamics*, 2nd ed., AIAA, Virginia, 2006.
- [56] Tauber, M. E., and Sutton, K., “Stagnation-Point Radiative Heating Relations for Earth and Mars Entries,” *Journal of Spacecraft and Rockets*, Vol. 28, No. 1, 1990, pp. 40–42.
- [57] Ozawa, T., Nompelis, I., Levin, D. A., Barnhardt, M., and Candler, G. V., “Continuum Method Comparison of a High Altitude, Extreme-Mach Number Reentry Flow,” *Journal of Thermophysics and Heat Transfer*, Vol. 24, No. 2, April–June 2010.
- [58] Boyd, I. D., Trumble, K., and Wright, M. J., “Nonequilibrium Particle and Continuum Analyses of Stardust Entry for Near-Continuum Conditions,” AIAA Paper 2007-4543, *39th AIAA Thermophysics Conference*, Miami, Florida, June 2007.
- [59] Z. Li, I. S., and Levin, D., “Effects of Non-Maxwellian Distributions on Shock-Layer Radiation from Hypersonic Reentry Flows,” *Journal of Thermophysics and Heat Transfer*, Vol. 27, No. 1, January–March 2013.
- [60] Huo, W., “Electron Recombination and Collisional Excitation in Air,” AIAA Paper 2009-1593, 2009.
- [61] Stone, E. J., and Zipf, E. C., “Excitation of Atomic Nitrogen by Electron Impact,” *Journal of Chemical Physics*, Vol. 58, No. 10, 1973.
- [62] Li, Z., Ozawa, T., Sohn, I., and Levin, D. A., “Modeling of Electronic Excitation and Radiation in Non-continuum Hypersonic Reentry Flows,” *Physics of Fluids*, Vol. 23, No. 6, 2011, pp. 066102-1–15.
- [63] Sohn, I., Li, Z., and Levin, D., “Effect of Nonlocal Vacuum Ultraviolet Radiation on Hypersonic Nonequilibrium Flow,” *Journal of Thermophysics and Heat Transfer*, Vol. 26, No. 3, July–September 2012.
- [64] Erdman, P., Zipf, E., Espy, P., Howlett, C., Levin, D., Loda, R., Collins, R., and Candler, G., “Flight Measurements of Low-Velocity Bow Shock Ultraviolet Radiation,” *Journal of Thermophysics and Heat Transfer*, Vol. 7, No. 1, Jan.–March 1993, pp. 37–41.
- [65] Erdman, P., Zipf, E., Espy, P., Howlett, C., Levin, D., Collins, R., and Candler, G., “Measurements of Ultraviolet Radiation from a 5 km/sec Bow Shock,” *Journal of Thermophysics and Heat Transfer*, Vol. 8, 1994, pp. 441.
- [66] Erdman, P., Zipf, E., Espy, P., Howlett, C., Christou, C., Levin, D., Loda, R., Collins, R., and Candler, G., “In Situ Plume Radiance Measurements from the Bow Shock Ultraviolet 2 Rocket Flight,” *Journal of Thermophysics and Heat Transfer*, Vol. 7, No. 4, Oct.–Dec. 1993, pp. 704–708.
- [67] Levin, D., Candler, G., Collins, R., Erdman, P., Zipf, E., Espy, P., and Howlett, C., “Comparison of Theory with Experiment for the Bow Shock Ultraviolet Rocket Flight,” *Journal of Thermophysics and Heat Transfer*, Vol. 7, 1993, pp. 30.
- [68] Levin, D., Candler, G., Collins, R., Erdman, P., Zipf, E., Espy, P., and Howlett, C., “Examination of Theory for the Bow Shock Ultraviolet Rocket Experiments-I,” *Journal of Thermophysics and Heat Transfer*, Vol. 8, 1994, pp. 447.
- [69] Levin, D., Braunstein, M., Candler, G., Collins, R., and Smith, G., “Examination of Theory for Bow Shock Ultraviolet Rocket Experiments-II,” *Journal of Thermophysics and Heat Transfer*, Vol. 8, 1994, pp. 453.
- [70] Levin, D., Laux, C., and Kruger, C., “A General Model for the Spectral Calculation of OH Radiation in the Ultraviolet,” *Journal of Quantitative Spectroscopy and Radiative Transport*, Vol. 61, No. 3, 1999, pp. 377–392.

- [71] Levin, D., Collins, R., Candler, G., Wright, M., and Erdman, P., "Examination of OH Ultraviolet Radiation from Shock-Heated Air," *Journal of Thermophysics and Heat Transfer*, Vol. 10, No. 200, 1996.
- [72] Li, Z., Sohn, I., and Levin, D., "Modeling of NO Formation and Radiation in Nonequilibrium Hypersonic Flows," *Journal of Thermophysics and Heat Transfer*, Vol. 28, 2014, pp. 365–380.
- [73] Kewley, D., and Hornung, H., "Free-piston shock-tube study of nitrogen dissociation," *Chemical Physics Letters*, Vol. 25, No. 4, April 1974, pp. 531–536.
- [74] Sharma, S. P., and Gillespie, W., "Nonequilibrium and Equilibrium Shock Front Radiation Measurements," *Journal of Thermophysics and Heat Transfer*, Vol. 5, No. 3, 1991, pp. 257–265.
- [75] Treanor, C. E., and Williams, M. J., "Kinetics of Nitric Oxide Formation Behind 3 to 4 km/s Shock Waves," Tech. Rept., 1993.
- [76] Gorelov, V., Gladyshev, M., Kireev, A., Yegorov, I., Plastinin, Y., and Karabazhak, G., "Experimental and numerical study of nonequilibrium ultraviolet NO and N-2(+) emission in shock layer," *Journal of Thermophysics and Heat Transfer*, Vol. 12, No. 2, 1998, pp. 172–179, AIAA 31st Thermophysics Conference, New Orleans, Louisiana, June 17–20, 1996.
- [77] Fujita, K., Sato, S., Abe, T., and Ebinuma, Y., "Experimental Investigation of Air Radiation from Behind a Strong Shock Wave," *Journal of Thermophysics and Heat Transfer*, Vol. 16, 2002, pp. 77–82.
- [78] Yee, J., and Abreu, V., "Visible Glow Induced by Spacecraft-Environment Interaction," *Geophysical Research Letters*, Vol. 10, No. 2, 1983, pp. 126–129.
- [79] Dogra, V., Collins, R., and Levin, D., "Modeling of Spacecraft Rarefied Environments Using a Proposed Surface Model," *AIAA Journal*, Vol. 3, No. 4, 1998.
- [80] Karipides, D., Boyd, I., and Caledonia, G., "Detailed Simulation of Surface Chemistry Leading to Spacecraft Glow," *Journal of Spacecraft and Rockets*, Vol. 36, No. 4, 1999.
- [81] Gimelshein, S., Levin, D., and Collins, R., "Modeling of Glow Radiation in the Rarefied Flow about an Orbiting Spacecraft," *Journal of Thermophysics and Heat Transfer*, Vol. 14, No. 4, October–December 2000, pp. 471–479.
- [82] Gimelshein, S., Levin, D., and Collins, R., "Modeling of Infrared Radiation in a Space Transportation System Environment," *AIAA Journal*, Vol. 40, No. 4, 2002, pp. 871–790.
- [83] Swenson, G., Raideren, R., Jennings, D., and Ahmadjian, M., "Vehicle Glow Measurements on Space Transportation System Flight 62," *Journal of Spacecraft and Rockets*, Vol. 33, No. 2, 1995.
- [84] Ahmadjian, M., and Jennings, D., "Analysis of STS-39 Space Shuttle Glow Measurements," *Journal of Spacecraft and Rockets*, Vol. 32, No. 3, May–June 1995.
- [85] Ahmadjian, M., Jennings, D., Mumma, M., Espenak, F., Rice, C., Russell, R., and Green, B., "Infrared Spectral Measurement of Space Shuttle Glow," *Geophysical Research Letters*, Vol. 19, No. 10, 1992.
- [86] Sakai, T., and Sawada, K., "Calculation of Nonequilibrium Radiation from a Blunt Body Shock Layer," *Journal of Thermophysics and Heat Transfer*, Vol. 15, No. 1, 2001.

- [87] Johnston, C. O., Gnoffo, P. A., and Sutton, K. A., "Influence of Ablation on Radiative Heating for Earth Entry," *Journal of Spacecraft and Rockets*, Vol. 46, No. 3, May–June 2009.
- [88] Sheikh, U., Morgan, R., McIntyre, T., and Laux, C., "Through Surface and Across Surface Vacuum Ultraviolet Spectral Measurements in an Expansion Tube," *44th AIAA Thermophysics Conference*, AIAA 2013-2644, June 24–27, 2013, San Diego, CA.
- [89] Porat, H., Sheikh, U., Morgan, R., Eichmann, T., and McIntyre, T., "Vacuum Ultraviolet and Ultraviolet Emission Spectroscopy Measurements for Titan and Mars Atmospheric Entry Conditions," *44th AIAA Thermophysics Conference*, June 24–27, 2013, San Diego, CA AIAA 2013-2770.
- [90] Helber, B., Chazot, O., Magin, T., and Hubin, A., "Space and Time-Resolved Emission Spectroscopy of Carbon Phenolic Ablation in Air and Nitrogen Plasmas," *44th AIAA Thermophysics Conference*, June 24–27, 2013, San Diego, CA AIAA 2013-2770.
- [91] Brandis, A., Wray, A., Liu, Y., Schwenke, D., Carbon, D., Huo, W., and Johnston, C., "Validation of HyperRad for Earth Entries," AIAA 2013-2777, *44th AIAA Thermophysics Conference*, June 24–27, 2013, San Diego, CA.
- [92] Seiff, A., Reese, D. E., Sommer, S. C., Kirk, D. B., Whiting, E. E., and Niemann, H. B., "PAET, An Entry Probe Experiment in the Earth's Atmosphere," *Icarus*, Vol. 18, No. 4, 1973, pp. 525–563.
- [93] Gasser, R. P. H., *An Introduction to Chemisorption and Catalysis by Metals*, Clarendon, Oxford, UK, 1985.

CFD Methods for Hypersonic Flows and Aerothermodynamics

Graham V. Candler*, Pramod K. Subbareddy†, and Ioannis Nompelis†

University of Minnesota, Minneapolis, Minnesota

NOMENCLATURE

A	convective flux Jacobian matrix
a	speed of sound
C, C^{-1}	eigenmatrices
c_{vs}	thermal specific heat of species s
E	total energy per unit volume
E_i	internal energy per unit volume
e	energy per unit mass
F	flux vector
g	damping parameter
h_s^o	heat of formation of species s
I	identity matrix
i	element number
k	kinetic energy, relaxation index
L_s	separation zone length in axial direction
M, N	viscous flux Jacobians
M_s	molecular mass of species s
N_x	number of grid elements in axial direction
\hat{n}	element face-normal unit vector
ns	number of chemical species
n_x, n_y, n_z	components of \hat{n}
p	pressure
\hat{R}	universal gas constant
R, R^{-1}	eigenmatrices
S, S^{-1}	variable transformation Jacobians
S	element face area
T	temperature
T_v	vibrational or internal temperature

*Russell J. Penrose and McKnight Presidential Professor, Fellow AIAA.

†Research Associate, Member AIAA.

t	time
U	conserved variables vector
\vec{u}	velocity vector
u'	velocity component in \hat{n} direction
u, v, w	components of velocity vector
V	primitive variables vector
V	element volume
W	thermochemical source term vector
x	axial or streamwise flow direction
α, β	parameters in higher-order flux formulation
α_d	dissipative flux factor
ϵ	eigenvalue limiter
ϕ	general scalar variable
Λ	diagonal matrix of eigenvalues
$\lambda, \lambda^\pm, \tilde{\lambda}, \hat{\lambda}$	eigenvalues
ρ	density
ρ_s	density of species s
ω	weight function

I. INTRODUCTION

The reliable prediction of aerodynamic heating to hypersonic vehicles remains a challenge. There are a number of reasons why aerothermal simulations are difficult. Obviously, heat fluxes require accurate predictions of temperature gradients at the vehicle surface, which is considerably more sensitive to the surface-normal grid resolution than the surface pressure (at least for attached flows). At least as important is the presence of strong shock waves which generate large error when the grid is not shock-aligned. This is particularly obvious in stagnation regions because the error can become trapped near the stagnation point. In extreme cases, the error can dominate the flowfield, causing the shock wave to artificially lens outward and develop a catastrophic breakdown in the numerical solution. Under this condition, the flowfield is unphysical and the predicted surface quantities are meaningless. This problem requires the addition of dissipation to numerical flux functions, the careful alignment or adjustment of the grid to the shock location, and the use of a grid patch in the stagnation region.

The resolution of temperature and other gradients across the boundary layer and at the vehicle surface present additional challenges to the numerical method. The dissipation that is required to control error across the bow shock and in the stagnation region can modify the boundary layer and result in poor heat transfer rate predictions. Furthermore, near-wall grid spacing must be very tight so as to resolve the key gradients; this often results in very large cell aspect ratios (order 10^4 or worse). Thus, the time integration method must converge to steady state

on this type of grid; for unsteady problems, it must be able to run in time-accurate mode at large time steps for practical applications.

Hypersonic and high-enthalpy flows are characterized by complex processes that take place within the gas and as the gas interacts with the surface. At high pressures or relatively slow flow conditions, the thermochemical state adjusts rapidly to the flow state and is close to thermodynamic equilibrium. However, for many aerothermodynamics applications, the flow is not close to equilibrium because the chemical kinetics and relaxation time scales are similar to the flow motion time scales. In this nonequilibrium condition, it is necessary to solve conservation equations for all relevant chemical species and for any gas internal energy states that are not equilibrated with the gas thermal state. The gas-surface boundary conditions can also be complicated because depending on the material properties, the surface may catalyze particular reactions, react with the flowfield gas, and inject ablation species into the flow. In the most general case, the surface mass and energy balance equations are very complicated, involving all aspects of transport to and from the surface. Thus, the surface boundary conditions can be as difficult to implement and to verify as the flowfield conservation equations [1, 2].

Essentially all practical high Mach number flow simulations are performed with second-order accurate upwind numerical fluxes with some form of limiting to control the solution near shock waves and other discontinuities. We present two popular methods and show how they are applied to gases with nontrivial equations of state. For hypersonic flows, standard textbook approaches do not produce reliable solutions for many relevant problems, and we discuss several ways to improve the robustness of the simulations. The key concern is adding dissipation to maintain stability, without adverse effect on the actual flow physics. Typically, this tradeoff becomes more delicate as the Mach number and size of the stagnation region increase.

High accuracy methods for finite volume approaches are being developed for high-speed flows. One such method uses a numerical flux function that is derived to be consistent with the compressible kinetic energy transport equation (unlike incompressible flows, kinetic energy is not a conserved quantity). This flux is inherently more stable than conventional upwind fluxes because it intrinsically limits aphysical undershoots and overshoots of kinetic energy in strong gradient regions. Some stabilization is required by adding upwind dissipation according to a shock/discontinuity detector. The design of this detector is critical for obtaining stable solutions with minimal levels of numerical dissipation.

In this article, we present a basic flux-vector split upwind method for the convective fluxes, and discuss some of its required extensions for the simulation of practical high Mach number flows. This method is compared to other widely used upwind flux methods on a challenging problem involving strong shock waves, shock interactions, and flow separation. This study focuses on second-order accurate methods, and demonstrates the importance of the slope limiter in setting the level of dissipation in a simulation. We then outline the

development of the kinetic energy consistent flux approach and illustrate its ability to resolve vastly larger ranges of length scales than the standard upwind fluxes.

We then turn to the time domain and briefly derive a parallelizable implicit method for compressible reacting flows. Again, special requirements for high Mach number applications are discussed. Finally, we introduce key ideas from recent work that reduce the cost of simulating nonequilibrium reacting flows with large numbers of chemical species.

We focus on finite volume methods because they are the most widely used approach for nontrivial high-speed flow simulations. The discontinuous Galerkin (DG) finite element method may have the potential to be the next generation numerical approach for hypersonic flows because it can produce high order of accuracy on arbitrary grid elements. However, DG has yet to be used for any large-scale practical problems—it may be possible to do so, but its large cost and the requirements for subelement shock/discontinuity capturing currently make it uncompetitive. Of course, there has been vastly more investment in the development of finite volume methods.

II. UPWIND NUMERICAL FLUX FUNCTIONS

In this section, we discuss two numerical flux functions that are widely used for the simulation of hypersonic flows and aerothermodynamics. In general, these methods are mostly used for steady-state applications in which the flow is either fully laminar or is modeled with a Reynolds-averaged Navier–Stokes (RANS) turbulence model. There are many other types of numerical flux methods in the literature, and some have been successfully applied to complex geometry high Mach number flows. For example, the AUSM+ class of schemes [3, 4] has some properties that make it an interesting candidate for hypersonic flows, and the weighted essentially nonoscillatory (WENO) methods [5] are becoming more widely used for unsteady flows or situations in which high-order of accuracy is required. It is beyond the scope of the present paper to discuss these methods in detail. However, the following derivation of the flux Jacobians and the discussion issues associated with the practical implementation of flux functions is applicable to most numerical methods for high Mach number flows.

The governing equations for a compressible flow with arbitrary equation of state may be written as

$$\frac{\partial U}{\partial t} + \frac{\partial}{\partial x_j} (F_j + F_{vj}) = W \quad (1)$$

where U is the vector of conserved quantities, F_j and F_{vj} are the inviscid (convective) and viscous fluxes in the j direction, and W is the vector of source terms. U must contain variables that represent the total mass, momentum, and energy per unit volume of the flowfield. It may also include additional quantities such as

species mass and internal energy, depending on the problem of interest. In the following, two important examples are given—a gas that is in local thermodynamic equilibrium, and a mixture of chemically reacting gases with thermal and chemical nonequilibrium.

In the following analysis, it is convenient to consider the convective flux normal to a grid element surface. That is, we define $F = F_j n_j$, where n_j is the unit surface-normal vector at an element face.

A. UPWIND FLUX METHODS

Consider the upwind evaluation of the inviscid flux vector F at a grid surface; here let the vector of conserved variables be given by U . We can use the classic Steger–Warming flux-vector splitting approach [6] to obtain the forward and backward moving fluxes, F^+ and F^-

$$F = F^+ + F^- = R^{-1} \Lambda^+ R U + R^{-1} \Lambda^- R U \quad (2)$$

where R^{-1} and R are the left and right eigenvector matrices, and Λ is the diagonal matrix of eigenvalues of the flux Jacobian, that is

$$\frac{\partial F}{\partial U} = A = R^{-1} \Lambda R \quad (3)$$

Here, Λ^+ and Λ^- are the elements of Λ that are positive and negative, respectively.

If we apply this method at a cell face denoted by the index $i + 1/2$, with the left cell denoted by i and the right cell by $i + 1$, we bias the evaluation of the fluxes in the upwind direction

$$F_{i+1/2} = (R^{-1} \Lambda^+ R)_i U_i + (R^{-1} \Lambda^- R)_{i+1} U_{i+1} \quad (4)$$

This original Steger–Warming formulation is known to be highly dissipative and gives poor predictions of gradients in shear layers. However, we can improve the method with a small change—by evaluating the eigenvalues and eigenvectors at the same location:

$$F_{i+1/2} = (R^{-1} \Lambda^+ R)_{i+1/2} U_i + (R^{-1} \Lambda^- R)_{i+1/2} U_{i+1} \quad (5)$$

where the subscript $i + 1/2$ indicates an average between the data on either side of the cell face. Recognizing that $\Lambda^+ = (1/2)(\Lambda + |\Lambda|)$ and $\Lambda^- = (1/2)(\Lambda - |\Lambda|)$ permits this expression for the flux to be written in a different form:

$$F_{i+1/2} = \frac{1}{2}(R^{-1} \Lambda R)_{i+1/2}(U_{i+1} + U_i) - \frac{1}{2}(R^{-1} |\Lambda| R)_{i+1/2}(U_{i+1} - U_i) \quad (6)$$

Note that because $F = AU = R^{-1}\Lambda RU$, this expression is effectively the combination of a flux based on the unbiased central average and a dissipative upwind flux.

This form of the modified Steger–Warming flux is closely related to the Roe flux, which is given by [7, 8]

$$F_{i+1/2} = \frac{1}{2}(F_{i+1} + F_i) - \frac{1}{2}(\tilde{R}^{-1}|\tilde{\Lambda}|\tilde{R})_{i+1/2}(U_{i+1} - U_i) \quad (7)$$

Where the tilde variables denote the Roe (density-weighted) variables, such as

$$\tilde{u}_{i+1/2} = \frac{\sqrt{\rho_i}u_i + \sqrt{\rho_{i+1}}u_{i+1}}{\sqrt{\rho_i} + \sqrt{\rho_{i+1}}} \quad (8)$$

Thus, the modified Steger–Warming and Roe flux functions differ only in how the variables are averaged across the element face. Both comprise an unbiased central average and a dissipative upwind component.

The computation of the eigenvalues and eigenvectors is simply a matter of algebra, which has been documented in the literature for perfect gases. For example, Rohde [9] derives the complete eigensystem for the three-dimensional (3-D) Euler equations. Below we consider two more general cases: an equilibrium gas mixture with an arbitrary equation of state and a gas composed of a nonequilibrium mixture of reacting thermally perfect gases.

B. EIGENSYSTEM FOR A GAS WITH AN ARBITRARY EQUATION OF STATE

Consider a gas in local thermodynamic equilibrium such that its thermodynamic state is uniquely determined by its elemental composition and two thermodynamic variables. The solution of the Euler or Navier–Stokes equations usually provides the density, ρ , the momentum per unit volume, $\rho\vec{u}$, and the total energy per unit volume, E . The internal energy per unit mass, e , can be obtained from

$$E = \rho e + \frac{1}{2}\rho\vec{u} \cdot \vec{u} \quad (9)$$

Thus, we have two thermodynamic variables, ρ and e . To close the system of equations, we require an expression for the pressure as a function of these two variables. In the most general form, we have:

$$p = p(\rho, e) \quad (10)$$

Where p could have a closed-form expression, such as the excluded volume equation of state, an algebraic expression fitted to theory and experimental data, or could be the result of minimizing the free energy for an arbitrary reacting gas. Here, let us assume that we have some means for evaluating this function for the problem of interest.

The vector of conserved variables and convective flux for a 3-D flow are given by

$$U = \begin{pmatrix} \rho \\ \rho u \\ \rho v \\ \rho w \\ E \end{pmatrix}, \quad F = \begin{pmatrix} \rho u' \\ \rho uu' + p n_x \\ \rho vu' + p n_y \\ \rho wu' + p n_z \\ (E + p)u' \end{pmatrix} \quad (11)$$

Here, we have taken F to be the component of the flux vector in the element face-normal direction, where $\hat{n} = n_x \vec{i} + n_y \vec{j} + n_z \vec{k}$ is the unit vector in that direction. The velocity in the face-normal direction is $u' = \vec{u} \cdot \hat{n}$.

It is convenient to define an additional vector of flowfield variables as

$$V = \begin{pmatrix} \rho \\ u \\ v \\ w \\ p \end{pmatrix} \quad (12)$$

These are commonly referred to as the primitive variables. Using the chain rule of differentiation, we can write the Jacobian of the flux vector as

$$A = \frac{\partial F}{\partial U} = \frac{\partial U}{\partial V} \frac{\partial V}{\partial U} \frac{\partial F}{\partial V} \frac{\partial V}{\partial U} = S^{-1} C^{-1} \Lambda C S \quad (13)$$

It is considerably easier to diagonalize the matrix $(\partial V / \partial U)(\partial F / \partial V)$ than the Jacobian expressed in terms of the conserved variables. We then construct the left and right eigenvector matrices with $R^{-1} = S^{-1} C^{-1}$ and $R = CS$.

Now, we can simply differentiate each term in this expression, diagonalize the system, and then multiply the results together to obtain the eigensystem. For example, we obtain

$$S = \frac{\partial V}{\partial U} = \begin{pmatrix} 1 & 0 & 0 & 0 & 0 \\ -u/\rho & 1/\rho & 0 & 0 & 0 \\ -v/\rho & 0 & 1/\rho & 0 & 0 \\ -w/\rho & 0 & 0 & 1/\rho & 0 \\ p_\rho & p_{\rho u} & p_{\rho v} & p_{\rho w} & p_E \end{pmatrix},$$

$$S^{-1} = \frac{\partial U}{\partial V} = \begin{pmatrix} 1 & 0 & 0 & 0 & 0 \\ u & \rho & 0 & 0 & 0 \\ v & 0 & \rho & 0 & 0 \\ w & 0 & 0 & \rho & 0 \\ E_\rho & E_u & E_v & E_w & E_p \end{pmatrix} \quad (14)$$

Here the subscripts on p and E represent the partial derivatives with respect to each variable, holding the appropriate variables fixed.

Returning to our description of the gas, we assumed that we could express the pressure in terms of the density and internal energy, $p = p(\rho, e)$. In order to evaluate the derivatives in the matrices above, we also need the derivatives of the pressure in the form: $\partial p / \partial \rho|_e$, $\partial p / \partial e|_\rho$. These expressions can be obtained by differentiating the expression for pressure for the given thermodynamic model, or in the case of free energy minimization, they are a result of the equilibrium state computation.

Using the definitions of the variables, we can evaluate the derivatives in (13) as

$$\begin{aligned} p_\rho &= \frac{\partial p}{\partial \rho} \Big|_{\rho u, \rho v, \rho w, E} = \frac{\partial p}{\partial \rho} \Big|_e - \frac{e}{\rho} \frac{\partial p}{\partial e} \Big|_\rho + \frac{1}{2} \vec{u} \cdot \vec{u} \frac{1}{\rho} \frac{\partial p}{\partial e} \Big|_\rho \\ p_{\rho u} &= \frac{\partial p}{\partial u} \Big|_{\rho, \rho v, \rho w, E} = - \frac{u}{\rho} \frac{\partial p}{\partial e} \Big|_\rho \\ p_{\rho v} &= \frac{\partial p}{\partial v} \Big|_{\rho, \rho u, \rho w, E} = - \frac{v}{\rho} \frac{\partial p}{\partial e} \Big|_\rho \\ p_{\rho w} &= \frac{\partial p}{\partial w} \Big|_{\rho, \rho u, \rho v, E} = - \frac{w}{\rho} \frac{\partial p}{\partial e} \Big|_\rho \\ p_E &= \frac{\partial p}{\partial E} \Big|_{\rho, \rho u, \rho v, \rho w} = \frac{1}{\rho} \frac{\partial p}{\partial e} \Big|_\rho \end{aligned} \quad (15)$$

$$\begin{aligned} E_\rho &= \frac{\partial E}{\partial \rho} \Big|_{u, v, w, p} = e - \rho \frac{\partial p}{\partial \rho} \Big|_e \left(\frac{\partial p}{\partial e} \Big|_\rho \right)^{-1} + \frac{1}{2} \vec{u} \cdot \vec{u} \\ E_u &= \frac{\partial E}{\partial u} \Big|_{\rho, v, w, p} = \rho u \\ E_v &= \frac{\partial E}{\partial v} \Big|_{\rho, u, w, p} = \rho v \\ E_w &= \frac{\partial E}{\partial w} \Big|_{\rho, u, v, p} = \rho w \\ E_p &= \frac{\partial E}{\partial p} \Big|_{\rho, u, v, w} = \rho \left(\frac{\partial p}{\partial e} \Big|_\rho \right)^{-1} \end{aligned} \quad (16)$$

Thus, we can express the derivatives of the flow variables in terms of the thermodynamic state.

The resulting diagonal matrix of eigenvalues is given as

$$\Lambda = \text{diag}(\lambda, \lambda^+, \lambda, \lambda, \lambda^-) \quad (17)$$

where $\lambda = u'$, $\lambda^+ = u' + a$, $\lambda^- = u' - a$, and a is the speed of sound. This is exactly what is expected, but for the arbitrary gas, the diagonalization gives the expression for the equilibrium speed of sound:

$$\rho a^2 = \frac{p}{\rho} \frac{\partial p}{\partial e} \Big|_e + \rho \frac{\partial p}{\partial \rho} \Big|_e \quad (18)$$

which is consistent with the results of equilibrium thermodynamics.

The left and right eigenvector matrices of the intermediate Jacobian are:

$$C^{-1} = \begin{pmatrix} 1 & 1/a^2 & 0 & 0 & 1/a^2 \\ 0 & n_x/\rho a & -n_y/n_x & -n_z/n_x & -n_x/\rho a \\ 0 & n_y/\rho a & 1 & 0 & -n_y/\rho a \\ 0 & n_z/\rho a & 0 & 1 & -n_z/\rho a \\ 0 & 1 & 0 & 0 & 1 \end{pmatrix} \quad (19)$$

$$C = \begin{pmatrix} 1 & 0 & 0 & 0 & -1/a^2 \\ 0 & \rho a n_x/2 & \rho a n_y/2 & \rho a n_z/2 & 1/2 \\ 0 & -n_x n_y & 1 - n_y^2 & -n_y n_z & 0 \\ 0 & -n_x n_z & -n_y n_z & 1 - n_z^2 & 0 \\ 0 & -\rho a n_x/2 & -\rho a n_y/2 & -\rho a n_z/2 & 1/2 \end{pmatrix} \quad (20)$$

The intermediate diagonalized matrix, $C^{-1} \Lambda C$, can be written in compact form by defining combinations of eigenvalues as:

$$\tilde{\lambda} = \frac{1}{2}(\lambda^+ - \lambda^-), \quad \hat{\lambda} = \frac{1}{2}(\lambda^+ + \lambda^- - 2\lambda) \quad (21)$$

Then we have:

$$C^{-1} \Lambda C = \begin{pmatrix} 0 & \rho n_x \tilde{\lambda} / a & \rho n_y \tilde{\lambda} / a & \rho n_z \tilde{\lambda} / a & \hat{\lambda} / a^2 \\ 0 & n_x n_x \hat{\lambda} & a n_x n_y \hat{\lambda} & n_x n_z \hat{\lambda} & n_x \hat{\lambda} / \rho a \\ 0 & n_y n_x \hat{\lambda} & a n_y n_y \hat{\lambda} & n_y n_z \hat{\lambda} & n_y \hat{\lambda} / \rho a \\ 0 & n_z n_x \hat{\lambda} & a n_z n_y \hat{\lambda} & n_z n_z \hat{\lambda} & n_z \hat{\lambda} / \rho a \\ 0 & \rho a n_x \tilde{\lambda} & \rho a n_y \tilde{\lambda} & \rho a n_z \tilde{\lambda} & \hat{\lambda} \end{pmatrix} + \lambda I \quad (22)$$

Note that considerable simplification to this expression occurs if we substitute the above expressions for the eigenvalues, as shown in Reference [10] for a one-dimensional (1-D) problem. However, for practical high Mach number applications we will see that it is necessary to modify the eigenvalues to reduce error accumulation in stagnation regions. Thus, we must explicitly carry the eigenvalues in the derivation.

The diagonalized flux Jacobian can be constructed by pre-multiplying by S^{-1} and post-multiplying by S . The final result can be expressed as the product of two

column and row vectors:

$$S^{-1}C^{-1}\Lambda CS = \begin{pmatrix} \hat{\lambda}/a^2 \\ (u\hat{\lambda} + an_x\tilde{\lambda})/a^2 \\ (v\hat{\lambda} + an_y\tilde{\lambda})/a^2 \\ (w\hat{\lambda} + an_z\tilde{\lambda})/a^2 \\ (h_0\hat{\lambda} + au'\tilde{\lambda})/a^2 \end{pmatrix} \begin{pmatrix} p_p & -up_E & -vp_E & -wp_E & p_E \end{pmatrix}$$

$$+ \begin{pmatrix} \tilde{\lambda}/a \\ u\tilde{\lambda}/a + n_x\hat{\lambda} \\ v\tilde{\lambda}/a + n_y\hat{\lambda} \\ w\tilde{\lambda}/a + n_z\hat{\lambda} \\ h_o\tilde{\lambda}/a + u'\hat{\lambda} \end{pmatrix} \begin{pmatrix} -u' & n_x & n_y & n_z & 0 \end{pmatrix} + \lambda I \quad (23)$$

where $h_o = e + p/\rho + \frac{1}{2}\vec{u} \cdot \vec{u}$ is the total enthalpy per unit mass. This is a closed-form expression for the diagonalized flux vector Jacobian for a 3-D flow of a gas with an arbitrary equation of state.

Note that for the modified Steger-Warming approach, we require that the flux vector can be written as $F^\pm = A^\pm U$, as in (1). However, for an arbitrary equation of state this is not always true. In this case, we follow the approach of Liou et al. [11] and construct a Jacobian matrix, A_e , such that $F = A_e U$ and define A_ρ such that $A = A_e + A_\rho$. Then we have $F = A_e U = AU - A_\rho U = A^+ + A^- - A_\rho U$ where we have diagonalized A , as discussed above. The Jacobians A_e and A_ρ can be found by considering the form of AU as compared the actual flux, F . See Reference [12] for a specific example.

C. EIGENSYSTEM FOR A CHEMICALLY REACTING MIXTURE OF PERFECT GASES

The above derivation applies to an equilibrium gas mixture with an arbitrary equation of state. This gas could be chemically reacting, but the chemical reaction time scales would have to be small relative to the flow time scales, so that the gas mixture is in local thermodynamic equilibrium. In this section, we consider a mixture of gases that are undergoing chemical reactions at reaction time scales similar to the flow time scale. In this nonequilibrium situation, we must solve conservation equations for each chemical species to track the variation of the chemical state.

In high-enthalpy flows, it is also common for the internal energy modes to lag the variation of the thermal (translational) energy state. Thus, we consider a gas with internal energy relaxation, which necessitates the solution of an internal energy conservation equation.

If we assume that the gas is composed of a mixture of thermally perfect gases, we can write the equations of state as:

$$p = \sum_s \rho_s \frac{\hat{R}}{M_s} T, \quad E = \sum_s \rho_s c_{vs} T + E_i + \sum_s \rho_s h_s^o + \frac{1}{2} \rho \vec{u} \cdot \vec{u} \quad (24)$$

where ρ_s is the density of species s and the summations are over all species. The universal gas constant is \hat{R} , the species molecular mass is M_s , the temperature that characterizes the thermal motion of the gas is T , the specific heat for the thermal modes is c_{vs} , the internal energy is $E_i = \rho e_i$, and the heat of formation of species s is h_s^o . A commonly used model is to assume that the translational and rotational modes are in equilibrium with one another, resulting in a translational–rotational energy. In this case, c_{vs} would be the translational–rotational specific heat of species s . The internal energy is often assumed to be the gas mixture vibrational energy, characterized by a single vibrational temperature, T_v . A more sophisticated model would treat the internal energy as the vibrational and electronic energy, assuming that these energy modes are equilibrated at the internal energy temperature. In some cases, it may be necessary to include more than one internal energy equation; the following derivation is easily extended to this case.

The vector of conserved variables and flux vector for this flow are:

$$U = \begin{pmatrix} \rho_1 \\ \vdots \\ \rho_{ns} \\ \rho u \\ \rho v \\ \rho w \\ E_i \\ E \end{pmatrix}, \quad F = \begin{pmatrix} \rho_1 u' \\ \vdots \\ \rho_{ns} u' \\ \rho u u' + p n_x \\ \rho v u' + p n_y \\ \rho w u' + p n_z \\ E_i u' \\ (E + p) u' \end{pmatrix} \quad (25)$$

Most of the pressure and energy derivatives are straight-forward, except for those with respect to the species densities; these are given by:

$$\begin{aligned} p_{\rho_s} &= \frac{\partial p}{\partial \rho_s} \Big|_{\rho_{r \neq s}, \rho u, \rho v, \rho w, E_i, E} = \left(\frac{\hat{R}}{M_s} - c_{vs} p_E \right) T + \left(\frac{1}{2} \vec{u} \cdot \vec{u} - h_s^o \right) p_E \\ E_{\rho_s} &= \frac{\partial E}{\partial \rho_s} \Big|_{\rho_{r \neq s}, u, v, w, e_i, p} = \left(c_{vs} - \frac{\hat{R}}{M_s} E_p \right) T + e_i + \frac{1}{2} \vec{u} \cdot \vec{u} + h_s^o \end{aligned} \quad (26)$$

The derivation of the eigensystem follows the same approach as discussed above. We obtain the expression:

$$S^{-1}C^{-1}\Lambda CS = \begin{pmatrix} (\rho_1/\rho)\hat{\lambda}/a^2 \\ \vdots \\ (\rho_{ns}/\rho)\hat{\lambda}/a^2 \\ (u\hat{\lambda} + an_x\tilde{\lambda})/a^2 \\ (v\hat{\lambda} + an_y\tilde{\lambda})/a^2 \\ (w\hat{\lambda} + an_z\tilde{\lambda})/a^2 \\ e_i\hat{\lambda}/a^2 \\ (h_o\hat{\lambda} + au'\tilde{\lambda})/a^2 \end{pmatrix} (p_{\rho_1} \cdots p_{\rho_{ns}} - up_E - vp_E - wp_E - p_E \quad p_E) \\ + \begin{pmatrix} (\rho_1/\rho)\tilde{\lambda}/a \\ \vdots \\ (\rho_{ns}/\rho)\tilde{\lambda}/a \\ u\tilde{\lambda}/a + n_x\hat{\lambda} \\ v\tilde{\lambda}/a + n_y\hat{\lambda} \\ w\tilde{\lambda}/a + n_z\hat{\lambda} \\ e_i\tilde{\lambda}/a \\ h_o\tilde{\lambda}/a + u'\hat{\lambda} \end{pmatrix} (-u' \cdots -u' \quad -n_x \quad n_y \quad n_z \quad 0 \quad 0) + \lambda I \quad (27)$$

With this gas model, a is the frozen speed of sound given by

$$a^2 = \left(1 + \frac{\bar{R}}{c_v}\right)\bar{R}T \quad (28)$$

where $\bar{R} = \sum_s (\rho_s/\rho)(\hat{R}/M_s)$ and $c_v = \sum_s (\rho_s/\rho)c_{vs}$ are the mass-averaged gas constant and thermal specific heat.

D. HIGHER-ORDER, ADDED DISSIPATION, AND LIMITING

There are a number of issues that arise when the above flux functions are applied to practical high Mach number flows on nonideal grids. The standard textbook flux formulation may work beautifully on standard 1-D test problems, but fail miserably when applied to an actual problem. This is especially true for multidimensional high-Mach number flows because it is impossible to design a grid that will be well aligned with strong shock waves, without first computing a solution. Thus, it is necessary that the flux functions produce physically-meaningful solutions on nonideal grids. However, the numerical method should not be required to work on *any* grid. For example, if a grid has massive changes in spacing at

critical locations in the flow, the method should not be expected to work—in fact, it may be preferable that it fails so as to provide a signal that the grid is of poor quality. In this section, we discuss the main difficulties that are encountered when computing realistic high Mach number flows and provide approaches for their resolution.

As written above, the upwind flux functions result in a method that is first-order accurate in space. Such a method is extremely dissipative and cannot be used for practical problems. To obtain second-order accuracy, a MUSCL (Monotone Upwind Schemes for Conservation Laws) [13] approach is usually used. In the case of the Roe flux, we first write (1) as

$$F_{i+1/2} = \frac{1}{2} [F(U^L) + F(U^R) - (\tilde{R}^{-1} |\tilde{\Lambda}| \tilde{R})_{i+1/2} (U^R - U^L)] \quad (29)$$

where U^L and U^R are higher-order estimates of the left and right data. For example, on a 1-D grid we could use the simple extrapolations to the $i+1/2$ face using neighboring data

$$\begin{aligned} U^L &= \frac{3}{2} U_i - \frac{1}{2} U_{i-1} \\ U^R &= \frac{3}{2} U_{i+1} - \frac{1}{2} U_{i+2} \end{aligned} \quad (30)$$

This would produce a second-order accurate numerical flux.

This numerical flux function is useless as written because it produces spurious unphysical overshoots and undershoots in the solution near strong gradients. Therefore, the left and right data must be limited so that new extrema are not produced. This is usually achieved by comparing changes in the solution, and taking a conservative value of the change. For example,

$$\begin{aligned} \tilde{U}^L &= U_i + \frac{1}{2} \text{limit}(\Delta U_{i-1/2}, \Delta U_{i+1/2}) \\ \tilde{U}^R &= U_{i+1} - \frac{1}{2} \text{limit}(\Delta U_{i+1/2}, \Delta U_{i+3/2}) \end{aligned} \quad (31)$$

where we are using a limiter to compare the changes in the solution at neighboring grid points; here $\Delta U_{i+1/2} = U_{i+1} - U_i$. Ideally, the limiter will detect an unphysical solution near a strong gradient and modify U^L and U^R to keep the flux physically meaningful. In general, this means that the flux function reverts to first-order accuracy in some regions of the flow. Clearly, the limiter should not be overly sensitive, because the solution could become only first-order accurate in the part of the flowfield that is of interest. Particularly for hypersonic flows, the choice of this limiter is crucial.

A widely used limiter is the minmod function which takes the smaller (in magnitude) of two arguments if they have the same sign, otherwise it returns zero. There are many other limiters available [14], each of which produces different

behavior on a particular problem. It is often tempting to use the most dissipative limiter because it will typically produce the best convergence to a steady state solution. However, this can have detrimental effects on the solution quality.

For high Mach number flows with strong shock waves, we must add dissipation to control numerical error. If the normal Mach number at a shock is greater than about 6, numerical error can overwhelm the flow physics and destroy a simulation. For example, in the stagnation region of a blunt body, numerical error can accumulate, forming a so-called carbuncle in which the shock wave lenses upstream and a large, unphysical recirculation region appears [15]. The usual way to prevent this problem is to align the grid with the primary bow shock wave to reduce error, and then to limit the eigenvalues that appear in the dissipative component of the flux. In particular, the eigenvalues are prevented from approaching zero via a function like:

$$\lambda' = \frac{1}{2} \left(\lambda \pm \sqrt{\lambda^2 + \epsilon^2} \right) \quad (32)$$

where λ is any one of the elements of Λ , and the sign is chosen depending on whether the eigenvalue is positive or negative (contributes to Λ^+ or Λ^- , respectively). The limiting value as λ approaches zero is $\epsilon = \epsilon_o a$, and ϵ_o is chosen large enough to keep the solution from becoming a physical in stagnation regions; typically, $0.1 \leq \epsilon_o \leq 0.3$. It should be noted that this type of eigenvalue limiting must not be performed in boundary layers because it induces an artificial flux across the boundary layer. This limiting is effective in stagnation regions because it prevents the $\lambda = u'$ eigenvalue from becoming zero as u' approaches zero. It is interesting that this modification is related to the entropy fix and sonic glitch correction applied to upwind methods at sonic points.

For very strong shock waves, even the first-order accurate form of the upwind fluxes may produce unphysical results, particularly on multidimensional grids with poor shock alignment. One approach to address this problem for the modified Steger–Warming flux is to make the flux expression revert to the original dissipative form of the flux in regions of strong pressure gradient. That is, we will smoothly transition from the flux given in (5) to (4). One such approach is to form a pressure-dependent weighting function that biases the data used to evaluate the Jacobians. Let us rewrite (4) as

$$F_{i+1/2} = (R^{-1} \Lambda^+ R)_+ U_i + (R^{-1} \Lambda^- R)_- U_{i+1} \quad (33)$$

where the data used to evaluate the Jacobians is

$$\begin{aligned} U_+ &= \omega_{i+1/2} U_i + (1 - \omega_{i+1/2}) U_{i+1} \\ U_- &= (1 - \omega_{i+1/2}) U_i + \omega_{i+1/2} U_{i+1} \end{aligned} \quad (34)$$

A typical pressure-dependent weighting function is

$$\omega_{i+1/2} = 1 - \frac{1}{2} \left(\frac{1}{(g\delta p)^2 + 1} \right), \quad \delta p = \frac{p_{i+1} - p_i}{\min(p_i, p_{i+1})} \quad (35)$$

with g a factor to control the sensitivity of the weighting function. From previous experience a value of $0.5 \leq g \leq 5$ produces good results, depending on the flow conditions, geometry, and alignment of the grid with the bow shock wave; larger values of g will increase the level of dissipation in the solution. Such an approach could be adapted to the Roe form of the upwind flux (6).

One additional consideration is which variables should be used in the averaging process. As written above, it is implied that the conserved variables are used to obtain the face-average data. However, in practice this can lead to poor behavior in boundary layers with strong temperature gradients. We favor forming the $i + 1/2$ flow state from the primitive variables (11).

There are many possible combinations of limiters, eigenvalue modifications, and other forms of added dissipation in practical upwind flux schemes. It is therefore critical that the user understand how these choices affect the computational results and the specific quantities of interest.

E. IMPLEMENTATION ON UNSTRUCTURED GRIDS

The above discussion assumes that the grid is ordered in the sense that each face has neighboring elements, and those elements also have neighbors. Furthermore, it is implicitly assumed that these two pairs of neighbors are well aligned so that extrapolations to the face are physically meaningful. In general, this requires a structured grid (or an unstructured grid composed of hexahedra) with a simple topology. This severely limits the geometries that can be represented, even if multiblock grids are used.

It is well known that unstructured tetrahedral grids produce poor answers for high-Mach number flows. We have shown that even first-order accurate methods produce very large numerical error if a tetrahedral grid is used across a strong shock [16]. The error is a result of an imbalance of momentum flux on the sides of a tetrahedral element, resulting in the production of spurious vorticity. Once this vorticity is created at the shock wave, it cannot be removed, even with the application of the forms of dissipation discussed above. Some progress has been made in reducing this source of error with rotated flux evaluation methods [17], but additional work is required to make this approach work on all grids.

For high-Mach number hypersonic flows, most geometries of interest tend to be fairly simple and many problems can be adequately represented by multi-block structured grids. However, this approach often requires compromises in

the grid design and the use of extra grid elements to resolve particular features. We have found that the use of three-point and five-point singularities in the grid topology can be used to alleviate much of these difficulties. It is possible to build grids with embedded refinement regions to capture key features, and to de-refine the grid in less critical regions. This approach may result in a very large number of small grid blocks, making it impossible to use a conventional multiblock structured grid code. Thus, for hypersonic flows the use of an unstructured grid approach is appealing, even if multiblock hexahedral element grids are used.

In this section, we discuss an approach for estimating the flow state at an element face for an unstructured grid approach. Here, we do not assume that the elements are ordered in the i direction in some clear fashion as above. Rather, for a given element, we know the location and values of the neighboring elements, and from this information it is possible to compute the gradient of the solution at each cell center. This can be done with weighted least squares or some other approach [18]. Therefore, at a given face, we are given the data and its gradients at left and right neighbors, and we must construct a higher-order flux from this information.

We use an approach suggested by Darwish and Moukalled [19] that is outlined here. Consider Fig. 1, which shows schematics of triangular and quadrilateral elements. The cell of interest is denoted by C , and assume that we are computing the flux across face f , and thus the flux is moving from C to D . This makes the cell denoted by D the downwind cell, and the point P is a virtual upwind cell centroid. P is located on the same line that connects C and D , and is the same distance from C as D .

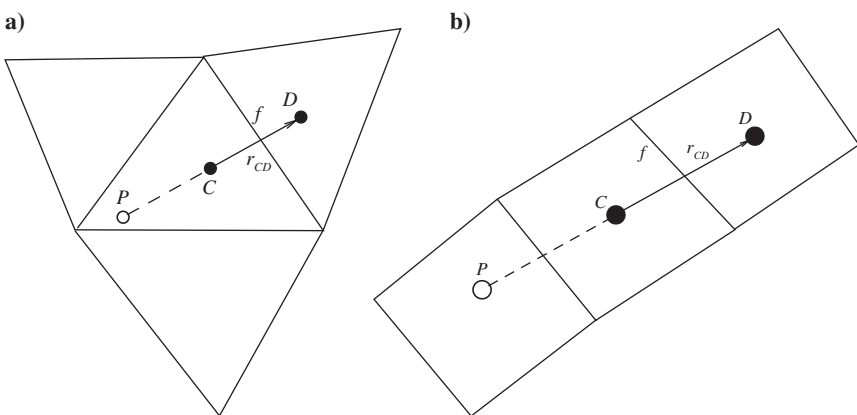


Fig. 1 Schematic of stencil used to extrapolate to cell faces.

We can then compute the value of the solution, U_P , at the virtual point using:

$$U_P = U_C - \nabla U_C \cdot \vec{r}_{CD} = U_D - 2\nabla U_C \cdot \vec{r}_{CD} \quad (36)$$

where ∇U_C is the gradient at C. Now we can form a second-order accurate extrapolation to the face as:

$$\begin{aligned} U_f^L &= U_C + \frac{1}{2}\text{limit}(U_C - U_P, U_D - U_C) \\ &= U_C + \frac{1}{2}\text{limit}(2\nabla U_C \cdot \vec{r}_{CD} - (U_D - U_C), U_D - U_C) \end{aligned} \quad (37)$$

where a limiter is applied to make the scheme total variation diminishing, and a similar approach is used to extrapolate the data from the right side of the face. Here, we have used the latter of the two representations for U_P in (35) because it is more accurate since the gradient is centered at C.

We have found one additional problem with evaluating viscous fluxes on grids with large stretching. In this case, a standard weighted least-squares approach may yield poor gradients, particularly for the viscous terms in the wall-normal direction. In this case, we use the deferred correction approach of Kim et al. [20].

III. LOW-DISSIPATION NUMERICAL FLUX

As is well known, accurate computation of compressible turbulent flow places conflicting demands on numerical algorithms. They must have low levels of numerical dissipation and must be nonlinearly stable; they must be capable of resolving shock waves as well as vortical structures. Negotiating these constraints efficiently with unstructured grid flow solvers that can handle complex geometries is critically important. There are many different ways to approach this issue: ideas that use underlying physical principles to construct or refine numerical schemes are particularly appealing.

Traditionally, compressible flows have been computed using upwind methods, most of which are based on the notion of solving a Riemann problem at each cell-face. These are appealing for a few reasons—they are stable and can capture shocks. However, they have an exorbitant amount of numerical dissipation: this wipes out fine scale features and makes their use in DNS and LES costly. In theory, regions of the flow that contain no discontinuities should be computed using nondissipative, central schemes; numerical sensors can be used to detect shocks and we can restrict the use of upwind schemes to these regions alone. In practice, although it is easy to build accurate, local, shock sensors (Ducros et al. [21]) and hybrid schemes, we must address aliasing errors that result from the nonlinearity of the convective terms in the equations of motion. So-called skew-symmetric schemes or energy-conserving schemes are a class of methods that deal with this issue.

A. SECONDARY CONSERVATION

The notion of using so-called secondary conservation laws is a related idea and has deep roots in the development of computational methods for compressible flow. Although one usually solves a set of conservation equations, typically for mass, momentum and energy, it is easy to show that in addition to these primary quantities, there are infinitely many derived (secondary) variables that obey conservation laws or inequalities. A classical example is the entropy inequality which forms the basis of the mechanism that enables one to pick out the physically relevant solution to nonlinear conservation laws. The challenge is to ensure that these secondary constraints are implicitly obeyed by the discrete solution as well as the differential equations that define them. We focus on kinetic energy as a variable of interest, primarily because the cascade of kinetic energy is a defining physical process in turbulence. If one solves the total energy equation, as most shock capturing methods do, kinetic energy only appears implicitly, as part of the definition of total energy. Although it is not a conserved quantity, it is, in a sense, redundant as the momentum and continuity equations implicitly define its evolution. Enforcing consistency between the flux of kinetic energy as part of the total energy equation and the flux of the same quantity implied by the momentum and continuity equations gives it a form that is strikingly similar to the skew-symmetric scheme. In addition, we can enforce this consistency for the time derivative terms as well and this gives a novel, fully discrete density weighted Crank–Nicolson type of time marching scheme. Recent papers by Jameson [22] and Morinishi et al. [23] focus on kinetic energy conservation as well.

There are other interesting approaches to using the ideas of secondary conservation. Tadmor [24] and Ismail and Roe [25] formulate fluxes that conserve entropy. Honein and Moin [26] also employ the second law of thermodynamics and the entropy equation to build difference schemes that have enhanced stability. Kennedy and Gruber [27] and Pirozzoli [28] deploy innovative splittings of the nonlinear convective terms to derive formulations that are stable.

The development of the kinetic energy consistent scheme is straightforward. Here we focus on the perfect gas 1-D Euler equations; extensions to multidimensional reacting flows are straightforward. Denoting the kinetic energy, $u^2/2$, by k , it is easy to show that for the 1-D Euler equations,

$$-k\left(\frac{\partial \rho}{\partial t} + \frac{\partial \rho u}{\partial x}\right) + u\left(\frac{\partial \rho u}{\partial t} + \frac{\partial \rho u^2}{\partial x}\right) \equiv \frac{\partial \rho k}{\partial t} + \frac{\partial \rho k u}{\partial x} \quad (38)$$

On the left-hand side we see the continuity equation multiplied by $(-k)$ and the momentum equation (ignoring pressure) multiplied by u . The right-hand side of the identity is just the kinetic energy portion of the total energy equation. Note that corresponding equivalences hold for the time derivative and convective

terms separately:

$$-k \frac{\partial \rho u}{\partial x} + u \frac{\partial \rho u^2}{\partial x} \equiv \frac{\partial \rho k u}{\partial x}, \quad -k \frac{\partial \rho}{\partial t} + u \frac{\partial \rho u}{\partial t} \equiv \frac{\partial \rho k}{\partial t} \quad (39)$$

Satisfying the first equality discretely leads to semi-discrete kinetic energy consistent schemes. Using the identity $\Delta k = \bar{u}\Delta u$, where Δ is the jump of some variable across a face and the bar denotes the centered average, we can show that using a flux vector for mass and momentum of the form

$$\rho_f u_f \begin{pmatrix} 1 \\ u \end{pmatrix} \quad (40)$$

for the fluxes of mass and momentum is a sufficient condition for the first identity to be true for finite volume formulations. Here, the reconstructed values of density and velocity at the element face (ρ_f and u_f) are left undetermined, we obtain non-dissipative fluxes if they are symmetric. Satisfying the second equality above leads to fully discrete kinetic energy consistent schemes and the process is only a little more involved. Firstly, observe that a straightforward use of average values in time does not yield a discrete equality, as can be readily verified:

$$-\frac{k^{n+1} + k^n}{2} \cdot \frac{\rho^{n+1} - \rho^n}{\Delta t} + \frac{(u^{n+1} + u^n)}{2} \cdot \frac{(\rho u)^{n+1} - (\rho u)^n}{\Delta t} \neq \frac{(\rho k)^{n+1} - (\rho k)^n}{\Delta t} \quad (41)$$

The key is to find a unique set of values k^* , u^* such that the relation

$$-k^* \frac{\rho^{n+1} - \rho^n}{\Delta t} + u^* \frac{(\rho u)^{n+1} - (\rho u)^n}{\Delta t} \equiv \frac{(\rho k)^{n+1} - (\rho k)^n}{\Delta t} \quad (42)$$

is identically true. We do this by using an idea due to Roe [7]: he constructs an elegant transformation which permits one to express the vector of conserved quantities (and ρk) as quadratic products of terms in a ‘parameter vector’, $Z = \sqrt{\rho}(1 \ u)$. After some algebra, this gives us

$$k^* = \frac{u^{*2}}{2}, \quad u^* = \frac{\sqrt{\rho^{n+1}} u^{n+1} + \sqrt{\rho^n} u^n}{\sqrt{\rho^n} + \sqrt{\rho^{n+1}}} \quad (43)$$

Using this result, the convective fluxes for mass and momentum are now

$$\rho_f u_f \begin{pmatrix} 1 \\ u^* \end{pmatrix} \quad (44)$$

For the full 3-D form of the fluxes and further details see Reference [29]. Note that the fully discrete scheme above is implicit: solution methods must be devised or adapted to solve the resulting system of equations which can be expressed

generically as

$$\frac{U^{n+1} - U^n}{\Delta t} + \frac{1}{V} \sum_f F'_f(U_f^n, U_f^{n+1}) S_f = 0 \quad (45)$$

A simple way is by the explicit iteration

$$U^{n+1,k+1} = U^n - \frac{\Delta t}{V} \sum_f F'_f(U_f^n, U_f^{n+1,k}) S_f \quad (46)$$

where k is an iteration index and we set the initial value $U^{n+1,0} = U^n$. The iteration is stopped when the residual drops below a pre-assigned threshold: typically three to four iterations are sufficient, making the cost similar to that of a multi-stage Runge–Kutta scheme (albeit of second order accuracy). However, the time step allowed is subject to a Courant–Friedrichs–Lewy number restriction such that $\text{CFL} \leq 1$.

Extending implicit schemes to solve the system of equations above is relatively straightforward: typically we linearize the flux around time index n and solve the resulting system of equations. Owing to the nonlinear combination of states at n and $n+1$ in the flux (the density dependence), exact linearization of the flux can be onerous. However, we find that simpler, approximate linearizations perform well in practice. Details can be found in Reference [29] and the discussion in Section IV can be adapted to this approach.

B. POSITIVITY PRESERVING SCHEMES

An important issue with almost all conservative numerical schemes for the Euler schemes is the occurrence of negative values of density or pressure in the solution process. The usual remedy is to change the parameters of the simulation—typically one lowers the time step. A related issue is the occurrence of negative values of transported scalar variables—for simulations of chemically reacting flows on coarse grids, this is an especially critical issue. Recent papers [30, 31] addressing this problem use an interesting flux limiting technique combining the high order flux with one that guarantees positivity (such a Lax–Friedrichs subject to a CFL condition). Extensions and simplifications of this approach show great promise for robust simulations.

C. PRACTICAL IMPLEMENTATION

The kinetic energy consistent flux approach is found to be more stable than would be expected from a method that uses unbiased data to obtain the face data. This is because the approach constrains the flow state to be consistent with the physically allowable variation in the kinetic energy, reducing the overshoots and undershoots in nonsmooth regions. However, for flows with strong shock waves and

other discontinuities, it is necessary to add dissipation (upwind bias) to the numerical flux.

To add dissipation, we can express the flux at the face as the sum of the non-dissipative unbiased kinetic energy consistent flux and the dissipative component discussed above:

$$F_f = F_{f,\text{KEC}} - \alpha_d \frac{1}{2} (R^{-1} |\Lambda| R)_f (U^L - U^R) \quad (47)$$

where $0 \leq \alpha_d \leq 1$ is a discontinuity sensor. As mentioned above, the shock sensor owing to Ducros is effective in many flows. However, for some cases, it may need to be augmented by a Mach number switch or other discontinuity detector. For example, when a cold gas of low molecular weight is injected into a hot high molecular weight stream, the large density gradient may not be identified by the Ducros sensor. The design of the sensor remains an open area of research—not just for the kinetic energy consistent flux scheme, but for all high-order, low-dissipation methods.

D. HIGHER THAN SECOND-ORDER ACCURACY

It is difficult to construct formally high-order schemes on generic unstructured meshes without resorting to more involved formulations such as discontinuous Galerkin methods and other variations on the theme. For finite-volume methods, the situation is slightly better for (unstructured) meshes that use hexahedral elements: if the grid lines are locally smooth enough, we can potentially use stencils and weights that give locally high order fluxes. Note that the onus is now on good grid design. The key to doing this efficiently is to recognize that gradients of the solution variables contain information that extends beyond the local connectivity. Gradients are almost always computed—the viscous fluxes, among other solution elements, depend explicitly on them. As a simple example of using gradient reconstruction, consider a uniform grid (cell size Δx) with minimal connectivity information: cell i can only access cells $i \pm 1$. As we can access the gradient of some variable, ϕ , say, at cells $i \pm 1$, it is possible to construct a flux with a larger stencil than is directly implied by the connectivity alone by linearly combining the neighboring cell gradients and the local solution values:

$$U_{i+1/2} = \alpha(U_i + U_{i+1}) + \beta \Delta x \left(\frac{\partial U}{\partial x} \Big|_i + \frac{\partial U}{\partial x} \Big|_{i+1} \right) \quad (48)$$

Different values of α and β give rise to schemes for which the modified wavenumber is different (alternatively, for fluxes, one can look at the transfer function in Fourier space). These can be adjusted and give some control over the characteristics of the flux derivative. If the connectivity has a larger bandwidth than in the example above, it is easy to iterate on the above notion to construct schemes with larger stencils.

IV. IMPLICIT TIME INTEGRATION

As discussed in the Introduction, realistic hypersonic flows usually require grids with strong stretching near vehicle surfaces. Typical grids may have very large cell aspect ratios, resulting in extremely small time steps if the explicit CFL condition is a binding constraint. Thus, for steady high-Reynolds number hypersonic flows, explicit time integration methods are essentially useless and implicit methods must be used. And for many unsteady flows, time-accurate implicit methods are required. In this section, we briefly discuss an implicit parallelizable line-relaxation method that has been shown to be effective for a wide class of problems. There are many other available methods; however, our experience is that because of the dominance of the near-wall flow physics in hypersonic flows, line-relaxation methods are the most effective for steady flows. For unsteady applications, the line-relaxation biases the solution, and a different type of method must be used [33].

Popular implicit methods for aerothermodynamics solve the governing equations in a fully-coupled fashion. That is, the species mass conservation equations, momentum equations, internal energy equation(s), and total energy equation are all solved simultaneously as one large linear system of equations. For example, the data-parallel line-relaxation method [2] requires the solution of block tridiagonal systems of equations, where the blocks have dimension of $(ns + 5) \times (ns + 5)$, assuming a 3-D problem with a single internal energy equation, and ns is the number of chemical species. This line-relaxation approach gives excellent convergence to steady-state, but the cost of the block tridiagonal solution scales quadratically with the number of equations being solved. The popular LAURA implicit method of Gnoffo [34] has similar quadratic scaling. Furthermore, these methods typically require the storage of up to seven large Jacobian matrices, which incurs large memory costs.

There are a number of approaches in the literature that attempt to reduce the quadratic cost of implicit methods for hypersonic flows. For example, Bussing and Murman [35] developed a semi-implicit approach in which the convective fluxes were computed explicitly and the chemical source term was solved implicitly, reducing issues with stiffness. Park and Yoon [36] developed an approach that takes advantage of elemental conservation to reduce the cost of the matrix inversion, though their approach is difficult to extend to arbitrary chemical kinetics models. Eberhardt and Imlay [37] proposed a modification to these methods to eliminate the need for the matrix inversion by replacing the full source term Jacobian with a diagonal matrix. This approach is appealing because it has a very low operation count, but it is not robust and may result in lack of elemental conservation owing to large disparities in chemical time scales. These approaches suffer from poor convergence on highly stretched grids owing to the approximations made in the development of the underlying implicit methods. Other, more recent

approaches for aerothermal and reacting flow simulations use multigrid approaches and approximations to the source term Jacobian to reduce simulation costs [38]. In work related to the approach discussed here, Schwer et al. [39] developed a operator splitting approach that involves a chemical state time integration followed by a fluid dynamic time integration. Recently, Katta and Roquemore [40] developed a semi-implicit method for very large chemical kinetics models, in which a portion of the source term Jacobian is included in the time integration.

A. DATA-PARALLEL LINE-RELAXATION

Consider an implicit time integration method, in which we evaluate the fluxes and source vector at the future time level. In finite-volume form, the governing equations may be written as

$$\frac{\partial U^n}{\partial t} + \frac{1}{V} \sum_f (F^{n+1} S)_f = W^{n+1} \quad (49)$$

where the summation is over the faces of the element, V is the volume of the element and S is the face area. We linearize using

$$\begin{aligned} F^{n+1} &\simeq F^n + \frac{\partial F^n}{\partial U} \delta U^n \\ W^{n+1} &\simeq W^n + \frac{\partial W^n}{\partial U} \delta U^n \end{aligned} \quad (50)$$

With $\delta U^n = U^{n+1} - U^n$. Then the discrete form of the conservation equation becomes

$$\frac{\delta U^n}{\Delta t} + \frac{1}{V} \sum_f (A_f^+ \delta U^L + A_f^- \delta U^R)^n S_f - \frac{\partial W^n}{\partial U} \delta U^n = -\frac{1}{V} \sum_f (F^n S)_f + W^n \quad (51)$$

This linear system of equations can be solved with a variety of methods; one approach is the data-parallel line-relaxation (DPLR) method [32]. This approach solves a line-relaxation problem along lines of elements near solid surfaces; the off-line terms on the left-hand side of the equation are updated during the relaxation process. For a structured grid, lines usually correspond to one of the computational coordinates, and for an unstructured grid they are constructed by starting at the surface and finding the connected hexahedral or prismatic elements in the direction away from the surface. The

DPLR method involves a series of relaxation steps for δU^n and can be written as:

$$\delta U^{(0)} = 0$$

for $k = 1, k_{\max}$

$$\begin{aligned} \frac{\delta U^{(k)}}{\Delta t} + \frac{1}{V} \sum_{f=\ell} (A_f^+ \delta U^L + A_f^- \delta U^R)^{(k)} S_f - \frac{\partial W^n}{\partial U} \delta U^{(k)} \\ = -\frac{1}{V} \sum_f (F^n S)_f + W^n - \frac{1}{V} \sum_{f \neq \ell} (A_f^+ \delta U^L + A_f^- \delta U^R)^{(k-1)} S_f \quad (52) \end{aligned}$$

end

$$\delta U^n = \delta U^{(k_{\max})}$$

where $f = \ell$ indicates the contribution to the left-hand side of the implicit problem owing to the change in the solution on the line of elements. Note that because the implicit problem solves along a line of elements, δU^L and δU^R involve each element and two of its neighbors. However, in practice we include only the Jacobian associated with the immediate neighbors for the implicit problem. This results in a block tridiagonal system of equations to be solved for each line of δU . If it is not possible to construct lines due to the grid topology or regions of tetrahedral elements, the line length is taken as one, and the method reverts to a locally point-wise relaxation method. Here, k_{\max} is the number of relaxation steps, which is typically taken as 4 for optimal convergence [32].

Here we have not included the viscous fluxes, however it is straight-forward to do so [32]. The approach is to linearize the $n + 1$ viscous flux, F_v^{n+1} as:

$$F_v^{n+1} = F_v^n + \delta F_v^n \simeq F_v^n + M \frac{\partial}{\partial \eta} (N \delta U) \quad (53)$$

where η is the direction normal to the face, and M and N are Jacobian matrices. This results in additional matrices added to the inviscid flux vector Jacobians in the above expression; this does not change the structure of the implicit problem to be solved.

The line relaxation approach is particularly effective for high-Reynolds number flows where the near-wall boundary layer must be resolved with highly stretched grids. It has been shown that this method can be run at large time steps and converges to the steady-state solution in a number of time steps that is essentially independent of the Reynolds number or the wall-normal grid stretching. The line-relaxation approach is much less expensive than solving the full linear system of equations. Recent work has compared this method to a direct solve using the preconditioned Generalized Method of Residuals

(GMRes) [41, 42]. It was found that the DPLR method is less costly except for certain problems where it is difficult or impossible to construct grids with lines of grid elements in the wall-normal direction.

B. DECOUPLED IMPLICIT METHOD

Recently, we have developed a decoupled implicit method that significantly reduces the cost of steady high Mach number simulations, while retaining the excellent convergence properties of the fully coupled line-relaxation approach [43]. We show that the cost of this approach has nearly linear scaling with the number of species in the chemical kinetics model. Furthermore, it requires the storage of just one large Jacobian matrix, which significantly reduces the memory requirements. With this method, the computational costs are dominated by the evaluation of the chemical source term and its Jacobian matrix.

The concept of the proposed method is to separate the mass, momentum, and energy equations from the species mass and internal energy equations. The first set of equations is solved with the DPLR method, involving the solution of 5×5 (for three dimensions) block tridiagonal systems. Then, the implicit problem for the species mass and internal energy equations is approximated, resulting in a scalar tridiagonal system of equation.

This drastically reduces the cost of the implicit system solution. This decoupled, modified DPLR method has been shown to produce similar convergence behavior for several reacting hypersonic flows and aerothermal problems [43]. Its performance does suffer somewhat when the chemical time scales are very small relative to the flow time scales; in these cases, it may be necessary to revert to the original DPLR method.

V. TEST CASE: DOUBLE-CONE FLOW

The hypersonic flow over a double-cone geometry produces many of the complex phenomena—such as shock/boundary-layer interactions, shock triple points, recirculation zones—that take place in hypersonic flows. Figure 2 shows a schematic diagram of a double-cone flowfield. The attached leading edge shock wave interacts with a detached bow shock wave formed from the second cone, and this interaction produces a transmitted shock wave that impinges on the second cone surface. This produces very high surface pressures and heat transfer rates on the second cone; the flow separates near the cone-cone juncture and a recirculation zone develops, which in turn alters the shock interaction. The size of the separation zone is very sensitive to the shock angles and to the strength of the shock interaction. Downstream of the shock impingement location, a supersonic jet develops near the second cone surface.

The double-cone flow was designed as a CFD validation test case with fully laminar flow and minimal effects of vibrational relaxation and chemical reactions [44].

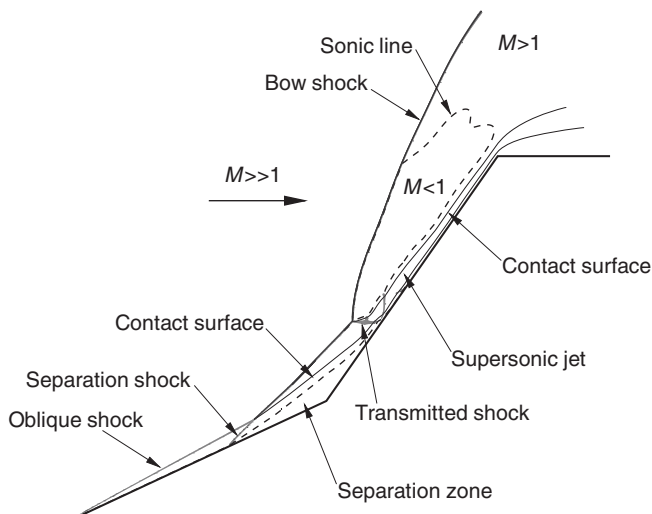


Fig. 2 Schematic of the hypersonic double-cone flow showing key flow features.

It has been shown that to accurately reproduce the experimental data, the vibrational nonequilibrium in the tunnel free-stream and weak accommodation of vibrational energy to the surface must be included in the simulations [45]. Rather, we focus on the numerical issues associated with simulating the double-cone flow, and neglect the physical modeling aspects of the problem. Therefore, we are not attempting to reproduce experimental measurements, but rather to use the double-cone flow as a test case for understanding the properties of a variety of popular numerical schemes. We show that the prediction of the shock interaction and the separation zone are very sensitive to the level of numerical dissipation, which depends on the accuracy of the numerical schemes and on the grid resolution. We show that the separation zone length can be used to quantitatively measure the accuracy of a numerical solution. See Reference [46] for more details.

The flow conditions were obtained from the 25° - 55° double-cone experiments of Holden and Wadham [47]. We study Run 35, with free-stream conditions $T_\infty = 138.9$ K, $\rho_\infty = 5.515 \times 10^{-4}$ kg/m³, and $u_\infty = 2713$ m/s; the wall temperature is fixed at 296.1 K. These conditions correspond to a Mach number of 11.30 and a unit Reynolds number of 133, 300 m⁻¹. The double-cone geometry has two conical sections of 10.16 cm surface length. For this model scale and free-stream conditions, the flow reaches a steady-state during the test time and the flow is completely laminar. This is supported by analysis of the shear layer Reynolds numbers, the number of characteristic flow times, and the excellent agreement obtained with laminar calculations [45, 48].

When simulating these flows, it is critical to obtain convergence in time; the separation zone takes a long time to reach a steady state, and in practice at least 150 flow times (based on free-stream speed and cone face length) must be simulated [48].

To show the influence of the numerical dissipation on these flows, various flux evaluation schemes were used. These include a set of flux evaluation schemes: modified Steger–Warming, Lax–Friedrichs, Harten–Lax–van Leer (HLL), Harten–Lax–van Leer–Contact (HLLC), and Roe; and a set of slope limiters: minmod, van Albada, van Leer, and superbee [49]. Each scheme has expected dissipation characteristics. Lax–Friedrichs is known to be extremely dissipative. The HLL scheme is known for its inability to capture contact surfaces because its construction relies only on the acoustic waves. The HLLC scheme is more reliable because it was designed to remedy the weaknesses of the HLL scheme. The Roe scheme is known to be accurate with good dissipation properties. The classical Steger–Warming scheme is known to be dissipative, but we will see that this is not true for modified Steger–Warming. Concerning the slope limiters, minmod is known to be dissipative, whereas superbee can introduce undesired oscillations. The results show how these schemes and slope limiters behave for the simulation of the double-cone flow.

We quantify the accuracy of the methods using the size of the separation zone, L_s , for each method. We define L_s as the axial (x) distance between the separation point on the first cone and the reattachment point on the second cone. Figure 3 plots the computed separation length for each grid used and various combinations of numerical flux functions and limiters. Here, N_x is the number of grid cells in the streamwise direction of the flow. We can see that as the grid is refined (N_x increases), the separation length converges to a single value. Thus, for this double-cone flow, the larger the separation zone, the less dissipative the method and the more accurate the simulation.

For coarse grid simulations, Roe + superbee, Roe + van Leer and modified Steger–Warming give the largest values of L_s ; all other methods give small separation lengths, indicating excessive dissipation. The superbee slope limiter is the least dissipative, but careful attention must be paid when using it, because it may introduce undesired spatial oscillations in the high-order reconstruction scheme [49]. We see that the choice of the slope limiter is at least as important as the choice of the flux evaluation method, and a dissipative limiter such as minmod can significantly degrade the quality of a good scheme.

On the largest 1536×768 grid, the three best methods are within 0.2% of one another, indicating that the different methods converge to the same unique solution. Interestingly, the two Roe solver based methods produce solutions that are essentially identical (0.04% difference), whereas the modified Steger–Warming method asymptotes to a slightly smaller separation length. The reason for this difference is not known, however it should be noted that on this grid, the axial-direction grid spacing in the vicinity of the separation and reattachment points is 0.01 cm; this is of the same size as the difference between the

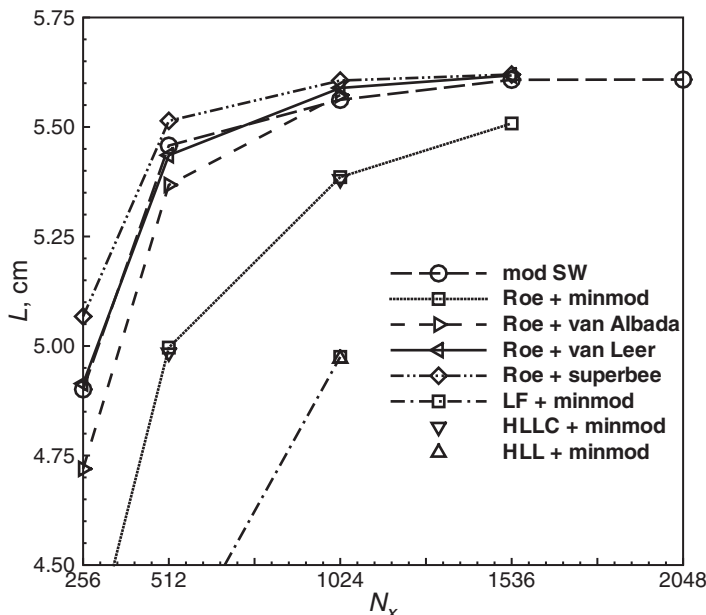


Fig. 3 Variation of recirculation zone size with grid spacing and numerical flux method.

methods. Therefore, even with this very fine grid we may not be fully resolving the separation length. Some key conclusions may be made from this plot.

- The separation length is a good measure of the dissipation qualities of a solution method.
- All methods converge to the same separation length, though some methods would require an impossibly large number of grid points to achieve convergence.
- The slope limiter is at least as important as the underlying flux evaluation scheme in these shock-dominated flows.
- The modified Steger–Warming, Roe + superbee, and Roe + van Leer methods are the best for this problem.
- The van Leer limiter is the best choice for this flow, whereas minmod is a poor choice because it introduces excessive levels of numerical dissipation.

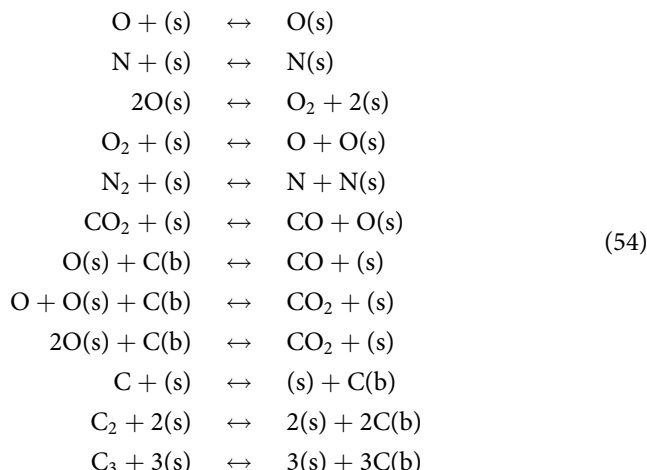
The double-cone flow is an excellent test case to evaluate the accuracy of new and existing numerical flux methods. It shows strong sensitivity to the dissipation levels in the method, and can be used to study how each component of the flux affects the solution. The single separation length parameter is easy to derive from a simulation and is a sensitive measure of the solution quality. It should

be noted that the surface heat flux is less sensitive to grid resolution than the separation zone size. This is because it is less expensive to resolve the grid in the wall-normal direction (affecting heat flux) than in the axial direction (affecting separation length).

VI. SIMULATION OF AN ABLATING THERMAL PROTECTION SYSTEM

A second example that illustrates the effect of finite-rate processes at high-enthalpy conditions is presented in this section. Consider a sphere-cone configuration with 10 cm nose radius and an 8° cone half-angle. The test article is assumed to be flying at zero angle of attack at an altitude of 30 km and a speed of 7.0 km/s. The body is assumed to be composed of graphite, and a surface temperature distribution is assumed (usually computed from a simplified aerothermal analysis tool).

For this simulation, a 20-species (ionized air and air–carbon reaction products), 40-reaction finite-rate air–carbon model is used to represent the gas-phase thermochemical processes; the rates for the reactions are taken from the work of Park et al. [50]. The gas-surface processes are represented with the 12-reaction finite-rate model from Zhluktov and Abe [51]. This model may be written as:



Here (s) represents an open bond site on the carbon surface, and O(s) and N(s) represent O and N atoms bonded to the surface. Each of these gas-surface reactions takes place at a finite rate, and appropriate equilibrium constants must be used so that the gas-phase and gas-surface processes are self-consistent and detailed balance is obtained. Additional details are available in the work of Marschall and MacLean [1].

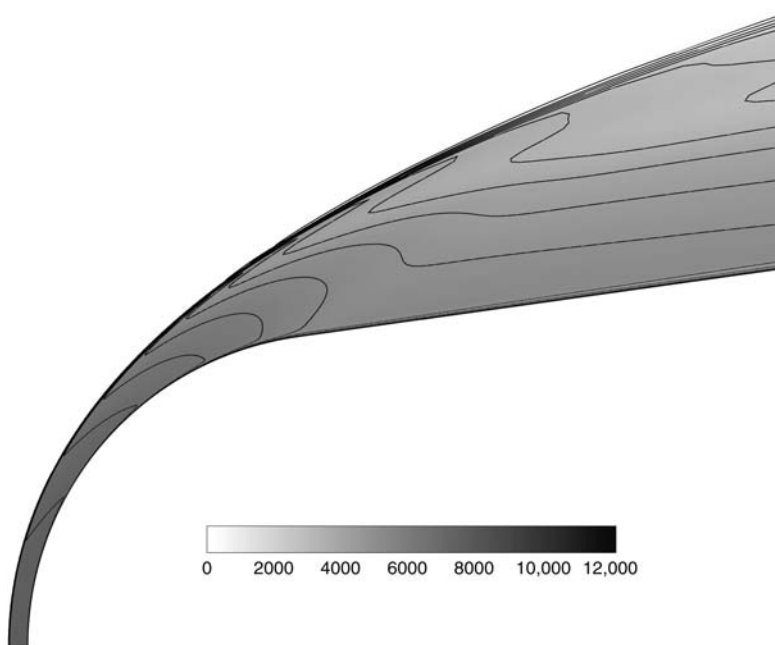


Fig. 4 Temperature distribution in the nose region of the sphere-cone example.

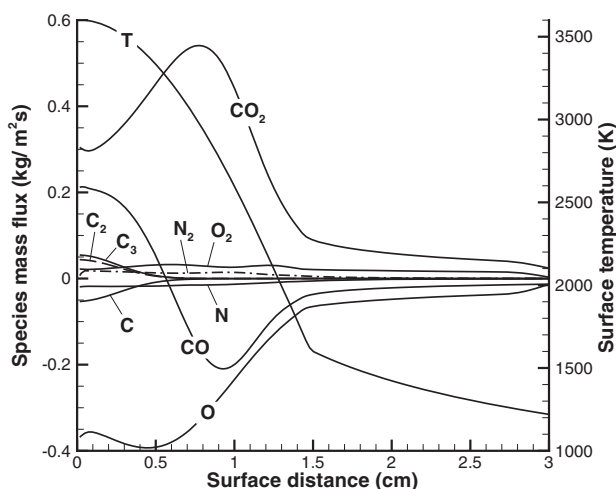


Fig. 5 Surface species mass fluxes and temperature distribution for the sphere-cone example.

Figure 4 plots the translational–rotational temperature distribution in the flowfield near the nose. Here, the grid has been aligned with the location of the bow shock to minimize errors; this significantly improves the quality of the solution and produces more reliable results in the stagnation region. Note that the shock standoff distance is small owing to the large level of chemical reactions that occur in the flow. Also, there is a small region of thermal nonequilibrium present just behind the bow shock where the temperature reaches a peak. Figure 5 plots the mass flux of key chemical species from the surface of the body as a function of the distance along the surface; also plotted is the assumed temperature distribution. Note that the Zhlukov–Abe model predicts changes in the species production as a function of location on the nosetip. At the stagnation point, the dominant species is CO, but off axis the CO₂ flux becomes much larger.

VII. FUTURE PROSPECTS

The field of computational fluid dynamics for hypersonic and high-enthalpy flows has made great progress over the last decade or so. It is now possible to perform full-vehicle simulations with finite-rate thermochemical models and nontrivial surface boundary conditions. Reliable numerical flux methods and parallelizable implicit methods have enabled these advances. The field is continuing to advance, and over the next decade hypersonic and aerothermal flow simulations will become much more sophisticated and accurate.

For example, the current reliance on dissipative second-order accurate upwind methods will diminish and improved low-dissipation, high-order methods will become more widely used. This will enable the simulation of unsteady hypersonic flows and open the field to large-eddy simulations (LES) of turbulent hypersonic flows. These simulations will be much larger as computers continue to increase in power, and codes are scaled to ever-larger systems. For some critical cases, extreme-scale direct numerical simulations (DNS) will be used to discover hypersonic flow physics. Advances in computational chemistry and novel experimental measurements will permit the development of improved chemical reaction models that correctly account for internal energy dynamics; the Park TT_v model will be supplanted with a more complex model based on physics. More complicated multiphysics simulations will become feasible; these will include the ability to “fly” a vehicle with moving control surfaces and operating thrusters. It will become possible to accurately simulate capsule dynamic stability. Fully-coupled flowfield, material response, and shape-change simulations will be possible for full vehicle configurations. The field has made great progress, but the best is yet to come.

VIII. CONCLUSIONS

We have discussed the key aspects of the derivation and application of upwind numerical fluxes for hypersonic flows and aerothermodynamics. The flux

Jacobian was diagonalized for an equilibrium gas with an arbitrary equation of state and for a mixture of chemically reacting thermally perfect gases. We show that the Jacobian can be written in a compact form, which is useful for analysis and implementation. We discuss approaches for obtaining higher-order extensions of the fluxes, and the required modifications of the standard schemes for high-Mach number applications. Several forms of added dissipation are illustrated, including a means of controlling error build up in stagnation regions behind normal shock waves. These approaches are not well founded in theory, but were developed through experience and application to a wide range of high Mach number flows. We then discuss a different type of numerical flux function that is not based on the solution of a Riemann problem, but uses conservation of a secondary quantity to obtain element face data for use in an unbiased flux evaluation. This approach produces significantly less dissipation than upwind methods, and can be stabilized for application to practical problems with a upwind-like dissipative flux and a shock sensor. This class of method is particularly useful for application to unsteady hypersonic flows. The importance of implicit methods is discussed, given that realistic hypersonic flows must use grids with extreme grid stretching and high cell aspect ratios. A powerful line-relaxation method is reviewed, and a novel approach for reducing the solution cost of chemically-reacting flows is outlined. Finally, the upwind methods and implicit time integration approaches are applied to two problems, the hypersonic flow over a double cone geometry and the finite-rate ablation of a carbon nosetip at hypersonic conditions. The first example shows that upwind methods have varying levels of dissipation, and a good method can be corrupted if an overly aggressive slope limiter is used. The double cone flow is an excellent test case for studying the properties of numerical methods for application to hypersonic flows. The ablation test case gives a sense that hypersonic flow simulations are becoming more complex with large numbers of chemical species and detailed gas-surface interaction models.

ACKNOWLEDGMENTS

This work was sponsored in part by the Air Force Office of Scientific Research under grants FA9550-10-1-0563 and FA9550-12-1-0133 and the National Security Science and Engineering Faculty Fellowship. The views and conclusions contained herein are those of the author and should not be interpreted as necessarily representing the official policies or endorsements, either expressed or implied, of the AFOSR or the U.S. Government.

REFERENCES

- [1] Marschall, J., and MacLean, M., "Finite-Rate Surface Chemistry Model, I: Formulation and Reaction System Examples," AIAA 2011-3783, June 2011.

- [2] MacLean, M., Marschall, J., and Driver, D. M., "Finite-Rate Surface Chemistry Model, II: Coupling to Viscous Navier–Stokes Code," AIAA 2011-3784, June 2011.
- [3] Liou, M. S., "A Sequel to AUSM: AUSM+," *Journal of Computational Physics*, Vol. 129, 1996, pp. 364–382.
- [4] Liou, M. S., "Probing Numerical Fluxes: Mass Flux, Positivity, and Entropy-Satisfying Property," AIAA 1997-2035, 1997.
- [5] Jiang, G.-S., and Shu, C.-W., "Efficient Implementation of Weight ENO Schemes," *Journal of Computational Physics*, Vol. 126, 1996, pp. 202–228.
- [6] Steger, J., and Warming, R. W., "Flux Vector Splitting of the Inviscid Gasdynamics Equations with Application to Finite Difference Methods," *Journal of Computational Physics*, Vol. 40, 1981, pp. 263–293.
- [7] Roe, P., "Approximate Riemann Solvers, Parameter Vectors, and Difference Schemes," *Journal of Computational Physics*, Vol. 43, 1981, pp. 357–372.
- [8] Roe, P., "Characteristic-Based Schemes for the Euler Equations," *Annual Review of Fluid Mechanics*, Vol. 18, 1986, pp. 337–365.
- [9] Rohde, A., "Eigenvalues and Eigenvectors of the Euler Equations in General Geometries," AIAA 2001-2609, 2001.
- [10] Montagné, J.-L., Yee, H. C., and Vinokur, M., "Comparative Study of High-Resolution Shock-Capturing Schemes for a Real Gas." *AIAA Journal*, Vol. 27, No. 10, 1989, pp. 1332–1346.
- [11] Liou, M. S., Van Leer, B., and Shuen, J. S., "Splitting of Inviscid Fluxes for Real Gas," *Journal of Computational Physics*, Vol. 87, No. 1, 1990, pp. 1–24.
- [12] Candler, G. V., "Hypersonic Nozzle Analysis Using an Excluded Volume Equation of State," AIAA 2005-2502, 2005.
- [13] van Leer, B., "Towards the Ultimate Conservative Difference Scheme, V. A Second Order Sequel to Godunov's Method," *Journal of Computational Physics*, Vol. 32, 1979, pp. 101–136.
- [14] Hirsch, C., *Numerical Computation of Internal and External Flows*, 2nd ed., Butterworth-Heinemann, Oxford, 2007.
- [15] MacCormack, R. W., "The Carbuncle CFD Problem," *Journal of Aerospace Information Systems*, Vol. 10, No. 5, 2013, pp. 229–239.
- [16] Candler, G. V., Barnhardt, M. D., Drayna, T. W., Nompelis, I., Peterson, D. M., and Subbareddy, P. K., "Unstructured Grid Approaches for Accurate Aeroheating Simulations," AIAA 2007-3959, 2007.
- [17] Gnoffo, P. A., "Updates to Multi-Dimensional Flux Reconstruction for Hypersonic Simulations on Tetrahedral Grids," AIAA 2010-1271, 2010.
- [18] Mavriplis, D. J., "Revisiting the Least-squares Procedure for Gradient Reconstruction on Unstructured Meshes," NASA CR-2003-212683, NIA Report No. 2003-06, 2003.
- [19] Darwish, M. S., and Moukalled, F., "TVD Schemes for Unstructured Grids," *International Journal of Heat and Mass Transfer*, Vol. 46, 2003, pp. 599–611.
- [20] Kim, S.-E., Makarov, B., and Caraeni, D., "Multi-Dimensional Linear Reconstruction Scheme for Arbitrary Unstructured Mesh," AIAA 2003-3990, 2003.
- [21] Ducros, F. et al., "Large-Eddy Simulation of the Shock/Turbulence Interaction," *Journal of Computational Physics*, Vol. 152, 1999, pp. 517–549.

- [22] Jameson, A., "Formulation of Kinetic Energy Preserving Conservative Schemes for Gas Dynamics and Direct Numerical Simulations of One-Dimensional Viscous Compressible Flow in a Shock Tube Using Entropy and Kinetic Energy Preserving Schemes," *Journal of Scientific Computing*, Vol. 34, No. 2, 2008, pp. 188–208.
- [23] Morinishi, Y., Vasilyev, O. V., and Ogi, T., "Fully Conservative Finite Difference Scheme in Cylindrical Coordinates for Incompressible Flow Simulations," *Journal of Computational Physics*, Vol. 197, No. 2, 2004, pp. 686–710.
- [24] Tadmor, E., "Numerical Viscosity and the Entropy Condition for Conservative Difference Schemes," *Mathematics of Computation*, Vol. 43, No. 168, 1984, pp. 369–381.
- [25] Ismail, F., and Roe, P. L., "Affordable, Entropy-Consistent Euler Flux Functions II: Entropy Production at Shocks," *Journal of Computational Physics*, Vol. 228, No. 15, 2009, pp. 5410–5436.
- [26] Honein, A. E., and Moin, P., "Higher Entropy Conservation and Numerical Stability of Compressible Turbulence Simulations," *Journal of Computational Physics*, Vol. 201, No. 2, pp. 531–545.
- [27] Kennedy, C. A., and Gruber, A., "Reduced Aliasing Formulations of the Convective Terms within the Navier Stokes Equations for a Compressible Fluid," *Journal of Computational Physics*, Vol. 227, No. 3, 2008, pp. 1676–1700.
- [28] Pirozzoli, S., "Generalized Conservative Approximations of Split Convective Derivative Operators," *Journal of Computational Physics*, Vol. 229, No. 19, 2010, pp. 7180–7190.
- [29] Subbareddy, P. K., and Candler, G. V., "A Fully Discrete, Kinetic Energy Consistent Finite-Volume Scheme for Compressible Flows," *Journal of Computational Physics*, Vol. 228, 2009, pp. 1347–1364.
- [30] Zhang, X., and Shu, C.-W., "On Positivity-Preserving High Order Discontinuous Galerkin Schemes for Compressible Euler Equations on Rectangular Meshes," *Journal of Computational Physics*, Vol. 229, No. 23, 2010, pp. 8918–8934.
- [31] Hu, X. Y., Adams, N. A., and Shu, C.-W., "Positivity-Preserving Method for High-Order Conservative Schemes Solving Compressible Euler Equations," *Journal of Computational Physics*, Vol. 242, 2013, pp. 169–180.
- [32] Wright, M. J., Bose, D., and Candler, G. V., "A Data-Parallel Line Relaxation Method for the Navier–Stokes Equations," *AIAA Journal*, Vol. 36, No. 9, 1998, pp. 1603–1609.
- [33] Wright, M. J., Candler, G. V., and Prampolini, M., "Data-Parallel Lower-Upper Relaxation Method for the Navier–Stokes Equations," *AIAA Journal*, Vol. 34, No. 7, 1996, pp. 1371–1377.
- [34] Gnoffo, P. A., "An Upwind-Biased, Point Implicit Relaxation Algorithm for Viscous, Compressible Perfect-Gas Flows," NASA TP-2953, 1990.
- [35] Bussing, T. R. A., and Murman, E. M., "A Finite Volume Method for the Calculation of Compressible Chemically Reacting Flows," AIAA 1985-0331, 1985.
- [36] Park, C., and Yoon, S., "A Fully-Coupled Implicit Method for Thermo-Chemical Nonequilibrium Air at Sub-Orbital Speeds," AIAA 1989-1974, 1989.
- [37] Eberhardt, S., and Imlay, S., "A Diagonal Implicit Scheme for Computing Flows with Finite-Rate Chemistry," AIAA 1990-1577, 1990.

- [38] Edwards, J. R., "An Implicit Multigrid Algorithm for Computing Hypersonic, Chemically Reacting Viscous Flows," *Journal of Computational Physics*, Vol. 123, 1996, pp. 84–95.
- [39] Schwer, D. A., Liu, P., Green, W. H., and Semiao, V., "A Consistent-Splitting Approach to Stiff Steady-State Reacting Flows with Adaptive Chemistry," *Combustion Theory and Modeling*, Vol. 7, 2003, pp. 383–399.
- [40] Katta, V. R., and Roquemore, W. M., "Calculation of Multidimensional Flames Using Large Chemical Kinetics," *AIAA Journal*, Vol. 46, No. 7, 2008, pp. 1640–1650.
- [41] MacLean, M., and White, T., "Implementation of Generalized Minimum Residual Krylov Subspace Method for Chemically Reacting Flows," *AIAA 2012-0441*, 2012.
- [42] Nompelis, I., Wan, T., and Candler, G., "Performance Comparisons of Parallel Implicit Solvers for Hypersonic Flow Computations on Unstructured Meshes," *AIAA 2007-4334*, 2007.
- [43] Candler, G. V., Subbareddy, P. K., and Nompelis, I., "Decoupled Implicit Method for Aerothermodynamics and Reacting Flows," *AIAA Journal*, Vol. 51, No. 5, 2013, pp. 1245–1254.
- [44] Harvey, J., Holden, M. S., and Candler, G. V., "Validation of DSMC/Navier–Stokes Computations for Laminar Shock Wave/Boundary Layer Interactions Part 3," *AIAA 2003-3643*, 2003.
- [45] Nompelis, I., Candler, G. V., and Holden, M. S., "Effect of Vibrational Nonequilibrium on Hypersonic Double-Cone Experiments," *AIAA Journal*, Vol. 41, No. 11, 2003, pp. 2162–2169.
- [46] Druguet, M.-C., Candler, G. V., and Nompelis, I., "Effects of Numerics on Navier–Stokes Computations of Hypersonic Double-Cone Flows," *AIAA Journal*, Vol. 43, No. 3, 2005, pp. 616–623.
- [47] Holden, M. S., and Wadhams, T. P., "Code Validation Study of Laminar Shock/Boundary Layer and Shock/Shock Interactions in Hypersonic Flow. Part A: Experimental Measurements," *AIAA 2001-1031*, 2001.
- [48] Gaitonde, D. V., Canupp, P. W., and Holden, M. S., "Heat Transfer Predictions in a Laminar Viscous/Inviscid Interaction," *Journal of Thermophysics and Heat Transfer*, Vol. 16, No. 4, 2002, pp. 481–489.
- [49] Toro, E. F., *Riemann Solvers and Numerical Methods for Fluid Dynamics. A Practical Introduction*, Springer, 1997.
- [50] Park, C., Howe, J. T., Jaffe, R. L., and Candler, G. V., "Review of Chemical-Kinetic Problems of Future NASA Missions II - Mars Entries," *Journal of Thermophysics and Heat Transfer*, Vol. 8, No. 1, 1994, pp. 9–23.
- [51] Zhlukov, S. V., and Abe, T., "Viscous Shock-Layer Simulation of Airflow Past Ablating Blunt Body with Carbon Surface," *Journal of Thermophysics and Heat Transfer*, Vol. 13, No. 1, 1999, pp. 50–59.

Surface Chemistry in Non-Equilibrium Flows

Jochen Marschall*

Molecular Physics Program, SRI International, Menlo Park, California

Matthew MacLean[†]

Aerosciences Sector, CUBRC, Inc., Buffalo, New York

Paul E. Norman[‡] and Thomas E. Schwartzentruber[§]

*Aerospace Engineering & Mechanics, University of Minnesota,
Minneapolis, Minnesota*

NOMENCLATURE

A_v	Avogadro's number, $6.0221 \times 10^{23} \text{ mol}^{-1}$
a_k	activity of species k
C_k	concentration of gas species k , mol m^{-3}
E_{ad}	adsorption energy barrier, J mol^{-1}
E_{des}	desorption energy barrier, J mol^{-1}
E_{diss}	dissociation energy, J mol^{-1}
E_{er}	Eley–Rideal energy barrier, J mol^{-1}
E_{lh}	Langmuir–Hinshelwood energy barrier, J mol^{-1}
E_m	surface diffusion energy barrier, J mol^{-1}
E_{sub}	sublimation energy barrier, J mol^{-1}
f_{ki}	branching fraction (fraction of net global production of species k by reaction i)
$G_k^o(T)$	Gibbs energy, J mol^{-1}
$H_k^o(T)$	enthalpy, J mol^{-1}
h	Planck constant, $6.6261 \times 10^{-34} \text{ J s}$
h_a	virgin TPS enthalpy per unit mass, J kg^{-1}
h_b	char enthalpy per unit mass, J kg^{-1}
I	total number of surface reactions
i	surface reaction index ($i = 1 \dots I$)
K	total number of species

*Senior Research Scientist

[†]Senior Research Scientist

[‡]Graduate Student

[§]Associate Professor

K_a	activity-based equilibrium constant
K_b	total numbers of bulk species
K_c	concentration-based equilibrium constant, units vary
K_g	total numbers of gas species
K_s	total numbers of surfaces pecies
K_{ns}	number of species on surface phase ns
$K_{ns,na}$	number of species in active-site set na on surface phase ns
K_{nb}	number of species in bulk phase nb
k	species index ($k = 1 \dots K$)
k_{bi}	backward reaction rate coefficient for reaction i , units vary
k_{fi}	forward reaction rate coefficient for reaction i , units vary
N	total number of phases
N_a	number of active site sets
N_b	number of bulk phases
N_{blw}	number of blowing gas mixtures
N_g	number of gas phases
$N_{ns,a}$	number of active site sets in surface phase ns
N_s	number of surface phases
na	active-site set index ($na = 1 \dots N_{ns,a}$)
nb	bulk-phase index ($nb = 1 \dots N_b$)
$nblw$	blowing gas mixture index ($nblw = 1 \dots N_{blw}$)
ns	surface-phase index ($ns = 1 \dots N_s$)
P	pressure, Pa
P_k	partial pressure of gas species k , Pa
R	universal gas constant, $8.3145 \text{ J mol}^{-1} \text{ K}^{-1}$
$r_{i,ns}$	reaction flux of reaction i on surface phase ns , $\text{mol m}^{-2} \text{ s}^{-1}$
$S_k^o(T)$	entropy, $\text{J mol}^{-1} \text{ K}^{-1}$
S_0	sticking coefficient
T	temperature, K
t	time, s
\bar{v}_k	thermal speed ($\sqrt{8RT_g/\pi M_k}$) of species k , m s^{-1}
v'_{ki}	reactant stoichiometric coefficient for species k in reaction i
v''_{ki}	product stoichiometric coefficient for species k in reaction i
v_{ki}	net stoichiometric coefficient for species k in reaction i , $(v''_{ki} - v'_{ki})$
ν_s	site exponent
\dot{w}_{ki}	production rate of species k in reaction i , $\text{mol m}^{-2} \text{ s}^{-1}$
\dot{w}_k	production rate of species in all reactions, $\text{mol m}^{-2} \text{ s}^{-1}$
X_k	generalized concentration of species k , units vary
y_k	mass fraction of species k
Γ_k	impingement flux of gas species k [$C_k \bar{v}_k / 4$], $\text{m}^{-2} \text{ s}^{-1}$
γ_{er}	Eley–Rideal reaction efficiency
Δ_{ns}	average distance between active sites on surface pages ns , m
$\theta_{ns,k}$	fraction of active sites occupied by species k on surface phase ns
ν	attempt frequency, s^{-1}

ρ_b	mass density of bulk environment, kg m^{-3}
ρ_{nb}	mass density of bulk phase nb , kg m^{-3}
Φ_{total}	total active site density on the surface, mol m^{-2}
Φ_{ns}	active site density on surface phase ns , mol m^{-2}
$\Phi_{ns,k}$	concentration of species k on surface phase ns , mol m^{-2}
ϕ_b	porosity of bulk environment
ϕ_{nb}	porosity of bulk phase nb
χ_k	mole fraction of species k
$\chi_{nb,k}$	mole fraction of bulk species k in bulk phase nb
$\chi_{nblw,k}$	mole fraction of gas species k in blowing gas mixture $nblw$
Ω_{ns}	surface fraction occupied by phase ns

I. INTRODUCTION

This chapter deals with the development and implementation of computational models to describe the effects of surface chemistry on the heat and mass transfer between the gas phase and the thermal protection system (TPS) of a hypersonic vehicle.

The range of possible gas–surface interactions, aerothermal heating mechanisms, and TPS materials responses is very wide and varies with vehicle size and shape, flight speed, altitude and trajectory, atmospheric composition, mission objectives, etc. We begin with a short summary of aerothermal heating mechanisms, TPS responses, and the role of nonequilibrium chemistry at the TPS surface. Then we describe in detail the formulation of a finite-rate surface chemistry model and its incorporation into the National Aeronautics and Space Administration (NASA) computational fluid dynamics (CFD) Data Parallel Line Relaxation (DPLR) [1, 2] code. This new computational capability allows for the development of mission-specific and TPS-specific surface chemistry models within a generic framework that ensures mass, energy, and element conservation at the gas–surface interface, as well as consistency with all available thermodynamic data, including those already in use for gas-phase CFD computations.

We then narrow our focus to the oxygen–silica system. The oxygen–silica system is relevant to many hypersonic applications since most current high-temperature oxidation-protection systems for leading edges on hypersonic vehicles involve silica-based or silica-forming coatings (e.g., the reinforced carbon–carbon systems used on the Space Shuttle and the X-43A). Furthermore, natural silica oxides form on SiC, Si_3N_4 , and most ultra-high temperature ceramic (UHTC) composite systems presently under development. The catalytic recombination of atomic oxygen is an important contributor to aerothermal heating during hypersonic flight through atmospheres of Earth and Mars, as well as during ground tests simulating these flight conditions.

A finite-rate model for catalytic recombination on a silica surface must capture the dominant atomistic processes and chemical pathways in operation, and once

assembled, requires “reasonable” numerical values (or ranges of values) for the many parameters that must be specified; e.g., activation energies, reaction probabilities, active site densities. In this context, “reasonable” means supported by a physics-based or chemistry-based justification, and consistent with experiment (when available). Unfortunately, many surface chemistry processes are not easily interrogated experimentally, and measured finite-rate surface chemistry model parameters are scarce. The rapidly evolving fields of computational chemistry and large-scale atomistic simulation can help fill this void, by providing unique insights into the surface chemistry at the atomic level and numerical values for finite-rate representation of these processes. We describe computational chemistry approaches for investigating gas–surface interactions between dissociated oxygen and “real” silica surfaces. Recent results are presented that identify silica surface defects important for catalytic oxygen recombination, and numerical values for finite-rate chemistry models associated with these defects.

We then give several examples of finite-rate surface chemistry computations, using both stand-alone numerical iteration to steady-state under fixed gas-phase conditions and DPLR solution of the implemented boundary condition for prescribed freestream flow conditions. The first of these examples exercises a simple empirical finite-rate model for oxygen atom recombination on silica, and the second example compares this model to a second finite-rate model derived using the discussed computational chemistry techniques for the oxygen/silica system. We then demonstrate some of the features of more complex surface reaction sets using an empirical model for catalysis in dissociated CO₂. After these surface catalysis examples, carbon oxidation models are compared for an ablating carbon wedge surface. Finally, an example demonstrating steady-state pyrolysis incorporated into the finite-rate surface chemistry system is shown. These examples show both the physical modeling features of the finite-rate surface chemistry formulation and the numerical performance of the implementation into a production CFD code. Finally, we discuss future directions in modeling and experiments.

II. BACKGROUND

The net heat flux experienced by a hypersonic vehicle is the result of complex and dynamic interactions between the flow field and the TPS surface. At hypersonic speeds, a bow shock forms in front of vehicle leading edges. Gases passing through the bow shock are compressed and increase in density, pressure, static enthalpy, and temperature. The shock standoff distance between the bow shock and the vehicle surface is determined by vehicle shape, velocity, and flight trajectory through the atmosphere. A boundary layer forms near the surface, characterized by large temperature, momentum, and chemical composition gradients. The gas flow is decelerated at the stagnation point, forming a thin boundary layer and a local subsonic region. The boundary layer thickens as the flow is redirected and accelerates around the vehicle, regaining supersonic

velocities. Shock and boundary layer conditions determine local aerothermal heating to the surface. Convective heating—the transfer of thermal energy from the gas phase to the surface through gas–surface collisions—is typically highest in the stagnation point region.

At sufficiently high velocities, gas molecules passing through the shock can be dissociated and ionized. In the terrestrial atmosphere, shock-induced dissociation means that N₂ and O₂ molecules break apart to become highly reactive N and O atoms. Because of their lower bond energy (~5.1 vs 9.8 eV), O₂ molecules dissociate at lower enthalpy levels than N₂ molecules. High-speed entries into the atmospheres of other solar system bodies may dissociate different species, for example CO₂ in the Martian atmosphere, CH₄ in the Titan atmosphere, and H₂ in Giant Planet atmospheres. The interaction of reactive gas species on and with vehicle surfaces can lead to chemical heating, which contributes diffusive energy transfer through gradients of chemical species.

Chemical and thermal relaxation occurs as gases transit the post-shock region towards the vehicle, particularly in the boundary layer where steep thermal and density gradients form near the surface. The extent that collisions and chemical reactions can drive the gases back towards thermochemical equilibrium before they interact with the vehicle surface is determined by specific flight conditions. It is very often the case that the chemical composition of the gas in direct contact with vehicle surface is not a thermochemical equilibrium composition at the temperature of the vehicle surface. In particular, the concentration of dissociated species is often orders of magnitude higher than the equilibrium value. Although not a universal approach, CFD simulations of reactive flows typically implement a thermal boundary condition at the gas–surface interface which sets the translational, vibrational, rotational, and electronic modes of gas species into thermal equilibrium at the temperature of the surface. However, the choice of chemical boundary conditions imposed at the surface—a complex balance of species mass production on the surface against diffusive and convective transport into the gas—can be a dominant effect on overall heat transfer to the surface.

Similar nonequilibrium boundary layer chemistry and gas–surface interactions are present in high-enthalpy ground test facilities, such as shock tunnels which are used to replicate shock formation and aerothermal heating phenomena in short duration tests (~milliseconds), and arc-jets and inductively coupled plasma (ICP) torches which are used to test TPS response to sustained aerothermal heating (~minutes).

Aerothermal environments can cause a wide range of TPS responses depending on the enthalpy level of the impinging flow. At low enthalpy levels, materials may simply heat up with no apparent physical or chemical changes; at intermediate enthalpy levels materials may experience moderate but permanent alterations, such as the formation of oxide layers that can alter the emittance or catalytic activity of the TPS surface; at extreme enthalpy levels, materials undergo major physical and chemical changes leading to mass loss, shape changes, and, in some instances, catastrophic failure.

Chemical TPS responses can be roughly divided into phenomena occurring at the gas–surface interface (GSI) or throughout a finite-depth in the bulk, and into chemistries involving species originating from the TPS and/or from the impinging gas phase.

Surface catalytic chemistry describes reactions in which the TPS surface mediates chemistry between impinging gas species. The surface acts solely as a host; none of the reactants originate from the bulk TPS material and none of the products remain on the surface. Catalytic reactions produce no net mass transfer between the impinging gas and the TPS, but can involve substantial heat transfer. For example, the surface recombination of atomic oxygen and atomic nitrogen into O₂, NO, and N₂ releases approximately 500, 630, and 950 kJ per mole of product, respectively.

Surface participating chemistry describes reactions which produce both mass and energy transfer between the TPS and the gas. Surface participating reactions always involve a reactant originating from the TPS material, but may or may not involve a reactant from the gas phase. Reaction products may leave the surface or augment the bulk material. Some examples of surface participating reactions include the oxidation of carbon by atomic and molecular oxygen to form gaseous carbon monoxide (CO) and carbon dioxide (CO₂); the formation of an adherent silica (SiO₂) scale during passive oxidation of silicon carbide (SiC) and the formation of volatile silicon monoxide (SiO) during active oxidation of SiC; and the sublimation of carbon in atomic and molecular forms (C, C₂, C₃, etc.). Surface participating reactions may be exothermic or endothermic.

Pyrolysis chemistry describes the thermochemical decomposition of materials into gaseous and condensed products, where gaseous (pyrolysis) products are typically driven into the boundary layer by internal pressure and the cohesive residual solid (char) is a bulk state that is chemically and elementally different from the virgin state of the material. Pyrolyzing TPS materials are generally polymeric composites of organic resins and fillers. Their char yield is defined as the ratio of the residual char density after pyrolysis divided by the initial virgin material density. Pyrolysis reactions are triggered by heat and progress from the surface into the bulk forming a traveling pyrolysis zone described by the relative movements of the pyrolysis and char fronts, which track the initiation and the completion of the pyrolysis process. Pyrolyzing materials with appreciable char yields, such as carbon/phenolic composites, form porous pyrolysis and char layers where additional internal gas-phase and surface chemistry may take place before reaction products enter the boundary layer. Pyrolyzing materials with negligible char yields, such as Teflon under most conditions, volatilize directly into the gas phase; the pyrolysis front and receding surface are coincident and there is no char front. This surface pyrolysis process is similar to sublimation, except that the chemistry is one of thermochemical decomposition instead of phase change. Pyrolysis reactions are endothermic and the injection (or “blowing”) of pyrolysis gases into the boundary layer lowers the convective heat flux to the surface.

Ablation is a generic term that describes the combined effect of many different chemical and physical processes acting in unison. Ablation may include catalytic, surface participating and pyrolysis chemistries, as well as other physical processes such as melting and spallation. In ablation, the net mass transfer is usually from the TPS bulk to the gas phase, although local mass deposition through coking reactions or condensation of supersaturated gases is also possible. Overall, ablation mitigates aerothermal heating through a combination of pyrolysis gas blowing and endothermic decomposition, although individual chemical reactions may be endothermic (pyrolysis, sublimation) or exothermic (oxidation, catalytic recombination.)

The coupling between the surface and flow field becomes stronger as the hypersonic flight conditions become more extreme. Increased convective heating causes higher surface temperatures; the extent of molecular dissociation in the shock and within the boundary layer becomes greater; and the concentration of reactants and the rates of various surface reactions rise. As surface reactions become more active, their contribution to aerothermal heating becomes more important; the balance between catalytic and surface-participating reactions determines the extent of TPS heating and surface degradation. When surface-participating reactions dominate, important surface properties like the catalytic activity, emittance, and surface roughness can change as TPS material is consumed and/or transformed.

III. A FINITE-RATE SURFACE CHEMISTRY MODEL

A variety of limiting surface chemistry approximations can be implemented into CFD simulations, which do not require mathematical descriptions of specific chemical pathways. For example, the TPS surface can be modeled as a completely inert wall—not participating as a reactant in surface chemistry and noncatalytic to surface recombination reactions. This boundary condition limits chemistry to the gas phase and sets the chemical heating component to the surface to zero. At the other extreme, the so-called supercatalytic boundary condition sets the surface-mass fractions to the state that results in maximum energy reclamation and therefore maximizes the convective heat delivered to the vehicle TPS. The supercatalytic boundary is often employed for mission design as a conservative prediction of heat flux to the TPS, but it also typically results in an overly conservative TPS system that limits scientific payload, constrains trajectory and landing options, and otherwise increases the stress placed on the design of other vehicle systems. Additionally, its nonphysical nature disconnects the TPS design from consistency with physical constraints and secondary processes (such as radiation). Another approach is to bring the gas-phase composition into equilibrium with the surface. This equilibrium boundary condition is computed using a thermochemical equilibrium solver such as the ACE [3], MAT [4, 5], and CEA [6] codes, and makes use of thermodynamic data rather than

chemical kinetic rates. The equilibrium boundary condition is, in most cases, equivalent to assuming infinitely fast reaction rates and reactant availabilities.

The difference in predicted aerothermal heating between the inert wall boundary condition and the supercatalytic or thermochemical equilibrium boundary condition can be considerable. The computation of more realistic chemical heating contributions between these bounding extremes requires modeling the kinetics of specific surface chemistry pathways. Traditionally, this has been done using “specified reaction efficiency” (SRE) surface chemistry models. In the SRE approach, species loss (negative) or production (positive) in a particular chemical pathway is computed as a specified probability times the flux of a gas-phase reactant impinging on the surface. A common example is the catalytic surface recombination pathway $O + O \leftrightarrow O_2$, in which O-atom loss from the gas phase (in $\text{mol m}^{-2} \text{ s}^{-1}$) is modeled as the gas-kinetic atom impingement flux, Γ_o , times a recombination coefficient, γ_o , whose value lies in the range 0 to 1:

$$\dot{w}_o = -\gamma_o \Gamma_o = -\gamma_o \frac{C_o \bar{v}_o}{4} \quad (1)$$

$$\dot{w}_{O_2} = -\frac{\dot{w}_o}{2} \quad (2)$$

The rate of chemical heating (in W m^{-2}), assuming total energy accommodation at the surface, is then related to the gas-phase O_2 dissociation energy as

$$\dot{q} = \dot{w}_{O_2} E_{\text{diss}, O_2} \quad (3)$$

The SRE approach is simple to implement for a case like this, but does not incorporate any physics-based mechanisms of surface reaction. Reverse reactions are not considered and thus the SRE model is not generally consistent with thermodynamics. The SRE approach typically assumes that multiple surface reactions, for example $O + O \leftrightarrow O_2$ and $N + N \leftrightarrow N_2$, operate independently, ignoring the finite nature of the surface, or more specifically, the competition for the limited number of sites on the surface where reactions can take place.

The SRE model also becomes extremely unwieldy when reactants can participate in multiple pathways. One example is the addition of the $O + N \leftrightarrow NO$ surface recombination pathway in dissociated air. Heterogeneous NO formation is typically ignored in aerothermal heating simulations. However, laser-based experiments have detected NO formation in front of test articles in plasma wind tunnels [7, 8], and Kurotaki [9] has championed its importance in matching flight data for the Orbital Re-entry Experiment (OREX) entry. A series of laboratory experiments using diffusion and flow tube reactors and laser-induced fluorescence species detection suggests that NO formation may be as important as the $O + O$ and $N + N$ pathways [10–12]. Because O and N atoms can participate in multiple reaction pathways, the SRE approach requires that both reaction efficiencies and branching factors be specified [11]. Moreover, the lack of reactant

availability may override the specified reaction efficiency. For example, in moderate enthalpy flows, nitrogen dissociation is much lower than oxygen dissociation, and NO formation can be limited by the availability of N atoms rather than the reaction efficiency. In general, complex rules must be implemented to ensure mass and element conservation.

A similar set of complications is encountered in dissociated CO₂ flows where O atoms may catalytically recombine via the competitive pathways O + CO \leftrightarrow CO₂ or O + O \leftrightarrow O₂ [13]. These reactions release similar amounts of energy on a unit basis (500 vs 530 kJ per mole of product); however, the energy deposition to the surface depends greatly on which reaction pathway is dominant. When O + O dominates, the number of potential recombination events drops by a factor of about 2 since CO is no longer a reactant partner, leading to less net energy release. Full recombination into CO₂ is usually assumed in CFD computations since this extracts the maximum energy from the flow field, but past laboratory experiments [14, 15] suggest that O + O is the dominant reaction pathway. The difference in catalytic heating between the two is very large and constitutes one of the significant uncertainties associated with aerothermal heating predictions of Mars entry and CFD simulations of ground tests in dissociated CO₂ atmospheres.

A logical step to improve surface chemistry modeling in aerothermal heating simulations is to move to a finite-rate formulation. Finite-rate surface chemistry models are in wide use in the chemistry and chemical engineering communities, particularly in the areas of catalysis and combustion. The major features of these models are: i) surface reactions occur at a finite number of “active sites” on the surface, ii) net surface chemistry is a result of multiple individual processes that proceed at finite, temperature dependent rates, and iii) reactant adsorption is a key step and all reactions between species involve at least one adsorbed reactant.

With this approach reactants compete for available active sites and chemistry in multi-pathway systems is inherently coupled. The efficiencies and branching fractions of specific reaction pathways are now a result of the surface chemistry model, rather than specified model inputs. Each rate process has forward and backward reaction rates linked by temperature-dependent equilibrium constants. These concepts ensure global mass and element conservation at the gas-solid interface, as well as consistency with all available thermodynamic data.

Several modeling groups in the European aerospace community have developed finite-rate catalysis and reaction models of various types for CFD simulations [16, 17]. Here we describe the recent development of a finite-rate surface chemistry framework for representing a wide range of chemical gas-surface interactions in aerothermal heating computations [1], and the implementation of this model in the NASA CFD code DPLR [2], although the presented framework should be applicable to any chemically reacting CFD code.

A. FINITE-RATE FORMULATION

1. SYSTEM DEFINITIONS: ENVIRONMENTS, PHASES, ACTIVE SITES, AND CHEMICAL SPECIES

The model system is defined in terms of “environments,” “phases,” “active site sets,” and “species”; see Fig. 1. Three environments are defined: the gas environment, the surface environment, and the bulk environment. Each environment comprises one or more phases, where each phase represents a physically distinct sub-environment. By definition, the gas environment is a single phase ($N_g = 1$) containing K_g chemically distinct gas-phase species. The gas phase must contain (at a minimum) all gas-phase species that interact with the surface: reactants and products involved in surface reactions, or species blown through or from the surface into the gas phase by gas-injection, transpiration, or in-depth pyrolysis.

The surface environment, which represents the interface between the gas and the bulk where gas and bulk species are allowed to chemically interact, can have multiple phases ($n_s = 1 \dots N_s$), each occupying a fraction Ω_{ns} of the total surface area. All surface reactions take place at “active sites” on the surface. Each surface phase can contain multiple sets of active sites ($na = 1 \dots N_{ns,a}$). Individual surface reactions must take place within a single surface phase, but can involve more than one set of active sites in that surface phase. Each set of active sites has a site density $\Phi_{ns,na}$ (mol m⁻²) and an associated set of $K_{ns,na}$ chemically distinct surface species. Thus each surface species is uniquely associated with a single set of active sites and each set of active sites is uniquely associated with a single surface phase. One surface species in each active site set is defined as an empty site, while all other species in that active site set represent adsorbed atoms or molecules. In our formulation, the number of active sites is conserved (no active sites are created, destroyed or converted), and each surface species occupies only a single surface site at one time. The surface concentration of a species k associated with the active site set na on phase n_s is designated by $\Phi_{ns,na,k}$.

The bulk environment can consist of one or more phases ($n_b = 1 \dots N_b$), each occupying a volume fraction ν_{nb} of bulk. Each bulk phase contains a unique set of K_{nb} species. The total number of phases in the model system is,

$$N = 1 + N_s + N_b \quad (4)$$

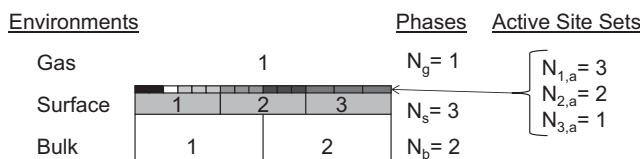


Fig. 1 Surface reaction model system consisting of environments, surface phases, and sets of active sites.

The total number of active site sets is,

$$N_a = \sum_{ns=1}^{N_s} N_{ns,a} \quad (5)$$

The total number of species in the system is,

$$K = K_g + \sum_{ns=1}^{N_s} \sum_{na=1}^{N_{ns,a}} K_{ns,na} + \sum_{nb=1}^{N_b} K_{nb} \quad (6)$$

Note that with these definitions, a particular atom (say atomic oxygen) is considered a different chemical species in the gas phase or in a particular active site set on the surface or in a particular bulk phase.

The purpose of including multiple phases in the surface environment is to allow for the representation of composite TPS materials wherein different components exhibit different chemical makeup and activity. An inert or porous area of the surface can be specified as a surface phase with no active sites, $N_{ns,a} = 0$. Such a phase will not participate directly in any surface chemistry, but will influence the conversion of local species production rates to global values since the total area fraction occupied by the chemically active surface phases will be less than one. The purpose of including multiple sets of active sites within a single phase is to allow for surface chemistry mechanisms that involve different species adsorbed to different sites on a surface, as is often done, for example, in carbon oxidation models.

All active sites in a single surface phase are pictured as homogeneously distributed over the surface of that phase and are treated as an ideal mixture of sites. The total site density on a given surface phase is therefore,

$$\Phi_{ns} = \sum_{na=1}^{N_{ns,a}} \Phi_{ns,na} \quad (7)$$

Because multiple sets of active sites on a single surface phase are treated as an ideal mixture and because each species associated with an active site set is unique to that set, the concentration of surface species k on surface phase ns is $\Phi_{ns,k} = \Phi_{ns,na,k}$. Given that multiple surface phases are treated as segregated areas on the surface, the effective (or average) active site density over the entire surface is,

$$\Phi_a = \sum_{ns=1}^{N_s} \Omega_{ns} \Phi_{ns} \quad (8)$$

The fraction of active sites in phase ns belonging to active site set na is,

$$\theta_{ns,na} = \frac{\Phi_{ns,na}}{\Phi_{ns}} \quad (9)$$

The fraction of active sites in phase ns that are occupied by species k is,

$$\theta_{ns,k} = \frac{\Phi_{ns,k}}{\Phi_{ns}} = \theta_{ns,na,k} = \frac{\Phi_{ns,na,k}}{\Phi_{ns}} \quad (10)$$

The average distance between active sites in a surface phase is,

$$\Delta_{ns} = \frac{1}{\sqrt{A_v \Phi_{ns}}} \quad (11)$$

Bulk phases are pictured as physically distinct volumes of the bulk environment with their individual chemical compositions, densities, and porosities. Multiple bulk phases can be used to model a composite material in a way consistent with known physical and chemical characteristics of the composite. Similar to inert areas on the surface, inert components in the bulk can be modeled as phases with no chemically active species ($K_{nb} = 0$). The density and the porosity of the bulk environment are given by,

$$\rho_b = \sum_{nb=1}^{N_b} v_{nb} \rho_{nb} \quad (12)$$

and,

$$\phi_b = \sum_{nb=1}^{N_b} v_{nb} \phi_{nb} \quad (13)$$

The amount of a species k in a gas, surface, or bulk phase is quantified by generalized species concentration X_k . The units of X_k vary depending on the environment. The generalized concentration for a gas-phase species is in units of mol m^{-3} and is related to the species partial pressure,

$$X_k \equiv C_k = \frac{P_k}{RT} = \chi_k \frac{P}{RT} \quad (14)$$

Since each surface reaction takes place within a single phase in the surface environment, the generalized concentration for a surface species k is in mol m^{-2} and represents the local concentration within its surface phase,

$$X_k \equiv \Phi_{ns,k} = \theta_{ns,k} \Phi_{ns} \quad (15)$$

This definition is consistent with treating each surface phase as an independent physical and chemical entity, and treating multiple sets of active sites in a given surface phase as an ideal mixture of active sites.

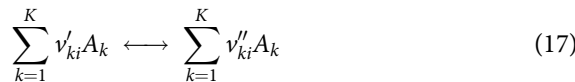
In the bulk environment, the generalized species concentration is dimensionless and equals the mole fraction of species k in within its bulk phase,

$$X_k \equiv \chi_{nb,k} \quad (16)$$

This definition is consistent with treating each reacting bulk phase as an ideal mixture of species with a fixed composition.

2. SURFACE REACTION FORMULATION, REACTION FLUXES, AND SPECIES PRODUCTION RATES

Consider a system with K species and I surface reactions; the general form for reaction i can be written as,



where A_k is the chemical symbol and v'_k and v''_k are the stoichiometric coefficients for species k on the reactant and product sides of the equation. The specification of a surface reaction mechanism begins by writing a set of chemical reactions involving surface species and their interactions with each other and/or species from the gas and bulk environments. The following conventions are adopted for writing surface reaction equations.

- At least one surface species must appear on each side of a reaction.
- No more than one gas and one bulk species should appear on each side of a reaction.
- Chemical elements must balance on both sides of a reaction.
- The number of like active sites must balance on both sides of a reaction.
- The number of surface species must balance on both sides of a reaction.
- No more than three different reactants and three different products are allowed in a single reaction.
- The order of species on both sides of a reaction should be written as: gas species; mobile surface species; immobile surface species; and bulk species.
- An adsorption reaction is required for every adsorbed species.
- Non-integer stoichiometric coefficients and arbitrary reaction orders are not allowed.

The reaction flux, $r_{i,ns}$, for reaction i on phase ns is given by,

$$r_{i,ns} = k_{fi} \prod_{k=1}^K X_k^{v'_{ki}} - k_{bi} \prod_{k=1}^K X_k^{v''_{ki}} \quad (18)$$

where k_{fi} and k_{bi} are the forward and backward reaction rate coefficients for reaction i at a given temperature. The reaction flux gives the number of reaction events in $\text{mol m}^{-2} \text{ s}^{-1}$ and can be used to compute a variety of chemical species production rates. The reaction-specific local production rate of species k via

reaction i on surface phase ns is,

$$\dot{w}_{ki, ns} = v_{ki} r_{i, ns} \quad (19)$$

where $v_{ki} = (v''_{ki} - v'_{ki})$. The net local production rate of species k on surface phase ns is the sum of production from all reactions operating in phase ns ,

$$\dot{w}_{k, ns} = \sum_i^I \dot{w}_{ki, ns} \quad (20)$$

The reaction-specific global production rate of species k via reaction i is,

$$\dot{w}_{ki} = \Omega_{ns} \dot{w}_{ki, ns} \quad (21)$$

and the net global production rate of species k by all reactions is,

$$\dot{w}_k = \sum_i^I \dot{w}_{ki} \quad (22)$$

For a gas species, the net global production rate is the rate that surface reactions are adding (positive) or removing (negative) that species from the gas environment. It is these net global production rates that couple the surface environment to the gas environment through the diffusive and convective mass flux boundary conditions.

For a bulk species, the net global production rate is the rate that surface reactions are adding (positive) or removing (negative) that species from the bulk environment. In the absence of a materials response model, these rates do not change the compositions of the bulk phases. Mass removed from the bulk environment is added to the gas environment and vice versa. It is this net mass transfer between the bulk and gas environments that produces a nonzero convective mass flux boundary condition.

For a surface species, the net global species production rate is the rate that surface reactions are augmenting or depleting the population of that species when averaged over the entire surface. Since each surface species is uniquely associated with a particular set of active sites, the net local chemical production rate of a surface species is the rate that surface reactions are augmenting (positive) or depleting (negative) the population of that species on its individual surface phase.

$$\dot{w}_{k, ns} = \frac{\partial \Phi_{ns, na, k}}{\partial t} \quad (23)$$

Because multiple surface species are competing for the same active sites and because surface reactions may involve different sets of active sites in the same surface phase, the surface species populations in a given phase are highly coupled. For steady-state conditions, local species surface coverage is determined

by the solution of the coupled equation set,

$$\dot{w}_{k,ns} = 0 \quad (24)$$

Both steady-state and transient surface populations are constrained by the requirement that the population of all species associated with a given active site set must sum to the total site density,

$$\Phi_{ns,na} = \sum_{k=1}^{K_{ns,na}} \Phi_{ns,na,k} \quad (25)$$

The forward reaction rate coefficient must be specified for each surface reaction in the model. The five different types of forward reaction rate coefficients that can be specified in the current formulation are listed in Table 1. In these rate formulas, β and T' are dimensionless ($T' = T/1K$ where T is in Kelvin) and the various activation energies E are in J mol^{-1} . The units of the A in the Arrhenius expression vary depending on reactant environments and reaction stoichiometries involved. For a reaction involving one gas and one surface reactant, the units of A would be $\text{m}^3 \text{ mol}^{-2} \text{ s}^{-1}$; for a reaction involving two surface reactants, the units of A would be $\text{m}^2 \text{ mol}^{-1} \text{ s}^{-1}$; for a reaction involving one surface and one bulk reactant, the units of A would be s^{-1} . Although the Arrhenius expression is the most general way to specify a surface reaction rate, the parameters are difficult to relate to physical, chemical or kinetic processes. A more insightful way to specify surface reaction rates is through kinetics-based formulations for specific types of reactions (adsorption, Eley–Rideal (ER), Langmuir–Hinshelwood (LH), and sublimation).

TABLE 1 FORWARD REACTION RATES

Reaction Type	Rate Formula	Parameters
0: Arrhenius	$k_f = AT'^\beta \exp\left(-\frac{E}{RT}\right)$	A, β, E
1: Adsorption	$k_f = \left[\frac{\bar{V}}{4\Phi_s^{\nu_s}} \right] S_0 T'^\beta \exp\left(-\frac{E_{ad}}{RT}\right)$	S_0, β, E_{ad}
2: Eley–Rideal	$k_f = \left[\frac{\bar{V}}{4\Phi_s^{\nu_s}} \right] \gamma_{er} T'^\beta \exp\left(-\frac{E_{er}}{RT}\right)$	$\gamma_{er}, \beta, E_{er}$
3: Langmuir–Hinshelwood	$k_f = \left[\bar{v}_{2D} \Phi_s^{(1.5-\nu_s)} \sqrt{A_v} \right] C_{lh} T'^\beta \exp\left(-\frac{E_{lh}}{RT}\right)$	C_{lh}, β, E_{lh}
4: Sublimation	$k_f = \left[\frac{\bar{V}}{4\Phi_s^{\nu_s} RT} \right] \gamma_{sub} T'^\beta \exp\left(-\frac{E_{sub}}{RT}\right)$	$\gamma_{sub}, \beta, E_{sub}$

In these kinetics-based rate formulations, the leading term in brackets does not have to be specified as part of the rate coefficient, but it can be computed internally from other surface chemistry model inputs. The leading term contains the following variables: Φ_s is the total active site density in the surface phase where the reaction takes place; v_s is the site density exponent equal to the sum of stoichiometric coefficients for all surface reactants; \bar{v} is the mean thermal velocity of the relevant gas species—the incoming reactant for the adsorption and ER reactions and the volatizing species in the sublimation reaction; and \bar{v}_{2D} is the mean thermal speed of the mobile surface species for the LH reaction,

$$\bar{v} = \sqrt{\frac{8RT}{\pi M}} \quad (26)$$

$$\bar{v}_{2D} = \sqrt{\frac{\pi RT}{2M}} \quad (27)$$

The sticking coefficient S_0 and the ER reaction efficiency γ_{er} are dimensionless, and their values should lie between 0 and 1. When specified with a nonzero value of β , the constraints $S_0 T'^\beta \leq 1$ and $\gamma_0 T'^\beta \leq 1$ are enforced. In the LH rate, C_{lh} is a dimensionless constant, A_v is Avogadro's number, and the activation energy is given by,

$$E_{lh} = \max(E_{mA}, E_{des,A} + E_{des,B} - E_{diss,AB}) \quad (28)$$

where E_{mA} is the surface diffusion energy barrier for the mobile reactant, $E_{des,A}$ and $E_{des,B}$ are the desorption energies for the adsorbed surface species, and $E_{diss,A,B}$ is the dissociation energy for the product molecule.

The sublimation rate expression is derived assuming the following two forms for the evaporation coefficient and the equilibrium vapor pressure,

$$\alpha = \alpha_0 \exp\left(-\frac{E_\alpha}{RT}\right) \quad (29)$$

and

$$P_{eq} = P_0 \exp\left(-\frac{E_{vap}}{RT}\right) \quad (30)$$

The dimensionless evaporation coefficient must lie between 0 and 1; $E_{sub} = E_{vap} + E_\alpha$ and $\gamma_{sub} = \alpha_0 P_0$ with units of Pa.

3. EQUILIBRIUM CONSTANTS AND THERMODYNAMIC DATA

Calculation of the reaction flux $r_{i,ns}$ from Eq. (18) also requires a backward rate coefficient. The backward rate coefficient is computed from the forward rate

coefficient and the concentration-based equilibrium constant as:

$$k_{bi} = \frac{k_{fi}}{K_{ci}} \quad (31)$$

The concentration-based equilibrium constant is related to the activity-based equilibrium constant by:

$$K_{ci} = K_{ai} \left(\frac{P_{\text{ref}}}{RT} \right)^{\nu_{gi}} \quad (32)$$

where the net stoichiometric exponent ν_{gi} runs only over the gas species:

$$\nu_{gi} = \sum_{k=1}^{K_g} (\nu''_{ki} - \nu'_{ki}) \quad (33)$$

The activity-based equilibrium constant for reaction i is defined by,

$$K_{ai} = \prod_{k=1}^K (a_k)^{\nu_{ki}} \quad (34)$$

Activity of ideal gas-phase species is its partial pressure divided by a reference pressure (typically 1 atmosphere or 1 bar). This is the same as the species mole fraction times the ratio of the total gas pressure to the reference pressure:

$$a_k = \left(\frac{P_k}{P_{\text{ref}}} \right) = \chi_k \left(\frac{P}{P_{\text{ref}}} \right) \quad (35)$$

The activity of a pure solid or liquid phase is taken as 1. The activity of a species in an ideal solid or liquid solution in phase nb is taken as its concentration divided by a reference concentration,

$$a_k = \left(\frac{C_k}{C_{nb,\text{ref}}} \right) = \chi_k \left(\frac{C_{nb}}{C_{nb,\text{ref}}} \right) \quad (36)$$

If potential concentration available to a solute species in bulk phase nb remains fixed, $C_{nb}/C_{nb,\text{ref}} = 1$. The activity of a species adsorbed to surface phase ns is taken as its surface concentration divided by a reference surface concentration,

$$a_k = \left(\frac{\Phi_{ns,k}}{\Phi_{ns,\text{ref}}} \right) = \theta_{ns,k} \left(\frac{\Phi_{ns}}{\Phi_{ns,\text{ref}}} \right) \quad (37)$$

If the total number of potential active sites available for an adsorbed species on surface phase ns remains constant, $\Phi_{ns}/\Phi_{ns,\text{ref}} = 1$.

The activity-based equilibrium constant is related to changes in the Gibbs energy of formation at temperature T in going from reactants to products,

$$\begin{aligned} K_{ai} &= \exp\left[\frac{-\Delta G_i^o(T)}{RT}\right] = \exp\left[-\sum_{k=1}^K v_{ki} \frac{G_k^o(T)}{RT}\right] \\ &= \exp\left[-\sum_{k=1}^K v_{ki} \left(\frac{H_k^o(T)}{RT} - \frac{S_k^o(T)}{R}\right)\right] \end{aligned} \quad (38)$$

The activity-based equilibrium constant can be calculated directly if the necessary thermodynamic functions are available for each species in the reaction. Thermodynamic function values are generally available for gases, pure liquids, and pure solids, but not surface phases.

The difference between the Gibbs energy of formation of an occupied active site and a vacant active site,

$$G_{[A]_s}^o(T) - G_{[s]}^o(T) \quad (39)$$

appears in most activity-based surface equilibrium constants computed by Eq. (38). Since experimental thermodynamic data are typically unavailable, this energy difference must be computed by some other means. One approach is to create empirically, or through ab initio computational methods, temperature-dependent enthalpy and entropy functions for the relevant surface species from which the Gibbs energies of formation can be calculated.

An alternate procedure is employed here: in addition to specifying k_{fi} for each adsorption reaction, we also specify either the backward (thermal desorption) rate coefficient k_{bi} or the concentration-based equilibrium constant K_{ci} . Analytic expressions for both k_{bi} and K_{ci} can be derived from simple statistical thermodynamics and/or kinetic theory. Then the missing Gibbs formation energy difference is computed as:

$$\begin{aligned} G_{[A]_s}^o(T) - G_{[s]}^o(T) &= G_A^o(T) - RT \ln(K_{ai}) \\ &= G_A^o(T) - RT \ln\left(K_{ci} \left(\frac{P_{\text{ref}}}{RT}\right)^{-v_{gi}}\right) \\ &= G_A^o(T) - RT \ln\left(\frac{k_{fi}}{k_{bi}} \left(\frac{P_{\text{ref}}}{RT}\right)^{-v_{gi}}\right) \end{aligned} \quad (40)$$

These calculated differences in Gibbs formation energy can be used together with tabulated thermodynamic data for bulk- and gas-phase species to evaluate the equilibrium constants for all other surface reactions, i.e., ER and LH recombination, oxidation, etc.

The desorption rate coefficient is represented by the general expression,

$$k_{\text{des}} = A_{\text{des}} T^{\beta} v \exp\left(-\frac{E_{\text{des}}}{RT}\right) \quad (41)$$

The attempt frequency $v(s^{-1})$ and the desorption energy E_{des} (J mol^{-1}) are taken as surface coverage independent, since the correct functional forms for this dependence are uncertain, and experimental data for systems of interest are scarce. Moreover, most aerothermal applications will take place at high surface temperatures at which adsorbed species coverage will be low, and the surface coverage-dependence of v and E_{des} should be weak. The desorption energy E_{des} is taken as a constant, while various functional choices exist for v . The simplest approach is to specify v as a constant, usually in the range $10^{12}\text{--}10^{15} \text{ s}^{-1}$ [18–20]. Another approach is to use approximations for v based on different levels of transition state theory (TST). The following forms for v can be invoked in this surface reaction model,

$$\text{Form 0, Arrhenius: } v = 1 \quad (42)$$

$$\text{Form 1, constant: } v = v_{sA,\perp} \quad (43)$$

$$\text{Form 2, simple TST: } v = \left(\frac{RT}{A_v h}\right) \quad (44)$$

$$\text{Form 3, complex TST: } v = \left(\frac{RT}{A_v h}\right) \frac{1 - \exp\left(-\frac{hA_v v_{sA,\perp}}{RT}\right)}{\exp\left(-\frac{hA_v v_{sA,\perp}}{2RT}\right)} \quad (45)$$

The concentration-based equilibrium constant for an adsorption/desorption reaction is expressed by the function,

$$K_c = A_{\text{eq}} T^{\beta} K_0 \exp\left(\frac{E_{\text{des}} - E_{\text{ad}}}{RT}\right) \quad (46)$$

where the form of the pre-exponential coefficient K_0 depends on the type of adsorption (mobile or immobile), and the level of transition state theory approximation is employed. The following forms for K_0 can be invoked in this surface reaction model:

$$\text{From 0, Arrhenius: } K_0 = 1 \quad (47)$$

$$\text{From 1, simple TST, immobile: } K_0 = \left(\frac{2\pi M_A RT}{(A_v h)^2}\right)^{-3/2} \quad (48)$$

From 2, complex TST, immobile: $K_0 = \left(\frac{2\pi M_A R T}{(A_v h)^2} \right)^{-3/2}$

$$\times \left(\frac{\exp\left(-\frac{h A_v v_{sA}}{2RT}\right)}{1 - \exp\left(-\frac{h A_v v_{sA}}{RT}\right)} \right)^3 \quad (49)$$

From 3, simple TST, mobile: $K_0 = \left(\frac{2\pi M_A R}{(A_v h)^2 T} \right)^{-1/2} \quad (50)$

From 4, complex TST, mobile: $K_0 = \left(\frac{2\pi M_A R}{(A_v h)^2 T} \right)^{-1/2}$

$$\times \left(\frac{\exp\left(-\frac{h A_v v_{sA,\perp}}{2RT}\right)}{1 - \exp\left(-\frac{h A_v v_{sA,\perp}}{RT}\right)} \right) \quad (51)$$

B. INCORPORATION INTO A CFD CODE

The finite-rate formulation described above is generally applicable to any generic CFD code via the surface boundary conditions. The implementation strategy into the DPLR CFD code is discussed below in detail, with a derivation of the boundary conditions enforced at the reacting surface. The DPLR code enforces wall boundary conditions implicitly. In our experience this requires accurate Jacobian contributions of the boundary condition to be specified. The boundary conditions are then advanced in time to steady-state along with the interior flowfield. This generalized finite-rate formulation has also been implemented into the US3D code [21] and into the LeMANS code [22, 23] by solving for the steady-state surface coverage and explicitly imposing the resulting coverage and associated gas production rates at each interior flowfield time step. Comparisons between results from the three codes show that both formulations can be expected to produce identical answers [24, 25].

1. DPLR

DPLR is a multi-block, structured, finite-volume code that solves the reacting Navier–Stokes equations including finite-rate chemistry and finite-rate vibrational nonequilibrium effects. This code is based on the data-parallel line relaxation method [26] which implements a modified (low dissipation) Steger-Warming flux-splitting approach [27] for the convection terms and central differencing for the diffusion terms. Finite-rate vibrational relaxation is modeled via a

simple harmonic oscillator vibrational degree of freedom [28] using the Landau-Teller model [29]. Vibrational energy relaxation time constants are computed by default from the semi-empirical expression owing to Millikan and White [30], but rates from the work of Camac [31] and Park et al. [32] are substituted for specific collisions for which experimental data exists. Vibration-dissociation coupling is currently modeled using the $T - T_v$ approach of Park [33] or with some preliminary implementation of coupled vibration-dissociation vibration (CVDV) coupling [34]. Transport properties are modeled in DPLR for high enthalpy flow [35, 36] using the binary collision-integral based mixing rules from Gupta et al. [37] with a database of relevant collision integral data for high temperature collisions [38, 39]. Diffusion fluxes can be modeled using either Fick's law of diffusion or the self-consistent effective binary diffusion (SCEBD) method [40].

2. SURFACE BOUNDARY CONDITIONS

The molar production or loss of any species at the surface (per unit surface area per unit time, e.g. $\text{mol m}^{-2} \text{ s}^{-1}$) is the summation of the individual production from each reaction, considering both forward and backward rate processes:

$$\dot{w}_k = \sum_{i=1}^I \left\{ (\nu''_{ki} - \nu'_{ki}) \left(k_{fi} \prod_{m=1}^{Ns} [X_m]^{\nu'_{mi}} - k_{bi} \prod_{m=1}^{Ns} [X_m]^{\nu''_{mi}} \right) \right\} \quad (52)$$

The chemical source term in Eq. (52) applies to species in any phase at the gas/surface interface, but species concentrations in the bulk phases are assumed to be constant in time as identical material replenishes the amount consumed in the reaction (as the surface recesses). However, the rate of loss or gain of bulk-phase material implies an addition or subtraction of mass from the gas phase. This results in an effective surface blowing or suction in the gas-phase boundary condition rather than the no-slip boundary condition:

$$\dot{m}_b = - \sum_{b=1}^{Nb} M_b \dot{w}_b \quad (53)$$

A limited form of pyrolysis is also included in the model formulation, in which additional blowing of gas-phase species can be added to the blowing implied by Eq. (53) either by entering explicit mass flow rates that must come from material response or via the steady-state approximation [41–43], in which the mass of pyrolysis gas passing through the surface is assumed to be proportional to the bulk (or char) blowing rate as in Eq. (54); here the char yield C_Y is equal to the ratio of the char density to the virgin material density and the relative composition of the pyrolysis gas must be explicitly specified.

$$\dot{m}_g = \dot{m}_b \left[\frac{1}{C_Y} - 1 \right] \quad (54)$$

For the integration of the finite-rate surface-chemistry model with DPLR, mass balance at the surface is utilized to set the boundary condition for the each species in the gas phase environment. For the infinitely thin control volume at the surface at any instant in time, the rate of diffusion of gaseous species away from the surface into the gas-phase interior and the rate that the entire mixture is convected away from the surface owing to bulk production exactly balances the rate of production from surface reactions of that species.

In this section, we use the subscripts g and s exclusively to indicate a vector length over all gas or surface species respectively. A partial derivative of a vector of an indicated length implies that the resulting term is a matrix with a number of rows matching the indicated length, whereas a partial derivative with respect to an indicated length vector implies that the result has a number of columns matching the indicated length.

Mass balance for each gaseous species, k , at the surface from Fig. 2a is written in Eq (55), which represents the rate at which mass of each gas-phase species changes at the surface. The source term from the finite-rate surface chemistry model is computed on a molar basis and the finite-rate framework allows for production to come from either finite-rate reactions occurring at the surface and/or from simple approximations to pyrolysis flow. Here, we note that the derivation of the implicit species mass balance relationship is performed assuming Fickian diffusion with mass fractions as the unknowns for simplicity in demonstrating the derivation, but it is straightforward to extend these results to better diffusion models such as SCEBD [40] or iterative Stefan–Maxwell [44], since those models amount to adding one or more correction terms to the form of the flux appearing in the first term of Eq (55). A major advantage of advanced diffusion models such as SCEBD over Fick’s law is that diffusive fluxes are automatically conserved (e.g. sum to zero) as they should. Thus, although DPLR uses SCEBD by default, the form of the implicitly coupled boundary equations remain the same, as shown here (with an added constant multiplier). Gosse and Candler [45] compare these improved flux schemes more thoroughly.

$$-\rho_w D_k \Delta y_k|_w + \rho_w v_w y_{k,w} = M_k \dot{w}_k \quad (55)$$

Energy balance at the surface is typically enforced using the radiative equilibrium boundary condition shown in Fig. 2b with the model formulation

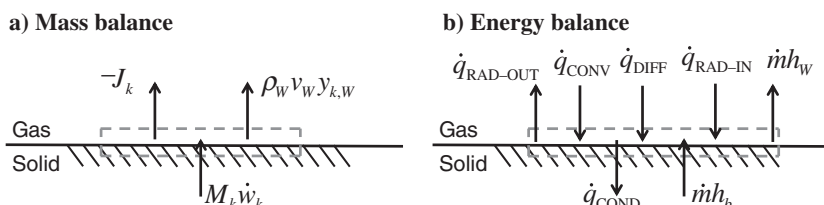


Fig. 2 Control volumes for the derivation of mass and energy balances at the surface.

constraint that material gained from the bulk phase has the same temperature as the gas at the surface and by assuming that the conduction term into the TPS is negligible. However, by assuming steady-state pyrolysis production, in which the surface recession rate owing to bulk loss and the pyrolysis front recession rate are equal, the control volume shown in Fig. 2b may be extended into the material to the unaffected front to eliminate the unknown conduction term. The solution of the steady-state energy balance (SSEB) equation is a straightforward extension of radiative equilibrium, since the only additional term imposed by the surface model is the enthalpy of the virgin material, h_a , which we consider to be a constant of the particular material. The SSEB equation is given in Eq. (56).

$$\sum_{m=1}^{N_T} k_m \nabla T_m \Big|_w + \sum_{k=1}^{N_g} h_k \rho D_k \nabla y_k \Big|_w + \alpha_w \dot{q}_{\text{rad}} = (\rho v)_w (h_w - h_a) + \sigma \epsilon T_w^4 \quad (56)$$

The discretized form of Eq. (55) for species mass-balance is given in Eq. (57), where the function, F_k , is defined to be zero and is enforced using a Newton iteration scheme. Because the boundary condition connects solution quantities (in this case species mass fractions) at the surface with those in the interior, the implicit dependence must be added to the solution matrix to maintain superior convergence behavior.

$$F_k = (y_{k,w} - y_{k,1}) + \frac{\Delta n}{D_k} v_w y_{k,w} - \frac{\Delta n M_k}{\rho_w D_k} \dot{w}_k = 0 \quad (57)$$

Purely for convenience in the derivation, the set of (assumed constant) terms in front of the production source term is defined with a single symbol in Eq. (58), and the term in front of the convection term is defined with a single symbol in Eq. (59).

$$\alpha_k \equiv \frac{\Delta n M_k}{\rho_w D_k} \quad (58)$$

$$\beta_k \equiv \frac{\Delta n}{D_k} \quad (59)$$

Implicit coupling is required for the production term that appears in the gas-phase boundary equations. The implicit form of the gas-phase boundary condition in Eq. (57) can be expressed as a series expansion about the $n+1$ time level and enforcing $F^{n+1} = 0$ as shown in Eq. (60) for each gaseous species, where the bracket notation, $[]$, is used to indicate a vector (with indicated length of g or s).

$$\frac{\partial F_k}{\partial [y]_{g,w}} \Delta^n [y]_{g,w} + \frac{\partial F_k}{\partial [y]_{g,1}} \Delta^n [y]_{g,1} + \frac{\partial F_k}{\partial [X]_s} \Delta^n [X]_s + \frac{\partial F_k}{\partial T} \Delta^n T + \frac{\partial F_k}{\partial v} \Delta^n v = -F_k \quad (60)$$

Expressed in this form, the boundary condition is dependent on the state of the gas-phase interior composition away from the wall (subscript “*g, 1*”), the gas-phase composition at the wall (subscript “*g, w*”), the gas-phase wall temperature, the wall-normal velocity, and the adsorbed surface composition (subscript “*s*”). The rate of change of the bulk phase is defined to be identically zero for all situations, so no term appears from bulk species dependencies.

The total production of each gaseous species is given in Eq. (61). The composite expression can include contributions from surface reactions (labeled with a “*c*”) as well as additional contributions from pyrolysis. For explicit pyrolysis or transpiration (labeled with an “*e*”), additional mass production is added to the total production rate. For steady-state pyrolysis (last term), the additional production of the gaseous species is proportional to the bulk-phase production rate, so the Jacobian of the source term must be modified.

$$\dot{w}_k = \dot{w}_{k,c} + \dot{w}_{k,e} + \frac{\chi_k}{\sum_{j=1}^{N_g} \chi_j M_j} \left(\frac{1}{C_Y} - 1 \right) \left(- \sum_{b=1}^{Nb} M_b \dot{w}_b \right) \quad (61)$$

The implicit Jacobian of this source term is given in Eq. (62), where *q* is used to represent a generic independent variable.

$$\frac{\partial \dot{w}_k}{\partial q} = \frac{\partial \dot{w}_{k,c}}{\partial q} + \frac{\chi_k}{\sum_{j=1}^{N_g} \chi_j M_j} \left(\frac{1}{C_Y} - 1 \right) \left(- \sum_{b=1}^{Nb} M_b \frac{\partial \dot{w}_b}{\partial q} \right) \quad (62)$$

For adsorbed surface species and bulk-phase species, there is no possibility of diffusion or convection, so the rate of change of the vector of surface phase species is given in Eq. (63).

$$\frac{\partial [X]_s}{\partial t} = [\dot{w}]_s \quad (63)$$

The implicit form of the adsorbed surface species concentration vector may be written by expanding Eq. (63) at the *n* + 1 time level as given in Eq. (64).

$$\frac{\Delta^n [X]_s}{\Delta t} = [\dot{w}]_s + \frac{\partial [\dot{w}]_s}{\partial [X]_s} \Delta^n [X]_s + \frac{\partial [\dot{w}]_s}{\partial [X]_g} \Delta^n [X]_g + \frac{\partial [\dot{w}]_s}{\partial T} \Delta^n T \quad (64)$$

This set of equations is dependent on the gas-phase composition at the wall, the gas-phase wall temperature (which is assumed to be equal to the surface phase wall temperature), and the surface-phase composition. The vector of nongaseous

concentrations may be solved for as shown in Eq. (65).

$$\Delta^n[X]_s = \left(\frac{[I]_s}{\Delta t} - \frac{\partial[\dot{w}]_s}{\partial[X]_s} \Big|_n \right)^{-1} [\dot{w}]_s \Big|_n + \left(\frac{[I]_s}{\Delta t} - \frac{\partial[\dot{w}]_s}{\partial[X]_s} \Big|_n \right)^{-1} \frac{\partial[\dot{w}]_s}{\partial[X]_g} \Big|_n \Delta^n[X]_g \\ + \left(\frac{[I]_s}{\Delta t} - \frac{\partial[\dot{w}]_s}{\partial[X]_s} \Big|_n \right)^{-1} \frac{\partial[\dot{w}]_s}{\partial T} \Big|_n \Delta^n T \quad (65)$$

The surface variable vector of unknowns in Eq. (65) may be substituted into Eq. (60). Additionally, a relationship is required for the conversion of the gas-phase concentrations to the gas-phase mass fractions, or whatever variable is used consistent with the flux approximation (mass fractions, mole fractions, concentrations, etc.). This is given in Eq. (66) for this derivation in terms of mass fractions.

$$\frac{\partial X_{k,w}}{\partial y_{k,w}} = \frac{\rho_w}{M_k} \quad (66)$$

After rearranging the remaining terms, the implicit form of the gas-phase boundary condition is given in Eq. (67), where all derivatives are evaluated at the n time level (the subscripts are dropped). All terms in the equation are known in the gas phase, but the implicit contribution of the surface reactions remain.

$$\left\{ (1 + \beta_k v_w) \delta_{g,k} - \alpha_k \left[\frac{\partial \dot{w}_k}{\partial [X]_{g,w}} + \frac{\partial \dot{w}_k}{\partial [X]_s} \left(\frac{[I]_s}{\Delta t} - \frac{\partial[\dot{w}]_s}{\partial[X]_s} \right)^{-1} \frac{\partial[\dot{w}]_s}{\partial[X]_{g,w}} \right] \frac{\partial[X]_{g,w}}{\partial[c]_{g,w}} \right\} \Delta^n[y]_{g,w} \\ - (1) \Delta^n y_{k,1} + (\beta_k y_{k,w}) \Delta^n v_w - \alpha_k \left[\frac{\partial \dot{w}_k}{\partial T} + \frac{\partial \dot{w}_k}{\partial [X]_s} \left(\frac{[I]_s}{\Delta t} - \frac{\partial[\dot{w}]_s}{\partial[X]_s} \right)^{-1} \frac{\partial[\dot{w}]_s}{\partial T} \right] \Delta^n T \\ = -[(y_{k,w} - y_{k,1}) + \beta_k v_w y_{k,w} - \alpha_k \dot{w}_k] + \alpha_k \frac{\partial \dot{w}_k}{\partial [X]_s} \left(\frac{[I]_s}{\Delta t} - \frac{\partial[\dot{w}]_s}{\partial[X]_s} \right)^{-1} [\dot{w}]_s \quad (67)$$

In addition to the equations for the gas-phase species masses, the rate of wall-normal velocity blowing also needs to be computed as a function of the nongas-phase production terms. Specifically, the wall-normal mass blowing (the product of wall density and the velocity normal to the surface) is equal to the negative of the production of the bulk-phase species, or the rate at which solid-phase material is removed from the surface. This relationship is shown in Eq. (68):

$$\rho_w v_w = -\frac{1}{C_Y} \sum_{b=1}^{Nb} M_b \dot{w}_b + \dot{m}_{p,e} \quad (68)$$

Here, the char yield parameter, C_Y , accounts for any steady-state pyrolysis, and C_Y is set equal to 1.0 if there is no pyrolysis present. Explicit gaseous mass

addition that is not proportional to bulk production is added to the explicit mass balance by the last term.

The implicit form of the wall blowing velocity is given in Eq. (69), which includes dependencies on the wall-normal velocity component, the gas-phase species mass fraction vector, and the surface-phase species concentrations.

$$\rho_w \Delta^n v_w + \left(\sum_{b=1}^{Nb} \frac{M_b}{C_Y} \frac{\partial \dot{w}_b}{\partial [X]_g} \frac{\partial [X]_{g,w}}{\partial [y]_{g,w}} \right) \Delta^n [y]_{g,w} + \left(\sum_{b=1}^{Nb} \frac{M_b}{C_Y} \frac{\partial \dot{w}_b}{\partial T} \right) \Delta^n T \\ + \left(\sum_{b=1}^{Nb} \frac{M_b}{C_Y} \frac{\partial \dot{w}_b}{\partial [X]_s} \right) \Delta^n [X]_s = - \left[\rho_w v_w + \sum_{b=1}^{Nb} \frac{M_b}{C_Y} \dot{w}_b - \dot{m}_{p,e} \right] \quad (69)$$

As before, the expression for the surface-phase concentration vector can be substituted in from Eq. (64) and the result is shown in Eq. (70).

$$\rho_w \Delta^n v_w + \left\{ \left(\sum_{b=1}^{Nb} \frac{M_b}{C_Y} \frac{\partial \dot{w}_b}{\partial [X]_s} \right) \left(\frac{[I]_s}{\Delta t} - \frac{\partial [\dot{w}]_s}{\partial [X]_s} \right)^{-1} \frac{\partial [\dot{w}]_s}{\partial T} \right\} \Delta^n T \\ + \left[\left(\sum_{b=1}^{Nb} \frac{M_b}{C_Y} \frac{\partial \dot{w}_b}{\partial [X]_g} \right) + \left(\sum_{b=1}^{Nb} \frac{M_b}{C_Y} \frac{\partial \dot{w}_b}{\partial [X]_s} \right) \right. \\ \times \left. \left(\frac{[I]_s}{\Delta t} - \frac{\partial [\dot{w}]_s}{\partial [X]_s} \right)^{-1} \frac{\partial [\dot{w}]_s}{\partial [X]_{g,w}} \right] \frac{\partial [X]_{g,w}}{\partial [y]_{g,w}} \Delta^n [y]_{g,w} \\ = - \left[\rho_w v_w + \sum_{b=1}^{Nb} \frac{M_b}{C_Y} \dot{w}_b - \dot{m}_{p,e} \right] \\ - \left(\sum_{b=1}^{Nb} \frac{M_b}{C_Y} \frac{\partial \dot{w}_b}{\partial [X]_s} \right)^T \left(\frac{[I]_s}{\Delta t} - \frac{\partial [\dot{w}]_s}{\partial [X]_s} \right)^{-1} [\dot{w}]_s \quad (70)$$

For systems with no bulk-phase production (i.e., only gas- and surface-phase production rates), the blowing velocity is zero. Together, Eqs. (67) and (70) represent the implicitly coupled implementation of the finite-rate surface system.

After each iterative solution the surface species concentrations are updated using Eq. (65) and the newly computed delta values of all gas-phase quantities. It should also be noted that the time step appears in the surface system. This time step should be the physical time step of the gas flow for a globally time-accurate method but, for steady-state problems, the possibility exists of adjusting this time step to improve stability or maximize convergence rate, but strategies for doing this have not yet been studied.

In general, this formulation results in a boundary condition that is far more complex than straight-forward Dirichlet or Neumann boundary conditions and stability depends on the stiffness of the gas/surface reaction rates, just as with

stiff source terms associated with the interior flowfield. For example, sublimation reaction rates that can increase by orders of magnitude with small changes in surface temperature can destabilize a problem. Strategies such as manipulating the surface reaction time step suggested above, suppressing rapid changes in surface temperature or reaction rates as the problem converges, or applying maximum limits to the change of surface concentrations can all be utilized to improve solution behavior on a case by case basis. In a later section, a number of test cases are shown that demonstrate that good solution behavior is obtained for most realistic problems of interest. For many examples, the formulation as outlined above converges as quickly as a simple Dirichlet boundary condition with the implicit coupling.

IV. COMPUTATIONAL CHEMISTRY APPROACHES FOR SURFACE CHEMISTRY MODELING

A. BACKGROUND

Section III demonstrates the increased flexibility and generality gained by the use of finite-rate surface chemistry models. However, such finite-rate models also require a large number of new physical parameters as input, many of which are not well characterized. Parameter values can have large uncertainties, and the overall gas–surface interaction will have a highly nonlinear dependence on these parameters [24].

At the same time, the finite-rate surface chemistry formulation presented above now describes elementary reactions and rate parameters (activation energies and steric factors) that could potentially be obtained by computational chemistry simulation. Furthermore, the set of reactions to include in a finite-rate model is also an input, and computational chemistry analyses may be useful for determining the dominant reaction mechanisms for particular gas–surface systems (e.g., reaction pathways occurring on specific active chemical surface sites).

There are four important aspects when employing computational chemistry methods to inform a macroscopic finite-rate gas–surface chemistry model. First, the accuracy of the computational chemistry model for the chemical system of interest must be established. Second, and arguably the most difficult, is that the surface of interest must be characterized at the atomistic level. Specifically, what does the surface look like, chemically, at the atomistic level under *in situ* conditions when exposed to a high temperature dissociated gas? If this can be determined, then the third aspect involves trajectory calculations of gas molecules impacting a realistic surface. Precisely, how do gas-phase atoms and molecules interact with the surface; what are the dominant reaction mechanisms and their associated energetics? Finally, the fourth aspect involves scaling the atomistic simulations of individual gas–surface reactions to form a macroscopic finite-rate model suitable for CFD simulation.

In this section, each aspect will be elaborated upon using the specific example of oxygen-silica interactions.

B. QUANTUM CHEMICAL DESCRIPTIONS OF GAS-SURFACE SYSTEMS

Quantum chemistry calculations often employ density functional theory (DFT). Although accurate and precise, DFT calculations are limited to fewer than 100 atoms owing to computational requirements. In contrast to the simulation of gas-phase collisions, for which only a few atoms participate in a given collision, large numbers of atoms must be simulated for gas-surface systems. This is especially true when predicting the *in situ* surface morphology by computational chemistry simulation. In order to simulate large atomic systems, single point energies computed by DFT can be used to fit a Potential Energy Surface (PES), also referred to as a Force Field. The equations of atomic motion can then be integrated using the specified PES using techniques from Molecular Dynamics (MD), thereby simulating interactions between large systems of atoms.

Molecular dynamics simulations based on empirical PES have been used widely in the study of gas-surface interactions of oxygen atoms and molecules with silica surfaces. A number of empirical force fields describing Si-O systems have been developed in the past [46–51], and they have been successful in describing the structures and energies of various polymorphs of silicon and silicon oxides. Specifically, the BKS potential [48] has been used for simulating bulk silica and silica surfaces [52]. Although these force fields provide valuable insights into the dynamics of silica polymorphs and their chemistry, they are applicable only close to the equilibrium structures of the morphologies against which they were parameterized. This imposes a severe restriction on the transferability of these potentials and their ability to simulate chemical reactions. Indeed, a number of researchers have used density functional calculations to fit a specific PES for reacting systems of interest [53–60]. There are certainly many ways to fit such a PES, however, the final PES should be verified to reproduce the DFT data used for the fit, the PES should be accurate within a useful (but limited) range outside of the DFT data, and ideally predictions using the PES within MD simulations should be validated with available experimental data relevant to chemical systems under study.

In this work, we utilize the ReaxFF PES formulation. ReaxFF is a classical potential parameterized from a training set of quantum chemical calculations [61]. The system energy in ReaxFF is calculated as the sum of a number of energy terms and a full description of these terms and their energy expressions can be found in the original work [62]. The ReaxFF potential has been shown to accurately model a diverse array of chemically reacting systems, including gas-surface interfaces. For example, ReaxFF MD simulations of the trapping probability of oxygen molecules as well as the adsorption and desorption of oxygen on a Pt(111) surface are in good quantitative agreement with experimental results [63, 64].

To describe the structures, properties, and chemistry specific to silicon and silicon oxide materials, ReaxFF_{SiO} was developed by van Duin et al. [62]. This specific parameterization has been shown to accurately reproduce the bulk phases of several polymorphs of SiO₂. Furthermore, ReaxFF_{SiO} simulations of the oxidation of Si(100) reconstructed surfaces [65, 66] and Si nanowires [67] have been shown to closely match the experimental radial distribution functions and bond angle distribution of amorphous silica thus formed, and have also been used to study hyperthermal oxygen atom interaction with silicon surfaces [68]. Thus, for the methodology and results presented in this chapter, the original ReaxFF_{SiO} parameterization [62] is used. All MD simulations presented in this chapter are carried out using the open-source LAMMPS program [69], distributed by Sandia National Laboratory (at lammps.sandia.gov), which contains many interatomic potentials, including ReaxFF_{SiO}. Thus, the simulations presented here are easily reproduced.

It is emphasized that although ReaxFF_{SiO} has been validated for bulk silica polymorphs and silica oxides, it has not been specifically validated for gas-phase oxygen interactions with silica surfaces. Recently, the ReaxFF_{SiO} potential has been re-parameterized with DFT data specific to oxygen-silica gas–surface interactions (GSI), resulting in a new ReaxFF_{SiO}^{GSI} interatomic potential [70, 71], and further validation is ongoing. However, as demonstrated in this chapter, the original ReaxFF_{SiO} potential accurately predicts many of the chemical structures found on real silica surfaces and leads to a realistic finite-rate model. The purpose of this chapter is to describe a *methodology* to construct a finite-rate gas–surface interaction model using MD simulation. Since the ReaxFF_{SiO} potential is not fully validated for gas–surface interactions, the resulting rate model is an example-model only. However, the methodology described in this chapter could be applied using other PES for oxygen-silica or PES specific to other gas–surface systems.

C. SILICA SURFACES

Fundamental to any description of recombination on a surface are the precise chemical structures on the surface with which gas-phase molecules interact under *in situ* conditions. A number of computational chemistry studies of high temperature oxygen-silica interactions have been performed for the interaction of atomic and molecular oxygen with a (001) β -cristobalite surface [53–57] and with a (001) β -quartz surface [58, 59]. In both series of studies the authors used idealized cleaved crystal surfaces, which are covered in highly reactive dangling bonds that, in reality, would reconstruct to lower energy states, and hence are not representative of real silica surfaces. In this section, we present a methodology to simulate the interaction of atomic and molecular oxygen with realistic, stable surface configurations that have been observed experimentally. Specifically, we focus on dry quartz and amorphous silica (a-SiO₂) surfaces. These two types of SiO₂ are chosen because there are experimental measurements for oxygen

recombination on them [58], and as discussed in the introduction, many TPSs involve silica-based or silica-forming coatings as well as natural silica oxide formations that are amorphous.

1. CRYSTALLINE QUARTZ SURFACES

In prior work, the ReaxFF_{SiO} potential has been shown to accurately reproduce the bulk structure of α/β -quartz [72]. To form a surface from a bulk, the simplest approach is to cleave the surface along a given crystallographic plane. The cleaved (0001) α -quartz surface is shown in Fig. 3a. Other works modeling oxygen recombination on silica surfaces have used cleaved quartz [58] or cleaved β -cristobalite [55, 57] surfaces as a model of the silica surface. However, such ideal cleaved surfaces are covered in highly reactive broken bonds and in thermodynamically meta-stable states. DFT calculations [73, 74] supported by experimental results [75, 76] show that the cleaved (0001) α -quartz surface reconstructs to form (1 \times 1) and (2 \times 1) patterns as shown in Figs. 3c and 3d, respectively. Additionally, there are semi-classical ab-initio MD simulations showing that the (011) α -quartz surface reconstructs into a disordered state at room temperature [77]. In general, we expect that cleaved silica surfaces will reconstruct to minimize the number of highly reactive broken bonds on the surface.

In our MD simulations, we use the reconstructed (0001) α -quartz surface as a model for a realistic quartz surface that has not yet been exposed to atomic

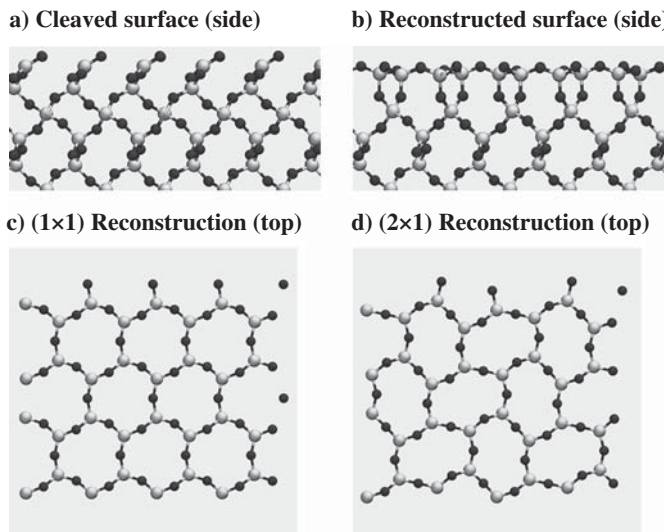


Fig. 3 Cleaved and reconstructed α -quartz surfaces.

oxygen. However, it is important to keep in mind that unless specifically processed, real quartz surfaces would present several crystal facets. To generate initial geometries for the reconstructed surface, we used the procedure described by Chen et al. [73] A $4 \times 4 \times 5$ supercell of 720 atoms of α -quartz cleaved along the (0001) plane is heated in increments of 100 K every 20 ps under constant particle number, volume, and temperature (NVT) dynamics using the BKS potential [48]. At each step, a copy of the surface is quenched to 0 K, and the resulting structure is minimized using the ReaxFF_{SiO} potential. We find that the (1 × 1) reconstruction forms at 100 K and the (2 × 1) reconstruction forms at higher temperatures. As seen in Table 2, the surface energies for the (1 × 1) and (2 × 1) reconstructions as predicted by the ReaxFF_{SiO} potential are in good agreement with published DFT results. The surface energy is defined as the difference between the energy of the slab exposed to vacuum and the energy of the slab in the bulk. Both reconstructions are significantly lower in surface energy than the cleaved surface.

The simulations of Chen et al. [73] predict several different types of the (1 × 1) and (2 × 1) reconstructions, distinguished by their orientation with respect to the crystal below. However, from a structural perspective the reconstructions are very similar, with all oxygen atoms two-coordinated and all silicon atoms four-coordinated. We will use the (0001) α -quartz surface with the (2 × 1) reconstruction generated through this method in further MD simulations of quartz surfaces. At temperatures greater than 300 K surfaces initialized from either reconstruction are indistinguishable, so we will simply refer to this surface as the reconstructed (0001) α -quartz surface.

2. AMORPHOUS SILICA SURFACES

Before we describe amorphous silica surfaces, we must first validate that the ReaxFF_{SiO} potential can accurately reproduce bulk amorphous silica (a-SiO₂). To generate bulk a-SiO₂, we performed molecular dynamics simulations following the annealing procedure described by Huff et al. [78]. Bulk β -cristobalite is given an initial temperature of 8000 K, and propagated for 20 ps under NVT dynamics to randomize its initial structure. The bulk is then cooled at 50 K ps⁻¹ under NVT

TABLE 2 SURFACE ENERGIES FOR α -QUARTZ SURFACES

Surface Reconstruction	Surface Energy, eV Å ⁻²		
	Chen (DFT) [73]	Rignanese (DFT) [74]	ReaxFF _{SiO}
Cleaved	0.167	0.17	0.150
1 × 1	0.031, 0.0308	0.05	0.0442
2 × 1	0.0273, 0.0298, 0.0343	0.09	0.0435

dynamics until it reaches 300 K. The system is propagated for a further 40 ps under constant particle number, pressure, and temperature (NPT) dynamics at 300 K, 1 atm, with the last 20 ps used to collect statistics about the structure. We used 11,616 atoms in our simulations, enough to ensure sufficient statistics about the structure were collected [78]. Simulations were performed with the ReaxFF_{SiO} potential and the BKS potential using the modifications outlined in the work by Jee et al. [79]. The BKS potential is used because it has been previously shown to reproduce the structure of bulk a-SiO₂ [80].

The total correlation function $T(r)$ can be used to directly compare the computationally generated annealed bulk structure to neutron scattering experiments. This function is generated from the partial radial distribution functions as described by Nakano et al. [81]. As shown in Fig. 4, the total correlation function of annealed a-SiO₂ created with both potentials is in relatively good agreement with experimental results. However, the ReaxFF_{SiO} potential under-predicts the location and magnitude of the secondary peak, which represents the average distance between O-O nearest neighbors, as well as several tertiary peaks. The BKS potential is in better agreement with experimental measurements on bulk a-SiO₂; however, this potential lacks the ability to describe chemical reactions because of its two body nature.

Table 3 shows a comparison to other available experimental measurements including coordination numbers and angle distributions. The results in Table 3 show that the ReaxFF_{SiO} potential is generally in good agreement with experimental measurements. This lends confidence that the ReaxFF_{SiO} potential can adequately model bulk a-SiO₂, which is prerequisite for modeling realistic a-SiO₂ surfaces.

The simplest way to generate an a-SiO₂ surface is to cleave the previously generated bulk along a convenient plane. However this method creates an idealized surface that is terminated by a number of highly reactive broken bonds. To generate more realistic surfaces, we performed MD annealing simulations on an a-SiO₂ surface cleaved from the previously generated bulk. The final state of an annealed surface or bulk is highly dependent on the annealing procedure [78, 87]. Unlike bulk a-SiO₂, there is relatively little information in the literature about the concentrations of specific features on an a-SiO₂ surface, so it is difficult to evaluate

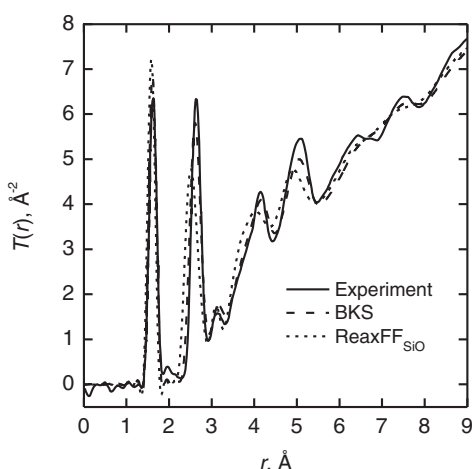


Fig. 4 Total correlation function.

TABLE 3 STRUCTURAL FEATURES OF BULK a-SiO₂

	Experiment	ReaxFF _{SiO}	BKS
Density, g cm ⁻³	2.20 [82]	2.24	2.21
% 2-coord. O	—	96.4	99.4
% 4-coord. Si	—	98.2	99.5
∠ Si-O-Si Ave.	152 [83]	153.25	149.4
∠ Si-O-Si RMS ^a	7.5 [84]	10.48	13.51
∠ O-Si-O Ave.	109.7 ± 0.6 [85]	108.61	109.30
∠ O-Si-O RMS	4.5 [86]	11.76	7.23

^aRoot Mean Square.

the effectiveness of a given annealing procedure. Owing to the limited time scale of MD simulations (~ 100 ns), the heating/cooling rates available in MD simulations are many orders of magnitude higher than those possible experimentally [80]. To create surfaces, we followed the procedure detailed in Fogarty et al. [87]. A slab of cleaved a-SiO₂ was heated at 25 K ps⁻¹ from 300 K to 4000 K under NVT dynamics and then cooled back to 300 K at same rate. The system was propagated for an additional 40 ps under NPT dynamics at 300 K, 1 atm. with the final 20 ps used to collect statistics. All slabs were 20 Å thick with areas chosen so that surfaces had a statistically significant number of defects.

In general we found that longer annealing simulations or additional annealing cycles produced surfaces with slightly lower surface energies and slightly fewer defects. However, we found that the same types of defects occur on surfaces annealed for longer times. Therefore we are confident that although surfaces may contain more defects than they would if annealed at slower and more experimentally realistic rates, they still contain the salient structural features of an a-SiO₂ surface. We use the annealed a-SiO₂ surfaces as a basis for realistic amorphous silica surfaces that have not yet been exposed to atomic oxygen.

D. ACTIVE CHEMICAL SITES (DEFECTS) ON SILICA SURFACES

Here we will examine the defects formed on both the reconstructed α -quartz and annealed amorphous SiO₂ surfaces upon exposure to high temperature dissociated oxygen. In order to simulate exposure to atomic oxygen, we use MD simulations with a Flux Boundary Condition (FBC), a method that exposes a surface to an ideal gas at a given temperature, pressure, and composition. A more detailed description of this method is given in our previous work [72]; however we will describe it briefly here. In Flux Boundary Condition simulations, atoms are generated at random points on a plane above the surface with a frequency corresponding to the flux of an ideal gas through that plane. This plane is 10 Å

above the surface, beyond the force cutoff of the potential. Impinging atoms are given velocities sampled from a Maxwell–Boltzmann distribution and a random incident angle. Atoms or molecules moving away from the surface at a distance greater than 10 Å are deleted, allowing us to simulate only the gas–surface interface region, and gas-phase collisions in this region are rare. A diagram of this method is shown in Fig. 5. Over the course of a simulation, gas atoms adsorb on the initially empty surface and a finite number of defects are created on the reconstructed surface. Eventually, the surfaces reach a steady state population of adsorbed atoms and defect chemistries.

We are primarily interested in structures on the surface where recombination can occur. The most prevalent structures on the surfaces are bridging oxygen atoms ($\text{Si}-\text{O}-\text{Si}$). These bridging oxygen atoms are typical of the reconstructions shown in Fig. 3, and are strongly bound to the surface (~ 10 eV). The energy released in gas-phase oxygen recombination is ~ 5.1 eV, so the direct recombination of an impinging gas-phase oxygen atom with a bridging oxygen atom is very unlikely, rendering the reconstructed (0001) α -quartz surface noncatalytic. Therefore, we expect that recombination will occur at defects on the reconstructed surface.

We find that the most populous defects on surfaces exposed to atomic oxygen are the nonbridging oxygen atom ($\equiv\text{Si}-\text{O}\bullet$, as shown in Fig. 6b) and adsorbed molecular oxygen ($\equiv\text{Si}-\text{O}_2$, as shown in Fig. 6c). Here (\equiv) indicates three bonds to other atoms on the surface and (\bullet) indicates a dangling bond. We also find that the amorphous SiO_2 (annealed) surface, which has not been exposed to atomic oxygen, has a significant number of under-coordinated silicon atoms ($\equiv\text{Si}\bullet$, as shown in Fig. 6a). We use an Si-O bond distance cutoff of 1.8 Å to identify Si-O bonds [80]. Visualizations of reconstructed quartz and annealed a- SiO_2 surfaces with these defects highlighted are shown in Figs. 7a and 7b, respectively.

There is experimental evidence for the existence of the $\equiv\text{Si}\bullet$ and $\equiv\text{Si}-\text{O}\bullet$ defects on silica surfaces under irradiation and fracture. Although there has been little work analyzing the structure of silica surfaces exposed to air plasma or atomic oxygen, it is possible that similar defects exist on silica surfaces under

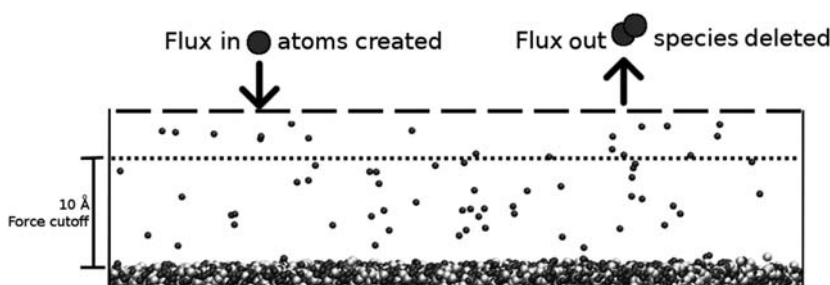


Fig. 5 Diagram of flux boundary condition.

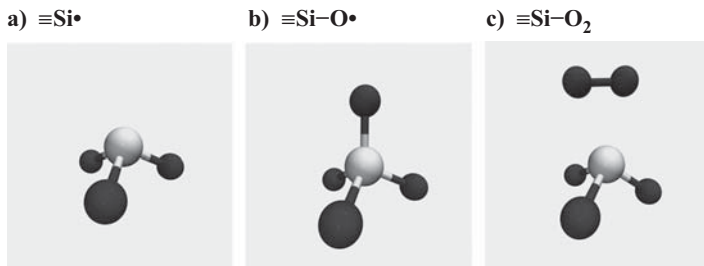


Fig. 6 Defect structures most prevalent on simulated silica surfaces.

a variety of conditions. The $\equiv\text{Si}\bullet$ defect has been extensively studied, and has been identified on irradiated and vacuum fractured quartz and amorphous silica using Electron Spin Resonance (ESR) [88, 89]. ESR in conjunction with isotope effects have been used to identify the $\equiv\text{Si}-\text{O}\bullet$ defect on irradiated amorphous SiO_2 [90]. Although the precise $\equiv\text{Si}-\text{O}_2$ structure predicted by ReaxFF_{SiO} has not be observed experimentally, adsorbed oxygen molecules in a similar configuration (called a peroxy defect) have been observed experimentally on irradiated and mechanically ground silica in the presence of O_2 [90, 91].

The $\equiv\text{Si}\bullet$ and $\equiv\text{Si}-\text{O}\bullet$ structures have also been observed in other MD simulations of a- SiO_2 surfaces simulated using different interatomic potentials [52, 92, 93]. In other works studying recombination on silica surfaces [55, 57, 58], the authors consider a single oxygen atom placed on a cleaved cristobalite or cleaved quartz surface. This effectively creates the $=\text{Si}-\text{O}\bullet$ defect on an otherwise empty surface. Our simulations show that although this defect does occur on

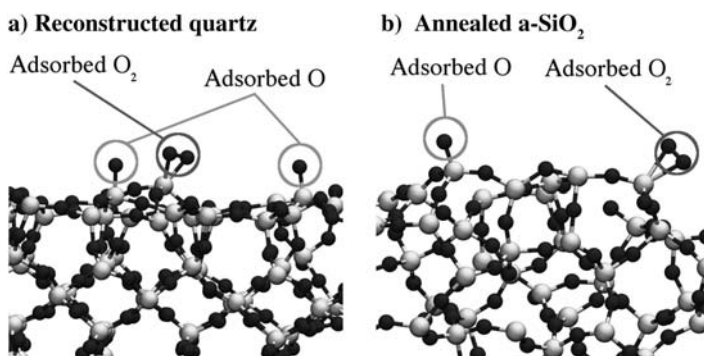


Fig. 7 Simulated silica surfaces exposed to high temperature atomic oxygen, showing nonbridging adsorbed O atoms ($\equiv\text{Si}-\text{O}\bullet$ see Fig. 6b) and adsorbed oxygen molecules ($\equiv\text{Si}-\text{O}_2$, see Fig. 6c).

the surface, it occurs in much smaller concentrations than the $\equiv\text{Si}\bullet$, $\equiv\text{Si}-\text{O}\bullet$, and $\equiv\text{Si}-\text{O}_2$ defects. Therefore our finite-rate catalytic model will focus only on the $\equiv\text{Si}\bullet$, $\equiv\text{Si}-\text{O}\bullet$, and $\equiv\text{Si}-\text{O}_2$ structures shown in Fig. 6.

E. GAS-SURFACE INTERACTIONS (TRAJECTORY CALCULATIONS)

Individual reactions considered in the rate model are based on the possible outcomes of the interaction of atomic and molecular oxygen with the defect sites. These reactions are shown in Table 4 (where reaction names are based on the forward reaction).

We use trajectory calculations and PESs to find the pre-exponential factors and activation energies used in the functional forms of the rate equations. Specifically, we will consider gas-phase species colliding with clusters of atoms, including off-normal collisions. We also show how detailed balance can be applied to the rate model to find the rates of reactions inaccessible in MD time scales.

The advantage of using clusters of atoms for gas-surface trajectory analysis is that such cluster representations can be carved out from any location on an amorphous surface, allowing our simulations to be easily extended to defects occurring in the slightly different geometries seen on disordered surfaces. For the present simulations, clusters are created from a large reconstructed quartz surface with one central defect. A $\equiv\text{Si}-\text{O}\bullet$ defect site can be created by running a short MD simulation of atomic oxygen impacting the surface. This defect can be converted to an under coordinated silicon defect ($\equiv\text{Si}\bullet$) by deleting the extruding oxygen atom, and the adsorbed molecular oxygen defect ($\equiv\text{Si}-\text{O}_2$) can be created by adding an additional oxygen atom and performing an energy minimization. We found that the binding energy of oxygen on this isolated defect is 4.21 eV, and that the binding energy of oxygen averaged over all of the defects identified on the a-SiO₂ and quartz surfaces exposed to atomic oxygen (see Fig. 7) was 4.29 eV \pm 0.31 eV.

Clusters are created by deleting all atoms that are a fixed bond connectivity away from the defect site. The under-coordinated atoms terminating the cluster

TABLE 4 ELEMENTARY GAS-SURFACE INTERACTIONS AT SILICA SURFACE DEFECTS

Reaction	
$\text{O} + \equiv\text{Si}\bullet \leftrightarrow \equiv\text{Si}-\text{O}\bullet$	O-atom adsorption
$\text{O} + \equiv\text{Si}-\text{O}\bullet \leftrightarrow \text{O}_2 + \equiv\text{Si}\bullet$	Eley-Rideal (ER) recombination
$\text{O} + \equiv\text{Si}-\text{O}\bullet \leftrightarrow \equiv\text{Si}-\text{O}_2$	Adsorbed O ₂ formation
$\text{O} + \equiv\text{Si}-\text{O}_2 \leftrightarrow \text{O}_2 + \equiv\text{Si}-\text{O}\bullet$	ER recombination II
$\text{O}_2 + \equiv\text{Si}\bullet \leftrightarrow \equiv\text{Si}-\text{O}_2$	O ₂ adsorption

are capped with hydrogen atoms, which are kept in fixed positions throughout the molecular dynamics simulations to keep the cluster stationary in space. We have found that simulations using clusters sized 13 bond connections away from the central defect (~ 500 atoms) produce results identical to those on larger surfaces. The adjacent N layers of atoms next to the fixed hydrogen atoms are thermalized with a Langevin thermostat to maintain the temperature of the cluster over the course of the simulation. We have found that one layer ($N = 1$) of thermostatted atoms was sufficient in the present simulations, and that larger thermostatted layers ($N > 1$) had no effect on the outcomes of the reactions.

To allow for a realistic range of collisions seen in real gas surface systems, our trajectory calculations also include impinging species at off-normal incident angles. To consider off-normal collisions, we must define the geometry of the surface site. Impinging gas-phase species have the opportunity to hit surface sites at a variety of incident angles and impact factors. We approximate a surface site as a sphere resting on a flat surface, as shown in Fig. 8a for the non-bridging oxygen defect ($\equiv\text{Si}-\text{O}^\bullet$). In the case of adsorbed molecular oxygen ($\equiv\text{Si}-\text{O}_2$) this sphere is centered on the midpoint in the O-O bond, whereas for the undercoordinated silicon defect ($\equiv\text{Si}^\bullet$) the sphere is centered on the adsorption minimum. Based on the PESs of atomic oxygen interacting with the defects, we have chosen a site radius (r_c) of 2.5 Å.

For the finite-rate catalytic model, we will consider the surface as perfectly flat. From Vincenti and Kruger [94], the flux of gas-phase species k hitting a surface

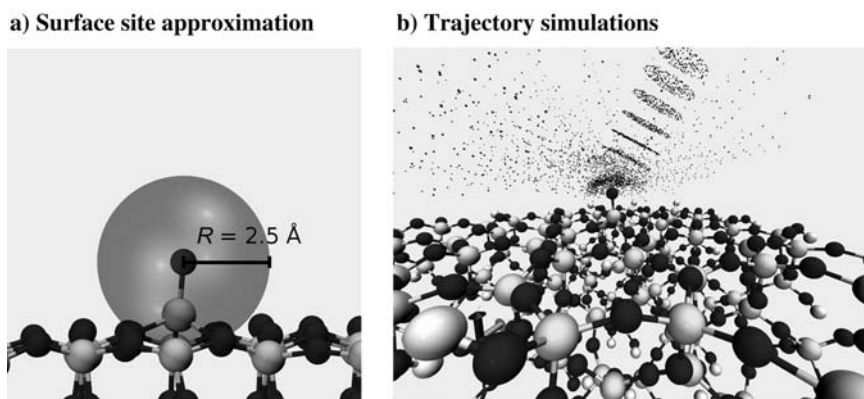


Fig. 8 a) Surface site approximated as a 2.5 Å radius sphere, and b) trajectory simulations for O atoms incident 30° off normal on a nonbridging oxygen defect ($\equiv\text{Si}-\text{O}^\bullet$); the cluster is frozen in its minimum energy configuration and impinging atoms are shown every 250 time steps.

(in mol m⁻² s⁻¹) can be written in spherical coordinates as

$$\Gamma_{\text{surf}} = C_k \left(\frac{M_k}{2\pi RT} \right)^{3/2} \int_0^{\pi/2} \sin(\varphi) \cos(\varphi) d\varphi \int_0^{2\pi} d\theta \int_0^{\infty} v^3 \exp(-M_k v^2 / 2RT) dv \quad (71)$$

If sites are considered as two-dimensional (2-D) discs resting on the surface, the flux of impinging atoms hitting sites on the surface is:

$$\Gamma_{\text{site},2D} = \Phi \pi r_c^2 \Gamma_{\text{surf}} \quad (72)$$

However, if we consider sites as spheres resting on a surface, the effective area of the site varies with the incident angle of the impinging atom ϕ . The effective area of a spherical site is the area of the orthographic ‘shadow’ cast by the site, which is an ellipse with an area of $\pi r_c^2 \cos(\phi)$. Considering this, the flux of atoms is given by:

$$\Gamma_{\text{surf},3D} = \Phi \pi r_c^2 C_k \left(\frac{M_k}{2\pi RT} \right)^{3/2} \int_0^{\pi/2} \sin(\varphi) d\varphi \int_0^{2\pi} d\theta \int_0^{\infty} v^3 \exp(-M_k v^2 / 2RT) dv \quad (73)$$

which is:

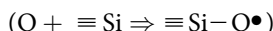
$$\Gamma_{\text{site},3D} = \Phi 2\pi r_c^2 \Gamma_{\text{surf}} = 2\Gamma_{\text{site},2D} \quad (74)$$

For molecular dynamics simulations, the speed and angles (θ, ϕ) of impinging atoms are sampled from the Maxwell-Boltzmann distribution for atoms passing through a plane as described by Garcia and Wagner [95]. Atoms are randomly placed within a disc of radius of r_c at a distance of 10 Å above the site. For example, a set of trajectories at $\phi = 30^\circ$ is shown in Fig. 8b. For the calculation of forward rates, the position of the impinging atom is rotated by the angles (θ, ϕ) about the surface site, where (θ, ϕ) are sampled from

$$\theta = 2\pi R_f \quad \text{and} \quad \phi = \arccos(R_f^{1/2}) \quad (75)$$

where R_f is a unit random number. The angle ϕ is sampled this way so impinging atoms have the same angular distribution as an ideal gas hitting a flat surface.

1. O-ATOM ADSORPTION:



In Fig. 9a gives the PES for O-atom adsorption on a $\equiv Si-O\bullet$ defect site, as illustrated in Fig. 9b. The energy of adsorption of atomic oxygen is -4.21 eV. Given this deep potential well and the lack of energy barrier, we assume that the sticking probability for O on this site is unity. We also assume that this is the case for the O₂ adsorption reaction. Thus for both reactions the pre-exponential factors are unity and the activation energies are zero.

a) PES for O-atom impingement on $\equiv\text{Si}\bullet$ b) O-atom impingement on $\equiv\text{Si}\bullet$

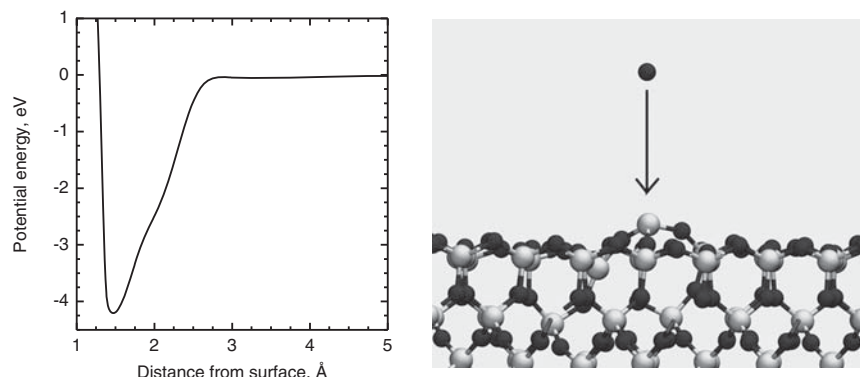


Fig. 9 Atomic oxygen adsorption on an under-coordinated silicon atom defect ($\equiv\text{Si}\bullet$).

2. MOLECULAR OXYGEN FORMATION AND ER-RECOMBINATION:

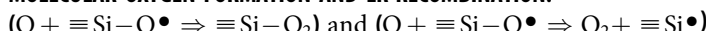
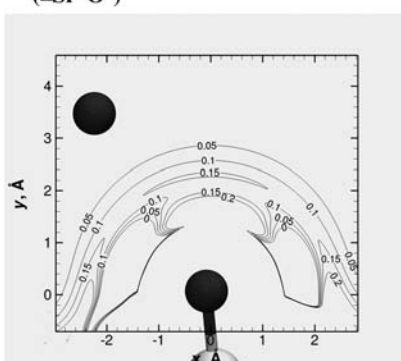


Figure 10(a) gives the PES for the process of O-atom impingement on a surface-adsorbed oxygen atom, as illustrated in Fig. 10b. The PES in Fig. 10a shows a well-defined transition state for O_2 formation. To find the pre-exponential factor and activation energy for this reaction, we performed molecular dynamics simulations. Over 2000 trajectories were carried out at each temperature, with temperatures ranging from 250–1750 K with an interval of 250 K. The results of these simulations are shown in Fig. 11a, where error bars are based on the Wald method with a 95% confidence interval. At all

a) PES for O-atom impingement on ($\equiv\text{Si}-\text{O}\bullet$)



b) O-atom impingement on ($\equiv\text{Si}-\text{O}\bullet$)

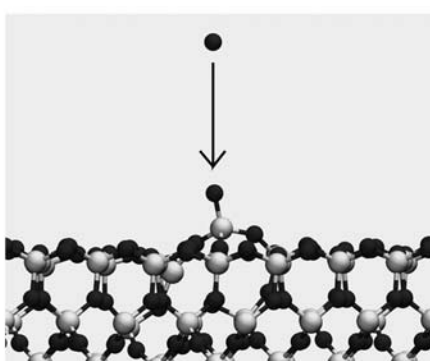


Fig. 10 Molecular oxygen formation on a nonbridging oxygen atom defect ($\equiv\text{Si}-\text{O}\bullet$).

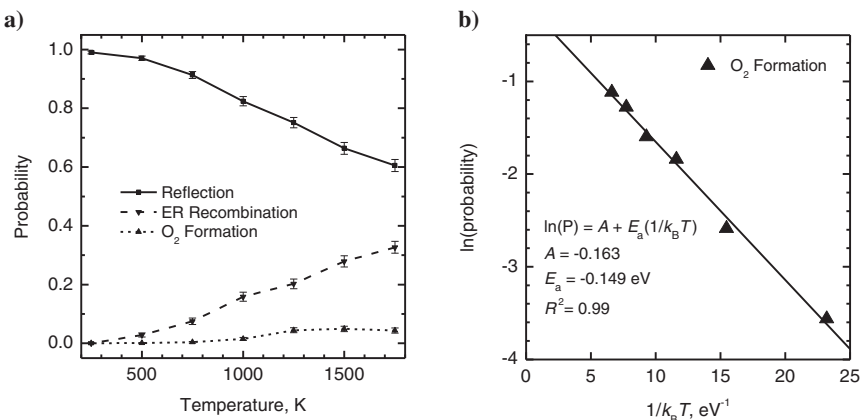


Fig. 11 a) Reaction probability for adsorbed O₂ formation, ER recombination, and reflection vs temperature, and **b)** activation energy for O₂ formation.

temperatures, the most probable reaction is O₂ formation, with a lesser probability of ER Recombination.

A log plot of the probability of O₂ formation, as seen in Fig. 11b, shows that the probability of this reaction follows an exponential trend, with activation energy $E_a = 0.149$ eV, in agreement with the PES in Fig. 10a. From the log plot, we also find that the pre-exponential factor for this reaction is 0.85. From a similar fit, the pre-exponential factor for the ER recombination reaction is 0.169 and the activation energy is 0.401 eV.

3. O₂ REPLACEMENT/ER-RECOMBINATION II: (O + ≡Si · O₂ ⇒ O₂ + ≡Si—O[•])

The impact of an oxygen atom on an adsorbed oxygen molecule is illustrated in Fig. 12, where there are two possible outcomes. The first is termed O₂ Replacement, where the incoming oxygen atom displaces the adsorbed O₂ molecule into the gas phase and fills the vacant silica bond on the surface. The second possible outcome is termed ER Recombination II, where the incoming oxygen atom forms a bond with one of the atoms in the adsorbed O₂ molecule, forming a new O₂

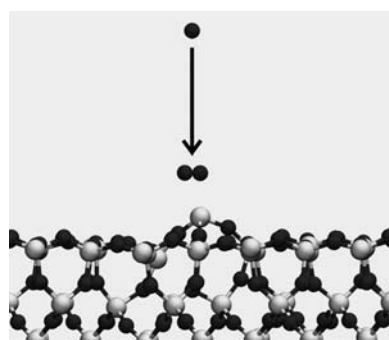


Fig. 12 O-atom impingement on an adsorbed oxygen molecule (≡Si—O₂).

molecule released into the gas phase with the remaining oxygen bonded to surface silica atom.

The probability of O₂ Replacement/ER Recombination II vs temperature is given in Fig. 13a. Uncertainty bars are found through the Wald method with a confidence interval of 95%. The dominant reaction is O₂ replacement, where the impinging oxygen atom replaces the molecular oxygen on the surface. There is also a small probability of ER Recombination II, where the impinging oxygen atom combines with one of the oxygen atoms in the adsorbed molecular oxygen.

The probability of the O₂ replacement reaction vs incident angle (ϕ) for clusters with a temperature of 1500 K and impinging atoms with a velocity of 2000 m s⁻¹ is shown in Fig. 13b, where we can clearly see that atoms at higher incident angles have a higher probability of reacting. This is reasonable because the impinging oxygen atom must displace the adsorbed O₂ molecule, an action that is frustrated in the direction of the surface. At higher incident angles ($\phi > 60^\circ$), we see a decrease in the probability of O₂ replacement, because the repulsive nature of the surface causes an increasing number of impinging oxygen atoms to scatter before interacting with the site. Because these two reaction paths produce identical products, we can add two probabilities together to find the probability of reaction as a function of temperature.

In practice, the contributions of the ER recombination II reaction are negligible. Thus, the activation energy for this reaction is $E_a = 0.303$ eV and the pre-exponential factor is $A = 0.172$. It is interesting to note that if only normal collisions are considered, the activation energy determined is the much larger value of $E_a = 0.457$ eV. This result highlights the importance of considering off-normal trajectory calculations when formulating a finite-rate model from MD calculations.

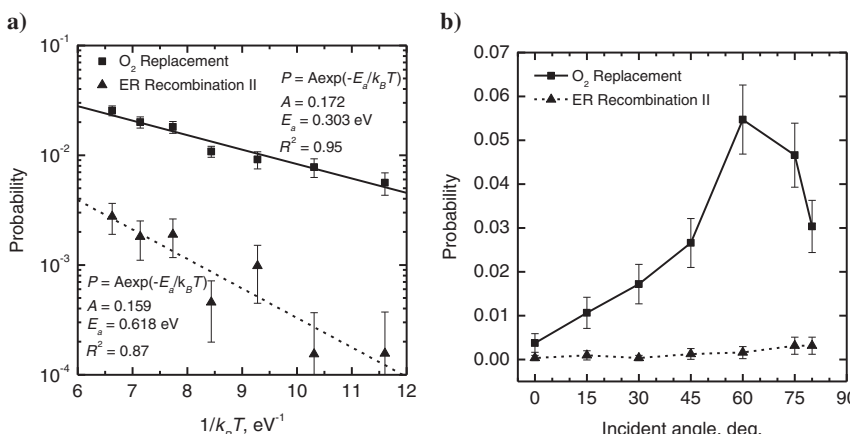


Fig. 13 O₂ replacement and ER Recombination II: a) reaction probability vs temperature, and b) reaction probability vs incident angle.

TABLE 5 GAS-SURFACE REACTIONS FOR THE COMPUTATIONAL CHEMISTRY FINITE-RATE CATALYSIS MODEL

	Reaction	Reaction Flux, mol m ⁻² s ⁻¹
1	$O + (s) \leftrightarrow O_s$	$r_1 = k_{f1}[O][E_s] - k_{b1}[O_s]$
2	$O + O_s \leftrightarrow O_2 + (s)$	$r_2 = k_{f2}[O][O_s] - k_{b2}[O_2][E_s]$
3	$O + O_s \leftrightarrow O_{2s}$	$r_3 = k_{f3}[O][O_s] - k_{b3}[O_{2s}]$
4	$O + O_{2s} \leftrightarrow O_2 + O_s$	$r_4 = k_{f4}[O][O_{2s}] - k_{b4}[O_2][O_s]$
5	$O_2 + (s) \leftrightarrow O_{2s}$	$r_5 = k_{f5}[O_2][E_s] - k_{b5}[O_{2s}]$

F. FORMATION OF A FINITE-RATE CATALYTIC MODEL FOR O-ATOM RECOMBINATION ON SILICA

The results of the computational chemistry calculations can now be applied to construct a simple finite-rate catalytic model consisting of the five gas-surface interactions summarized in Table 4. The silica surface is modeled as single surface phase with a single set of active sites of constant site density Φ_s . The variables are the gas-phase O-atom and O₂ concentrations ([O] and [O₂] in mol m⁻³) and the surface concentrations of three surface defects $\equiv Si^\bullet$, $\equiv Si-O^\bullet$, and $\equiv Si-O_2$ ([E_s], [O_s] and [O_{2s}] in mol m⁻²). Table 5 gives the surface reactions and their reaction fluxes, and Table 6 lists the various forward and backward rate coefficient expressions required for the computation of reaction fluxes.

The results of the trajectory calculations give the pre-exponential factors and activation energies for the five forward reactions in the finite-rate model. These values are listed in second and third columns of Table 7. The activation energies for the two adsorption processes are zero. The activation energies for the other three reactions represent energy barriers associated with the transition states between reactant and product states. The state energies for the full catalytic cycle are shown in Fig. 14.

TABLE 6 RATE COEFFICIENT EXPRESSIONS FOR THE COMPUTATIONAL CHEMISTRY FINITE-RATE CATALYSIS MODEL

	Forward Rate Expression	Backward Rate Expression
1	$k_{f1} = (\pi r_c^2 \bar{v}_O / 2A_v) A_{f1} \exp(-E_{f1}/RT)$	$k_{b1} = (1/A_v) A_{b1} \exp(-E_{b1}/RT)$
2	$k_{f2} = (\pi r_c^2 \bar{v}_O / 2A_v) A_{f2} \exp(-E_{f2}/RT)$	$k_{b2} = (\pi r_c^2 \bar{v}_{O2} / 2A_v) A_{b2} \exp(-E_{b2}/RT)$
3	$k_{f3} = (\pi r_c^2 \bar{v}_O / 2A_v) A_{f3} \exp(-E_{f3}/RT)$	$k_{b3} = (1/A_v) A_{b3} \exp(-E_{b3}/RT)$
4	$k_{f4} = (\pi r_c^2 \bar{v}_O / 2A_v) A_{f4} \exp(-E_{f4}/RT)$	$k_{b4} = (\pi r_c^2 \bar{v}_{O2} / 2A_v) A_{b4} \exp(-E_{b4}/RT)$
5	$k_{f5} = (\pi r_c^2 \bar{v}_{O2} / 2A_v) A_{f5} \exp(-E_{f5}/RT)$	$k_{b5} = (1/A_v) A_{b5} \exp(-E_{b5}/RT)$

TABLE 7 MODEL PARAMETERS FOR THE COMPUTATIONAL CHEMISTRY FINITE-RATE CATALYSIS MODEL

Trajectory Calculations			TST	ReaxFF _{SiO}	Detailed Balance	
	A_{fi}	E_{fi} , eV	A_{bi}	E_{bir} , eV	A_{bi}	E_{bir} , eV
1	1.0	0.0	$10^{13} - 10^{15} \text{ s}^{-1}$	4.19	10^{14} s^{-1} ^a	4.19 ^a
2	0.169	0.401	0.0–1.0	1.33	1.07	1.38
3	0.850	0.149	$10^{13} - 10^{15} \text{ s}^{-1}$	3.96	10^{14} s^{-1} ^a	3.96 ^a
4	0.172	0.303	0.0–1.0	1.61	0.92	1.66
5	1.0	0.0	$10^{13} - 10^{15} \text{ s}^{-1}$	2.88	$4.65 \times 10^{13} \text{ s}^{-1}$	2.84

^aFixed at TST and ReaxFF_{SiO} values during detailed balance.

At this point, it is important to again emphasize that a more accurate PES (such as the ReaxFF_{SiO}^{GSI} potential) may predict different pre-exponential factors, activation energies, and single point energies for these reactions. If a finite-rate model developed through MD simulation is highly sensitive to one or more of these energies, then these values should ultimately be computed to a high level

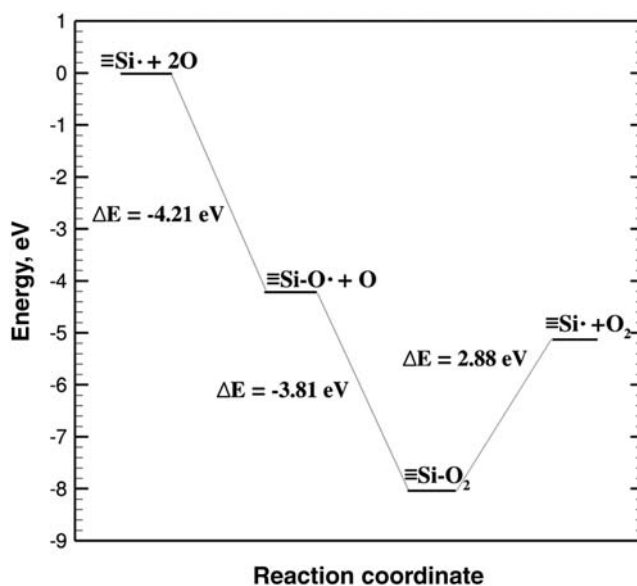


Fig. 14 Relative structure energies within catalytic cycle.

of precision by finding transition states using DFT [70, 71]. Such an iterative approach involving both MD trajectory calculations and matching DFT analysis is crucial in order to develop a consistent and accurate model for gas–surface interactions.

The pre-exponential factors for the backward reaction rates are given in column four of Table 7. For the desorption reactions these are estimated from transition state theory (TST) as $10^{13} - 10^{15} \text{ s}^{-1}$, as described in by Lieberman and Lichtenberg [96], and for the backward rates involving a collision process the pre-exponential factors are nondimensional and lie between zero and one. The activation energies for the backward reactions are found by adding the energy difference between the reactant and product states to the activation energy of the corresponding forward reaction. For example, the activation energy for dissociative oxygen desorption (the backward direction of reaction 3) is given by $E_{b3} = \Delta E_3 + E_{f3} = 3.81 + 0.149 = 3.96 \text{ eV}$. These energies are listed in column five of Table 7.

Although numerical values for all the pre-exponential factors and activation energies parameters needed to perform a model calculation are now available in columns 2–5 of Table 7, we note that the forward and backward rate coefficients should be related by detailed balance and consistent with the known thermodynamics of the gas-phase reactants. Here, we apply detailed balance to the high temperature rate model in a similar manner to Sorenson et al. [24]. This ensures that the rate model maintains gas-phase chemical equilibrium, as defined by known thermodynamic properties. It can be shown that the concentration based equilibrium constant, $K_{c,ox}$, for the gas-phase equilibrium reaction $[\text{O}_2] \leftrightarrow 2[\text{O}]$ is equal to the following combinations of reaction rate coefficients in the finite-rate surface catalysis model:

$$K_{c,ox} = \frac{k_{b1}k_{b2}}{k_{f1}k_{f2}} = \frac{k_{b3}k_{b4}}{k_{f3}k_{f4}} = \frac{k_{f1}k_{f3}k_{b5}}{k_{b1}k_{b3}k_{f5}} \quad (76)$$

Thus, by specifying the values of $K_{c,ox}$ and all MD-derived forward rate parameters, only two of the five backward rate coefficients are independent. In addition to ensuring that detailed balance is obeyed at equilibrium, this method acts as a sanity check for the reverse reactions in the rate model: if the parameters for the chosen rate constant fall within reasonable bounds, so should the rate constant found from detailed balance. This level of agreement can only be expected if the O_2 bond energy as predicted by the ReaxFF_{SiO} potential is in agreement with the experimental value of 5.12 eV [94]. Any deviation from this will cause the activation energies of the reverse rates from detailed balance to disagree with results from the ReaxFF_{SiO} potential. The ReaxFF_{SiO} potential predicts an O_2 bond energy of 5.14 eV, so good agreement is expected.

As an example, we parameterize k_{b1} and k_{b3} using the values $A_{b1} = A_{b3} = 1 \times 10^{14} \text{ s}^{-1}$, $E_{b1} = 4.19 \text{ eV}$, and $E_{b3} = 3.96 \text{ eV}$, and then use detailed balance

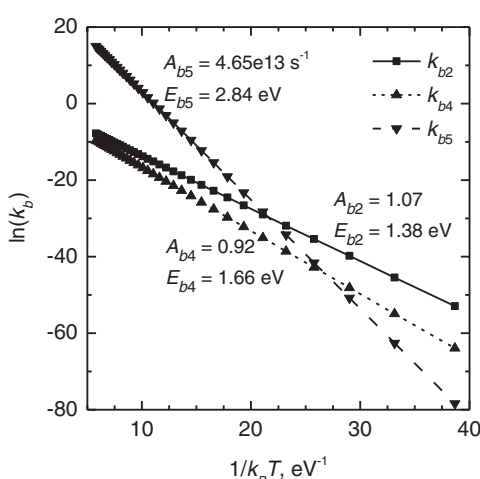
to compute the remaining three rate constants k_{b2} , k_{b4} , and k_{b5} . We compute $K_{c,ox}$ from ΔG° , which we find by using the partition functions of atomic oxygen and the harmonic-oscillator rigid-rotor model of molecular oxygen with the first few electronic energy levels included, as described by Vincinti and Kruger [94]. As a validation, this equilibrium constant was compared to the predictions of NASA's CEA program [6] and found to be in excellent agreement over the temperature range 300 K–2000 K.

The reverse rate constants k_{b2} , k_{b4} , and k_{b5} computed by detailed balance are shown in Fig. 15, and the extracted pre-exponential and activation energy parameters are given in the final two columns of Table 7. As shown in Table 7, the pre-exponential factors of the reverse rate constants are within the range predicted by transition state theory, and the reverse activation energies are in good agreement with the values predicted by ReaxFF_{SiO}. The rate constants predict that the probabilities of reactions 2 and 4 in the backward direction are very low ($<10^{-4}$ at 2000 K) and would rarely be seen in trajectory calculations.

Since the reaction-specific production rates of species k are given by $\dot{w}_k = v_{ki}r_i$ (Eq. (19)) and all stoichiometric coefficients $v_{ki} = 1$ in this model (see Table 5), the instantaneous change in surface concentrations of adsorbed O-atom and O₂ molecules can be written in terms of the reaction fluxes as

$$\frac{d[O_s]}{dt} = r_1 - r_2 - r_3 + r_4 \quad (77)$$

$$\frac{d[O_{2s}]}{dt} = r_3 - r_4 + r_5 \quad (78)$$



The concentration of empty sites is determined from the active site conservation constraint

$$[E_s] = \Phi_s - [O_s] - [O_{2s}] \quad (79)$$

Within this catalytic model the loss efficiency of impinging O atoms, defined as the fraction of collisions with the surface that result in permanent removal

Fig. 15 Backward rate constants from detailed balance vs temperature.

from the gas phase, is given by

$$\gamma_O \equiv \frac{-\dot{w}_O}{\Gamma_O} = \frac{r_1 + r_2 + r_3 + r_4}{\Gamma_O} \quad (80)$$

Under steady-state conditions, the surface concentrations of adsorbed O and O₂ are constant and the rate of O atoms removed from the gas phase exactly equals twice the rate of O₂ molecules added to the gas phase. The loss efficiency of Eq. (80) is then equivalent to the “recombination coefficient” described in Section III, Eq. (1). However, note that here the recombination coefficient is not specified as in the conventional SRE approach. Rather it is a result of finite-rate kinetics representing various individual processes supported by detailed computational chemistry calculations and molecular dynamics simulations.

Equations (76–79) can be iterated to steady state for a fixed temperature and gas-phase oxygen concentrations through the Newton–Raphson method or through time integration to steady state as detailed in previous sections.

It is noted that in other works [56], quasi-steady-state surface coverages (chosen from some arbitrary time prior to steady state) were used to determine recombination coefficient values. However, we believe it is more consistent to use only steady state surface coverages, since compared to the time scales of vehicle reentry, the surface coverage would instantaneously adapt to the local gas conditions, and continued catalytic reactions occur throughout the reentry trajectory.

From a macroscopic viewpoint the concentration of sites per unit area varies with the total surface area, which can vary between silica samples used in different experiments [97, 98]. Therefore, we treat Φ_s as a variable that is used to match specific experimental results. As shown in Fig. 16, changing the concentration of surface sites changes the magnitude of recombination coefficients, but not their trend with temperature.

A number of independent experiments have observed that at high temperatures ($T > 1000$ K) oxygen recombination coefficients on silica show a weak exponential trend with temperature [98–100]. For example, the activation energy for this exponential trend on quartz has been

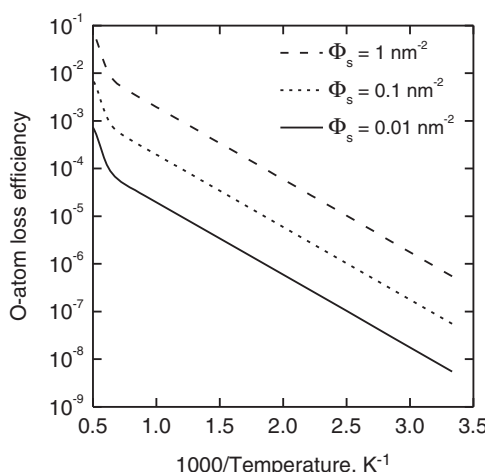


Fig. 16 O-atom loss efficiency as a function of active site concentration on the surface.

measured as 0.19 ± 0.01 eV by Balat-Pichelin et al. [99] and 0.18 ± 0.04 eV by Kim and Boudart [98]. Although the experiments by Kim and Boudart and Balat-Pichelin et al. show similar trends in recombination coefficients with temperature, there is a difference of over an order magnitude in the measured recombination coefficients. This variation could come, in-part, from a difference in the concentration of active sites on the surfaces and mesoscopic morphology (surface area). Such variation could also come from differences in the gas-phase pressures and compositions, as well as the diffusion models employed to interpret a recombination coefficient from experimental measurements.

The finite-rate description obtained through this computational chemistry process is compared to an empirical set of rates for the oxygen/silica system in the next section. Again, the rate model developed in this section through molecular dynamics simulation is an example-model only. The ReaxFF_{SiO} interatomic potential has not been validated with DFT energy calculations for silica surfaces and gas–surface interactions. Future effort will address this.

V. COMPUTATIONAL EXAMPLES

In this section we present some computational examples of the finite-rate surface reaction modeling approach. We begin with several simple examples to exercise different features of the finite-rate surface reaction formulation, demonstrate consistency with thermochemical equilibrium where it is expected, and show how the present implementation differs from traditional surface reaction boundary conditions that directly specify reaction efficiencies and branching fractions. For these examples, we fix the gas-phase temperature, pressure, and composition and simply iterate the appropriate rate equations for each surface species to steady-state together with the constraint that active sites are conserved [1]. We then give some examples that demonstrate the implementation of the finite-rate surface reaction formulation as part of a CFD solution in the DPLR code [2]. In general, the parameters used in most of these examples are representative and illustrative, derived by a combination of literature review and chemical intuition and have not been validated against particular experimental datasets.

A. EMPIRICAL MODEL (EM) FOR CATALYTIC O-ATOM RECOMBINATION ON SILICA

We consider a simple finite-rate surface chemistry model for partially dissociated oxygen in contact with a catalytic surface. The surface reaction model has a gas phase containing O and O₂ and a surface phase with a single set of active sites containing empty and filled sites, E(s) and O(s). Surface chemistry is limited to three reaction types: O-atom adsorption, ER recombination of a gas-phase O atom with an adsorbed O atom, and LH recombination of two adsorbed O atoms with each other. With this approach it is possible to choose parameters

TABLE 8 REACTIONS AND RATES FOR EMPIRICAL MODEL (EM)

	Reaction	Type	S_0 , γ_{er} , C_{lh}	E_{ad} , E_{er} , E_m , kJ mol^{-1}
1	$O + (s) \leftrightarrow O_s$	Ads	0.05	0
2	$O + O_s \leftrightarrow O_2 + (s)$	ER	0.001	9
3	$2O_s \leftrightarrow O_2 + 2(s)$	LH	0.1	300

that will reproduce representative values and temperature variations of O-atom recombination coefficients that have been reported in the literature on silica surfaces [98, 101–103].

Reaction rate parameters are given in Table 8. Because no thermodynamic data are available for adsorbed O atoms, we specify a thermal desorption reaction of Form 1 (Eq. (43)) with $A_{des} = 1$, $\beta = 0$, $v = 1.0 \times 10^{12} \text{ s}^{-1}$ and $E_{des} = 350 \text{ kJ mol}^{-1}$. The active site density is set to $\Phi_s = 7.5 \times 10^{-6} \text{ mol m}^{-2}$.

In this particular model, O atoms are pictured to adsorb strongly to the surface, with large barriers for thermal desorption and surface diffusion. A lower energy barrier for ER recombination is set because the exothermic recombination of two O atoms releases more energy than the energy barrier for thermal desorption of a single O atom.

Figure 17 shows how the computed O-atom and O₂ loss efficiencies vary with temperature at 2000 Pa for a fixed bounding gas composition of 90% O₂–10% O.

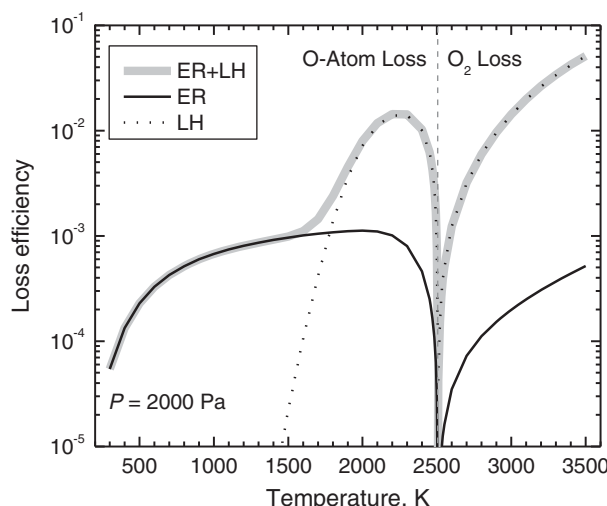


Fig. 17 O-atom or O₂ loss efficiencies as a function of temperature for catalytic recombination on silica in a 90% O₂–10% O mixture at 2000 Pa.

These loss efficiencies are computed as the absolute values of the steady-state O-atom and O₂ production rates at the surface, divided by their kinetic surface impact flux, as given by Eq. (1). Results for three different recombination models are presented: ER recombination only (thin solid lines), LH recombination only (thin dotted lines), and simultaneous ER and LH recombination (thick gray lines.) For the chosen parameters, the loss efficiency is dominated by the ER process at low temperatures and the LH process at high temperatures.

Figure 18 shows how the O-atom surface coverage and the O-atom and O₂ loss efficiencies vary with temperature for three different pressures of 20,000, 2000, and 200 Pa at the same 90% O₂-10%O bounding gas composition, for the ER + LH recombination model. Since the adsorbed O atom is bound tightly to the surface, surface coverage is high at low temperatures. As the temperature increases, the rates of thermal desorption and ER and LH recombination

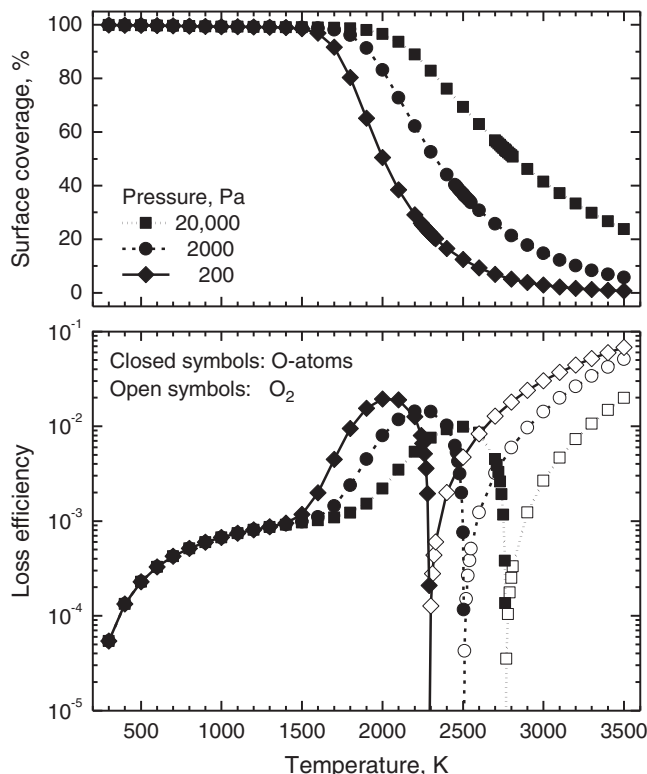


Fig. 18 O-atom surface coverage (top panel) and O-atom or O₂ loss efficiency (bottom panel) as a function of temperature for ER + LH surface catalytic recombination in a 90% O₂-10% O mixture at 20,000, 2000, and 200 Pa.

overwhelm the rate of adsorption, and the surface coverage rapidly decreases. This drop in coverage happens at lower temperatures when the gas pressure is low because the rate of adsorption depends on the gas-phase O-atom concentration, whereas the O-atom desorption and LH recombination mechanisms only depend on temperature.

The O-atom loss efficiency shows three characteristic regimes with increasing temperature. At low temperatures, the loss efficiency increases as the ER recombination rate increases and the O-atom surface coverage remains high. The LH mechanism is not effective in the low temperature regime. At moderate temperatures, LH recombination accelerates with increasing temperature as the available thermal energy becomes sufficient for effective surface diffusion. At even higher temperatures, O-atom loss rate drops sharply with increasing temperature, as the O-atom surface coverage falls and the ER and LH recombination reactions are effectively countered by their corresponding backward dissociative adsorption reactions. Above a certain temperature, the dissociation reactions dominate and the net effect is a loss of O₂ from the gas phase, with a loss efficiency that increases with temperature.

The activity-based equilibrium constant for the gas phase of this simple system can be written in terms of the system pressure and oxygen species mole fractions as,

$$K_a(T) = \frac{P_{\text{ref}} \chi_{O_2}}{P \chi_O^2} \quad (81)$$

This equilibrium constant equals 456, 4560, and 45,600, for a 90% O₂-10% O mixture at the pressures 20,000 Pa, 2000 Pa, and 200 Pa, respectively. The corresponding equilibrium temperatures can be found as 2765 K, 2506 K, and 2291 K [104]. Since a catalytic surface should not alter the thermochemical equilibrium state of the gas phase, the net production of both O atoms and O₂ molecules should equal zero under these conditions. From Figs. 17 and 18, it is seen that the loss efficiencies for O and O₂ tend to zero at exactly these three temperatures (as they should).

Marschall and Maclean [1] have shown that the finite-rate equations can also be iterated to steady-state together with a constant pressure or constant volume constraint. They found that these solutions correspond exactly to the thermochemical equilibrium states obtained by constant volume or constant pressure free-energy minimization, again demonstrating consistency between the finite-rate model and thermodynamic data.

For this simple example, it is also possible to derive analytic solutions for the steady-state surface coverage and the loss efficiencies in terms of the reaction rate coefficients and the fixed gas-phase concentrations. The surface concentration of adsorbed O atoms is obtained from the quadratic equation,

$$a\Phi_{s,O}^2 + b\Phi_{s,O} + c = 0 \quad (82)$$

TABLE 9 SURFACE COVERAGE COEFFICIENTS

Model	<i>a</i>	<i>b</i>	<i>c</i>
ER	0	$-k_{f1}C_O - k_{b1} - k_{b2}C_{O_2} - k_{f2}C_O$	$k_{f1}C_O + k_{b2}C_{O_2}$
LH	$2k_{b3}C_{O_2} - 2k_{f3}$	$-k_{f1}C_O - k_{b1} - 4k_{b3}C_{O_2}\Phi_s$	$(k_{f1}C_O + 2k_{b3}C_{O_2}\Phi_s)\Phi_s$
ER + LH	$2k_{b3}C_{O_2} - 2k_{f3}$	$-k_{f1}C_O - k_{b1} - k_{b2}C_{O_2}$ $-k_{f2}C_O - 4k_{b3}C_{O_2}\Phi_s$	$(k_{f1}C_O + k_{b2}C_{O_2} + 2k_{b3}C_{O_2}\Phi_s)\Phi_s$

with the coefficients given in Table 9 for the three different surface recombination models. Once the surface coverage is known, the loss efficiencies can be computed using the expressions for γ_O and γ_{O_2} listed in Table 10. Excellent agreement between these analytic functions and numerical integration of the finite-rate model was confirmed for all three models.

B. RELATIONSHIP TO SRE CATALYSIS MODELS

In the finite-rate surface reaction formulation, the effective reaction efficiency for a gas-phase reactant consumed in a surface reaction process is a result of competing finite-rate processes under a given set of experimental conditions. Traditionally, surface reactions in CFD simulations have been implemented by specifying these reaction rate efficiencies, either as constants or as functions of temperature.

TABLE 10 O AND O₂ LOSS EFFICIENCIES

ER	$\gamma_O = \frac{\Phi_s(k_{f1}C_O - k_{b2}C_{O_2}) - \Phi_{s,O}(k_{f1}C_O + k_{b1} - k_{f2}C_O - k_{b2}C_{O_2})}{\Gamma_O}$
	$\gamma_{O_2} = \frac{\Phi_s(k_{b2}C_{O_2}) - \Phi_{s,O}(k_{f2}C_O + k_{b2}C_{O_2})}{\Gamma_{O_2}}$
LH	$\gamma_O = \frac{\Phi_s(k_{f1}C_O) - \Phi_{s,O}(k_{f1}C_O + k_{b1})}{\Gamma_O}$
	$\gamma_{O_2} = \frac{\Phi_s^2(k_{b3}C_{O_2}) - \Phi_{s,O}(k_{b3}C_{O_2}2\Phi_s) - \Phi_{s,O}^2(k_{f3} - k_{b3}C_{O_2})}{\Gamma_{O_2}}$
ER + LH	$\gamma_O = \frac{\Phi_s(k_{f1}C_O - k_{b2}C_{O_2}) - \Phi_{s,O}(k_{f1}C_O + k_{b1} - k_{f2}C_O - k_{b2}C_{O_2})}{\Gamma_O}$
	$\gamma_{O_2} = \frac{\Phi_s(k_{b2}C_{O_2}) + \Phi_s^2(k_{b3}C_{O_2}) - \Phi_{s,O}(k_{f2}C_O + k_{b2}C_{O_2} + k_{b3}C_{O_2}2\Phi_s) - \Phi_{s,O}^2(k_{f3} - k_{b3}C_{O_2})}{\Gamma_{O_2}}$

Although the general finite-rate reaction approach is a more physically justified model for surface reactions, we note that it is still possible to implement the specified-reaction-efficiency (SRE) approach within its framework through the judicious choice of reaction types and parameters.

As an example, consider an SRE model of catalytic oxygen recombination with a specified temperature-dependent surface recombination efficiency of $\gamma_o = \gamma \exp(-E/RT)$. Curve fits of this type are given, for example by Stewart [103, 105] for a wide range of TPS materials. This simple SRE model can be recreated in the finite-rate framework by neglecting the backward reactions in the ER model described above. With this simplification and inputting the appropriate rate formula from Table 1 (with all $\beta = 0$) the expressions for O-atom surface coverage and the O-atom loss coefficient from Tables 9 and 10 become,

$$\Phi_{s,O} = \frac{\Phi_s k_{f1}}{k_{f1} + k_{f2}} = \frac{\Phi_s S_0 \exp\left(-\frac{E_{ad}}{RT}\right)}{S_0 \exp\left(-\frac{E_{ad}}{RT}\right) + \gamma_{er} \exp\left(-\frac{E_{er}}{RT}\right)} \quad (83)$$

$$\begin{aligned} \gamma_O &= \frac{\Phi_s (k_{f1} C_O) - \Phi_{s,O} (k_{f1} C_O - k_{f2} C_O)}{\Gamma_O} \\ &= \frac{2S_0 \gamma_{er} \exp\left(-\frac{E_{ad}}{RT} - \frac{E_{er}}{RT}\right)}{S_0 \exp\left(-\frac{E_{ad}}{RT}\right) + \gamma_{er} \exp\left(-\frac{E_{er}}{RT}\right)} \end{aligned} \quad (84)$$

From Eqs. (83) and (84), it is easy to show that the choices $S_0 = \gamma_{er} = \gamma$ and $E_{ad} = E_{er} = E$ lead directly to $\Phi_{s,O} = \Phi_s/2$ and $\gamma_O = \gamma \exp(-E/RT)$. One can also show that any combination of S_0 and γ_{er} that satisfies $2S_0 \gamma_{er}/(S_0 + \gamma_{er}) = \gamma$ will reproduce the even simpler $\gamma_O = \gamma$ (constant gamma or $E = 0$) SRE model.

Often two (or more) independent surface reactions are modeled using the SRE approach (e.g., O + O and N + N recombination in dissociated air). These models can also be reproduced by the approach described above, with each process restricted to its own set of active sites on a single surface phase. However, with multiple active site sets in a single surface phase, the site density fraction of a particular active site set also scales these simple relationships.

So, for example, for two independent constant gamma SRE models of oxygen and nitrogen recombination reacting on independent active site sets 1 and 2 in the same surface phase, the specified loss coefficients are reproduced by:

$$\gamma_O = \frac{\Phi_1}{\Phi_1 + \Phi_2} \left[\frac{2S_{0,O} \gamma_{er,O}}{S_{0,O} + \gamma_{er,O}} \right] \quad \text{and} \quad \gamma_N = \frac{\Phi_2}{\Phi_1 + \Phi_2} \left[\frac{2S_{0,N} \gamma_{er,N}}{S_{0,N} + \gamma_{er,N}} \right] \quad (85)$$

C. COMPARISON OF THE CCM AND EM RATES FOR O-ATOM RECOMBINATION ON SILICA

The two sets of rates presented for the recombination of oxygen on a silica surface may be easily compared and contrasted both in a stand-alone environment of fixed temperature, pressure, and gas concentrations, as well as in a CFD boundary condition for a high-enthalpy flow environment. We will refer to these models as the computational chemistry model (CCM) and the empirical model (EM).

For a fixed gas environment by specifying temperature, pressure, and gas concentration, the steady state response of these two rate models may be compared by iterating the system to a steady state as measured by the L1 and L2 norms of the concentration change vector. To demonstrate this, the mole fraction of gaseous atomic oxygen is fixed to $\chi_O = 0.1$ and gaseous molecular oxygen is fixed to $\chi_{O_2} = 0.9$. The trend with temperature is measured by running a series of cases from 300 K to 2000 K, and the pressure is adjusted for each case (from 3 kPa to 20 kPa) to maintain a constant mixture concentration of 1.203 mol m^{-3} .

As noted before in the discussion related to Fig. 16, the site density in the CCM may be adjusted to match particular experiments or material samples. Here, the site density is computed by the assumed effective site radius of 2.5 \AA (see Fig. 8). Using this estimate, the site density for the CCM is $\Phi_s = 1/(2\pi r_c^2 A_v)$ or $4.2286 \times 10^{-6} \text{ mol m}^{-2}$, as compared to the site density assumed for the EM of $\Phi_s = 7.5 \times 10^{-6} \text{ mol m}^{-2}$.

The steady-state surface coverage concentrations of these two models shows very different behavior as demonstrated in Fig. 19a. For the CCM, the surface sites are mostly occupied by adsorbed molecular oxygen. In contrast, the EM empirical rate set does not allow O_2 adsorption, so adsorbed atomic oxygen dominates the system. In both cases, the surface is filled by something other than empty sites. The effective loss efficiency of atomic oxygen is plotted for both models in Fig. 19b, showing very different efficiency levels. The CCM system predicts lower efficiency at low temperatures but higher efficiency at higher temperatures.

As the effective O-atom loss efficiency is dependent on the mechanisms and parameter values included in the finite-rate model, it is of interest to examine the mechanisms by which oxygen atoms are converted to oxygen molecules in the two surface reaction systems. This is summarized in Figs. 19c and 19d, which plot the fractional contribution (branch) of each individual reaction to the total O-atom consumption or O_2 production, respectively. For the EM system, the catalytic process is dominated by ER recombination until approximately 1600 K, above which LH recombination begins to contribute. This is evident because atom loss comes 50% from adsorption and 50% from ER reaction (which also uses the adsorbed atom) until 1600 K, when adsorption becomes the dominant O-atom loss mechanism in Fig. 19c and LH recombination becomes a prominent source of O_2 production in Fig. 19d.

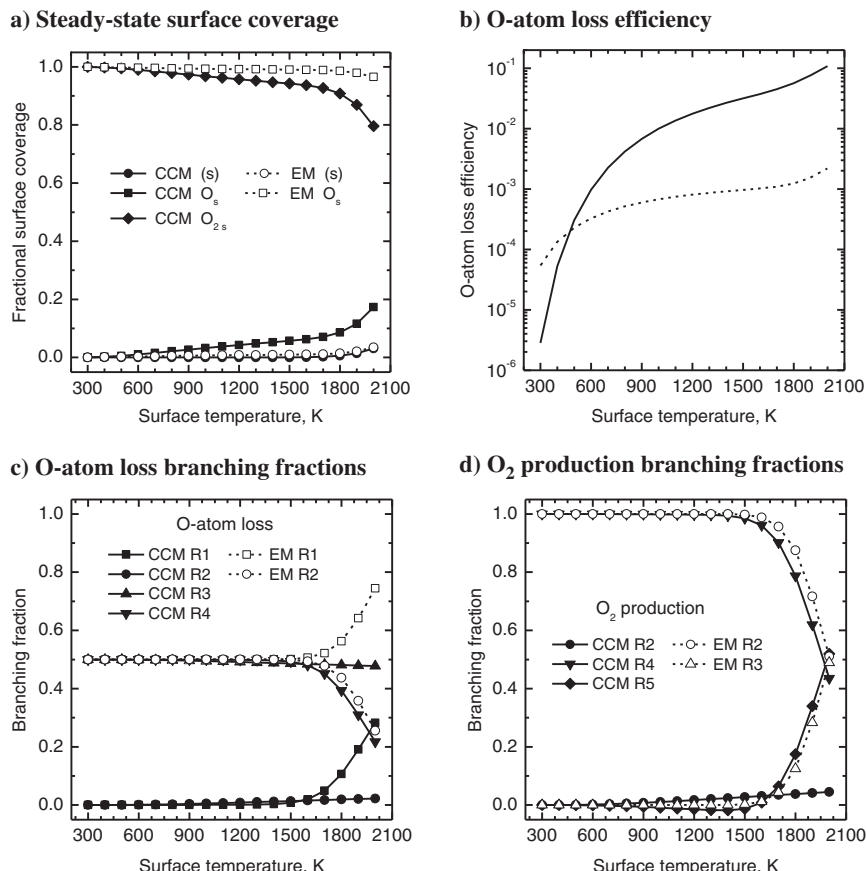


Fig. 19 CCM and EM simulations of dissociated oxygen recombination on silica.

The CCM system is very different in that no LH mechanism is included. Instead, adsorbed molecular oxygen is produced by an ER-like process (reaction 3 in Table 5) that produces a surface-bound molecular product. This adsorbed O_2 is subsequently liberated by the ER II mechanism (reaction 4 in Table 5) that replaces the adsorbed molecule with an adsorbed oxygen atom at temperatures up to about 1500 K. At higher temperatures, the surface is hot enough for direct molecular desorption to occur. Although a number of different reactions can contribute to the O-atom recombination at different temperatures, the most important reaction releasing O_2 into the gas phase at $T < 1500$ K is ER Recombination II. The exponential trend in loss efficiency with temperature exactly matches the activation energy of $E_{f4} = 0.3$ eV up to this temperature. Any change in the activation energy of this dominant reaction will change the slope in recombination coefficients with temperature.

It is insightful to analyze the behavior of the systems to fixed boundary conditions to gain understanding of the nature of the response to varying inputs. When used as a boundary condition to the CFD, this model will experience varying temperatures, pressures, and concentrations and respond to produce a physical set of production rates that result in an effective reactant loss efficiency or product gain efficiency at the surface which is balanced by diffusion into the gas.

As a demonstration of the coupling of the boundary condition into the DPLR CFD code, a 1 m radius cylinder is considered with freestream conditions of $\rho = 0.001 \text{ kg m}^{-3}$, $U = 6 \text{ km s}^{-1}$, and $T = 200 \text{ K}$. This is the same case and geometry that was previously used to make comparisons between DPLR, US3D, and LeMANS for reacting air [24, 25] (exact agreement was demonstrated), but the results presented here considered pure oxygen. The comparison between the two rate systems is made for two fixed wall temperatures of 1750 K and 2750 K in Fig. 20a and 20b, respectively. As expected from the previous fixed gas simulations, the higher effective loss efficiency of the CCM system results in higher heat flux rates to the surface. At the 1750 K surface temperature, the EM rates are close to noncatalytic, whereas the CCM rates are close to fully catalytic, resulting in approximately a 20% increase in heat flux. At the 2750 K surface temperature, the EM rates predict a more reactive response and the two models are closer in predicted heat flux.

We note that this high temperature computation is for illustrative purposes only; 2750 K is well above the melting point of silica and in a regime of high silica volatility where a more sophisticated finite-rate boundary condition model including surface participating reactions would need to be formulated.

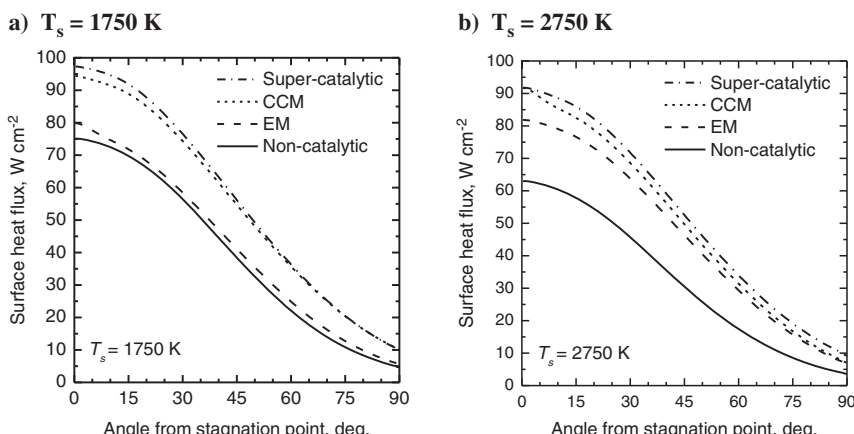


Fig. 20 CCM and EM simulations for a 1 meter radius silica cylinder at 6 km s^{-1} freestream velocity using the DPLR CFD code.

D. COUPLED CATALYSIS MODELS: MARTIAN ATMOSPHERIC ENTRY SURFACE CHEMISTRY

The Martian atmosphere is predominately carbon dioxide with approximately 3% nitrogen. Dissociation of these molecules during atmospheric entry gives rise to the possibility of various surface recombination reactions involving CO, C, O, and N. Under moderate entry conditions, the predicted C-atom and N-atom concentrations near the surface are much smaller than those of O atoms and CO molecules, and the main surface reactions contributing to catalytic heating are recombination to molecular oxygen and carbon dioxide.

Various surface recombination models have been developed and implemented into CFD computations for Martian entry simulations; however, most have been SRE-type models, which do not incorporate competing surface reactions nor the reverse reactions consistent with thermodynamics [106–111]. More recently, some attempts have been made to incorporate finite-rate surface chemistry effects into these models [20, 112, 113].

Independent specification of reaction efficiencies in systems in which reactants can participate in multiple surface reactions can lead to violations of element conservation if the reactions are not allowed to compete for a finite set of active sites on the surface. Thus, additional constraints on the values of specified reaction efficiencies must be derived and implemented based on specified branching fractions and/or species flux limitations, a complication that is avoided in finite-rate surface reaction formulations. A simple finite-rate surface reaction model can be constructed within the present framework based on two adsorption reactions and three ER recombination reactions, as shown in Table 11.

This is the same reaction set presented by Gupta et al. [108] and similar to that of Micheltree and Gnoffo [107], who omitted the oxygen recombination reaction 3. This reaction set was also used by Afonina et al. [113], although in most of their work CO adsorption reaction 5 was neglected. Using this model, we illustrate how species production rates, and the loss efficiencies and branching fractions for O and CO, vary with the values of the sticking coefficients, ER probabilities, and bounding gas compositions.

TABLE 11 REACTIONS AND RATES FOR MARS ENTRY CATALYSIS

	Reaction	Type	Case a: S_0 , γ_{er}	Case b: S_0 , γ_{er}
1	$O + (s) \leftrightarrow O_s$	Ads	0.01	0.01
2	$CO + (s) \leftrightarrow CO_s$	Ads	0.01	0.001
3	$O + O_s \leftrightarrow O_2 + (s)$	ER	0.01	0.01
4	$O + CO_s \leftrightarrow CO_2 + (s)$	ER	0.01	0.001
5	$CO + O_s \leftrightarrow CO_2 + (s)$	ER	0.01	0.001

The gas phase contains O₂, O, CO, and CO₂, and the surface phase has one set of active sites with three surface species, E(s), O(s), and CO(s). We set $\Phi_s = 7.5 \times 10^{-6} \text{ mol m}^{-2}$, all $\beta = 0$, and all energy barriers $E_{\text{ad}} = E_{\text{er}} = 0$. We specify both O-atom and CO thermal desorption by Form 1 (Eq. (43)) with $A_{\text{des}} = 1$, $\beta = 0$, $v = 1.0 \times 10^{12} \text{ s}^{-1}$ and $E_{\text{des}} = 300 \text{ kJ mol}^{-1}$. The surface temperature and pressure are taken as 2500 K and 10,000 Pa, respectively.

First, consider Case A where the probability of reaction for all surface reactions is identical: $S_{0,1} = S_{0,2} = \gamma_{\text{er},3} = \gamma_{\text{er},4} = \gamma_{\text{er},5} = 0.01$. We compute the species production rates, the reactant loss efficiencies, and the reactant branching ratios as the surface is exposed to a series of fixed gas compositions ranging from CO to O rich; see Table 12.

The results are plotted in Fig. 21a. The production rates of O and CO are negative because they are consumed, whereas those of O₂ and CO₂ are positive, which indicates species generation. As expected, CO loss and CO₂ generation are maximized when the gas-phase O and CO concentrations are similar, whereas O-atom loss and O₂ generation increase monotonically with increasing gas-phase O concentration.

Note that the O and CO loss efficiencies (the fraction of collisions with the surface that remove the gas species from the gas phase) as well as their branching fractions (the relative amounts of each species lost via different surface reactions) vary smoothly with changes in the bounding gas composition. In the finite-rate formulation, loss efficiencies and branching fractions are a result of finite-rate reactions competing for active surface sites in response to the imposed boundary conditions. This is a fundamental difference from SRE models, and we argue it is a more physically justified representation of surface chemistry in systems with multiple reactants participating in multiple reactions.

The O-atom loss efficiency is relatively constant, but the dominant loss pathway changes from adsorption and ER CO₂ formation to adsorption and ER O₂ formation as the gas-phase O-atom mole fraction increases. The CO branching fractions are about evenly split between adsorption and ER CO₂ formation, but the CO loss efficiency increases with decreasing gas-phase CO.

There is some evidence that O-atom recombination to O₂ is a more likely outcome than O + CO recombination to CO₂, at least under some conditions [14, 15]. A rationalization for this behavior is that O atoms may adsorb more

TABLE 12 BOUNDING GAS COMPOSITIONS (MOLE FRACTIONS)

	1	2	3	4	5	6	7	8	9
O ₂	0.01	0.01	0.01	0.01	0.01	0.01	0.01	0.01	0.01
O	0.09	0.19	0.29	0.39	0.49	0.59	0.69	0.79	0.89
CO	0.89	0.79	0.69	0.59	0.49	0.39	0.29	0.19	0.09
CO ₂	0.01	0.01	0.01	0.01	0.01	0.01	0.01	0.01	0.01

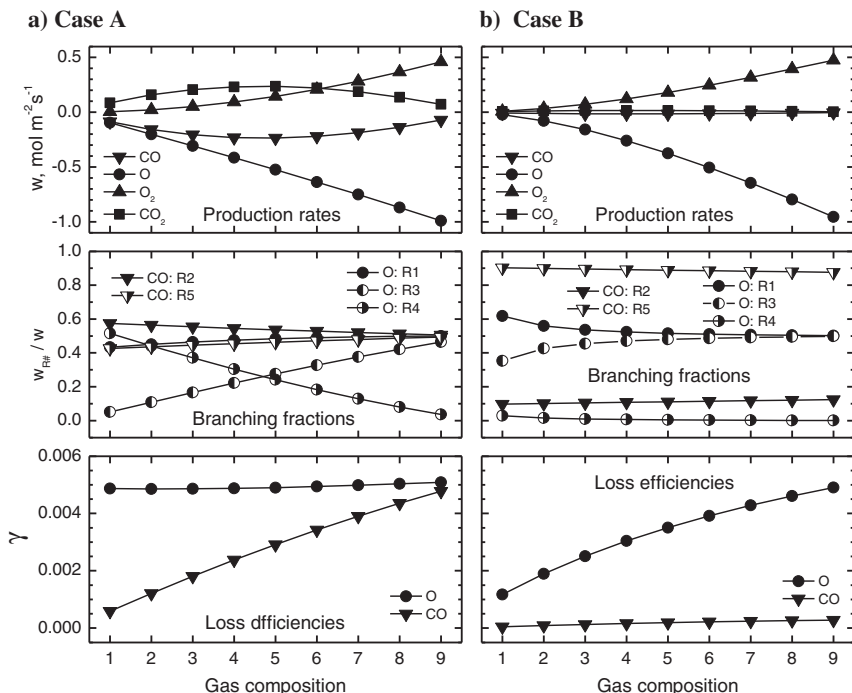


Fig. 21 Species production rates at the surface (top panels), O and CO branching fractions (middle panels), and O and CO loss efficiencies (bottom panels), at 2500 K and 10,000 Pa for the compositions listed in Table 12.

efficiently to a surface because they do not suffer from steric hindrances associated with the orientation of the impinging CO on the surface. A similar argument can be made for ER reactions involving O and CO partners. Although the issue is not settled, it is straightforward to incorporate this idea into the surface reaction model by lowering the efficiencies of the reactions involving CO. For Case B we reset $S_{0,2} = \gamma_{er,4} = \gamma_{er,5} = 0.001$ and repeat the previous simulation. The results are shown in Fig. 21b.

With these changes, the production rates of CO and CO₂ are much smaller than those of O and O₂. The branching fractions show that almost all O-atom loss is attributable to adsorption and ER O₂ generation. Both the O-atom and CO loss efficiencies increase with increasing gas-phase O-atom mole fraction, but the former is much larger than the latter. The small CO loss is predominately attributable to ER formation of CO₂ by reaction with an adsorbed O atom. Of course, many other reaction mechanisms and possible parameter choices exist, but these examples show the flexibility of the finite-rate formulation for modeling surface catalysis in the dissociated CO₂ system.

E. AIR-CARBON SURFACE CHEMISTRY

The oxidation of carbon is considered by comparing to the numerical solution and the experimental data published by Driver et al. [114] for a Fiberform[©] sample ablated on a copper wedge model in an arcjet facility. Driver et al employed a hard-wired version of a carbon oxidation model with a constant loss efficiency [115] to successfully model the interaction of atomic oxygen on the Fiberform[©] substrate downstream of a cooled copper wall and demonstrated that uncoupled material response without accounting for the interaction of the surface reactions and the gaseous boundary layer will under predict recession rates by 50% to 100%. Effects such as shape change, catalytic efficiency, and molecular versus atomic oxidation mechanisms were considered by the authors in order to best model the experimental data. MacLean et al. [2] later showed that the generalized finite-rate surface chemistry model can exactly replicate the behavior of the hardwired reaction model in the DPLR code by using the generalized model to emulate SRE behavior; see Table 13.

The SRE model is emulated in the following way. The oxidation of carbon bulk mass by atomic oxygen at the wall is modeled as an irreversible ER reaction with zero activation energy and a constant reaction probability of $\gamma = 0.9$. As we require in the finite-rate model framework, the interaction of bulk and gaseous species must occur through a surface phase, so a single, empty surface site appears on each side of reaction 1 as given in Table 13.

The catalysis of nitrogen with constant atomic loss efficiency can be accomplished in the finite-rate model framework via the inclusion of a pair of reactions—an irreversible adsorption reaction with a constant sticking coefficient and zero adsorption energy followed by an irreversible ER reaction with zero activation energy and a constant reaction efficiency.

For this system, the net reactant loss efficiency for steady-state coverage can be shown to follow the relationship in Eq. (86) as a function of the sticking coefficient and ER reaction probability.

$$\gamma = \frac{2S_0\gamma_{er}}{S_0 + \gamma_{er}} \quad (86)$$

To achieve a net reactant loss efficiency of $\gamma_N = 0.05$, we set $S_0 = \gamma_{er} = 0.05$. This reaction system is given in reactions 2 and 3 in Table 13.

TABLE 13 REACTIONS AND RATES FOR SRE MODEL

	Reaction	Type	S_0	$E_{ad}, E_{er}, \text{ kJ mol}^{-1}$
1	$O + (s1) + C_b \rightarrow CO + (s1)$	ER	0.9	0
2	$N + (s2) \rightarrow N_{s2}$	Ads	0.05	0
3	$N + N_{s2} \rightarrow N_2 + (s2)$	ER	0.05	0

It is also essential to note that the surface is modeled with two independent active site sets, in which one active site set is dedicated to the oxidation reaction, and the second is dedicated to the nitrogen catalysis reactions. Two active site sets are necessary, because the desired approximation is that the reaction efficiencies of the two processes are independent. If only one active site set were used, the adsorption of nitrogen atoms onto the surface partially fills up the available empty surface sites and reduces the observed reaction probability of the oxidation process. In some situations, such an interaction may be desirable and physically meaningful, but here we neglect it to match the behavior of the previous simulations. For the finite-rate model, the effective atomic loss efficiencies can be post-processed from the converged solution to verify that they are equal to the target values.

The density of available surface sites for both active site sets was taken as $1 \times 10^{-5} \text{ mol m}^{-2}$. This selection is arbitrary for this particular case since we note that, for this simple set of reactions replicating the constant loss efficiency, both the steady-state and time-accurate response of the gas phase is independent of the site density. The only effect of the surface site density is to control the non-dimensional fill rate of adsorbed nitrogen atoms. This may potentially be a means to control numerical stability issues in certain situations, but no issues were observed in this case.

Using the SRE reaction set, the CFD flow field of the model is shown in Fig. 22a. Driver et al. [114] considered additional effects, such as shape change, point wise specification of the freestream, and three-dimensional (3-D) flow in order to obtain better agreement with the measured recession distribution.

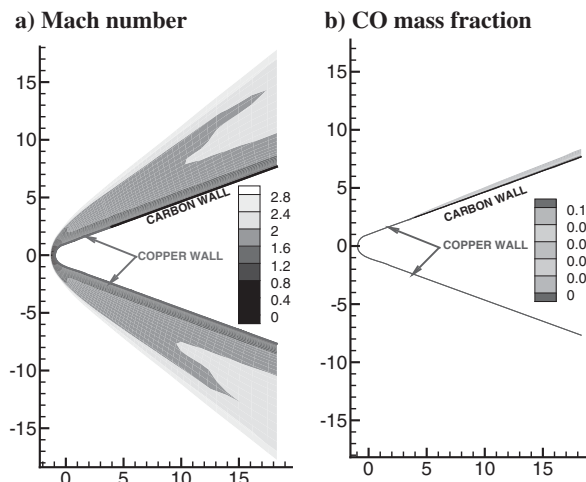


Fig. 22 Wedge flow field computed with DPLR (see color section).

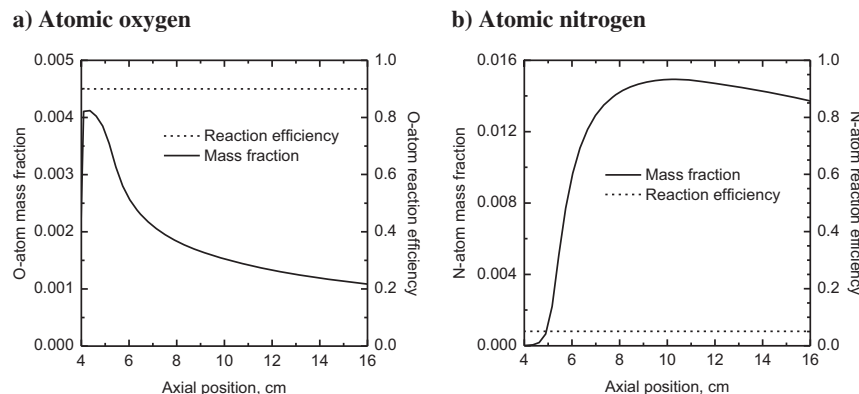


Fig. 23 Atom mass fractions and effective loss efficiency.

Here, only the initial (flat) shape of the wedge model was used, and shape change effects were neglected; we assume that the freestream is uniform at the following conditions: $U = 4.818 \text{ km s}^{-1}$, $\rho = 0.00671 \text{ kg m}^{-3}$, $T = 4744 \text{ K}$, $T_v = 4535 \text{ K}$, $y_{N2} = 0.5107$, $y_{NO} = 0.0006$, $y_N = 0.2079$, $y_O = 0.2172$, and $y_{Ar} = 0.0636$. The nose piece and lower side of the flow field have a cold, copper wall (350 K) considered to be fully catalytic to atoms, whereas the back of the upper side is modeled with the finite-rate boundary condition and radiative equilibrium with an emissivity $\varepsilon = 0.90$. The formation of CO as the gas hits the carbon surface is evident in the flow in Fig. 22b.

The atomic mass fractions of oxygen and nitrogen along the carbon surface and the associated effective loss efficiencies are plotted in Figs. 23a and 23b. As expected, the loss efficiencies are the exact values of 0.9 and 0.05 required from the model. The upstream copper surface has been modeled as fully catalytic to nitrogen, whereas the carbon surface is only partially catalytic; thus, there is a slight increase in the population of nitrogen atoms as the boundary layer moves onto the carbon wall. The same is true for oxygen atoms, which are fully consumed at the copper wall, but 10% of the diffusing atoms remain on the carbon surface.

The SRE model assuming constant carbon oxidation efficiency of atomic oxygen that has been used initially in this case is simplistic, but it has been shown to be effective in for this case [114] and in other cases [115]. However, since the finite-rate model that has been implemented in DPLR is capable of modeling more complex surface systems, we have chosen to include results using several popular carbon oxidation models from the literature including the Park model and the Zhlukov and Abe model [116]. Beerman et al. [117] and Candler [118] compare these two models in great detail.

The Park model is an extended version of the baseline oxidation model that includes irreversible oxidation by both atomic and molecular oxygen, irreversible nitridation by atomic nitrogen, and C₃ sublimation/condensation. The four-mechanism model and the associated rates actually come from Chen and Milos [119], who suggested a model that was loosely inspired by some earlier work of Park [120]; however, this model continues to be commonly called “the Park model” in the literature despite the fact that it is not really directly attributable to Park’s published work, and we will continue that convention here. In this model, the oxidation and nitridation processes are represented as ER reactions in the forward direction, with the backward reactions set to zero. The sublimation/condensation reactions are modeled as two separate reactions, sublimation and ER (for condensation), with zero backward reaction rates. The earliest oxidation model actually published by Park [121] is also implemented and will be referred to as the “Park (1976) model.” This model includes O-atom and O₂ carbon oxidation as well as O-atom surface recombination. These processes are modeled by three ER reactions and one adsorption reaction, again with all backward reactions set to zero. The reactions and rates parameters for the Park and Park 1976 models are given in Tables 14 and 15.

The Zhlukov and Abe model takes full advantage of the new features now in DPLR for modeling finite-rate surface chemistry. It makes use of ER, LH, sublimation, adsorption, and desorption reactions on the surface, and includes a number of adsorbed surface species, consistent with the latest thinking on gas/surface interaction modeling. The Zhlukov and Abe model is a finite-rate model with 12 defined forward and reverse rates that are thermodynamically constrained for each process. The reactions and rate parameters for the Zhlukov and Abe model are given in Table 16.

The recession rate predicted by these three models is compared to the baseline SRE model in Fig. 24. It is readily noted that the Park model predicts a significantly higher recession rate than the baseline model, whereas the Zhlukov and Abe model predicts a significantly lower recession rate. Noting again that the SRE model accurately predicted the measured recession rate of the experiment

TABLE 14 REACTIONS AND RATES FOR PARK MODEL

	Reaction	Type	$\gamma_{er}, \gamma_{sub}$	$E_{er}, E_{sub}, \text{kJ mol}^{-1}$
1	O + (s) + C _b → CO + (s)	ER	0.63	9.644
2	O ₂ + 2(s) + 2C _b → 2CO + 2(s)	ER	0.50	0
3	N + (s) + C _b → CN + (s)	ER	0.30	0
4	3(s) + 3C _b → C ₃ + 3(s)	Sub	5.19×10^{13}	775.81
5	C ₃ + 3(s) → 3(s) + 3C _b	ER	0.10	0

TABLE 15 REACTIONS AND RATES FOR PARK (1976) MODEL

	Reaction	Type	S_0, γ_{er}	$E_{er}, E_{sub}, \text{kJ mol}^{-1}$
1	$O_2 + (s1) + C_b \rightarrow CO + O + (s1)$	ER	0.01	0
2	$O + (s1) + C_b \rightarrow CO + (s1)$	ER	0.63	9.644
3	$O + (s2) \rightarrow O_{s2}$	Ads	0.63	9.644
4	$O + O_{s2} \rightarrow O_2 + (s2)$	ER	0.63	9.644

when accounting for an accurate freestream distribution and shape change, the differences predicted by the other two models are not desirable. The Park (1976) model accurately matches the SRE model recession rate in the downstream portion of the surface, but it is more limited upstream by availability of atomic oxygen immediately following the fully catalytic copper surface, as demonstrated by the effective atomic loss efficiency of this model shown in Fig. 25a. This effect was forecasted to possibly occur downstream of a highly catalytic surface in this situation by Driver et al. [114].

TABLE 16 REACTIONS AND RATES FOR ZHLUKTOV AND ABE MODEL

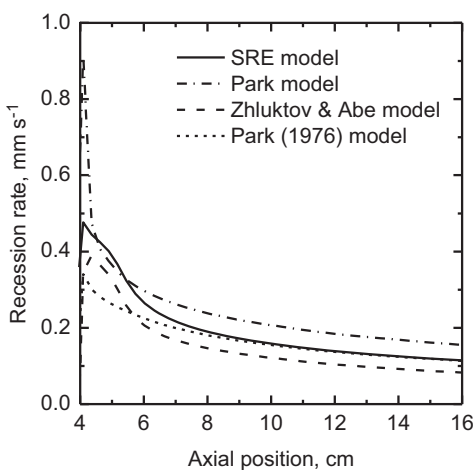
	Reaction	Type	S_0, γ_{er}, A, ν	β	$E_{ad}, E_{er}, E_A, E_{des}, \text{kJ mol}^{-1}$
1	$O + (s) \rightarrow O_s$	Ads	1	0	0
2	$N + (s) \rightarrow N_s$	Ads	1	0	0
3	$2O_s \rightarrow O_2 + 2(s)$	Arrh	3.58×10^{10}	1	256.07
4	$O_2 + (s) \rightarrow O + O_s$	ER	1	0	118.06
5	$CO_2 + (s) \rightarrow CO + O_s$	ER	0.9	0	0
6	$O_s + C_b \rightarrow CO + (s)$	Arrh	2.08×10^9	1	332.56
7	$O + O_s + C_b \rightarrow CO_2 + (s)$	ER	0.8	0	16.63
8	$2O_s + C_b \rightarrow CO_2 + (s)$	Arrh	3.58×10^{14}	1	332.56
9	$C + (s) \rightarrow (s) + C_b$	ER	0.24	0	0
10	$C_2 + 2(s) \rightarrow 2(s) + 2C_b$	ER	0.5	0	0
11	$C_3 + 3(s) \rightarrow 3(s) + 3C_b$	ER	0.023	0	0
12	$N_2 + (s) \rightarrow N + N_s$	ER	1	0	636.85
1b	$O_s \leftrightarrow O + (s)$	K_c^a	1.72×10^4	0	374.13
2b	$N_s \leftrightarrow N + (s)$	K_c^a	1.72×10^4	0	304.29

^aConcentration-based equilibrium constants in the simple TST approximation for mobile adsorption: Eqs. (46) and (50).

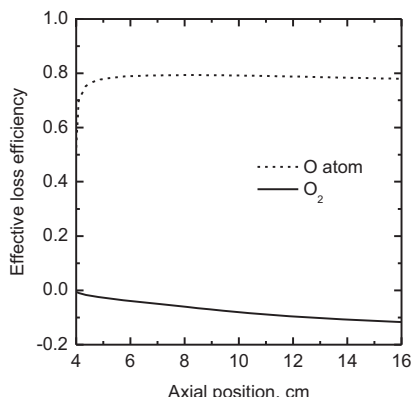
Fig. 24 Surface recession rates as function of position on carbon wall.

The reasons for the differences in predicted recession rates between the other models may be more closely examined by looking at the distribution of several gaseous species at the surface. The effective loss efficiencies for the Park model are shown in Fig. 25b. The loss efficiency of molecular oxygen and atomic nitrogen are fixed at 0.5 and 0.3, respectively. In addition, the loss efficiency of atomic oxygen is shown to vary because of the temperature dependence of the expression, but the average is approximately 0.4.

The production of the CN species is shown in Fig. 26a. The Park model produces a significant amount of CN, whereas the other three models do not. Driver et al. noted as part of their analysis that the production of CN predicted with the nitrogen atomic loss rate of 0.3 from the Park model did not correlate well with similar measurements of recession rate in a pure nitrogen gas.



a) The Park (1976) Model



b) The Park model

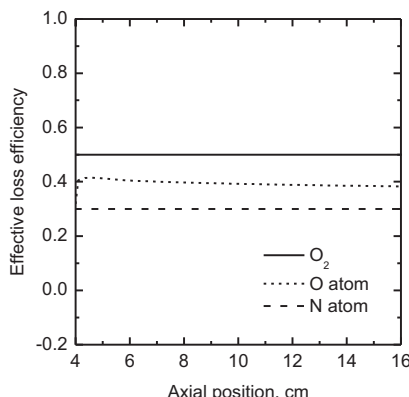
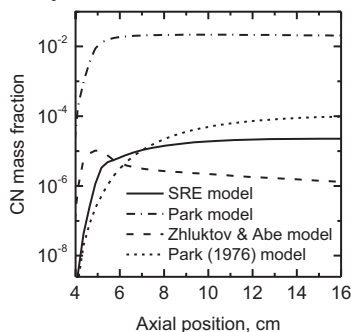
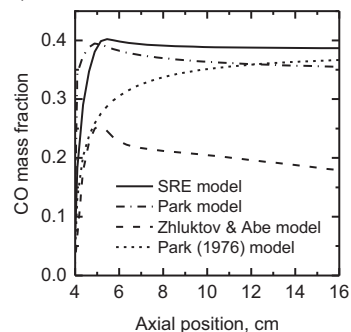


Fig. 25 Effective O_2 , O-atom, and N-atom loss efficiencies as a function of position on the carbon wall.

a) Cyano radical



b) Carbon monoxide



c) Carbon dioxide

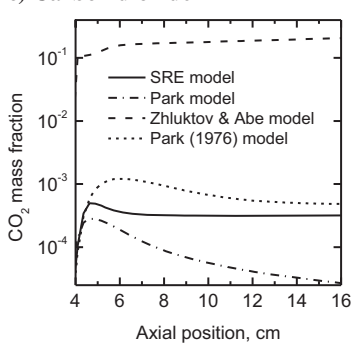


Fig. 26 Product mass fractions as a function of position on the carbon wall.

The mass fraction of carbon monoxide shown in Fig. 26b is similar for both the Park and the SRE models, although the Park model produces carbon monoxide through both molecular and atomic oxidation. The total fraction of the diffusing oxygen that is consumed in the Park model is similar to the SRE model. It was verified that the change in recession rate is caused primarily by the CN formation reaction by testing the Park model with reaction 3 (Table 14) turned off.

The production of CO from the Zhlukov and Abe model is significantly lower than the others. The same calculation shows a significant production of carbon dioxide in Fig. 26c. Simple stoichiometry suggests creation of CO_2 will liberate one carbon atom for every two oxygen atoms, making it half as effective at promotion of surface blowing. Although the complex production/diffusion interactions produce recession rates that are not exactly in this proportion, this fact explains why the overall predicted recession rate is qualitatively lower than the SRE model. Driver et al. [114] argue that a significant production of either CN or CO_2 is not likely based on agreement with available arcjet data. The finite-rate model formulation provides a powerful framework to test potential systems to help improve the accuracy of surface reaction rates for applications such as this.

F. PHENOLIC ABLATOR IN AIR WITH PYROLYSIS

To demonstrate the addition of pyrolysis gas products to the finite-rate surface model system, a test case published by Driver and MacLean [122] is considered that models reacting air ablating a phenolic impregnated carbon ablator (PICA) surface. The shape that has been considered is a 4-in. diameter “Iso-Q” shape,

thus named because it exhibits approximately uniform heat flux and recession rate across the surface. The predicted recession rates were successfully compared to measurements made in an arc-jet facility at nominal freestream conditions of: $U = 3.860 \text{ km s}^{-1}$, $\rho = 0.00345 \text{ kg m}^{-3}$, $T = 1470 \text{ K}$, $T_v = 1787 \text{ K}$, $y_{\text{N}_2} = 0.7096$, $y_{\text{NO}} = 0.0202$, $y_{\text{O}_2} = 0.0242$, $y_{\text{O}} = 0.1824$, and $y_{\text{Ar}} = 0.0636$. The flow field is given in Fig. 27, in which Mach number contours are shown on the upper half of the figure, and temperature contours are shown on the lower half of the figure.

The surface reaction model is the same SRE model used in the previous example of flow over a wedge (see Table 13). In addition to the surface reactions, pyrolysis is modeled via the steady-state pyrolysis approximation, in which the mass of the pyrolysis gas injected from the surface is proportional to the bulk phase (carbon) loss rate governed by Eq. (54). The surface temperature is assumed to be in radiative equilibrium. Driver and MacLean [122] performed a detailed analysis and determined that the char yield for the PICA sample is $C_Y = 0.83683$ with a pyrolysis gas molar composition that is 60% H₂, 20% CO, and 20% C. The use of atomic carbon here is consistent with the approximation made by Driver and MacLean [122], who noted that the injection of C₃ is sufficiently unstable and immediately decomposes in the boundary layer. Thus, atomic carbon is used for simplicity both here and in the referenced analysis.

The predicted unit mass blowing rate from the surface is shown in Fig. 28. The figure shows multiple solutions. One is without pyrolysis injection, so the blown mass comes purely from the bulk-phase loss rate at the surface. When the pyrolysis injection is included, the overall blowing rate increases as it should. However, the magnitude is somewhat less than the 19.5% increase that might be expected if the pyrolysis is uncoupled by applying Eq. (54) to the production rate from the bulk-phase-only case. Because additional products are injected into the near-wall boundary layer region, the amount of atomic oxygen that can diffuse to the surface to oxidize the bulk is diluted. The reduction in bulk oxidation, of course,

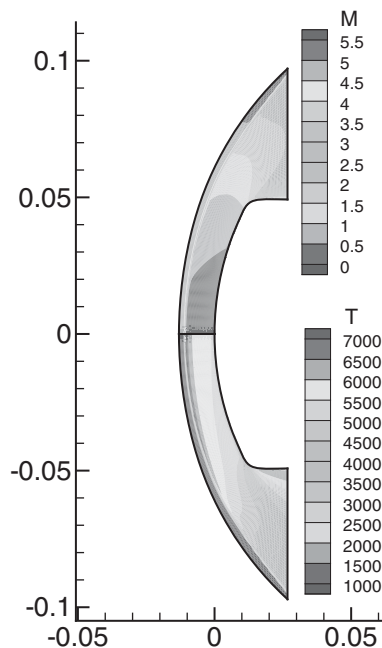


Fig. 27 Mach number (upper half) and temperature (lower half) contours of the Iso-Q flow field (see color section).

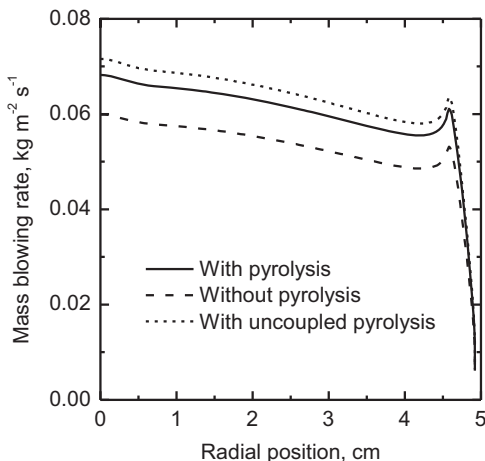


Fig. 28 Mass blowing rate as a function of radial position; without pyrolysis and with coupled and uncoupled pyrolysis.

affects the rate of pyrolysis in the steady-state pyrolysis approximation, and the overall effect is nonlinear.

The mass fractions of the pyrolysis species at the surface are shown in Fig. 29. The relative fractions of the pyrolysis products are not equal to the specified steady-state pyrolysis mass

proportionality constants, because the model enforces the ratio of the production rates and not the species concentrations themselves. The production rate controls the mass balance at the surface, but diffusion and convection play a role also. With unequal diffusion of the gaseous species, the effect is somewhat unintuitive.

The terms of the mass balance of the converged solution at the stagnation point are given in Table 17. In addition to showing that mass is properly conserved at the surface for all participating species, the ratio of the molar production rates, \dot{w}_k , of the pyrolysis participants should follow the target proportionality assumed for the steady-state pyrolysis model. With the prescribed char yield fraction that has been specified – 1.051 moles of CO, 0.051 moles of C, and 0.153

moles of H₂ – these are expected for each 1.0 mole of bulk carbon loss. The molar production rates of the participant species are observed to follow exactly these proportions.

The response of the surface with time at the stagnation point has been considered as part of the finite-rate solution. It is useful to monitor the surface coverage

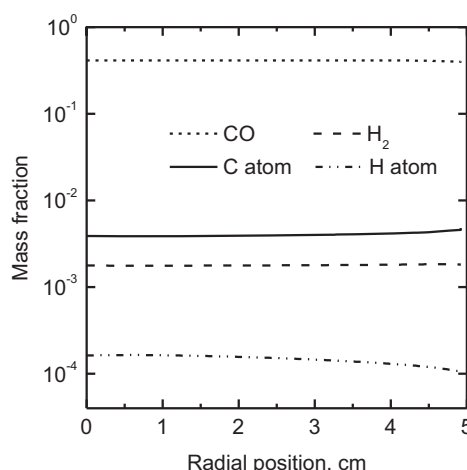


Fig. 29 Pyrolysis species mass fractions as a function of radial position.

TABLE 17 STAGNATION POINT MASS BALANCE TERMS; UNITS OF $\text{kgmol m}^{-2} \text{s}^{-1}$

	$+ J_k/M_k$	$- \rho_w v_w y_{k,w}/M_k$	\dot{w}_k	sum
O	0.00476	-0.00001	-0.00475	4.52×10^{-16}
C _b	—	—	-0.00475	-4.75×10^{-3}
CO	-0.00399	-0.00100	0.00499	4.34×10^{-18}
C	-0.00022	-0.00002	0.00024	-3.11×10^{-16}
H ₂	-0.00066	-0.00006	0.00072	-1.14×10^{-16}

while the flow evolves as one metric of convergence. The evolution of the adsorbed N-atom concentration is shown in Fig. 30a, and its production rate is shown in Fig. 30b. The N_{s1} production rate decreases to machine zero as the empty surface fills. The loss rate of the bulk-phase carbon is shown in Fig. 30c. Unlike the surface phase, the production or loss rate of the bulk phase constituents do not tend to zero since the bulk loss rate determines the blowing mass rate in to the gas. However, it does reach a steady-state value, indicating convergence of the solution.

The overall convergence of the CFD solver is plotted in Fig. 30d as measured by the L₂-norm of the continuity equation residual. This again emphasizes that the flow and the surface evolve together. The change in the density residual slope after approximately 1100 iterations indicates the surface has reached steady-state coverage. Once the rate of nitrogen atoms adsorbing to the surface is equal to the rate adsorbed N atoms are lost owing to ER recombination, the shock-layer convergence proceeds at a different rate as the interior of the flow finishes its evolution.

Finally, the effect of the inclusion of the steady-state energy balance is shown in Fig. 31. The SSEB is an extension of the common radiative equilibrium boundary condition that accounts for conduction into the ablating surface under the steady-state ablation approximation. The use of the radiative equilibrium boundary condition is the same as a situation in which the virgin enthalpy is equal to the enthalpy of the gas mixture at the wall (and thus the extra term is zero). In this case, the radiative equilibrium energy balance boundary condition predicts an average mixture enthalpy blown from the surface of approximately 2.2 MJ kg⁻¹. The surface temperature for the SSEB boundary condition using this value for the virgin enthalpy is shown in Fig. 31a along with the surface temperature from the radiative equilibrium case. The match is excellent, as expected. In addition, several other solutions are shown for virgin enthalpy increments spanning likely values for this type of ablator. The solution with a virgin enthalpy of 0.0 MJ kg⁻¹ is shown simply as a reminder that, when using the SSEB boundary condition, this choice of virgin material enthalpy does not mean that the term is not active.

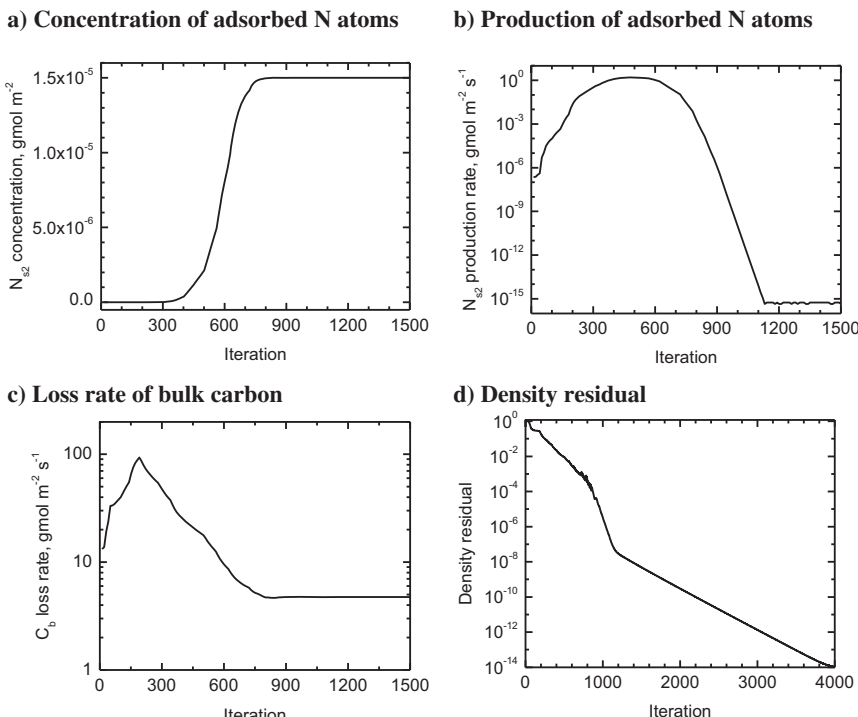


Fig. 30 Surface and bulk species convergence and CFD continuity equation residual.

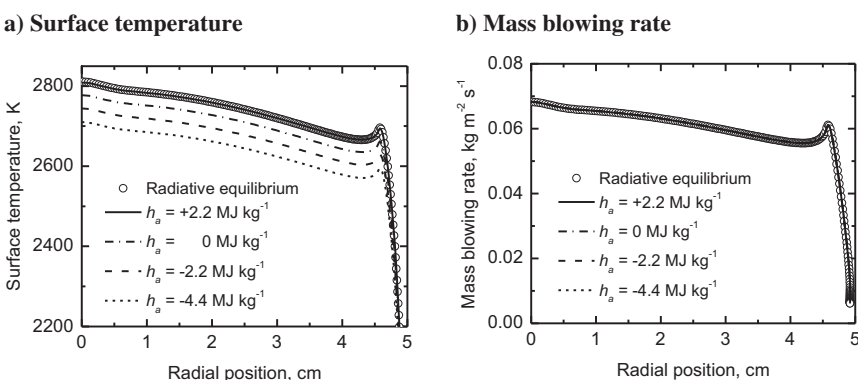


Fig. 31 Surface temperature and mass blowing rate as a function of radial position; effect of the SSEB model for various virgin enthalpy values.

An ablator with a negative absolute enthalpy results in a decrease in surface temperature relative to radiative equilibrium because of the implied surface conduction. However, all of the predictions for surface blowing rate are shown in Fig. 31b, and it is observed that the change in energy balance has no discernible effect on the blowing rate for this model since the oxidation rate chosen for this case is not a function of temperature. For a general finite-rate model with reaction rates that depend on surface temperature, we might expect to see a coupling from this additional term. The use of the steady-state pyrolysis and the steady-state energy balance boundary conditions should result in a solution that is close to a detailed material response analysis undergoing steady-state ablation.

VI. FUTURE DIRECTIONS

The modeling work described here can be extended in many different ways to provide a more detailed representation of the actual TPS response during hypersonic flight or ground testing. It is also obvious that carefully designed experiments for the calibration and validation of surface reaction models are essential. Here we discuss a few particular areas where future effort could be productively focused.

A. TIGHTLY COUPLED CFD AND MATERIALS RESPONSE COMPUTATIONS

The implementation of the finite-rate surface chemistry framework into the DPLR code demonstrates tight coupling of the surface reactions into the Navier–Stokes surface mass and energy balance, while neglecting certain material response effects such as internal heat conduction, surface shape change (owing to recession), and generalized pyrolysis or similar sub-surface decomposition processes. For many applications, the approach presented here may be sufficient since the effect of the surface reactions and resulting mass injection on the gaseous flow-field are accurately captured. In other cases, where the time accurate simulation of transient materials responses to the environment are critical, a clear improvement to the modeling fidelity is to couple the materials response modeling tightly into the CFD simulation.

This type of integration between CFD and material response codes has been demonstrated to varying degrees by a number of authors [123–125] using an equilibrium ablation approach where surface mass loss is computed using free-energy minimization or equilibrium constants with available reactants reaching the surface, often using the classical “B” tables [126]. Although the exact exchange of information between the codes varies from author to author, the process usually involves passing surface pressure and heat flux from the CFD solution, conduction heat flux and pyrolysis mass/composition from the material response solution, and iteratively solving surface mass and energy balance relationships to determine surface mass loss, surface composition, and surface temperature until

some convergence threshold is reached. A direct approach was even recently demonstrated by Nompelis et al. [127] for a pure carbon surface ablator with pure equilibrium shock layer chemistry and thermodynamics by marching the gas and solid solutions together through a trajectory with real-time, 3-D surface recession.

However, incorporation of finite-rate surface kinetics into this process is relatively new. In principle, the same approach can be used by substituting the calculation of the finite-rate reaction production rates instead of the equilibrium B' table to determine the surface mass loss and surface composition. This has been very recently demonstrated by Alkandry et al. [128]. Similar work is also in process with the NASA Johnson Space Center Fully-Implicit Navier–Stokes (FIN-S) and CHarring Ablator Response (CHAR) codes. In addition, MacLean [129] has recently developed an equilibrium ablation boundary condition that allows the DPLR CFD code to perform boundary layer simulations with equilibrium ablation in a tightly coupled manner. Continued research related to managing the range of time-scales associated with the coupled simulations, maintaining grid quality in both fluid and solid domains as the surface recesses [130], and, of course, development and validation of kinetic models and mechanisms will likely remain challenging in the near future.

B. BOUNDARY-LAYER DIFFUSION AND CHEMISTRY

The computational examples of catalysis, oxidation and pyrolysis shown in the previous sections demonstrated the effects of finite-rate surface reactions on the species mass balance at the wall (Eq. (55)). However, the mass balance equation is equally affected by the gas-phase diffusion of species between the surface and the adjacent boundary layer. Moreover, near-surface gas-phase chemistry will further affect the species mass balance, since species loss or production will respectively decrease or increase the concentration gradients that drive diffusion through the boundary layer.

The DPLR code used the SCEBD model which enforces total flux conservation and allows for unequal diffusion of species of differing molecular weights. MacLean et al. [2] have demonstrated that substituting a constant Schmidt number diffusion model with a Schmidt number of 0.70 for the SCEBD diffusion model in DPLR, decreases the computed blowing rates for a PICA Iso-Q pyrolysis computation by ~30% and the computed catalytic heating of a platinum cylinder by ~10%. Unequal species diffusion changes the relative availability of reactants at the surface and impacts the net energy reclamation from the gas.

Similar impacts on surface energy transfer and mass balance could be anticipated for different gas-phase reaction and rate coefficient sets applied within the boundary layer. Traditionally, CFD models for hypersonic and re-entry flow fields have emphasized gas-phase chemistries at very high temperatures (2000–15,000 K), with mechanisms and rates often derived from shock tube or combustion experiments. However, in many cases—reusable TPS applications, water

cooled specimens and probes, test environments like shock tunnels and diffusion/flow tubes—surface temperatures are relatively low, in the 300–2000 K range. Note that finite-rate gas-phase chemistry effects will be most pronounced in the low temperature, high density regions of the boundary layer directly adjacent to the surface and so the accuracy of the reaction rates is most important in this regime. The extrapolation of rate coefficients measured at many thousands of degrees to this low temperature regime may lead to significant errors that propagate into computed reactant and product concentrations at the surface and thus impact the surface energy and mass balances.

We therefore emphasize that diffusion and near-surface gas-phase chemistry modeling must be considered in parallel with the development and implementation of finite-rate surface chemistry models. In particular, the uncertainties associated with each modeling component and the impact of these uncertainties on the surface mass and energy balances must be understood, before the accuracy of the entire computation can be evaluated. This coupling between surface chemistry, near-wall gas-phase chemistry and diffusion also means that a surface chemistry model tuned to reproduce experimental results within a particular CFD code cannot be ported to another CFD code and retain its accuracy, unless the gas-phase chemistry and diffusion modeling are also consistent between the two codes.

C. FINITE-RATE MODELS AND COMPUTATIONAL CHEMISTRY

The approach described here for the oxygen-silica system, of using computational chemistry to identify chemical pathways and parameter values/ranges for a finite-rate surface chemistry model, could be applied to other species-materials systems.

Two obvious systems are the nitrogen-silica and nitrogen-oxygen-silica systems, relevant to surface catalysis under high-enthalpy air. Although various ReaxFF nitrogen descriptions have been used by a number of groups and authors [131–133], only a preliminary silicon nitride force field has appeared in open literature [134]. This Si/N ReaxFF description needs to be updated to the currently used ReaxFF formulism by first extending the DFT-based training set with Si_3N_4 equations of state, heats of formation and elastic properties, N-atom binding energies to silicon surfaces, and N_2 dissociation barriers in silicon surfaces, and then training the force field against mixed silicon nitride/oxide phases to generate a fully transferable Si/N/O description. As discussed in the Section III, laboratory experiments have confirmed the surface formation of NO on silica in dissociated air. The prediction of surface defect structures and trajectory calculations in these N-atom containing environments would provide a great deal of insight into the proper construction and parameterization of finite-rate models for competitive $\text{O} + \text{O}$, $\text{N} + \text{N}$ and $\text{O} + \text{N}$ recombination processes on silica.

Extension of the computational chemistry techniques for formulating a finite-rate model has recently been applied to oxygen-carbon interactions [135]. The

main challenge in extending such methods to actively oxidizing materials is that the surface structure changes. To analyze a TPS material during oxidation with computational chemistry requires the determination of a representative atomistic-level surface morphology. However, in the same way that surface defect structures for silica were predicted by the integrated MD-DFT methodology presented in this chapter, the atomistic structure of other oxidizing systems could also be determined. This has been demonstrated for Highly Oriented Pyrolytic Graphite (HOPG) [135], but remains a challenge for other actively oxidizing materials with more complex microstructures.

Beyond purely catalytic or purely oxidative systems lie more complicated gas–surface chemistries that include both phenomena, and exhibit transitions between different chemical pathways under changing environmental conditions. The prototypical example of such a system is the passive-to-active oxidation transition observed for TPS systems containing silicon carbide. Passive oxidation of SiC leads to condensed SiO_2 formation in a self-limiting process that preserves a stable surface of low catalytic efficiency. Active oxidation of SiC produces only gaseous products (SiO and CO) and exposes a bare SiC surface to the dissociated gas environment that is more catalytically efficient than SiO_2 . Generally active oxidation is favored at higher temperatures and lower oxygen partial pressures than passive oxidation. Both heating and mass loss rates are much higher under active than passive oxidation conditions. Changes in the aerothermal environment can trigger a passive-to-active transition leading to dramatic temperature jumps and material degradation, as have been observed in plasma wind tunnel tests on SiC-based ceramic matrix composites [136–139] and SiC-containing ultra-high temperature composites [140, 141].

So far, only very a limited attempt has been made to formulate a finite-rate model that incorporates both catalytic recombination and active/passive oxidation of SiC [142]. The complexities are substantial, in that many of the elementary processes competing at the SiO_2 and SiC surfaces, as well as at their interfaces with each other, are not well characterized making the selection of a dominated reaction set and a thermodynamically consistent criteria for passive–active transition difficult. There is much room for the computational chemistry analyses of the surface and interface reactions in the oxygen–nitrogen–silicon–carbon system, and the subsequent application of the insights and results provided by these analyses on the formulation of finite-rate models.

D. ENERGY ACCOMMODATION

The finite-rate modeling formulation presented here does not explicitly address energy accommodation. It is assumed that surface reaction products are fully accommodated to the surface temperature, and that the energy transfer to (from) the surface is equivalent to the net exothermicity (endothermicity) of all acting surface chemistry. This is a conservative approach from a design perspective, since the predicted heating rate for a particular finite-rate surface chemistry

model is maximized. However, it has been shown experimentally that the heat deposited during surface recombination implies less-than full energy accommodation [100, 143, 144], and that recombination products can leave a catalytic surface with excess energy stored in translational, vibrational, rotational and electronic modes [145–148]. Computational chemistry calculations have also shown that recombined molecules can leave the surface in vibrationally excited states [149, 150]. Likewise, the MD simulations presented in this chapter could be post-processed to determine the rotational and vibrational energies of recombined product molecules.

During the 1980s, Black and Slanger [147] and Ali et al. [151] reported laboratory experiments, using an NO-titrated nitrogen discharge flow and optical absorption and emission diagnostics, that indicated the formation of electronically excited $O_2(a^1\Delta_g)$ by atom recombination on silica surfaces. Recent measurements in a similar flow configuration, using resonance enhanced multi-photon ionization diagnostics, also confirm $O_2(a^1\Delta_g)$ formation [152]. The lowest vibrational level of the $O_2(a^1\Delta_g)$ state lies approximately 1 eV above the lowest vibrational level in the electronic ground state $O_2(X^3\Sigma_g^-)$ and has a very long radiative lifetime of about 75 minutes [153]. Any chemical energy stored in the long lived $O_2(a^1\Delta_g)$ state may remain “locked-up” long enough to be transported away from the surface. The computational chemistry analysis of $O_2(a^1\Delta_g)$ surface formation and quenching on silica are currently under investigation.

The explicit representation of gas–surface energy transfer through finite-rate surface-chemistry models will require tracking molecules and atoms in specific internal energy states both on the surface and in the gas phase. The vibrational energy distributions of molecules leaving the surface and relaxing in the boundary layer are markedly non-Boltzmann. The gradients of state-specific reactants and products adjacent to the surface will be affected by collisional energy transfer processes that redistribute internal energies between species and modes. Even if internally excited molecules leave the surface and enter the boundary layer, gas-phase collisional-processes may convert excess vibrational and electronic energy into translational and rotational energy modes, heating the boundary layer and increasing the convective heating of the surface. The extent to which partial energy accommodation is counteracted by increased convection will depend on the relative rates of excited-state surface formation and gas-phase collisional transfer.

The inclusion of state-specific finite-rate surface chemistry thus complicates CFD considerably by adding many more species and processes into the computations. It is highly unlikely that all the rate coefficients for the myriad collisional energy transfer processes could be measured; thus computational chemistry may need to play a prominent role in identifying dominant energy-transfer mechanisms, both in the gas phase and on the surface, and in providing physics-based estimates of rate coefficient parameters and temperature dependencies.

Finally, we point out that models for material microstructure (characteristic of real TPS materials) must be considered for energy accommodation, since

recombination products may undergo multiple surface impacts before leaving the TPS surface and re-entering the boundary layer flow. Although an individual surface collision may not result in full energy accommodation, multiple surface impacts could certainly lead to full accommodation. These issues make determination of energy accommodation between a hypersonic boundary layer and real TPS a difficult problem that remains to be fully investigated.

E. CONSISTENCY BETWEEN EXPERIMENTAL ANALYSES AND CFD SIMULATIONS

One of the lingering issues in aerothermal heating simulations is the disconnect between published experimental results for the efficiency of surface reactions and their use in predictive CFD computations. This is particularly true in the area of surface catalysis, where for decades measurements of “recombination coefficients” have been presented for O-atom and N-atom recombination on a variety of surfaces [102, 103, 105, 154, 155].

It is important to remember that such recombination coefficients are not uniquely associated with a single chemical process in the same way that a reaction rate coefficient is associated with a specific gas-phase reaction. Rather, they reflect the total efficiency of all operating surface reaction pathways that remove a species on a particular surface under a particular combination of temperature, pressure, and gas composition. Moreover, recombination coefficients are never measured directly. Experiments probe the effects of surface reactions on the gas-phase concentrations of reactants or products near a surface or the flow of heat into the surface, and numerical values of recombination coefficients are extracted from these measurements in the framework of specific assumptions and models for species chemistry, mass transport, and heat transfer.

These realities make numerical values of experimental recombination coefficients extremely dependent on both the experimental conditions and the data analyses procedures employed, and render their direct application in predictive CFD simulations problematic. One clear avenue for improving this situation is the consistent application of the same CFD code—including all transport models, and finite-rate gas-phase and surface chemistry models—for both the analysis of experiments and for flight simulations.

A barrier to this approach has been the wide range of flow, temperature, and gas conditions spanning experimental and flight regimes. The CFD codes used for hypersonic flight simulation are typically structured to compute solutions efficiently for high-Mach number flows, however much laboratory data originates from setups with relatively low flow speeds (flow tubes) [156] or under stagnant conditions (diffusion tubes) [101]. A great deal experimental data is also generated in subsonic inductively coupled plasma flow facilities [157, 158]. Efficient computation of the subsonic flows encountered in the above facilities requires some coding modifications and re-optimization of the solution procedures currently used for supersonic and hypersonic flows. A second issue, already mentioned above, is the need incorporate more accurate and complete gas-phase chemistry

models for low temperature environments. Once these tasks are accomplished, it will be possible to simulate experiments in these subsonic facilities directly, with the same transport property approximations, thermodynamic data, and finite-rate gas and surface chemistry models that will be used to compute arc-jet and shock tunnel test environments, and to predict in-flight aerothermal environments. Such a capability eliminates the need for empirical representations of surface reactions in terms of “recombination coefficients” or “reaction probabilities”, replacing it with a full finite-rate chemistry model tuned to reproduce a collection of experiments within a consistent computational framework.

F. ADVANCED DIAGNOSTICS FOR PLASMA FACILITIES

Carefully designed experiments for the calibration and validation of surface reaction models are essential. The performance of most TPS materials is ultimately evaluated in high-speed plasma tunnels—typically arcjets or ICP facilities—which provide the best long-duration (~minutes) representation of the aeroconvective heating environment expected in flight. The data generated in these facilities is generally of a global or macroscopic nature: stagnation point pressure and heat flux measurements conducted with water cooled probes; surface and internal specimen temperature histories; test documentation in the form of videos or photography; and post-test specimen analysis. Although reproduction of observed heating rates (and in some cases mass loss rates) is a requirement for a valid surface reaction model, this requirement does not tightly constrain the chemical mechanisms in operation, nor any of the rate parameters in the model.

In recent years a variety of optical diagnostics, based on emission and absorption spectroscopy and laser-induced fluorescence, have been applied in these facilities to better document the freestream test conditions, to establish the composition of the gas-phase near test surfaces, and to capture transient volatilizations from test specimen surfaces.

The importance and future promise of these optical diagnostics lies in their species-specificity, which in combination with well-defined spatial and temporal resolution, can impose much stricter criteria on surface reaction models, and their coupling to gas-phase chemistry and transport in the boundary layer. As one example, we highlight recent laser-induced fluorescence measurements detecting O atoms, N atoms and NO molecules in the boundary layer over copper, quartz, and SiC specimens in a laboratory-scale ICP facility [8, 159]. These measurements are the first that attempt to measure the concentration profiles of the reactant O and N atoms, as well as the surface-reaction product NO, through the boundary layer to the specimen surface. The measurements also provide the temperature profile through the boundary layer. Measurements of this type appear more feasible in subsonic ICP facilities than in supersonic arc-jet facilities because the subsonic boundary layers are thicker allowing for more spatial resolution of concentrations and temperatures between the surface

and the boundary layer edge. While still in the preliminary stages, such measurements provide a wealth of information to which surface reaction models can be anchored.

VII. SUMMARY/CONCLUSION

In this chapter we have presented a general framework in which finite-rate surface chemistry models can be constructed for specific gas–surface systems of interest. This framework incorporates the concept that surface reactions proceed at finite rates at a finite number of active sites on the surface. Each process has forward and backward reaction rates linked by temperature-dependent equilibrium constants, ensuring consistency with all available thermodynamic data. Global mass and element conservation at the gas-solid interface are automatically enforced.

This surface chemistry framework has been incorporated in the NASA DPLR CFD code, as an implicit species boundary condition, making it possible to implement finite-rate chemistry models using user inputs, without the necessity of “hardwiring” a specific model into the code as has been done in the past. Although demonstrated here for DPLR, this general formulation (or adaptations of it) should be equally applicable to other reacting flow CFD solvers.

The finite-rate surface chemistry modeling approach is based on the selection of a set of elementary reactions and a variety of numerical parameters as inputs. Often both the identity of the dominate processes and the numerical values of the associated input parameters are uncertain. Here, we have described a methodology by which a finite-rate gas–surface reaction model can be formulated using Molecular Dynamics simulation and single-point energy calculations obtained using DFT. This computational chemistry approach has been detailed for the oxygen-silica system, but analogous procedures should be applicable to other systems of interest.

Specifically, an interatomic potential for silica (ReaxFF_{SiO}) was used to construct a finite-rate model for oxygen interactions with realistic quartz and amorphous SiO₂ surfaces at high temperatures, characteristic of real TPS materials. The first crucial aspect of the methodology involved determining the chemical defect structures present on real silica surfaces exposed to atomic oxygen at high temperatures that participate in recombination reactions. For example, nondefective surface reconstructions were found to be highly stable and noncatalytic and recombination was energetically favorable only on surface defects (also called active sites). The defect structures predicted by MD simulations with the ReaxFF_{SiO} potential were shown to be in excellent agreement with experimentally observed defects.

The second crucial aspect of the methodology involved trajectory calculations of gas-phase oxygen interacting with these defect structures in order to determine specific reaction pathways with associated pre-exponential factors and activation energies. It was noted that ultimately, further DFT calculations should be

performed in order to obtain activation energies for dominant reactions with much higher precision than is possible using MD with a PES. It was also demonstrated that the inclusion of off-normal impact trajectories was important to determine the correct activation energy to be included in the finite-rate model. Finally, the third crucial aspect of the methodology involved combining the reaction pathways and associated reaction parameters into a consistent finite-rate model that satisfies detailed balance and is suitable for implementation as a boundary condition for CFD.

When the finite-rate model constructed by MD simulation was implemented as a boundary condition in CFD, the overall behavior of the model was qualitatively similar to an existing empirical model. However, in contrast to the empirical model, the model constructed by MD simulation contained reaction pathways specific to real surface defect structures, which differed substantially from the generic ER and LH reactions contained in the empirical model. For example, although the MD simulations did predict a direct ER mechanism for recombination, the dominant reaction pathway was through the formation of molecular oxygen on the surface followed by its release into the gas phase owing to subsequent collisions.

The final parameterization presented for the oxygen-silica finite-rate model is qualitative and has not been validated by accurate computational chemistry data specific to the interactions studied and has not been validated by experimental data. However, the methodology for constructing a finite-rate surface reaction model through MD simulation and DFT calculation is general, and could be repeated using increasingly accurate PESs (based on new DFT data) as data becomes available for materials of interest.

The combination of the finite-rate surface chemistry approach in CFD, supported by computational chemistry analyses for mechanism understanding and parameter evaluation, is a powerful combination. As discussed above, there are many promising directions for future work that further develop this approach and support it with the high-fidelity experimental data that are currently lacking.

ACKNOWLEDGMENTS

This paper draws heavily on the authors' own research, conducted over the last decade and supported primarily by funding from the National Aeronautics and Space Administration (NASA) and the Air Force Office of Scientific Research (AFOSR). The views and conclusions contained herein are those of the authors and should not be interpreted as necessarily representing the official policies or endorsements, either expressed or implied, of the AFOSR or the U.S. Government.

Dr. Marschall acknowledges that the development of the finite-rate model described in Section II was supported by NASA Ames Research Center through grant NNX08AR52G and by NASA's Fundamental Aeronautics Hypersonics Project through grant NNX09AK38A. He acknowledges funding from the

AFOSR Hypersonics and Ceramics programs through contract FA9550-05-1-0490, the AFOSR Aerospace Materials for Extreme Environments Program through contracts FA9550-08-C-0049 and FA9550-11-1-0201, and the AFOSR Basic Research Initiatives program through FA9550-12-1-0486.

Dr. MacLean acknowledges support for this activity from NASA's Fundamental Aeronautics Hypersonics Project, Prime Award NNX09AK38A, and from AFOSR under the Multidisciplinary University Research Initiative entitled Fundamental Processes in High-Temperature Hypersonic Flows, Prime Award FA9550-10-1-0563.

Drs. Norman and Schwartzentruber acknowledge support for this activity from AFOSR under Grant FA9550-12-1-0202 and Grant FA9550-12-1-0486.

REFERENCES

- [1] Marschall, J., and MacLean, M., "Finite-Rate Surface Chemistry Model, I: Formulation and Reaction System Examples," AIAA Paper 2011-3783, June 2011.
- [2] MacLean, M., Marschall, J., and Driver, D. M., "Finite-Rate Surface Chemistry Model, II: Coupling to Viscous Navier-Stokes Code," AIAA Paper 2011-3784, June 2011.
- [3] Anon., *User's Manual: Aerotherm Chemical Equilibrium Computer Program*, Aerotherm Division, Acurex Corporation, Mountain View, California, 1981.
- [4] Milos, F. S., and Chen, Y.-K., "Comprehensive Model for Multicomponent Ablation Thermochemistry," AIAA Paper 97-0141, January, 1997.
- [5] Milos, F. S., and Marschall, J., "Thermochemical Ablation Model for TPS Materials with Multiple Surface Constituents," AIAA Paper 94-2042, June, 1994.
- [6] McBride, B. J., and Gordon, S., "Computer Program for Calculation of Complex Chemical Equilibrium Compositions and Applications II. Users Manual and Program Description," NASA RP-1311-P2, June 1996.
- [7] Laux, T., Feigl, M., Stöckle, T., and Auweter-Kurtz, M., "Estimation of the Surface Catalytic Properties of PVD-Coatings by Simultaneous Heat Flux and LIF Measurements in High Enthalpy Air Flows," AIAA Paper 2000-2364, June 2000.
- [8] Meyers, J. M., Owens, W. P., and Fletcher, D. G., "Surface Catalyzed Reaction Efficiencies in Air Plasmas Using Laser Induced Fluorescence Measurements," AIAA Paper 2013-3140, June 2013.
- [9] Kurotaki, T., "Catalytic Model on SiO₂-Based Surface and Application to Real Trajectory," *Journal of Spacecraft and Rockets*, Vol. 38, No. 5, 2001, pp. 798–800.
- [10] Copeland, R. A., Pallix, J. B., and Stewart, D. A., "Surface-Catalyzed Production of NO from Recombination of N and O Atoms," *Journal of Thermophysics and Heat Transfer*, Vol. 12, No. 4, 1998, pp. 496–499.
- [11] Pejaković, D., Marschall, J., Duan, L., and Martin, M. P., "Nitric Oxide Production from Surface Recombination of Oxygen and Nitrogen Atoms," *Journal of Thermophysics and Heat Transfer*, Vol. 22, No. 2, 2008, pp. 178–186.

- [12] Pejaković, D., Marschall, J., Duan, L., and Martin, M. P., "Direct Detection of NO Produced by High-Temperature Surface-Catalyzed Atom Recombination," *Journal of Thermophysics and Heat Transfer*, Vol. 24, No. 3, 2010, pp. 603–611.
- [13] Bose, D., Wright, M. J., and Palmer, G. E., "Uncertainty Analysis of Laminar Aeroheating Predictions for Mars Entries," *Journal of Thermophysics and Heat Transfer*, Vol. 20, No. 4, 2006, pp. 652–662.
- [14] Sepka, S., Chen, Y.-K., Marschall, J., and Copeland, R. A., "Experimental Investigation of Surface Reactions in Carbon Monoxide and Oxygen Mixtures," *Journal of Thermophysics and Heat Transfer*, Vol. 14, No. 1, 2000, pp. 45–52.
- [15] Marschall, J., Copeland, R. A., Hwang, H. H., and Wright, M. J., "Surface Catalysis Experiments on Metal Surfaces in Oxygen and Carbon Monoxide Mixtures," AIAA Paper 2006-181, January 2006.
- [16] Nasuti, F., Barbato, M., and Bruno, C., "Material-Dependent Catalytic Recombination Modeling for Hypersonic Flows," *Journal of Thermophysics and Heat Transfer*, Vol. 10, No. 1, 1996, pp. 131–136.
- [17] Deutschmann, O., Riedel, U., and Warnatz, J., "Modeling of Nitrogen and Oxygen Recombination on Partial Catalytic Surfaces," *Journal of Heat Transfer*, Vol. 117, No. 2, 1995, pp. 495–501.
- [18] Lefèvre, L., Belmonte, T., and Michel, H., "Modeling of Nitrogen Atom Recombination on Pyrex: Influence of the vibrationally excited N₂ Molecules on the Loss Propability of N," *Journal of Applied Physics*, Vol. 87, No. 10, 2000, pp. 7497–7507.
- [19] Guerra, V., "Analytical Model of Heterogeneous Atomic Recombination on Silicalike Surface," *IEEE Transactions On Plasma Science*, Vol. 35, No. 5, 2007, pp. 1397–1412.
- [20] Thömel, J., Lukkien, J. J., and Chazot, O., "A Multiscale Approach for Building a Mechanism Based Catalysis Model for High Enthalpy CO₂ Flow," AIAA Paper 2007-4399, June 2007.
- [21] Nompelis, I., Drayna, T., and Candler, G., "A Parallel Unstructured Implicit Solver for Hypersonic Reacting Flow Simulation," AIAA Paper 2005-4867, June 2005.
- [22] Scalabrin, L. C., and Boyd, I. D., "Numerical Simulation of Weakly Ionized Hypersonic Flow for Reentry Configurations," AIAA Paper 2006-3773, June 2006.
- [23] Martin, A., Scalabrin, L. C., and Boyd, I. D., "High Performance Modeling of Atmospheric Re-Entry Vehicles," *Journal of Physics: Conference Series*, Vol. 341, 2012, pp. 012002.
- [24] Sorenson, C., Valentini, P., and Schwartzentruber, T. E., "Uncertainty Analysis of Reaction Rates in a Finite-Rate Surface-Catalysis Model," *Journal of Thermophysics and Heat Transfer*, Vol. 26, No. 3, 2012, pp. 407–416.
- [25] Alkandry, H., Farbar, E. D., and Boyd, I. D., "Evaluation of Finite-Rate Surface Chemistry Models for Simulation of the Stardust Reentry Capsule," AIAA Paper 2012-2874, June 2012.
- [26] Wright, M. J., Candler, G. V., and Bose, D., "Data-Parallel Line Relaxation Method for the Navier–Stokes Equations," *AIAA Journal*, Vol. 36, No. 9, 1998, pp. 1603–1609.
- [27] MacCormack, R. W., and Candler, G. V., "The Solution of the Navier–Stokes Equations Using Gauss–Seidel Line Relaxation," *Computers and Fluids*, Vol. 17, No. 1, 1989, pp. 135–150.

- [28] Candler, G. V., "Chemistry of External Flows," *Von Karman Institute for Fluid Dynamics Lecture Series, VKI LS 1995-04*, 1995.
- [29] Landau, L., and Teller, E., "Theory of Sound Dispersion," *Physikalische Zeitschrift der Sowjetunion*, Vol. 10, No. 34, 1936, pp.
- [30] Millikan, R. C., and White, D. R., "Systematics of Vibrational Relaxation," *Journal of Chemical Physics*, Vol. 39, No. 12, 1963, pp. 3209–3213.
- [31] Camac, M., "CO₂ Relaxation Processes in Shock Waves," in *Fundamental Phenomena in Hypersonic Flow*, edited by J. G. Hall, Cornell University Press, Buffalo, NY, 1964, pp. 195–215.
- [32] Park, C., Howe, J. T., Jaffe, R. J., and Candler, G. V., "Review of Chemical-Kinetic Problems of Future NASA Missions II: Mars Entries," *Journal of Thermophysics and Heat Transfer*, Vol. 8, No. 1, 1994, pp. 9–23.
- [33] Park, C., "Assessment of Two-temperature Kinetic Model for Ionizing Air," AIAA Paper 87-1574, June 1987.
- [34] Marrone, P. V., and Treanor, C. E., "Chemical Relaxation with Preferential Dissociation from Excited Vibrational Levels," *Physics of Fluids*, Vol. 6, No. 9, 1963, pp. 1215–1221.
- [35] Palmer, G. E., and Wright, M. J., "A Comparison of Methods to Compute High Temperature Gas Viscosity," *Journal of Thermophysics and Heat Transfer*, Vol. 17, No. 2, 2003, pp. 232–239.
- [36] Palmer, G. E., and Wright, M. J., "A Comparison of Methods to Compute High Temperature Gas Thermal Conductivity," AIAA Paper 2003-3913, June 2003.
- [37] Gupta, R., Yos, J., Thompson, R., and Lee, K., "A Review of Reaction Rates and Thermodynamic and Transport Properties for an 11-Species Air Model for Chemical and Thermal Nonequilibrium Calculations to 30000 K," NASA RP-1232, NASA, August 1990.
- [38] Wright, M. J., Bose, D., Palmer, G. E., and Levine, E., "Recommended Collision Integrals for Transport Property Computations, Part 1: Air Species," *AIAA Journal*, Vol. 43, No. 12, 2005, pp. 2558–2564.
- [39] Wright, M. J., Hwang, H. H., and Schwenke, D. W., "Recommended Collision Integrals for Transport Property Computations Part 2: Mars and Venus Entries," *AIAA Journal*, Vol. 45, No. 1, 2007, pp. 281–288.
- [40] Ramshaw, J. D., "Self-Consistent Effective Binary Diffusion in Multicomponent Gas Mixtures," *Journal of Non-Equilibrium Thermodynamics*, Vol. 15, No. 3, 1990, pp. 295–300.
- [41] Rindal, R. A., Flood, D. T., and Kendall, R. M., "Analytical and Experimental Study of Ablation Materials for Rocket-Engine Application," NASA CR-54757, ITEK Corporation, Palo Alto, May 1966.
- [42] Quan, V., "Quasi-Steady Solutions for the Ablation-Erosion Heat Transfer," *Journal of Spacecraft and Rockets*, Vol. 7, No. 3, 1970, pp. 355–357.
- [43] Lin, W.-S., "Quasi-Steady Solutions for the Ablation of Charring Materials," *International Journal of Heat and Mass Transfer*, Vol. 50, No. 5–6, 2007, pp. 1196–1201.
- [44] Sutton, K., and Gnoffo, P.A., "Multi-Component Diffusion with Application to Computational Aerothermodynamics," AIAA Paper 98-2575, June 1998.
- [45] Gosse, R., and Candler, G., "Diffusion Flux Modeling: Application to Direct Entry Problems," AIAA Paper 2005-389, January 2005.

- [46] Sanders, M. J., Leslie, M., and Catlow, C. R. A., "Interatomic Potentials for SiO₂," *Journal of the Chemical Society, Chemical Communications*, Vol. 19, 1984, pp. 1271–1273.
- [47] Tsuneyuki, S., Tsukada, M., Aoki, H., and Matsui, Y., "First-Principles Interatomic Potential of Silica Applied to Molecular Dynamics," *Physical Review Letters*, Vol. 61, No. 7, 1988, pp. 869–872.
- [48] van Beest, B. W., Kramer, G. J., and van Santen, R. A., "Force Fields for Silicas and Aluminophosphates Based on Ab Initio Calculations," *Physical Review Letters*, Vol. 64, No. 16, 1990, pp. 1955–1958.
- [49] de Vos Burchart, E., Verheij, V. A., van Bekkum, H., and van de Graaf, B., "A Consistent Molecular Mechanics Force Field for All-Silica Zeolites," *Zeolites*, Vol. 12, No. 2, 1992, pp. 183–189.
- [50] Belonoshko, A. B., and Dubrovinsky, L. S., "Molecular Dynamics of Stishovite Melting," *Geochimica et Cosmochimica Acta*, Vol. 59, No. 9, 1995, pp. 1883–1889.
- [51] Ermoshin, V. A., Smirnov, K. S., and Bougeard, D., "Ab initio Generalized Valence Force Field for Zeolite Modelling 2. Aluminosilicates," *Chemical Physics*, Vol. 209, No. 1, 1996, pp. 41–51.
- [52] Roder, A., Kob, W., and Binder, K., "Structure and Dynamics of Amorphous Silica Surfaces," *Journal of Chemical Physics*, Vol. 114, No. 17, 2001, pp. 7602–7614.
- [53] Arasa, C., Gamallo, P., and Sayós, R., "Adsorption of Atomic Oxygen and Nitrogen at β -Cristobalite (100): A Density Functional Theory Study," *Journal of Physical Chemistry B*, Vol. 109, No. 31, 2005, pp. 14954–14964.
- [54] Arasa, C., Busnengo, H. F., Salin, A., and Sayos, R., "Classical Dynamics Study of Atomic Oxygen Sticking on the β -Cristobalite (100) Surface," *Surface Science*, Vol. 602, No. 4, 2008, pp. 975–985.
- [55] Arasa, C., Moron, V., Busnengo, H. F., and Sayos, R., "Eley-Rideal Reaction Dynamics between O-atoms on β -Cristobalite(100) Surface: A New Interpolated Potential Energy Surface and Classical Trajectory Study," *Surface Science*, Vol. 603, No. 17, 2009, pp. 2742–2751.
- [56] Moron, V., Gamallo, P., Martin-Gondre, L., Crespos, C., Larregaray, P., and Sayos, R., "Recombination and Chemical Energy Accommodation Coefficients from Chemical Dynamics Simulations: O/O₂ Mixtures Reacting over a β -Cristobalite (001) Surface," *Physical Chemistry Chemical Physics*, Vol. 13, No. 39, 2011, pp. 17494–17504.
- [57] Caciato, M., Rutigliano, M., and Billing, G. D., "Eley-Rideal and Langmuir-Hinshelwood Recombination Coefficients for Oxygen on Silica Surfaces," *Journal of Thermophysics and Heat Transfer*, Vol. 13, No. 2, 1999, pp. 195–203.
- [58] Bedra, L., Rutigliano, M., Balat-Pichelin, M., and Caciato, M., "Atomic Oxygen Recombination on Quartz at High Temperature: Experiments and Molecular Dynamics Simulation," *Langmuir*, Vol. 22, No. 17, 2006, pp. 7208–7216.
- [59] Zazza, C., Rutigliano, M., Sanna, N., Barone, V., and Caciato, M., "Oxygen Adsorption on beta-Quartz Model Surfaces: Some Insights from Density Functional Theory Calculations and Semiclassical Time-Dependent Dynamics," *Journal of Physical Chemistry A*, Vol. 116, No. 9, 2012, pp. 1975–1985.
- [60] Rutigliano, M., Zazza, C., Sanna, N., Pieretti, A., Mancini, G., Barone, V., and Caciato, M., "Oxygen Adsorption on β -Cristobalite Polymorph: Ab Initio Modeling and Semiclassical Time-Dependent Dynamics," *Journal of Physical Chemistry A*, Vol. 113, No. 52, 2009, pp. 15366–15375.

- [61] van Duin, A. C. T., Dasgupta, S., Lorant, F., and Goddard, W. A., "ReaxFF: A Reactive Force Field for Hydrocarbons," *Journal of Physical Chemistry A*, Vol. 105, No. 41, 2001, pp. 9396–9409.
- [62] van Duin, A. C. T., Strachan, A., Stewman, S., Zhang, Q. S., Xu, X., and Goddard, W. A., "ReaxFF(SiO) Reactive Force Field for Silicon and Silicon Oxide Systems," *Journal of Physical Chemistry A*, Vol. 107, No. 19, 2003, pp. 3803–3811.
- [63] Valentini, P., Schwartzenruber, T. E., and Cozmuta, I., "Molecular Dynamics Simulation of O₂ Sticking on Pt(111) Using the ab initio Based ReaxFF Reactive Force Field," *Journal of Chemical Physics*, Vol. 133, No. 8, 2010, pp. 084703.
- [64] Valentini, P., Schwartzenruber, T. E., and Cozmuta, I., "ReaxFF Grand Canonical Monte Carlo Simulation of Adsorption and Dissociation of Oxygen on Platinum (111)," *Applied Surface Science*, Vol. 605, No. 23–24, 2011, pp. 1941–1950.
- [65] Khalilov, U., Neyts, E. C., Portois, G., and van Duin, A. C. T., "Hyperthermal Oxidation of Si(100)2x1 Surfaces: Effect of Growth Temperature," *Journal of Physical Chemistry*, Vol. 116, No. 15, 2012, pp. 8649–8656.
- [66] Khalilov, U., Neyts, E. C., Portois, G., and van Duin, A. C. T., "Can We Control the Thickness of Ultrathin Silica Layers by Hyperthermal Silicon Oxidation at Room Temperature?", *Journal of Physical Chemistry C*, Vol. 115, No. 50, 2011, pp. 24839–24848.
- [67] Khalilov, U., Pourtois, G., van Duin, A. C. T., and Neyts, E. C., "Self-limiting Oxidation in Small Diameter Si Nanowires," *Chemistry of Materials*, Vol. 24, No. 11, 2012, pp. 2141–2147.
- [68] Neyts, E. C., Khalilov, U., Portois, G., and van Duin, A. C. T., "Hyperthermal Oxygen Interacting with Silicon Surfaces: Adsorption, Implantation and Damage Creation," *Journal of Physical Chemistry C*, Vol. 115, No. 11, 2011, pp. 4818–4823.
- [69] Plimpton, S., "Fast Parallel Algorithms for Short-Range Molecular Dynamics," *Journal of Computational Physics*, Vol. 117, No. 1, 1995, pp. 1–19.
- [70] Kulkarni, A., Truhlar, D. G., Srinivasan, S. G., van Duin, A. C. T., Norman, P., and Schwartzenruber, T. E., "Oxygen Interactions with Silica Surfaces: Coupled Cluster and Density Functional Investigation and the Development of a New ReaxFF Potential," *Journal of Physical Chemistry C*, Vol. 117, No. 1, 2013, pp. 258–269.
- [71] Norman, P., Schwartzenruber, T. E., Leverentz, H., Luo, S., Meana-Pañeda, R., Paukku, Y., and Truhlar, D. G., "The Structure of Silica Surfaces Exposed to Atomic Oxygen," *Journal of Physical Chemistry C*, Vol. 117, No. 18, 2013, pp. 9311–9321.
- [72] Norman, P., Schwartzenruber, T. E., and Cozmuta, I., "Modeling Air-SiO₂ Surface Catalysis under Hypersonic Conditions with ReaxFF Molecular Dynamics," AIAA Paper 2010-4320, June 2010.
- [73] Chen, Y.-W., Cao, C., and Cheng, H.-P., "Finding Stable α -quartz (0001) Surface Structures via Simulations" *Applied Physics Letters*, Vol. 93, No. 18, 2008, pp. 181911.
- [74] Rignanese, G. M., De Vita, A., Charlier, J. C., Gonze, X., and Car, R., "First-Principles Molecular-Dynamics Study of the (0001) Alpha-Quartz Surface," *Physical Review B*, Vol. 61, No. 19, 2000, pp. 13250–13255.

- [75] Bart, F., Gautier, M., Jollet, F., and Duraud, J. P., "Electronic Structure of the (0001) and (1010) Quartz Surfaces and of Their Defects as Observed by Reflection Electron Energy Loss Spectroscopy (REELS)," *Surface Science*, Vol. 306, No. 3, 1994, pp. 342–358.
- [76] Steurer, W., Apfolter, A., Koch, M., Sarlat, T., Søndergård, E., Ernst, W. E., and Holst, B., "The Structure of the α -quartz (0001) Surface Investigated Using Helium Atom Scattering and Atomic Force Microscopy," *Surface Science*, Vol. 601, No. 18, 2007, pp. 4407–4411.
- [77] Lopes, P. E. M., Demchuk, E., and Mackerell, A. D., Jr., "Reconstruction of the (011) Surface on α -Quartz: A Semiclassical Ab Initio Molecular Dynamics Study," *International Journal of Quantum Chemistry*, Vol. 109, No. 1, 2009, pp. 50–64.
- [78] Huff, N. T., Demiralp, E., Çagin, T., and Goddard, W. A., III, "Factors Affecting Molecular Dynamics Simulated Vitreous Silica Structures," *Journal of Non-Crystalline Solids*, Vol. 253, No. 1–3, 1999, pp. 133–142.
- [79] Jee, S. E., McGaughey, A. J. H., and Sholl, D. S., "Molecular Simulations of Hydrogen and Methane Permeation through Pore Mouth Modified Zeolite Membranes," *Molecular Simulation*, Vol. 35, No. 1–2, 2009, pp. 70–78.
- [80] Vink, R., and Barkema, G., "Large Well-Relaxed Models of Vitreous Silica, Coordination Numbers, and Entropy," *Physical Review B*, Vol. 67, No. 24, 2003, pp. 245201.
- [81] Nakano, A., Kalia, R. K., and Vashishta, P., "First Sharp Diffraction Peak and Intermediate-Range Order in Amorphous Silica: Finite-Size Effects in Molecular Dynamics Simulations," *Journal of Non-Crystalline Solids*, Vol. 171, No. 2, 1994, pp. 157–163.
- [82] Mozzi, R. L., and Warren, B. E., "The Structure of Vitreous Silica," *Journal of Applied Crystallography*, Vol. 2, No. 4, 1969, pp. 164–172.
- [83] Coombs, P. G., Natale, J. F. D., Hood, P. J., McElfresh, D. K., Wortman, R. S., and Shackelford, J. F., "The Nature of the Si-O-Si Bond Angle Distribution in Vitreous Silica," *Philosophical Magazine B*, Vol. 51, No. 4, 1985, pp. L39–L42.
- [84] Neufeind, J., and Liss, K.-D., "Bond Angle Distribution in Amorphous Germania and Silica," *Berichte der Bunsengesellschaft für Physikalische Chemie*, Vol. 100, No. 8, 1996, pp. 1341–1349.
- [85] Grimley, D. I., and Wright, A. C., "Neutron Scattering from Vitreous Silica IV. Time-of-Flight Diffraction," *Journal of Non-Crystalline Solids*, Vol. 119, No. 1, 1990, pp. 49–64.
- [86] Susman, S., Volin, K. J., Montague, D. G., and Price, D. L., "Temperature Dependence of the First Sharp Diffraction Peak in Vitreous Silica," *Physical Review B*, Vol. 43, No. 13, 1991, pp. 11076–11081.
- [87] Fogarty, J. C., Aktulga, H. M., Grama, A. Y., van Duin, A. C. T., and Pandit, S. A., "A Reactive Molecular Dynamics Simulation of the Silica Water Interface," *Journal of Chemical Physics*, Vol. 132, No. 17, 2010, pp. 174704.
- [88] Warren, W. L., PoINDEXER, E. H., Offenberg, M., and Müller-Warmuth, W., "Paramagnetic Point Defects in Amorphous Silicon Dioxide and Amorphous Silicon Nitride Thin Films I. $a\text{-SiO}_2$," *Journal of the Electrochemical Society*, Vol. 139, No. 3, 1992, pp. 872–880.

- [89] Costa, D., Fubini, B., Giamello, E., and Volante, M., "A Novel Type of Active Site at the Surface of Crystalline SiO₂ (*a*-Quartz) and Its Possible Impact on Pathogenicity," *Canadian Journal of Chemistry*, Vol. 69, No. 9, 1991, pp. 1427–1434.
- [90] Griscom, D. L., and Friebele, E. J., "Fundamental Defect Centers in Glass: 29Si Hyperfine Structure of the Nonbridging Oxygen Hole Center and the Peroxy Radical in *a*-SiO₂," *Physical Review B*, Vol. 24, No. 8, 1981, pp. 4896–4898.
- [91] Legrand, A. P., *The Surface Properties of Silicas*, John Wiley & Sons, New York, 1999.
- [92] Levine, S. M., and Garofalini, S. H., "A Structural Analysis of the Vitreous Silica Surface via a Molecular Dynamics Computer Simulation" *Journal of Chemical Physics*, Vol. 86, No. 5, 1987, pp. 2997–3002.
- [93] Wilson, M., and Walsh, T. R., "Hydrolysis of the Amorphous Silica Surface. I. Structure and Dynamics of the Dry Surface," *Journal of Chemical Physics*, Vol. 113, No. 20, 2000, pp. 9180–9190.
- [94] Vincenti, W. G., and Kruger, C. H., Jr., *Introduction to Physical Gas Dynamics*, Krieger Publishing Company, Malabar, 1967.
- [95] Garcia, A. L., and Wagner, W., "Generation of the Maxwellian Inflow Distribution," *Journal of Computational Physics*, Vol. 217, No. 2, 2006, pp. 693–708.
- [96] Lieberman, M., and Lichtenberg, A. J., *Principals of Plasma Discharges and Materials Processing*, John Wiley and Sons, Inc., New York, NY, 1994.
- [97] Alfano, D., Scatteia, L., Monteverde, F., Beche, E., and Balat-Pichelin, M., "Microstructural Characterization of ZrB₂-SiC Based UHTC Tested in the MESOX Plasma Facility," *Journal of the European Ceramic Society*, Vol. 30, No. 11, 2010, pp. 2345–2355.
- [98] Kim, Y. C., and Boudart, M., "Recombination of O, N, and H Atoms on Silica: Kinetics and Mechanism," *Langmuir*, Vol. 7, No. 12, 1991, pp. 2999–3005.
- [99] Balat-Pichelin, M., Badie, J. M., Berjoan, R., and Boubert, P., "Recombination Coefficient of Atomic Oxygen on Ceramic Materials Under Earth Re-Entry Conditions by Optical Emission Spectroscopy," *Chemical Physics*, Vol. 291, 2003, pp. 181–194.
- [100] Carleton, K. L., and Marinelli, W. J., "Spacecraft Thermal Energy Accommodation from Atomic Recombination" *Journal of Thermophysics and Heat Transfer*, Vol. 6, No. 4, 1992, pp. 650–655.
- [101] Marschall, J., in *Experiment, Modelling, and Simulation of Gas-surface Interactions for Reactive Flows in Hypersonic Flights*, Educational Notes RTO-EN-AVT-142, Paper 11. (RTO, Neuilly-sur-Seine, France, 2006), pp. 11-11–11-32.
- [102] Bedra, L., and Balat-Pichelin, M., "Comparative Modeling Study and Experimental Results of Atomic Oxygen Recombination on Silica-Based Surfaces at High-Temperature," *Aerospace Science and Technology*, Vol. 9, No. 4, 2005, pp. 318–328.
- [103] Stewart, D. A., "Surface Catalysis and Characterization of Proposed Candidate TPS for Access-to-Space Vehicles," NASA TM-112206, July 1997.
- [104] Gordon, S., and McBride, B. J., "Computer Program for Calculation of Complex Chemical Equilibrium Compositions and Applications I. Analysis," NASA RP-1311, NASA Lewis Research Center, Cleveland, Ohio, October 1994.

- [105] Stewart, D. A., "Surface Catalytic Efficiency of Advanced Carbon Carbon Candidate Thermal Protection Materials for SSTO Vehicles," NASA TM-110383, February 1996.
- [106] Chen, Y.-K., Henline, W. D., Stewart, D. A., and Candler, G. V., "Navier-Stokes Solutions with Surface Catalysis for Martian Atmospheric Entry," *Journal of Spacecraft and Rockets*, Vol. 30, No. 1, 1993, pp. 32–42.
- [107] Mitcheltree, R. A., and Gnoffo, P. A., "Wake Flow about the Mars Pathfinder Entry Vehicle," *Journal of Spacecraft and Rockets*, Vol. 32, No. 5, 1995, pp. 771–776.
- [108] Gupta, R. N., Lee, K. P., and Scott, C. D., "Aerothermal Study of Mars Pathfinder Aeroshell," *Journal of Spacecraft and Rockets*, Vol. 33, No. 1, 1996, pp. 61–69.
- [109] Bose, D., Wright, M. J., and Palmer, G. E., "Uncertainty Analysis of Laminar Aeroheating Predictions for Mars Entries," *Journal of Thermophysics and Heat Transfer*, Vol. 20, No. 4, 1996, pp. 652–662.
- [110] Kolesnikov, A. F., Pershin, I. S., Vasil'evskii, S. A., and Yakushin, M. I., "Study of Quartz Surface Catalycity in Dissociated Carbon Dioxide Subsonic Flows," *Journal of Spacecraft and Rockets*, Vol. 37, No. 5, 2000, pp. 573–579.
- [111] Rini, P., Garcia, A., Magin, T., and Degrez, G., "Numerical Simulation of Nonequilibrium Stagnation-Line CO₂ Flows with Catalyzed Surface Reactions," *Journal of Thermophysics and Heat Transfer*, Vol. 18, No. 1, 2004, pp. 114–121.
- [112] Valentini, P., Schwartzenruber, T. E., and Cozmuta, I., "A Mechanism-Based Finite-Rate Surface Catalysis Model for Simulating Reacting Flows," AIAA Paper 2009-3935, June 2009.
- [113] Afonina, N. E., Gromov, V. G., and Kovalev, V. L., "Catalysis Modeling for Thermal Protection Systems of Vehicles Entering into Martian Atmosphere," AIAA Paper 2001-2832, June 2001.
- [114] Driver, D., Olsen, M., Barnhardt, M., and MacLean, M., "Understanding High Recession Rates of Carbon Ablators Seen in Shear Tests in an Arc Jet," AIAA Paper 2010-1177, January 2010.
- [115] MacLean, M., Barnhardt, M., and Wright, M., "Implicit Surface Boundary Conditions for Blowing, Equilibrium Composition, and Diffusion-Limited Oxidation," AIAA Paper 2010-1179, January 2010.
- [116] Zhluktov, S. V., and Abe, T., "Viscous Shock-Layer Simulation of Airflow Past Ablating Blunt Body with Carbon Surface," *Journal of Thermophysics and Heat Transfer*, Vol. 13, No. 1, 1999, pp. 50–59.
- [117] Beerman, A. F., Lewis, M. J., Starkey, R. P., and Cybyk, B. Z., "Nonequilibrium Surface Interactions Ablation Modeling with the Fully Implicit Ablation and Thermal Response Program," AIAA Paper 2008-1224, January 2008.
- [118] Candler, G. V., "Nonequilibrium Processes in Hypervelocity Flows: An Analysis of Carbon Ablation Models," AIAA Paper 2012-0724, January 2012.
- [119] Chen, Y.-K., and Milos, F. S., "Finite-Rate Ablation Boundary Conditions for a Carbon-Phenolic Heat-Shield," AIAA Paper 2004-2270, June 2004.
- [120] Park, C., "Stagnation-Point Ablation of Carbonaceous Flat Disks—Part I: Theory," *AIAA Journal*, Vol. 21, No. 11, 1983, pp. 1588–1594.
- [121] Park, C., "Effects of Atomic Oxygen on Graphite Ablation," *AIAA Journal*, Vol. 14, No. 11, 1976, pp. 1640–1642.
- [122] Driver, D., and MacLean, M., "Improved Predictions of PICA Recession in Arc Jet Shear Tests," AIAA Paper 2011-0141, January 2011.

- [123] Martin, A., and Boyd, I., "Strongly Coupled Computation of Material Response and Nonequilibrium Flow for Hypersonic Ablation," AIAA Paper 2009-3597, June 2009.
- [124] Olynick, D., Chen, Y.-K., and Tauber, M., "Aerothermodynamics of the Stardust Sample Return Capsule," *Journal of Spacecraft and Rockets*, Vol. 36, No. 3, 1999, pp. 442–462.
- [125] Kuntz, D., Hassan, B., and Potter, D., "Predictions of Ablating Hypersonic Vehicles Using an Iterative Coupled Fluid/Thermal Approach," *Journal of Thermophysics and Heat Transfer*, Vol. 15, No. 2, 2001, pp. 129–139.
- [126] Kendall, R. M., Bartlett, E. P., Rindal, R. A., and Moyer, C. B., "An Analysis of the Coupled Chemically Reacting Boundary Layer and Charring Ablator, Part I. Summary Report," NASA CR-1060, June 1968.
- [127] Nompelis, I., Candler, G., and Conti, R., "A Parallel Implicit CFD Code for the Simulation of Ablating Re-Entry Vehicles," AIAA Paper 2009-1562, January 2009.
- [128] Alkandry, H., Boyd, I., and Martin, A., "Coupled Flow Field Simulations of Charring Ablators with Nonequilibrium Surface Chemistry," AIAA Paper 2013-2634, June 2013.
- [129] MacLean, M., "An Equilibrium Ablation Boundary Condition for the Data-Parallel Line-Relaxation Code," AIAA Paper 2013-304, January 2013.
- [130] Martin, A., and Boyd, I. D., "Mesh Tailoring for Strongly Coupled Computation of Ablative Material in Nonequilibrium Hypersonic Flow," AIAA Paper 2010-5062, June 2010.
- [131] Zhang, L.-H., Zybin, S. V., van Duin, A. C. T., and Goddard, W. A., III, "Modeling High Rate Impact Sensitivity of Perfect RDX and HMX Crystals by ReaxFF Reactive Dynamics," *Journal of Energetic Materials, Supplement 1*, Vol. 28, 2010, pp. 92–127.
- [132] Zhang, L. Z., van Duin, A. C. T., Zybin, S. V., and Goddard, W. A., "Thermal Decomposition of Hydrazines from Reactive Dynamics Using the ReaxFF Reactive Force Field," *Journal of Physical Chemistry B*, Vol. 113, No. 31, 2009, pp. 10770–10778.
- [133] Strachan, A., Kober, E. M., van Duin, A. C. T., Oxgaard, J., and Goddard, W. A., "Thermal Decomposition of RDX from Reactive Molecular Dynamics," *Journal of Chemical Physics*, Vol. 122, No. 5, 2005, pp. 054502.
- [134] Hudson, T. S., Nguyen-Manh, D., van Duin, A. C. T., and Sutton, A. P., "Grand canonical Monte Carlo simulations of intergranular glassy films in beta silicon nitride," *Materials Science and Engineering a-Structural Materials Properties Microstructure and Processing*, Vol. 422, No. 1–2, 2006, pp. 123–135.
- [135] Poovathingal, S., Schwartzentruber, T. E., Srinivasan, S. G., and Duin, A. C. T. V., "Large Scale Computational Chemistry Modeling of the Oxidation of Highly Oriented Pyrolytic Graphite," *Journal of Physical Chemistry A*, Vol. 117, No. 13, 2013, pp. 2692–2703.
- [136] Panerai, F., Chazot, O., and Helber, B., "Gas/Surface Interaction Study on Ceramic Matrix Composite Thermal Protection System in the VKI Plasmatron Facility," AIAA Paper 2011-3642, June 2011.
- [137] Herdrich, G., Fertig, M., Löhle, S., Pidan, S., and Augweter-Kurtz, M., "Oxidation Behavior of Siliconcarbide-Based Materials by Using New Probe Techniques," *Journal of Spacecraft and Rockets*, Vol. 42, No. 5, 2005, pp. 817–824.

- [138] Laux, T., Herdrich, G., and Auweter-Kurtz, M., "Oxidation Behavior of Sintered Silicon Carbide in Various Plasma Wind Tunnels," in *Hot Structures and Thermal Protection Systems for Space Vehicles, Proceedings of the 4th European Workshop held 26–29 November, 2002 in Palermo, Italy.*; Vol. ESA SP-521, edited by A. Wilson, European Space Agency, Paris, 2003, pp. 377–379.
- [139] Lacombe, A., and Lacoste, M., "Investigation of C/SiC "Breaking Point" Under Arc Jet Environment at NASA-J.S.C.," *High Temperature Chemical Processes*, Vol. 3, No. 3, 1994, pp. 285–296.
- [140] Marschall, J., Pejaković, D. A., Fahrenholtz, W. G., Hilmas, G. E., Panerai, F., and Chazot, O., "Temperature Jump Phenomenon During Plasmatron Testing of ZrB₂-SiC Ultrahigh-Temperature Ceramics," *Journal of Thermophysics and Heat Transfer*, Vol. 26, No. 4, 2012, pp. 559–572.
- [141] Glass, D. E., "Physical Challenges and Limitations Confronting the Use of UHTCs on Hypersonic Vehicles," AIAA Paper 2011-2304, April 2011.
- [142] Fertig, M., Frühauf, H.-H., and Auweter-Kurtz, M., "Modelling of Reactive Processes at SiC Surfaces in Rarified Nonequilibrium Airflows," AIAA Paper 2002-3102, June 2002.
- [143] Melin, G. A., and Madix, R. J., "Energy Accommodation During Oxygen Atom Recombination on Metal Surfaces," *Transactions of the Faraday Society*, Vol. 67, 1971, pp. 198–211.
- [144] Melin, G. A., and Madix, R. J., "Energy Accommodation During Hydrogen Atom Recombination on Metal Surfaces," *Transactions of the Faraday Society*, Vol. 67, 1971, pp. 2711–2719.
- [145] Murphy, M. J., Skelly, J. F., and Hodgson, A., "Translational and Vibrational Energy Release in Nitrogen Recombinative Desorption from Cu(111)," *Chemical Physics Letters*, Vol. 279, No. 1-2, 1997, pp. 112–118.
- [146] Thorman, R. P., Anderson, D., and Bernasek, S. L., "Internal Energy of Heterogeneous Reaction Products: Nitrogen-Atom Recombination on Iron," *Physical Review Letters*, Vol. 44, No. 11, 1980, pp. 743–746.
- [147] Black, G., and Slanger, T. G., "Production of O₂(a1Δg) by Oxygen Atom Recombination on a Pyrex Surface," *Journal of Physical Chemistry*, Vol. 74, No. 11, 1981, pp. 6517–6519.
- [148] Myasnikov, I. A., Grigor'ev, E. I., and Tsivenko, V. I., "Electronically Excited Atoms and Molecules in Solid-Gas Systems," *Russian Chemical Reviews*, Vol. 50, No. 2, 1986, pp. 161–190.
- [149] Armenise, I., Barbato, M., Capitelli, M., and Kustova, E., "State-to-State Catalytic Models, Kinetics, and Transport in Hypersonic Boundary Layers," *Journal of Thermophysics and Heat Transfer*, Vol. 20, No. 3, 2006, pp. 465–476.
- [150] Armenise, I., Capitelli, M., Gorse, C., Cacciatore, M., and Rutigliano, M., "Nonequilibrium Vibrational Kinetics of an O₂/O Mixture Hitting a Catalytic Surface," *Journal of Spacecraft and Rockets*, Vol. 37, No. 3, 2000, pp. 318–323.
- [151] Ali, A. A., Ogryzlo, E. A., Shen, Y. Q., and Wassell, P. T., "The Formation of O₂(a1Δg) in Homogeneous and Heterogeneous Atom Recombination," *Canadian Journal of Physics*, Vol. 64, No. 12, 1986, pp. 1614–1620.
- [152] White, J. D., Copeland, R. A., and Marschall, J., "Singlet O₂ Formation by O-atom Recombination on Fused Quartz Surfaces," AIAA Paper 2014-0000, January 2014.

- [153] Slanger, T., and Copeland, R. A., "Energetic Oxygen in the Upper Atmosphere and the Laboratory," *Chemical Reviews*, Vol. 103, No. 12, 2003, pp. 4731–4765.
- [154] Wise, H., and Wood, B.J., "Reactive Collisions Between Gas and Surface Atoms," in *Advances in Atomic and Molecular Physics; Vol. 3*, edited by D. R. Bates, and I. Estermann, Academic Press, New York, 1967, pp. 291–353.
- [155] Brennan, D., "Heterogeneous Atomisation and Recombination," in *Comprehensive Chemical Kinetics. Volume 21, Reactions of Solids with Gases*, edited by C. H. Bamford, C. E. H. Tripper, and R. G. Compton, Elsevier, New York, 1984, pp. 151–231.
- [156] Balat, M., Czerniak, M., and Badie, J. M., "Thermal and Chemical Approaches for Oxygen Catalytic Recombination Evaluation on Ceramic Materials at High Temperature," *Applied Surface Science*, Vol. 120, No. 3-4, 1997, pp. 225–238.
- [157] Chazot, O., Krassilchikoff, H. W., and Thömel, J., "TPS Ground Testing in Plasma Wind Tunnel for Catalytic Properties Determination," AIAA Paper 2008-1252, January 2008.
- [158] Chazot, O., Paris, S., Collin, P., Bickel, M., and Ullman, T., "TPS Testing and Catalycity Determination in the VKI Plasmatron Facility," VKI RP 2003-80, March 2003.
- [159] Meyers, J. M., Owens, W. P., and Fletcher, D. G., "Surface Catalyzed Reaction Efficiencies in Nitrogen and Oxygen Plasmas from Laser Induced Fluorescence Measurements," AIAA Paper 2013-3139, June 2013.

High-Enthalpy Facilities and Plasma Wind Tunnels for Aerothermodynamics Ground Testing

Olivier Chazot* and Francesco Panerai†

Von Karman Institute for Fluid Dynamics, Rhode St-Genèse, Belgium

I. INTRODUCTION

Planetary entries remain to date a major challenge for aerospace engineers. Aerothermodynamics and hypersonic effects yield a complex flow environment around the space vehicle, where high velocities, gas radiation, and extreme temperatures are tightly coupled to each other and interact with the heatshield materials producing complex transport and chemical phenomena. The schematic in Fig. 1 highlights the several regions of interests around a blunt-shaped hypersonic body, with different leading phenomena.

Space exploration requires a continuous involvement with improved design for mission spacecraft based on cumulated experience and databases generated through wind tunnel and flight testing and analysis. The ability to model entry flow physics progresses as well, together with an improved understanding in physical gas dynamics. However, several key areas of aerothermodynamics remain to be better understood and are the focus of intensive investigations. Current efforts are devoted to develop a more accurate knowledge on critical phenomena such as laminar to turbulence transition, gas–surface interactions (GSIs), and flow radiation. These latter are directly related to hypersonic non-equilibrium flows and are chiefly important because of their major impact on Thermal Protection System (TPS) design. The limited knowledge on modeling of nonequilibrium flows is a demanding challenge in computational fluid dynamics of entry systems, which are one of the main tools for aerospace mission analysis.

In this scenario, ground test facilities are an invaluable tool to extract material and flow information for computational models and to provide validation data for numerical tools. In this chapter we offer an overview of the challenges encountered when attempting a simulation in ground of hypersonic flight conditions. As detailed description of existing testing techniques and facilities has been

*Professor, Head of Aeronautics/Aerospace Department at Von Karman Institute

†Post-Doctoral fellow

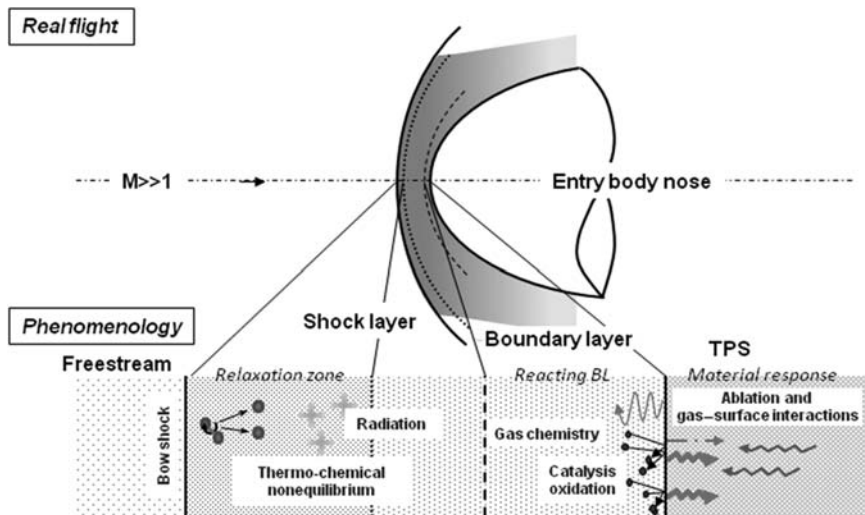


Fig. 1 Typical nonequilibrium effects behind a bow shock in reentry flights.

extensively treated in the literature [1–6], our objectives are: 1) recall the basic similarity concepts behind high-speed and high-enthalpy facility and aerothermodynamic ground testing, 2) illustrate the operating principles of different classes of wind tunnels and 3) to review the states-of-the-art of ground hypersonic facilities currently operational in the form of a single page datasheet summarizing the main testing capabilities, operational envelopes and measurement techniques. The selection presented in the appendix is narrowed to the hypersonic facilities able to provide a minimum of 5 km/s as testing conditions with a total temperature above 7000 K.

II. AEROTHERMODYNAMIC GROUND TESTING

Aerothermodynamics testing is essential for the development and design of aerospace vehicles. Firstly, it represents a convenient step in the testing procedure at reduce cost, compared to a real flight experiment. Secondly, ground tests allow a better control of the environment and a direct application of the measurement techniques to investigate the complexities of nonequilibrium phenomena in high-speed flows. They also have a very practical use to assess the performance of TPS materials, to determine their surface and in-depth properties and to characterize their high temperatures response when exposed to dissociated flows.

To provide relevant data, the severe environment encountered by a space-craft during reentry has to be reproduced at best in ground based facilities. However a complete experimental simulation of hypersonic conditions in a ground test facility, where high-speed flow and high thermal loads are provided

simultaneously to a test model is beyond the current technical capabilities [7]. Facilities able to provide high Mach number flows are characterized by limited test time, insufficient to reproduce heat load for thermal protection material performance testing. Plasma wind tunnels instead allow long duration heating tests, but flow Mach numbers is limited.

To overcome this limitation, testing methodologies have been elaborated to simulate high temperature effects in hypersonic flows in ground wind tunnels, as the so-called binary scaling [8–10] and the Local Heat Transfer Simulation (LHTS) [11, 12], presented in the following paragraphs.

The binary scaling provides a framework to simulate the features of nonequilibrium postshock environment in high-enthalpy facilities for forebody stagnation regions when binary reactions are dominant. Considering a blunt body at a velocity of 7 km/s, the temperature immediately after the shock is around 14,000 K, and around 8000 K downstream the shock, where the flow may return to equilibrium. At such high temperatures, thermo-chemical effects have a significant influence on the flow. To give typical reference for air at a pressure of 1 atm, vibrational excitation begins at 800 K, O₂ begins to dissociate at 2500 K and is fully dissociated for 4000 K, point for which N₂ begins to dissociate. At 9000 K, N₂ is fully dissociated and ionization begins. In the aim at reproducing high-temperature flow phenomena in ground testing facilities one need to consider the mass conservation equation where thermo-chemical reactions appear in production terms. From the nondimensional expression of the equation the Damköhler number (Da) could be identified as the characteristic parameter for the reaction phenomena. This number is defined as $Da = \tau_F/\tau_D$ where τ_F is the characteristic time for the flow and τ_D the characteristic time associated to the dissociation reaction. Da allows to range the nonequilibrium phenomena of a reacting gas mixture.

Regarding the flow as composed of a single species the dissociation rate is proportional to the density (ρ), whereas the recombination rate is proportional to the square of density (ρ^2), because of three body reactions. At high altitude, typical for reentry situations of interest, recombination will take much longer time to happen compare to dissociation. Da could be expressed with the flow parameters for the dissociation phenomena as follows:

$$Da = \frac{k_D \cdot \rho \cdot L}{U_\infty}$$

U_∞ being the flow velocity, ρ the gas density, L a characteristic length of the flow around the model and k_D the dissociation rate coefficient. Neglecting the diffusion process, in the shock layer, the condition of similarity for a dissociated flow in a high-enthalpy facility is to reproduce the same Da number as in flight. It leads to consider the same nature of the gas to respect the reaction partners, to replicate the flow velocity and to preserve the product ρL , between the flight, in real dimensions, and the scaled model in the ground testing facility conditions.

Some limitations could be mentioned at this point. Firstly the required density to be achieved in the wind tunnel could become too large on the reduced model, in order to maintain the proper value of the binary scaling parameter (ρL) for duplication of flight at lower altitude, and lead to practical problems for the facility operation. Secondly, the binary scale methodology is built upon the hypothesis of a single species mixture. That approach has to be carefully used when applied to more complex mixtures such as air [13]. Finally, as altitude decreases, density increases and recombination can no longer be neglected. The binary scaling parameter does not hold anymore, as both ρL and $\rho^2 L$ should be reproduced at the same time. These remarks remind that the experimental hypersonic simulation for studying nonequilibrium phenomena requires an accurate understanding of the ground testing facility operation and a careful interpretation of the experimental data.

The LHTS methodology considers all the reactions and transport phenomena in the dissociated flow. It is mostly adapted for chemical nonequilibrium boundary layer duplication and it allows to study GSI in ground facilities. It comes from a detailed inspection of the heat transfer at hypersonic flight where one could underline that all the important phenomena are laying in the boundary layer. This is presented in Fig. 1, which gives an illustration of real flight situation in front of an Aerospace vehicle, accounting for a negligible contribution from radiation. The study could then be focused on this confined layer in particular for the heat-transfer problems in hypersonic. In this situation the full-scale environment is reproduced by duplicating solely the characteristics of the boundary layer in the ground testing facilities. Figure 2 gives the general frame of the LHTS conditions applied to TPS testing in plasma wind tunnels.

The methodology for stagnation point heat transfer duplication is based on the theoretical work of Fay and Riddell [14], from the sixties. It was firstly applied to shock tube experiments in air by Rose and Stark [15]. An extension of the method to induction plasmatron, that use subsonic dissociated flow to reproduce in ground the boundary layer chemistry around a thermal protection materials, was documented in the nineties by Kolesnikov [11]. The LHTS methodology applies at the stagnation point for which the total enthalpy (He), stagnation pressure (Ps) and velocity gradient ($\beta = du/dx$) need to be reproduced to return at the surface of the test model the same total heat flux as in flight. By doing so the gas Damköhler number (Da_g), which characterizes the chemical nonequilibrium in the boundary layer, is correctly replicate. Here also this number corresponds to the ratio between the typical time of the flow, to cross the boundary layer, to a typical reaction time for the gas chemistry: $Da_g = \tau_F/\tau_c$. When $Da_g \rightarrow \infty$ the boundary layer reaches a local thermodynamic equilibrium (LTE). On the contrary when $Da_g \rightarrow 0$ it leads to a frozen boundary layer, where no chemistry happen. In this framework the wall reactions are also represented, at the stagnation point on the tested article, and are characterized by a wall Damköhler number (Da_w). This second number compares the time of diffusion for the species across the boundary layer to the time of reaction at the

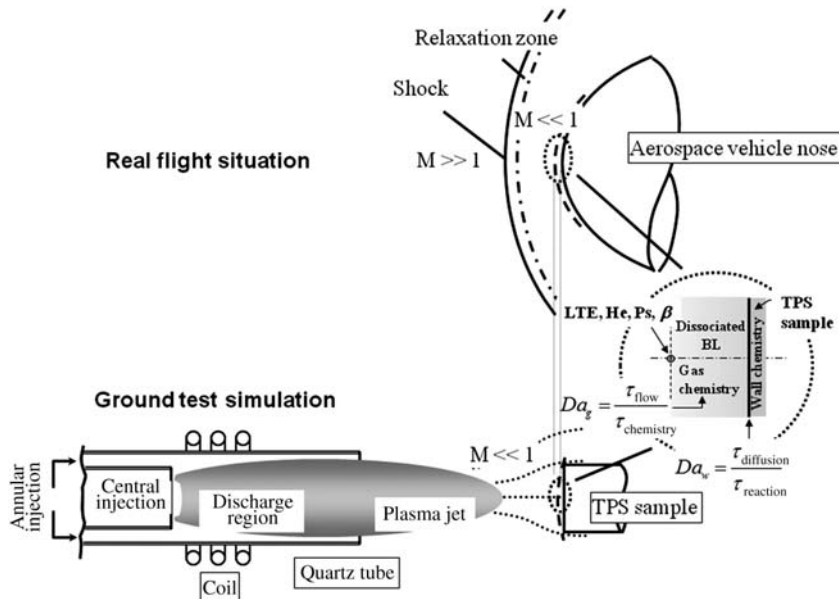


Fig. 2 TPS testing in plasma wind tunnel in LHTS conditions.

wall: $Da_w = \tau_{\text{Diff}}/\tau_{\text{React}}$. When $Da_w \rightarrow \infty$ it does not necessarily imply that the reaction rate at the wall tend to infinity ($k_w \rightarrow \infty$), but simply that the surface reaction are much more faster than the diffusion process. It is said that the GSI phenomena are “limited by diffusion.” In the other extreme case, when $Da_w \rightarrow 0$ the diffusion is much faster than the reaction and the GSI phenomena are “limited by reaction” or “reaction controlled.” Applications of the LHTS methodology for plasmatrons play a key role in the characterization of the thermal protection materials, as it allows determination of catalytic rates for reusable surfaces expose to high-enthalpy flows.

The two ground testing methodologies have been developed for two types of ground testing facilities that address different aspects of nonequilibrium in hypersonic flows. Binary scaling better applied for high-enthalpy facilities to study post-shock nonequilibrium with thermo-chemical effects, including flow radiation. LHTS methodology is specifically suited for plasma wind tunnels where nonequilibrium flow enters to play in GSI phenomena and offers a dedicated environment to characterize thermal protection material response.

These ground testing strategies are often used as complementary approaches for nonequilibrium hypersonic research. They cannot go without a sharp understanding of the working principles of the facilities and their range of operation as well as a precise characterization of the testing conditions. A summarizing schematic of the aerothermodynamic testing is illustrated in Fig. 3.

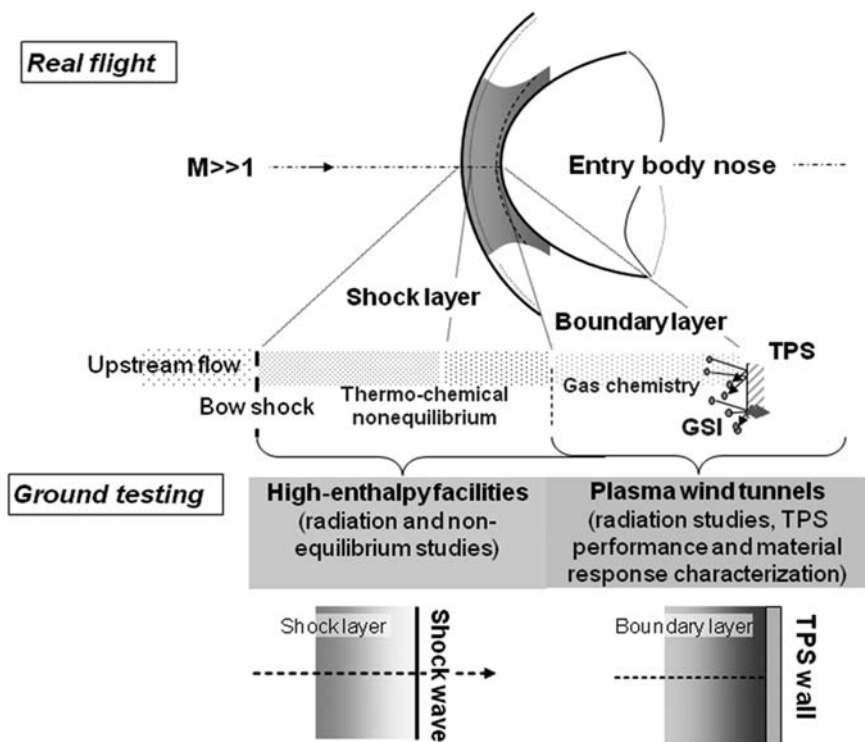


Fig. 3 Ground testing strategy for high-speed reentry simulation.

III. HIGH-ENTHALPY FACILITIES

The operating principles of the different types of high-enthalpy facilities that allow the duplication of high-speed reentry conditions are briefly presented below. The description is focus on the main elements of the wind tunnel and recalls their basic functioning, followed by an illustrative sketch.

A. BLOW DOWN WIND TUNNEL

This type of facility delivers a flow at constant stagnation pressure. This pressure is equal to the plenum pressure which is monitored by pressure regulators in a separate tank section. During testing time, the tank pressure decreases continuously to equilibrate the plenum pressure. A regulator valve coordinates the pressure equilibrium by moving progressively. Typical runs usually last 20–200s. This kind of facility usually provides moderate enthalpies which are limited by the heating capacity of its pebble-bed heater. Figure 4 shows the facility schematic.

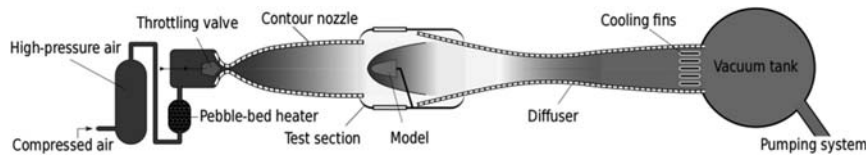


Fig. 4 Schematic of a blowdown wind tunnel.

B. BALLISTIC RANGE

In the ballistic range facility, a gun launches a model into a range where chemical composition, temperature and pressure are adjusted in order to match with conditions of interest. This configuration allows for testing in a quiet environment similar to the real flight situation. At several points on the model's trajectory the characteristics of the flight are measured such as velocity, angle of attack and yaw angle but also the properties of the flow around the model. Measurements from on-board sensors are obtained as well with remote transmission or from flash memory after the model recovery. Figure 5 illustrates the basic operation of a ballistic range facility.

C. HOT SHOT TUNNEL

The hot shot tunnel stores electrical energy in condensers and coils which is then discharged in an arc chamber through electrodes. This apparatus allows the test gas to be pressurized and heated, reaching high total temperature, in a constant volume process. The pressure breaks a diaphragm and lets the gas expand through a nozzle. A quasi steady flow is obtained. The experiments usually last 20 to 100 milliseconds. Very high total conditions could be generated from the discharge process, but a careful characterization of the high-enthalpy flow is required to well qualify the testing conditions. An illustration of its working principles is given in Fig. 6.

D. SHOCK TUBE

A shock tube is a short duration facility (or impulse facility) which has been developed to simulate high-speed flows on ground. Basically a shock tube is composed

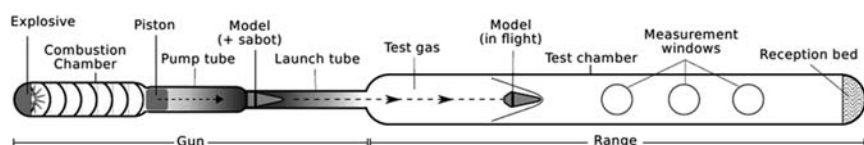


Fig. 5 Schematic of a ballistic range facility.

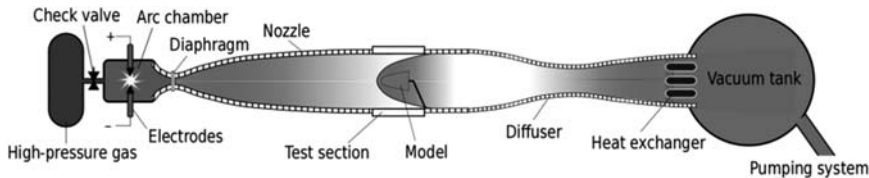


Fig. 6 Schematic of a hot shot tunnel.

of two tubes of constant area filled with two different gases. The first one, called driver tube, contains a light gas set at high pressure. It is separated by a diaphragm from the second one, called driven tube, which contains the test gas at much lower pressure. Increasing the reservoir pressure, in the driver tube, leads to the burst of the diaphragm. This phenomenon initiates a shock wave using the open space created by the rupture of the diaphragm. The low-pressure gas contained in the second tube allows propagating the shock wave. On the opposite way, an expansion wave propagates toward the high-pressure region. The traveling shock wave produces post shock conditions that could be observed at tube exit. Figure 7 illustrates the shock tube operation.

E. SHOCK TUNNEL

To provide high Mach number flows around models and improve the performances a nozzle could be added at the end of the shock tube. It is then called a shock tunnel. It operates with the same principles as the shock tube and can use a reflected shock at the end of the driven tube to generate high-pressure and high-temperature conditions in the reservoir (Fig. 8). Mach numbers over 15 and high Reynolds number can be obtained, from constant total pressure process in the reservoir. But, those conditions cannot be maintained continuously. This implies short test time duration, typically in the order of few milliseconds or shorter. Besides, the high temperature and heat flux attained in these facilities could highlight the high material resistance level needed.

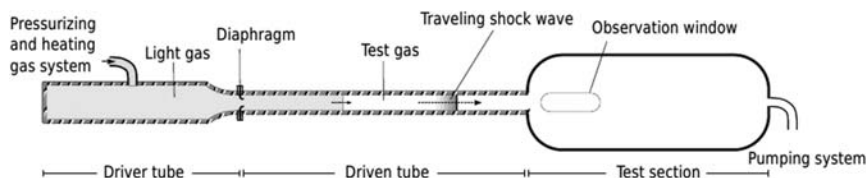


Fig. 7 Schematic of a shock tube facility.

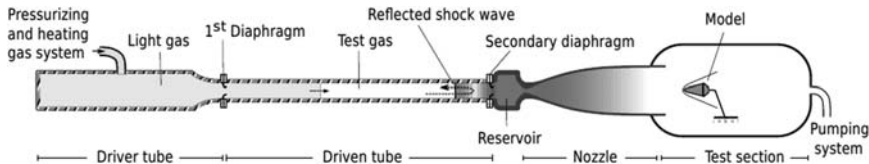


Fig. 8 Schematic of a shock tunnel facility.

F. FREE PISTON DRIVER TUBE

To reach higher enthalpies and generate higher flow velocities, in the test section, shock tunnels could be run with a free piston driver tube. This facility section, corresponding to a compression tube, is added between the high pressurized driver tube and the driven tube. It involves heating the driver gas by a rapid quasi isentropic compression using a free piston apparatus. Such a technique was pioneered by Stalker in the early sixties in Australia [16, 17]. The free piston compressor configuration can provide high stagnation pressure and temperature. It also presents the advantages of a compact driver configuration and leads to minimize the contamination problem caused by the heaters. A sketch of a free piston-driven section is given Fig. 9.

G. EXPANSION TUBE/TUNNEL

The expansion tube is similar to a shock tube connected at the end to a tube section in which the test gas is accelerated, through an expansion, to reach hypervelocities. It is an impulse flow device consisting in three sections of tubing aligned in tandem. To separate sections, two diaphragms, made of metal for the main one and of thin plastic for the second one, are used. The first tube is the driver section which is filled with high-pressure gas. The driven section is filled with a lower pressure test gas. The last section is called the acceleration tube and filled with a light gas at a very low pressure.

At the rupture of the first diaphragm, the driver gas expands into the driven section and a shock wave is created. Propagating in the second section, the shock wave increases the pressure and temperature behind it. Reaching the secondary diaphragm that breaks, the shock wave does not get reflected but pass through and continues in the last tube. Therefore, the test gas, which follows, is cooled

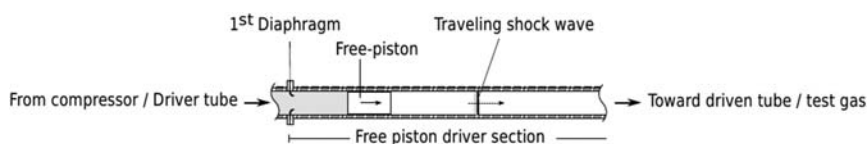


Fig. 9 Sketch of piston-driven shock tube with free piston motion.

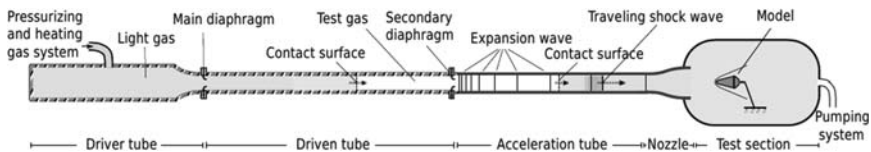


Fig. 10 Schematic of an expansion tunnel.

and accelerated by an unsteady expansion from the driven section into the acceleration section.

It is possible to complete the expansion tube with a nozzle to accommodate a larger exit section for testing. In this latter configuration the facility is sometime called expansion tunnel. It has to be noticed that the test gas is never stagnated along the facility until it reaches the model. Expansion tubes are, from the high-enthalpy facilities, the ones able to provide the highest flow velocities reaching typically superorbital reentry conditions. They are also the facilities offering the smallest test time, i.e., in the order of millisecond. The different elements of a typical expansion tube configuration are presented in Fig. 10.

IV. PLASMA WIND TUNNELS

A. ARCJET FACILITY

Arcjet facilities are long duration, plasma wind tunnels where the dissociated flow is generated by means of an inter-electrodes current, passed through a high-pressure flow of gas. The discharge, in a form of an arc column, is produced in a segmented heater of metal elements with magnetically spun electrodes, arranged in a large length-to-diameter ratio column. The heated test gas is flown through a converging-diverging nozzle producing a supersonic flow blown into a test chamber. Supersonic nozzles have usually a conical shape, though few examples of elliptical nozzles exist. Pressure levels in the arc chamber are adapted whether ballistic or planetary entry aerothermal conditions are simulated around the sample in the test section. The test chamber is kept at partial pressure to match at best the conditions of the supersonic plasma jet at nozzle exit. Typical powers for arcjet facilities used for aerospace range from 10 to 70 MW. Figure 11 provides a schematic of the arcjet operation.

B. INDUCTIVELY COUPLED PLASMA FACILITY

Similarly to arcjets, inductively coupled plasma (ICP) generators provide long duration plasma flows for thermal protection systems testing and GSI studies. They are also called plasmatron facilities. ICP generation is achieved by an electromagnetic (EM) discharge at high frequency, produced by a coil, into a flow of gas passing through a quartz tube. The gas heats up by Joule effect, in the

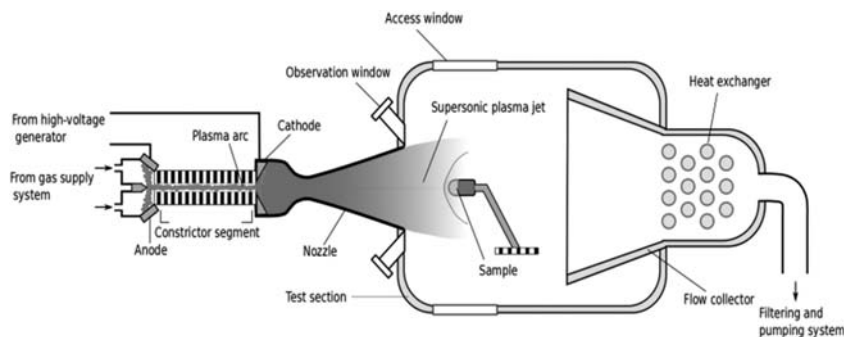


Fig. 11 Schematic of an arcjet facility.

inductive zone, promoting further ionization in the flow that develops into plasma in the torch and exits in the form of a subsonic jet. The plasma jet is blown into the test chamber at subatmospheric pressure which is adapted depending on the conditions to be duplicated. Recent extensions of performance envelopes of ICP wind tunnel have led to the development of sonic nozzles, producing supersonic flows with higher energy contents. ICP generators range from tens of kilowatts to 1 MW in power. ICP are mostly specific because of the quality of the flow chemistry they could provide thanks to their plasma discharge produced without any contact with the electrodes in the torch. A schematic of an ICP facility is shown Fig. 12.

V. CONCLUSION

Ground-based facilities dedicated to high-speed reentry are fundamental for the development of aerospace vehicles. These wind tunnels used for

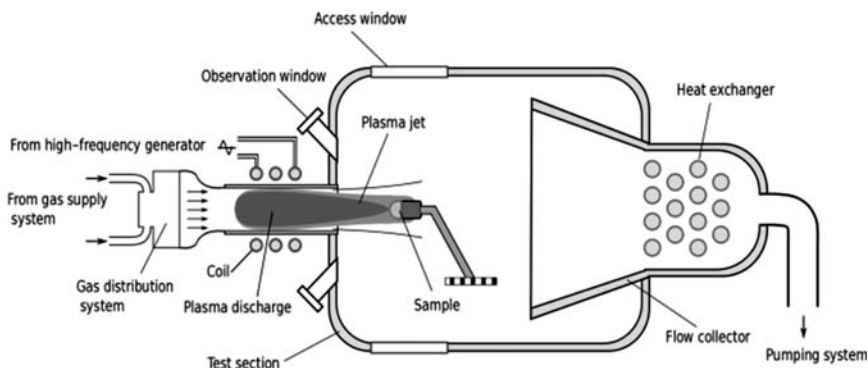


Fig. 12 Schematic of plasmatron facility.

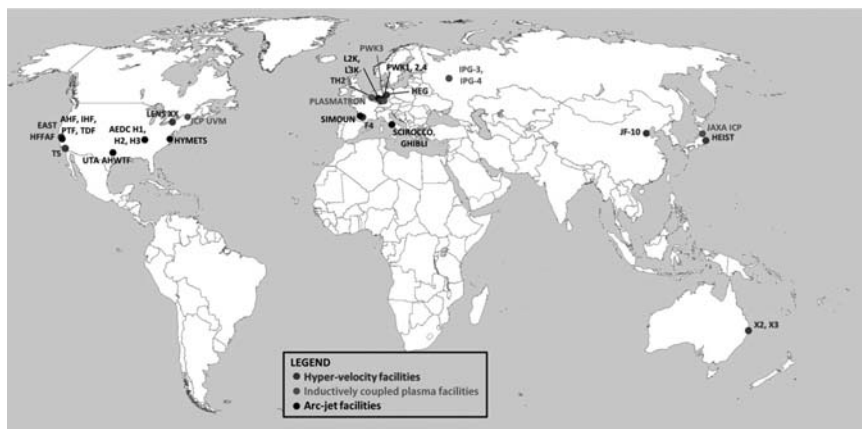


Fig. 13 Location of the high enthalpies and plasma wind tunnels in the world.

aerothermodynamic testing can be grouped in two categories: high-enthalpy facilities and plasma wind tunnels. This chapter exposed the different type of facilities and their basic operating principles to generate high-speed conditions on ground. The review of the high-enthalpy facilities and plasma wind tunnels in operation worldwide revealed also the variety of ground testing facilities used to reproduce nonequilibrium flow situations.

High-enthalpy facilities are unique to achieve the flow velocity and the nonequilibrium features of the post shock conditions of hypersonic flights. Even if those facilities are limited to short test duration they allow to capture enough flow physics to feed the development of nonequilibrium modeling.

Plasma wind tunnels are designed to duplicate the complete environment on some critical part of reentry vehicles. These facilities are focus on the simulation of dissociated boundary layers and usually disregard the coupling with the radiation feature of the flow. Nevertheless they are very well adapted for GSI studies. Thanks to the extreme heat-flux conditions they could provide, with long test duration, they are heavily used for TPS qualification.

Most of the time these facilities are used with complementary approaches defined in a testing strategy to generate experimental databases needed to progress with the physical modeling [18]. To enlarge the perspective, the ground-based facilities presented in the following annex are situated on the world map in Fig. 13. They stand as precious companions for researchers and engineers as they constantly bring out result of reference, but they allow also to question and reveal the aerothermodynamic nature of high-speed flows. These experimental resources appear as strong assets for the advancement in knowledge and technical development for the aerospace field.

REFERENCES

- [1] Lu, F. K., and Marren, D. E., *Advanced Hypersonic Test Facilities, Progress in Astronautics and Aeronautics Series*, Vol. 198, AIAA, Reston, MA, 2002.
- [2] Park, C., *Nonequilibrium Hypersonic Aerothermodynamics*, 1st ed., Wiley-Interscience, New York (February 1990), ISBN-10: 0471510939.
- [3] Goodrich, M., and Gorham, J., "Wind Tunnels Of The Western Hemisphere," A report prepared by the Federal Research Division, Library of Congress, for the Aeronautics Research Mission Directorate, National Aeronautics and Space Administration, June 2008.
- [4] Goodrich, M., Gorham, J., Ivey, W. N., Kim, S., Lewis, M., and Minkus, C., "Wind Tunnels Of The Eastern Hemisphere," A report prepared by the Federal Research Division, Library of Congress for the Aeronautics Research Mission Directorate, National Aeronautics and Space Administration, August 2008
- [5] Pélissier, C., Trainau, J. C., Kharitonov, A. M., Lapygin, V. I., and Gorelov, V. A., *Review of the Aerothermodynamics Facilities in Europe: The High Enthalpy Facilities Example*, ICMAR, Novosibirsk, 2002.
- [6] Bugel, M., Reynier, Ph., and Smith, A., "Survey of European and Major ISC Facilities for Supporting Mars and Sample Return Mission Aerothermodynamics and Tests Required for Thermal Protection System and Dynamic Stability," *International Journal of Aerospace Engineering* 2011, Article ID 937629, 18 pp., doi: 10.1155/2011/937629.
- [7] Neumann, R. D., "Experimental Methods for Hypersonics: Capabilities and Limitations," *2nd Joint Europe-US Short Course on Hypersonic*, GAMNI-SMAI and University of Texas at Austin, USAF Academy, Colorado Springs, CO 80840, Jan. 1989.
- [8] Freeman, N. C., "Non equilibrium Flow of an Ideal Dissociating Gas," *Journal of Fluid Mechanics*, Vol. 4, No. 4, Aug. 1958.
- [9] Gibson, W. E., and Marrone, P. V., "A Similitude for Non-equilibrium Phenomena in Hypersonic Flight," *The High Temperature Aspect of Hypersonic Flow*, AGARDograph 69, edited by W. C. Nelson, Pergamon, Oxford, England, U.K./New York, 1964.
- [10] Inger, G. R., Higgins, C., and Morgan, R., "Generalized Nonequilibrium Binary Scaling for Shock Standoff on Hypersonic Blunt Bodies," *Journal of Thermophysics and Heat Transfer*, Vol. 17, No. 1, 2003, pp. 126–128.
- [11] Kolesnikov, A. F., "Condition of Simulation of Stagnation Point from High Enthalpy Flow," *Fluid Dynamics* (tr. from Russian), Vol. 28, No. 1, 1993, pp. 131–137.
- [12] Barbante, P. F., and Chazot, O., "Flight Extrapolation of Plasma Wind Tunnel of Stagnation Region Flowfield," *Journal of Thermophysics and Heat Transfer*, Vol. 20, No. 3, July–Sept. 2006, pp. 493–499.
- [13] Ellington, D., "Binary Scaling Limits for Hypersonic Flight," *AIAA Journal*, Vol. 5, No. 9, 1967, pp. 1705–1706.
- [14] Fay, J. A., and Riddell, F. R., "Theory of Stagnation Point Heat Transfer in Dissociated Air," *Journal of the Aeronautical Sciences*, Vol. 25, No. 2, Feb. 1958, pp. 73–85.

- [15] Rose, P. H., and Stark, W. I., "Stagnation Point Heat-Transfer Measurements in Dissociated Air," *Journal of the Aeronautical Sciences*, Vol. 25, No. 2, Feb. 1958, pp. 86–97.
- [16] Stalker, R. J., "The Free Piston Shock Tube," *Aero Quarterly*, Vol. 17, 1966, pp. 351–370.
- [17] Stalker, R. J., "Study of the Free Piston Shock Tunnel," *AIAA Journal*, Vol. 5, 1967, pp. 2160–2165.
- [18] Chazot, O., "Ground Testing Strategy for High Speed Re-entry," STO-VKI AVT 218 Lecture Series, edited by O. Chazot, and T. Magin, von Karman Institute, Rhode St. Genèse, Belgium, May 6–8, 2013.

Molecular-Based Optical Diagnostics for Hypersonic Nonequilibrium Flows

Paul M. Danehy* and **Brett F. Bathel***

NASA Langley Research Center, Hampton, Virginia

Craig T. Johansen[†]

University of Calgary, Calgary, Canada

Michael Winter[‡]

University of Kentucky, Lexington, Kentucky

Sean O'Byrne[§]

University of New South Wales Canberra, Canberra, Australia

Andrew D. Cutler[¶]

The George Washington University, Newport News, Virginia

I. INTRODUCTION

Departure from thermal and chemical equilibrium occurs frequently in hypersonic flow. When a fluid element travels through a flowfield it will stay in equilibrium with its surroundings if the molecular collision rate is sufficiently high. On the other hand, if the fluid element experiences sudden changes in conditions and the collision rate is relatively low, then departure from thermodynamic equilibrium, or *nonequilibrium*, occurs. In hypersonic flight nonequilibrium can occur, for example, as gas passes through shock waves, suddenly expands, or undergoes combustion. The resulting nonequilibrium can affect the population of molecules in translational, rotational, and vibrational internal energy modes as well as the chemical composition. Such nonequilibrium phenomena, if ignored, can lead to erroneous predictions of lift, drag, aeroheating, and engine performance.

*Research Scientist

[†]Assistant Professor

[‡]Assistant Professor

[§]Senior Lecturer

[¶]Professor

In a gas in thermal equilibrium the distribution of population among its various thermal energy levels (translational, rotational, and vibrational) is governed by the Boltzmann distribution law, which is expressed in terms of a temperature. If the gas is not in thermal equilibrium, then no unique temperature can be assigned. In moderate density (nonrarified) hypersonic flows it is often useful to define separate vibrational and translational–rotational temperatures (where translation and rotational modes are assumed to be in equilibrium among themselves and with each other). For example, the translational–rotational temperature will rise abruptly across a shock wave, but the distribution of energy in the vibrational levels will take some time (distance) before it comes into equilibrium. It has been shown that under certain conditions an intermediate vibrational temperature may be defined (i.e., a Boltzmann distribution of population among the vibrational levels) at various times in the relaxation [1]. In rarefied hypersonic flows, the rotational and translation temperatures can be unequal; furthermore they can have non-Boltzmann distributions [2].

Computation of fluid dynamical flowfields is greatly complicated when non-equilibrium must be considered. Instead of computing chemical equilibrium, finite rate chemistry must be included, resulting in the calculation of tens to thousands of equations instead of just a few. Similarly, thermal nonequilibrium conditions require bookkeeping of different temperatures for different energy modes such as translational, rotational, and vibrational temperatures, T_{trans} , T_{rot} and T_{vib} , respectively, assuming that each of those energy modes can be described by a Boltzmann distribution. Further complicating matters, different species in the same flow can have different vibrational temperatures, or may even have nonequilibrium distributions that cannot be described by a temperature. For example, the products of some exothermic chemical reactions are formed with a non-Boltzmann distribution of vibrational energy [1].

While thermodynamic and chemical nonequilibrium occur in many different fields of chemistry, physics and engineering, hypersonic flows are particularly susceptible to these complicating effects. Hypersonic vehicles (e.g., entry vehicles or hypersonic cruise vehicles) typically fly at high altitude where the pressure is low. Because of the high speed, kinetic energy from the vehicle is converted to thermal energy in the gas flowing over the vehicle. Thus hypersonic gas flow typically encounters low-pressure, P , and high-temperature, T , conditions. As gaseous collision rates scale as P/\sqrt{T} , low-pressure high-temperature flows can have relatively low collision rates. These low collision rates, coupled with flow phenomena such as shock waves, expansions and boundary layers which have steep gradients, cause sudden changes in flow conditions, resulting in nonequilibrium.

The different thermal and chemical phenomena mentioned above require different numbers of collisions to maintain equilibrium. Translational and rotational modes of a molecule can be brought into equilibrium with 10 or fewer collisions, occurring in less than 1 ns at $P = 1$ atm and $T = 273$ K [3]. For comparison, it takes about 20,000 collisions to vibrationally excite an O_2

molecule [4]. Chemical changes can occur even more slowly. Dissociation of the O₂ molecule by collisions requires on the order of 200,000 collisions [4]. Thus vibrational and chemical changes in a gas occur much more slowly than translational and rotational changes. Consequently, vibrational and chemical nonequilibrium are more commonly observed in hypersonic flow than translational and rotational nonequilibrium, and measurements of these phenomena will be emphasized in this chapter. The complexity of modeling these nonequilibrium phenomena, and the strong effect that they can have on the heating of aerospace vehicles, makes it essential to develop experimental techniques capable of quantifying the degree of nonequilibrium in the flowfield without interfering with the distributions that they are measuring. The nonintrusive and quantum-state-specific characteristics of spectroscopic techniques make them uniquely suitable for this purpose. Spectroscopy, then, can provide direct experimental evidence of these equilibrium or nonequilibrium thermal distributions and chemical compositions. Nonintrusive spectroscopic techniques can be used in ground-based flow simulation facilities and sometimes even in flight to probe individual atomic and molecular states, thereby measuring population distributions, translational, rotational, and vibrational temperatures, chemical compositions, and other data that can help modelers compute these challenging flowfields.

A variety of different molecular-based optical measurement techniques will be detailed in this chapter. Optical emission spectroscopy (OES) is the only technique detailed herein that does not require a light source (e.g., a laser). OES instead disperses naturally emitted light to provide quantitative flow field information. However, OES can only be used to study luminous environments. Also it is difficult to determine spatially specific information using OES, as the collection optics average all the light along its optical path. These limitations can be overcome by using a light source such as a lamp or a laser. If a light source is incident upon a gaseous medium the incident photons can either be absorbed, scattered, or can transmit through the medium. These different possible light paths present opportunities for different methods to probe and measure the gas. Absorption spectroscopy uses the transmitted light to diagnose the sample: the method compares the transmitted intensity with a sample present to a reference thereby determining the sample's absorption integrated along the optical path. Rayleigh scattering, Raman scattering and laser induced fluorescence (LIF) collect scattered light at an angle to the incoming light. This localizes the measurement point at the intersection between the incoming light and the optical path of the detection optics. Measurements can be made at a single spatial location or, using a camera, measurements can be made along a line or in an image plane. Whereas Rayleigh scattering is an elastic scattering process, Raman scattering is inelastic, with a small amount of energy either gained from or lost to the surrounding medium. LIF is a two-step process wherein a photon from the incident beam is absorbed and then is subsequently emitted. These scattering processes emit light approximately isotropically in three dimensions (into 4π steradians)

so that the intensity of the light drops off as one over the distance from the measurement point squared (*inverse square law*). Consequently, using conventional lenses, only a small fraction (typically $\sim 1\%$) of the scattered light can be collected [5]. The abovementioned scattering techniques do not require the coherence property of a laser and are known as *incoherent* measurement techniques.

Coherent measurement approaches involve the use of multiple laser beams which are directed into and interact with the flowfield. These techniques make use of the coherence of laser light to perform nonlinear wave-mixing which generates coherent signal beams. The resulting laser-like beam does not follow the inverse square law. Instead, it can propagate long distances without loss. It can also be spatially filtered to reject flow luminosity (which does follow the inverse square law) without losing signal intensity. For coherent measurement techniques, the measurement volume is determined by the location of the crossing of the laser beams. Unfortunately, these coherent techniques are much more complicated to set up and harder to keep aligned than incoherent techniques. Also, these methods are nonlinear and are therefore generally more difficult to analyze and interpret than incoherent techniques. However, coherent techniques, such as coherent anti-Stokes Raman spectroscopy (CARS), provide high signal-to-noise ratio data in applications with limited optical access and/or flow luminosity.

This chapter mainly focuses on spectroscopic measurement techniques for studying gaseous hypersonic nonequilibrium flow. In particular, we will focus on techniques that have either been used to study hypersonic nonequilibrium flowfields or techniques that show promise for studying these flows. Several classes of measurement techniques that are, or could be, used to study hypersonic nonequilibrium flows are *not* described herein. For example, surface measurement techniques such as pressure and temperature sensitive paint, phosphor thermography, skin friction measurements and photogrammetry (for model attitude and deformation measurement) are excluded to limit the scope of the chapter. Physical probes such as pitot probes, static pressure probes, heat flux gauges, total temperature probes, and others are excluded to limit scope. We further exclude measurement techniques that require particle seeding because of practical difficulties in seeding particles into hypersonic nonequilibrium flow facilities and because the particles may not faithfully follow the flow through steep gradients [6] often associated with hypersonic nonequilibrium flow. However, particle based methods may still be useful in certain hypersonic nonequilibrium flow applications. The chapter emphasizes quantitative techniques, so excluded are techniques that typically provide only flow visualization, such as schlieren.

Hypersonic facilities present many challenges to the implementation of optical measurement techniques. Facilities capable of producing high-enthalpy flow often have hazards that must be accommodated in order to make measurements. Such hazards include those associated with high pressure, explosives, high voltage, high acoustic noise and toxic gas generated by the facility and the measurement system. Consequently, in many facilities the operator cannot be near the facility

during operation so the equipment must be operated remotely or must operate autonomously. To reduce costs and increase test section size and operating pressure range many hypersonic facilities operate for very short duration, for example 100 msec or less. These are known as *impulse* facilities. For laser systems operating at 10 Hz only one measurement can be acquired in these facilities per tunnel run. As some impulse facilities can operate only once per day it is difficult to obtain a statistically significant number of measurements with some measurement techniques. In such facilities higher-speed measurement systems that can obtain data at kHz or MHz rates are desirable. Large impulse facilities can move a few centimeters during operation, complicating measurement technique alignment. The flow through longer-run-duration facilities induces vibrations that can misalign optical measurement systems and changes in the model position may occur via thermal expansion of the support system. Furthermore, many large hypersonic facilities have poor or no optical access; if there is optical access the window material may not be suitable for the desired measurement technique. Hypersonic facilities are often located in dirty operating environments and for practical considerations the lasers often are placed far from the test section requiring long path lengths resulting in misalignment and reduced laser energy delivered to the test section. Finally, some hypersonic facilities produce very luminous flow, making difficult the detection of weak light signals. In such flowfields, coherent optical measurement techniques are desirable.

In some instances, it is desired to study nonequilibrium effects. However, nonequilibrium also frequently occurs as a byproduct of heating and accelerating the test gas in hypersonic facilities. For example, in order to achieve the required high flow enthalpy and Mach number, gas is often heated to thousands of Kelvin and then expanded through a nozzle. Energy can be added to the flow using electricity (via convection over a heating element or by an electric arc), by driving shockwaves through the gas, or by combustion [7, 8]. Upstream of the nozzle, the gas can be vibrationally excited and may reach chemical equilibrium in which minor species such as NO, O, and N are present for the case of air. When the gas expands through the nozzle, the collision rate is not sufficient to keep the chemical composition in equilibrium and the chemical composition effectively freezes at an intermediate composition. Similarly, vibrational energy modes do not stay in equilibrium with rotational and translational modes, which can result in $T_{\text{vib}} > T_{\text{rot}} \approx T_{\text{trans}}$. This test gas in a state of chemical and/or thermal nonequilibrium, expanded to the desired Mach number, then passes over the test article being studied. An accurate understanding of the nozzle exit, or *freestream* conditions, is required to properly characterize the test stream, calibrate the facility, interpret the test results and to scale the test results to flight. For a detailed description of the different types of hypersonic test facilities see the chapter 7 titled “*High Enthalpy Facilities and Plasma Wind Tunnels for Aerothermodynamics Ground Testing*” in this manuscript.

The next section of this chapter reviews some of the equipment commonly used to perform the different measurement techniques. The following sections

introduce and develop the theory behind some of the most important measurement techniques used to study hypersonic nonequilibrium flows. Theoretical developments are limited to introductory material with references provided for more detailed analysis. Then, selected measurement examples are described. These examples do not provide an exhaustive review but are meant to illustrate typical applications. When possible, applications to hypersonic nonequilibrium flows are shown. However, examples of other flowfields are provided if the measurements demonstrate the potential for application to hypersonic nonequilibrium flows.

II. EQUIPMENT USED FOR MOLECULAR-BASED OPTICAL MEASUREMENT

There are similarities in the hardware used in most optical spectroscopic measurement systems. Some of the more common lasers and detection systems will be summarized here. References for commercially available equipment described are not cited to avoid preferential treatment to certain vendors. It is difficult to capture all possible types of lasers and optical detection systems in a few paragraphs. This section is intended to provide an introduction and overview to the uninitiated and is not a comprehensive discussion. The various specifications described are approximate and are presented only to provide rough orders of magnitude.

Laser systems can be classified as continuous wave or pulsed, though hybrid systems also exist. Continuous wave (CW) lasers operate continuously and are specified by their operating power in Watts. CW lasers can be made to operate with very narrow spectral resolution suitable for high-resolution spectroscopy where the spectral width of the laser is negligible compared to the spectrum being measured. Inexpensive, low powered diode lasers having power on the order of 1 mW are used for absorption measurements. Higher powered CW lasers on the order of 10 W are used for Rayleigh scattering measurements. These higher powered CW lasers are generally not broadly tunable, so for resonant techniques such as LIF only coincidental spectral overlaps between available laser frequencies and atomic or molecular transitions can be exploited. To perform spectroscopic measurements at arbitrary wavelengths, high-powered CW lasers can be converted to tunable light using dye lasers and/or other energy conversion systems such as doubling or mixing crystals, sometimes in combination with other CW lasers. Currently, high-resolution (i.e., laser linewidth much narrower than the typical absorption linewidths) CW lasers are available commercially from the ultraviolet (UV) to the infrared (IR). The main limitations of CW lasers are their relatively low power output which may require long integration times to acquire data with sufficient signal-to-noise ratio in some applications. Whereas absorption spectroscopy, which detects the full laser beam, can be performed at hundreds of kHz, scattering approaches such as the Rayleigh, Raman and LIF that use CW lasers typically acquire

data several orders of magnitude slower because of low signal levels. For comparison, a typical hypersonic flow with a gas velocity of 2000 m/s, a 1 mm resolution would require 500 ns time resolution, corresponding to 2 MHz data acquisition rate.

Diode lasers provide CW light in most wavelength ranges of spectroscopic interest from the ultraviolet to the far infrared. Wavelengths can be varied over a limited range by modulating the temperature or injection current of the diode, at up to MHz scan rates [9], providing extremely high time resolution for wavelength-scanning measurements. Because the lasers and detectors are small, have no moving parts, and the lasers are often coupled to optical fibers, these devices can be used to produce relatively robust measurement systems that are particularly well suited to the often harsh environments associated with nonequilibrium hypersonic flows. These characteristics have made diode laser absorption spectroscopy a particularly desirable technology for hypersonic flight testing programs [10].

Pulsed lasers typically producing much higher power (on the order of 10^8 Watts) for short durations, typically over a few nanoseconds, have been commercially available for about three decades. Such powers are usually required to perform nonlinear spectroscopic measurement techniques such as CARS. These lasers are usually specified in terms of the energy per pulse. For example, frequency doubled Nd:YAG laser systems can produce 1 J per pulse at 532 nm. Again, this type of laser is not broadly tunable but it can be used to pump a dye laser or optical parametric amplifier and together with other conversion devices (doubling and/or mixing crystals) can produce high-energy tunable output from the UV to the IR. Ten ns duration pulsed lasers allow measurements to be made with time resolution that “freezes” the flow (prevents blurring). Raman, Rayleigh, PLIF and CARS systems based on Nd:YAG lasers typically integrate signals over 10 to 500 ns time durations. Unfortunately, commercially available high energy pulsed laser systems typically operate at repetition rates of 10 to 100 Hz, which according to the calculations above, are too slow to resolve unsteady flow fluctuations. Therefore, individual measurements can be considered instantaneous, but successive measurements are not correlated in time. The linewidth of pulsed lasers is typically broader than high-resolution narrowband lasers because of a number of factors. A consequence of the Heisenberg uncertainty principle is that the shorter the duration of a laser pulse the spectrally more broad the laser pulse will be. Consequently, the spectrally narrowest 10 ns pulses typically have line widths equal to 0.004 cm^{-1} . These pulses are routinely obtained by injection seeding pulsed Nd:YAG lasers so that only a single longitudinal mode is amplified. These injection-seeded pulses are much broader than commercially available CW Nd:YAG lasers. Without seeding, the same Nd:YAG laser would have an even larger linewidth of about 1 cm^{-1} . Nd:YAG-pumped narrowband dye lasers typically have line widths within the range of 0.03 to 0.5 cm^{-1} , although modifications such as injection seeding or intercavity etalons can be used to reduce the linewidth of a pulsed dye laser. Conversely,

spectrally selective elements can be removed to create a broadband (red) dye laser with a linewidth of 20 nm ($\sim 500 \text{ cm}^{-1}$) or more [11].

There are several new laser technologies that have been developed in the past decade with high output power and fast repetition rates. This allows for flow freezing, temporally resolved measurements to be obtained with good signal-to-noise levels. *Pulse burst laser* technology uses Nd:YAG lasers that have been optimized to be pulsed 25–100s of times in succession at frequencies up to 1 MHz. Pulse burst laser technology is not yet widely commercially available although it is being brought to market. Another relatively new technology that produces high power and high repetition rates is known as *ultrafast* or *femtosecond* lasers. As the name implies, the duration of the laser pulses can be nearly a million times shorter than a typical nanosecond laser. While the energy per pulse (typically less than 10 mJ, for commercially available systems) is much lower than ns-based systems, the output power can be on the order of 10^{10} Watts, opening up new opportunities for coherent measurement approaches. Such high powers can be efficiently converted using optical parametric amplifiers and doubling or mixing crystals to extend the tuning range of femtosecond lasers to the UV and IR. Femtosecond lasers are commercially available at repetition rates up to 10 kHz—still two orders of magnitude too slow to time-resolve unsteady hypersonic flows. Even though the resulting measurements would not be time correlated, such high data rates are especially useful for acquiring statistics in short duration or expensive-to-operate test facilities. The higher data rate allowed by femtosecond lasers would be beneficial in most experiments. Picosecond-duration lasers are also available for spectroscopic measurement applications though picosecond lasers have neither the high energy per pulse of nanosecond lasers nor the high peak power of femtosecond lasers. The linewidth of a femtosecond laser is closely related to the duration of the pulse. Typical off-the-shelf femtosecond lasers with pulse duration on the order of 100 fs have linewidths of ~ 10 nanometers. Although this relatively large linewidth prevents conventional high-resolution spectral-domain spectroscopy, the time domain can instead be used to obtain detailed spectral information.

Most measurement techniques use some type of spectrally selective optic or optical system to collect or process signal. The simplest spectrally selective optic consists of filters that are placed in front of detectors or cameras. Absorptive and reflective filters are commercially available (or can be custom manufactured at a reasonable cost) at many wavelengths, for example to block the laser's wavelength and collect the signal in another wavelength. In some applications, the narrower the spectral filter the better, as the signal is often very close to the laser's wavelength such as in Rayleigh and rotational Raman scattering. Spectral filters blocking a 10–20 nm full width half maximum (FWHM) wide band near the laser's wavelength with greater than 6 orders of magnitude of attenuation while transmitting $>95\%$ of the Raman shifted signal can be purchased. However, such filters do not provide sufficient resolution to observe Doppler broadening

and Doppler shifts required for gas temperature and velocity measurement from Rayleigh scattering, for example. Gaseous filters, such as I₂ vapor contained in a heated cell, can provide spectrally narrow (0.0015 nm or 0.05 cm⁻¹ FWHM) and high (6 or more orders of magnitude) absorption which is useful in many applications [12]. Etalons are spectrally dispersive optics or optical systems that are made of a pair of partially reflective mirrors. An etalon's resolution depends on its flatness and reflectivity; the resolution can be high enough (0.01 cm⁻¹) to resolve the Doppler broadening (0.05–0.5 cm⁻¹) in typical hypersonic flow experiments and have an advantage over gas filters in that they can operate at any wavelength. Spectrometers, containing a dispersive optic such as a prism or grating, are typically used to disperse a signal beam into a spectrum that can be acquired by a detector or camera. Small (100 mm focal length), easy-to-use fiber-optic coupled spectrometers are commercially available for applications in which spectral resolution on the order of 0.02 nm (5 cm⁻¹) is acceptable. Larger spectrometers (for example with 1 meter or longer focal length) provide higher resolution spectra—the resolution generally increasing linearly with the focal length. Coupled with a charge coupled device (CCD) camera, such spectrometers can typically achieve resolutions of 0.15 cm⁻¹/pixel [13]. Resolution can sometimes be improved by using a camera with smaller pixels or by using a telescope at the exit of the spectrometer to enlarge the spectrum [14].

For spectroscopic measurement techniques, light is detected with a variety of different single point, line, or imaging devices. Among single point detectors, photodiodes are typically used in applications where the intensity of the collected light is high, for example in absorption spectroscopy. Photodiodes are used because they are linear over a wide range of light intensities, have fast time response, require relatively simple electronics and are inexpensive to produce. Photomultiplier tubes (PMTs) are usually single-point detectors but they allow variable gain useful for amplifying light at low signal levels, while also providing fast (sub-ns) time response. Although photodiodes and PMTs are both available as linear and even two-dimensional (2-D arrays, other camera technologies are usually used in spectroscopic applications where high-resolution spatial or spectral information is required. CCD cameras provide the linear response (less than 1% nonlinearity), high dynamic range (12–16 bits) and high sensitivity required by many spectroscopic imaging or spectral applications. For applications requiring short exposures, for example to freeze the flow or to reject unwanted luminosity while capturing a transient signal, CCD cameras can be fitted with an image intensifier allowing exposure times down to hundreds of picoseconds. CCD cameras having 1 million pixels or more typically frame at tens of Hz consistent with high-powered YAG laser systems. CCD camera technology has been extended to much higher speeds (up to MHz rates) albeit with lower spatial resolution (e.g., 160 × 160 pixels). Recently, CMOS camera technology has allowed megapixel cameras to frame at tens of thousands of Hz allowing new opportunities for optical measurement techniques.

III. OPTICAL EMISSION SPECTROSCOPY

Optical emission spectroscopy (OES) is one of the oldest diagnostic techniques and has been applied to various fields of research. Traditionally, astronomy was one of the first fields to apply this passive method. Due to the large distances to even the nearest stars, emission spectroscopy continues to be one of the main techniques for understanding the stars. Despite its disadvantages, OES presents an often simple experimental method to access the thermochemical state of emitting gases. The experimental setups are relatively simple (not requiring a laser, for example) and the underlying optical principles well understood. However, the scope of this chapter does not allow for a complete description of emission spectroscopy methods applied to plasma diagnostics, even if restricted to nonequilibrium applications. Instead, selected examples of successful applications to nonequilibrium environments will be shown to demonstrate fundamental approaches to access these complicated problems.

In general, emission spectroscopy (if properly calibrated) can provide absolute, quantitative information on excited states (electronic, vibrational, or rotational). However, even in strongly radiating environments, the majority of particles will be in the ground state or in weakly excited levels. Therefore, an extrapolation of the measured quantities to the low lying states is necessary to obtain information about the gas chemistry. In thermodynamic equilibrium, the upper state population distributions are linked to the ground state through known relations, given by Boltzmann distributions. Even if temporal or spatial changes occur in a medium, an equilibrium assumption may be justified if the variations are slow enough that, for any point, one can assume thermodynamic equilibrium in some neighborhood about that point. This condition is widely called local thermodynamic equilibrium (LTE). When nonequilibrium processes are involved, these relations may no longer hold. Hence, a combination with other methods (LIF, CARS, absorption spectroscopy, etc.), which can access the ground and excited states not covered by emission spectroscopy, may better describe the thermodynamic state of the plasma. However, even without knowledge of the relation to the total particle density of the species under consideration or under nonequilibrium conditions, basic information may be extracted from spectral features. In particular, the line shape of individual lines carries important information on translational temperature which often can be determined from Doppler broadening or the electron density can be inferred from the line's Stark broadening. Line ratios may be used to determine rotational, vibrational, or electronic excitation temperatures as opposed to the absolute intensity of the detected emission. Ratios between lines from inert elements (e.g., argon) and reacting components such as oxygen may carry information on chemical processes, even in nonequilibrium situations, without the need to compute total species densities.

One major difficulty of emission spectroscopy measurements is that each measurement provides integrated intensities along the entire line of sight.

Furthermore, absorption along this line cannot be separated from single measurements. In case of an optically thin medium, local distributions can be obtained through tomographic methods or through deconvolution of vertical profiles (e.g., through Abel-inversion or related methods if rotational symmetry of the emitting volume can be assumed). In the general case of an absorbing medium, only indirect methods made through a comparison with computed radiation based on numerical simulation are feasible.

Emission spectroscopy is typically performed in atmospheric entry wind tunnel tests for at least two different reasons: 1) to determine radiation as a load factor for design purposes (typical examples are given by recent testing in the NASA Ames EAST facility) [15], and 2) to use radiation as a tool for diagnostic purposes, e.g., for facility characterization [16] or to gather information for comparisons to numerical simulation (e.g., material response). One further important application of emission spectroscopy is flight measurements which can provide validation data for theoretical simulation and extrapolation to flight of ground test data, either by flight experiments [17, 18] or by airborne or ground based observation [19–21]. In industrial plasma applications (e.g., coating or edging), OES may be used for process control through empirical correlations or even to provide information on the underlying physics.

The more recent development of off-the-shelf miniaturized spectrometers and the availability of fiber-coupled instrumentation have simplified emission instruments. The hardware requirements can be roughly grouped into systems with 1) low resolution for survey and overview applications, 2) more sophisticated instruments (usually with larger focal length) for higher spectral resolutions of specific spectral features such as molecular band structures, and 3) high-resolution systems (e.g., Fabry–Perot interferometers) for detailed investigation of single spectral lines in particular for the investigation of line shapes and broadening mechanisms.

The following sections will give a short introduction to basic physics for emission of radiation of atoms and molecules followed by examples for plasma diagnostics to determine temperatures, velocities, or even particle densities. A description of some simulation codes with particular respect to hypersonic flows and examples for successful simulation of equilibrium plasmas with these codes will also be given. In a second part, the effect of nonequilibrium on plasma radiation will be discussed with examples showing emission spectroscopy applied under nonequilibrium conditions.

A. BASIC PHYSICS DESCRIBING THE EMISSION OF ATOMS AND MOLECULES

Unlike the emission of thermal radiation of solid bodies, which yields continuum radiation following Planck's formula, the emission of flames and plasmas usually consists of discrete emission lines. If measured in lower spectral resolution these lines appear as bands. These lines and bands originate from bound–bound transitions (i.e., in both upper and lower states of the transition, the participating

electron is bound to an atom or molecule). These line spectra may overlap with continuum radiation produced through free-free or bound-free radiation generated through interaction of electrons with each other or heavy particles (nonelectrons) which, in the latter case, involves ionization and recombination processes. In general, the prediction of single emission lines can be divided into three problems:

1. determination of the spectral position of the line using empirical or quantum mechanical information on the governing energy difference,
2. determination of the line strength using thermodynamic information about the plasma state (i.e., the upper state population), and
3. determination of the spectral shape of the line determined by broadening processes, again from the thermodynamic state (e.g., the gas temperature for Doppler broadening and pressure/species information for pressure or/and Stark broadening).

For bound-bound emission processes, each emission line will be produced through a radiative transition from an upper energetic state E_2 to an energetically lower state E_1 as indicated in Fig. 1. The resulting photon will carry the energy difference $\Delta E = E_2 - E_1$ which determines its frequency

$$\nu = \Delta E / h \quad (1)$$

with Planck's constant h . This frequency is equivalent to the speed of light divided by the wavelength of the emitted radiation, in a vacuum:

$$\nu = c_0 / \lambda \quad (2)$$

Often, the energy is used and tabulated normalized by the product of $(h c_0)$, given in the unit [cm^{-1}]. Consequently, the spectral position of an emission line might be characterized by its wave number, $\bar{\nu}$, which is the inverse of its wavelength, again often given in [cm^{-1}].

The energy emitted by one emission line, often called the volumetric emission coefficient, can be written as the energy of one photon ($h\nu$) times the number of atoms which undergo this transition per unit time, defined as a probability (Einstein coefficient of spontaneous

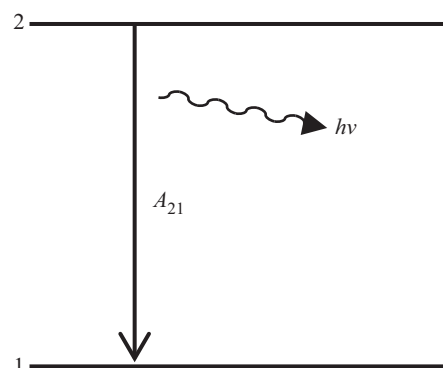


Fig. 1 Energy level diagram for spontaneous emission.

emission, A_{21}) times the population density in the upper energy state, emitted into full space of 4π :

$$\varepsilon_{21} = \frac{h\nu}{4\pi} A_{21} n_2 \quad (3)$$

We recognize that the emitted power depends on the product of the transition probability A_{21} , which only depends on the quantum mechanical characteristics of the energy level E_2 , and the upper state particle density n_2 which depends on the thermodynamic state of the emitting medium. For a computation of the emitted power, we therefore have to determine the quantum mechanical relations for the species and the energy level of concern and the thermodynamic state of the emitting gas.

First, let us consider the emission of atoms, which then will be extended to molecule emission. For atoms, the only degree of freedom for excited states is given by electronically excited levels. These excited levels are not arbitrary but characteristic for each species. In the simplest case of a hydrogen atom with only one electron, the energy levels can be calculated through the Rydberg formula, resulting in a series of spectral lines emitting at wavelengths, λ :

$$\frac{1}{\lambda} = R_H \left(\frac{1}{n_1^2} - \frac{1}{n_2^2} \right) \quad (4)$$

where R_H is the Rydberg empirical constant. The energy levels can also be expressed in terms of the angular momentum of the electrons (by Planck) as:

$$\Delta E = \frac{k^2 e^4 m}{2} \left(\frac{1}{L_1^2} - \frac{1}{L_2^2} \right) \quad (5)$$

who also expressed R_H is given by universal constants:

$$R_H = \frac{2\pi^2 k^2 e^4 m}{ch^3} \quad (6)$$

For more complex atoms with more electrons, such laws cannot be easily derived and laws for allowed radiative transitions between electronically excited states must be extracted from quantum mechanics. Detailed descriptions of the nomenclature and the basic governing processes are found for example in References [22] and [23], tables for transition probabilities for the different atoms can be found in Reference [24] or in online databases, for example published and maintained by the National Institute of Standards and Technology (NIST) [25]. These transitions can be summarized in so-called Grotian diagrams [26].

To determine the final emission coefficient, the number of particles in the upper excited state must be known. In general, this could be done by balancing all populating and depopulating processes, such as collisions (excitation and quenching), radiative transitions (absorption and emission), and chemical reactions. In thermodynamic equilibrium, the forward and backward processes

equal each other and the plasma will achieve a stationary state in which the populations of the excited states, n_2 , are related to the total density of the species of concern, n_0 , by a Boltzmann distribution:

$$n_2 = \frac{g_2}{Q(T_{\text{ex}})} n_0 \exp\left(-\frac{E_2}{kT_{\text{ex}}}\right) \quad (7)$$

with the excited state energy, E_2 , the excitation temperature, T_{ex} , the multiplicity (sometimes called degeneracy) of the upper state, g_2 , and the temperature dependent partition function, Q :

$$Q(T_{\text{ex}}) = \sum_i g_i \exp\left(-\frac{E_i}{kT_{\text{ex}}}\right) \quad (8)$$

Under nonequilibrium conditions, the population balance for each individual state has to be determined separately by considering all individual processes. Common approaches for such situations will be discussed in the second part of this chapter.

For molecular emission, the same principles used for atoms apply but additional degrees of freedom of rotation and vibration have to be considered. Internal energy now can be stored in all three degrees of freedom and a radiative transition may contain contributions of all three energies. Therefore, the relation for one photon becomes:

$$\Delta E = \Delta E_{\text{el}} + \Delta E_{\text{vib}} + \Delta E_{\text{rot}} = h\nu = \frac{hc}{\lambda} \quad (9)$$

The following considerations are restricted to diatomic molecules, which are relatively well understood and also are the major molecular constituents of high-temperature air (N_2 , O_2 , and NO). The governing processes for poly atomic molecules become rapidly too complicated to be considered in this work. Although simplified models for diatomic (considering the molecule as two point masses with a rigid massless connection (rigid rotator) or as two point masses connected by a perfectly elastic massless spring (harmonic oscillator)) are sometimes used in computational fluid dynamics to account for the internal energies, these models are not sufficient for spectroscopic considerations, in particular at high temperatures. The molecular potential are usually described by an anharmonic oscillator where the energy approaches infinity as the nuclear distance decreases and approaches the dissociation energy with increasing internuclear distance. The solutions of the Schrodinger equation yield discrete energy levels, characterized by the vibrational and rotational quantum numbers V and J . Figure 2 illustrates a molecular transition.

Recently, ab initio computations for molecular potentials were performed using quantum chemistry [27]. However, these models require substantial computational effort both during the initial calculations and in post processing. More commonly, approximations as proposed by Dunham [28] are used where

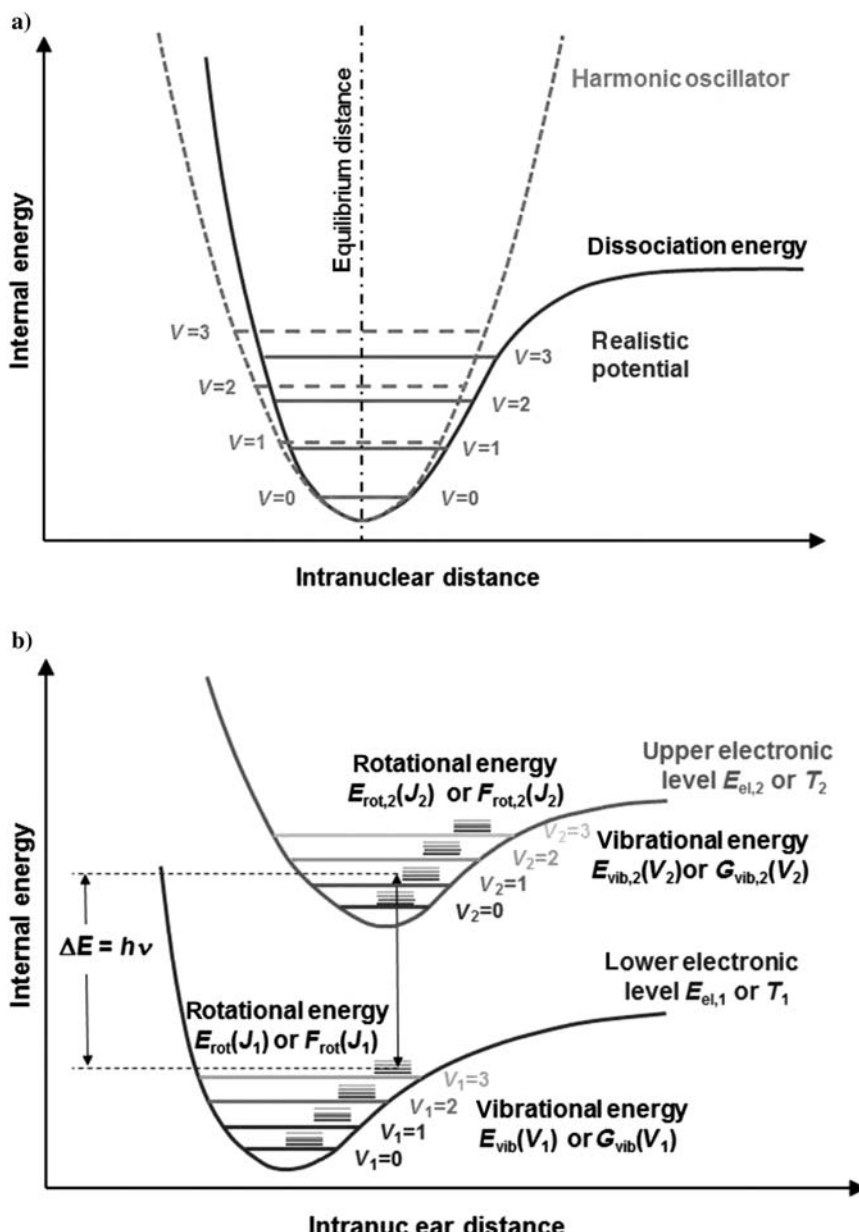


Fig. 2 Illustrations of a) vibrational potentials of a harmonic oscillator and a realistic molecular potential, and b) a ro-vibrational transition between two electronic levels.

vibrational and rotational energies are approximated through polynomial series depending on the rotational and vibrational quantum numbers J and V . Usually, vibrational and rotational energies, respectively, are computed in the normalized form with the units [cm^{-1}] with the spectroscopic constants derived from empirical observation [22]:

$$G(V) = \omega_e \left(V + \frac{1}{2} \right) - \omega_e x_e \left(V + \frac{1}{2} \right)^2 + \omega_e y_e \left(V + \frac{1}{2} \right)^3 + \omega_e z_e \left(V + \frac{1}{2} \right)^4 + \dots \quad (10)$$

$$F_V(V, J) = B_V J(J+1) - D_V J^2(J+1)^2 + \dots \quad (11)$$

where the coupling constants B_V and D_V are given by:

$$B_V = B_e - \alpha_e \left(V + \frac{1}{2} \right) + \gamma_e \left(V + \frac{1}{2} \right)^2 + \dots \quad (12)$$

$$D_V = D_e + \beta_e \left(V + \frac{1}{2} \right) + \delta_e \left(V + \frac{1}{2} \right)^2 + \dots \quad (13)$$

The coefficients for these series can be found in the literature. Detailed computation of different molecules may take additional effects into account such as spin splitting, lambda doubling, etc. A rather complete description was given by Herzberg [22], whereas more current molecular constants for air were published by Gilmore et al. [23].

The dependence of rotational energies on vibrational quantum numbers shown in Eq. (11) yields a deformation of the molecular potential with rotational excitation rather than just a vertical shift in energy as suggested by the illustration in Fig. 2.

The resulting potentials show a potential well above the dissociation limit (and therefore stable excited molecules with energies higher than the dissociation energy) [30] as shown in Fig. 3.

If a truncated Dunham series (10 and 11) after second-order terms is used, Morse showed that an exact solution for the Schrodinger equation representing the motions of the nuclei in a diatomic molecule can be found [31]. He proposed a molecular potential in the form:

$$U(x) = D_e \left(1 - e^{-\beta x} \right)^2 \quad (14)$$

With the well depth of the potential D_e , the difference x to the equilibrium distance r_e , and the parameter β that depends on the Eigen-frequency of the oscillator ω_0 , the reduced mass of the molecule μ_A and D_e [31]:

$$\beta = 1.2177 \cdot 10^{-7} \omega_e \sqrt{\frac{\mu_A}{D_e}} \quad (15)$$

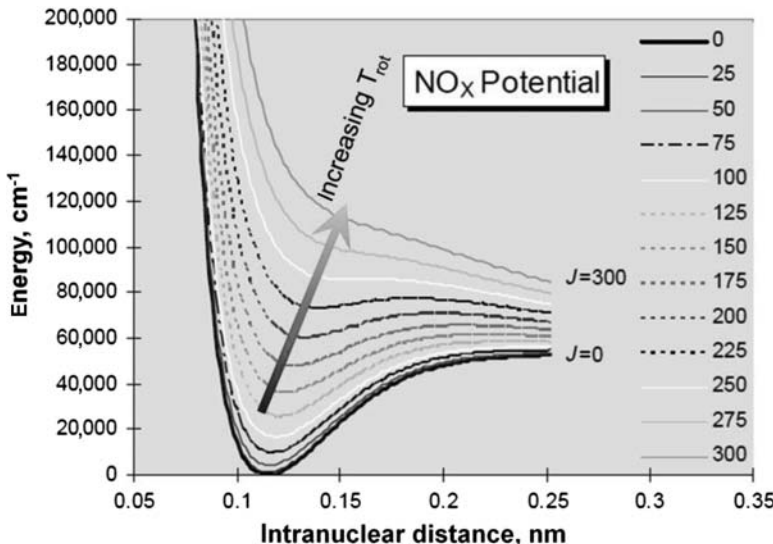


Fig. 3 Deformation of the NO ground state potential with rotational quantum number [30]. Modified and reprinted with permission of the author.

This representation, however, becomes inaccurate for high quantum numbers and more sophisticated potentials may be used, e.g., the three parameter Lippincott potential [32], the five parameter Hulbert–Hirschfelder potential [32], or Rydberg–Klein–Rees (RKR) potentials [33].

For the computation of line strengths, the definition of the volumetric emission coefficient remains but the transition probability becomes a function of the relation between the upper and lower state rotational and vibrational configuration, the indices ' and " indicating the upper and lower state, respectively:

$$\varepsilon_{2-1} = \frac{\Delta E}{4\pi} A_{2-1} n_2 = \frac{16\pi^3 c \bar{v}^4}{3} (R_e(\bar{r}_{v'v''}))^2 q_{v'v''} \frac{S'_{J''\Lambda''}^{J'\Lambda'}}{2J'+1} n_2 \quad (16)$$

(1) (2)

J' is the rotational quantum number of the upper state, the electronic transition moment $(R_e(\bar{r}_{v'v''}))^2 q_{v'v''}$ describes the probability of a particular electronic transition depending on the inter-nuclear distance, the Honl–London factor $S'_{J''\Lambda''}^{J'\Lambda'}/2J'+1$ indicates how the total intensity of a transition is distributed among the different branches (in the easiest case the P-, R-, and Q- branches defined by a change in rotational quantum number from the upper state to the lower state of -1, 1, or 0, respectively).

Fig. 4 Illustration of the Franck-Condon principle. Reprinted from Reference [60] with permission of Springer Science and Business Media.

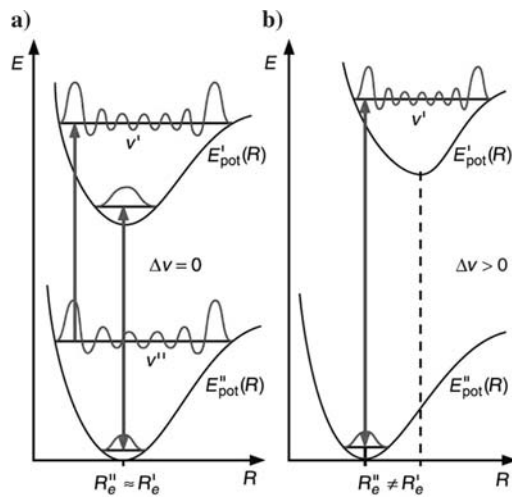
The electronic transition moment is based on the Franck-Condon principle which postulates that the internuclear distance does not change during the transition. Therefore, the wave functions of the upper and lower level will yield a higher transition probability when the overlap of the upper and lower molecular potentials is larger as illustrated in Fig. 4. The transitions indicated by solid lines are probable because of the overlap of wave functions. The hypothetical transition indicated by the dashed line on the right side of Fig. 4 is not possible because of nonoverlap of the wave functions caused by the different internuclear spacing in ground and electronic states. Both the electronic transition moment and the Honl-London factor depend on the molecular species of concern.

In equilibrium, population of each energy level is distributed through a Boltzmann distribution. Although the definition of thermodynamic equilibrium postulates that only one temperature governs all distribution functions, separate temperatures for rotational, vibrational, and electronic excitation are already introduced at this point to be able to extend these considerations to different degrees of nonequilibrium. Therefore, the upper-state density now depends on three temperatures and can be described through a combination of three Boltzmann distributions of rotational, vibrational, and electronic energy:

$$N_2 = N_{\text{tot}} \frac{g_{e'} (2J' + 1)}{Q(T_{\text{el}}, T_{\text{vib}}, T_{\text{rot}})} \exp\left(-\frac{E_{\text{el}}^{e'}}{kT_{\text{el}}}\right) \exp\left(-\frac{E_{\text{vib}}^{e'V'}}{kT_{\text{vib}}}\right) \exp\left(-\frac{E_{\text{rot}}^{e'V'J'}}{kT_{\text{rot}}}\right) \quad (17)$$

with the partition function:

$$\begin{aligned} Q &= \sum_{e'V'J'} Q_{\text{el}}^{e'} Q_{\text{vib}}^{e'V'} Q_{\text{rot}}^{e'V'J'} \\ &= \sum_{e'V'J'} g_{e'} \exp\left(-\frac{E_{\text{el}}^{e'}}{kT_{\text{el}}}\right) \exp\left(-\frac{E_{\text{vib}}^{e'V'}}{kT_{\text{vib}}}\right) (2J' + 1) \exp\left(-\frac{E_{\text{rot}}^{e'V'J'}}{kT_{\text{rot}}}\right) \end{aligned} \quad (18)$$



B. LINE SHAPE OF EMISSION LINES AND LINE BROADENING

So far, each emission line was considered to be emitted at one discrete wavelength determined by the energy difference of the upper and lower different states. However, emission and absorption lines can be broadened through different processes (some of which are detailed in the next section on Absorption Spectroscopy) such as the following.

1. Natural broadening owing to the Heisenberg uncertainty principle (Lorentzian)
2. Doppler broadening due to the thermal motion of the emitting particles (Gaussian)
3. Collision broadening (Lorentzian)
 - i) Van-der-Waals owing to collisions with neutrals
 - ii) Resonance broadening due to collisions with the like species (perturber's state connected by an allowed transition to the upper or lower state of the transition)
 - iii) Stark for interactions with ions or electrons, specific for each transition/line
4. Zeeman effect owing to interaction with magnetic fields (Lorentzian)

Each of these processes actually causes a line shift for each photon. The integration over many photons with different shifts produces a broadening by distributing the transition energy over a certain wavelength (or wave number) range. Depending on the physical effect, the final line shape will follow a Gaussian or a Lorentzian profile. Usually, the broadening is described by the linewidth at its half maximum (full width, FWHM, or half width, HWHM). Half widths of Lorentz profiles can be summed up linearly, half widths of Gaussian profiles can be summed in quadrature: $FWHM_{G,\text{total}} = \sqrt{FWHM_{G,1}^2 + FWHM_{G,2}^2}$. If several processes occur simultaneously, the resulting broadening may be described by a Voigt profile. Spectral lineshapes are detailed in Sec. IV of this manuscript, which focuses on Absorption Spectroscopy.

C. SPATIAL RESOLUTION

One major disadvantage of emission spectroscopy (shared with absorption spectroscopy) is the integrating character of the measurements. Even if the setup is focused on one particular point in the field of view (e.g., the centerline of a flow field), the detected signal is not limited to that point. In a radiating volume, the measured signal will result from an integration along the line of sight with all cross sections along this line contributing with equal efficiency as long as the local cross section defined by the limiting rays does not exceed the

volume dimensions. The measured integrated intensity $I(z)$ is coupled to the local emission coefficient $\varepsilon(r)$ by the Abel equation [34]:

$$I(z) = 2 \int_{r=z}^R \frac{r}{\sqrt{r^2 - z^2}} \varepsilon(r) dr \quad (19)$$

where R is the outer radius of the measured volume, z the off-axis position, and r the local radius. Solving for $\varepsilon(r)$ yields

$$\varepsilon(r) = -\frac{1}{\pi} \int_{z=r}^{\infty} \frac{(dI/dz)}{\sqrt{z^2 - r^2}} dz \quad (20)$$

In the special case of axi-symmetry and an optically thin volume radiator, local emission values can be determined by analyzing a series of off-axis lines of sight. For the example of a homogeneously emitting medium, an elliptic distribution of the measured emission vs off-axis position will be obtained. Local values may be obtained by applying a so-called Abel-inversion. However, an analytical solution can only be found if the measured profile vs off-axis position can be described by particular functions (such as a Gaussian distribution, a pair polynomial function, or elliptic functions). In the general case, i.e., if the measured profile $I(z)$ cannot be described by one of the above mentioned functions, approximate methods can be used. The most common one is the “onion peeling” method:

Each measurement is interpreted as an average over a ring with constant emission coefficient measured at an off-set value z_j . The emission along the lines of sight is then the sum of the individual emission coefficients e_i times the length $L_{j,i}$ with which the line of sight cuts each individual ring r_i , yielding a rather simple system of linear equations. The geometric principle is illustrated in Fig. 5a for four measurement positions. The system for four lines of sight reads as:

$$\begin{aligned} I_{3,int}(z_3) &= \varepsilon(r_3) L_3(r_3) \\ I_{2,int}(z_2) &= \varepsilon(r_3) L_2(r_3) + \varepsilon(r_2) L_2(r_2) \\ I_{1,int}(z_1) &= \varepsilon(r_3) L_1(r_3) + \varepsilon(r_2) L_1(r_2) + \varepsilon(r_1) L_1(r_1) \\ I_{0,int}(z_0) &= \varepsilon(r_3) L_0(r_3) + \varepsilon(r_2) L_0(r_2) + \varepsilon(r_1) L_0(r_1) + \varepsilon(r_0) L_0(r_0) \end{aligned} \quad (21)$$

and can even be solved recursively for small numbers of off-axis positions or through matrix inversion for a larger set of measurements. For this method, the individual lines of sight do not have to be parallel to each other, e.g., if the variation of z is realized through tilting the optical axis rather than moving the setup, as illustrated in Fig. 5b. To reach higher accuracy, radial distributions over each ring element might be assumed and included in the set of equations.

D. ANALYSIS OF EMISSION SPECTROSCOPY DATA

The most traditional application (e.g., in astronomy, or process control in industrial applications) of emission spectroscopy is probably the identification of

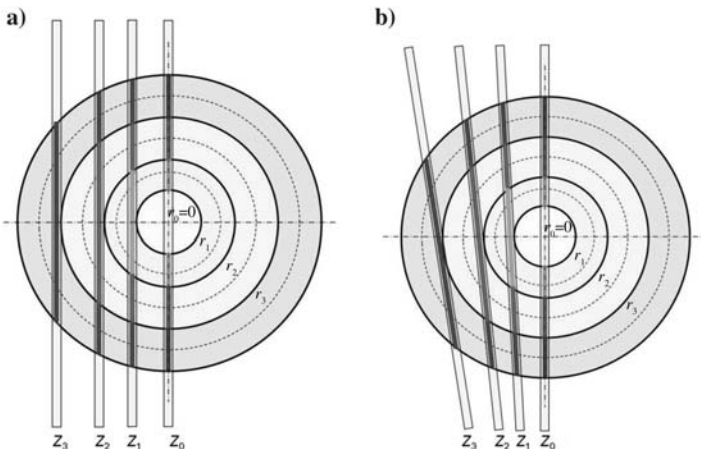


Fig. 5 Illustration of the Abel-inversion principle for a set of off-axis measurements a) parallel to the rotational symmetric radiation field, and b) realized through tilting the detection setup (from Reference [35]). Reprinted with permission of the authors.

radiating species in the emitting medium. Even for an unknown thermodynamic state of the emitting medium, the simple occurrence of particular emission lines is proof for the existence of the element of concern. If a number of species contribute to the unknown spectrum, the occurrence of multiple lines of the same element can provide a conclusive identification. As the emitted spectrum will change with temperature, some basic knowledge of the thermodynamic state might be required already at that stage of interpretation. For industrial applications, an engineering approach might be suitable where spectra are recorded at the desired condition, and only deviations from these spectra are used as indication for a possible failure of the process without even knowing the cause.

If quantitative measurements of the chemical composition are intended, however, the thermodynamic state of the emitting medium has to be known to a significant accuracy. All atomic emission lines (and most molecular spectra in the visible to near-infrared region) will originate from electronically excited states. Quantitative interpretation of these spectra requires detailed knowledge of the population of these excited states and their link to the ground state of the species of concern which, even at high temperatures, usually contains the highest density. Without detailed collisional models, quantitative interpretation usually requires the validity of Boltzmann distributions, and therefore an assumption of equilibrium. In general, equilibration will be reached through collisional energy exchange. As described in the introduction, the various forms of internal energies (rotational, vibrational, and electronic excitation) require different numbers of collisions to equilibrate. Whereas some 10s of collisions are needed to equilibrate rotational excitation, vibrational equilibration already requires

some 100s of collisions, and electronic excitation may be reached after several 1000s of collisions during the life time of the excited states [36]. Therefore, equilibration of electronic excitation with the ground states is most likely achieved at high pressures.

1. TEMPERATURE DETERMINATION METHODS

Although number densities usually require quantitative knowledge of the absolute measured emission, temperatures can be obtained from the qualitative spectral appearance, e.g., from relative line ratios or line shapes. At low pressures, the dominant broadening mechanism of emission lines is the Doppler broadening which is related to the translational temperature through Eq. (21). If the emission lines are measured with sufficiently high spectral resolution, a Gaussian profile can be fitted to the measured line shape and the extracted half width can be evaluated with respect to the governing temperature. The basic assumption is only that the concept of temperature is defined which implies that the thermal velocities are distributed according to a Maxwell distribution. No information about the strength of the measured line is needed. Typical half widths for temperatures up to 10s of thousands of Kelvins are on the order of 10s of picometers (~ 0.5 cm) at maximum. Such spectral resolution is usually obtained through interferometers (e.g., Fabry–Perot interferometers) or Echelle spectrometers. The main influences on the measured data are usually the instrument broadening of the setup used and line broadening caused by other physical effects that are potential error sources that need to be modeled and corrected for. The higher the pressure, the more dominant collisional broadening becomes but collision broadening typically decreases with $T^{0.5}$, whereas Doppler broadening increases with $T^{0.5}$ (from Eq. (11)) [36]. For the individual lines of carbon dioxide (CO_2) or water (H_2O), for example, the Doppler broadening will be dominant at 0.1 atm or below for temperatures higher than 1000 K, whereas at 1 atm Doppler and collisional broadening are on the same order of magnitude for temperatures of 3000 K (compare Fig. 10-7 in Reference [36]).

If a significant amount of ionization occurs (e.g., in electrically heated plasmas), Stark broadening through interaction of excited electronic states with the electrons may contribute to the line broadening. This can potentially interfere with temperature measurements or alternately, allow electron number density measurements. However, Stark broadening factors are different for each individual transition [37], so an appropriate choice of emission lines under investigation may provide useful temperature measurements, even at significant degrees of ionization. On the other hand, the broadening of selected lines (e.g., the hydrogen lines H_α or H_β) may provide measurement of electron density [15, 38]. If no hydrogen is available in the original plasma composition (e.g., for air plasmas) it has been shown that even intentional seeding with small amounts of hydrogen enables electron density measurements at hypersonic conditions while not significantly altering the plasma state.

If lines originating from the same atom or molecule but different excitation energies are measured simultaneously, governing temperatures can be determined from ratios of the total emission of the individual transitions. These data are obtained by integrating the measured spectrum over the line shape (in the following refer to as line emission). If a Boltzmann distribution of the excited states can be assumed, the ratio of different emission lines can be analyzed by evaluating the distribution function with respect to temperature. If the thermodynamic state of the emitting medium is not known to be in equilibrium it is appropriate to analyze more than two emission lines to determine the temperature and, at the same time, prove the validity of the Boltzmann distribution using a so-called Boltzmann plot. If the equation for the electronic excitation of atoms is written as

$$\ln\left(\frac{I_{2-1}}{vA_{2-1}g_2}\right) + \text{const} = -\frac{E_2}{kT_{\text{ex}}} \quad (22)$$

with I_{2-1} being measured line intensities for upper state excited energies E_2 . A plot of the logarithmic terms vs excitation energy follows a straight line if the upper state densities are Boltzmann distributed. The agreement with this straight line shows the validity of a Boltzmann distribution, the slope contains the desired excitation temperature (slope = $-1/(kT_{\text{ex}})$). The higher the difference in excitation energy, the better the accuracy of the measurement, a rule that will be discussed in more detail in the context of PLIF in Sec. IV.E.

However, even if the Boltzmann plot indicates a Boltzmann distribution of the excited levels under consideration, the resulting temperature might not necessarily equal the equilibrium temperature. As illustrated in Fig. 6, in a recombining or ionizing plasma, the population of high electronic lev-

els might be modified with respect to the equilibrium population through the chemical processes (overpopulation of highly excited levels in a recombining plasma, underpopulation in the ionizing case) yielding a Boltzmann-

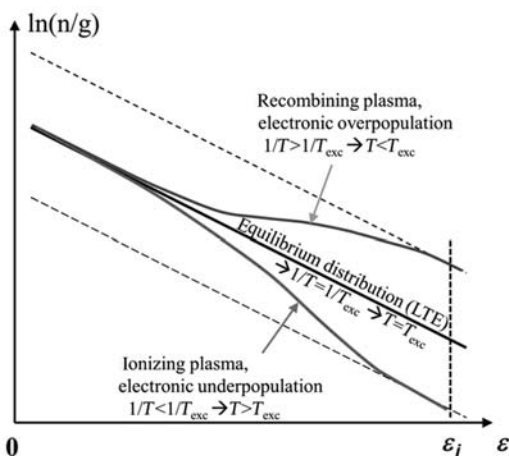


Fig. 6 Effects of the plasma state on electronic excitation temperature in comparison to equilibrium temperature, based approximately on data in Reference [39].

like distribution within the measurement accuracy with a governing temperature different from the equilibrium temperature.

If the same procedure as described above is applied to molecules, similar equations can be derived for rotational, vibrational, and electronic excitation. The individual temperatures can be determined by appropriate selection of evaluated emission lines (for T_{rot} , all lines under consideration should originate from the same upper and lower vibrational and electronic levels, etc.). Figure 7 gives an example of a Boltzmann plot to determine the rotational temperature of N_2^+ in an air plasma from different rotational lines of the 0-0 transition of the N_2^+ 1st Neg. System.

A more common approach in the last few decades, however, to determine vibrational or rotational temperatures is a comparison of a low resolution molecular spectrum with theoretical simulation. The band shapes are usually characteristic for the rotational temperature, band ratios of different upper vibrational excitation levels may be used to determine vibrational temperatures. Again, this method does not necessarily require intensities calibrated to absolute values as only band ratios are used. It is, however, mandatory to at least perform a relative calibration within the wavelength range of concern, even if this range is rather narrow.

2. SIMULATION CODES

Over the years, several codes for the simulation of plasma emission with particular respect to the application to hypersonic flows have been developed worldwide. In the following, only line-by-line approaches are summarized. In these codes, emission, absorption, and broadening properties for each individual transition of the species of concern are calculated, and a final spectrum is composed through a superposition of all lines under consideration. In comparison with other methods (smeared band, narrowband, or wideband models) that are usually faster, line by line models still yield the most accurate simulation and offer the advantage of covering all ranges of spectral resolution (e.g., through simulation in high spectral resolution, followed by a spectral integration). Typically, lines of

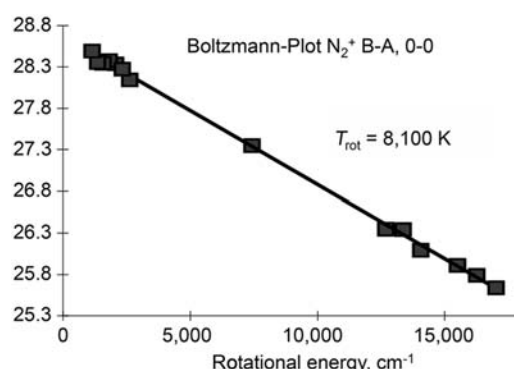


Fig. 7 Boltzmann-Plot for the determination of rotational temperature from rotational lines of the 0-0 transition of the N_2^+ 1st Neg. system in an air plasma based on data from Reference [29]. Reprinted with permission of the American Institute of Aeronautics and Astronautics.

sight through a radiating volume with known composition are constructed and the emission is propagated through this volume. Typical applications are found in rebuilding experimental conditions in ground experiments or flight for a comparison of measured data. Another task is to determine radiation loads in ground test facilities or, even more important, in flight situations to determine final loads and support the design process. A list of some important codes is given in Table 1. Again, it is not possible to cover all existing codes, so the list was compiled with the intention of being representative but not comprehensive. Typically, these codes are under continuous development to account for recent simulation demands (e.g., adding radiating species for atmospheric entries into other celestial bodies' atmospheres, the most recent examples being Mars, Titan, or Venus) and new physics models being developed.

E. APPLICATION EXAMPLES OF EMISSION SPECTROSCOPY

Below we present some typical examples of the application of emission spectroscopy to hypersonic flows in ground test facilities. There is a wide spectrum of facilities operational around the world which may be divided up into impulse and stationary facilities. Shock tubes belong to the first category. They typically recreate the hypersonic flight regime accurately but provide only short test times. Stationary facilities provide sufficient test time to yield a realistic material response for thermal protection system (TPS) qualification but only partially rebuild a true flight environment. Both types of facilities need plasma diagnostic methods to characterize the flow, emission spectroscopy being widely applied.

In impulse facilities, imaging setups have been used in recent years to take a snapshot of the flow propagating through the test section while gaining simultaneous spectral information from the entire shock and post-shock system [15, 50]. Figure 8 shows such an image with extracted spectra and spatial intensity distributions across the shock and the post-shock region.

The purpose of recent work was to experimentally quantify radiation loads to spacecraft during atmospheric entry to reduce margins in the design process, mainly due to equilibrium radiation generated in the post-shock region. However, increased interest in the nonequilibrium radiation inside the shock and in the immediate relaxation region has been expressed recently [51].

A simple to interpret case of emission spectroscopy is plasma states in thermodynamic equilibrium. For most high-temperature air species, the simulation capabilities are sufficient to reproduce measured spectra. A good example is given by data taken at Stanford University in an atmospheric, inductively coupled plasma torch by Laux et al. [38]. Figure 9 shows measured and simulated emission spectra in that equilibrium case that are in excellent agreement.

These measurements demonstrate the ability to make absolute concentration measurements using OES; in this case the absolute intensity of N₂ emission matches the predicted emission assuming equilibrium chemistry.

TABLE 1 REPRESENTATIVE (BUT NOT COMPREHENSIVE) LIST OF CODES FOR THE SIMULATION OF PLASMA RADIATION

Code (organization, country)	Simulated species	Radiation trans- port capabilities	Restrictions/ availability	Ref.
<i>N</i> _{EQAIR} (NASA Ames, USA)	Air, H, H ₂ , C, CN, CO ₂	Line of sight, spherical cap, infinite slab	EAR restricted	[40]
<i>HARA</i> (NASA Langley, USA)	Air, H, H ₂ , C, CN, CO ₂ , Ar	Line of sight, spherical cap, infinite slab	EAR restricted	[41]
<i>SPRADIAN/RADIPAC</i> (JAXA, Japan/ South Korea)	Air, H, H ₂ , C, CN, CO ₂ , Ar	Line of sight, spherical cap, infinite slab	None, available through JAXA	[42]
<i>PARADE</i> (ESA, Europe)	Air, NH, C, CN, CH, C ₂	Ray tracing through additional Fortran code (Herta)	None, available through ESA	[43]
<i>SPECAIR</i> (Ecole Centrale, France)	Air, H, H ₂ , C, CN, CO ₂ , Ar	None	Reduced version available for download [44]	[38]
<i>LIFBASE</i> (SRI, USA)	OH, OD, NO, H, CN, CF, SiH, N, ⁺	None	None, available for download [45]	[46]
<i>SPARTAN</i> (<i>ipfn</i> , Instituto de Plasmas e Fusão Nuclear, Portugal)	Air		Freely distributed for academic and research	[47]
<i>HYPERRAD</i> , (NASA Ames, USA)	Air		EAR restricted	[27]
CNRS-RAD DATABASE, (Ecole Centrale, France)	Air, CN, CO, CO ⁺ , C ₂	None	Available as spectroscopic database	[48, 49]

Note: Air is N₂, O₂, NO, N, O, N₂⁺

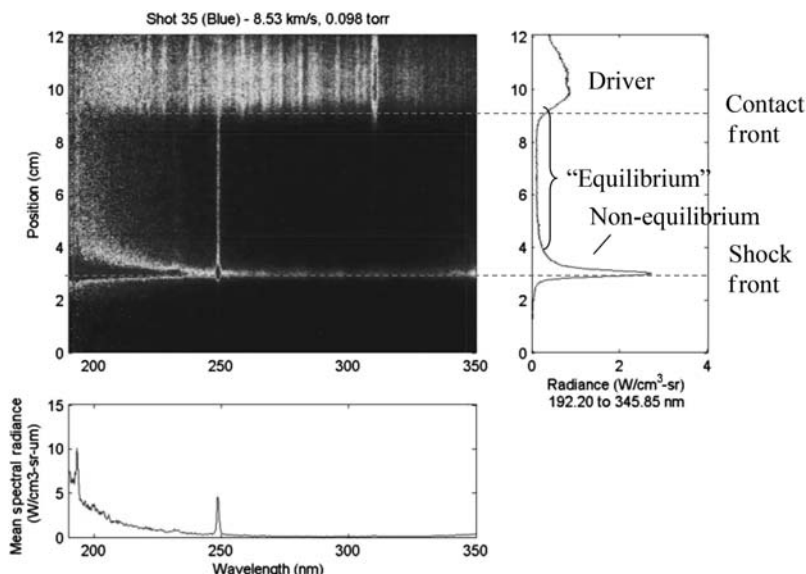


Fig. 8 Example of data obtained from a single spectrograph in the EAST facility. Vertical and horizontal cross sections of the data shown depict the spatial and wavelength resolved data, respectively [50]. Reprinted with permission of the American Institute of Aeronautics and Astronautics (see color section).

Sometimes changes in the gas dynamic state happen too fast for the plasma to reach equilibrium (both in the thermal and chemical sense). In this case, populations of the excited states may no longer follow well defined (Maxwellian) distribution functions. An analysis requires a detailed balance of population and depopulation for each excited state, yielding the necessity of collisional radiative models. The assumption of a quasi-steady-state, where the time change of the excited states is considered small against the population processes themselves, is often applied as described by Park [30] and may hold over a wide regime of conditions. However, additional population processes may become dominant, in particular those through chemical reactions, requiring knowledge of excited-state chemistry. Evidence of excited state chemistry was found during the space shuttle development in the so-called shuttle glow. This basic process was thoroughly described by Golde and Thrush [52]. Excited states are populated through chemical reactions that end up directly in these states without the need of collisional excitation from the ground state. The final radiating level might even be populated through overlapping potentials (usually of molecules) through level crossing processes [53]. An experimental realization was given by Laux et al. by rapidly cooling down an equilibrium plasma. The molecular

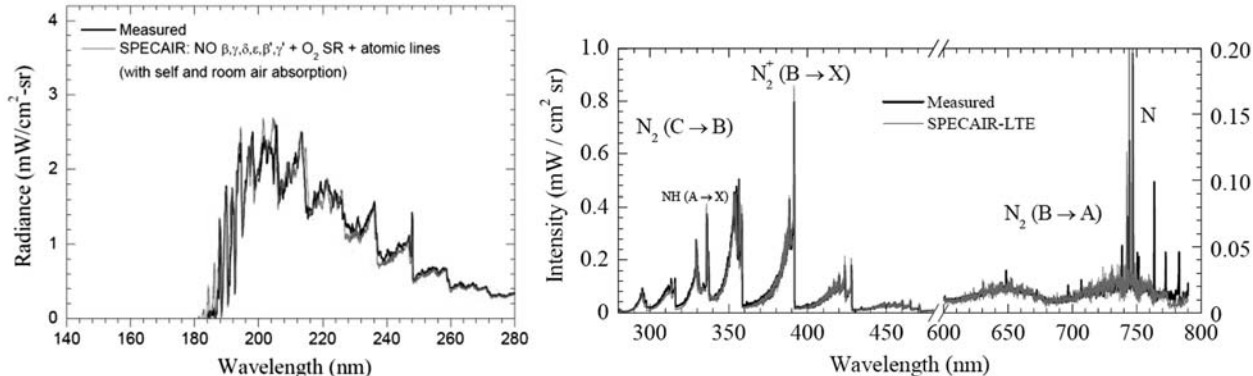


Fig. 9 SPECAIR: NO $\beta, \gamma, \delta, \epsilon, \beta', \gamma'$, O_2 SR and atomic lines, including self-absorption within plasma and absorption in 5 m of room air in the low UV (left), and measured and computed LTE spectra of the nitrogen/argon plasma at the generator nozzle exit from the near-UV to the near infrared [38]. Credentials to von Karman Institute for Fluid Dynamics, in Radiation and Nonequilibrium Collisional-Radiative Models by C.O. Laux, VKI LS 2002-07.

emission of N₂ from the 1st Pos. System (N₂ B³Π_g → N₂ A³Σ_u⁺) was monitored and showed strong deviations from the simulation based on thermal excitation with significant overpopulations of high vibrational quantum numbers, as illustrated in Fig. 10.

Indeed, these overpopulations could be related to the aforementioned level crossing processes (also known as inverse pre-dissociation) and the spectrum was rebuilt applying collisional radiative models [53]. Recently, the same processes have been shown to be dominant for the emitted radiation of N₂ in highly expanding high-enthalpy flows used for TPS material testing at NASA by Winter and Prabhu [35] as demonstrated in Fig. 11. The measured spectrum can only be rebuilt by introducing significant overpopulation factors for high upper vibrational quantum numbers ($V_u = 8$ to $V_u = 13$) of the emitting electronic state of N₂. It was shown that the molecular radiation (at least of these high vibrational levels) is not produced by excitation of N₂ ground state molecules but by recombination of N atoms into electronically excited N₂ levels. This provides a potential method for measuring ground state atom concentrations in nonequilibrium flows without the need of much more complicated techniques such as two-photon laser-induced fluorescence (TALIF).

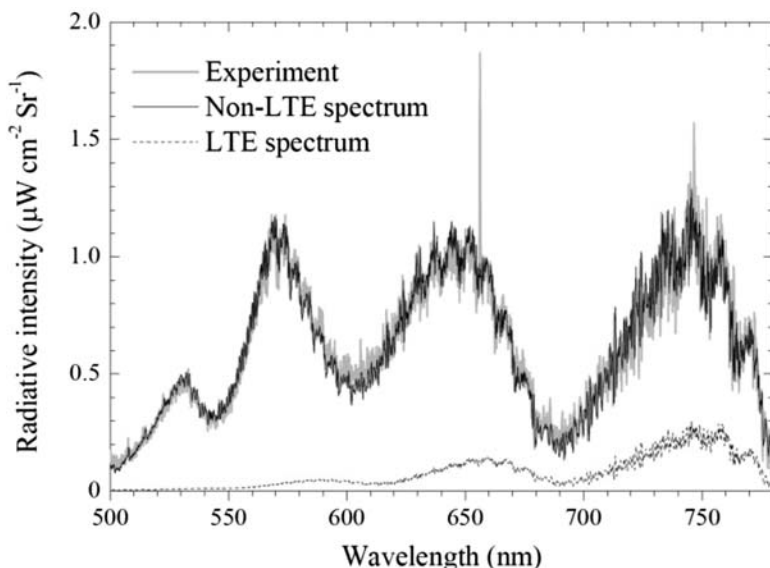


Fig. 10 Measured spectra and computation assuming LTE and non-LTE simulation of a nitrogen/argon plasma after rapid cooling from an equilibrium state from Reference [38]. Credentials to von Karman Institute for Fluid Dynamics, in Radiation and Nonequilibrium Collisional-Radiative Models by C.O. Laux, VKI LS 2002-07.

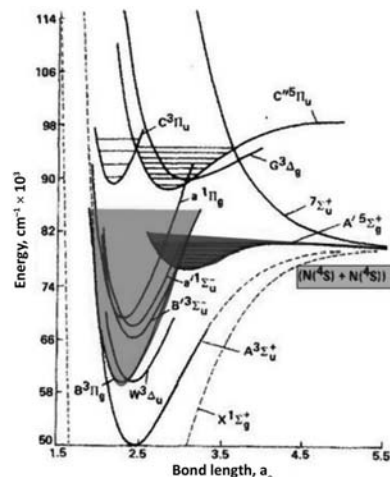
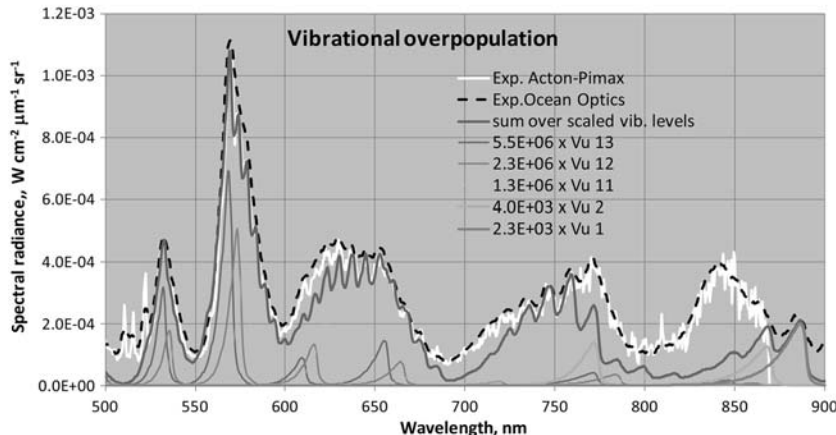


Fig. 11 Measurements of the N₂ 1st Pos System in the free stream of the IHF arc-jet facility in comparison to LTE simulation with NEQAIR and superposition of individually scaled spectra simulated separately for each upper vibrational level (left) [35], and potential crossing between the N₂A^{5Σ_g^+}, and N₂B^{3Π_g} states [53] (right), which is reproduced with permission from the authors. Right hand figure is Copyright 1988, AIP Publishing LLC.

IV. ABSORPTION SPECTROSCOPY

Absorption spectroscopy has been used to study nonequilibrium flows since at least 1961 [54]. In their textbook on gas dynamics, Vincenti and Kruger describe how Camac (1961) used the technique to measure vibrational relaxation times behind normal shock waves in oxygen-argon mixtures [55]. Camac used a xenon-filled microwave-excited resonance lamp, a hot cathode hydrogen discharge tube, and a high-voltage Lyman discharge lamp to produce the UV light needed for the absorption measurements. Absorption spectroscopy has been since used to extract other quantitative thermodynamic and fluid dynamic properties flows such as temperature, pressure, species concentration, and velocity.

A. ABSORPTION THEORY

Quantitative measurements are achieved with absorption through the analysis of the fluid's interaction with light. As light, with spectral irradiance I_ν [$\text{W}/\text{cm}^2/\text{cm}^{-1}$] propagates through an infinitesimal thickness dx [cm] of an absorbing medium of concentration C [molecules/ cm^3] with a molar absorption coefficient ε [$\text{cm}^2/\text{molecule}$], its intensity decreases according to [56]:

$$-dI_\nu = I_\nu \varepsilon C dx \quad (23)$$

Using a spectral absorption coefficient k_ν [cm^{-1}], which is equivalent to the product of ε and C , Eq. (23) can also be written as [57, 58]:

$$-dI_\nu = k_\nu I_\nu dx \quad (24)$$

Integration of this equation gives the well-known Beer–Lambert law:

$$\frac{I_\nu}{I_0} = e^{-\int k_\nu dx} \quad (25)$$

In this equation, I_0 is the incident irradiance prior to absorption. If the medium can be specified by a single temperature, velocity, and absorbing species concentration and the pressure is uniform and absorbs linearly over the path length L , the relationship can be simplified to:

$$\frac{I_\nu}{I_0} = e^{-k_\nu L} \quad (26)$$

The parameter k_ν contains key information about the absorbing medium, including the population of potential absorbers and the probability of absorption. Strategies that exploit the relationship between this information and thermodynamic properties lead to various quantitative measurement techniques. Contributions to k_ν can be better explained with the aid of an energy diagram. Figure 12 shows incident light being absorbed, which causes molecules to transition from an energy ground state (E_1) to an energy excited state (E_2). The

Fig. 12 Two-level energy diagram of absorption process.

energy of the incident photon, which is the product of Planck's constant h and the frequency of the light ν , is transferred to the excited molecule.

Not all potential absorbers in the ground state are excited. The rate of absorption is governed by the transition line shape function Y_ν [cm] and the transition line-strength factor S_{12} [cm $^{-2}$]. These two components contribute to the spectral absorption coefficient [59]:

$$k_\nu = S_{12} Y_\nu \quad (27)$$

If we assume that the population in the upper state is negligible, S_{12} is proportional to the population of absorbers in the ground state N_1 , Einstein's coefficient of stimulated absorption B_{12} [s $^{-1}$ (W/cm 2 /cm $^{-1}$) $^{-1}$] and the energy of the incident photon. Y_ν describes the shape of the transition, spectrally, and is related to the probability that molecules will absorb photons at various frequencies. By definition, the transition line shape function is integrated to give:

$$\int Y_\nu d\nu = 1 \quad (28)$$

Light sources typically have a discrete spectral width, which further complicates the process. The spectral irradiance of light can be calculated from:

$$I_\nu = I L_\nu \quad (29)$$

where I [W/cm 2] is irradiance and L_ν [cm] is the line shape function of the light source. Similar to Y_ν , L_ν is defined as:

$$\int L_\nu d\nu = 1 \quad (30)$$

To account for these two different line shape functions, the integrated absorption coefficient is used:

$$k_{\text{int}} = S_{12} G \quad (31)$$

where G is the spectral overlap integral defined as:

$$G = \int Y_\nu L_\nu d\nu \quad (32)$$

The spectral overlap integral represents the amount of intersection between the light source line shape and the transition line shape. There are two extreme cases to consider [58]. The first case assumes a monochromatic light source and a relatively broad absorption transition. Here, G approaches the value of Y_v at the light source's frequency. A spectral scan of a relatively broad transition using a narrow-band laser to determine the absorption line shape is an example of this case. The second case assumes a monochromatic absorption transition and a broadband light source. Here, G approaches the value of L_v at the absorption transition's frequency. Note that Eq. (32) can be used to calculate G for all cases. For single-mode diode lasers the approximation of a monochromatic laser is frequently used. This is because the laser line-width is of the order of 10s of MHz, whereas transitions are of the order of a few GHz at standard atmospheric conditions. However, at low-density conditions, such as those appropriate to flight in the upper atmosphere, the monochromatic approximation may no longer be valid. In these cases, corrections such as Eq. (32) need to be used.

B. BROADENING MECHANISMS

The transition line shape is influenced by broadening mechanisms, which have various thermodynamic dependencies. Typically, the spectral width and shape of the transition are affected by natural ($\Delta\nu_N$), collision ($\Delta\nu_c$), and Doppler-based ($\Delta\nu_D$) broadening mechanisms. Natural and collision broadening are homogenous where each absorber has the same transition energy and frequency. Natural broadening is related to the Heisenberg uncertainty principle, as the frequency of the transition cannot be perfectly known. Natural broadening is usually small in comparison to the other broadening mechanisms [60]. Collision or pressure broadening occurs from physical collisions with other molecules. Not only do collisions increase the spectral width ($\Delta\nu_c$), they also cause a shift ($\Delta\nu_s$) in the center frequency and asymmetry in the line shape. For a multi-component gas mixture, these values can be calculated from [61]:

$$\Delta\nu_c = P \sum_i (\chi_i 2\gamma_i) \quad (33)$$

$$\Delta\nu_s = P \sum_i (\chi_i \delta_i) \quad (34)$$

where P , χ_i , $2\gamma_i$, and δ_i are the pressure, mole fraction, collision width per unit pressure, and collision shift per unit pressure, respectively, of the absorbing molecules. The terms γ_i , and δ_i have temperature dependencies, which for many species of interest to absorption spectroscopy, can be evaluated with the High Resolution Transmission (HITRAN) database [62]. As we shall see, the temperature can be determined through the area ratio of two transitions. Because the effects of pressure are the same for both transitions, these effects cancel in the integrated signal ratio allowing for an unambiguous temperature measurement. If the temperature is known, then the analysis of the collision shift and/or collision

broadening can be used to calculate the gas pressure. Homogeneous broadened transitions have a Lorentzian line shape function:

$$g_H = \frac{\Delta\nu_H}{2\pi} \frac{1}{(\nu - \nu_0)^2 + (\Delta\nu_H/2)^2} \quad (35)$$

where $\Delta\nu_H$ is the spectral width of a homogeneous broadened transition (full width half maximum).

Doppler broadening is inhomogenous, where each absorbing molecule has a transition frequency that is Doppler shifted according to its velocity component in the laser propagation direction. This is because of thermal motion, which induces Doppler shifts. Doppler broadened transitions have a Gaussian line shape function:

$$g_D = \frac{2\sqrt{\ln 2}}{\pi^{1/2}\Delta\nu_D} e^{\left[\frac{-4(\ln 2)(\nu - \nu_0)}{\Delta\nu_D^2}\right]} \quad (36)$$

where ν_0 is the center frequency corresponding to a stationary absorber.

When both homogeneous and inhomogeneous broadening mechanisms contribute to the line shape function, the Voigt function is used [57]. The Voigt function is a convolution of the Lorentzian and Gaussian profiles and requires numerical methods to calculate the shape [63]:

$$V(a, x) = \frac{a}{\pi} \int_{-\infty}^{\infty} \frac{e^{-y^2}}{a^2 + (x - y)^2} dy \quad (37)$$

where

$$a = \sqrt{\ln 2} \frac{\Delta\nu_H}{\Delta\nu_D} \quad (38)$$

$$x = 2\sqrt{\ln 2} \frac{(\nu - \nu_0)}{\Delta\nu_D} \quad (39)$$

Physically, the use of the Voigt profile can be justified by each collection of molecules or atoms in a particular Doppler subgroup being subject to the effects of collisional broadening, and this is expressed through the convolution operation. Figure 13 illustrates the different line shapes computed using an approximation to Eq. (37) [64]. Figure 14 shows the effect of Lorentzian and Gaussian broadening on the spectral shape of a line using the fraction of the total transition energy contained within a given frequency difference from the line center. With Gaussian broadening dominant, 99% of the transition strength is contained within two half widths at half maximum ($\Delta\nu_{\text{HWHM}}$), whereas for a Lorentzian profile, this value is not reached for ~ 50 half widths. In other words, a strong Lorentzian-broadened line might significantly influence distant spectral regions if Lorentz broadening is dominant.

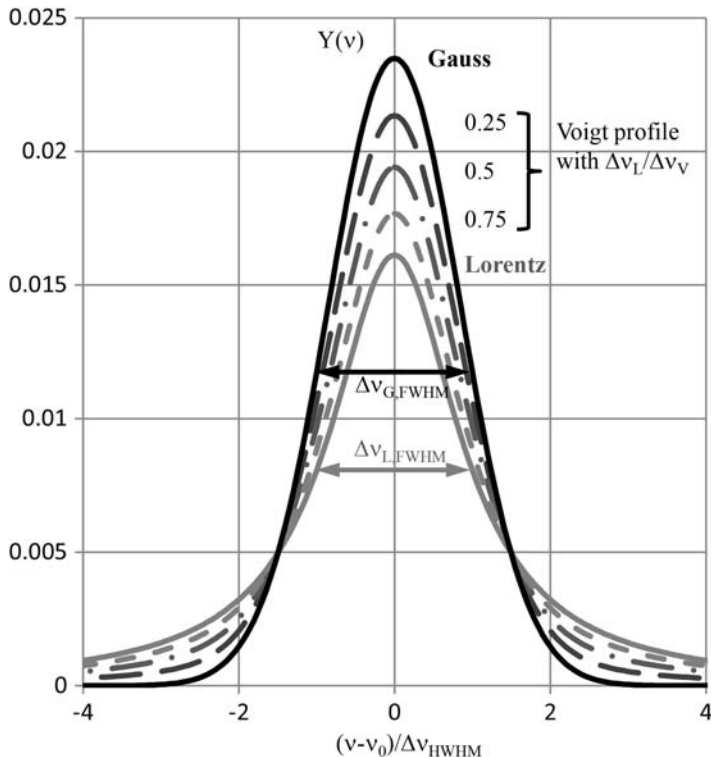


Fig. 13 Spectral line shape for Lorentz (collision), Gaussian (Doppler) and Voigt broadening for equal transition strength and half-width.

C. TRANSLATIONAL TEMPERATURE

If $\Delta\nu_D$ can be measured, then the translational temperature T_{trans} can be determined by the following relationship [58]:

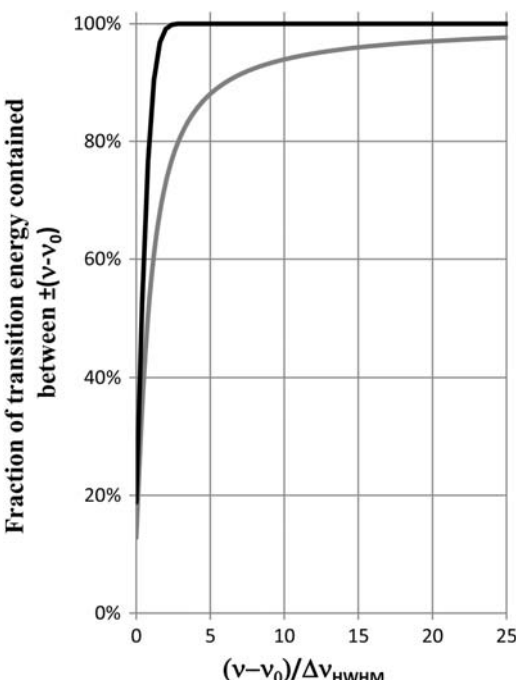
$$\Delta\nu_D = 2\nu_0 \sqrt{\frac{2kT_{\text{trans}}}{(\text{MW})c^2} \ln 2} \quad (40)$$

where k is Boltzmann's constant and MW is the molecular weight of the absorber. If other broadening mechanisms are small in comparison and a spectrally narrow light source is used to spectrally scan across the transition, then $\Delta\nu_D$ can be extracted with relative ease to determine the translational temperature. Even in flows with considerable homogeneous broadening the translational temperature

Fig. 14 Fraction of transition energy contained between $(v - v_0)$ for a Lorentzian (collision) and a Gaussian (Doppler) line profile.

can be determined from the Doppler component of the Voigt line shape [65]. Using linewidth to determine translational temperature has the advantage of only requiring a single absorption line. This is particularly useful for absorption measurements of atomic species where there may only be one transition available within a laser's output range, or for lasers that have a very limited tuning range. It is also necessary for measurements in cases where there is nonequilibrium between rotational and translational energies. Measurements of translational temperature based upon transition width may have higher uncertainties compared to measurements of rotational or vibrational temperature based upon a Boltzmann plot [66]. This is because of the square-root dependence of the Doppler width on temperature and the additional challenge of separating the Doppler width from other broadening mechanisms, especially at high pressures, when measuring translational temperature [67]. For example, an uncertainty of 1.5% in the measurement of the Doppler width in A-band Doppler-broadened oxygen lines at 296 K leads to an uncertainty in temperature of 3%. Zhang et al. [68] measured the translational temperature in an arcjet facility using absorption of Argon at 811 nm. The Doppler width was measured with an uncertainty of 12% after the effects of homogeneous broadening, Stark broadening and noise were accounted for, leading to an uncertainty in the translational temperature of less than 30% over temperatures from 2000 K to 10,000 K. The difference in sensitivity between line-strength-based temperature measurements and Doppler width measurement depends strongly on the difference in ground-state energies between the available transitions.

Another example of a translational temperature measurement is described in the work of Parker et al., where absorption experiments were performed in the Large Energy Shock Tunnel (LENS I) at the Calspan-University of Buffalo Research Center (CUBRC) [69]. Quantum cascade lasers were used to obtain absorption measurements of NO deep into the infrared spectrum. Figure 15 shows



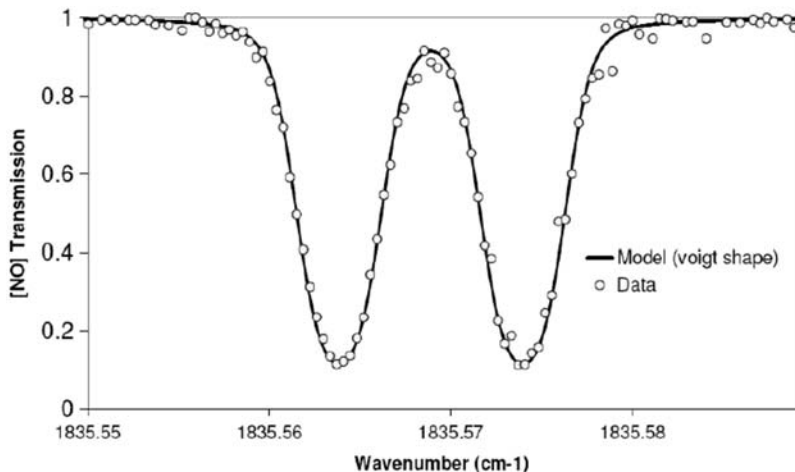


Fig. 15 Absorption spectra measured in the CUBRC LENS I facility used to calculate translational temperature. Reproduced from Reference [69] with permission of the authors.

a sample absorption spectra from that work near 5447 nm (1835.56 cm^{-1}), which corresponds to one of six fundamental NO rovibrational transitions used in that study. Using the Doppler width contribution based on the fitted Voigt line shape, a translational temperature of 190 K was computed (Eq. (40)). This temperature, measured in the test section, corresponds to a lower enthalpy condition (5 MJ/kg) and using a helium driver gas. At highenthalpy conditions, the LENS I facility produces free-stream flows that are characterized by chemical and thermal nonequilibrium. In the work, translational temperatures were compared to rotational temperatures and to CFD predictions at these conditions. Although the measurement uncertainty was not reported, the authors predict a temperature resolution of 50 K.

D. ROTATIONAL TEMPERATURE

Rotational temperatures are typically measured by analyzing multiple absorption features that have line-strengths with different rotational temperature dependencies. Usually either multiple light sources are used to excite separate isolated transitions or a single light source is used to spectrally scan over adjacent absorption features. This technique is referred to as multiline or ratio thermometry. The spectrally integrated absorbance that is measured experimentally is defined as [70]:

$$a_j = \int -\ln\left(\frac{I_\nu}{I_0}\right) d\nu \quad (41)$$

The subscript j refers to the absorption feature that is probed. Often a modified version of the spectral absorption coefficient is used [71]:

$$k_v = P\chi_i SY_v \quad (42)$$

The subscript ‘12’ in the line strength term S has been dropped for clarity. With this change, a modified version of the line-strength factor S [cm^{-2} atm^{-1}] is used [72]:

$$S(T_{\text{rot}}) = S(T_0) \frac{Q(T_0)}{Q(T_{\text{rot}})} e^{\frac{-hcE_{\text{rot}}}{k}} \left(\frac{1}{T_0} - \frac{1}{T_{\text{rot}}} \right) \left(\frac{1 - e^{\frac{-hc\Delta E}{kT_{\text{rot}}}}}{1 - e^{\frac{-hc\Delta E}{kT_0}}} \right) \quad (43)$$

where T_{rot} , T_0 , Q , and E_{rot} are the rotational temperature, reference rotational temperature (296 K), the total internal partition function, and the total rotational energy of the molecular quantum state absorbing the light, respectively. ΔE is the difference in energy between the upper and lower states of the transition. It should be noted that the final term in the equation is due to stimulated emission, and is negligible at temperatures below approximately 2500 K and at wavelengths below 2.5 μm [73].

If the light source is spectrally narrow, the integrated absorbance for each j transition can be simplified:

$$a_j = \int k_v L d\nu = \int P\chi_i LS_j Y_v d\nu = P\chi_i LS_j \int Y_v d\nu \quad (44)$$

If the entire transition can be resolved using a scanning technique, then the integrated absorbance becomes:

$$a_j = P\chi_i LS_j \quad (45)$$

The ratio of two separate absorption features, denoted by subscripts $j = 1$ and $j = 2$, with different rotational energies, becomes:

$$\frac{a_1}{a_2} = \frac{S_1}{S_2} = \frac{S_1(T_0)}{S_2(T_0)} e^{-\frac{hc\Delta E_{\text{rot}}}{k}} \left(\frac{1}{T_{\text{rot}}} - \frac{1}{T_0} \right) \quad (46)$$

where ΔE_{rot} is the change in lower state rotational energy between the two absorption lines. Because many terms are cancelled in this ratio, it is possible to extract T_{rot} . Note that it is also possible to calculate this ratio based on peak absorbances instead of spectrally integrated values to extract temperature if the line shape function is included. This assumes that the pressure shift and broadening coefficients are similar for both transitions.

Wehe et al., performed rotational and translational temperature calculations from H_2O absorption measurements in the high-enthalpy (10 MJ/kg) Calspan 96-inch Hypersonic Shock Tunnel using a diode-laser sensor [74]. A probe, which housed the critical optical components, was placed directly into the core

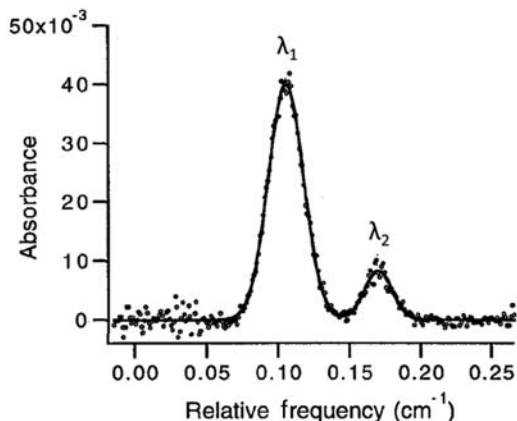


Fig. 16 Absorption spectra and fit through H_2O transitions in Calspan 96-inch Hypersonic Shock Tunnel. Adapted from Reference [74] with permission of the authors.

transition ($\nu_1 + \nu_3$ band) near 1396 nm (λ_2) and 1400 nm (λ_1). A Gaussian fit, shown as a solid line in the figure, was applied to the experimental data to determine the spectrally integrated absorbances and Doppler broadening of each transition. The ratio of the absorbances was used to compute the rotational temperature Eq. (46) and the Doppler broadening was used to calculate the translational temperature Eq. (39). The measurement uncertainty of the rotational temperature measurement was ± 13 K ($\pm 2.3\%$ of mean) whereas the measurement uncertainties of the translational temperatures based on the two absorption profiles (λ_1 and λ_2) were ± 15 K ($\pm 2.7\%$ of mean) and ± 35 K ($\pm 6.4\%$ of mean), respectively.

These high-resolution line shapes were recorded every 125 μsec (8 kHz), allowing for time-resolved temperature measurements. Figure 17 shows the time-resolved rotational and translational temperatures extracted during the facility run time. Agreement indicates that the flow was in thermal equilibrium, which was expected based on equilibrium calculations reported in the work.

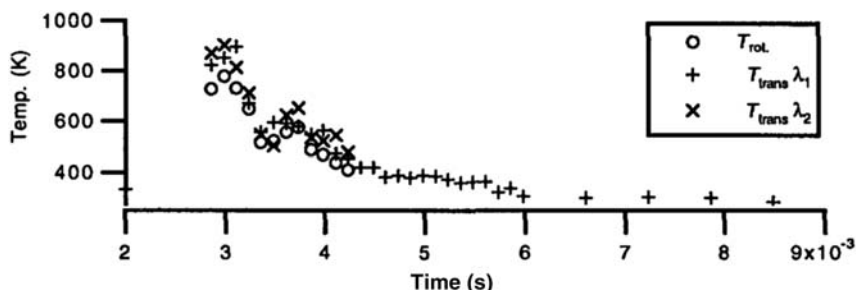


Fig. 17 Translational and rotational temperature measurements in the Calspan 96-inch Hypersonic Shock Tunnel. Adapted from Reference [74] with permission of the authors.

of the flow. In order to improve the signal-to-noise ratio, the hypersonic air flow was seeded with 6% water vapor. Absorption measurements, shown as solid data points in Figure 16, correspond to an H_2O absorption

It can be difficult to accurately measure the line-strength due to problems in determining the zero absorbance intensity near the absorption feature wings, which is needed for baseline levels [75]. Using diode lasers, for example, the laser intensities can drift over time due to thermal, mechanical, and electronic effects. Liu et al. discuss how low signal levels, baseline-fitting errors, beam steering effects, and others can affect the estimation of the line shapes [75]. To combat these problems, wavelength modulation spectroscopy (WMS) with second harmonic ($2f$) detection can be used. Detailed theory about WMS can be found in the literature [76–79]. Through the superposition of a modulation of frequency f onto the light source, the problem of excessive DC noise that occurs at low absorbances can be greatly reduced. The absorbing medium converts some of the wavelength modulation into amplitude modulation of the laser intensity. The amplitude modulation occurs at the modulation frequency f and at its integral harmonics, nf . Then, by using phase-sensitive electronics, a selected harmonic can be isolated (e.g., $n = 2$). At sufficiently high frequencies f , excess noise from the light source (e.g., laser diode) can be reduced.

Goldstein et al. performed WMS- $2f$ rotational temperature measurements using a tunable diode laser absorption sensor in the University of Virginia's supersonic combustion facility [80]. In this work, the facility was run with water injection to simulate vitiating effects and with hydrogen combustion (equivalence ratio of 0.33). Figure 18 shows sample experimental direct absorption (a) and WMS- $2f/1f$ absorption (b) line shapes of H_2O obtained at the combustor exit.

The two absorption features in Fig. 18a allow for the ratio thermometry technique to be used. However, the small magnitude of the neighboring feature results in a higher measurement uncertainty compared to the WMS- $2f$ technique. Both techniques give temperatures that agree reasonably well with CFD predictions (Table 2). However, the direct absorption technique has consistently larger measurement uncertainties compared to the WMS technique. The authors discuss the discrepancy in temperatures observed in the H_2 -air combustion case.

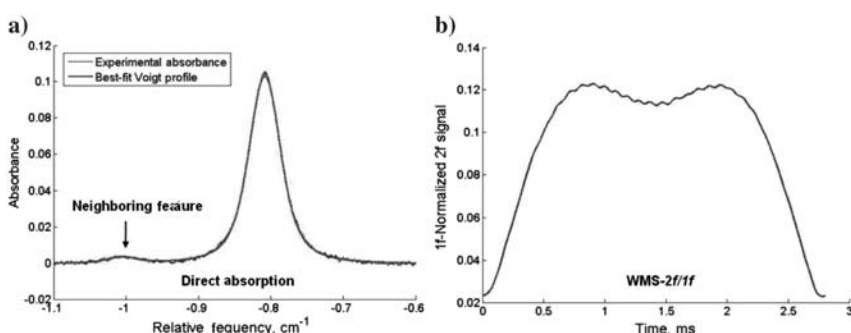


Fig. 18 a) Direct absorption vs b) WMS- $2f/1f$ in UVa supersonic combustion experiment. Reproduced from Reference [80] with permission of the authors.

TABLE 2 COMPARISON OF DIRECT AND WMS ABSORPTION CALCULATIONS OF ROTATIONAL TEMPERATURE. REPRODUCED FROM REFERENCE [80] WITH PERMISSION OF THE AUTHORS

Operation Mode	Expected Value	DA	WMS
11% Steam	700–1000 K	776 ± 10 K	742 ± 9 K
(Combustor Entrance)	$11.4 \pm 0.2\%$ H ₂ O	$10.9 \pm 0.1\%$ H ₂ O	$10.8 \pm 0.1\%$ H ₂ O
9% Steam	700–1000 K	860 ± 30 K	831 ± 9 K
(Exit Plane)	$9 \pm 0.2\%$ H ₂ O	$9.1 \pm 0.2\%$ H ₂ O	$9.1 \pm 0.1\%$ H ₂ O
12% Steam	700–1000 K	875 ± 50 K	850 ± 6 K
(Exit Plane)	$12 \pm 0.2\%$ H ₂ O	$12.1 \pm 0.5\%$ H ₂ O	$11.5 \pm 0.1\%$ H ₂ O
H ₂ -Air Combustion $\varphi = 0.33$	1800–2200 K	1802 ± 94 K	1765 ± 41 K
(Exit Plane)	13% H ₂ O	$12.8 \pm 0.5\%$ H ₂ O	$13.3 \pm 0.3\%$ H ₂ O

An alternative to wavelength modulation that has also been used with success in high-speed flows is ratiometric detection [81, 82]. For this technique, the laser beam is split into a signal beam that propagates through the flowfield and a reference beam that does not. The photocurrents from the two beams are passed through a log-ratio amplifier, providing a direct measurement of the absorbance. If the photocurrents for the two beams are equal, the log-ratio detection removes the intensity modulation due to varying current on the beams, and the common-mode laser intensity noise, leaving only the absorption signal on the detector. The balanced variant of this technique includes an additional low-frequency feedback circuit that ensures that the photocurrents balance, zeroing the baseline of the measurement. This method, because it uses two beams rather than one, is optically more complex than WMS but electronically simpler, and provides similar absorbance detection limits. The output of the circuit is a signal that is directly proportional to the absorbance, making the analysis of the data straightforward.

Upschulte et al. [83] used the balanced ratiometric method to measure temperature, mole fraction and velocity in a supersonic combustion facility at the US Air Force Research Laboratory at Wright-Patterson Air Force base at Mach 2.1, using balanced ratiometric detection of water vapor near 1390 nm. The temperature and mole fraction measurements were made to within 100 K and around 0.3%, respectively, whereas beam steering adversely affected the velocity measurements. Griffiths and Houwing have also made measurements of water vapor temperature, mole fraction and velocity in a model scramjet engine at a flight Mach number of 10, in the Australian National University's T3 free-piston

shock tunnel [84]. They used two time-multiplexed distributed feedback diode lasers and balanced ratiometric detection at scan rates of up to 20 kHz. Temperatures ranging from 600 K to 1800 K were measured in the turbulent, combusting environment of the scramjet engine.

E. VIBRATIONAL TEMPERATURE

Similar to multiline thermometry for rotational temperature, vibrational temperatures can be measured by probing absorption features at different vibrational levels. Pan and Oka measured vibrational temperatures of ArH^+ ions in a glow discharge by separately measuring the integrated absorbance of transitions in two vibrational levels [85]. They compared the vibrational temperature to the translational kinetic temperature measured using the Doppler width of the transition and quantified the thermal nonequilibrium in the plasma.

Brandt and Roth measured the absorption in the nonequilibrium flow behind a normal shock wave in a shock tube, in mixtures of CO and Ar, using a lead-salt IR diode tuned to absorption transitions lying between 2100 and 2200 cm^{-1} [86]. Once again, the vibrational temperature was compared with the translational temperature to determine the degree of nonequilibrium downstream of the shock wave. The measured translational and vibrational temperatures corresponded well to the values predicted by Landau–Teller theory.

F. SPECIES CONCENTRATIONS

Similar to the thermometry techniques, species concentrations can be determined through the analysis of the integrated absorbance. If the temperature can be determined from one of the thermometry techniques, then the concentration of absorbers C_i of species i can be determined from the integrated absorbance (Eq. (45)) and ideal gas law [87]:

$$C_i = \frac{6.02 \times 10^{23} P \chi_i}{RT} \left(\frac{101325 \cdot \text{Pa}}{1 \cdot \text{atm}} \frac{1 \cdot \text{m}^3}{100^3 \text{cm}^3} \right) = \frac{6.1 \times 10^{22} a_j}{RT S_j L} \left[\frac{\text{molecules}}{\text{cm}^3} \right] \quad (47)$$

where R [$\text{J} \cdot \text{mol}^{-1} \cdot \text{K}^{-1}$] is the gas constant. Concentration can also be extracted from analysis of the broadening mechanisms, which have pressure and temperature dependencies, using a spectroscopic model that is fitted to the experimental data [88].

Lin et al. obtained CO concentration measurements using TDLAS in a Martian simulant gas (70% CO_2 and 30% N_2) that was accelerated in a shock tube [87]. The flow immediately behind the 6.31 km/s shock wave was in thermal nonequilibrium. Figure 19 shows a sample absorption spectra taken at 50 kHz near 2335.8 nm (4281.2 cm^{-1}) corresponding to the targeted CO transition. Even with excessive noise in the wings of the line shape, a good Voigt fit was applied to the data, which is shown as the smooth line through the data. The spectrally integrated absorbance was used to calculate the concentration.

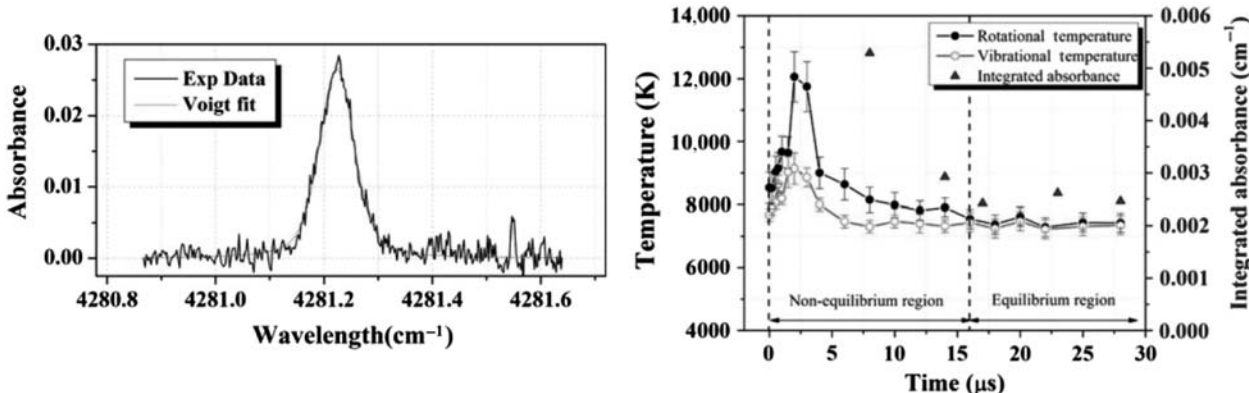


Fig. 19 Sample absorption measurement with Voigt fit (left) and nonequilibrium temperature measurements (right). Reproduced from Reference [87] with permission of the authors and Springer Science and Business Media.

A room temperature cavity cell of CO was used to validate the technique. The authors report an average CO concentration of 7.46×10^{12} molecules/cm³ behind the shock wave (Eq. (47)). Errors in the Voigt fitting process resulted in a 1% uncertainty in the spectrally integrated absorbance values, which result in a 10% error in the CO concentration measurement.

G. VELOCIMETRY

Doppler-shift based velocimetry is based on the analysis of the spectral shift that occurs in an absorption feature when gas molecules have a component of velocity that is in the same direction as the excitation source. From the absorbing molecule's frame of reference, the excitation source appears either red- or blue-shifted, depending on the molecule's velocity. As a result, the spectral frequency at which the light beam is absorbed is either blue- or red-shifted, respectively, from the laboratory frame of reference. If the Doppler shift can be measured experimentally, usually through a spectral scan, then the gas velocity can be calculated from the following relationship:

$$U = \frac{c\Delta\nu_{\text{Doppler Shift}}}{\nu_{\text{Light Source}}} \quad (48)$$

The velocity can be determined by passing the laser beam through a duct at two different angles and measuring the absorption of a spectral feature for each of the two transmitted beams, as shown in Figure 20 [89]. The Doppler shift in the peak of the absorption feature can be used to directly measure the velocity using Eq. (48).

Infrared DLAS velocimetry measurements from CO, NO, and H₂O molecules were performed in the S4MA, F4, and DLR piston driven HEG facilities [90].

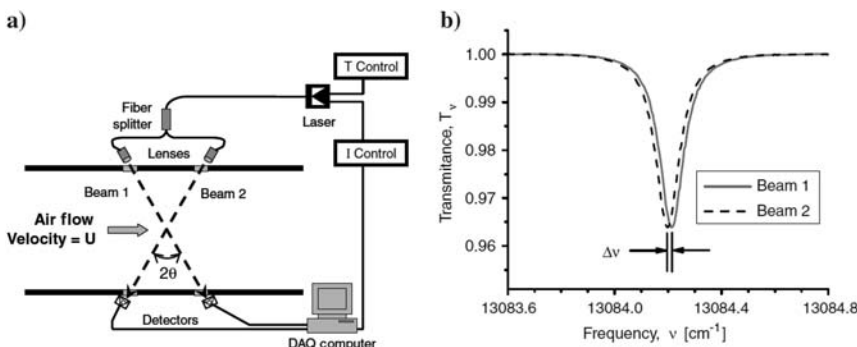


Fig. 20 a) Typical arrangement for diode laser absorption measurement, and b) Doppler-shifted absorption features for the two beams. Reproduced from Reference [32] with permission of the authors.

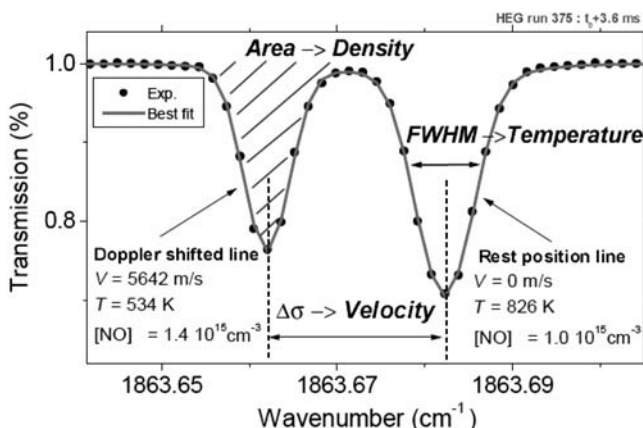


Fig. 21 NO absorption line indicating how velocimetry, concentration, and translational temperature are calculated. Reproduced from Reference [90] with permission of the authors.

In that work, enthalpy conditions ranged from $\sim 1 \text{ MJ/kg}$ to 20 MJ/kg and test times ranged from 100 s to 1 ms . In addition to velocimetry, thermometry (translational), and concentration measurements were also performed. Figure 21 shows a sample NO absorption line shape ($R\ 3/2$) near 536 nm (1863.6 cm^{-1}) obtained in the DLR facility. The Doppler shift, which is used to calculate velocity (Eq. (48)) is visible in the figure. The integrated absorbance and Doppler width used to calculate concentration and translational temperature are also shown in the figure.

Figure 22 shows DLAS velocimetry measurements in the F4 facility at an enthalpy condition of 15 MJ/kg . The velocimetry measurements are compared to CFD calculations using both equilibrium and frozen assumptions. The

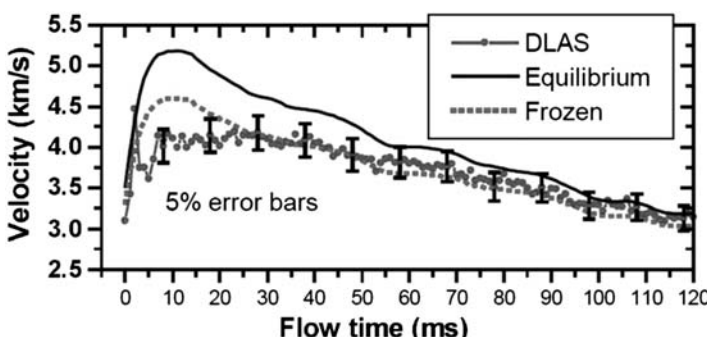


Fig. 22 DLAS Doppler-shift based velocimetry measurements in the F4 facility (50 MPa ; 15 MJ/kg). Reproduced from Reference [90] with permission of the authors.

velocimetry measurements show a closer agreement to the frozen calculations, indicating nonequilibrium.

The first oxygen velocity measurement in a high-speed flow was made by Philippe and Hanson using wavelength modulation detection at scan rates of 10 kHz in the *A*-band of molecular oxygen [91]. Velocities were measured to within ± 50 m/s, and agreed with theoretical estimates to within 5%. More recently, velocity has been measured in a Mach 6 nozzle flow, using absorption in the same wavelength range, excited by a vertical cavity surface-emitting laser (VCSEL) emitting near 760 nm [92]. The laser was able to be current-scanned over four oxygen transitions. Velocities of around 950 m/s were measured with an uncertainty of ± 40 m/s. These measurements were made by propagating the laser beam through two opposing retroreflectors, imposing opposite Doppler shifts as the beam propagates in the two opposing directions. This method allows the velocity to be measured using a single laser beam.

H. TOMOGRAPHY

Absorption tomography involves using multiple absorption measurements, which are path averaged, to reconstruct a spatial distribution (e.g., 2-D) of the measured property. Hanson suggested that new low-power fiber-based absorption sensor arrays may bring tomographic imaging inside aeroengine and airframe models for hypersonic ground tests [93]. Tunable diode lasers have features that make them especially suitable for tomography. They can scan at very high rates, providing information at tens or hundreds of kHz, and the lasers are typically routed to and from the flowfield using optical fibers, simplifying the experimental setup. Technology from the telecommunications industry, such as fiber couplers and multiplexers, can be used to split the laser light into many channels and/or to combine many wavelengths into a single fiber, allowing multiple species to be probed with multiple colors along many paths through the flow. The light from the fibers is coupled into lenses, propagated across the flow and captured by lens-coupled multimode fibers, separated into wavelengths and directed onto detectors. Thus, different species and spectral lines can be probed at different locations in a ducted flow, for example, allowing some spatially resolved concentration and temperature information to be determined from the line-of-sight measurements.

Recent advancements in TDLAS tomography include systems that scan a single laser or multiple lasers spatially across the flow and from different directions to allow time-averaged tomographic reconstruction of temperature and species concentrations in turbulent combustible flowfields [94] or a grid of fixed optical paths transmitting across the flow, allowing a low-resolution but time-resolved tomographic reconstruction of concentration and temperature [95, 96]. Figure 23 (from Reference [96]) shows temperature and mole fraction maps obtained in a General Electric J85 gas turbine engine. Thirty individual laser beams—15 in the horizontal direction and 15 in the vertical direction, making

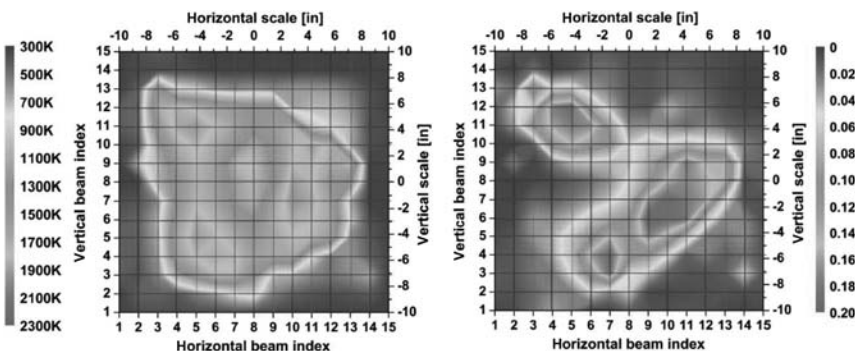


Fig. 23 Temperature (left) and water vapor mole fraction (right) measured at the exit of a General Electric J85 engine, with 50 kHz diode laser tomography, adapted from Reference [96]. The paper online has links to play animated movie clips of these data. Reprinted with permission of the authors and publisher (see color section).

a square mesh of 225 grid points—were used to probe the flow. The laser was rapidly scanned over multiple water vapor absorption lines near $1.35\text{ }\mu\text{m}$ with scans occurring at a rate of 50 kHz. Although the smaller turbulent length (and time) scales of the flow are not resolved with this system, the large-scale spatial (and temporal) distribution of the temperature and mole fraction are resolved.

I. CAVITY RING-DOWN SPECTROSCOPY (CRDS) AND OTHER CAVITY-ENHANCED METHODS

Even when using sensitive detection techniques such as wavelength modulation or balanced ratiometric detection, it can be challenging to measure absorbances below 10^{-5} . As many nonequilibrium flows occur at low number densities, and many important absorbing species such as oxygen have only very weak accessible absorption features, it becomes necessary to investigate even more sensitive optical systems. CRDS is a highly sensitive technique that is based on increasing the amount of absorbance in a medium by increasing the effective path length (L) through the use of an optical system [97]. For example, if an absorbing medium is placed between two highly reflective dielectric mirrors, then the energy of light resonating between the mirrors will decrease with each pass. A small amount of light passing through one of the mirrors is detected and monitored as a function of time. The “ring-down time” is the time it takes for the light to decrease to an intensity threshold. It is also equivalent to the mean time that any photon will survive between the two mirrors (i.e., within the cavity). Analysis of the absorption features using a CRDS setup can lead to quantitative measurements similar to those described for direct absorption (e.g., velocity, temperature, concentration). Though it is more sensitive than conventional absorption spectroscopy, it is more

difficult to set up and to maintain alignment. Scherer et al. describes the history, development and application of CRDS to pulsed supersonic flows [98]. Similarly, Romanini et al., performed CRDS measurements in NO₂ in a supersonic slit jet using a narrow line, continuous wave laser source [99].

CRDS, owing to its extreme sensitivity and the requirement of locking a laser to a cavity, can prove difficult to employ in the often-hostile environments where nonequilibrium aerospace measurements need to be made. Cavity-enhanced absorption (CEA) techniques have been developed that provide enhanced absorption using an optical cavity for enhancing the effective path length without requiring complex cavity-locking mechanisms. Two of the more commonly used CEA variants are cavity-enhanced absorption spectroscopy (CEAS) [100] and integrated cavity output spectroscopy (ICOS) [101, 102]. These methods measure the output signal of the cavity as the laser is scanned across a transition, rather than measuring the ring-down at a discrete set of frequencies. The noise immunity of CRDS is traded for a simpler and more robust arrangement, while still having enhanced sensitivity compared to TDLAS. All cavity-enhanced systems are sensitive to degradation of the quality of the cavity mirrors, which can be a consideration when used in harsh environments.

Most studies involving cavity-enhanced techniques in high-speed or nonequilibrium flows have concentrated on cold supersonic jets and plasmas. Bakowski et al., have used CEAS to make measurements of translational and rotational temperatures of N₂ in an inductively coupled plasma, by exciting transitions from the A³Σ_u⁺(v = 0) band near 686 nm [103]. Fiedler et al. have also expanded the CEAS method to the use of an incoherent broadband light source, and have performed measurements in a cold supersonic jet of azulene over a 40-nm wavelength range [104].

J. HARDWARE USED FOR ABSORPTION

The most common excitation sources used for absorption measurements in hypersonic nonequilibrium flows are semiconductor diode lasers that provide tunable light in the infrared [105]. Tunable diode lasers are relatively inexpensive compared to dye-pumped lasers and have narrow linewidths, which is necessary to resolve the absorption features in many common atoms and molecules. By adjusting the current through and the temperature of the diode, the wavelength can easily be controlled. Furthermore, the wavelength can be scanned at high frequencies (kHz), which is useful for some of the above-mentioned techniques. As a result of these advantages, the diode laser is the preferred choice for absorption measurements although many other laser and nonlaser sources are used.

K. STRENGTHS AND WEAKNESSES OF ABSORPTION METHODS

There are many advantages of absorption methods over other optical diagnostics. In contrast to emission spectroscopy, absorption techniques can probe

nonluminous flows, including both ground and excited states. Furthermore, optical setups for absorption experiments are simpler to set up and interpret compared to other techniques. Light sources, such as diode lasers, are relatively small and inexpensive compared to large pulsed laser systems needed for many techniques such as PLIF and CARS. The frequency and scanning rate of diode lasers are also fast compared to Nd:YAG pumped dye lasers, allowing for high frequency temperature and concentration measurements to be obtained. Because of its simplicity, the absorption technique is also very robust. Also, unlike PLIF, there are no problems with quenching for absorption measurements, making them much simpler to analyze.

The main weaknesses of absorption spectroscopy are that measurements are path-averaged and are normally restricted to a point normal to the flow. Multiple absorption measurements in combination with tomographic reconstruction techniques can be used to invert the data and produce spatial distributions of the desired properties. In contrast, PLIF can easily obtain 2-D measurements along a thin sheet that interrogates the flow. If there is axial symmetry in the flow, then Abel transforms (described in the emission spectroscopy section) can be used to obtain radial distributions.

Because absorption is a path-averaged technique, uniform flow conditions across the path are desired for accurate measurements. Many practical flows have nonuniformities along the optical path, such as boundary layers, heat transfer at walls, and gas dynamic phenomena. These nonuniformities cause problems in the traditional signal analysis described above. In addition to the tomographic approaches described above, work reported in the literature describes methods to correct for these problems [106, 107]. Sanders et al., describe a method to deduce nonuniformity along the path by probing many absorption transitions [70].

V. LASER-INDUCED FLUORESCENCE (LIF)

Laser-induced fluorescence (LIF) uses a laser to probe individual species within the flowfield, providing information pertaining to both the thermodynamic (pressure, temperature, mole fraction) and fluid dynamic state (velocity) of the gas. The laser can be focused to a point for LIF measurements, formed into a thin sheet using a cylindrical and focusing lens in combination for planar LIF measurements (PLIF), or used to illuminate a volume for three-dimensional (3-D) or stereoscopic imaging. Reviews of the laser-induced fluorescence measurement technique are available from Eckbreth [5] and others [108, 109]. The measurement technique works by inducing a transition, usually of an electron, from a lower energy state (E_1) to an excited energy state (E_2) via stimulated absorption of one or more photons in the atomic or molecular species of interest. In a two-level model assumption, the atom or molecule of interest in the E_2 state then returns to the E_1 state by transferring energy via spontaneous emission of a

photon (fluorescence), or by transferring energy nonradiatively through a collision with another atom or molecule (collisional quenching).

For an atom, such as N or O, the energy required to induce an absorption transition of an electron to the E_2 state from the ground (E_1) state is equal to the energy difference between the atom with an electron occupying the excited electronic orbital and the atom's ground electronic orbital configuration, respectively. For molecules, such as N_2 and O_2 , the energies of the E_2 and E_1 states include the energies associated with the vibrational and rotational motion of the molecule in addition to the energy associated with the molecule's electronic configuration. Figure 24 shows a generalized two-level model for fluorescence with the stimulated absorption transition induced by a single photon.

In Fig. 24, the rate at which the absorbing medium in the E_1 state transitions to the E_2 state is proportional to the product of the Einstein coefficient for stimulated absorption, B_{12} , and the laser's spectral irradiance (power per unit area per unit frequency), $I_\nu = IL_\nu$, where I is the irradiance (power per unit area) and L_ν is the laser spectral profile or laser line shape (per unit of frequency) [5]. The energy of the absorbed and emitted photons is the frequency, ν , multiplied by Planck's constant, h . The Einstein A_{21} and B_{12} coefficients describe the probabilities for emission and absorption [110], respectively, whereas Q_{21} is the collisional quenching rate. For absorbing species, the line shape function, Y_ν , describes the spectral width for a particular energy level.

As detailed in Sec. IV.B, the line shape function combines effects from Gaussian-shaped Doppler broadening and Lorentzian-shaped homogeneous broadening mechanisms. The integral of the product of the absorption line shape function, Y_ν , and the laser's spectral profile, L_ν , is defined by the overlap integral, $G = \int Y_\nu L_\nu d\nu$, and describes what portion of a particular absorption transition is affected by the incident laser radiation. The rate constant for stimulated absorption, W_{12} , which describes the rate at which species in E_1 transition to E_2 via absorption of a single photon [5, 109] is then given by:

$$W_{12} = B_{12}IG \quad (49)$$

As the laser passes through a flowfield, it is absorbed at a rate corresponding to Eq. (5.1), inducing a transition between the E_1 and E_2 states. Consequently, as the laser continues to propagate through the flowfield, the irradiance is continually diminished as a result of the absorption process as described by the Beer-Lambert law (Eq. (25)).

In certain circumstances, the energy separation between the E_1 and E_2 states for the species being examined with LIF is such that the

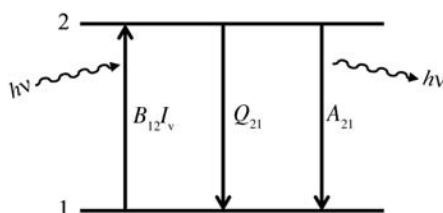


Fig. 24 Two-level model of single-photon fluorescence.

frequency of a photon necessary to induce an absorption transition is far into the UV portion of the electro-magnetic spectrum. However, achieving frequencies far into the UV with conventional laser systems can be difficult [110]. Additionally, strong absorption of UV radiation by many materials and gases (including air) below approximately 200 nm limits the application of laser systems capable of producing such frequencies [5]. One solution is to use two-photon LIF techniques to probe species having absorption transitions in the deep UV. With a two-photon technique, the frequency (and therefore energy) of each photon is half that required by a single photon for the same transition. Figure 25 shows a generalized two-photon fluorescence energy model for two-photon LIF. For atomic species, such as N or O, spontaneous emission is often observed between E_2 and an intermediate energy state, E_3 .

For the two-photon LIF process in Fig. 25, the two-photon absorption cross section results in a rate constant different from that in Eq. (49) and has the form [5, 110–114]:

$$W_{12} = C_{12} I^2 G \quad (50)$$

where C_{12} relates to the two-photon absorption cross section. Note that the dependence of the rate constant scales with the square of the incident laser irradiance, I . This behavior arises from the probability of observing the simultaneous arrival of two photons, which is the square of the probability for the arrival of a single photon [110].

In both Figs. 24 and 25, Q_{21} is the so-called quenching rate constant. It describes the rate at which energy is transferred through nonradiative collisions between excited atoms or molecules in the E_2 state and atomic or molecular collision partners of species i . This rate constant is computed similarly to that in Reference [5] as:

$$Q_{21} = N_T \sum_i \chi_i \sigma_{s,i} v_{s,i} \quad (51)$$

where $N_T = P/k_B T$ is the total population of the excited state, χ_i is the mole fraction of quenching species i , $\sigma_{s,i}$ is the collision cross section between the excited species, s , and quenching species, i , and $v_{s,i} = \sqrt{8k_B T_{\text{trans}}/\pi\mu_{s,i}}$ is the mean relative velocity [115, 116] between the excited species and quenching species, with $\mu_{s,i}$ being their reduced mass and T_{trans} their translational temperature. The spontaneous emission coefficient, A , in

Figs. 24 and 25 is also known as the Einstein A coefficient and describes the probability for spontaneous emission of a photon by an atom or molecule in the excited state [110].

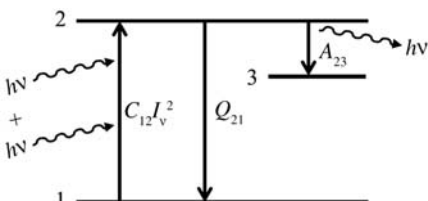


Fig. 25 Three-level model of two-photon fluorescence.

For the two-level model in Fig. 24, the rate of change of the populations N_1 and N_2 , in the E_1 and E_2 states, respectively, can be obtained from relations similar to those presented in Reference [5]:

$$\frac{dN_1}{dt} = -\frac{dN_2}{dt} = -N_1 W_{12} + N_2(Q_{21} + A_{21}) \quad (52)$$

$$N_1 + N_2 = N_s = \chi_s f_B N_T \quad (53)$$

Equation (53) is a conservation law saying that the combined populations of the E_1 and E_2 states is equal to the initial population of the excitation species' E_1 state, N_s , which is in turn the product of the species mole fraction, χ_s , the total population, N_T , and the temperature-dependent Boltzmann fraction, f_B . Equation (52) assumes that the laser intensity is sufficiently weak such that stimulated emission (W_{21}) can be neglected.

The Boltzmann fraction, f_B , describes the ratio of the number of absorbers initially occupying E_1 relative to all possible energy states at a particular temperature, T , when a system is in thermodynamic equilibrium [116]. This term has a general form given by [5, 116, 117]:

$$f_B = \frac{g_j e^{-E_j/k_B T}}{\sum_j g_j e^{-E_j/k_B T}} \quad (54)$$

where g_j is the degeneracy of state j . Degeneracy refers to the number of quantized states that exist in a given energy level, E_j [116]. The summation in the denominator is termed the *partition function*, Q as described in Eq. (18).

More involved differential rate equations can be formulated for the two-photon method such as those presented in Reference [115]. It should be noted that the models presented in Figs. 24 and 25 neglect transitions from E_1 to E_2 resulting from collisions, with a rate constant of Q_{12} . This is usually a good assumption for large energy separations associated with the visible or UV transitions typically employed for LIF. Transitions from the E_2 and E_3 states resulting from pre-dissociation (Q_{pre}) and ionization (Q_{ion}), which are described in References [5] and [109], have also been neglected.

A. LINEAR, STEADY STATE SOLUTION

If a continuous laser source is used to populate the E_2 state and detection of fluorescence occurs well after this source is turned on, then N_2 can be assumed to have reached its steady-state value. From this assumption, the left-hand-side of Eq. (52) is set to zero, resulting in two algebraic equations (Eqs. (52) and (53)) for two unknowns (N_1 and N_2). The same assumption can be made to determine the population, N_2 , achieved by a pulsed laser source if the time required to reach

steady state is short compared to the duration of the pulse. This population is computed as:

$$N_2 = \frac{\chi_s f_B N_T W_{12}}{W_{12} + Q_{21} + A_{21}} \quad (55)$$

The product of this excited state population and the spontaneous emission rate constant is $N_2 A_{21}$ and represents the number of transitions per unit time and per unit volume. Integrating this constant value with respect to time gives the total number of transitions per unit volume during the detection period. Substituting Eq. (49) for W_{12} , and assuming that W_{12} is small compared to A_{21} and Q_{21} (which is valid for low-intensity excitation), a relation for the total number of photons collected via fluorescence by the detection device is [109]:

$$S_{LIF} = \chi_s f_B N_T B_{12} I G \Phi t_{\text{det}} V \frac{\Omega}{4\pi} \eta \quad (56)$$

where $\Phi = A_{21}/(Q_{21} + A_{21})$ is the fluorescence yield, t_{det} is the period of detection, V is the volume probed by the laser source, Ω is the solid angle over which detection occurs, and η is the detection efficiency. The fluorescence yield, Φ , describes the fraction of de-excitation transitions that occur via spontaneous emission (fluorescence) relative to all de-excitation transitions (i.e., spontaneous emission and collisional quenching, assuming pre-dissociation and ionization are negligible). Neglecting the constants in Eq. (56), a generalized form for the fluorescence signal similar to that presented in References [109] and [118] including its thermodynamic (χ, P, T) dependencies and velocity dependence (arising from the Doppler effect), is:

$$S_{LIF} \propto \chi_s N_T f_B(T) B_{12} I G(\chi_s, P, T, U) \Phi(\chi_s, \chi_i, P, T) t_{\text{det}} \quad (57)$$

B. NONSTEADY STATE SOLUTION

For a pulsed laser source, if N_2 is changing during the period of detection, then the entirety of Eq. (52) must be solved to obtain the time-dependent population, $N_2(t)$. Similarly, if the duration of the laser pulse is of the same order of magnitude as the time required to reach steady state, then the population at the end of the laser pulse, $N_2(t_{\text{laser}})$, can be obtained by solving Eq. (52). By assuming the laser intensity behaves as a Heaviside step function in time, the population $N_2(t)$, existing during laser excitation can be calculated by substituting the relation for N_1 from Eq. (53) into Eq. (52) and integrating with respect to time [109]:

$$N_2(t) = \chi_s f_B N_T \frac{W_{12}}{r} \cdot (1 - e^{-rt}), \quad 0 < t \leq t_{\text{laser}} \quad (58)$$

where $r = W_{12} + Q_{21} + A_{21}$. The inverse of this value, r^{-1} , is the characteristic time needed to achieve steady state. This solution assumes an initial condition which typically specifies the initial excited state population to be zero ($N_2(0) = 0$).

When the laser source is turned off, the only pathways to return to the ground state from the excited state are assumed to be through either spontaneous emission or collisional quenching. Therefore, for the period following laser excitation, the first term on the right-hand-side of Eq. (52) is zero. This modified version of Eq. (52) is then used to determine the excited-state population for the period after laser excitation by integrating with respect to time [109]:

$$N_2(t) = \chi_s f_B N_T \frac{W_{12}}{r} \cdot (1 - e^{-rt_{\text{laser}}}) \cdot e^{-(t-t_{\text{laser}})/\tau_{\text{LIF}}}, \quad t > t_{\text{laser}} \quad (59)$$

This solution assumes that the laser intensity is turned off instantaneously, with an initial condition given by Eq. (58), evaluated at $t = t_{\text{laser}}$. This solution shows that the population in the excited state decreases exponentially in time after the laser pulse.

The term $\tau_{\text{LIF}} = (Q_{21} + A_{21})^{-1}$ in Eq. (59) is referred to as the fluorescence lifetime and describes the rate at which the population in a particular excited state transitions to a lower state. As with the derivation of Eq. (56), the total number of photons collected via fluorescence over the detection period is determined by multiplying Eqs. (58) and (59) by the spontaneous emission rate Einstein coefficient A_{21} , accounting for the collection volume and detection system, and integrating with respect to time [109]:

$$S_{\text{LIF}} = \chi_s f_B N_T \Phi B_{12} I G t_{\text{laser}} \left\{ \left[1 - \frac{1 - e^{-rt_{\text{laser}}}}{rt_{\text{laser}}} \right] + \left[\frac{(1 - e^{-rt_{\text{laser}}})}{t_{\text{laser}}/\tau_{\text{LIF}}} \right] \right\} V \frac{\Omega}{4\pi} \eta \quad (60)$$

Like Eq. (56), this solution assumes that W_{12} is small compared to A_{21} and Q_{21} . However, if the laser irradiance, I , is sufficiently large such that W_{12} and W_{21} are of the same order of magnitude as Q_{21} and A_{21} , then both must be included in the solution. This gives $r = W_{12} + W_{21} + Q_{21} + A_{21}$ during laser excitation. By defining the irradiance at which the fluorescence signal saturates as [5, 109] $I_{\text{sat}} = (Q_{21} + A_{21})/(B_{12} + B_{21})$ and rearranging such that $r = \tau_{\text{LIF}}^{-1}[I/I_{\text{sat}} + 1]$, a more detailed formulation for the fluorescence signal, including effects from laser saturation, is given as [109]:

$$S_{\text{LIF}} = \chi_s f_B N_T \Phi B_{12} \frac{I}{1 + I/I_{\text{sat}}} G t_{\text{laser}} \left\{ 1 + \frac{1 - e^{-rt_{\text{laser}}}}{rt_{\text{laser}}} \left(\frac{I}{I_{\text{sat}}} \right) \right\} V \frac{\Omega}{4\pi} \eta \quad (61)$$

When $I \ll I_{\text{sat}}$, Eq. (61) simplifies to a form similar to that of Eq. (58).

C. MULTILEVEL FLUORESCENCE MODELING

In the preceding discussion, a simplified two-level model of fluorescence was put forth, which provides for an understanding of the most basic physical mechanisms and energy transfer processes involved. This basic description allows for the development of a general analytic relation between the fluorescence signal and these mechanisms and processes. However, such a simple description does not

account for rotational or vibrational energy transfer occurring between the absorbing species and the surrounding gas mixture. As each electronic energy level depicted in Fig. 24 can have vibrational and rotational fine structure for molecular species, such energy transfer processes result in a redistribution of the populations to various vibrational and rotational states. To account for these processes, analytical models including multiple energy states and a system of population rate equations are used. Discussion of such modeling aspects can be found in References [5], [108], and [109].

D. TRANSLATIONAL TEMPERATURE

Translational temperature resulting from the random thermal motion of the absorbing species can be determined by measuring the Doppler-broadened width of the absorption line shape function of Eq. (36). If the temperature, pressure, and mole fractions at a particular location are assumed to be constant, then the Boltzmann fraction and fluorescence yield in Eq. (5.9) at that location are also assumed to be constant. If these assumptions are valid, and if the laser line shape function is known, then the fluorescence signal will be proportional to the overlap integral at a particular frequency. By scanning the laser's spectral frequency across a particular transition, the absorption line shape function can be obtained.

Once the absorption line shape is obtained, the contribution of homogeneous broadening mechanisms to the line shape must be determined to allow for calculation of the Doppler-broadened line width. Homogeneous broadening can include components from Van der Waals broadening and Stark broadening effects [119], in addition to collisional pressure-broadening effects. In many cases, the Van der Waals and Stark effects can be ignored, resulting in homogeneous broadening from pressure alone. If the pressure is known, then the component of the line shape due to homogeneous broadening can be determined. Alternately, if the pressure is sufficiently low, then collisional pressure broadening can be ignored. A fitting algorithm can then be used to determine the contribution of Doppler broadening to the line shape. This allows for a more accurate temperature calculation as only one parameter, $\Delta\nu_D$, must be iterated upon to fit the line shape. The translational temperature, T_{trans} , of the absorbing species can then be obtained by modifying Eq. (50):

$$T_{\text{trans}} = \frac{m}{8 \ln(2)k_B} \left(\frac{c\Delta\nu_D}{v_o} \right)^2 \quad (62)$$

Both single-photon [119–121] and two-photon [122–126] methods have been used to measure translational temperature. The requirement of scanning a laser's frequency to resolve the Doppler-broadened line shape can limit the time resolution of the temperature measurement such that only average translation temperatures can be obtained.

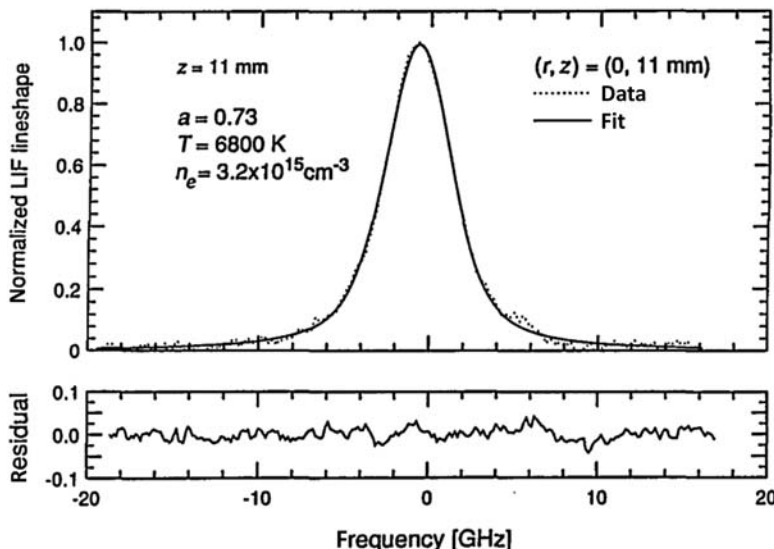


Fig. 26 Experimental LIF data measured (dotted line, upper plot) in an Argon plasma and corresponding fit of Voigt line shape (solid line, upper plot) to the experimental data (upper plot) and difference between experimental data and fit (lower plot). Image reprinted from Reference [119] with permission of the authors and the publisher.

Figure 26 shows LIF data (dotted line, upper plot) from Reference [119] obtained by performing a frequency scan with a semiconductor laser source over an argon metastable transition centered at 810.4 nm. Each frequency scan over the absorption transition took 500 seconds to complete. In the experiment, argon plasma was generated using an inductively coupled plasma torch. The translation temperature, T , and electron number density, n_e , were obtained by fitting the Voigt line shape function, which accounted for both Doppler-broadening and several collisional broadening mechanisms, to the experimental LIF data (solid line, upper plot). The lower plot in Fig. 26 shows the residual: the difference between the experimental LIF data and the fitted line shape. An analysis of one of the scans in Reference [119] gave $T_{\text{trans}} = 6800 \pm 690$ K, resulting in a $\sim 10\%$ measurement uncertainty.

E. ROTATIONAL TEMPERATURE

For molecules, the rotational temperature, T_{rot} , can be obtained by exciting two absorption transitions and relating the signal intensities observed from each transition to the rotational temperature through modification of Eq. (57). This method was demonstrated in Reference [127] using a two-photon excitation method to

measure rotational temperature at a point in a cold (~ 300 K) turbulent flow. For each rotational transition, the population fraction, f_B , is dependent on the rotational energy, F_j , rotational quantum number, J , and rotational temperature, T_{rot} , of the absorbing species. This assumes that excitation occurs in the same vibrational state, v , such that the vibrational energy, G_v , is constant for each probed rotational transition. If χ_s , G , Φ , and t_{det} are assumed to be independent of the rotational state of the absorbing species, then the ratio, R , of fluorescence signals can be simplified to the following relation, similar to that in References [109, 128–131]:

$$\frac{S_{\text{LIF},i}}{S_{\text{LIF},j}} = R = C \frac{B_{12,i}E_i(2J_i + 1) \exp[-F_{J,i}/k_B T_{\text{rot}}]}{B_{12,j}E_j(2J_j + 1) \exp[-F_{J,j}/k_B T_{\text{rot}}]} \quad (63)$$

where the subscripts i and j refer to the particular excited absorption transition, E is the laser energy such that $E = at_{\text{laser}}I$, a is the beam cross-sectional area, t_{laser} is the temporal pulse width of the laser, and C is a constant which includes all terms that are independent of the rotational state of the absorbing species. Solving for T_{rot} in Eq. (63) yields:

$$T_{\text{rot}} = \frac{-\Delta E_{\text{rot}}}{k_B \ln \left[CR \frac{B_{12,j}E_j(2J_j + 1)}{B_{12,i}E_i(2J_i + 1)} \right]} \quad (64)$$

Here, $\Delta E_{\text{rot}} = (F_{J,i} - F_{J,j})$, and is the difference in energy between the probed rotational levels. To minimize the uncertainty associated with the measured rotational temperature, δT_{rot} , a propagation-of-error analysis can be performed on Eq. (63) by computing the derivative of the signal ratio, R , with respect to T_{rot} [129, 132]:

$$\frac{\delta T_{\text{rot}}}{T_{\text{rot}}} = \frac{k_B T_{\text{rot}}}{\Delta E_{\text{rot}}} \frac{\delta R}{R} \quad (65)$$

This analysis suggests that by increasing ΔE_{rot} , and thereby probing two widely separated rotational energy levels, the uncertainty in T_{rot} can be proportionally decreased for a given error in R [129].

Figure 27 shows a mean rotational temperature map of nitric oxide measured in the wake of a 6.35-mm-thick flat plate in a Mach 3 turbulent flow, taken from Reference [132]. The map was obtained by averaging a series of images taken for excitation from rotational levels $J = 8.5$ and $J = 10.5$, computing the ratio of the two averaged images, and using a relation similar to that in Eq. (64) to compute T_{rot} . In this experiment, it was shown that the turbulent nature of the flowfield required excitation of two relatively closely spaced rotational levels ($J = 8.5$ and 10.5). This requirement arose from the nonlinear relation between R and T_{rot} in Eq. (64), which can be heavily influenced by flowfield turbulence.

Figure 27 shows a time-averaged temperature measurement obtained using a single laser, which probed the two transitions in separate wind tunnel runs.

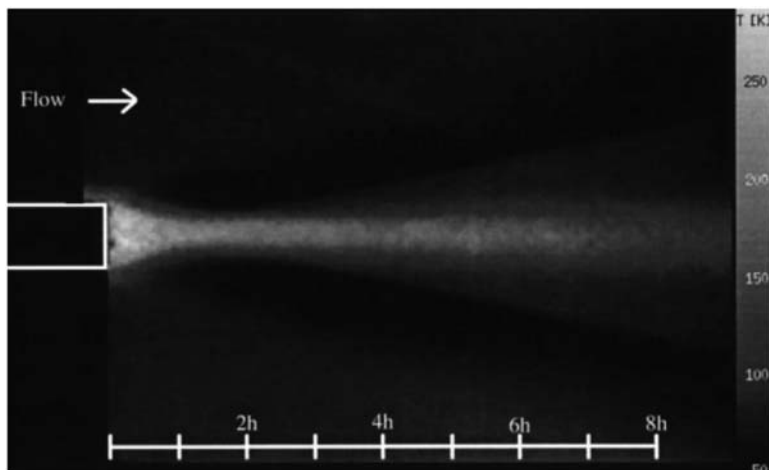


Fig. 27 Rotational temperature map obtained in the supersonic wake of a flat plate using two-line rotational thermometry. Image reprinted from Reference [132] with permission from the authors and Springer Science and Business Media.

To obtain instantaneous temperature measurements in a plane using this method, a two-laser, two-camera system can be used, as in References [128–130]. In Reference [129], instantaneous two-line temperature imaging of OH in a shock tube at a nominal pressure of 40.53 kPa and temperature range of 1500–2950 K resulted in temperature measurements with errors of ~20%–25%.

Multirotational-line temperature methods also exist and can potentially provide relatively higher sensitivity and dynamic range T_{rot} measurements, particularly at lower temperatures where rotational energy levels are closely spaced [133]. Such methods are appropriate when large variations in T_{rot} are expected, requiring probing of several rotational levels. The rotational temperature is computed by exciting multiple rotational lines and measuring the signal. This measured fluorescence signal, together with the measured laser energy are then substituted into the following relation [131]:

$$\ln \left[\frac{S_{\text{LIF},i}}{B_{12,i} E_i (2J_i + 1)} \right] \quad (66)$$

A plot of this logarithmic term vs $F_{j,b}$ known as a Boltzmann plot, yields a linear trend with a slope of $-k_B T_{\text{rot}}$. References [133–136] used this method to characterize rotational temperatures in arc jet flows. An alternative multiline approach used in Reference [137] for measurements in a flame involved fitting a simulated rotational spectrum to experimental data to obtain T_{rot} .

F. VIBRATIONAL TEMPERATURE

The vibrational temperature, T_{vib} , can be measured using an approach similar to that used for rotational temperature. For T_{vib} measurements, a two-line approach can be used. Such an approach is presented in Reference [138], in which the same rotational levels, $J_i = J_f$, are probed in two different vibrational levels, $v_i \neq v_f$, resulting in nearly constant rotational energies, F_j , but different vibrational energies, G_v . Assuming χ_s , G , Φ , and t_{det} to be independent of the rotational and vibrational levels, the ratio of fluorescence signals, R , can be used to measure vibrational temperature, T_{vib} , in a way analogous to that in Eqs. (63) and (64).

As with rotational temperature measurements, a multivibrational-line temperature measurement method can also be used to infer T_{vib} by modifying the logarithmic term from Eq. (5.18) [131]:

$$\ln \left[\frac{S_{\text{LIF},i}}{B_{12,i} E_i (2J_i + 1) \exp [-F_{J,i}/k_B T_{\text{rot}}]} \right] \quad (67)$$

If the rotational level, J_i , is fixed and the rotational energy, $F_{J,i}$, is kept approximately constant, then the vibrational temperature can be computed independently of rotational temperature [131]. This is done by generating a Boltzmann plot of vibrational energy, $G_{v,i}$, vs this logarithmic term, resulting in a linear relation with a slope equivalent to $-1/(k_B T_{\text{vib}})$.

Figure 28a, taken from Reference [131], shows a Boltzmann plot generated using a relation like that in Eq. (5.19) to infer vibrational temperature. The image data in the experiment were used to measure T_{vib} at a point downstream of a free-piston shock tunnel nozzle on the centerline of the flow. In this experiment, three absorption transitions were selected that had nearly constant rotational energies, F_j , but differing vibrational energies, G_v . In Fig. 5(b), also

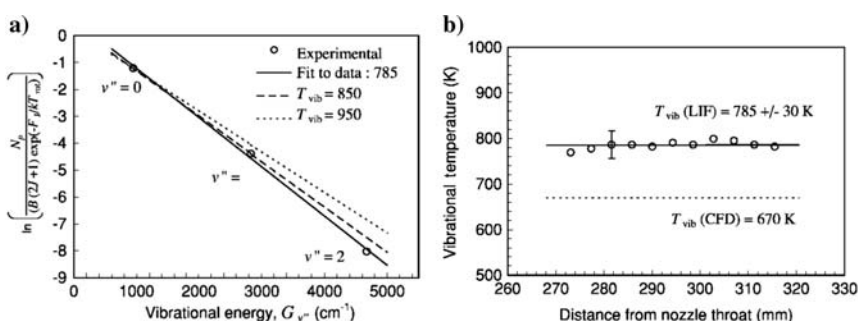


Fig. 28 Vibrational temperature measurement obtained by probing multiple vibrational levels and generating a) a Boltzmann plot and b) vibrational temperatures plotted as a function of distance downstream. Images taken from Reference [131] with permission of the authors.

taken from Reference [131], the vibrational temperature of NO was observed to be constant with distance downstream of the nozzle, even though the nozzle was conical and the rotational temperature was shown to be decreasing with distance downstream, as the flow expanded. A simple computational model (shown in Fig. 5(b)) was not able to accurately predict the measured vibrational temperature [131]. As shown in Fig. 5(b), $T_{\text{vib}} = 785 \pm 30$ K, giving an uncertainty of $\sim 4\%$.

G. SPECIES CONCENTRATION

Returning to the simplified Eq. (56), it is possible to quantify the number density, $\chi_s N_T$, using LIF. However, several factors complicate the interpretation of a LIF signal and its relation to concentration. For instance, Q_{21} in Eq. (51) depends on the concentration and temperature of the absorbing species and all other constituent species in the probed mixture. If the temperature of the mixture were unknown, then a separate measurement of temperature would be required to determine both Q_{21} and the temperature-dependent Boltzmann fraction. The measurement system also requires an appropriate absolute intensity calibration to a known reference, which can be further complicated by the collection optics and filters used in such a measurement. The response of the detection system as a function of S_{LIF} intensity and spectral frequency must also be well understood. The following discussion highlights some of the methods that have been used to provide concentration measurements that address some of these issues.

1. NONQUANTITATIVE FLOW VISUALIZATION

A relatively simple approach to obtaining a qualitative visualization of species concentration is to use laser-induced fluorescence to visualize the spatial distribution of the absorbing species. To first-order, the fluorescence signal in Eq. (57) is proportional to the relative species concentration, $\chi_s N_T$, assuming all other terms are constant. In hypersonic nonequilibrium test facilities, the formation of reactive species at the high enthalpies required to simulate true flight conditions can influence the gas dynamics under study. For example, arc-heated facilities are often used to simulate true flight enthalpy conditions by depositing significant energy into a test gas and then expanding that gas to hypersonic Mach numbers. This process can result in a nonuniform species distribution resulting from the unsteady nature of the electrical arc.

Figure 29 (from Reference [139]) shows instantaneous nitric oxide (NO) planar LIF images in false color acquired in the Hypersonic Materials Environmental Test System (HyMETS) arc-heated facility at the NASA Langley Research Center for a flow simulating earth's atmosphere at several enthalpy conditions. The flow in this figure is from left to right. The object on the right-hand edge of the field of view is a 25 mm diameter silicon carbide tipped probe aligned with the axis of symmetry of the facility nozzle. For the lowest enthalpy condition

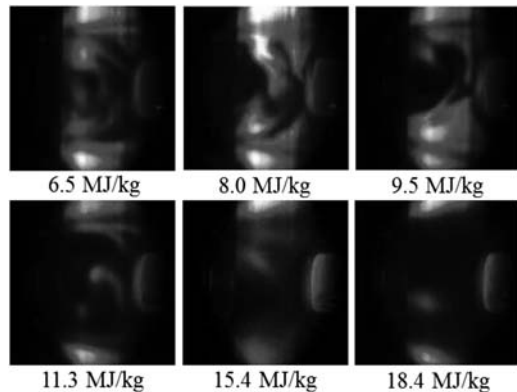


Fig. 29 Instantaneous nitric oxide planar LIF flow visualization images in false color acquired in the Hypersonic Materials Environmental Test System (HyMETS) arc-heated facility at NASA Langley Research Center. Flow is from left to right. Images taken from Reference [139] with permission of authors (see color section).

shown (6.5 MJ/kg), the spatial distribution of NO within the core of the nozzle flow is irregular, suggesting that the energy deposition by the arc upstream of the nozzle is nonuniform. As the flow enthalpy increases to 18.4 MJ/kg, the distribution of NO remains irregular and the total production of NO appears to decrease.

Other examples of such LIF-based flow visualization experiments are provided in Reference [140]. The interpretation of such flow visualization images and their relation to quantitative species concentration measurement is complicated. The remaining terms in Eq. (5.9), such as the quenching rate constant, often vary significantly in high-speed nonequilibrium flows and can be difficult to determine. The sections that follow detail approaches for quantitative measurements of concentration which address such complicating factors.

2. SATURATED LIF

To avoid the complications associated with an unknown quenching rate constant, a relatively high laser irradiance where $I \gg I_{\text{sat}}$ can be used to probe the absorbing species [5]. In this instance, the stimulated absorption and emission rates dominate both collisional quenching and spontaneous emission rates; that is, $(W_{12} + W_{21}) \gg (Q_{21} + A_{21})$. The result of this leads to a modified form of Eq. (56) where stimulated emission is included and the fluorescence signal is of a form similar to that in Reference [5].

$$S_{\text{LIF}} = \chi_s f_B N_T A_{21} \frac{B_{12}}{B_{12} + B_{21}} t_{\text{det}} V \frac{\Omega}{4\pi} \eta \quad (68)$$

If A_{21} , B_{12} , and B_{21} are known, then this method can be used to measure concentration if the remaining terms, such as f_B , can be determined. In practice, it is difficult to achieve $I \gg I_{\text{sat}}$ because high powered pulsed laser beams are typically Gaussian, both spatially and temporally, so much of the acquired signal can originate from the lower intensity edges of the Gaussian beam, which excite the fluorescence linearly [5]. Further discussion of this method is found in References [5] and [108].

3. PRE-DISSOCIATION LIF

Pre-dissociative fluorescence involves inducing a transition to a level in the excited state, which can then couple to a dissociative state, resulting in dissociation of the molecule into smaller molecules or atoms. Pre-dissociative fluorescence concentration measurements are similar to saturated fluorescence measurements in that the dependence on Q_{21} in Eq. (56) can be removed, in this case by exciting the absorbing species to a pre-dissociative state where the pre-dissociation rate, Q_{pre} , is faster than both Q_{21} and A_{21} [5]. A discussion of this mechanism can be found in References [141] and [142] and a general discussion of the method can be found in References [5] and [108]. An application of the pre-dissociative technique was presented in Reference [143] to measure time-averaged OH concentrations in a supersonic hydrogen-air turbulent combusting flow. Concentrations as high as $5.4 \times 10^{16} \text{ cm}^{-3}$ with uncertainties of 21% or less were reported [143].

4. SHORT-PULSE LIF

There are two methods of using short laser pulses to quantitatively determine concentration. The first probes the species of interest with a laser pulse having a duration much shorter than the time between collisions with other species. With this method, the concentration can be determined by relating the measured exponential fluorescence decay behavior to the initial signal magnitude during the short-pulse excitation period. Although this decay is a function of both A_{21} and Q_{21} , extrapolation of the exponential behavior to initial excitation provides an inferred peak intensity magnitude, which is assumed to be independent of collisional quenching effects [108]. This independence is assumed since a sufficient number of collisions, required to transfer energy nonradiatively from the excited state, would not yet have occurred. A discussion of this method can be found in Reference [108]. Reference [144] uses a form of this short-pulse method for OH concentration measurements in a turbulent flame.

A second method for measuring concentration involves using a laser pulse that is shorter than or comparable to the fluorescence lifetime but not shorter than the collisional timescales described in Reference [5]. In this approach, the fluorescence lifetime is measured directly, usually using a PMT. This short-pulse LIF method can also be used to determine spontaneous emission [145]

and collisional quenching [146, 147] rate constants when the thermodynamic conditions of the probed mixture are known. Even for unknown conditions, measurement of the fluorescence lifetime allows for the quenching rate to be determined and accounted for. References [148] and [149] use a two-photon LIF technique in which fluorescence lifetime measurements are used to correct for collisional quenching effects in a similar manner. Figure 30a, taken from Reference [148], shows spectral scans of atomic nitrogen in the NASA Ames Aerodynamic Heating Facility arc jet flow (arcjet) and laboratory flow reactor (lab). Fluorescence measurements from the flow reactor and a krypton reference cell were used for intensity calibration in order to provide absolute atomic nitrogen number densities. The fluorescence lifetimes observed in the arc jet and flow reactor were used to correct for collisional quenching effects. Figure 30b, also taken from Reference [148], shows radial atomic nitrogen number density measurements for two air/argon arc jet runs taken 35.6 cm downstream of the nozzle exit. The reported uncertainty in number density was $\sim 12\%$ [148].

A similar approach is being developed for mole fraction measurements in hypersonic turbulent boundary layers using naphthalene PLIF [150, 151]. One benefit of using naphthalene is that it sublimates at slightly elevated temperatures (with respect to room temperature), allowing for the study of scalar transport effects in transitional boundary layers, turbulent boundary layers, and ablating surfaces.

5. BI-DIRECTIONAL BEAM LIF

If two overlapping, counter-propagating beams are tuned to the same transition, the ratio of fluorescence signals results in the cancellation of all terms in Eq. (57) at

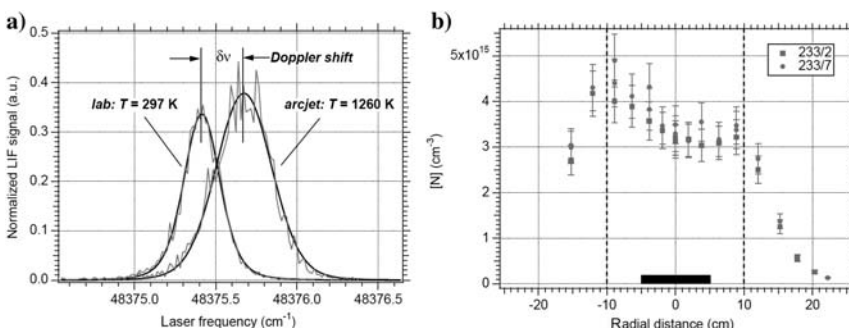


Fig. 30 a) Spectral scans of atomic nitrogen in the NASA Ames Aerodynamic Heating Facility arc jet flow and in a laboratory flow reactor and b) measured number densities spanning the radial direction of the arc jet 35.6 cm downstream of the nozzle exit. Image taken from Reference [148] with permission of the authors.

a point in the flow, with the exception of the spatially dependent laser irradiance. Thus, the spatially varying ratio of fluorescence signals can be equated to the spatially varying ratio of irradiances of the respective beams. The Beer–Lambert law of Eq. (25) can then be used to relate irradiance, and therefore fluorescence signals, to number density via the relation [57]

$$k_s(v) = N_s \varphi_s(v) \quad (69)$$

where $\varphi_s(v)$ is the transition cross section of the absorbing species, describing the absorbing species' interaction with the incident irradiance on a per atom or molecule basis [110]. Combining Eq. (69) with Eq. (26) allows for a relation between the natural logarithm of the signal ratio and the absorbing species number density to be made [152]:

$$N_s(x) = \frac{1}{2\varphi_{s,0}} \frac{d}{dx} \ln \left[\frac{S_{\text{LIF},1}(x)}{S_{\text{LIF},2}(x)} \right] \quad (70)$$

where $S_{\text{LIF},1}(x)$ and $S_{\text{LIF},2}(x)$ are the spatially varying fluorescence signal intensities of the forward- and backward-propagating beams, respectively. In Eq. (70), $\varphi_{s,0}$ is the peak transition cross section, with $\varphi_{s,0} = \varphi_s(v_0)$ [110].

This concentration measurement technique was first demonstrated in Reference [152]. The technique only requires that a value for $\varphi_{s,0}$ be known in order to make an absolute concentration measurement of N_s [152]. For total absolute concentration, however, f_B must either be assumed or measured, as from Eq. (5.5), $N_s = \chi_s f_B N_T$. Figure 31 (taken from Reference [152]), graphically depicts the process of obtaining a concentration of OH in a methane-air flame. In the top plot, the fluorescence intensities are plotted vs position across the flame. The middle plot shows the natural logarithm of the ratio of these two signals with position and the bottom plot shows the calculated absolute OH concentration using Eq. (5.22). Measurements of OH concentration were also made in a plane in Reference [152] by imaging fluorescence from two counter-propagating laser sheets. Equation (5.22) was applied using each row of pixels to compute signal ratios. Single-shot imaging of a hydrogen/air/oxygen flame allowed for calculation of means and standard deviations of OH concentration. Using 10 images for each laser sheet direction (20 total images), Figure 31 (from Reference [152]) showed a mean peak OH concentration of $\sim 8.8 \times 10^{14} \text{ cm}^{-1}$ with a standard deviation of $\sim \pm 1.7 \times 10^{14} \text{ cm}^{-1}$, which is $\sim 19.7\%$ of the mean.

6. COMBINED LIF/RAYLEIGH/RAMAN

In reacting flows, flows undergoing transition-to-turbulence, and turbulent flows, the time-varying nature of flow properties make it difficult to ascertain concentration. By making simultaneous time-resolved measurements of temperature and major species concentrations, the thermodynamic-dependent parameters in

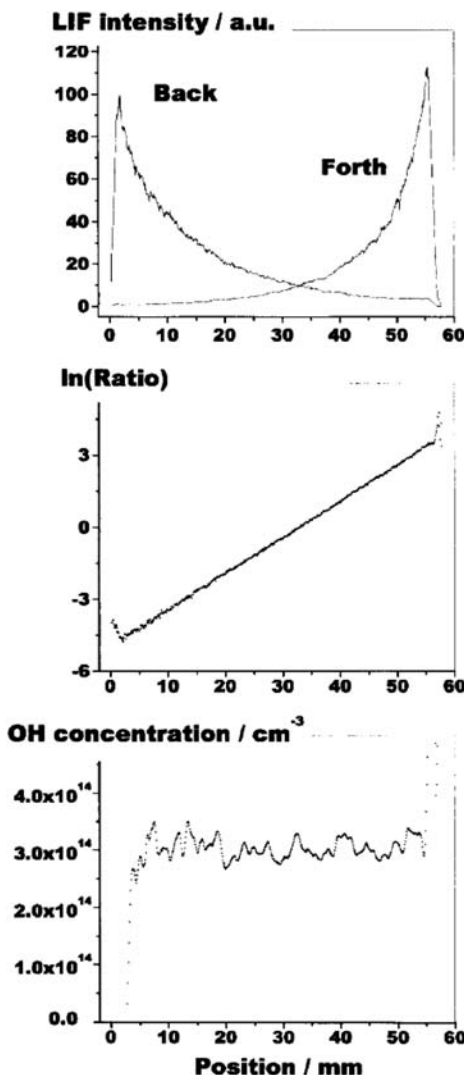


Fig. 31 Graphical depiction of methodology used to measure concentration using bi-directional beam LIF. Top plot shows spatially varying fluorescence signals, middle plot shows natural logarithm of ratio of these signals, and bottom plot shows OH concentration calculated using Eq. (70). Image reprinted from Reference [152] with permission of the authors and Springer Science and Business Media.

Eq. (57) (Boltzmann fraction, overlap integral, and fluorescence yield) can be determined, and a direct relation between concentration and fluorescence signal established. A combined fluorescence, Rayleigh scattering, and Raman scattering measurement technique was used for this purpose in Reference [153]. In that experiment, the Raman scattering was used to measure instantaneous concentrations for major species (O_2 , N_2 , H_2O , and H_2) in a turbulent hydrogen jet flame. This allowed for the mole fractions of the collision partners, χ_i , in Eq. (51) to be calculated. The combined Rayleigh/Raman scattering measurements were then used to measure temperature. The temperature-dependent collisional cross sections and relative velocity in Eq. (51) could then be calculated, and the collisional

quenching rate, Q_{21} , determined. The temperature-dependent absorption line shape and Boltzmann fraction could also be determined from the temperature measurement. The additional measurement of laser energy then provided for a direct relation between NO fluorescence signal and concentration to be established. In Reference [154], this technique was used to make concentration measurements of CO in turbulent premixed and stratified CH_4 /air flames.

A stated CO concentration accuracy and precision (single standard deviation) of 10% and 4.5%, respectively, were given [154].

H. PRESSURE

Measurements of pressure can also be obtained using a LIF-based approach, although such measurements are not as commline shapeon as LIF-based temperature and species concentration measurements (described in the preceding sections) for determination of the thermodynamic state of a gas. This is in part due to the implicit relationship between fluorescence signal and pressure in Eq. (57), as opposed to the explicit relationships with temperature and concentration.

One method by which pressure can be measured is by tuning to the center frequency of an absorption transition and relating the measured fluorescence signal to pressure. For such measurements, the selected absorption transition must be carefully chosen such that the temperature dependence (i.e., f_B) can be removed over the range of temperatures expected for the experiment. When this is done, the fluorescence signal is inversely proportional to the static pressure if certain additional simplifying assumptions are made. This approach has been used in low-quenching ($Q_{21} \ll A_{21}$) flows [132] or quenching-dominated ($Q_{21} \gg A_{21}$) flows where the pressure broadening is much larger than the Doppler broadening [155, 156].

Often for quenching-dominated LIF-based pressure measurements, however, the dependence of fluorescence signal on pressure when tuned to the center of an absorption transition is nearly removed, as N_T (and hence pressure) can be factored out of both the numerator and denominator in Eq. (57). An alternative approach is to infer pressure from the absorption lineshape function. This can be accomplished if a separate measure of temperature can be made so that the absorption lineshape dependence on temperature can be isolated from its dependence on pressure. Common methods include those which relate the width of the absorption lineshape to pressure [157], those which resolve the entire absorption lineshape function [158], and those which relate the ratio of fluorescence signal from the wing of the lineshape to the signal from the center of the lineshape [159–161].

I. DOPPLER-BASED VELOCIMETRY

The Doppler effect can be used to determine flow velocities for atomic and molecular species. The translational motion of the absorbing species in the direction of the excitation laser's propagation, described by a velocity component U , results in a shift of the absorption line shape function away from its transition center frequency, ν_0 , according to [57]:

$$\Delta\nu = \frac{U}{c} \nu_0 \quad (71)$$

This velocity-dependent frequency shift of the absorption line shape function is implicit in the overlap integral, G , and thus, its effect on fluorescence signal can be seen through the dependence of G on the velocity component, U , in Eq. (57). When a component of translational motion of the absorbing species opposes the laser's direction of propagation, corresponding to the negative (-) solution of Eq. (71), the incident laser radiation appears to be at a higher frequency from the perspective of the gas. Hence, as the laser's frequency is scanned over the absorption transition, Y_v , the measured intensity of fluorescence corresponding to this profile is shifted toward a lower frequency, or red-shifted. The converse is true when motion is in the same direction as the laser's propagation, corresponding to the positive (+) solution of Eq. (71), where the absorption profile is shifted toward a higher frequency, or blue-shifted.

In one implementation, velocity component measurements can be made by scanning the laser over an absorption transition in both the measurement volume and a reference cell. In this case, the Doppler shift between the absorption profiles is used to compute an average velocity according to Eq. (71). Examples of such measurements include those in an arcjet [120, 121, 125, 162], supersonic underexpanded jets [157, 158, 163–165], shock tunnel [166, 167], and nonreacting supersonic flow with a rearward-facing step [168–170]. Such measurements require that the flowfield be relatively steady, as shot-to-shot fluctuations in fluorescence intensity from thermodynamic and fluid dynamic variations can affect the measured line-shape. The velocity measurements can also be complicated by a frequency shift in the line shape function resulting from collisional effects (pressure). In compressible flows, the pressure field can vary significantly, and hence the collisional shift in the line shape function can likewise vary. Absorption of laser energy can also result in an apparent frequency shift in the line shape function. Recall that the line shape function must be inferred from the overlap integral, G , which represents the convolution of the absorption line shape and laser spectral line shape. If absorption is significant, then irradiance will vary spatially according to Eq. (25), resulting in a spatially varying overlap integral. An analysis of how absorption affects the line shape frequency shift is presented in Reference [167]. If flow symmetry is assumed, then the frequency shift due to pressure can be estimated [166]. Flow symmetry can also be used in the application of Eq. (25) to correct for the frequency shift resulting from absorption [121]. Alternatively, if two counter-propagating laser beams are used, these frequency shift effects can be completely removed. The use of counter-propagating beams results in two excitation peaks, separated in frequency by twice the velocity-induced Doppler shift. The need for a reference cell measurement to ascertain velocity can also be removed, as a counter-propagating beam approach is self-referencing [164, 171, 172].

Figure 32 shows a two-component velocity measurement about a heat shield model taken in a hypersonic free-piston shock tunnel. In this experiment, laser

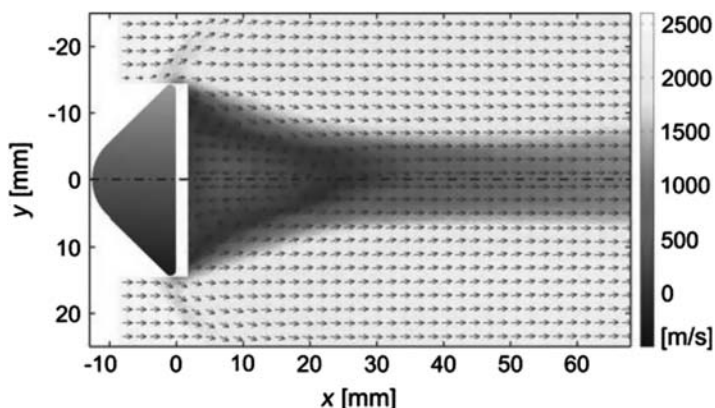


Fig. 32 Two-component velocity measurement using fluorescence-based Doppler velocimetry technique. Vectors denote flow direction and color map represents magnitude. Image reprinted from Reference [167] with permission of the authors and Springer Science and Business Media (see color section).

sheets were directed in both the radial (vertical) and axial (horizontal) directions so that measurements of the Doppler-shifted absorption profiles for the respective directions could be obtained and compared with measurements from a static reference cell to infer velocities. An estimation of velocity errors incurred from the frequency shifts due to absorption and collisional effects was also performed. In Reference [167], three separate absorption transitions were probed to measure two different velocity components, with one transition being used for both components. This resulted in a measured axial freestream velocity of 2394 ± 68 m/s and a measured radial velocity of 53 ± 50 m/s, giving respective uncertainties of $\sim 2.8\%$ and $\sim 94.3\%$ [167].

Another form of the fluorescence-based Doppler velocity measurement is a fixed frequency method, which can allow for an instantaneous velocity component measurement. With the fixed frequency technique, a narrow linewidth laser is tuned off the absorption profile peak to a point where the slope of the profile is maximum, as described in References [159] and [173]. Assuming that the absorption profile is approximately linear in the region of maximum slope, the measured signal intensity can be related to the Doppler shift of the profile. This fixed frequency Doppler velocimetry technique has been applied to a free jet [174], supersonic underexpanded jet [175], and reacting supersonic flow [176]. The stated random and systematic errors in Reference [175], when added in quadrature, gave a total uncertainty of $\sim 12\%$. In Reference [176], the stated lowest time-averaged and single-shot uncertainties achieved were $\sim 3\%$ and $\sim 15\%$, respectively, for a 1600 m/s velocity range.

J. FLOW-TAGGING VELOCIMETRY

Another technique by which velocity can be measured using fluorescence is flow-tagging velocimetry. Fluorescence-based flow-tagging velocimetry is a time-of-flight technique that involves laser excitation—or tagging—of the gas along a line, series of lines, or grid pattern. With this form of velocimetry, the species of interest in the gas absorbs the incident radiation from a laser source, which induces either of the following: 1) fluorescence, 2) a reaction that forms a product that then emits a photon via fluorescence, or 3) a reaction that forms a product that can then be probed with another laser source to induce fluorescence. Images of the fluorescence pattern are acquired at two time delays, with velocity computed by measuring the displacement of the tagged molecules between images. Typically, a line or series of lines can be used to measure a single-component of velocity, whereas a crossed grid pattern can be used to measure two-components. Two general fluorescence-based methods of flow-tagging velocimetry are discussed here; one that requires a single laser source and another that requires multiple laser sources. The main advantage of flow-tagging velocimetry, as compared to most Doppler-based methods (which are time averaged), is that it can make instantaneous (single-shot) measurements with fast time resolutions (as short as a few hundred nanoseconds). A disadvantage, however, is that flow-tagging velocimetry cannot provide full velocity field information. A broader discussion of molecular-tagging velocimetry, which relies on molecular tracers for flow-tagging, is provided in Reference [177].

1. SINGLE-LASER METHODS

The first method involves either direct or indirect excitation of fluorescence with a single laser source. The first application of this method to a gaseous flow involved excitation of phosphorescence of biacetyl molecules, as described in Reference [178]. If this method is used, the fluorescence lifetime of the tagged molecules must be long enough so that advection provides for measurable displacements with tagged regions having signal intensities that are still above the detection limit of the imaging system at the time the second image is acquired. Typical experiments involve capturing a reference image acquired during the tagging process, or a relatively short time thereafter. If a single-framing camera is used, such as in Reference [179], a single reference image or set of reference images is acquired. The timing of the single-frame camera is then delayed and a subsequent image or set of images is then acquired. If a two-camera system or dual-framing camera is used, such as in Reference [180], the delayed image is acquired in sequence after the reference image. The velocity is computed by measuring the displacement of the tagged molecules that occurs in the time between when the reference and delayed images were acquired. The form of this technique relying on direct excitation of fluorescence for flow tagging has been applied to the study of supersonic

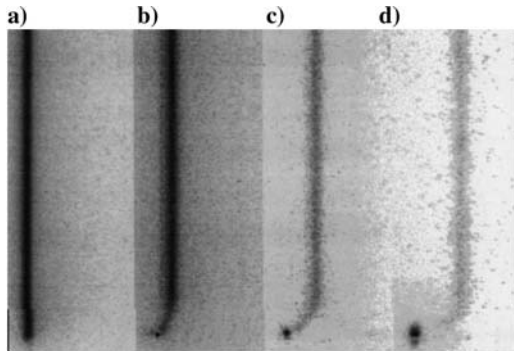


Fig. 33 Single-line excitation of nitric oxide fluorescence used to study hypersonic boundary layer flow over a flat plate. Images, from left to right, correspond to camera delay settings of 0 ns, 250 ns, 500 ns, and 750 ns. Image reprinted from Reference [179] with permission of the authors.

jets [181–187], hypersonic boundary layers [179, 180 188, 189], and arcjet flowfields [121].

Figure 33, taken from Reference [179], shows images from tagging a single line of nitric oxide using direct excitation of fluorescence within a flat plate hypersonic laminar boundary layer. In this figure, the left-most image corresponds to the reference image, whereas the remaining images, from left to right, correspond to delayed images taken at 250 ns, 500 ns, and 750 ns after tagging, respectively. Measurements of freestream velocity, spatially averaged from a point just above the velocity boundary layer (3 mm) to 15 mm above the flat plate, resulted in a mean of 3035 ± 100 m/s at 90% confidence, giving an uncertainty of 3.3% of the mean [179]. Single-shot uncertainty estimates for a 3000 m/s freestream flow and for camera delay settings of 250 ns, 500 ns, and 750 ns were 4.6%, 3.5%, and 3.5%, respectively [179].

An indirect excitation scheme, as described in References [190–192], relies on photodissociation of molecular nitrogen for flow tagging. The technique uses a femtosecond laser pulse to dissociate molecular nitrogen into two nitrogen atoms, which then recombine after a collision, forming molecular nitrogen in an intermediate state. A subsequent collision brings the molecular nitrogen to an excited electronic B state, which then emits a photon via fluorescence upon transitioning to the excited electronic A state. Reference [192] provides a description of this process. One benefit of this indirect technique, known as Femtosecond Laser Electronic Excitation Tagging (FLEET), is that the recombination rate of dissociated atomic nitrogen allows for a much longer fluorescence lifetime. This would allow displacements to be measured over greater time scales, providing for accurate measurements of velocity in low-speed flow regions, such as in a

hypersonic wake flow. Additionally, the technique relies on molecular nitrogen for tagging, which is present in most hypersonic facilities.

2. MULTILASER METHODS

A second method of fluorescence-based flow-tagging velocimetry involves writing a line, series of lines, or grid pattern into the flowfield by one of several laser-based mechanisms. This pattern can then be interrogated, or read, by subsequent laser pulses to induce fluorescence, allowing for the determination of velocity through measurement of the displacement of the pattern. Such techniques usually involve two or three different lasers and are therefore more time consuming to set up and more difficult to execute.

One mechanism by which a pattern can be written into the flowfield is via ionization of the absorbing species, known as Laser Enhanced Ionization (LEI) flow tagging. The tagging process is accomplished by promoting the species (such as sodium in References [193–195]) to a higher energy state via laser excitation near the ionization limit. Collisions then result in the ionization of the species, with the tagging pattern corresponding to the ionized regions. Subsequent laser pulses are used to induce fluorescence of the absorbing species in regions that have not been photo-ionized. Supersonic measurements of velocity in a shock tube were performed using LEI flow-tagging in References [193] and [194], and hypersonic velocity measurements in an expansion tube were performed in Reference [195].

A second mechanism that can be used to write a pattern into the flowfield is by vibrational excitation of molecular oxygen via Raman pumping. This is followed by reading the pattern of the vibrationally excited oxygen by inducing fluorescence. The technique, known as Raman Excitation and Laser-Induced Electronic Fluorescence (RELIEF) [196], is advantageous as it relies on the flow-tagging of oxygen which is a common working gas of most hypersonic facilities. This technique has been used to characterize turbulence in a free jet [197] and underexpanded jet [198]. The RELIEF technique, however, is limited to temperatures below 750 K. Above this temperature, a significant fraction of oxygen molecules are vibrationally excited, making it difficult to distinguish the tagged molecules from the background [199].

Yet another mechanism involves using one laser to photo-dissociate a molecular species. This results in the formation of a product species for which a second laser can be used to read the location of the written pattern by exciting laser-induced fluorescence in the product species. The formation of the product species typically occurs through one or more reactions. A list of partner species used in the writing and reading process include: H₂O-OH [200–206], N₂O-NO [207], O₂-O₃ [208, 209], N₂/O₂-NO [210–213], and NO₂-NO [183, 215–221].

Figures 10a and 10b, taken from Reference [218], show images of vibrationally excited NO fluorescence in a grid pattern formed via photodissociation of NO₂ in a mixture containing 6.3% NO₂ in N₂. The images were taken in a supersonic

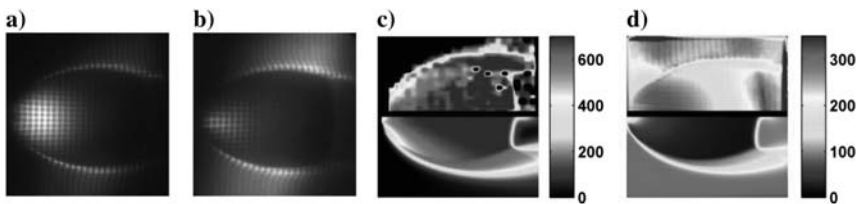


Fig. 34 Flow-tagging images of vibrationally excited NO fluorescence obtained a) 400 ns and b) 800 ns after photodissociation of NO_2 . The 2-D grid pattern allows for calculation of two velocity components. Measured (c, top) and computed (c, bottom) streamwise velocity maps. Measured (d, top) and computed (d, bottom) rotational temperature map. Image reprinted from Reference [218] with permission of the authors and the publisher (see color section).

underexpanded jet 400 ns (Fig. 34a) and 800 ns (Fig. 34b) after the pattern was written into the flow with a 2-D array of 355 nm beams. Two components of velocity were obtained by relating the displacement of the grid in the left image to a grid imaged in a stationary gas. The upper half of Fig. 34c, taken from Reference [218], shows measured streamwise velocities compared with computation, shown in the lower half of Fig. 34c. The use of two pulsed dye lasers in this experiment permitted the excitation of both a low ($J = 1.5$) and high ($J = 8.5$) rotational level within the same vibrationally excited ($v = 1$) NO state. The fluorescence images corresponding to the low- J (Fig. 34a) and high- J (Fig. 34b) rotational levels also allowed for measurement of the rotational temperature by using a calculation similar to that presented in Eq. (5.16). The top half of Fig. 34d, from Reference [218], shows measured rotational temperature compared with computation, shown in the lower half of Fig. 34d. Stated root-mean-square (RMS) uncertainties in the velocity measurement were $\sim 5\%$ with high signal-to-noise [218]. The stated RMS uncertainties in rotational temperature ranged from 9% to 35% prior to the Mach disk [218].

NO_2 -NO flow tagging velocimetry has also been used to study boundary layer transition on a flat plate in a Mach 10 wind tunnel [220, 221]. Pure NO_2 was seeded into the boundary layer through a spanwise slot located downstream of the sharp leading edge. The angle of attack of the flat plate was 20 deg, reducing the edge Mach number to about 4.2. Parallel focused beams of 355 nm light oriented normal to the surface of the flat plate (and in a plane parallel with the streamwise direction of the flow) dissociated the NO_2 , creating NO. After a 40 ns delay, the NO was probed by a 226 nm laser, at which time the camera acquired an image. One microsecond later, a second 226 nm laser probed the NO and the second image was acquired with the same camera. The two images were compared to compute velocity profiles. Figure 35 shows the resulting velocity profiles for two cases, one with no trip (i.e., tripping element, a protuberance designed to trip the flow from laminar to turbulent) and one with a 1-mm tall cylindrical trip, where the measurements were made downstream of,

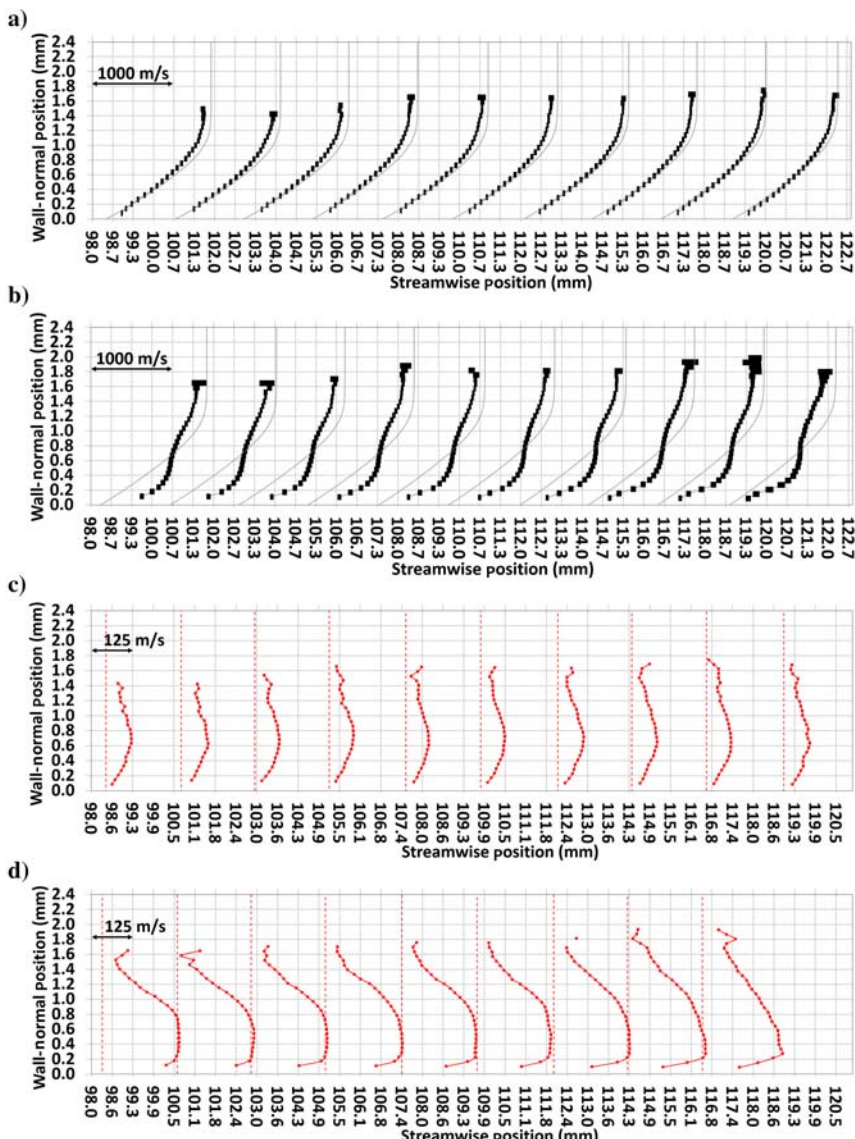


Fig. 35 Streamwise velocity profiles on a flat plate in a Mach 10 facility for: a) the case of no trip, b) $k = 1$ mm tall, 4 mm diameter cylinder trip, c) the fluctuating streamwise velocity for no trip, and d) a $k = 1$ mm tall, 4 mm diameter cylinder trip. Images reprinted from Reference [221] with permission of the authors.

and on the centerline of, the trip. (The laminar boundary layer thickness was also approximately 1 mm thick.) The figure shows mean profiles (black, top two charts) as well as profiles of the fluctuating component of velocity, u' (bottom two charts). For the case of no trip, the velocity profiles compare well with a compressible Blasius solution (shown in light gray). When the trip is present, the measured mean profiles depart from the laminar solution, showing a profile that is fuller than the laminar profile near the plate surface with a pronounced velocity deficit near the edge of the profile. The fluctuating streamwise velocity increases by a factor of three, up to 250 m/s, between the two cases, with the fluctuations highest in the wake of the trip. The single-shot measurement precision was 15–25 m/s, which was 1–2% of the maximum velocity in the boundary layer. The accuracy was estimated to be 5–15 m/s [220].

K. ADVANTAGES AND LIMITATIONS OF LASER-INDUCED FLUORESCENCE

The time scales associated with inducing fluorescence via laser excitation are typically a few hundred nanoseconds, which is much shorter than hypersonic flow time scales, therefore providing sufficient temporal resolution for high-speed transition-to-turbulence measurements. The availability of pulsed lasers capable of picosecond and femtosecond excitation allow for fluorescence measurements with time scales much less than those associated with collision and reaction time scales. Recently developed kHz- and MHz-rate pulsed laser systems have allowed image sequences consisting of tens to thousands [223] of images to be acquired, providing time-resolved information pertaining to high-speed fluid dynamic behavior. Both fluorescence-based velocimetry [217] and visualization [223, 224] experiments in hypersonic flow fields have been performed with these types of laser systems. The spatial resolution of a LIF technique is also sufficient for many applications, and higher than other techniques such as Raman or CARS, with laser sheet thicknesses typically in the range of 0.1 to 1 mm and magnifications of tens of pixels per mm, depending on the experimental setup. Fluorescence-based measurements are more sensitive than other techniques (for example Raman spectroscopy) with sensitivity on the order of parts-per-million or better [5].

Additionally, a wide range of species including intermediate combustion species can be probed using fluorescence techniques. Reference [108] provides an extensive listing of many species that have been detected using LIF and other methods. Another advantage of LIF is that it is readily extended to planar or volumetric measurement (see References [225] and [226]).

Several factors complicate acquisition and interpretation of LIF signals, complicating quantitative measurements. Quenching of the fluorescence, which prevents easy quantification of signal intensities, was discussed extensively above. Absorption of laser energy as the laser light passes through the flowfield can limit the effectiveness of fluorescence-based measurements, as the energy will

decrease in an exponential manner over a given spatial path length according to the Beer–Lambert relations in Eqs. (25) and (26). This makes quantitative measurements difficult, as the laser energy at a particular location may not be easily determined. Absorption can be significant when the concentration of the absorbing ground state population is high, the transition cross section is relatively large, the Einstein B coefficient for stimulated absorption is relatively large, and/or the path length through which the laser radiation passes is relatively long. To avoid strong absorption, a transition may be selected for which the population is small based on analysis of the Boltzmann fraction, as was done for PLIF visualization measurements in a hypersonic shock tunnel described in Reference [227]. Absorption can also limit measurement capabilities when fluorescence from the probed volume is re-absorbed by the species of interest. This effect, known as *radiative trapping*, occurs when fluorescence emission at frequencies readily absorbed by highly populated states must pass through gas containing these potential absorbers before reaching the imaging system. Measurements in a nonuniform or turbulent mixture are especially susceptible to errors associated with absorption and radiative trapping effects, as the absorption coefficient is a spatially and temporally varying property. A discussion of these issues, and some methods used to circumvent them, is provided in Reference [5].

Another disadvantage of LIF is that it usually probes only a single species at a time, compared to Raman or CARS, which can interrogate many species simultaneously. However, the fact that PLIF can measure spatial distributions of species can compensate for the single-species capability in some applications.

Consideration must also be given to the optical access of the test facility. As much of the work described in this discussion requires fluorescence excitation using laser frequencies in the UV portion of the electromagnetic spectrum, the window material used in hypersonic facilities must be capable of transmitting such frequencies with minimal absorption. Also, typically two or three windows are required for LIF or PLIF applications. The laser (beam or sheet) is typically brought in from one window and observed through another window at right angles to the first window. A third window can allow the laser to leave the test section, reducing scattered light, and allowing the quantification of absorption of the laser beam/sheet in some applications. These windows are typically relatively large compared to those required for CARS or diode laser absorption measurements. When short-pulse LIF experiments are performed, the inverse relationship between the pulse temporal width and spectral width (which for a Gaussian pulse is $\tau_{\text{laser}} = 0.44/\Delta\nu$) [110] can result in distortion of the temporal characteristics of the pulse. This is because the refractive properties of the optical windows of the test facility affect the speed with which the frequency components of the short pulse pass through the window material. Reference [110] discusses issues related to short pulse excitation and interaction with optical components.

VI. RAYLEIGH AND RAMAN SCATTERING

A. INTRODUCTION

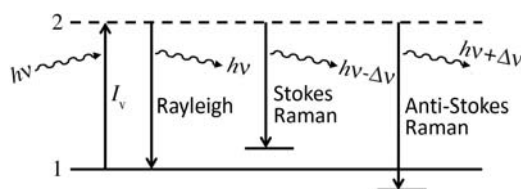
When a light beam passes through a gaseous medium, it can interact with the gas molecules or particles in the gas, thereby scattering light away from the path of the incident beam. *Elastic* scattering occurs if no energy is gained or lost to the medium. If energy is either absorbed or lost by the medium, the scattering is *inelastic*. Light scatter from particles that have a diameter, d , on the order of or larger than the light wavelength, λ , is termed Mie scattering. Scattering for which $d \ll \lambda$ is known as *spontaneous Rayleigh scattering* if elastic and *spontaneous Raman scattering* if inelastic. These processes are shown schematically in Figs. 36 and 37. Represented on the energy level diagram in Fig. 36, a photon excites a molecule from an originating state, 1, to a ‘virtual’ state, 2, from which the scattered photon is emitted. The virtual state, represented by a dashed line, is not an actual resonant state of the molecule. Instead, it indicates a nonresonant, short-lived state in which the electron distribution of the molecule is distorted. This virtual state immediately relaxes to the originating state (in the case of Rayleigh scattering) or another state (in the case of Raman scattering). Relaxation to a higher lying (e.g., vibrational) state than the originating state is termed *Stokes Raman* scattering. In this case, the molecule absorbs a quantum of energy through this process. In *anti-Stokes Raman* scattering the molecule imparts a quantum of energy to the scattered photon so that the scattered photon has higher energy than the incident photon. In this case, the originating state must not have been a ground state.

Figure 37 shows notional Raman/Rayleigh spectra, not drawn to scale. Rayleigh scattering is shown at the laser’s wavelength. Discrete pure rotational Raman lines, associated with rotational quanta imparted to or subtracted from the incident laser frequency, are shown on opposite sides of the Rayleigh peak. Vibrational Raman bands are located further away, spectrally shifted towards the red (Stokes) and the blue (anti-Stokes). The vibrational Raman bands show rotational fine structure. Raman scattering is much weaker than Rayleigh scattering. Raman scattering is typically three orders of magnitude smaller than Rayleigh scattering for most gases of interest to supersonic and hypersonic flows [5].

B. THEORY OF SPONTANEOUS RAYLEIGH AND RAMAN SCATTERING

Comprehensive reviews of the theory and application of Rayleigh and Raman scattering

Fig. 36 Energy level diagram indicating incident radiation, Rayleigh scattering and Raman scattering.



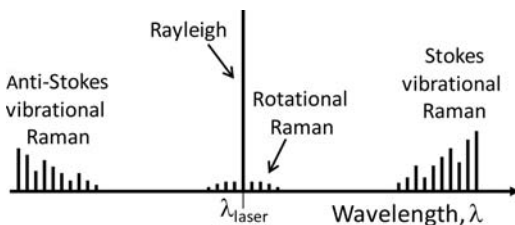


Fig. 37 Notional Raman/Rayleigh spectra.

have been given by others [5, 108, 228, 229]. Herein we provide a brief introduction and overview. Later sections will show how this theory is

applied to measure thermodynamic properties. Consider an electromagnetic wave incident upon a molecule, perturbing the molecule's electron cloud and making it oscillate at the same frequency as the incident wave. These oscillations cause a periodic charge separation within the molecule, known as an induced dipole moment. Oscillating dipole moments act like antennas, emitting radiation. As described in more detail by Baldwin [230], if these oscillations are in-phase, the emission adds constructively, producing a coherent beam. If out-of-phase (for example, in the direction orthogonal to the beam), the emitted light interferes destructively and the radiation cancels. For a monochromatic plane wave passing through a gas, the constructive interference occurs only in the forward direction. The resulting emitted coherent light is perfectly in-phase with and indistinguishable from the incident wave. In a gas composed of a finite number of molecules, the destructive interference at other angles is not fully complete because of statistical variations in the number of particles located in different wavelength-sized volumes of the gas [230, 231]. That is, there are not exactly the same number of particles in each wavelength sized volume, which would be required to cancel out the radiation perfectly. This statistical variation in the number density then leads to Rayleigh and Raman scattering. Rayleigh and Raman increase significantly in intensity at shorter wavelengths: both scale approximately as $1/\lambda^4$ [5].

The radiant intensity, I^Ω , which is the scattered power per unit solid angle, is proportional to the square of the induced dipole moment. The induced dipole moment, \vec{p} is given by [5]:

$$\vec{p} = \epsilon_0 \alpha \vec{E} \quad (72)$$

where ϵ_0 is the permittivity of free space, α is the molecular polarizability and \vec{E} is the incident electric field given by $\vec{E} = \vec{E}_0 \cos(\omega_0 t)$, where \vec{E}_0 is the amplitude of the electric field, ω_0 is the frequency of the laser light and t is time.

The polarizability of a molecule depends on its internal structure and varies with time during vibrational oscillations at the natural frequency of the molecule, ω_v , vibrating in the direction of its normal spatial coordinate, Q . The polarizability can be approximated with a Taylor series expansion:

$$\alpha = \alpha + \left(\frac{\partial \alpha}{\partial Q} \right)_0 dQ \quad (73)$$

where the small physical displacement, dQ , of the atoms about their equilibrium positions (denoted by the subscript 0) during vibrations is:

$$dQ = Q_0 \cos(\omega_v t) \quad (74)$$

Combining Eqs. (72)–(74):

$$\vec{p} = \left[\alpha_0 + \left(\frac{\partial \alpha}{\partial Q} \right)_0 Q_0 \cos(\omega_v t) \right] \varepsilon_0 \vec{E}_0 \cos(\omega_0 t) \quad (75)$$

Expanding and using a trigonometric identity [5]:

$$\vec{p} = \alpha_0 \varepsilon_0 \vec{E}_0 \cos(\omega_0 t) + \frac{1}{2} \left(\frac{\partial \alpha}{\partial Q} \right)_0 \varepsilon_0 Q_0 \vec{E}_0 [\cos(\omega_0 - \omega_v) t + \cos(\omega_0 + \omega_v) t] \quad (76)$$

The first term on the right side of Eq. (76) describes Rayleigh scattering at a frequency corresponding to the incident laser's wavelength. The second term indicates Raman scattering which is shifted from the Rayleigh scattering by $\pm \omega_v$ resulting in upshifted (anti-Stokes) and downshifted (Stokes) Raman scattering. While significant theory has been developed to describe the physics of Raman and Rayleigh scattering, the strengths of the scattering for different gases is generally measured and reported as a temperature-independent differential cross section [5]:

$$\left(\frac{\partial \sigma}{\partial \Omega} \right)_{zz} \equiv \frac{I_{zz}^\Omega}{NI} \quad (77)$$

which can be rearranged as:

$$I_{zz}^\Omega = \left(\frac{\partial \sigma}{\partial \Omega} \right)_{zz} NI \quad (78)$$

where the subscript zz refers to a polarization in the z (vertical) direction caused by an incident electric field oriented in the z direction, N is the number density of the gas and I is the laser irradiance [5]. The differential cross sections vary by process (Rayleigh vs Raman), by molecule, and vary with the laser wavelength but are independent of pressure and temperature.

Rayleigh scattering from different molecules cannot be distinguished spectrally, so it is not usually used to detect individual species. Under circumstances where the composition is fixed or known, or limited to vary under controlled conditions [232, 233], Rayleigh scattering can be used to measure the gas density, ρ . As discussed further below, the Rayleigh scattering cross section varies from molecule to molecule, with some hydrocarbon species having cross sections more than an order of magnitude larger than N_2 . The cross section for a mixture of gases is equal to the mole-fraction-weighted average of the individual cross sections. If the composition can be estimated or measured, for example by Raman scattering

[234], then the effective cross section for the gas mixture can be determined, allowing the density to be determined from the measured Rayleigh scattering. Under conditions where the pressure and composition are known or can be determined and where the perfect gas law applies, the gas temperature can be inferred from the measured density [5]. Such measurements can suffer from interference from Mie scattering from particles and laser scattered light [5]. To avoid Mie interferences, the gases can be filtered to remove particles. Careful experimental design and blackening of surfaces can minimize scattered laser light.

Spectral analysis of Rayleigh scattering yields additional parameters that can be measured. Figure 38 shows a schematic of the dispersed Rayleigh scattered light (solid line), separated from the incident laser light (dashed line). The spectral shift of the Rayleigh from the laser is caused by the Doppler shift of the gas relative to the incident light beam and depends on the detection angle. The width of the Rayleigh spectrum depends, in part, on the gas temperature. The amplitude of the scattering, as described above, depends on the gas density (and composition). Thus, in principle, by spectrally dispersing the Rayleigh scattered light, the temperature, velocity, and density of a gas can be measured simultaneously. These effects are detailed below with examples given.

Revisiting Eq. (76), notice that for Raman scattering to occur, $(\partial\alpha/\partial Q)_0$ must be nonzero. This happens when a molecule exhibits a *change* in its polarizability with vibrational displacement. For example, as the atoms in the N_2 molecule vibrate, they become less polarizable as the atoms approach each other (charges exhibiting more force because they are closer to each other) and more polarizable when further apart (charges more weakly interacting). This results in a nonzero $(\partial\alpha/\partial Q)_0$. Such vibrations are *Raman active*. On the other hand, some vibrational modes do not change the molecule's polarizability, for example the asymmetric stretch of CO_2 has the following vibration pattern: $O \rightarrow \leftarrow C O \rightarrow$. Such modes have $(\partial\alpha/\partial Q)_0 = 0$ and are termed *Raman inactive*. Further quantum mechanical selection rules and molecular structure considerations (atomic mass, bond length, moment of inertia, etc.) determine the shape and structure of the Raman spectra [5]. As the frequency of Raman spectra depend strongly on the individual species' molecular structure (each vibrational resonance occurring at a different energy), Raman spectra from different molecules appear spectrally separated when they are dispersed, typically using a grating-based

spectrometer equipped with a camera to acquire the spectra. Because Raman scattering is species-specific, it can be used to measure individual species

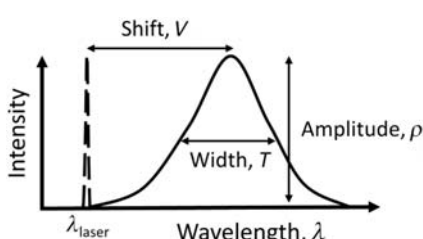


Fig. 38 Notional sketch of spectrally dispersed Rayleigh scattered light (solid line) which has been Doppler shifted from the incident laser light (dashed).

concentrations, where in Eq. (77), N is the species being detected and the differential cross section is that of the individual species.

C. ADVANTAGES AND DISADVANTAGES OF RAYLEIGH AND RAMAN SCATTERING

Rayleigh and Raman scattering have many inherent advantages compared to other measurement techniques. Both use just a single laser and the laser need not be resonant with any particular molecular resonance as in absorption or LIF. This allows high-powered, fixed frequency lasers to be used for Rayleigh or Raman. As they are linear laser techniques involving only a single excitation beam, Raman and Rayleigh are relatively easy to set up and understand, and the data are, in general, easier to analyze than nonlinear techniques such as CARS. Neither Raman nor Rayleigh is sensitive to collisional quenching, a phenomenon which complicates the interpretation of LIF signals. Absolute intensity calibration of both techniques is relatively straight forward and easily performed. Raman and Rayleigh can be performed simultaneously using the same laser to measure species concentrations (Raman), temperature (Raman and/or Rayleigh), density (Raman and/or Rayleigh) and velocity (Rayleigh).

The major disadvantage of Raman and Rayleigh scattering is the low signal intensity. The low signal from Raman scattering generally prevents minor species (less than a few percent by mole fraction) from being detected using this technique. Because the signals are so low, large (low f -number) collection optics are usually used. Ideally, the detection optics need to be placed close to the measurement region and, in ducted flows, large windows are required. Hypersonic and combusting flows can sometimes be luminous. Natural luminosity, such as spontaneous Rayleigh and Raman scattering, emits light in all directions. In order to improve the signal-to-noise ratio, temporal, spatial, and spectral filtering can be used to collect the desired radiation and block unwanted natural luminosity. For example, gated detection of pulsed signals (or lock-in detection of continuous signals) can be used.

D. TRANSLATIONAL TEMPERATURE, VELOCITY, AND DENSITY MEASUREMENTS

The gas temperature and velocity can be determined from the Rayleigh spectrum by resolving the Doppler broadening and Doppler shift, respectively. The Rayleigh scattering linewidth is typically in the range of 1–6 GHz ($0.03\text{--}0.17\text{ cm}^{-1}$) for supersonic and hypersonic flow experiments in the range of a few hundred to a few thousand kelvins, depending on the temperature and angle of incidence of detection and collection of the light (see Reference [228] for detailed information about the Rayleigh scattering lineshape and angular dependence). A high-resolution laser can be used so that the broadening caused by the laser's lineshape is negligible compared to this Doppler broadening. For example, injection seeded, pulsed Nd:YAG lasers typically have linewidths of about 0.1 GHz (0.004 cm^{-1}), whereas continuous sources can have linewidths that are orders of magnitude

smaller. To spectrally resolve Rayleigh scattering, a high-spectral-resolution instrument is required. Two methods, described below and also in the introduction, are typically used: gas vapor cells and Fabry–Perot etalons.

A gaseous cell filled with iodine vapor can be used in combination with excitation in the visible wavelength range, where I_2 has many absorption lines, by placing a low-pressure gas cell containing crystalline iodine and I_2 vapor in front of a detector or camera. The diameter of the cell should be larger than the diameter of the collection lens. The cell length, pressure and temperature of the I_2 cell are chosen to control the I_2 gas concentration and spectral line shape and therefore the absorption magnitude and profile. Attenuation of transmitted light by a factor of 10^5 can be achieved using high-resolution cw lasers, though it is more difficult to achieve attenuations greater than $\sim 10^3$ with off-the-shelf injection-seeded, pulsed Nd:YAG lasers [235]. The absorptions can be used to reject spurious scattered laser light, while passing the pressure- and Doppler-broadened and Doppler-shifted Rayleigh scattering, allowing background-scatter-free density measurements. These sharp absorption features can also be used for temperature and velocity measurements by using the steep edge of the absorption spectral profile to provide spectral resolution. As the absorption spectrum of the gas filter is well known, if the laser frequency is scanned across the filter, then the Doppler-broadened and Doppler-shifted Rayleigh-scattered light will transmit through the filter, being acquired by the camera. Each pixel on the camera will then have obtained a convolution of the Rayleigh-scattered light with the absorption spectrum. These spectra can then be deconvolved to determine the gas temperature through the thermal broadening and gas velocity through the observed Doppler shift. Miles et al. [228] demonstrated this approach in a Mach 2 pressure-matched jet flow, shown in Fig. 39. Variations of this technique can provide both time-averaged and single-shot measurements. For single-shot measurements, the dynamic range of velocities that can be measured is limited, although by increasing the gas cell buffer gas pressure, the dynamic range has

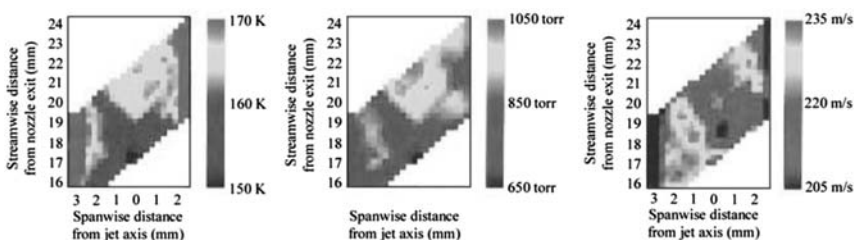


Fig. 39 Temperature (left), pressure (center) and velocity (right) measured in a Mach 2 supersonic jet flow using Rayleigh scattering observed through a gas vapor cell using a frequency-scanned, injection-seeded Nd:YAG laser [228]. © IOP Publishing. Reproduced with permission of the authors and of IOP Publishing. All rights reserved (see color section).

been increased by Elliot et al., who made single-shot measurements with $\sim 9\%$ uncertainty over a velocity range from 200 to 600 m/s [236, 237].

By using a Fabry–Perot etalon, single-shot Rayleigh spectra can be obtained, allowing instantaneous (in ~ 100 ns) and simultaneous measurement of temperature, density and velocity. A Fabry–Perot etalon consists of two planar, reflective surfaces that cause interference, dispersing the transmitted light spatially, so that in the focal plane of the etalon, the spectrum of the light is separated spatially and can be resolved spectrally. Two different strategies have been developed to acquire these spectra. The first uses a CCD camera in the focal plane of the etalon to capture the dispersed spectrum [238–241]. The second method uses spatial masks or mirrors to direct the Rayleigh-scattered light to single-point detectors such as photo-multiplier tubes (PMTs) [242, 243]. Typically, CCD cameras read out more slowly than single-point detectors such as PMTs, so using PMTs generally results in higher-speed detection. Measurement rates up to 32 kHz have been reported using this approach [244]. However, using a CCD camera offers several measurement advantages, described below.

Figure 40 shows one such example of CCD-based detection of Rayleigh-scattered light from Bivolaru et al. [240]. A pulsed Nd:YAG laser is focused into a heated Mach 1.6 jet flow. The Rayleigh-scattered light is collected at right angles by a lens system that down-collimates the collected light and passes it through a solid etalon. The etalon-processed light is then focused on an electron-multiplying charged-coupled device camera (EMCCD) where the

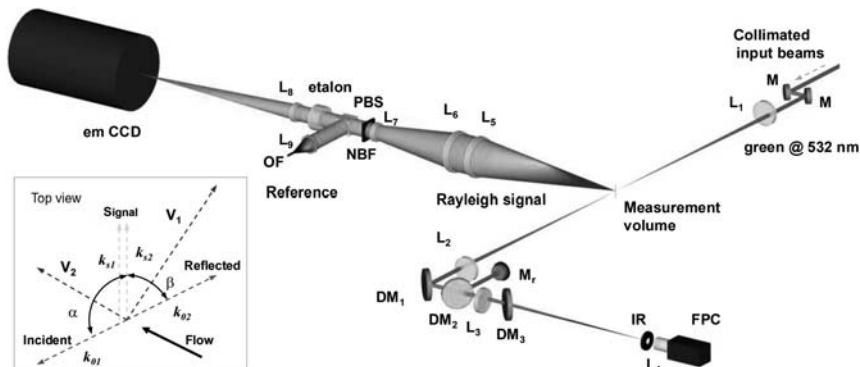


Fig. 40 Two-component interferometric Rayleigh scattering system from Reference [240]. Mirrors are denoted by M, dichroic mirrors by DM and lenses by L. PBS is a polarizing beam splitter while NBF is a narrowband filter. IR is an iris and FPC is a focal plane camera used to monitor the beam alignment. In this experiment, the dichroic mirrors were required to filter out other laser beams associated with a dual-pump CARS measurement that was being performed simultaneously. Reprinted with permission of the authors.

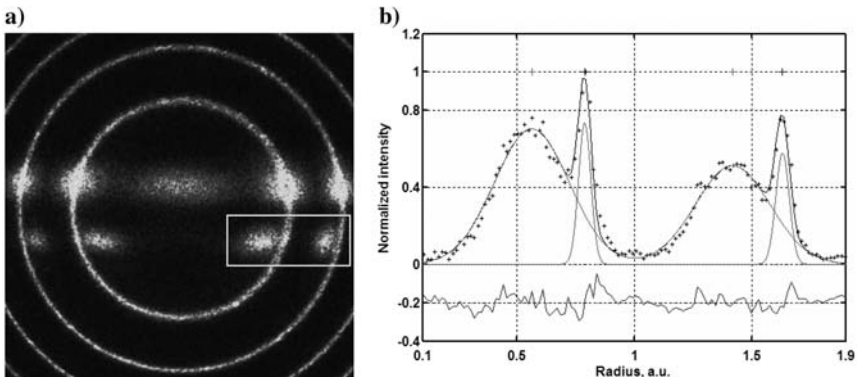


Fig. 41 a) Fabry-Perot interferogram of Rayleigh-scattered light obtained by laser beams from two different directions as well as laser-light, resulting in the circular pattern. b) The linearized Rayleigh-scattered spectrum obtained from the boxed region in a), showing best fits to the reference and Doppler-shifted light [240]. Reprinted with permission of the authors.

interference fringes are realized. This image is called an interferogram. An optical fiber (OF) directs some of the spectrally narrow laser light into the optical path so that a circular reference fringe will appear in the interferogram, as in Fig. 41a. The pair of oval patterns located in the white rectangle show Doppler-shifted, Doppler-broadened, Rayleigh-scattered light collected by the lenses and dispersed by the etalon. A similar pattern is shown on the left side of the interferogram. These four oval patterns originate from four different spatial locations a few mm apart in the flow, thus resulting in four simultaneous, spatially separated measurements. The gas velocity, V , and the Doppler shift, Δf , are related by: $\Delta f = ((\mathbf{k}_s - \mathbf{k}_o) \cdot \mathbf{V})/\lambda$ where λ is the wavelength of the incident light, \mathbf{k}_o is the wave vector of the incident light and \mathbf{k}_s is the wave vector of the collected light. (The wave vector points in the direction of light propagation and has a magnitude of $2\pi/\lambda$.) In the vector diagram shown in Fig. 40, \mathbf{k}_{o1} is the wave vector of the incident light and \mathbf{k}_{s1} is the wave vector of the collected light. The observed Doppler shift measures the velocity component V_1 in the direction defined by $\mathbf{k}_{s1} - \mathbf{k}_{o1}$, which bisects the angle β between the laser and collection wave vectors. Similarly, a mirror M_r reflects this incident beam back through the lens, L_2 , and into the measurement volume with wave vector \mathbf{k}_{o2} resulting in collected Rayleigh signal having a wave vector \mathbf{k}_{s2} . This signal is sensitive to the velocity component V_2 . The reflected beam was slightly misaligned in the downward direction so that the two measurements would be spatially separated on the interferogram, shown in Fig. 41a. Furthermore, the geometry of this experiment was constructed so that the V_1 would be orthogonal to the jet axis, measuring a radial velocity

component, whereas V_2 was parallel to the jet axis, measuring the axial velocity component. In Fig. 41a, four spatially separated measurements of axial velocity are collected in the bottom half of the interferogram, while four measurements of radial velocity are collected in the top half. Figure 41b shows the two boxed peaks after they have been processed to linearize the interferograms and to bin the data into single spectra [239, 240]. These spectra were fitted with Gaussians to determine the Doppler shift and broadening associated with Rayleigh scattering, relative to the reference peaks. Subsequent work by this team and others has been able to simultaneously determine the gas velocity, temperature and density from similar spectra [244, 245].

In Reference [240], Bivolaru et al. reported velocity measurements with a precision of ~ 40 m/s in a flow with ~ 1200 m/s, or about 3% of the maximum velocity. The dynamic range of the instrument was ~ 3000 m/s. (The dynamic range is mainly determined by the thickness of the etalon, which sets the free spectral range, or fringe-to-fringe spectral separation.) Thus, expressed as a percentage of the dynamic range of the instrument, the measurement precision is $\sim 1\%$. To obtain more precise measurements at lower temperatures, the experiment can be designed to use higher spectral resolution.

The use of the camera-based approach has some advantages over the PMT-based approach. First, it can tolerate (and in fact, benefits from) scattering from stationary surfaces in the flow. Such scattering, as long as it is not too large, provides a reference frequency to determine the Doppler shift. Second, having a laser frequency reference in each interferogram makes the system insensitive to variations in the etalon transmission spectrum or the laser wavelength. In typical PMT-based experiments, the etalon must be temperature controlled, vibration isolated (if it is an air spaced etalon) and the laser frequency must be carefully controlled. Uncontrolled drift in either the etalon or laser would result directly in a systematic error in the PMT-based approach, whereas it is automatically corrected in the CCD-based approach. A third advantage of the CCD-based approach is that it is somewhat more tolerant of scattering from clusters and particles in the flow, lessening the need for gases to be filtered. Scattered light from particles typically appears in CCD-based interferograms as spatially distinct, circular artifacts. These can sometimes be removed by image processing. However, if the scattering is too large either spatially or in intensity, it can corrupt the measurement; even in this case, other spatial locations in the flow may yield measurements from the same interferogram. As shown in Fig. 41, the CCD-based detection allows multiple spatial points to be measured simultaneously, allowing measurements at adjacent spatial locations to be correlated. Furthermore, with CCD-based detection, it is straightforward to measure multiple velocity components with the same instrument, also shown in Fig. 41. Finally, CCD-based detection has often been combined with pulsed-laser excitation, which has two benefits: it makes the measurement instantaneous, occurring in ~ 10 ns, and the signal intensity is much higher, allowing measurement in much lower density flows, such as atmospheric-pressure flames and low-pressure gas flows.

Instantaneous measurements at 1/5 of atmospheric density or lower are possible with this approach [240].

E. ROTATIONAL AND VIBRATIONAL TEMPERATURE MEASUREMENTS

Raman scattering is sensitive to individual molecular rotational and vibrational transitions. As the population of these lines depends on (actually defines) the temperature, it is possible to measure rotational and vibrational temperatures from spontaneous Raman spectra. Figure 42 shows a typical Raman spectrum obtained in a hydrocarbon-air flame at high pressure [246]. A pulse-stretcher was used to extend the duration of the 500-mJ, 532-nm pulse by nearly a factor of 10, thereby lowering the peak laser power to avoid laser-induced breakdown while maintaining high pulse energy to yield a sufficiently high signal-to-noise ratio [246]. This spectrum shows many temperature and concentration dependent features. The relative heights and shapes of the different bands depend on temperature and gas concentration. Modeling, calibration and analysis of such Raman spectra can yield rotational and vibrational temperatures as well as concentrations.

Several different strategies for temperature measurement based on spontaneous Raman scattering exist. Rotational temperatures can be measured from pure-rotational Raman scattering either using high-resolution or low-resolution detection, as indicated in Fig. 43 [248]. The advantage of low-resolution detection is that the spectrum can be acquired simultaneously with the same instrument used to acquire multispecies spectra like that shown in Fig. 42. A disadvantage of this low-resolution technique is that many different species have similar pure

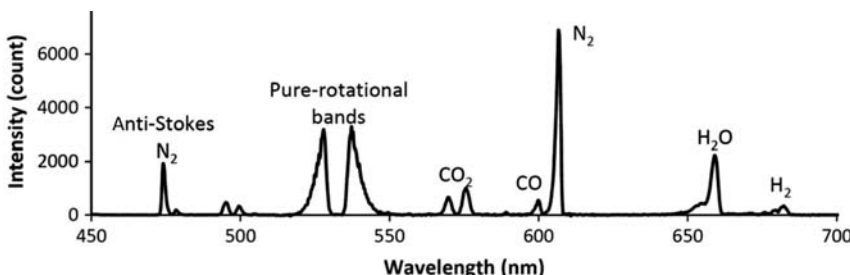


Fig. 42 Five-hundred-pulse-average Raman spectrum in a high-pressure CH_4 air flame. The excitation laser wavelength was 532 nm. A 532 nm filter blocks Mie, Rayleigh and spurious laser scattering as well as some of the low-rotational-quantum-number rotational Raman lines. A subframe burst gating (SBG) technique was also used to subtract background emission from this spectrum [247]. Reprinted with permission of the authors and publishers. Combustion science and technology by Taylor & Francis Inc. Reproduced with permission of Taylor & Francis Inc. in the format reuse in a book/textbook via Copyright Clearance Center.

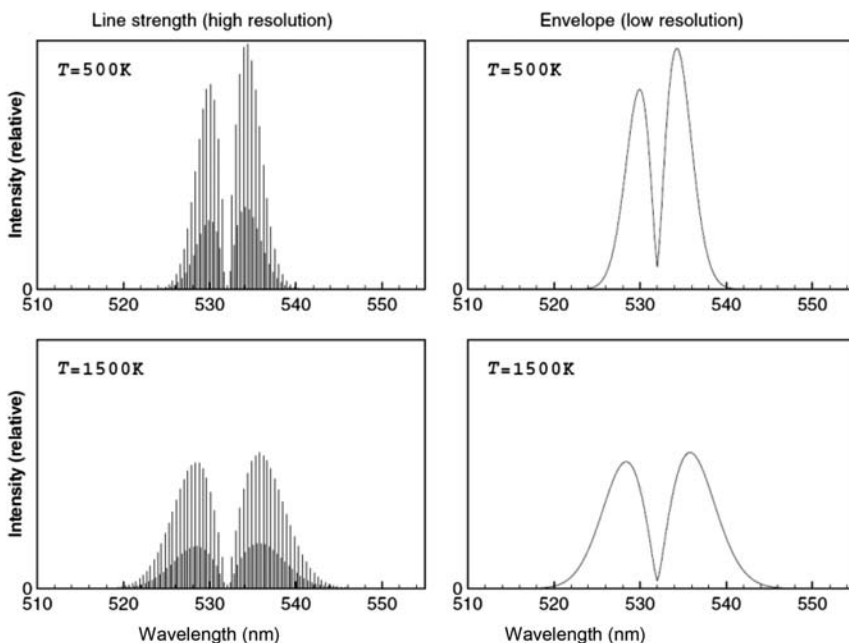


Fig. 43 Theoretical calculation of the pure rotational Raman spectra of N_2 at two different temperatures and two different spectral resolutions, adapted from Reference [248]. © IOP Publishing. Reproduced with permission of the authors and of IOP Publishing. All rights reserved.

rotational Raman shifts, so they overlap in the same spectral region close to the excitation laser. Such interferences from different species can lead to measurement errors. This technique works over a wide temperature range, including at room temperature. Alternately, rotational temperatures could be determined by resolving the rotational-vibrational Raman scattering, typically of N_2 [249], as is often done for CARS [250]. When flows are in rotational-vibrational equilibrium, it is more common to measure the temperature using vibrational bands, as described below, because they result in higher signal-to-noise ratios and consequently, more precise temperature measurements.

Vibrational temperatures can be measured from the relative heights of different vibrational Raman bands. A commonly used method compares the ratio of the Stokes to anti-Stokes (S-AS) vibrational Raman bands of N_2 [5, 251–253]. N_2 is often used because it is present in high concentration in many supersonic, hypersonic and combusting flows, resulting in adequate signal-to-noise ratio. Also, N_2 is used because it is relatively well understood and well resolved spectrally from other species. Recall from Fig. 36 that the anti-Stokes scattering originates from an excited vibrational state whereas the Stokes scattering can originate from the

ground vibrational state. Thus, the integrated intensity of the anti-Stokes N_2 spectrum at 473 nm in Fig. 42 can be compared to the Stokes scattering at 607 nm. This ratio, which is a monotonic function of temperature, can be used to determine the temperature. As this method integrates the signal intensity in the two different bands, it improves the signal-to-noise ratio, allowing single-shot determination of temperature. Single shot precisions of $\sim 20\%$ of the measured temperature have been obtained at several points along a line using this method [251]. This technique becomes insensitive to temperature below about 700 K because the low population in the excited vibrational state causes low signal-to-noise ratio [5].

A second method of measuring the vibrational temperature is to spectrally resolve the different vibrational bands of a molecule such as N_2 , though the individual rotational lines need not be resolved. The relative heights of the vibrational levels can be plotted on a Boltzmann plot or can be fitted spectrally to determine the vibrational temperature [254]. For example, Sharma and coworkers [254] used a KrF excimer laser operating at 248 nm to generate spontaneous Raman scattering in the Electric Arc Shock Tube (EAST) facility at NASA Ames Research Center. The EAST facility, normally operated as a shock tube, was fitted with a 2-D converging-diverging nozzle so that a shock reflection generated a high pressure (100 atm), high temperature (5600 K) reservoir of N_2 gas that expanded through the nozzle. The sudden expansion through the nozzle results in vibrational–rotational nonequilibrium, which was monitored with Raman scattering. Measurements were performed at different distances downstream to study the evolution of the vibrational relaxation. Figure 44 shows a sample spectrum generated and spectrally fit to determine the rotational and vibrational temperatures. The vibrational temperatures were then plotted vs distance downstream in the flow so that different vibrational relaxation models could be tested

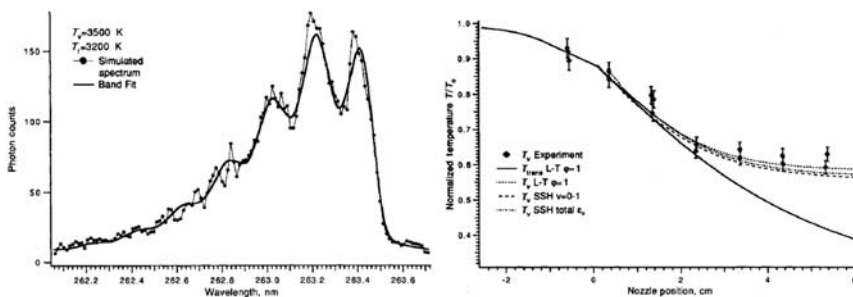


Fig. 44 An experimental Raman spectrum of N_2 , fitted for rotational and vibrational temperature (left), and resulting vibrational temperatures measured as a function of distance downstream of the nozzle (right), adapted from Reference [254] with permission of the authors.

[254]. Though not explicitly stated in the paper, the temperature measurement precision appears to be about 5%.

F. SPECIES CONCENTRATION MEASUREMENT

Rayleigh scattering has been used in some specialized experiments for determining species concentration. For example, the Rayleigh scattering cross section for propane is 13.5 times larger than for air, allowing mixing to be quantified in propane/air jets [255]. However, Raman scattering is much more commonly used to measure species concentrations. Sandia National Laboratories have extensively used Raman scattering for major-species concentration measurements (along with Rayleigh and LIF measurements for temperature and minor-species concentration measurements, respectively) [154]. This system uses a series of four frequency-doubled Nd:YAG lasers to produce temporally stretched 1.8 Joule pulses which are focused to a 0.22 mm ($1/e^2$) diameter spot size. A separate laser excites LIF of CO. An imaging system directs the collected Raman/Rayleigh/LIF scattered light into the optical analysis system shown in the bottom-right panel of Fig. 45. The system contains two mechanical chopper wheels (one

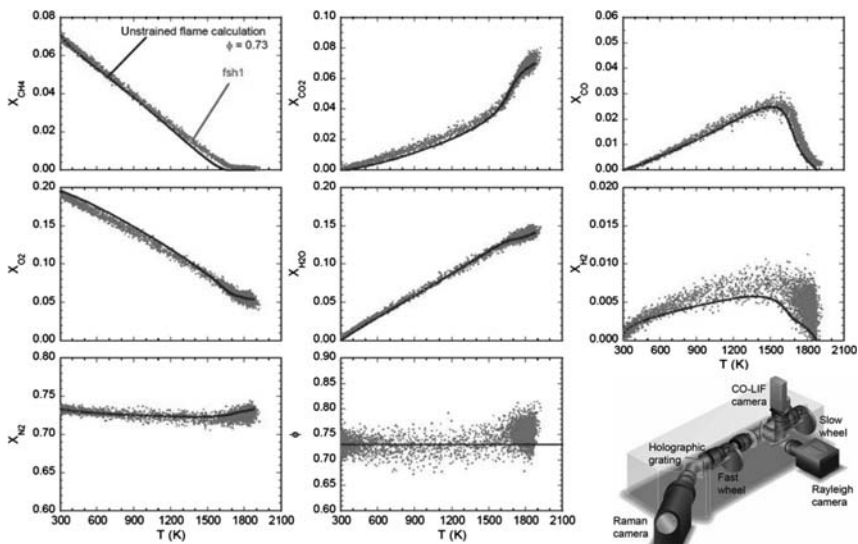


Fig. 45 Scatter plots of mole fraction and equivalence ratio (ϕ) data at one location in an atmospheric pressure, methane-air flame compared with a calculation, and a schematic of the optical components associated with the collection and analysis of light from the Sandia Raman/Rayleigh/LIF imaging system (bottom right). Adapted from Reference [154] with permission of the authors and The Combustion Institute.

“slow” and one “fast”) that are synchronized with the laser to transmit the signals while rejecting flow luminosity. It also has a transmission grating and multiple lenses, beam splitters and cooled (low noise) CCD cameras. This system images a 6-mm-long segment of the Rayleigh, Raman and LIF probe volume, allowing concentrations and temperature to be obtained along a line. The spatial resolution for the Raman measurements was ~ 10 pixels/mm along the 6-mm-long probe volume, though the actual spatial resolution was slightly worse due to optical distortions from the flame [154].

A sample of the resulting concentration measurements are shown in Fig. 45. Raman has been used to measure N_2 , O_2 , CH_4 , CO_2 , H_2O , and H_2 , whereas CO was measured with two-photon LIF excited at 230.1 nm. Temperature was measured from the intensity of the Rayleigh-scattered light, using the ideal gas law to convert density to temperature as described above. The data are graphed vs temperature to show the correlation of species with temperature and to allow comparison with an unstrained flame calculation, shown by the smooth curve. The individual data points correspond to different single pulses of the laser. Thus, these measurements are ‘single shot’ having been obtained with flow freezing (~ 100 ns) time resolution. Data such as these have been acquired at many locations in a variety of different flames, allowing the development of a large database of turbulent flames. The accuracy of the Raman concentration measurements varies from 2% to 10% of the measured concentration, while the precision (based on one standard deviation) varies from 0.7% to 7.5% depending on the species. The accuracy of the temperature measurement, based on Rayleigh scattering signal intensity, was reported to be 2% with a $1-\sigma$ precision of 0.75%.

VII. COHERENT ANTI-STOKES RAMAN SPECTROSCOPY

A. INTRODUCTION

Comprehensive reviews of the theory and application of Coherent anti-Stokes Raman spectroscopy, often called coherent anti-Stokes Raman *scattering*, or CARS, in a gas have been given by others [5, 108]. A brief introduction and overview are provided herein. CARS is a nonlinear optical process in which three laser beams interact with the gas generating a fourth, laser-like signal beam. The energy level diagram of this process (each arrow represents a change in state due to photon absorption, an up arrow, or emission, a down arrow, and the length of the arrow is proportional to energy change or, equivalently, photon frequency) is shown in Fig. 46.

The pump beam and the lower frequency Stokes beam interact with the gas, a pump frequency photon is absorbed and a Stokes frequency photon is emitted coherently with the Stokes beam, and the gas is excited to a higher energy state via a state that in most CARS setups is a virtual state (although it could also be a real state). The difference between the frequencies of the upper and lower

Fig. 46 Energy level diagram showing the CARS process.

state, $\omega_{\text{pump}} - \omega_{\text{Stokes}}$, is called the Raman shift. A probe beam photon is coherently scattered from this excited state, shifted up in frequency by the Raman shift to form part of the signal beam, and the gas molecule returns to its original state.

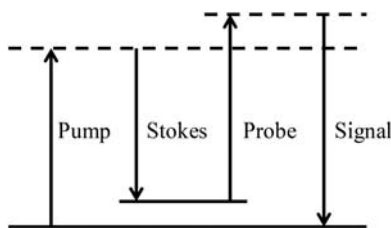
Total momentum as well as energy is conserved. Therefore, the momentum of the scattered photons equals that of the incident photons, leading to the following equation:

$$\overrightarrow{k_{\text{pump}}} + \overrightarrow{k_{\text{probe}}} = \overrightarrow{k_{\text{Stokes}}} + \overrightarrow{k_{\text{signal}}} \quad (79)$$

As the k 's are the wave vectors (length proportional to photon frequency with direction the same as that of the beam), this equation allows the direction of the signal beam to be found from the directions of the pump, Stokes, and probe beams.

A physical interpretation of this process is that the interaction of the pump and Stokes beams establishes an optical fringe pattern in the gas. If the pump and Stokes frequencies are the same, as with a related technique called degenerate four-wave mixing (DFWM), this fringe pattern is stationary. In CARS, the frequencies are different and the fringe pattern moves across the interaction region, modulating the intensity at any particular point at the beat frequency, i.e., the Raman shift frequency. This moving fringe pattern excites a polarization response in the gas which acts as a moving grating from which a probe beam photon is scattered, in a manner similar to Bragg scattering, to form the signal beam photon. As the grating is moving, the frequency of the signal photon is shifted relative to the probe photon by the Raman shift frequency. (An analogous effect occurs in an acousto-optical modulator where acoustical waves in a solid material, such as glass, form a moving grating of varying index of refraction, and incident laser light is coherently or Bragg scattered from this volumetric “grating” with its frequency shifted by the acoustical frequency [256].)

If the pump, probe, and Stokes lasers are all single frequencies, then the signal is also at a single frequency, as indicated in Fig. 46. If the pump and/or Stokes lasers are broadband lasers, while the probe is single frequency, then the signal is broadband also, and contains a spectrum that reflects the variation of CARS susceptibility of the molecules in the probe volume as a function of Raman shift. In many broadband CARS setups, the probe and pump frequencies are the same (derived from the same laser source). In the dual-pump CARS technique [5, 257], pump and probe frequencies are different and these two laser beams have interchangeable roles (each beam performs the role of pump in one CARS process and probe in a second CARS process). The signal is thus the coherent



superposition of the signal from the two processes, generated over two different ranges of Raman shift. When the desired Raman shift is small, as in rotational CARS (i.e., when the transitions probed are pure rotational transitions, which differ by relatively small quanta of energy and are thus relatively closely spaced spectrally), the pump and Stokes beams can be derived from the same broadband laser, whereas the probe beam is single frequency (dual-broadband CARS) [5].

As CARS is a nonlinear process (see Sec. I.B) it requires high irradiance levels. Consequently, CARS signal in a gas is typically generated by focusing pump, Stokes, and probe beams, and overlapping them at their common focus. If the beams are initially separate and crossed at the common focus, the arrangement is called BOXCARS; if they lie in a plane (Fig. 47), it is called planar BOXCARS. In this arrangement the measurement volume is the small region of overlap of all three beams.

B. CARS THEORY

CARS, as with Raman and Rayleigh scattering, arises because of time-varying polarization induced in the gas in the presence of electromagnetic radiation [5, 108, 256]. CARS, specifically, arises due to the third order susceptibility, χ_{CARS} , for which the induced polarization is described as follows:

$$P^{(3)}(\omega_{\text{signal}}) = \epsilon_0 \chi_{\text{CARS}} E(\omega_{\text{pump}}) E(\omega_{\text{Stokes}}) E(\omega_{\text{probe}}) \quad (80)$$

The E 's are the complex electrical field amplitudes. This equation can be substituted into the wave equation relating the electrical field to the induced polarization and solved by integration along the direction of the signal beam. The CARS irradiance is thus:

$$I_{\text{signal}} \propto I_{\text{pump}} I_{\text{Stokes}} I_{\text{probe}} |\chi_{\text{CARS}}|^2 L^2 \quad (81)$$

L is the length of the measurement volume, i.e., the length of the region along which the pump, Stokes, and probe beams all overlap. Rigorous calculations of the CARS susceptibility require quantum mechanical treatments, but classical derivations are simpler to understand. The gas is modeled as a simple harmonic oscillator in which the variation of the normal coordinate, Q (intermolecular spacing in the case of vibrational states), with time is described by a second order linear ordinary differential equation, with a time-dependent forcing function proportional to the average over an optical cycle of the square of the electrical field. (Thus, the forcing term oscillates at the Raman shift frequency.) The constant of proportionality in the forcing

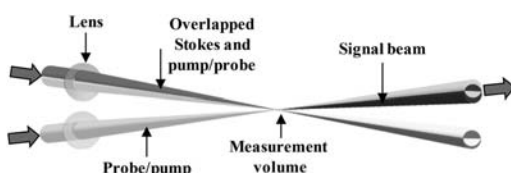


Fig. 47 Planar BOXCARS beam geometry (see color section).

term is proportional to $(\partial\alpha/\partial Q)_0$, and consequently to the Raman scattering cross section, where α is the optical polarizability of the molecule. The CARS susceptibility is found by solving for the time dependence of the normal coordinate, combining with Eqs. (72) and (73) for the polarization (from the chapter on Rayleigh and Raman scattering), and comparing with Eq. (80):

$$\chi_{\text{CARS}} \propto \frac{N \left(\frac{\partial\sigma}{\partial\Omega} \right)}{\Delta\omega \left(2 - \frac{\Delta\omega}{\omega_v} \right) + i \left(1 - \frac{\Delta\omega}{\omega_v} \right) \Gamma} \quad (82)$$

The susceptibility is proportional to the molecule number density, N , and the differential Raman cross section, $(\partial\sigma/\partial\Omega)$, and reaches a peak where the detuning, $\Delta\omega \equiv \omega_v - (\omega_{\text{pump}} - \omega_{\text{Stokes}})$, approaches zero. The damping coefficient, Γ , determines the line width. A quantum-mechanical treatment yields the following equation:

$$\chi_{\text{CARS}} = \sum_j \frac{K_j \Gamma_j}{2\Delta\omega_j - i\Gamma_j} + \chi_{nr} \quad \text{where} \quad K_j \propto N \Delta_j \left(\frac{\partial\sigma}{\partial\Omega} \right)_j \quad (83)$$

The index j refers to a particular transition and Δ_j is the fractional difference in the population of the two states of the gas between which a transition is taking place (the two real levels in the energy level diagram of Fig. 46); χ_{nr} is the nonresonant susceptibility, a nearly constant term for the CARS process in which all the states in Fig. 46, other than the ground state, are virtual states. The (real part of the) line shape in Eq. (83) is a Lorentz function with full-width at half maximum equal to Γ_j . This line shape is the same as the (complex conjugate of the) line shape for the classical solution when the detuning is small relative to the vibrational frequency. The line width depends inversely upon the lifetimes of the two states involved in the transition, which depend upon the rate of collisions between molecules (collisional broadening). Light emitted by molecules in motion is observed at a slightly different frequency by a stationary observer by an amount proportional to the velocity component towards the observer. This effect, when averaged over many molecules travelling in different directions, results in Doppler broadening. As the distribution of molecular velocity components about the bulk mean in a gas in equilibrium is Gaussian, the line shape becomes a Voigt profile, a convolution between Gaussian and Lorentzian functions. At pressures much above atmospheric, additional line narrowing effects occur.

As the CARS signal is proportional to $|\chi_{\text{CARS}}|^2$, a CARS spectrum reflects the populations of the molecular energy states involved in the transitions. As these populations, in equilibrium, are related via the Boltzmann equation to the temperature, CARS can measure temperature. Integrated CARS signal is also strongly

dependent upon number density and, in principle, could be used to measure density. This is not typically done because of experimental difficulties in maintaining a consistent geometry of the laser beams at the beam intersection. Small uncontrolled motions of the beams due to refraction in inhomogeneous gas fields, movements of the optical system, variation in the quality of the laser beams, etc., cause changes in signal intensity, and calibrations fail. However, where two gas species are resonant in a spectrum, the ratio of the population of one species to another may be found from the shape of the spectrum. Where only one species present is resonant, but χ_{nr} is known, the fraction of that species may be found from the relative amplitude of the resonant signal to the nonresonant “background”; however, χ_{nr} depends on the number density of all species present. If all species but one are resonant in the spectrum then the composition can be fully determined by reference to the nonresonant background [258]. Use of CARS as a diagnostic tool requires comparison of experimental and theoretical spectra [259]. Calculation of theoretical spectra is quite complex and numerically time-consuming: after computation of theoretical susceptibility, spectra must be convolved with laser line shapes and instrument probe function [260].

Nitrogen is a very useful species for measurement of temperature as it is usually present in fuel-air combustion or hypersonic flows, and is readily probed by CARS. The band head of the N₂ Q branch is located at a Raman shift of 2330 cm⁻¹ (units of inverse wavelength, proportional to frequency divided by the speed of light), and is readily accessible using available lasers. The Q branch occurs as a result of transitions between adjacent vibrational states ($\Delta\nu = +1$, where ν is the vibrational quantum number) with no change in the rotational state ($\Delta J = 0$, where J is the rotational quantum number). Figure 48 shows a portion of the N₂ Q-branch spectrum near the band head. Transitions are between $\nu = 0$ and $\nu = 1$ and each peak corresponds to a different J value. As rotation of the molecules affects the energy associated with a given vibrational state, the energy difference between $\nu = 0$ and $\nu = 1$ (at given rotational level) is a function of the rotational level. Two spectra are shown in this figure—the first is the CARS susceptibility and the second is a computed typical broadband CARS spectrum formed by convolution of typical laser line shapes and a typical instrument function with the susceptibility [260]. As may be seen, line shapes are typically not fully resolved in experiments.

Figure 49 shows the sensitivity of the signal spectrum to a) temperature and b) concentration. The calculations are for a) air and b) either air (79% N₂) or 10% N₂, 21% O₂, 69% H₂O, with a pressure of 1 atmosphere. The CARS signal strength varies strongly with temperature, partly through the effect of temperature on density (N) via the N^2 dependence of the CARS susceptibility. By using the Sandia CARSFT code [259], the pressure and temperature dependence was determined to be proportional to $p^2 T^{-3.5}$ at moderate to high pressures [261]. However, the shape of the spectrum also changes. At low temperature, only one vibrational band is present, associated with $\nu = 0$ to $\nu = 1$ transitions, and is

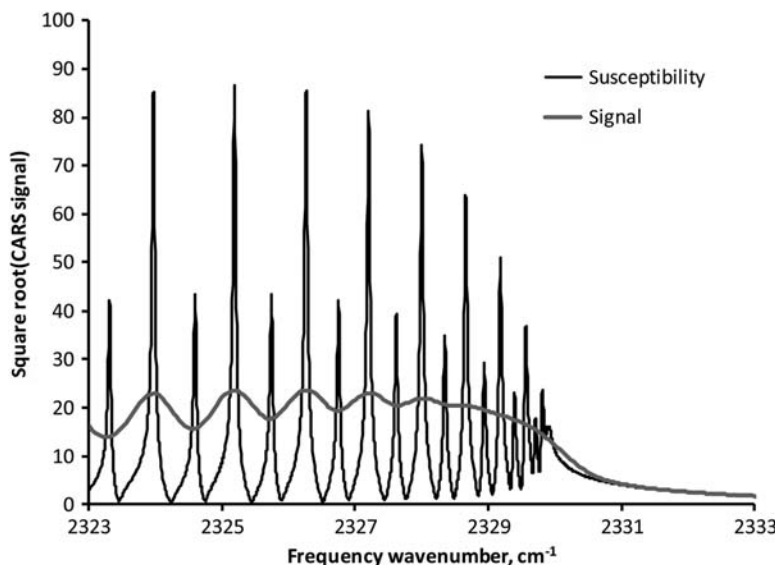


Fig. 48 CARS N_2 Q-branch susceptibility and spectrum near band head at 1 atm., 1400 K.

relatively narrow (because fewer J levels are occupied). At the higher temperatures, “hot” bands are present also, associated with $v = 1$ to $v = 2$ and $v = 2$ to $v = 3$ transitions, and more J levels are populated. As the fraction of N_2 is reduced, the amplitude of the band structure becomes smaller relative to the nonresonant background, and sensitivity to N_2 is lost for concentrations less than a few percent. This lack of sensitivity below a few percent is typical and prevents measurement of minor species, although a number of CARS techniques, for example *resonance* CARS (e.g., Reference [262]), have been developed to circumvent this limitation.

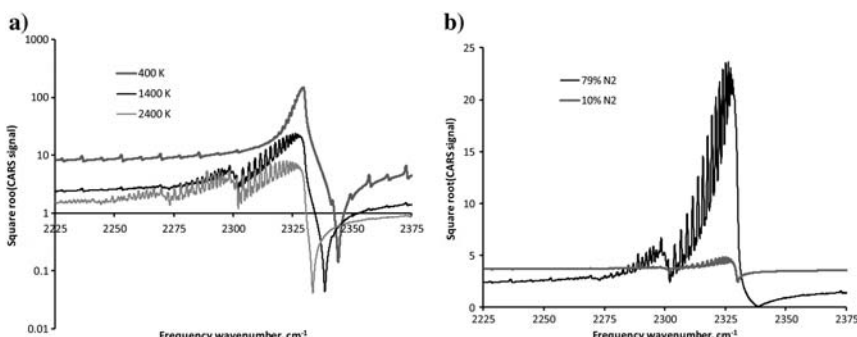


Fig. 49 Effects of a) temperature and b) concentration on the CARS N_2 Q-branch spectrum.

C. ULTRAFAST CARS

Ultrafast techniques have been surveyed by Roy et al. [263]. The CARS technique as described above is a steady-state process involving the mixing of four beams simultaneously present. For given laser energy available in the pump, probe, and Stokes laser beams, the energy in the signal beam is proportional to t^{-2} , where t is the time over which the measurement is made. Nanosecond ($\text{ns} = 10^{-9} \text{ s}$) CARS is performed with Q-switch pulsed lasers where the pulse energy is distributed over 5 ns to 10 ns, at a pulse rate on the order of 10 Hz. There are many 10's or 100's of thousands of Raman frequency cycles during each laser pulse, so that CARS is effectively a steady-state process. However, with the advent of femtosecond ($\text{fs} = 10^{-15} \text{ s}$) lasers (e.g., titanium-sapphire), very short pulse widths of order 10^{-14} seconds are possible at high pulse repetition rate (1 kHz or more), and the pulse width is less than the period of a Raman cycle. Due to the t^{-2} scaling, strong signal energy is available with modest pulse energy.

The theory of fs CARS is different from ns CARS as a steady state problem is replaced with an impulsively initiated, time-dependent one [264]. First, a polarization grating is established in the gas by the interaction of pump and Stokes beams. This grating evolves in time through rotational-vibrational relaxation and then, after some delay (typically up to several hundred picoseconds in measurement applications), a signal is generated by scattering the probe pulse off the grating. By making measurements at different probe delays the relaxation of the grating, which carries with it an imprint of the vibrational and rotational state of the probed molecules, may be observed. “Chirping” techniques have been developed where the probe beam is broadened both temporally and spectrally in such a way that the frequency of the probe varies with time. The temporal relaxation is thus mapped into frequency space, obtained in a single laser pulse, and may be analyzed with an optical spectrometer [265].

Picosecond ($\text{ps} = 10^{-12} \text{ s}$) CARS employs mode-locked solid state lasers with pulse lengths on the order of 10 ps and has characteristics of both ns and fs CARS. As with fs CARS, generation of the grating by the pump and Stokes beams, and scattering of the probe to form the signal, are typically separate steps. However, the probe pulse is still relatively long compared with the Raman cycle period, and the signal contains an optical spectrum similar to that of ns CARS [266]. An advantage of ps CARS over ns CARS is that the ps pulses required to obtain adequate signal-to-noise ratio CARS spectra are better suited to pass through commercially available optical fibers without damaging the fibers [267]. Both fs and ps CARS have the potential advantages over ns CARS of much higher data (pulse) rates and the absence, when the probe is delayed relative to the pump-Stokes laser pulses, of nonresonant background effects. Another advantage of fs CARS is simpler theoretical modeling, as few or no collisions occur in the time of the measurement (negligible collisional effects) [263].

D. ADVANTAGES AND DISADVANTAGES OF CARS FOR PROBING SUPERSONIC, HYPERSONIC AND NONEQUILIBRIUM FLOW

In hypersonic propulsion systems (scramjets), flow velocities are supersonic in inlets and nozzles, and may be supersonic or a mixture of subsonic and supersonic in the combustors. In combustors, pressures are roughly one atmosphere, whereas temperatures are similar to those of low speed combustion. Thermal nonequilibrium (not typically present in low speed combustion) as well as chemical non-equilibrium can be present due to the short flow through time (on the order of milliseconds). CARS has several advantages in this application. The signal comes as a laser beam, which means that it can be collected through a relatively small aperture and may be separated from noncoherent interferences by spatial filtering. This is particularly useful in an engine combustor where there may be emission from the gases and thermal radiation from the wall, and where, for structural reasons, it may not be possible to incorporate large windows. Typical CARS measurements are spatially and temporally resolved, with ~ 1.5 mm long and $50\ \mu\text{m}$ diameter measurement volume, and a 10 ns time scale. CARS is able to nonintrusively measure local temperature and composition. As the Q-branch spectrum reflects the rotational–vibrational state of the molecule, the populations of these states may be directly determined, which is useful when thermal equilibrium (and therefore a single “temperature”) does not exist.

CARS has been used much less frequently in hypersonic freestreams, where temperatures and pressures can be very low. Owing to the previously mentioned $p^2 T^{-3.5}$ scaling of the CARS signal, the signal to noise ratio may be low. At low temperatures only the vibrational ground state and far fewer rotational states of molecules are populated. Vibrational CARS (e.g., of the N₂ Q-branch) then depends upon measuring high-resolution spectra of the rotational structure of the “cold” band near the band head, which depends upon the pressure-dependent collisional effects on line shape, as well as temperature. Measurements of both pressure and temperature, at pressures down to about 0.1 atm., have been made in an underexpanded supersonic jet using this approach [268]. If the $v > 0$ bands are populated at low rotational temperature (vibrational nonequilibrium), this can be easily measured. Alternatively, pure rotational CARS ($\Delta v = 0$, $\Delta J = \pm 2$) is sometimes used at low temperatures as the lines have greater separation than in the Q-branch, but no information on the vibrational state is obtained [269].

In nonequilibrium flows CARS has a significant advantage that it can simultaneously monitor multiple individual state populations. Thus non-Boltzmann distributions can be probed, as in the examples below. Using vibrational broadband CARS, separate rotational and vibrational temperatures can be determined from CARS spectra.

CARS has some disadvantages compared to other measurement techniques. It typically measures at only a single point, and so does not typically provide simultaneous information at multiple spatial locations. Instead, the probe volume is

typically scanned around the flow allowing time-averaged spatial properties to be measured. The data rate is low in ns systems (order 10 Hz) so that in pulsed hypersonic facilities only one single measurement is obtained per facility run. Also, its ~ 1.5 mm long probe volume can be too large in certain applications where it is desired to resolve small length scales such as shock waves, shear layers or turbulent eddies. Many of these limitations are being overcome with fs CARS where 1-D [270] and 2-D [271] imaging have been demonstrated recently with smaller probe volumes and data acquisition rates in the kHz regime have been achieved [263]. CARS requires optical access on two sides of the flow, which may limit application in some facilities. The experimental setup for CARS, involving two or three pulsed laser systems along with large spectrometer(s), is relatively complicated and time consuming to set up. Furthermore, the nonlinear nature of the theory of CARS complicates the interpretation and analysis of the resulting spectra. However, with the combination of accurate and precise temperature and multispecies measurement capabilities, CARS is used in many supersonic, hypersonic, and nonequilibrium flow applications.

E. MOLE FRACTION AND NONEQUILIBRIUM TEMPERATURE MEASUREMENT

Extensive dual-pump CARS measurements have been made in a dual-mode scramjet burning hydrogen [272]. The experiments were conducted in a facility which provided electrically heated clean air to the scramjet combustor via a Mach 2 nozzle. The CARS lasers, which were located outside the scramjet lab, consisted of an injection-seeded Nd:YAG, frequency doubled to 532 nm, an in-house broad band dye laser (Stokes laser) centered around 603 nm with FWHM of 10 nm, and a commercial narrow-band dye laser centered around 550.5 nm. Beams were relayed to the experiment via a translation system that could move the measurement volume and through special slotted windows in the scramjet. Beams were focused and crossed in the scramjet in a planar BOXCARS arrangement (Fig. 47) to form the measurement volume. The signal beam was transmitted out of the scramjet, recollimated, separated from one of the pump beams, relayed to a 1 m spectrometer, then imaged onto a cooled CCD array with 1340×100 pixels. The measured spectra had background subtracted and were normalized by a CARS spectrum in argon, which has no resonances, to remove the spectrum of the broad-band laser. The resulting spectra were fitted to theory, using the Sandia CARSFIT code [259] to generate the theoretical spectra and an in-house fitting code [260] to do the fitting, resulting in temperature standard deviations of $\sim 3\%$ [273]. The fitted parameters included vibrational temperature of N₂, a single rotational temperature for all resonant species, and mole fractions of N₂, O₂, and H₂.

Vibrational nonequilibrium was observed in the flow at the exit of the nozzle and in the freestream of the scramjet flow, which could be fitted to around 1200 K in vibrational temperature of N₂ and 1000 K in vibrational temperature of O₂, whereas the facility air stagnation temperature was 1200 K and the nozzle exit

static temperature was around 680 K [274]. The low rate of relaxation of N₂ vibrational energy relative to rotational (which rapidly comes into equilibrium with translational), and the higher but still relatively low rate for O₂ is consistent with known rates in the literature [275]. Measurements in which a varying amount of steam was added to the air flow are consistent with the known effect of water vapor to promote equilibrium [276]. Figure 50 shows the effect of water vapor in the dual-pump CARS spectrum; notice the large effect of steam on the hot band of the N₂ spectrum and a lesser effect on the hot band of the O₂. The intensity of these bands is proportional to the population difference between the $\nu = 1$ and $\nu = 2$ vibrational states (roughly proportional to the population of $\nu = 1$ as the population of $\nu = 2$ is small).

Figure 51 shows some typical (averaged) measured spectra and fits to theory in the scramjet. Spectrum (a) was in the freestream air of the flow and is shown with a fitted rotational temperature of 923 K and N₂ vibrational temperature of 1133 K. N₂ and O₂ Q-branch resonances may be seen. Spectrum (b) is in the combustion plume and shows H₂ rotational (S) lines as well as the aforementioned Q-branches, with fitted rotational and vibrational temperatures of 1588 K and 1766 K, respectively. Figure 52 shows contour maps of vibrational temperature in the combustor operated in the “scram” mode. The wireframe represents the corners of the flow path; a single hydrogen injection nozzle is located at the downstream end of the small ramp visible on the top surface of the flow path. Flow enters at Mach 2 from the test facility nozzle and is from left to right. The development of the combustion may be seen; combustion is initiated on the top of the plume of hydrogen, near the fuel injector, and wraps around and engulfs the plume further downstream.

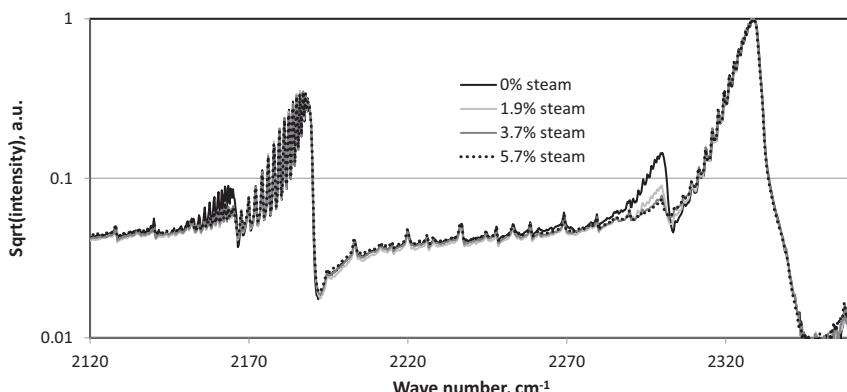


Fig. 50 Experimental dual-pump CARS spectra in a Mach 2 flow with varying amounts of steam added to the air. The N₂ Q-branch is on the right and the O₂ on the left. Reprinted from Reference [274] with permission of the authors.

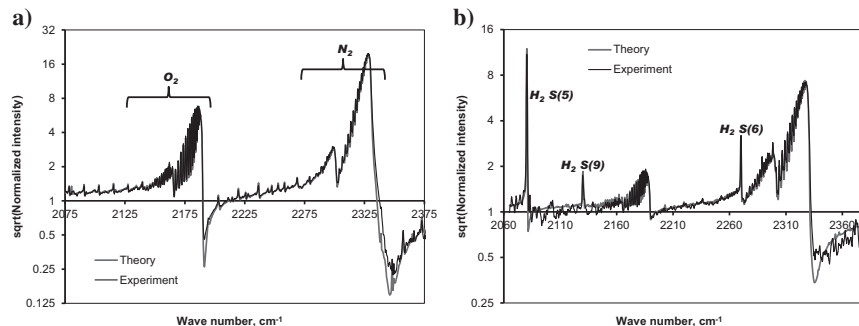


Fig. 51 Typical fits of theory to experimental dual-pump CARS spectra in a dual-mode scramjet: a) freestream, b) combustion plume. Reprinted from Reference [274] with permission of the authors.

Simultaneous with the temperature measurements, species concentrations were also determined from CARS data. The concentration information was derived from the relative intensity of the different resonant features in the CARS spectra, comparing to the intensity of the nonresonant background, and considering that the mole fractions must sum to one [259]. Figure 53 shows CARS mole fraction measurements obtained at the same conditions as Fig. 52. The mole fraction is uniform air in the first plane at the left of each of the figures. Evidence of the cold H_2 fuel jet is seen in the temperature map (Fig. 52) and all three mole fraction maps in the second plane, which is located just downstream of the fuel injector (Fig. 53). As the fuel jet spreads spatially and is consumed by combustion, the presence of N_2 in the center of the downstream fuel plume shows evidence of fuel-air mixing. However, the O_2 mole

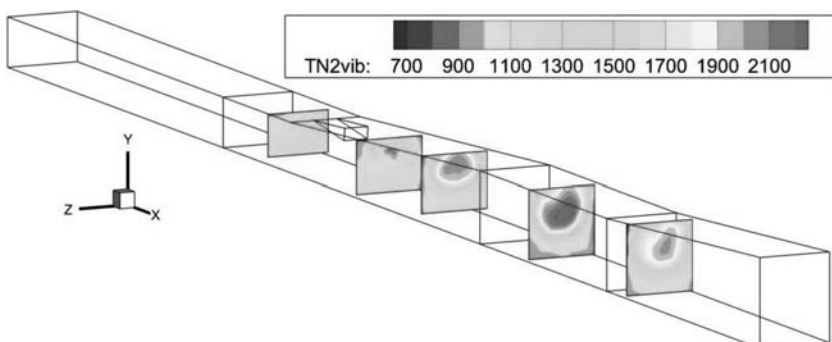


Fig. 52 Contour plots of CARS-measured mean vibrational temperature in a dual-mode scramjet. Reprinted from Reference [272] with permission of the authors (see color section).

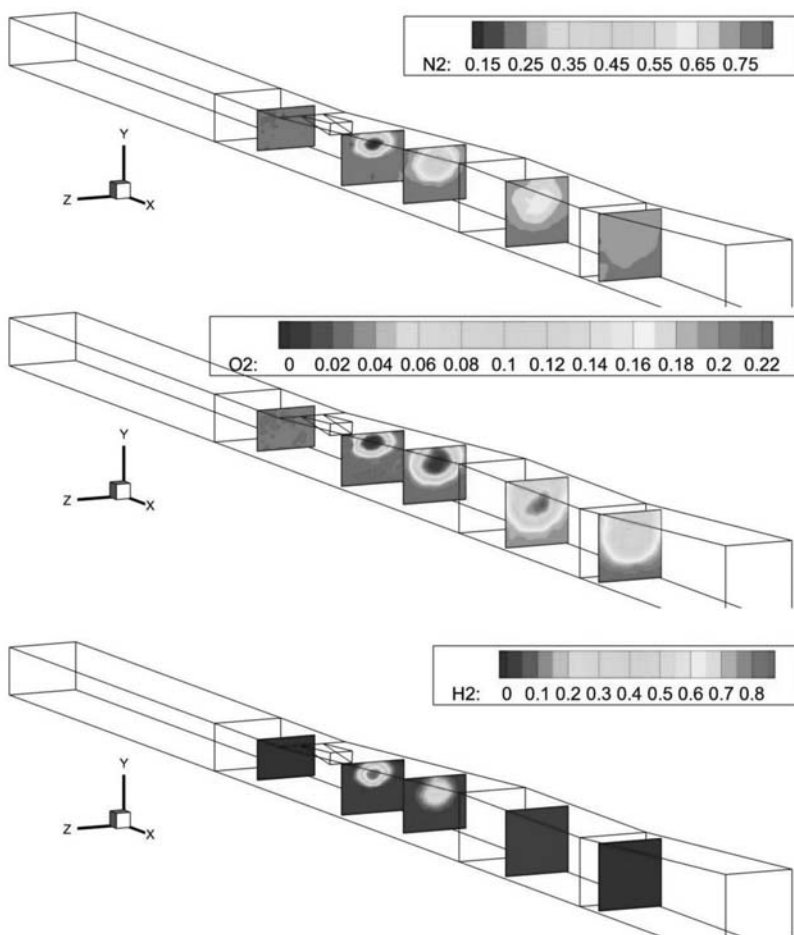


Fig. 53 Contour plots of CARS-measured mean mole fractions of N₂ (top), O₂ (middle) and H₂ (bottom) in a dual-mode scramjet at the same conditions as Fig. 8.52 [272]. Reprinted from Reference [272] with permission of the authors (see color section).

fraction does not track exactly with the N₂ because it is reacting with the H₂. Not until the final plane at the right side of each figure, when all the H₂ is consumed, does the O₂ penetrate to the center of the duct, in the wake of the fuel plume.

F. MEASUREMENT OF NONTHERMALIZED POPULATION DISTRIBUTIONS USING CARS

Nonequilibrium flows sometimes result in non-Boltzmann distributions, for example among rotational or vibrational states. Montello et al. [277] used

picosecond CARS to probe nonthermal vibrational distributions in N₂ generated in low pressure (100 Torr) N₂ and air pulsed discharges. They used a 150 ps duration, frequency doubled Nd:YAG laser to generate the two green pump beams. The Nd:YAG laser also pumped a red broadband dye laser for the Stokes beam. These frequencies were chosen to probe the Q-branch Raman spectrum of N₂. The CARS signal was dispersed on a spectrometer, allowing instantaneous quantification of the N₂ vibrational distribution function (VDF). By varying the time between the CARS acquisition and the pulsing of the plasma discharge, the time evolution of the VDF could be studied.

Figure 54a shows vibrational N₂ CARS spectra obtained at different times after the beginning of the ~100 ns duration pulsed discharge. The narrowness of the bands indicates a relatively low rotational temperature, compared to the VDF. The populations of the excited vibrational levels are observed to increase with time (though the rotational distribution stays relatively constant). Vibrational levels from 0–9 were observed to have measurable population. When the vibrational populations are graphed with respect to vibrational quantum number (Fig. 54b) a thermalized population distribution would appear as a nearly straight line on this semi-log plot. Instead, departure from the Boltzmann distribution is observed, as evident from the nonlinear trends in the data. A theoretical model captures much of the nonequilibrium physics occurring in this plasma [277].

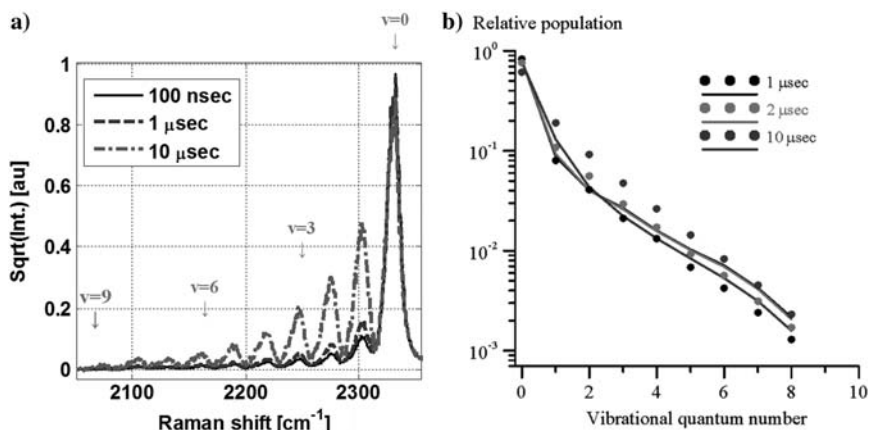


Fig. 54 a) N₂ Q-branch CARS spectrum obtained in a pulsed discharge operating with 100 Torr of N₂ shown for three different measurement times after the beginning of the ~100 ns discharge pulse. b) Experimental and predicted vibrational energy level populations based on a), showing nonthermal vibrational distributions which evolve with time. Reprinted from Reference [277] with permission of the authors. © IOP Publishing. Reproduced by permission of IOP Publishing. All rights reserved (see color section).

G. CARS SUMMARY

In summary, CARS is a powerful technique for simultaneously and quantitatively measuring multiple flow parameters in gas flows with thermal and/or chemical nonequilibrium. If the gas is in thermal equilibrium, CARS can be used to measure temperature; if not it can provide information on rotational and vibrational (for rotational–vibrational CARS) state populations, allowing separate determinations of rotational and vibrational temperature or rotational and vibrational distribution functions in nonthermalized flows. It also can be used to quantify the relative concentration of the species probed. It is spatially and temporally resolved, with a short measurement time (sub-ps to 10 ns) and a measurement volume that is typically on the order of 1 mm long. Nanosecond CARS is limited by available lasers to measurement rates of about 10 Hz, but femtosecond CARS data rates are often 1 kHz or more. Nanosecond CARS is a well-established technique, picosecond and femtosecond CARS in gases is quite recent, due to the advent of suitable lasers, and techniques are still under development. The primary limitations of state-of-the art CARS systems include its complexity (which has meant relatively few applications to large-scale test facilities), the fact that measurements are pointwise and not planar or volumetric, and (for nanosecond CARS) the low data rate. Other issues include sensitivity to optical misalignment due to vibrations or refractive index variations along the beam path, and lack of spectral and collision-rate modeling for some species.

VIII. OTHER MOLECULAR-BASED MEASUREMENT TECHNIQUES

A. INTRODUCTION

Many different surface-based, probe-based and particle-based instruments have been used to study nonequilibrium hypersonic flows. However, this manuscript focuses only on molecular-based measurement techniques. Optical emission spectroscopy, absorption spectroscopy, Raman scattering, Rayleigh scattering, laser-induced fluorescence (LIF) and CARS are some of the most commonly used techniques, and for this reason have been detailed in the preceding sections. This section briefly describes additional molecular-based measurement techniques that have been used, or that show some promise for use, in studying nonequilibrium hypersonic flows.

B. INTERFEROMETRY

Interferometry uses interference of light to measure small changes in optical path length. Variation in gas flow properties along the optical path cause the index of refraction to vary, which generates these path length changes relative to a reference path. The two paths are then aligned onto a 1- or 2-D detector where interference (or a so-called interferogram) is observed. This method is very sensitive

because it can measure optical path differences that are fractions of a wavelength of the light from which they are generated.

In fluid mechanical applications, interferometry is usually used for flow visualization or to measure the gas density. The gas density is related to the index of refraction through the Gladstone-Dale equation:

$$n - 1 = K\rho \quad (84)$$

where n is the index of refraction, ρ is the density and K is the Gladstone-Dale constant, which depends on the gas and the wavelength of light. The Springer Handbook of Experimental Fluid Mechanics recently reviewed applications of various types of interferometry to fluid mechanics [229]. These include Mach Zehnder interferometry, holographic interferometry, shearing interferometry and others. The different interferometric methods can be sensitive to the density or the gradient in density [229]. Interferograms typically have light and dark fringes, which correspond to interference in the light caused by index of refraction variations introduced to one of the paths. Sometimes, to enable post-processing, the optics are purposely misaligned producing a series of mostly parallel sinusoidal fringes that act as a spatial carrier frequency allowing Fourier transforms to be used in post processing. Such interferograms are called *finite fringe interferograms* (as opposed to *infinite fringe interferograms* wherein the two paths are precisely aligned).

As a path-averaged measurement technique, most interferometry techniques require experimental methods and/or analysis to determine spatially resolved information. If measurements along multiple lines of sight can be obtained, tomographic reconstruction can be used to deconvolve spatial information. Or, in axisymmetric flows, an Abel inversion can be used, as described previously. However, in the general case of 3-D turbulent flows, these approaches are challenged by the short spatial and temporal scales of the experiments, which require many simultaneous high-resolution views from different angles. Although time-averaged measurements in such turbulent flow fields are possible, it is more difficult to use these methods to resolve small temporal or spatial scales.

Interferometry is particularly useful in luminous high-enthalpy flow facilities, where spectral, spatial and temporal discrimination can be used to obtain the interferograms, while rejecting flow luminosity. Interferometry was used extensively to study nonequilibrium hypersonic flows several decades ago. See, for example, the use of Mach-Zehnder interferometry to study the effect of non-equilibrium flow on the shock stand-off distance and post-shock density field [278]. More recently, holographic interferometry has been used in expansion tube facilities which are simply too luminous to use other techniques such as laser-induced-fluorescence. In one experiment [279], the 532 nm and 355 nm outputs from an Nd:YAG laser were used to produce two simultaneous finite fringe interferograms in air passing over a cylinder at 12 km/sec in the X1 super-orbital expansion tube at the University of Queensland, Australia. Both holographic finite fringe interferograms were acquired on the same photographic

plate. After reconstruction, a Fourier transform method was used to process the interferograms. In this experiment the fringe shift is sensitive to both the density and the electron concentration, necessitating the two measurements to determine the two properties. Density and electron concentration maps were determined from the interferograms [279].

C. BACKGROUND ORIENTED SCHLIEREN (BOS)

A relatively new measurement technique that is sensitive to density (through index of refraction gradients) is known as Background Oriented Schlieren (BOS) [280, 281]. BOS uses a CCD camera equipped with a lens to image a flow placed in front of a *background* consisting of a random dot pattern (or other [282, 283] random pattern). A *reference* image of the background pattern is acquired with the flow absent and then a second image is acquired with the flow present. Refractive index gradients cause the dots to move slightly from one image to the other. The pair of dot pattern images is processed using particle-image velocimetry (PIV) software to recover the path-integrated light deflections (pixel shifts) caused by the refractive index (density) gradients.

To obtain the highest possible spatial resolution, both the dot pattern and the flow disturbance should be in crisp focus. This suggests the use of small lens apertures to obtain a large depth of field. To obtain maximum sensitivity, the flow disturbance should be located as close to the camera lens as possible [284]. As it is difficult to achieve a long enough depth of field to optimize both of these requirements, in practice, the object is usually put closer to the background dot pattern, for example from 0.5 to 0.875 of the way from the camera to the background pattern [284, 285]. Also affecting spatial resolution are the camera pixel size, the resolution and quality of the background pattern used and the interrogation window size used in image processing.

In a 2-D flow, the pixel shifts can be used to directly compute the density gradient and thus the density field [284]. In an axisymmetric flow, the density gradient varies along the optical path and additional processing of the data is required to make quantitative measurements. In such axisymmetric cases, an Abel or Radon inversion can be used to compute the density field, for example in the supersonic flow over a cone at zero degrees angle of attack [286]. In nonaxisymmetric flows, tomography using multiple camera views is required to obtain density information [284]. The multiple views can either be obtained using a single camera that observes the flow from different angles at different times, resulting in time-averaged measurements [284], or by using multiple cameras to take many simultaneous images, providing time resolution, which is a current research topic. As BOS measures gradients and is thus a relative measurement technique, the density in one point in the flow must be known or estimated to obtain the density field. BOS has the advantages of being a low-cost technique and being able to provide both qualitative flow visualization and quantitative measurements for large fields of view. One disadvantage is that BOS does not

produce real-time visualization and measurement results as the raw images require processing. Also, as a tomographic technique using a limited number of views, it has much lower spatial resolution than laser-sheet based techniques such as planar LIF, at least in unsteady flows where it is impractical to have a large number of views.

D. ELECTRON-BEAM FLUORESCENCE

In low-density ($<10^{16}$ molecules/cm³) hypersonic flows, electron beam fluorescence is an attractive measurement approach [287]. An electron beam can be directed into the flow to excite a line, or swept through the flow to stimulate fluorescence in a plane. Multiple species, such as NO and N₂, can be excited and detected at different wavelengths. The fluorescence signal, if quenching is negligible, can be related to species concentration. Decades ago, density and temperature were measured in hypersonic boundary layers using electron beam fluorescence [288]. More recently, electron-beam fluorescence has been used to distinguish rotational and vibrational temperatures by spectrally resolving the emitted fluorescence, as well as to measure the gas velocity from time-of-flight measurements, using a technique similar to that shown in Fig. 33 [287]. However, at higher pressures, several problems complicate the use of electron-beam fluorescence. First, quenching becomes significant, complicating interpretation of concentration data and minimizing fluorescence lifetimes used to obtain flow tagging velocity. Second, the beam begins to disperse at higher densities, preventing measurement in a line or plane. Finally, excitation from scattered electrons becomes significant at higher pressures, which complicates interpretation of the images. Nonetheless, the electron beam fluorescence method has been shown to be useful in a wide variety of low-pressure hypersonic flows and even has potential for measurements in flight [287, 289].

E. DEGENERATE FOUR-WAVE MIXING (DFWM)

Like CARS, Degenerate Four-Wave Mixing (DFWM) is a nonlinear, four-wave mixing measurement technique that involves the crossing of three laser beams to generate a fourth beam that is detected. DFWM's three input laser beams are all of the same color (degenerate) and are usually tuned to an absorption in the atom or molecule being probed. The signal beam from DFWM measurements is typically analyzed in the spectral domain using scanned or broadband lasers to measure a spectrum of signal intensity vs wavelength. DFWM has been used to measure gas concentration, temperature and velocity [5]. Compared to LIF, it has an advantage for measuring species concentrations because it is relatively insensitive to collisional quenching, owing to the fact that it is an absorption-based technique (not depending on fluorescence) [290]. As each beam is resonant, it is also relatively sensitive and can be used for detecting minor species [5]. As the DFWM signal is a laser-like beam, it is suitable for studying luminous flows since

background radiation can be spatially filtered with an aperture. DFWM is usually implemented as a single-point measurement, though it has been extended to line and 2-D imaging applications [5]. The main drawbacks of DFWM are that it is more difficult to align and implement than LIF, it has much lower spatial resolution than LIF (because of its elongated probe volume), it is sensitive to absorption of the laser beams, it is sensitive to saturation of the molecular transitions, and it requires very high beam quality to obtain 2-D images [5]. DFWM temperature measurements in a flame have reported accuracies and precisions more than a factor of two worse than CARS [5, 291] while also having a larger probe volume.

F. LASER-INDUCED THERMAL ACOUSTICS (LITA)

Another four-wave mixing technique, laser-induced thermal acoustics (LITA), uses two pump beams to generate acoustic waves that scatter a probe laser into a signal beam that is detected [292]. The two pumps and probe can be the same wavelengths, in which case it is also DFWM. Or, the probe beam can be a different wavelength than the pumps, which reduces light interferences from the incident, high-powered pump beams. Whereas the signal beam from the DFWM techniques described in the previous section is usually analyzed in the *spectral* domain, LITA usually uses the *time* domain (signal beam intensity vs time) to measure gas velocity, speed of sound (which can be converted to temperature if the gas composition is known) [292, 293] and gas pressure [294]. In the time domain, the signal intensity is characterized by a damped oscillation, which can have beat frequencies containing the velocity and temperature information. Velocity and temperature accuracies and precisions on the order of 1 m/s and 1 K, respectively, have been reported in air flows [293, 295]. These accuracies and precisions are the best reported in this manuscript for these parameters. LITA is usually implemented as a single-point, single-velocity-component measurement. The main limitations of LITA are its relative complexity and that the measurements are obtained over relatively long probe volumes—on the order of 1 to 2 cm. Although this is much longer than most turbulent length scales occurring in hypersonic flows, it can be sufficient to probe laminar flows if the probe volume is oriented with its long axis oriented perpendicular to the steepest gradients in the flow.

IX. CONCLUSIONS

This manuscript has described numerous molecular-based measurement techniques that are potentially applicable to the investigation of hypersonic nonequilibrium flows. One might ask, “*Which technique is best?*” or “*Which one should I use?*” The answer to the first question is that no one is best. The different techniques measure different properties in different ways and have relative merits. In addition, flow conditions and facility constraints may prevent application of specific measurement techniques. The answer to the second, more important

question, depends on many factors. It depends on the measurement requirements as well as the past experience of the research team. It depends on the available equipment, the budget for new equipment and the time frame available to make the measurement. Some techniques, such as CARS, require a year or years of training to gain enough experience to apply the technique expertly. Dual-pump CARS requires home-built equipment (i.e., a broadband dye laser) as well as two commercially available lasers, a spectrometer, a low noise CCD camera, and other equipment. It is therefore relatively time consuming and expensive to set up. If a researcher or research team has experience with similar technology (for example Nd:YAG lasers, dye lasers, CCD cameras), then the work will progress faster. Less complicated (easier to set up and to understand) methods might yield usable results in a shorter time frame. These practical issues are certainly important, but a major consideration in planning an experiment is tailoring the chosen technique to the measurement requirements, the characteristics of the facility and the expertise of the scientist or engineer performing the experiment.

A measurement campaign should begin by answering the following questions, for example by interviewing the final “customer” of the data:

- What parameter(s) need to be measured?
- Must multiple parameters be obtained simultaneously to determine correlations?
- What spatial resolution is required?
- Is imaging required or are single-point or line measurements sufficient?
- What temporal resolution is required? (e.g., time required for a single measurement)
- Do measurements need to be time resolved? (e.g., a continuous sequence of data)
- What accuracy is needed?
- What precision is needed?
- What quantity of data is required?
- When are the data needed? Are instant (real-time) data required?
- Where in the flow are measurements required? (inflow, exit, near walls, etc.)
- What type of optical access is available?
- Can (toxic) seed gases be introduced? Will they influence the properties being measured?
- What is the ordered priority of the above requirements?

This list of requirements must be matched with available measurement technologies such as those reported in the sections above. There is rarely a perfect solution for this exercise. Instead, there is a compromise between the needs of the

customer and the capabilities of the instrumentation team and the chosen technique. Goals should then be established before the research actually starts. This exercise is fruitful for the measurement scientist because it often results in a need for a new measurement technique that can be developed if existing techniques are not suitable.

ACKNOWLEDGMENTS

The authors wish to thank Jennifer Inman and Joel Everhart of NASA Langley Research Center, Christopher Combs from The University of Texas at Austin and Christopher Peters from Princeton University for assistance in reviewing this manuscript. The authors acknowledge support from the NASA Fundamental Aeronautics Program, Hypersonics and High Speed Projects. Dr. Cutler received support from the National Center for Hypersonic Combined Cycle Propulsion grant FA 9550-09-1-0611. The technical monitors on the grant are Chiping Li (AFOSR), and Aaron Auslender and Rick Gaffney (NASA).

REFERENCES

- [1] Schuler, K. E., "Studies in Nonequilibrium Rate Processes. II. The Relaxation of Vibrational Nonequilibrium Distributions in Chemical Reactions and Shock Waves," *Journal of Physical Chemistry*, Vol. 61, No. 7, 1957, pp. 849–856.
- [2] Bird, G. A. "Breakdown of Translational and Rotational Equilibrium in Gaseous Expansions," *AIAA Journal*, Vol. 8, No. 11, 1970, pp. 1998–2003.
- [3] Vincenti, W. G., and Kruger, C. H. Jr., *Introduction to Physical Gas Dynamics*, Robert E. Krieger Publishing Company, Malabar, Florida, 1986, originally published by Wiley, New York, 1965.
- [4] Anderson, J. D. Jr., *Hypersonic and High-Temperature Gasdynamics*, 2nd ed., AIAA Education Series, Reston, Virginia, 2006.
- [5] Eckbreth, A. C., *Laser Diagnostics for Combustion Temperature and Species*, 2nd ed., Combustion Science & Technology Book Series, Volume 3, Taylor & Francis, New York, 1996.
- [6] Tedeschi, G., Gouin, H., and Elena, M., "Motion of Tracer Particles in Supersonic Flows," *Experiments in Fluids*, Vol. 26, 1999, pp. 288–296.
- [7] Lu, F. K., and Marren, D. E., *Advanced Hypersonic Test Facilities*, AIAA, Reston, Virginia, 2002, p. 17.
- [8] Chue, R. S. M., Tsai, C. Y., Bakos, R. J., and Erdos, J. I., *Advanced Hypersonic Test Facilities*, AIAA, Reston, Virginia, 2002, p. 29.
- [9] Lackner, M., Totschnig, G., Winter, F., Ortsiefer, M., Amann, M. C., Shau, R., and Rosskopf, J., "Demonstration of methane spectroscopy using a vertical-cavity surface-emitting laser at 1.68 μm with up to 5 MHz repetition rate," *Measurement Science and Technology*, Vol. 14, No. 1, 2003, p. 101.
- [10] Kurtz, J. J., Aizengendler, M., Krishna, Y., Walsh, P., and O'Byrne, S. "A Rugged, High-sensitivity, TDLAS-based Oxygen Sensor for a Scramjet Inlet,"

- ISABE-2013-1605, *Proceedings of the 21st International Symposium on Air-Breathing Engines*, Busan, Korea, Sept. 9–13, 2013.
- [11] Tedder, S. A., Wheeler, J. L., Cutler, A. D., and Danehy, P. M., “Width-increased Dual-pump Enhanced Coherent Anti-Stokes Raman Spectroscopy,” *Applied Optics*, Vol. 49, No. 8, 2010, pp. 1305–1313.
 - [12] Seasholtz, R. G., and Buggele, A. E., “Improvement in Suppression of Pulsed Nd: YAG Laser Light with Iodine Absorption Cells for Filtered Rayleigh Scattering Measurements,” NASA Technical Memorandum 113177, November 1997.
 - [13] Naik, S. V., Laurendeau, N. M., Lucht, R. P., Roy, S., and Gord, J. R., “Single-laser-shot Detection of Nitric Oxide in Reacting Flows using Electronic Resonance Enhanced Coherent Anti-Stokes Raman Scattering,” *Applied Physics Letters*, Vol. 93, No. 9, 2008, pp. 091115–09111.
 - [14] Woodmansee, M. A., Iyer, V., Dutton, J. C., and Lucht, R. P., “Nonintrusive Pressure and Temperature Measurements in an Underexpanded Sonic Jet Flowfield,” *AIAA Journal*, Vol. 42, No. 6, 2004, pp. 1170–1180.
 - [15] Cruden, B., “Electron Density Measurement in Reentry Shocks for Lunar Return,” *Journal of Thermophysics and Heat Transfer*, Vol. 26, No. 2, 2012, pp. 222–223.
 - [16] Winter, M. W., Raiche, G., and Prabhu, D. K., “Emission Spectroscopy and Radiometry Measurements in the NASA Ames IHF Arc Jet Facility,” *Proceedings of the 5th ESA-CNES RHTG Workshop*, Barcelona, Spain, 16th to 19th Oct. 2012.
 - [17] Cauchon, D. L., Radiative Heating Results from the FIRE II Flight Experiment at a Re-entry Velocity of 11.4 Kilometers per Second, TM X-1402, NASA, 1967.
 - [18] Erdman, P. W., Zipf, E. C., Espy, P., Howlett, C. L., Levin, D. A., Collins, R. J., and Candler, G. V., “Measurements of Ultraviolet Radiation from a 5-km/s Bow shock,” *Journal of Thermophysics and Heat Transfer*, Vol. 8, No. 3, 1994, pp. 441–446.
 - [19] Kontinos, D. A., and Wright, M. J., “Introduction: Atmospheric Entry of the Stardust Sample Return Capsule,” Vol. 47, No. 5, 2010, pp. 705–707.
 - [20] Trumble, K. A., Cozmuta, I., Sepka, S., Jenniskens, P., and Winter, M., “Postflight Aerothermal Analysis of the Stardust Sample Return Capsule,” *Journal of Spacecraft and Rockets*, Vol. 47, No. 5, 2010, pp. 765–774.
 - [21] Winter, M. W., McDaniel, R. D., Chen, Y.-K., Liu, Y., Saunders, D., and Jenniskens, P., “Radiation Modeling for the Reentry of the Hayabusa Sample Return Capsule,” *50th AIAA Aerospace Sciences Meeting*, Nashville, Tennessee, 9–12 Jan 2012, AIAA-2012-1296.
 - [22] Herzberg, G., *Molecular Spectra and Molecular Structure: Vol. I, Spectra of Diatomic Molecules*, D. Van Nostrand Company, Ltd, 1950.
 - [23] Gilmore, F. R., Laher, R. R., and Espy, P. J., “Franck-Condon Factors, r-centroids, Electronic transition Moments, and Einstein Coefficients for Many Nitrogen and Oxygen Band Systems,” *Journal of Physical Chemistry Reference Data*, Vol. 21, 1992, p. 1005.
 - [24] Wiese, W. L., Smith, M. W., and Miles, B. M., *Atomic Transition Probabilities, Volume I, Hydrogen through Neon*, Institute for Basic Standards, National Bureau of Standards, Washington, D. C., October 1969.
 - [25] NIST-database: physics.nist.gov/cgi-bin/At_Data/main_asd
 - [26] Bashkin, S., and Stoner, J.O. Jr, *Atomic Energy Levels and Grotian Diagrams*, Vol. 2, North-Holland, Amsterdam, 1982.

- [27] Brandis, A. M., Wray, A., Liu, Y., Schwenke, D. W., Huo, W. M., and Johnston, C. O., "Validation of HyperRad for Earth Entries," *44th AIAA Thermophysics Conference*, 2013, AIAA 2013-2777.
- [28] Dunham, J., "The Energy Levels of a Rotating Vibrator," *Physical Review*, Vol. 41, 1932, p. 721.
- [29] Winter, M., "Emissionsspektroskopische Untersuchung der Umströmung von Probenkörpern in hochenthalpen Plasmaströmungen/Emission Spectroscopic Investigation of the Flow Field around a Blunt Body in a High Enthalpy Flow," Dissertation (in German), Universität Stuttgart, Germany, Dec. 2006.
- [30] Park, C., *Nonequilibrium Hypersonic Aerothermodynamics*, John Wiley and Sons, New York, 1989.
- [31] Morse, P. M., "Diatom Molecules according to the Wave Mechanics: II. Vibrational Levels," *Physical Review*, Vol. 34, 1929, p. 57.
- [32] Steele, D., Lippincot, E. R., and Vanderslice, J. T., "Comparative Study of Empirical Internuclear Potential Functions," *Review of Modern Physics*, Vol. 34, 1962, pp. 239–251.
- [33] Le Roy, R. J., *RKR1 2.0 - A Computer Program Implementing the First-Order RKR Method for Determining Diatomic Molecule Potential Energy Functions*, Guelph-Waterloo Centre for Graduate Work in Chemistry, University of Waterloo, Waterloo, Ontario N2L 3G1, Canada, April 2004.
- [34] Vest, C. M. *Holographic Interferometry*, New York, John Wiley and Sons, Inc., Vol. 476, 1979.
- [35] Winter, M. W., and Prabhu, D. K., "Excited State Chemistry in the Free Stream of the NASA IHF Arc Jet Facility Observed by Emission Spectroscopy," *42nd AIAA Thermophysics Conference*, Honolulu, Hawaii, 27–30 Jun 2011.
- [36] Modest, M., *Radiation Heat Transfer*, Academic Press, Elsevier Science, USA, 2003.
- [37] Griem, H. R., *Plasma Spectroscopy*, McGraw-Hill Book Company, New York, USA, 1964.
- [38] Laux, C. O., *Radiation and Nonequilibrium Collisional-Radiative Models*, VKI Special Course on Physico-Chemical Models for High Enthalpy and Plasma Flows Modeling, Belgium, June 4–7, 2002. See also Laux, C. O., Pierrot, L., and Gessman, R. J., "State-to-state Modeling of a Recombining Nitrogen Plasma Experiment," *Chemical Physics*, Vol. 398, pp. 46–55, DOI: 10.1016/j.chemphys.2011.10.028, 2012.
- [39] Quintero, M. C., Rodero, A., Garcia, M. C., and Sola, A. "Determination of the Excitation Temperature in a Nonthermodynamic-Equilibrium High-Pressure Helium Microwave Plasma Torch," *Applied Spectroscopy*, Vol. 51, no. 6, 1997, pp. 778–784.
- [40] Whiting, E. E., Park, C., Liu, Y., Arnold, J. O., and Paterson, J. A., "NEQAIR96, Nonequilibrium and Equilibrium Radiative Transport and Spectra Program: User's Manual," NASA RP-1389, NASA, December 1996.
- [41] Johnston, C. O., Hollis, B. R., and Sutton, K., "Spectrum Modeling for Air Shock-Layer Radiation at Lunar-Return Conditions," *Journal of Spacecraft and Rockets*, Sep.–Oct. 2008.
- [42] Fujita, K., and Abe, T., "SPRADIAN, Structured Package for Radiation Analysis: Theory and Application," The Institute of Space and Astronautical Science Report No. 669, July 1997.

- [43] Smith, A. J., Wood, A., Dubois, J., Fertig, M., and Pfeiffer, B., Plasma Radiation Database PARADE V22 Final Report Issue 3, ESTEC contract 11148/94/NL/FG, FGE TR28/96, Issue 3, October 2006.
- [44] <http://www.specair-radiation.net> (last accessed in Feb 2013).
- [45] <http://www.sri.com/contact/form/libase> (last accessed in Feb 2013).
- [46] Luque, J., and Crosley, D. R., "LIFBASE: Database and spectral simulation (version 1.5)," SRI International Report MP 99-009 (1999).
- [47] <http://cfp.ist.utl.pt/radiation/SPARTAN/SPARTAN.html> (last accessed in April 2013).
- [48] Babou, Y., Riviere, P., Perrin, M., and Soufiani, A., "Spectroscopic Data for the Prediction of Radiative Transfer in CO₂-N₂ Plasmas," *Journal of Quantitative Spectroscopy & Radiative Transfer*, Vol. 110, 2009, pp. 89–108.
- [49] Perrin, M.-Y., Rivière, P., and Soufiani, A., Radiation Database for Earth and Mars Entry, RTO-EN-AVT-162 Nonequilibrium Gas Dynamics – From Physical Models to Hypersonic Flights (2009) 8.1.8.40.
- [50] Cruden, B., Martinez, R., Grinstead, J. H., and Olejniczak, J., "Simultaneous Vacuum Ultraviolet through Near IR Absolute Radiation Measurement with Spatiotemporal Resolution in an Electric Arc Shock Tube," *41st AIAA Thermophysics Conference*, June 22–25 2009, San Antonio, Texas, AIAA Paper 2009-4240.
- [51] Brandis, A., Johnston, C., Panesi, M., Cruden, B., Prabhu, D., and Bosem, D., "Investigation of Nonequilibrium Radiation for Mars Entry," *51st AIAA Aerospace Sciences Meeting including the New Horizons Forum and Aerospace Exposition*, 2013, AIAA Paper 2013-1055.
- [52] Golde, M. F., and Thrush, B. A., "Afterglows," *Reports on Progress in Physics*, Vol. 36, 1973, pp 1285–1364.
- [53] Partridge, H., Langhoff, S. R., Bauschlicher, C. W. Jr., and Schwenke, D. W., "Theoretical Study of the A⁵ Σ_g^+ and C⁵ Π_u States of N₂: Implications for the N₂ Afterglow," *Journal of Chemical Physics*, Vol. 88, No. 5, 1 March 1988. Figure 3.11b reproduced with permission from the authors. Copyright 1988, AIP Publishing LLC. DOI: 10.1063/1.453962.
- [54] Camac, M., "O₂ Vibration Relaxation in Oxygen-argon Mixtures," *Journal of Chemical Physics*, Vol. 34, No. 2, 1961, p. 448.
- [55] Vincenti, W. G., and Kruger, C. H., *Introduction to Physical Gas Dynamics*, Wiley, New York, 1967.
- [56] Gauglitz, G., and Vo-Dinh, T., *Handbook of Spectroscopy*, Wiley-VCH Verlag GmbH & Co. KGaA, Weinheim, 2003.
- [57] Thorne, A. P., *Spectrophysics*, 2nd ed., Chapman and Hall, 1988.
- [58] Palma, P. C., "Laser-Induced Fluorescence Imaging in Free-Piston Shock Tunnels" PhD Thesis, Australian National University, 1999.
- [59] Webster, C. R., Menzies, R. T., and Hinkley, E. D., "Infrared Laser Absorption: Theory and Applications," in *Laser Remote Chemical Analysis, Chemical Analysis*, edited by R. M. Measures, Vol. 94. John Wiley and Sons, New York, 1988.
- [60] Demtroder, W., "Atoms, Molecules and Photons," Heidelberg, Springer-Verlag Berlin Heidelberg, 2006.
- [61] Di Rosa, M. D., "Collision-broadening and–shift of NO $\gamma(0,0)$ Absorption Lines by H₂O, O₂, and NO at 295 K," *Journal of Molecular Spectroscopy*, Vol. 164, 1994, pp. 97–117,

- [62] Rothman, L. S., Gordon, I. E., Barbe, A., Bernath, P. F., and Birk, M. et al., "The HITRAN 2008 Molecular Spectroscopic Database," *Journal of Quantitative Spectroscopy and Radiative Transfer*, Vol. 110, pp. 533–572, 2009.
- [63] Humlincek, J., "Optimized Computation of the Voigt and Complex Probability Functions," *Journal of Quantitative Spectroscopic Radiative Transfer*, Vol. 27, No. 4, 1982, pp. 437–444.
- [64] Arnold, J. O., Whiting, E. E., and Lyle, G. C., "Line by Line Calculation of Spectra from Diatomic Molecules and atoms Assuming a Voigt Line Profile," *Journal of Quantitative Spectroscopy and Radiative Transfer*, Vol. 9, No. 6, 1969, pp. 775–798.
- [65] Baer, D. S., and Hanson, R. K., "Tunable Diode Laser Absorption Diagnostics for Atmospheric Pressure Plasmas," *Journal of Quantitative Spectroscopic Radiative Transfer*, Vol. 47, No. 6, 1992, pp. 455–475.
- [66] Haverlag, M., Stoffels, E., Stoffels, W. W., Kroesen, G. M. W., and De Hoog, F. J., "Measurement of the Gas Temperature in Fluorocarbon Radio Frequency Discharges using Infrared Absorption Spectroscopy," *Journal of Vacuum Science & Technology A: Vacuum, Surfaces and Films*, Vol. 14, No. 2, 1996, pp. 380–383.
- [67] Haverlag, M., Stoffels, E., Stoffels, W. W., Kroesen, G. M. W., and De Hoog, F. J., "Measurement of the Gas Temperature in Fluorocarbon Radio Frequency Discharges using Infrared Absorption Spectroscopy," *Journal of Vacuum Science & Technology A: Vacuum, Surfaces and Films*, Vol. 14, No. 2, 1996, pp. 380–383.
- [68] Zhang, F.-Y., Komurasaki, K., Iida, T., and Fujiwara, T., "Diagnostics of an Argon Arcjet Plume with a Diode Laser," *Applied Optics*, Vol. 38, No. 9, 1999, pp. 1814–1822.
- [69] Parker, R. A., Wakeman, T., MacLean, M., and Holden, M., "Measuring Nitric Oxide Freestream Concentration using Quantum Cascade Lasers at CUBRC," *44th AIAA Aerospace Sciences Meeting and Exhibit*, Jan 2006, AIAA Paper 2006-926.
- [70] Sanders, S. T., Wang, J., Jeffries, J. B., and Hanson, R. K., "Diode-laser Absorption Sensor for Line-of-sight Gas Temperature Distributions," *Applied Optics*, Vol. 40, 2001, pp. 4404–4415.
- [71] Silver, J. A., and Kane, D. J., "Diode Laser Measurements of Concentration and Temperature in Microgravity Combustion," *Measurement Science and Technology*, Vol. 10, 1999, pp. 845–852.
- [72] Rothman, L. S., Rinsland, C. P., and Goldman, A. et al., "The HITRAN molecular spectroscopic database and HAWKS (HITRAN atmospheric workstation): 1996 Edition," *Journal of Quantitative Spectroscopy and Radiative Transfer*, Vol. 60, 1998, pp. 665–710.
- [73] Allen, M. G., "Diode Laser Absorption Sensors for Gas Dynamic And Combustion Flows," *Measurement Science and Technology*, Vol. 9, No. 4, 1998, pp. 545–562.
- [74] Wehe, S. D., Baer, D. S., and Hanson, R. K., "Tunable Diode-laser Absorption Measurements of Temperature, Velocity, and H₂O in Hypervelocity Flows," *33rd Joint Propulsion Conference and Exhibit*, Seattle, WA, 1997, AIAA Paper 97-3267.
- [75] Liu, J. T. C., Jeffries, J. B., and Hanson, R. K., "Wavelength Modulation Absorption Spectroscopy with 2 f Detection using Multiplexed Diode Lasers for Rapid Temperature Measurements in Gaseous Flows," *Applied Physics B*, Vol. 78, 2004, pp. 503–511.
- [76] Wilson, G. V. H., "Modulation Broadening of NMR and ESR Line Shapes," *Journal of Applied Physics*, Vol. 34, 1963, pp. 3276–3285.

- [77] Reid, J., and Labrie, D., "Second Harmonic Detection with Tunable Diode Lasers—Comparison of Experiment and Theory," *Applied Physics B*, Vol. 26, 1981, pp. 203–210.
- [78] Silver, J. A., "Frequency-modulation Spectroscopy for Trace Species Detection: Theory and Comparison among Experimental Methods," *Applied Optics*, Vol. 31, 1992, pp. 707–717.
- [79] Cooper, D. E., and Warren, R. E., "Two-tone Optical Heterodyne Spectroscopy with Diode Lasers: Theory of Line Shapes and Experimental Results," *Journal of Optical Society America B*, Vol. 4, 1987, pp. 470–480.
- [80] Goldstein, C. S., Schultz, I. A., Jeffries, J. B., and Hanson, R. K., "Tunable Diode Laser Absorption Sensor for Measurements of Temperature and Water Concentration in Supersonic Flows," 49th AIAA Aerospace Sciences Meeting including the New Horizons Forum and Aerospace Exposition, Orlando FL, Jan 4–7, 2011, AIAA Paper 2011-1094.
- [81] Haller, K. L., and Hobbs, P. C. D., "Double-beam Laser Absorption Spectroscopy: Shot noise-limited Performance at Baseband with a Novel Electronic Noise Canceler," In *Optics, Electro-Optics, and Laser Applications in Science and Engineering*, pp. 298–309. International Society for Optics and Photonics, 1991.
- [82] Allen, M. G., and Kessler, W. J., "Simultaneous Water Vapor Concentration and Temperature Measurements using 1.31-micron Diode Lasers," *AIAA Journal*, Vol. 34, No. 3, 1996, pp. 483–488.
- [83] Upschulte, B. L., Miller, M. F., and Allen, M. G., "Diode Laser Sensor for Gasdynamic Measurements in a Model Scramjet Combustor," *AIAA Journal*, Vol. 38, No. 7, 2000, pp. 1246–1252.
- [84] Griffiths, A. D., and Houwing, A. F. P., "Diode Laser Absorption Spectroscopy of Water Vapor in a Scramjet Combustor," *Applied Optics*, Vol. 44, No. 31, 2005, pp. 6653–6659.
- [85] Pan, F., and Oka, T., "Radial Distribution of Molecular Ions in the Positive Column of de Glow Discharges using Infrared Diode-Laser Spectroscopy," *Physical Review A*, Vol. 36, 1987, pp. 2297–2310.
- [86] Brandt, O., and Roth, P., "Temperature Measurements behind Shock Waves using a Rapid Scanning IR-diode Laser," *Physics of Fluids*, Vol. 30, No. 5, 1987, pp. 1294–1298.
- [87] Lin, X., Yu, X. L., Li, F., Zhang, S. H., Xin, J. G., and Chang, X. Y., "CO Concentration and Temperature Measurements in a Shock Tube for Martian Mixtures by Coupling OES and TDLAS," *Applied Physics B*. 2012.
- [88] Farooq, A., Jeffries, J. B., and Hanson, R. K., "CO₂ Concentration and temperature Sensor for Combustion Gases using Diode-laser Absorption Near 2.7 μm," *Applied Physics B*, Vol. 90, 2008, pp. 619–628.
- [89] Lyle, K. H., Jeffries, J. B., and Hanson, R. K., "Diode-laser Sensor for Air-mass Flux 1: Design and Wind Tunnel Validation," *AIAA Journal*, Vol. 45, No. 9, 2007, pp. 2204–2212.
- [90] Mohamed, A. K., Henry, D., Falni, J. P., Sagnier, P., Soutad, J., Beck, W. H., and Martinez Schramm, J., "Infrared Diode Laser Absorption Spectroscopy Measurements in the S4MA, F4, and HEG Hypersonic Flows," *International Symposium on Atmospheric Reentry Vehicles and Systems*, ONERA Paper No. TP 1999–45, March 1999.

- [91] Philippe, L. C., and Hanson, R. K., "Laser Diode Wavelength-modulation Spectroscopy for Simultaneous Measurement of Temperature, Pressure, and Velocity in Shock-heated Oxygen Flows," *Applied Optics*, Vol. 32, No. 30, 1993, pp. 6090–6103.
- [92] Wittig, S., and O'Byrne, S., "Characterization of Supersonic Combustor Inlet Flows using Diode Laser Absorption Spectroscopy," *49th AIAA Aerospace Sciences Meeting*, Orlando, Florida, January 4–7, 2011, AIAA Paper 2011-0073.
- [93] Hanson, R. K., "Application of Quantitative Laser Sensors to Kinetics, Propulsion and Practical Energy Systems," *Proceedings of the Combustion Institute*, Vol. 33, 2011, pp. 1–40.
- [94] Busa, K. M., Ellison, E. N., McGovern, B. J., Diskin, G. S., DePiro, M. J., Capriotti, D. P., and Gaffney, R. L., "Measurements on NASA Langley Durable Combustor Rig by TDLAT: Preliminary Results," *51st AIAA Aerospace Sciences Meeting including the New Horizons Forum and Aerospace Exposition*, Grapevine TX., 7–10 January 2013, AIAA Paper 2013-096.
- [95] Brown, M. S., Herring, G. C., Cabell, K., Hass, N., Barhorst, T. F., and Gruber, M., "Optical Measurements at the Combustor Exit of the HIFIRE 2 Ground Test Engine," *50th AIAA Aerospace Sciences Meeting including the New Horizons Forum and Aerospace Exposition*, Nashville, TN, January 9–12, 2012, AIAA Paper 2012-0857.
- [96] Ma, L., Li, X., Sanders, S. T., Caswell, A. W., Roy, S., Plemons, D. H., and Gord, J. R., "50-kHz-rate 2D Imaging of Temperature and H₂O Concentration at the Exhaust Plane of a J85 Engine Using Hyperspectral Tomography," *Optics Express*, Vol. 21, No. 1, 2013, pp. 1152–1162.
- [97] Berden, G., and Engeln, R., *Cavity Ring-Down Spectroscopy: Techniques and Applications*, John Wiley, New York, 2009.
- [98] Scherer, J. J., Paul, J. B., O'Keefe, A., and Saykally, R. J., "Cavity Ringdown Laser Absorption Spectroscopy: History, Development, and Application to Pulsed Molecular Beams," *Chemical Review*, Vol. 97, 1997, pp. 25–51.
- [99] Romanini, D., Dupré, P., and Jost, R., "Non-linear Effects by Continuous Wave Cavity Ringdown Spectroscopy in Jet-Cooled NO₂," *Vibrational Spectroscopy*, Vol. 19, 1999, pp. 93–10.
- [100] Engeln, R., Berden, G., Peeters, R., and Meijer, G., "Cavity Enhanced Absorption and Cavity Enhanced Magnetic Rotation Spectroscopy," *Review of Scientific Instruments*, Vol. 69, No. 11, 1998, pp. 3763–3769.
- [101] O'Keefe, A., "Integrated Cavity Output Analysis of Ultra-Weak Absorption," *Chemical Physics Letters*, Vol. 293, No. 5, 1998, pp. 331–336.
- [102] Paul, J. B., Lapson, L., and Anderson, J. G., "Ultrasensitive Absorption Spectroscopy with a High-finesse Optical Cavity and Off-axis Alignment," *Applied Optics*, Vol. 40, No. 27, 2001, pp. 4904–491.
- [103] Bakowski, B., Hancock, G., Peverall, Ritchie, G. A. D., and Thornton, L. J., "Characterization of an N₂ Plasma Using Sensitive Diode Laser Spectroscopy," *Journal of Physics D: Applied Physics*, Vol. 37, No. 15, 2004, pp. 2064–2072.
- [104] Fiedler, S. E., Hese, A., and Ruth, A. A., "Incoherent Broad-Band Cavity-Enhanced Absorption Spectroscopy," *Chemical Physics Letters*, Vol. 371, No. 3, 2003, pp. 284–294.

- [105] Bonnet, J. P., Gresillon, D., and Taran, J. P., "Nonintrusive Measurements for High-Speed, Supersonic, and Hypersonic Flows," *Annual Review of Fluid Mechanics*, Vol. 30, 1998, pp. 231–273.
- [106] Ouyang, X., and Varghese, P. L., "Line-of-sight Absorption Measurements of High Temperature Gases with Thermal and Concentration Boundary Layers," *Applied Optics*, Vol. 28, 1989, pp. 3979–3984.
- [107] Schoenung, M., and Hanson, R. K., "CO and Temperature Measurements in a Flat Flame by Laser Absorption Spectroscopy and Probe Techniques," *Combustion Science and Technology*, Vol. 24, 1980, pp. 227–237.
- [108] Kohse-Höinghaus, K., and Jeffries, J. B. (eds.) *Applied Combustion Diagnostics*, Combustion: An International Series, Taylor & Francis, New York, 2002.
- [109] Palma, P. A., *Laser-Induced Fluorescence Imaging in Free-Piston Shock Tunnels*, PhD Thesis, Australian National University, submitted May 1998, revised February 1999.
- [110] Saleh, B. A. E., and Teich, M. C., *Fundamentals of Photonics*, 2nd ed., John Wiley & Sons, Inc., Hoboken, New Jersey, 2007.
- [111] Bischel, W. K., Kelly, P. J., and Rhodes, C. K., "High-resolution Doppler-free two-photon Spectroscopic Studies of Molecules. II. The ν_2 Bands of NH₃14," *Physical Review A*, Vol. 13, no. 5, 1976, 1829.
- [112] McIlrath, T. J., Hudson, R., Aikin, A., and Wilkerson, T. D., "Two-photon Lidar Technique for Remote Sensing of Atomic Oxygen," *Applied Optics*, Vol. 18, no. 1, 1989, pp. 1887–1896.
- [113] Bischel, W. K., Perry, B. E., and Crosley, D. R., "Detection of Fluorescence from O and N Atoms Induced by two-photon Absorption," *Applied Optics*, Vol. 21, No. 8, 1982, 1419–1429.
- [114] Meier, U., Bittner, J., Kohse-Höinghaus, K., and Just, Th., "Discussion of Two-photon Laser-excited Fluorescence as a Method for Quantitative Detection of Oxygen Atoms in Flames," In *Symposium (International) on Combustion*, Elsevier, Vol. 22, no. 1, 1989, 1887–1896.
- [115] Crosley, D. R., "Rotational and Translational Effects in Collisions of Electronically Excited Diatomic Hydrides," *Journal of Physical Chemistry*, Vol. 93, 1989, pp. 6273–6282.
- [116] Anderson, J. D. Jr., *Hypersonic and High-Temperature Gas Dynamics*, 2nd ed., AIAA Education Series, AIAA, Reston, VA, 2006.
- [117] Vincenti, W. G., and Kruger, C. H. Jr., *Introduction to Physical Gas Dynamics*, Reprint of 1967 ed., John Wiley, New York, 1975.
- [118] Paul, P. H., Gray, J. A., Durant, J. L., and Thoman, J. W., "Collisional Quenching Corrections for Laser-Induced Fluorescence Measurements of NO A² Σ^+ ," *AIAA Journal*, Vol. 32, No. 8, August 1994.
- [119] Baer, D. S., Chang, H. A., and Hanson, R. K., "Fluorescence Diagnostics for Atmospheric-pressure Plasmas using Semiconductor Lasers," *Journal of the Optical Society of America B*, Vol. 9, No. 11, 1992, pp. 1968–1978.
- [120] Liebeskind, J. G., Hanson, R. K., and Cappelli, M. A., "Laser-induced Fluorescence Diagnostic for Temperature and Velocity Measurements in a Hydrogen Arcjet Plume," *Applied Optics*, Vol. 32, No. 30, 1993, pp. 6117–6127.
- [121] Inman, J. A., Bathel, B. F., Johansen, C. T., Danehy, P. M., Jones, S. B., Gragg, J. G., and Splinter, S. C., "Nitric Oxide PLIF Measurements in the Hypersonic Materials

- Environmental Test System (HYMETS)," *49th AIAA Aerospace Sciences Meeting*, Orlando, FL, January 4–7, 2011, AIAA Paper 2011-1090.
- [122] Storm, P. V., and Cappelli, M. A., "LIF Characterization of Arcjet Nozzle Flows," *AIAA, ASME, SAE, and ASEE, Joint Propulsion Conference*, Lake Buena Vista, FL, July 1–3, 1996, AIAA Paper 1996-2987.
- [123] Fletcher, D. G., "Arcjet Flow Properties Determined from Laser-induced Fluorescence of Atomic Nitrogen," *36th AIAA Aerospace Sciences Meeting*, AIAA Paper 1998-0205.
- [124] Fletcher, D. G., "Arcjet Flow Properties Determined from Laser-induced Fluorescence of Atomic Nitrogen," *Applied Optics*, Vol. 38, No. 9, March 20, 1999.
- [125] Grinstead, J. H., Porter, B. J., and Carballo, J. E., "Flow Property Measurement Using Laser-Induced Fluorescence in the NASA Ames Interaction Heating Facility," *49th AIAA Aerospace Sciences Meeting*, Orlando, FL, January 4–7, 2011, AIAA Paper 2011-1091.
- [126] Lutz, A., Meyers, J., Owens, W., Smith, S., and Fletcher, D. G., "Experimental Analysis of Carbon Nitridation and Oxidation Efficiency with Laser-Induced Fluorescence," *51st AIAA Aerospace Sciences Meeting*, Grapevine, TX, January 7–10, 2013, AIAA Paper 2013-0924.
- [127] McKenzie, R. L., and Gross, K. P., "Two-photon Excitation of Nitric Oxide Fluorescence as a Temperature Indicator in Unsteady Gas Dynamic Processes," *Applied Optics*, Vol. 20, No. 12, June 15, 1981.
- [128] McMillin, B. K., Palmer, J. L., and Hanson, R. K., "Temporally Resolved, Two-line Fluorescence Imaging of NO Temperature in a Transverse Jet in a Supersonic Cross Flow," *Applied Optics*, Vol. 32, No. 36, December, 20, 1993.
- [129] Seitzman, J. M., Hanson, R. K., DeBarber, P. A., and Hess, C. F., "Application of Quantitative Two-line OH Planar Laser-induced Fluorescence for Temporally Resolved Planar Thermometry in Reacting Flows," *Applied Optics*, Vol. 33, No. 18, June 20, 1994.
- [130] McMillin, B. K., Seitzman, J. M., and Hanson, R. K., "Comparison of NO and OH Planar Fluorescence Temperature Measurements in Scramjet Model Flowfields," *AIAA Journal*, Vol. 32, No. 10, October 1994.
- [131] Palma, P. C., Danehy, P. M., and Houwing, A. F. P., "Fluorescence Imaging of Rotational and Vibrational Temperature in Shock-Tunnel Nozzle Flow," *AIAA Journal*, Vol. 41, No. 9, September 2003.
- [132] Lachney, E. R., and Clemens, N. T., "PLIF Imaging of Mean Temperature and Pressure in a Supersonic Bluff Wake," *Experiments in Fluids*, Vol. 24, 1998, pp. 354–36.
- [133] Koch, U., Gülhan, A., and Esser, B., "Determination of NO-rotational and Vibrational Temperature Profiles in a High Enthalpy Flow Field with Nonequilibrium," *1st Joint French-German Symposium on Simulation of Atmospheric Entries by Means of Ground Test Facilities*, Stuttgart, Germany, 1999.
- [134] Del Vecchio, A., Palumbo, G., Koch, U., and Gülhan, A., "Temperature Measurements by Laser-induced Fluorescence Spectroscopy in Nonequilibrium High-Enthalpy Flow," *Journal of Spacecraft and Rockets*, Vol. 14, No. 2, April–June 2000.

- [135] Löhle, S., Auweter-Kurtz, M., Herdrich, G., and Laux, T., "LIF Measurements of NO in N₂/O₂ and N₂/CO₂ Plasma Flows," *36th AIAA Thermophysics Conference*, Orlando, FL, June 23–26, 2003, AIAA Paper 2003-3487.
- [136] Brinkman, E. A., Raiche, G. A., Brown, M. S., and Jeffries, J. B., "Optical Diagnostics for Temperature Measurement in a DC Arcjet Reactor used for Diamond Deposition," *Applied Physics B*, Vol. 64, No. 6, 1997, pp. 689–697.
- [137] Bessler, W. G., and Schulz, C., "Quantitative Multi-line NO-LIF Temperature Imaging," *Applied Physics B*, Vol. 78, 2004, pp. 519–533.
- [138] Palmer, J. L., and Hanson, R. K., "Planar Laser-induced fluorescencE Temperature Measurements in Free Jet Flows with Vibrational Nonequilibrium," *31st AIAA Aerospace Sciences Meeting*, Reno, NV, January 11–14, 1993, AIAA Paper 1993-0046
- [139] Inman, J. A., Bathel, B. F., Johansen, C. T., Danehy, P. M., Jones, S. B., Gragg, J. G., and Splinter, S. C., "Nitric-Oxide Planar Laser-Induced Fluorescence Measurements in the Hypersonic Materials Environmental Test System," *AIAA Journal*, Vol. 51, No. 10, 2013, pp. 2365–2379.
- [140] Smits, A. J., and Lin, T. T. (eds.) *Flow Visualization: Techniques and Examples*, 2nd ed., Imperial College Press, London, 2012.
- [141] Katô, H., and Baba, M., "Dynamics of Excited Molecules: Predissociation," *Chemical Review*, Vol. 95, 1995, pp. 2311–2349.
- [142] Herzberg, G., *Molecular Spectra and Molecular Structure: I. Spectra of Diatomic Molecules*, New York, Van Nostrand Reinhold, 1950.
- [143] Laufer, G., Quagliaroli, T. M., Krauss, R. H., Whitehurst III, R. B., McDaniel, J. C., and Grinstead, J. H., "Planar OH Density and Apparent Temperature Measurements in a Supersonic Combusting Flow," *AIAA Journal*, Vol. 34, No. 3, March 1996.
- [144] Zhang, J., King, G. B., Laurendeau, N. M., and Renfro, M. W., "Two-point Time-series Measurements of Hydroxyl Concentration in a Turbulent Nonpremixed Flame," *Applied Optics*, Vol. 46, No. 23, August 10, 2007.
- [145] Settersten, T. B., Patterson, B. D., and Humphries, W. H., "Radiative Lifetimes of NO A^{2Σ⁺(v' = 0,1,2) and the Electronic Transition Moment of the A^{2Σ⁺-X^{2Π} System," *Journal of Chemical Physics*, Vol. 131, No. 10, 2009, 104309.}}
- [146] Settersten, T. B., Patterson, B. D., and Gray, J. A., "Temperature- and Species-dependent Quenching of NO A^{2Σ⁺(v' = 0) Probed by Two-photon Laser-induced Fluorescence using a Picosecond Laser," *Journal of Chemical Physics*, Vol. 124, No. 23, 2006, 234308.}
- [147] Settersten, T. B., Patterson, B. D., and Carter, C. D., "Collisional Quenching of NO A^{2Σ⁺(v' = 0) between 125 and 294 K," *Journal of Chemical Physics*, Vol. 130, No. 20, 2009, 204302.}
- [148] Grinstead, J. H., Driver, D. M., and Raiche, G. A., "Radial Profiles of Arcjet Flow Properties Measured with Laser-induced Fluorescence of Atomic Nitrogen," *41st AIAA Aerospace Sciences Meeting*, Reno, NV., January 6–9, 2003, AIAA Paper 2003-400.
- [149] Fletcher, D. G., and Playez, M., "Characterization of Supersonic and Subsonic Plasma Flows," *25th AIAA Aerodynamic Measurement Technology and Ground Testing Conference*, San Francisco, CA., June 5–8, 2006, AIAA Paper 2006-3294.

- [150] Lochman, B. J., Murphree, Z. R., Narayanaswamy, V., and Clemens, N. T., "PLIF Imaging of Naphthalene-ablation Products in a Mach 5 Turbulent Boundary Layer," *27th AIAA Aerodynamic Measurement Technology and Ground Testing Conference*, Chicago, IL, June 28–July 1, 2010, AIAA Paper 2010-4346.
- [151] Buxton, O. R., Lochman, B. J., Sharma, M., and Clemens, N. T., "Simultaneous PIV and PLIF Imaging of Low-Temperature Ablation in a Mach 5 Turbulent Boundary Layer," *50th AIAA Aerospace Sciences Meeting*, Nashville, TN, January 9–12, 2012, AIAA Paper 2012-440.
- [152] Versluis, M., Georgiev, N., Martinsson, L., Aldén, M., and Kröll, S., "2-D Absolute OH Concentration Profiles in Atmospheric Flames using Planar LIF in a Bi-directional Laser Beam Configuration," *Applied Physics B: Lasers and Optics* Vol. 65, No. 3, 1997, pp. 411–417.
- [153] Carter, C. D., and Barlow, R. S., "Simultaneous Measurements of NO, OH, and the Major Species in Turbulent Flames," *Optics Letters*, Vol. 19, No. 4, 1994, pp. 299–301.
- [154] Barlow, R. S., Wang, G.-H., Anselmo-Filho, P., Sweeney, M. S., and Hochgreb, S., "Application of Raman/Rayleigh/LIF Diagnostics in Turbulent Stratified Flames," *Proceedings of the Combustion Institute* Vol. 32, 2009, pp. 945–953.
- [155] McDaniel, J. C., "Nonintrusive Pressure Measurement with Laser-Induced Iodine Fluorescence," *18th AIAA Thermophysics Conference*, Montreal, Canada, June 1–3, 1983, AIAA Paper 1983-1468.
- [156] Lemoine, F., and Leporcq, B., "An Efficient Optical Pressure Measurement in Compressible Flows: Laser-induced Iodine Fluorescence," *Experiments in Fluids*, Vol. 19, 1995, pp. 150–158.
- [157] Chang, A. Y., Battles, B. E., and Hanson, R. K., "Simultaneous Measurements of Velocity, Temperature, and Pressure Using Rapid CW Wavelength-Modulation Laser-induced Fluorescence of OH," *Optics Letters*, Vol. 15, No. 12, June 15, 1990.
- [158] Naik, S. V., Kulatilaka, W. D., Venkatesan, K. K., and Lucht, R. P., "Pressure, Temperature, and Velocity Measurements in Underexpanded Jets Using Laser-Induced Fluorescence Imaging," *AIAA Journal* Vol. 47, No. 4, April 2009.
- [159] Hiller, B., and Hanson, R. K., "Simultaneous Planar Measurements of Velocity and Pressure Fields in Gas Flows using Laser-induced Fluorescence," *Applied Optics*, Vol. 27, No. 1, January 1, 1988.
- [160] Hartfield, J., Jr., Hollo, S. D., and McDaniel, J. C., "A Unified Planar Measurement Technique for Compressible Flows Using Laser-induced Iodine Fluorescence," *30th AIAA Aerospace Sciences Meeting*, Reno, NV, January 6–9, 1992, AIAA Paper 1992-0141.
- [161] Rothamer, D. A., and Hanson, R. K., "Temperature and Pressure Imaging Using Infrared Planar Laser-induced Fluorescence," *Applied Optics*, Vol. 49, No. 33, 2010, pp. 6436–6447.
- [162] Marinelli, W. J., Kessler, W. J., Allen, M. G., Davis, S. J., Arepalli, S., and Scott, C. D., "Copper Atom Based Measurements of Velocity and Turbulence in Arc Jet Flows," *29th Aerospace Sciences Meeting*, Reno, NV., January 7–10, 1991, AIAA Paper 1991-358.
- [163] McDaniel, J. C., Hiller, B., and Hanson, R. K., "Simultaneous Multiple-point Velocity Measurements Using Laser-induced Iodine Fluorescence," *Optics Letters*, Vol. 8, No. 1, 1983, pp. 51–53.

- [164] Klavuhn, K. G., Gauba, G., and McDaniel, J. C., "OH Laser-Induced Fluorescence Velocimetry Technique for Steady, High-Speed, Reacting Flows," *Journal of Propulsion and Power*, Vol. 10, No. 6, 1994, pp. 787–797.
- [165] Kulatilaka, W. D., Naik, S. V., and Lucht, R. P., "Development of High-Spectral-Resolution Planar Laser-Induced Fluorescence Imaging Diagnostics for High-Speed Gas Flows," *AIAA Journal*, Vol. 46, No. 1, January 2008.
- [166] Danehy, P. M., Mere, P., Gaston, M. J., O'Bryne, S., Palma, P. C., and Houwing, A. F. P., "Fluorescence Velocimetry of the Hypersonic, Separated Flow over a Cone," *AIAA Journal*, Vol. 39, No. 7, 2001, pp. 1320–1328.
- [167] Hruschka, R., O'Byrne, S., and Kleine, H., "Two-component Doppler-shift Fluorescence Velocimetry Applied to a Generic Planetary Entry Probe Model," *Experiments in Fluids*, Vol. 48, 2010, pp. 1109–1120.
- [168] Fletcher, D. G., and McDaniel, J. C., "Laser-Induced Iodine Fluorescence Technique for Quantitative Measurement in a Nonreacting Supersonic Combustor," *AIAA Journal*, Vol. 27, No. 5, May 1989.
- [169] Hartfield, R. J., Hollo, S. D., and McDaniel, J. C., "Planar Measurement Technique for Compressible Flows Using Laser-Induced Iodine Fluorescence," *AIAA Journal*, Vol. 31, No. 3, March 1993.
- [170] Donohue, J. M., and McDaniel, J. C., "Computer-Controlled Multiparameter Flowfield Measurements Using Planar Laser-Induced Iodine Fluorescence," *AIAA Journal*, Vol. 34, No. 8, August 1996.
- [171] Zimmerman, M., and Miles, R. B., "Hypersonic-helium-flow-field Measurements with the Resonant Doppler Velocimeter," *Applied Physics Letters*, Vol. 37, No. 10, November 15, 1980.
- [172] Bathel, B. F., Johansen, C., Inman, J. A., Jones, S. B., and Danehy, P. M., "Review of Fluorescence-Based Velocimetry Techniques to Study High-Speed Compressible Flows," *51st AIAA Aerospace Sciences Meeting*, Grapevine, TX, January 7–10, 2013, AIAA Paper 2013-0339.
- [173] Hiller, B., and Hanson, R. K., "Two-frequency Laser-induced Fluorescence Technique for Rapid Velocity-field Measurements in Gas Flows," *Optics Letters*, Vol. 10, No. 5, May, 1985.
- [174] Westblom, U., and Aldén, M., "Spatially Resolved Flow Velocity Measurements using Laser-induced Fluorescence from a Pulsed Laser," *Optics Letters*, Vol. 14, No. 1, January 1, 1989.
- [175] Paul, P. H., Lee, M. P., and Hanson, R. K., "Molecular Velocity Imaging of Supersonic Flows Using Pulsed Planar Laser-induced Fluorescence of NO," *Optics Letters*, Vol. 14, No. 9, May 1, 1989.
- [176] Allen, M., Davis, S., Kessler, W., Legner, H., McManus, K., Mulhall, P., Parker, T., and Sonnenfroh, D., "Velocity Field Imaging in Supersonic Reacting Flows near Atmospheric Pressure," *AIAA Journal*, Vol. 32, No. 8, August 1994.
- [177] Koochesfahani, M. M., and Nocera, D. G., "Molecular Tagging Velocimetry," *Handbook of Experimental Fluid Dynamics*, Chap. 5.4, edited by J. Foss, C. Tropea, and A. Yarin, Springer-Verlag, Berlin, 2007.
- [178] Hiller, B., Booman, R. A., Hassa, C., and Hanson, R. K., "Velocity Visualization in Gas Flows Using Laser-Induced Phosphorescence of Biacetyl," *Review of Scientific Instruments*, Vol. 55, No. 12, 1984, pp. 1964–1967.

- [179] Danehy, P. M., O'Byrne, S., Houwing, A. F. P., Fox, J. S., and Smith, D. R., "Flow-Tagging Velocimetry for Hypersonic Flows Using Fluorescence of Nitric Oxide," *AIAA Journal*, Vol. 41, No. 2, February 2003.
- [180] Bathel, B. F., Danehy, P. M., Inman, J. A., Jones, S. B., Ivey, C. B., and Goyne, C. P., "Velocity Profile Measurements in Hypersonic Flows Using Sequentially Imaged Fluorescence-Based Molecular Tagging," *AIAA Journal*, Vol. 49, No. 9, September 2011.
- [181] Lempert, W. R., Jiang, N., Sethuram, S., and Samimy, M., "Molecular Tagging Velocimetry Measurements in Supersonic Microjets," *AIAA Journal*, Vol. 40, No. 6, June, 2002.
- [182] Lempert, W. R., Boehm, M., Jiang, N., Gimelshein, S., and Levin, D., "Comparison of Molecular Tagging Velocimetry Data and Direct Simulation Monte Carlo Simulations in Supersonic Micro Jet Flows," *Experiments in Fluids*, Vol. 34, 2003, pp. 403–411.
- [183] Hsu, A. G., Srinivasan, R., Bowersox, R. D. W., and North, S. W., "Two-component Molecular Tagging Velocimetry Utilizing NO Fluorescence Lifetime and NO₂ Photodissociation techniques in an Underexpanded Jet Flowfield," *Applied Optics*, Vol. 48, No. 22, August 1, 2009.
- [184] Inman, J. A., Danehy, P. M., Bathel, B. F., Alderfer, D. W., and Nowak, R. J., "Laser-Induced Fluorescence Velocity Measurements in Supersonic Underexpanded Impinging Jets," *48th AIAA Aerospace Sciences Meeting*, Orlando, FL., January 4–7, 2010, AIAA Paper 2010-1438.
- [185] Johansen, C. T., Danehy, P. M., Ashcraft, S. W., Bathel, B. F., Inman, J. A., and Jones, S. B., "PLIF study of Mars Science Laboratory Capsule Reaction Control System Jets," *41st AIAA Fluid Dynamics Conference*, Honolulu, HI., June 27–30, 2011, AIAA Paper 2011-3890.
- [186] Johansen, C. T., Novak, J., Bathel, B., Ashcraft, S. W., and Danehy, P. M., "Comparison of MSL RCS Jet Computations with Flow Visualization and Velocimetry," *50th AIAA Aerospace Sciences Meeting*, Nashville, TN., January 4–7, 2012, AIAA Paper 2012-0594.
- [187] Balla, R. J., "Iodine Tagging Velocimetry in a Mach 10 Wake," *AIAA Journal*, Technical Note (accepted).
- [188] Houwing, A. F. P., Smith, D. R., Fox, J. S., Danehy, P. M., and Mudford, N. R., "Laminar Boundary Layer Separation at a Fin-Body Junction in a Hypersonic Flow," *Shock Waves*, Vol. 11, 2001, pp. 31–42.
- [189] Bathel, B. F., Danehy, P. M., Inman, J. A., Watkins, A. N., Jones, S. B., Lipford, W. E., Goodman, K. Z., Ivey, C. B., and Goyne, C. P., "Hypersonic Laminar Boundary Layer Velocimetry with Discrete Roughness on a Flat Plate," *40th Fluid Dynamics Conference and Exhibit*, Chicago, IL, June 28–July 1, 2010, AIAA Paper 2010-4998.
- [190] Michael, J. B., Edwards, M. R., Dogariu, A., and Miles, R. B., "Femtosecond Laser Electronic Excitation Tagging for Quantitative Velocity Imaging in Air," *Applied Optics*, Vol. 50, No. 26, 2011, pp. 5158–5162.
- [191] Michael, J. B., Edwards, M. R., Dogariu, A., and Miles, R. B., "Velocimetry by Femtosecond Laser Electronic Excitation Tagging (FLEET) of Air and Nitrogen," *50th AIAA Aerospace Sciences Meeting*, Nashville, TN., January 9–12, 2012, AIAA Paper 2012-1053.

- [192] Edwards, M. R., Dogariu, A., and Miles, R. B., "Simultaneous Temperature and Velocity Measurement in Unseeded Air Flows with FLEET," *51st AIAA Aerospace Sciences Meeting*, Grapevine, TX, January 7–10, 2013, AIAA Paper 2013-0043.
- [193] Barker, P., Bishop, A., and Rubinsztein-Dunlop, H., "Supersonic Velocimetry in a Shock Tube using Laser Enhanced Ionization and Planar Laser induced Fluorescence," *Applied Physics B*, Vol. 64, No. 3, 1997, pp. 369–376.
- [194] Barker, P. F., Thomas, A. M., McIntyre, T. J., and Dunlop-Rubinsztein, H., "Velocimetry and Thermometry of Supersonic Flow Around a Cylindrical Body," *AIAA Journal*, Vol. 36, No. 6, 1998, pp. 1055–1060.
- [195] Littleton, B. N., Bishop, A. I., McIntyre, T. J., Barker, P. F., and Dunlop-Rubinsztein, H., "Flow Tagging Velocimetry in a Superorbital Expansion Tube," *Shock Waves*, Vol. 10, 2000, pp. 225–228.
- [196] Miles, R., Cohen, C., Connors, J., Howard, P., Huang, S., Markovitz, E., and Russell, G., "Velocity Measurements by Vibrational Tagging and Fluorescent Probing Of Oxygen," *Optics Letters*, Vol. 12, No. 11, 1987, pp. 861–863.
- [197] Miles, R. B., Zhou, D., Zhang, B., Lempert, W. R., and She, Z-S., "Fundamental Turbulence Measurements by Relief Flow Tagging," *AIAA Journal*, Vol. 31, No. 3, March, 1993.
- [198] Miles, R. B., Connors, J., Markovitz, E., Howard, P., and Roth, G., "Instantaneous Supersonic Velocity Profiles in an Underexpanded Sonic Air Jet by Oxygen Flow Tagging," *Physics of Fluids A*, Vol. 1, No. 2, 1989, pp. 389–393.
- [199] Miles, R. B., Grinstead, J., Kohl, R. H., and Diskin, G., "The RELIEF Flow Tagging Technique and its Application in Engine Testing Facilities and for Helium-air Mixing Studies," *Measurement Science and Technology*, Vol. 11, No. 9, 2000, pp. 1272–1281.
- [200] Boedeker, L. R., "Velocity measurement by H_2O photolysis and laser-induced fluorescence of OH," *Optics Letters*, 14 (10), pp. 473–475, May 15, 1989.
- [201] Wehrmeyer, J. A., Ribarov, L. A., Oguss, D. A., Batliwala, F., Pitz, R. W., and DeBarber, P. A., "Flow Tagging Velocimetry for Low and High Temperature Flowfields," *37th AIAA Aerospace Sciences Meeting*, Reno, NV, 1999.
- [202] Wehrmeyer, J. A., Ribarov, L. A., Oguss, D. A., and Pitz, R. W., "Flame Flow Tagging Velocimetry with 193-nm H_2O Photodissociation," *Applied Optics*, Vol. 38, No. 33, 1999, pp. 6912–6917.
- [203] Ribarov, L. A., Wehrmeyer, J. A., Hu, S., and Pitz, R. W., "Multiline Hydroxyl Tagging Velocimetry Measurements in Reacting and Nonreacting Experimental Flows," *Experiments in Fluids*, Vol. 37, 2004, pp. 65–74.
- [204] Ribarov, L. A., Hu, S., Wehrmeyer, J. A., and Pitz, R. W., "Hydroxyl Tagging Velocimetry Method Optimization: Signal Intensity and Spectroscopy," *Applied Optics*, Vol. 44, No. 31, 2005, pp. 6616–6626.
- [205] Pitz, R. W., Lahr, M. D., Douglas, Z. W., Wehrmeyer, J. A., Hu, S., Carter, C. D., Hsu, K-Y., Lum, C., and Koochesfahani, M. M., "Hydroxyl Tagging Velocimetry in a Supersonic Flow over a Cavity," *Applied Optics*, Vol. 44, No. 31, 2005, pp. 6692–6700.

- [206] Lahr, M. D., Pitz, R. W., Douglas, Z. W., and Carter, C. D., "Hydroxyl-Tagging-Velocimetry Measurements of a Supersonic Flow over a Cavity," *Journal of Propulsion and Power*, Vol. 26, No. 4, 2010, pp. 790–797.
- [207] ElBaz, A. M., and Pitz, R. W., "N₂O Molecular Tagging Velocimetry," *Applied Physics B* vol. 106, pp. 961–969, 2012.
- [208] Pitz, R. W., Brown, T. M., Nandula, S. P., Skaggs, P. A., DeBarber, P. A., Brown, M. S., and Segall, J., "Unseeded Velocity Measurement by Ozone Tagging Velocimetry," *Optics Letters*, Vol. 21, No. 10, 1996, pp. 755–757.
- [209] Ribarov, L. A., Wehrmeyer, J. A., Batliwala, F., Pitz, R. W., and DeBarber, P. A., "Ozone Tagging Velocimetry Using Narrowband Excimer Lasers," *AIAA Journal*, Vol. 37, No. 6, June 1999.
- [210] Dam, N. J., Klein-Douwel, R. J. H., Sijtsema, N. M., and Jter Meulen, J. J., "Nitric Oxide Flow Tagging in Unseeded Air," *Optics Letters*, Vol. 26, No. 1, 2001, pp. 36–38.
- [211] Sijtsema, N. M., Dam, N. J., Klein-Douwel, R. J. H., and ter Meulen, J. J., "Air Photolysis and Recombination Tracking: A New Molecular Tagging Velocimetry Scheme," *AIAA Journal*, Vol. 40, No. 6, 2002, pp. 1061–1064.
- [212] Van der Lann, W. P. N., Tolboom, R. A. L., Dam, N. J., and ter Meulen, J. J., "Molecular Tagging Velocimetry in the Wake of an Object in Supersonic Flow," *Experiments in Fluids*, Vol. 34, 2003, pp. 531–534.
- [213] Bominaar, J., Pashttrapanska, M., Elenbaas, T., Dam, N., ter Meulen, H., and van de Water, W., "Writing in Turbulent Air," *Physical Review E*, Vol. 77, No. 4, 2008, 046312.
- [214] Orleemann, C., Schulz, C., and Wolfrum, J., "NO-flow Tagging by Photodissociation of NO₂. A New Approach for Measuring Small-scale Flow Structures," *Chemical and Physical Letters*, Vol. 307, 1999, pp. 15–20.
- [215] Shinji, N., Kasahara, M., Tsue, M., and Kono, M., "Velocity Measurements of Reactive and Non-reactive Flows by NO-LIF Method Using NO₂ Photodissociation," *Heat Transfer-Asian Research*, Vol. 34, No. 1, 2005, pp. 40–52.
- [216] Hsu, A. G., Srinivasan, R., Bowersox, R. D. W., and North, S. W., "Molecular Tagging Using vibrationally Excited Nitric Oxide in an Underexpanded Jet Flowfield," *AIAA Journal*, Vol. 47, No. 11, 2009, pp. 2597–2604.
- [217] Jiang, N., Nishihara, M., and Lempert, W. R., "500 kHz NO₂ Molecular Tagging Velocimetry in a Mach 5 Wind Tunnel," *27th AIAA Aerodynamic Measurement Technology and Ground Testing Conference*, Chicago, IL., Jun 28–July 1, 2010, AIAA Paper 2010-4348.
- [218] Sánchez-González, R., Srinivasan, R., Bowersox, R. D. W., and North, S. W., "Simultaneous Velocity and Temperature Measurements in Gaseous Flow Fields Using the VENOM Technique," *Optics Letters*, Vol. 36, No. 2, 2011, pp. 196–198.
- [219] Sánchez-González, R., Srinivasan, R., Bowersox, R. D. W., and North, S. W., "Simultaneous Velocity and Temperature Measurements in Gaseous Flowfields using the vibrationally Excited Nitric Oxide Monitoring Technique: A Comprehensive Study," *Applied Optics*, Vol. 51, No. 9, 2012, pp. 1216–1228.
- [220] Bathel, B. F., Danehy, P. M., Johansen, C. T., Jones, S. B., and Goyne, C. P., "Hypersonic Boundary Layer Measurements with Variable Blowing Rates Using Molecular Tagging Velocimetry," *28th AIAA Aerodynamic Measurement*

- Technology, Ground Testing, and Flight Testing Conference*, New Orleans, LA., June 25–28, 2012, AIAA Paper 2012-2886.
- [221] Bathel, B. F., Johansen, C. T., Jones, S. B., Danehy, P. M., and Goyne, C. P., “Trip-induced Transition Measurements in a Hypersonic Boundary Layer Using Molecular Tagging Velocimetry,” *51st AIAA Aerospace Sciences Meeting*, Grapevine, TX., January 7–10, 2013, AIAA Paper 2013-0042.
 - [222] Boxx, I., Stöhr, M., Carter, C., and Meier, W., “Sustained Multi-kHz Flamefront and 3-Component Velocity-field Measurements for the Study of Turbulent Flames,” *Applied Physics B*, Vol. 95, No. 1, 2009, pp. 23–29.
 - [223] Jiang, N., Webster, M., Lempert, W. R., Miller, J. D., Meyer, T. R., Ivey, C. B., and Danehy, P. M., “MHz-rate Nitric Oxide Planar Laser-induced Fluorescence Imaging in a Mach 10 Hypersonic Wind Tunnel,” *Applied Optics*, Vol. 50, No. 4, February 1, 2011.
 - [224] Jiang, N., Bruzzese, J., Patton, R., Sutton, J., Yentsch, R., Gaitonde, D. V., Lempert, W. R., Miller, K. D., Meyer, T. R., Parker, R., Wadham, T., Holden, M., and Danehy, P. M., “NO PLIF Imaging in the CUBRC 48-inch Shock Tunnel,” *Experiments in Fluids*, Vol. 53, 2012, pp. 1637–1646.
 - [225] Yip, B., Schmitt, R. L., and Long, M. B., “Instantaneous Three-dimensional Concentration Measurements in Turbulent Jets and Flames,” *Optics Letters*, Vol. 13, No. 2, 1988, pp. 96–98.
 - [226] Danehy, P. M., Bathel, B. F., Inman, J. A., Alderfer, D. W., and Jones, S. B., “Stereoscopic Imaging in Hypersonic Boundary Layers using Planar Laser-Induced Fluorescence,” *26th AIAA Aerodynamic Measurement Technology and Ground Testing Conference*, Seattle, WA., June 23–26, 2008, AIAA Paper 2008-4267.
 - [227] Combs, C. S., Clemens, N. T., Danehy, P. M., Bathel, B. F., Parker, R., Wadhams, T., Holden, M., and Kirk, B., “NO PLIF Visualizations of the Orion Capsule in LENS-I,” *51st AIAA Aerospace Sciences Meeting*, Grapevine, TX., January 7–10, 2013, AIAA Paper 2013-0033.
 - [228] Miles, R. B., Lempert, W. R., and Forkey, J. N., “Laser Rayleigh Scattering,” *Measurement Science Technology*, Vol. 12, 2001, p. R33–R51, doi: 10.1088/0957-0233/12/5/201
 - [229] *Springer Handbook of Experimental Fluid Mechanics*, edited by C. Tropea, A. L. Yarin, and J. F. Foss, Vol. 1, ISBN-10: 3540251413 Springer, 1st ed. 2007.
 - [230] Baldwin, G. C., *An Introduction Nonlinear Optics*, Plenum Press, New York, 1969.
 - [231] Thorne, A., Litzén, U., and Johansson, S., *Spectrophysics: Principles and Applications*, Berlin Heidelberg, 1999.
 - [232] Magre, P., and Dibble, R. W., “Finite Chemical Kinetic Effects in a Subsonic Turbulent Hydrogen Flame,” *Combustion and Flame*, Vol. 73, 1988, p. 195.
 - [233] Bergmann, W., Meier, W., Wolff, D., and Stricker, W., “Application of Spontaneous Raman and Rayleigh Scattering and 2D LIF for the characterization of a Turbulent CH₄/H₂/N₂ Jet Diffusion Flame,” *Applied Physics B*, Vol. 66, 1998, pp. 489–502.
 - [234] Nguyen, Q. V., Dibble, R. W., Carter, C. D., Fiechtner, G. J., and Barlow, R. S., “Raman-LIF Measurement of Temperature, Major Species, OH and NO in a Methane-Air Bunsen Flame,” *Combustion and Flame*, Vol. 105, 1996, pp. 499–510.

- [235] Seasholtz, R. G., and Buggele, A. E., "Improvement in Suppression of Pulsed Nd:YAG Laser Light With Iodine Absorption Cells for Filtered Rayleigh Scattering Measurements," NASA TM-113177.
- [236] Elliott, G. S., Samimy, M., and Arnette, S. A., "Details of a Molecular Filter-Based Velocimetry Technique," *32nd Aerospace Sciences Meeting & Exhibit*, Reno, NV, January 10–13, 1994, AIAA Paper -94-0490.
- [237] Elliott, G. S., Samimy, M., and Arnette, S. A., "A Molecular Filter Based Velocimetry Technique for High Speed Flows," *Experiments in Fluids*, Vol. 18, No. 1–2, 1994, pp 107–118.
- [238] Seasholtz, R. G., Buggele, A. E., and Reeder, M. F., "Flow Measurements Based on Rayleigh Scattering and Fabry-Perot Interferometer," *Optics and Lasers in Engineering*, Vol. 27, No. 6, 1997, pp. 543–570.
- [239] Bivolaru, D., Otugen, M. V., Tzes, A., and Papadopoulos, G., "Image Processing for Interferometric Mie and Rayleigh Scattering Velocity Measurements," *AIAA Journal*, Vol. 37, No. 6, June 1999.
- [240] Bivolaru, D., Danehy, P. M., Gaffney, R. L., Jr., and Cutler, A. D., "Direct-View Multi-Point Two-Component Interferometric Rayleigh Scattering Velocimeter," *46th AIAA Aerospace Sciences Meeting and Exhibit*, Reno, Nevada, January 7–10, 2008, AIAA Paper 2008-236
- [241] Mielke-Fagan, A. F., Elam, K. A., and Clem, M. M., "Multiple-Point Mass Flux Measurement System Using Rayleigh Scattering," *47th AIAA Aerospace Sciences Meeting Including The New Horizons Forum and Aerospace Exposition*, Orlando, Florida, January 5–8, 2009, AIAA Paper 2009-528.
- [242] Panda, J., Seasholtz, R. G., and Elam, K. A., "Investigation of Noise Sources in High-Speed Jets via Correlation Measurements," *Journal of Fluid Mechanics*, Vol. 537, 2005, pp. 349–385.
- [243] Mielke, A. F., Elam, K. A., and Sung, C. J., "Multiproperty Measurements at High Sampling Rates Using Rayleigh Scattering," *AIAA Journal*, Vol. 47, No. 4, 2009, pp. 850–862.
- [244] Bivolaru, D., Cutler, A. D., and Danehy, P. M., "Spatially- and Temporally-resolved Multi-parameter Interferometric Rayleigh Scattering," *49th AIAA Aerospace Sciences Meeting including the New Horizons Forum and Aerospace Exposition*, Orlando, Florida, January 4–7, 2011, AIAA Paper 2011-1293.
- [245] Fagan, A. F., Clem, M. M., and Elam, K. A., "Improvement in Rayleigh Scattering Measurement Accuracy," *50th AIAA Aerospace Sciences Meeting including the New Horizons Forum and Aerospace Exposition*, Nashville, TN, January 9–12, 2012, AIAA Paper 2012-1060.
- [246] Kojima, J., and Fischer, D. G., "Multiscalar Analyses of High-Pressure Swirl-Stabilized Combustion via Single-Shot Dual-SBG Raman Spectroscopy," *Combustion Science and Technology*, Vol. 185, No. 12, 2013, pp. 1735–1761.
- [247] Kojima, J., Fischer, D., and Nguyen, Q-V., "Subframe burst gating for Raman spectroscopy in combustion," *Optics Letters*, Vol. 35, No. 9, pp. 1323–1325, May 1, 2010.
- [248] Kojima, J., and Nguyen, Q-V., "Single-shot Rotational Raman Thermometry for Turbulent Flames using a Low-resolution Bandwidth Technique," *Measurement Science and Technology*, Vol. 19, 2008. doi: 10.1088/0957-0233/19/1/015406

- [249] Schoenung, S. M., and Mitchell, R. E., "Comparison of Raman and Thermocouple Temperature Measurements in Flames," *Combustion and Flame*, Vol. 35, 1979, pp. 207–211.
- [250] Cutler, A. D., Magnotti, G., Cantu, L. M. L., Gallo, E. C. A., Danehy, P. M., Baurle, R., Rockwell, R., Goyne, C., and McDaniel, J., "Measurement of Vibrational Nonequilibrium in a Supersonic Freestream using Dual-Pump CARS," *28th Aerodynamic Measurement Technology, Ground Testing, and Flight Testing Conference*, New Orleans, Louisiana, June 25–28, 2012, AIAA Paper 2012-3199.
- [251] Wehrmeyer, J. A., Yeralan, S., and Tecu, K. S., "Linewise Raman-Stokes/Anti-Stokes Temperature Measurements in Flames Using an Unintensified Charge-coupled Device," *Applied Physics B*, Vol. 62, 1996, pp. 21–27.
- [252] Rabenstein, F., and Leipertz, A., "Two-Dimensional Temperature Determination in the Exhaust Region of a Laminar Flat-Flame Burner with Linear Raman Scattering," *Applied Optics*, Vol. 36, 1997, pp. 6989–6996.
- [253] Kojima, J., and Nguyen, Q.-V., "Strategy for Multiscalar Raman Diagnostics in High-Pressure Hydrogen Flames," In: *New Developments in Combustion Research*, edited by Carey W. J., ISBN: 1-59454-826-9, NOVA Science Publishers, New York, 2006, pp. 227–256.
- [254] Sharma, S. P., Ruffin, S. M., Gillespie, W. D., and Meyer, S. A., "Vibrational Relaxation Measurements in an Expanding Flow Using Spontaneous Raman Scattering," *Journal of Thermophysics and Heat Transfer*, Vol. 7, No. 4, Oct.–Dec. 1993.
- [255] Dyer, T. M., "Rayleigh scattering measurements of time-resolved concentration in a turbulent propane jet," *AIAA Journal*, vol. 17, Aug. 1979, pp. 912–914.
- [256] Boyd, R. W., *Nonlinear Optics*, 3rd ed., Academic International Press, New York/London/Orlando, FL, 2008.
- [257] Lucht, R. P., "Three-laser Coherent Anti-Stokes Raman Scattering Measurements of two Species," *Optics Letters*, Vol. 12, No. 2, 1987, pp. 78–80.
- [258] O'Byrne, S., Danehy, P. M., Tedder, S. A., and Cutler, A. D., "Dual-Pump Coherent Anti-Stokes Raman Scattering Measurements in a Supersonic Combustor," *AIAA Journal*, Vol. 45, No. 4, pp. 922–933, April 2007.
- [259] Palmer, R. E., The CARSFT Computer Code for Calculating Coherent Anti-Stokes Raman Spectra: User and Programmer Information, Sandia Rpt. SAND89-8206, Feb. 1989.
- [260] Cutler, A. D., and Magnotti, G., "CARS Spectral Fitting with Multiple Resonant Species Using Sparse Libraries," *Journal of Raman Spectroscopy*, Vol. 42, No. 11, 2011, pp. 1949–1957.
- [261] Bultitude, K. M., Danehy, P. M., Fraval, E., Fox, J. S., and Houwing, A. F. P., "Broadband Coherent Anti-Stokes Raman spectroscopy (BB-CARS) in Flames and Hypersonic flows," *2nd Australian Conference on Laser Diagnostics in Fluid Mechanics and Combustion*, Monash University, Melbourne Australia, 1999.
- [262] Kulatilaka, W. D., Chai, N., Naik, S. V., Laurendeau, N. M., Lucht, R. P., Kuehner, J. P., Roy, S., and Gord, J. R., "Measurement of Nitric Oxide Concentrations in Flames by Using Electronic-resonance-enhanced Coherent Anti-Stokes Raman Scattering," *Optics Letters*, Vol. 31, No. 22, 2006, pp. 3357–3359, <http://dx.doi.org/10.1364/OL.31.003357>.

- [263] Roy, S., Gord, J. R., and Patnaik, A. K., "Recent Advances in Coherent Anti-Stokes Raman Scattering Spectroscopy: Fundamental Developments and Applications in Reacting Flows," *Progress in Energy and Combustion Science*, Vol. 36, No. 2, 2010, pp. 280–306, ISSN 0360-1285, 10.1016/j.pecs.2009.11.001, April 2010.
- [264] Lucht, R. P., Kinnius, P. J., Roy, S., and Gord, J. R., "Theory of Femtosecond Coherent Anti-Stokes Raman Scattering Spectroscopy of Gas-phase Transitions," *Journal of Chemical Physics*, Vol. 127, 2007, p. 044316, <http://dx.doi.org/10.1063/1.2751184>.
- [265] Lucht, R. P., Roy, S., Meyer, T. R., and Gord, J. R., "Femtosecond Coherent Anti-Stokes Raman Scattering Measurement of Gas Temperatures from Frequency-spread Dephasing of the Raman Coherence," *Applied Physics Letters*, Vol. 89, 251112, <http://dx.doi.org/10.1063/1.2410237>, 2006.
- [266] Meyer, T. R., Roy, S., and Gord, J. R., "Improving Signal-to-Interference Ratio in Rich Hydrocarbon-Air Flames Using Picosecond Coherent Anti-Stokes Raman Scattering," *Applied Spectroscopy*, Vol. 61, No. 11, 2007, pp. 1135–1140.
- [267] Hsu, P. S., Patnaik, A. K., Gord, J. R., Meyer, T. R., Kulatilaka, W. D., and Roy, S., "Investigation of Optical Fibers for Coherent Anti-Stokes Raman Scattering (CARS) Spectroscopy in Reacting Flows," *Experiments in Fluids*, Vol. 49, No. 4, 2010, pp. 969–984.
- [268] Woodmansee, M. A., Dutton, J. C., and Lucht, R. P., "Experimental Measurements of Pressure, Temperature, and Density Measurements in an Underexpanded Sonic Jet Flowfield," presented at the *30th AIAA Fluid Dynamics Conference*, Norfolk, VA, June 28–July 1, 1999, AIAA Paper 99-3600.
- [269] Zheng, J., Snow, J. B., Murphy, D. V., Leipertz, A., Chang, R. K., and Farrow, R. L., "Experimental Comparison of Broadband Rotational Coherent anti-Stokes Raman Scattering (CARS) and Broadband Vibrational CARS in a Flame," *Optics Letters*, Vol. 9, No. 8, pp. 341–343, August 1984.
- [270] Bohlin, A., Patterson, B. D., and Kliewer, C. J., "Simplified Two-beam Rotational CARS Signal Generation Demonstrated in 1D," *Journal of Chemical Physics*, Vol. 138, 2013, p. 081102.
- [271] Bohlin, A., and Kliewer, C. J., "Two-dimensional Gas-phase Coherent Anti-Stokes Raman Spectroscopy (2D-CARS): Simultaneous Planar Imaging and Multiplex Spectroscopy in a Single Laser Shot," *The Journal of Chemical Physics*, Vol. 138, 2013, p. 221101.
- [272] Cutler, A. D., Magnotti, G., Cantu, L. M. L., Gallo, E.C. A., Danehy, P. M., Rockwell, R. D., Goyne, C. P., and McDaniel, J. C., "Dual-Pump CARS Measurements in the University of Virginia's Dual-Mode Scramjet: Configuration 'C,'" *51st Aerospace Sciences Meeting*, Grapevine, TX, 7–10 Jan 2013, AIAA Paper 2013-0335.
- [273] Magnotti, G., Cutler, A. D., and Danehy, P. M., "Development of a Dual-Pump CARS System for Measurements in a Supersonic Combusting Free Jet." Presented at the *50th AIAA Aerospace Sciences Meeting*, Nashville TN., January 9–12, 2012, AIAA Paper 2012-1193.
- [274] Cutler, A. D., Magnotti, G., Cantu, L. M. L., Gallo, E. C. A., Danehy, P. M., Baurle, R., Rockwell, R. D., Goyne, C. P., and McDaniel, J. C., "Measurement of Vibrational Nonequilibrium in a Supersonic Freestream using Dual-Pump CARS,"

- 28th AIAA Aerodynamic Measurement Technology, Ground Testing, and Flight Testing Conference, New Orleans, June 25–28, 2012, AIAA Paper 2012-3199.
- [275] Vincenti, W. G., and Kruger, C. H., *Introduction to Gas Dynamics*, Robert Krieger Pub. Co., New York, 1977.
- [276] Center, R. E., and Newton, J. F., "Vibrational Relaxation of N₂ by H₂O," *Journal of Chemical Physics*, Vol. 68, No. 8, April 1978.
- [277] Montello, A., Yin, Z., Burnette, D., Adamovich, I. V., and Lempert, W. R., "Picosecond CARS Measurements of Nitrogen Vibrational Loading and Rotational/Translational Temperature in Nonequilibrium Discharges," *Journal of Physics D: Applied Physics*, Vol. 46, No. 46, 2013, p. 464002. doi: 10.1088/0022-3727/46/46/464002
- [278] Hornung, H. G., "Nonequilibrium Dissociating Nitrogen Flow over Spheres and Circular Cylinders," *Journal of Fluid Mechanics*, Vol. 53, No. 01, 1972, pp. 149–176.
- [279] McIntyre, T. J., Wegener, M. J., Bishop, A. I., and Rubinsztein-Dunlop, H., "Simultaneous Two-wavelength Holographic Interferometry in a Superorbital Expansion Tube Facility," *Applied Optics*, Vol. 36, No. 31, 1997, pp. 8128–8134.
- [280] Meier, G. E. A., "Hintergrund Schlierenmessverfahren," *Deutsche Patentanmeldung DE*, Vol. 199, No. 42, 1999, p. 856.
- [281] Richard, H., and Raffel, M., "Principle and applications of the background oriented schlieren (BOS) method," *Measurement Science and Technology*, Vol. 12, No. 9, 2001, pp. 1576–1585.
- [282] Hargather, M. J., and Settles, G. S., "Natural-background-oriented Schlieren Imaging," *Experiments in Fluids*, Vol. 48, No. 1, 2010, pp. 59–68.
- [283] Mizukaki, T., Tsukada, H., Wakabayashi, K., Matsumura, T., and Nakayama, Y., In "Quantitative Visualization of Open-air Explosions by Using Background-oriented Schlieren with Natural Background," *28th International Symposium on Shock Waves*, edited by K. P. Kontis, Vol. 2, 2012, pp. 465–470.
- [284] Goldhahn, E., and Seume, J., "The Background Oriented Schlieren Technique: Sensitivity, Accuracy, Resolution and Application to a Three-dimensional Density Field," *Experiments in Fluids*, Vol. 43, No. 2–3, 2007, pp. 241–249.
- [285] Hargather, M. J., and Settles, G. S., "A Comparison of Three Quantitative Schlieren Techniques," *Optics and Lasers in Engineering*, Vol. 50, No. 1, 2012, pp. 8–17.
- [286] Venkatakrishnan, L., and Meier, G. E. A., "Density Measurements Using the Background Oriented Schlieren Technique," *Experiments in Fluids*, Vol. 37, No. 2, 2004, pp. 237–247.
- [287] Mohamed, A. K., Bonnet, J., Larigalde, S., Pot, T., Soutadé, J., and Diop, B., "Electron Beam Fluorescence in Hypersonic Facilities," *Aerospace Lab, the ONERA Journal*, Vol. 1, 2009.
- [288] Smith, J. A., and Driscoll, J. F., "The Electron-beam Fluorescence Technique for Measurements in Hypersonic Turbulent Flows," *Journal of Fluid Mechanics*, Vol. 72, 1975, pp. 695–719.
- [289] Cattolica, R. J., Schmitt, R. L., and Palmer, R. E., "Feasibility of Non-intrusive Optical Diagnostic Measurements in Hypersonic Boundary Layers for Flight Experiments," In *AIAA, Aerospace Sciences Meeting*, Vol. 1. 1990.

- [290] Danehy, P. M., Friedman-Hill, E. J., Lucht, R. P., and Farrow, R. L., "The Effects of Collisional Quenching on Degenerate Four-wave Mixing," *Applied Physics B*, Vol. B57, 1993, pp. 243–248.
- [291] Lloyd, G. M., Hughes, I. G., Bratfalean, R., and Ewart, P., "Broadband Degenerate Four-wave Mixing of OH for Flame Thermometry," *Applied Physics B*, Vol. 67, 1998, pp. 107–113.
- [292] Cummings, E. B., "Laser-induced Thermal Acoustics: Simple Accurate Gas Measurements," *Optics Letters*, Vol. 19, 1994, pp. 1361–1363.
- [293] Hart, R. C., Balla, R. J., and Herring, G. C., "Simultaneous Velocimetry and Thermometry of Air by Use of Nonresonant Heterodyned Laser-induced Thermal Acoustics," *Applied Optics*, Vol. 40, No. 6, 2001, pp. 965–968.
- [294] Hart, R. C., Herring, G. C., and Balla, R. J., "Pressure Measurement in Supersonic Air Flow by Differential Absorptive Laser-Induced Thermal Acoustics," *Optics Letters*, Vol. 32, No. 12, 2007, pp. 1689–1691.
- [295] Hart, R. C., Herring, G. C., and Balla, R. J., "Common-Path Heterodyne Laser-Induced Thermal Acoustics for Seedless Laser Velocimetry," *Optics Letters*, Vol. 27, No. 9, 2002, pp. 710–712.

High-Enthalpy Facilities and Plasma Wind Tunnels for Aerothermodynamics Ground Testing

Olivier Chazot* and Francesco Panerai†

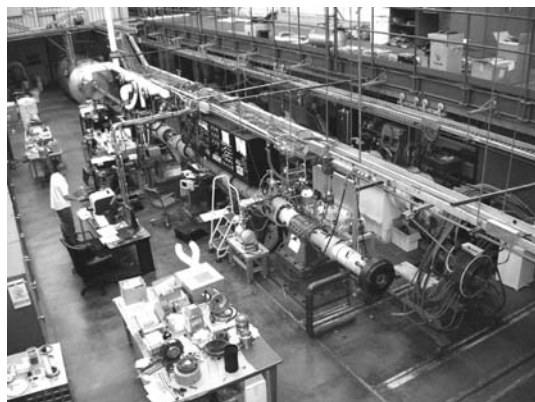
Von Karman Institute for Fluid Dynamics, Rhode St-Genèse, Belgium

Electric Arc Shock Tube (EAST)	472
F4 Hypersonic Arc-Jet Wind Tunnel	474
High Enthalpy Shock Tunnel Göttingen (HEG)	476
Hypervelocity Free Flight Aerodynamic Facility (HFFGAF)	478
High Enthalpy Shock Tunnel (HIEST)	480
JF-10 Oxygen-Hydrogen Detonation-Driven High-Enthalpy Shock Wind Tunnel.....	482
Large Energy National Shock Tunnel (LENS) XX.....	484
T5 Hypervelocity Shock Tunnel Facility	486
TH2 Hypersonic Shock Tunnel.....	488
X2 Super Orbital Expansion Tube	490
X3 Super Orbital Expansion Tube	492
NASA Ames Aerodynamic Heating Facility (AHF)	494
NASA Ames Interaction Heating Facility (IHF)	496
NASA Ames Panel Test Facility (PTF)	498
NASA Turbulent Flow Duct (TFD).....	500
NASA Langley Hypersonic Materials Environmental Test System (HYMETS)	502
DLR ARC-Heated Wind Tunnel 2 (L2K)	504
DLR ARC-Heated Wind Tunnel 3 (L3K)	506
CIRA Plasma Wind Tunnel SCIROCCO	508
CIRA Plasma Wind Tunnel Ghibli	510
IRS Plasma Wind Tunnels (PWK1, 2, 4)	512
VKI Inductively Coupled Plasma Wind Tunnel (Plasmatron)	514
IRS Plasma Wind Tunnel (PWK 3).....	516
IPM Induction Plasma Generator (IPG-3 and IPG-4).....	518
UVM 30 kW Inductively Coupled Plasma Torch Facility	520

*Professor, Head of Aeronautics/Aerospace Department at Von Karman Institute

†Post-Doctoral fellow

ELECTRIC ARC SHOCK TUBE (EAST)



Photograph of the EAST laboratory

Mission: Spatially and temporally resolved measurements of absolute spectral radiance behind a traveling shock wave. Conditions replicate shock radiation phenomenon for entry into a variety of planetary atmospheres.

Location: THERMOPHYSICS FACILITIES BRANCH, NASA Ames Research Center, Moffett Field, California

Type of tunnel: Shock tube

Driven tube diameter	$\varnothing 101.6 \text{ mm}$	Running time	1–100 μs
Mach number	10–50	Velocity	Up to 46 km/s
Arc discharge driver temperature	$>10,000 \text{ K}$	Driver gases	H ₂ , He, Ar
Reservoir enthalpy	930 MJ/m ³	Driven gases	Air, CO ₂ , N ₂ , H ₂ , CH ₄ , He, Ar

Instrumentation

Four imaging spectrometers with 2-D CCD and ICCD arrays, spanning from Vacuum Ultraviolet through Mid-IR. PMTs, Pressure Transducers, Ionization Gauges.

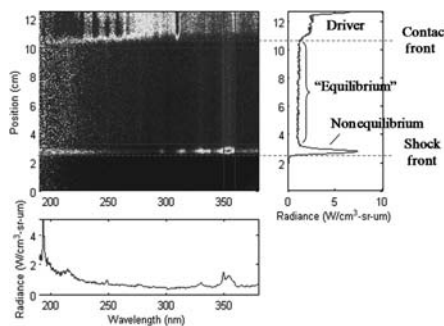
References

Cruden, B. A., Martinez, R. et al., "Simultaneous Vacuum Ultraviolet through Near IR Absolute Radiation Measurement with Spatiotemporal Resolution in an Electric Arc Shock Tube," *41ST AIAA Thermophysics Conference*, AIAA 2009-4240.

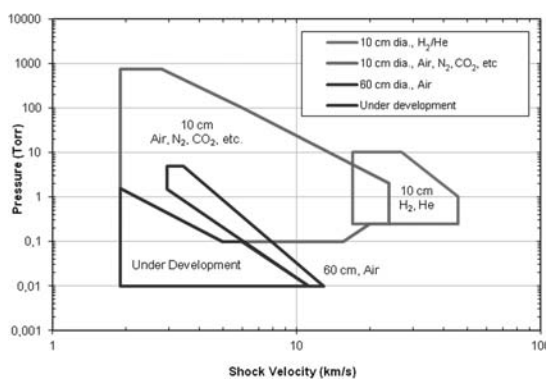
<http://www.nasa.gov/centers/ames/thermophysics-facilities>

Grinstead, J. H., Wilder, M. C., Reda, D. C., Cornelison, C. J., Cruden B. A., and Bogdanoff, D. W., "Shock Tube and Ballistic Range Facilities at NASA Ames Research Center," AVT-186 RTO AVT/VKI Lecture Series, von Karman Institute for Fluid Dynamics, Rhode St. Genèse, Belgium, 2010, Paper 4.

Grinstead, J. H., Wilder, M. C., Reda, D. C., Cruden, B. A., and Bogdanoff, D. W., "Advanced spectroscopic and Thermal Imaging instrumentation for Shock Tube and Ballistic Range Facilities," AVT-186 RTO AVT/VKI Lecture Series, von Karman Institute for Fluid Dynamics, Rhode St. Genèse, Belgium, 2010, Paper 6.



**Example of a spectrograph image
Earth lunar return: 10.0 km/s, 0.2 torr**



EAST operating envelopes

Information Contacts

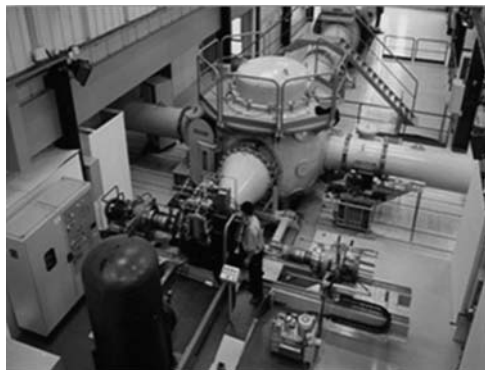
Dr. Brett A. Cruden (PI)

Brett.A.Cruden@nasa.gov

Mark McGlaughlin (Facility Manager)

Mark.S.McGlaughlin@nasa.gov

F4 HYPERSONIC ARC-JET WIND TUNNEL



Mission: Simulation of hypervelocity flows involved with the aerobreaking of space vehicles during their reentry into planetary atmosphere; combustion tests of scramjet configurations.

Location: ONERA, Fauga-Mauzac, France

Type of tunnel: Hot-shot

Nozzle exit diameter	\varnothing 43, 67 cm	Running time	400 ms
Mach number	8–15	Reservoir pressure	<100 MPa
Temperature range	>7500 K	Velocity	2.5 to 5 km/s
Reservoir enthalpy	<18 MJ/kg	Working gases	Air, N ₂ , CO ₂ , Argon

Instrumentation

- Forces: 3 or 6 component balance
- Temperature: thermocouples, IR, thin film
- Visualization: Schlieren, OH* Chemiluminescence
- Optical system: DLAS

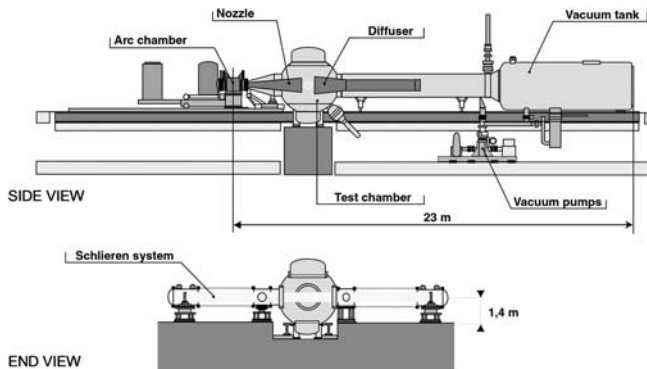
References

Masson, A., Sagnier, P., and Mohammed, A. K., "The ONERA F4 High-Enthalpy Wind Tunnel," *Advanced Hypersonics Test Facilities, Progress in Astronautics and Aeronautics*, Vol. 198, 2002.

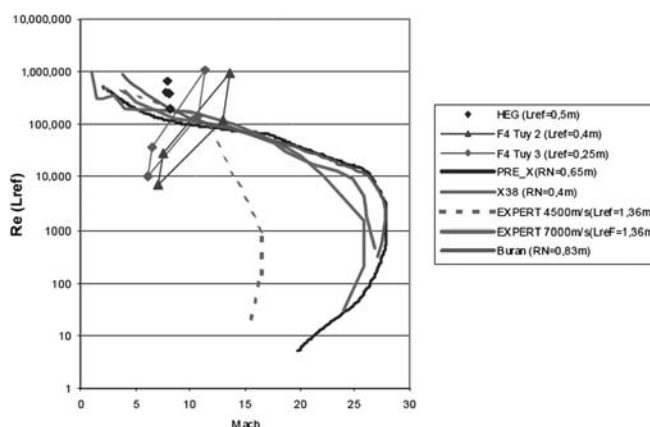
Sagnier, Ph., and Verant, J. L., "Flow characterization in the ONERA F4 High Enthalpy Wind Tunnel," *AIAA Journal*, Vol. 36, No. 4, 1998.

Viguier, P. et al., "Development of F4 Hot-Shot Wind Tunnel for High Enthalpy Scramjet Tests," AIAA 2012-5970, 18th AIAA Int. Spaces Planes and Hypersonic Systems and Technologies Conference, Tours, France, 2012.

Wolf, S., and Viguier, P., "F4 Hypersonic Arc-Jet Wind Tunnel Evolves to Advance Re-Entry Design," STAI 107th Semi-annual Meeting, Cleveland, OH, 2007.



Sketch of the F4 hot-shot wind tunnel



Standard envelopes of F4 and HEG reference conditions with trajectories of lifting and ballistic entry vehicles

Information Contacts

Paul Viguier
 (Manager of Research Wind Tunnel Unit)
 Tel: 33(0)5 61 56 63 44, Fax.: 33(0)5 61 56 63 63
 paul.viguier@onera.fr

HIGH ENTHALPY SHOCK TUNNEL GÖTTINGEN (HEG)



Mission: The HEG is one of the major European hypersonic test facilities. It was commissioned for use in 1991 and has been utilized extensively since then in a large number of national and international space and hypersonic flight projects. The HEG was designed for the investigation of high temperature effects during entry or reentry of space vehicles. The operating range was continuously extended and now also includes conditions to simulate the flow past hypersonic configurations from low altitude Mach 6 up to Mach 10 in approximately 33 km altitude. Further, combustion of hydrogen in complete supersonic combustion ramjet configurations is studied.

Location: German Aerospace Center (DLR), Göttingen, Germany

Type of tunnel: Free piston driven shock tunnel

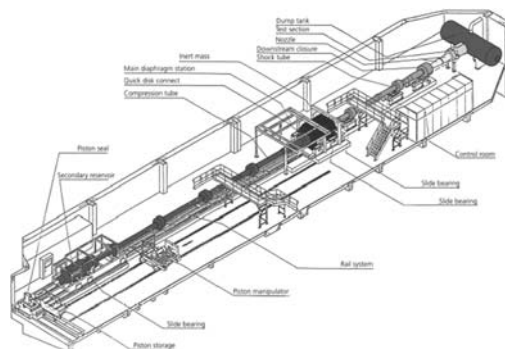
Nozzle exit diameter	Ø 430,590,880 mm	Test time	1–8 ms
Mach number	6–10	Reservoir pressure	8–180 MPa
Reservoir temperature	1600 to 9900 K	Velocity	1.7–6.2 km/s
Reservoir enthalpy	1.5–23 MJ/kg	Test gases	Air, N ₂ , CO ₂ , ...

Instrumentation

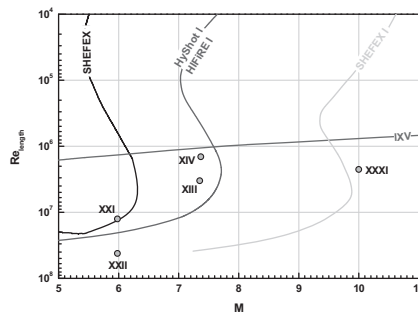
- Forces: Free Flight Techniques by optical tracking of motion and measurement of acceleration, stress wave force balance
- Heat Flux: thermocouples, thin film, temperature sensitive paint
- Pressure: Pitot, static, surface
- Visualization: time resolved Schlieren/shadowgraph, holographic interferometry
- Gas State: OH* chemiluminescence, diode laser absorption techniques, spectroscopy

References

- Hannemann, K., "High Enthalpy Flows in the HEG Shock Tunnel: Experiment and Numerical Rebuilding," AIAA 2003, 41st AIAA Aerospace Sciences Meeting and Exhibit, Reno, Nevada, 2003.
- Hannemann, K., and Martinez Schramm, J., "High Enthalpy, High Pressure Short Duration Testing of Hypersonic Flows," *Springer Handbook of Experimental Fluid Mechanics*, edited by C. Tropea, J. Foss and A. Yarin, Springer Berlin, Heidelberg, 2007, pp.1081–1125.
- Hannemann, K., Martinez Schramm, J., and Karl, S., "Recent extensions to the High Enthalpy Shock Tunnel Göttingen (HEG)," *Proceedings of the 2nd International ARA Days "Ten Years after ARD,"* Arcachon, France, 2008.



Schematic of HEG



HEG operating conditions in terms of
Mach and Reynolds number

Information Contact

Prof. Dr. Klaus Hannemann
Tel: +49 551 709-2477
klaus.hannemann@dlr.de

HYPERVELOCITY FREE FLIGHT AERODYNAMIC FACILITY (HFFGAF)



Mission: Free-flight experiments to study aerodynamic and aerothermodynamic phenomenology of atmospheric entry.

Location: Thermophysics Facilities Branch, NASA Ames Research Center, Moffett Field, California

Type of facility: Aeroballistics range

Range length	23 m	Launch tube diameter	\varnothing 7–38 mm
Velocity	0.2–8.5 km/s	Launch mass	0.2–400 g
Total enthalpy	Up to 36 MJ/kg	Test gases	Air, CO ₂

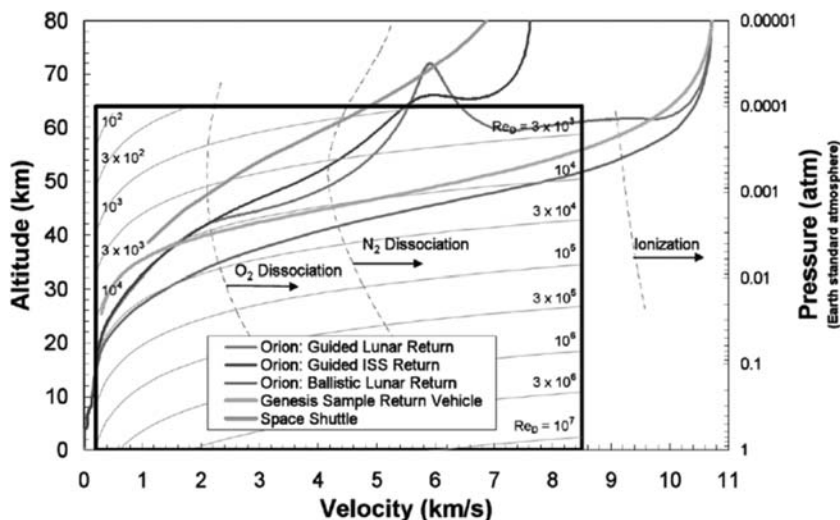
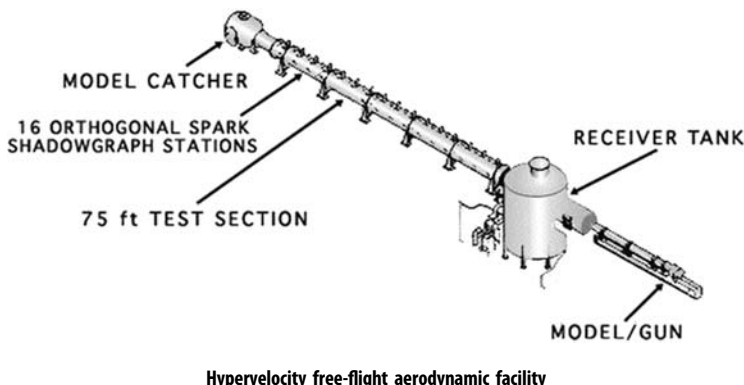
Instrumentation

- Thermal imaging: Time-gated visible, near infrared and mid-wave infrared cameras
- Spectroscopy: Time-gated imaging spectrographs
- Aerodynamics: Shadowgraphy

References

Grinstead, J. H., Wilder, M. C., and Reda, D. C., Cruden, B. A., and Bogdanoff, D. W., "Advanced Spectroscopic and Thermal Imaging Instrumentation for Shock Tube and Ballistic Range Facilities," *AVT-186 RTO AVT/VKI Lecture Series*, von Karman Institute for Fluid Dynamics, Rhode St. Genèse, Belgium, 2010, Paper 6.

Grinstead, J. H., Wilder, M. C., Reda, D. C., Cornelison, C. J., Cruden, B. A., and Bogdanoff, D. W., "Shock Tube and Ballistic Range Facilities at NASA Ames Research Center," *AVT-186 RTO AVT/VKI Lecture Series*, von Karman Institute for Fluid Dynamics, Rhode St. Genèse, Belgium, 2010, Paper 4.



Testing envelope for HFFGAF overlaid with selected Earth entry trajectories

Information Contacts

Michael. C. Wilder (PI)

Michael.C.Wilder@nasa.gov

Ernest Fretter (Business Manager)

Ernest.F.Fretter@nasa.gov

HIGH ENTHALPY SHOCK TUNNEL (HIEST)



Mission: Simulate the aerothermodynamic properties of the flow around re-entry vehicles and the supersonic combustion properties in the space engines.

Location: Japan aerospace Exploration Agency (JAXA), Kakuda Space Center, Miyagi, Japan

Type of tunnel: Shock tunnel

Nozzle exit diameter	Ø 880, 1200 mm	Running time	2 to 10 ms
Nozzle flow Mach number	6 to 10	Max stagnation pressure	150 MPa
Max stagnation temperature	10,000 K	Velocity	4 to 7 km/s
Max stagnation enthalpy	25 MJ/kg	Working gases	Air, N ₂

Instrumentation

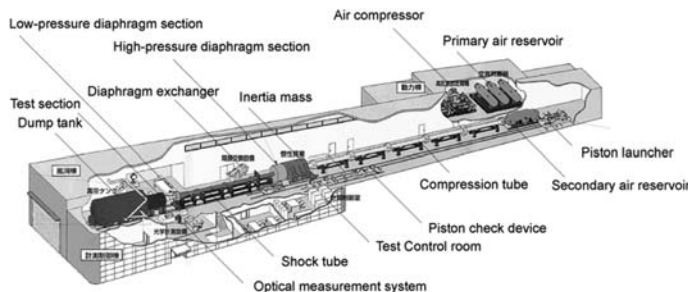
- 250 channels;
- Optical measurement system: schlieren device and double exposure hologram interferometer

References

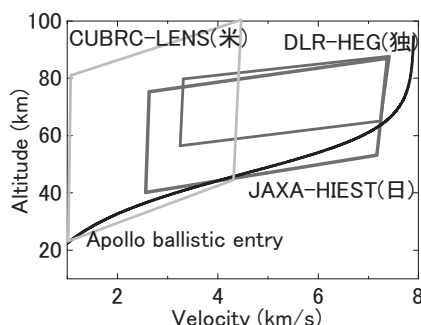
Itoh, K., Ueda, S., Takahashi, M., Tanno, H., Komuro, T., and Sato, K., "Characteristics of the High Enthalpy Shock Tunnel HIEST."

Itoh, K., Ueda, S., Takahashi, M., Komuro, T., Sato, K., Miyajima, H., and Koga, K., "Design and Construction of HIEST(High Enthalpy Shock Tunnel)," *Proceedings of International Conference on Fluid Engineering, ICFE'97*, 1997.

http://www.mhi.co.jp/en/products/expand/shock_wind_tunnel_supply_result_01.html
<http://www.rocket.jaxa.jp/kspc/english/tf/hiest.html>



Overview of the facility



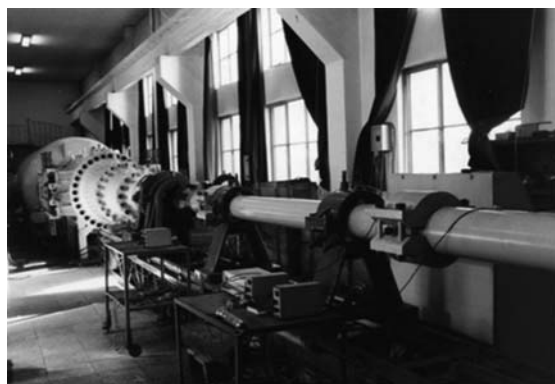
Operating envelope of Hiest compared to that of LENS XX and HEG

Information Contact

Katsuhiro Ito

Tel: (81) 224 68 3111; Fax: (81) 224 68 2860
ito.katsuhiro@jaxa.jp

JF-10 OXYGEN-HYDROGEN DETONATION-DRIVEN HIGH-ENTHALPY SHOCK WIND TUNNEL



Mission: Experimental research on real gas effects of high temperature flows

Location: State Key Laboratory of High-Temperature Gas Dynamics (LHD), Beijing, China

Type of tunnel: Detonation driven shock tunnel

Nozzle exit diameter	\varnothing 500/800 mm	Running time	3–6 ms
Mach number	10 to 20	Stagnation pressure	25 MPa
Temperature range	4500–9000 K	Velocity	3.5–6.0 km/s
Stagnation enthalpy	15–25 MJ/kg	Test gases	Air

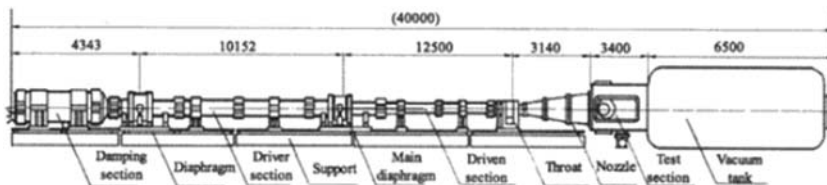
Instrumentation

- Pressure transducers
- Heat flux sensors
- Schlieren system

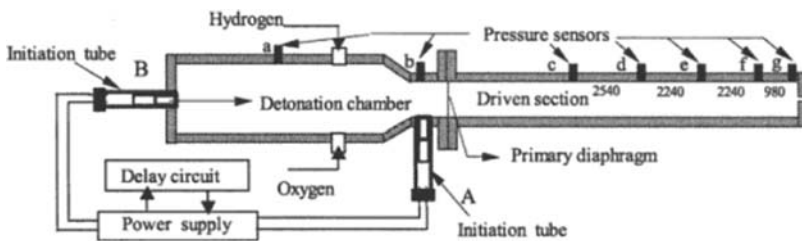
References

Jiang, J., Zhao, W., Wang, C., and Takayama, K., "Forward-running Detonation Drivers for High-enthalpy Shock Tunnels," *AIAA J.*, Vol. 40, No. 10, 2002, pp. 2009–2016.

Zhao, W., Jiang, Z., Saito, T., Lin, J. M., Yu, H. R., and Takayama, K., "Performance of a Detonation Driven Shock Tunnel," *Shock Wave*, Vol. 14, No. 1/2, 2005, pp. 53–59.



Sketch of the JF-10 detonation shock tunnel



Schematic of the initiation tube and transducers arrangement in downstream mode

Information Contact

Professor Jiang Zonglin (Director)

Tel: (86) 10 82543995

Fax: (86) 10 82543996

zjjiang@imech.ac.cn

LARGE ENERGY NATIONAL SHOCK TUNNEL (LENS) XX



Mission: Generate clean hypervelocity flows to evaluate nonequilibrium and real gas effects in the shock and to study shock layer radiation and the properties of plasmas surrounding hypersonic vehicles as they enter planetary atmosphere.

Location: CUBRC, Inc., Buffalo, New York, USA

Type of tunnel: Expansion tunnel

Exit diameter	Ø 610 mm	Running time	Up to 4 ms
Mach number	8 to 25	Velocity	2.4 to 12.2 km/s
Total enthalpy	10–100 MJ/kg	Driver gas	Hydrogen

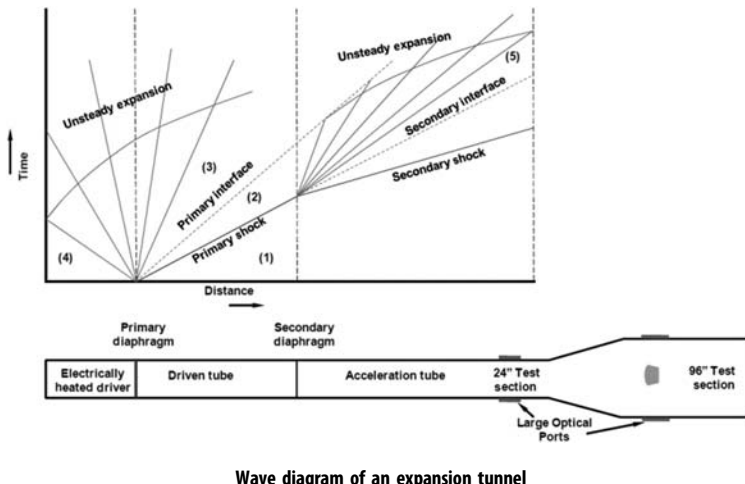
Instrumentation

- Flowfield measurements:
 - intrusive: hot wires, hot films, thin-film, pitot pressure
 - nonintrusive: Laser absorption differential velocimetry, spatial laser differential interferometry
- Surface measurements:
 - Thin-film
 - Pressure sensors

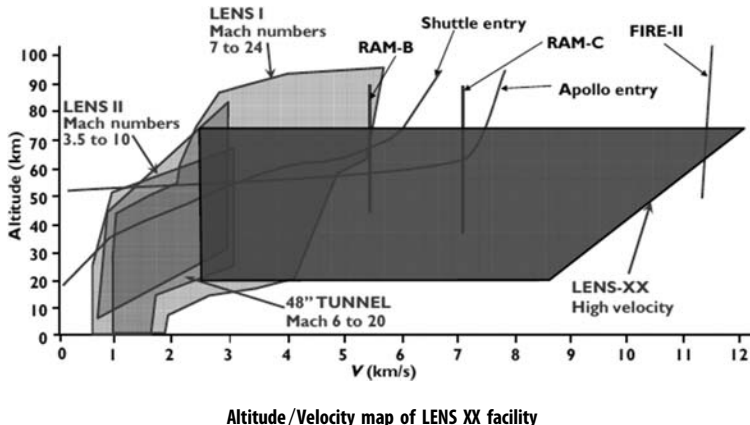
References

Dufrene, A., MacLean, M., Parker, R., Wadhams, T., and Holden, M., "Characterization of the New LENS Expansion Tunnel Facility," *48th AIAA Aerospace Sciences Meeting & Exhibit*, Orlando, FL, 4–7 January 2010, AIAA Paper 2010-1564.

MacLean, M., Dufrene, A., Wadhams, T., and Holden, M., "Numerical and Experimental Characterization of High Enthalpy Flow in an Expansion Tunnel Facility," *48th AIAA Aerospace Sciences Meeting & Exhibit*, Orlando, FL, 4–7 January 2010, AIAA Paper 2010-1562.



Wave diagram of an expansion tunnel



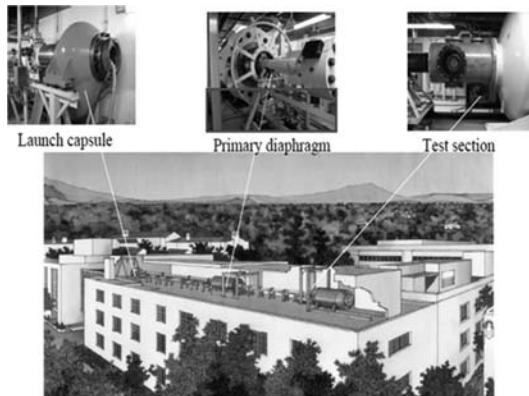
Altitude/Velocity map of LENS XX facility

Information Contacts

Matthew MacLean, Ph.D.
 maclean@cubrc.org

Michael S. Holden; CUBRC, 4455 Genesee Street,
 Buffalo, NY 14225, USA
 holden@cubrc.org

T5 HYPERVELOCITY SHOCK TUNNEL FACILITY



Mission: Simulate the chemical nonequilibrium effects encountered in the aerothermodynamics of transport to and from space through planetary atmosphere.

Location: California Institute of Technology, Pasadena, California

Type of tunnel: Free piston shock tunnel

Nozzle exit diameter	\varnothing 300 mm	Running time	1–2 ms
Mach number	5	Stagnation pressure	15 to 100 MPa
Reservoir temperature	10,000 K	Velocity	2–6 km/s
Reservoir enthalpy	4 to 27 MJ/kg	Test gases	Air, N ₂ , CO ₂ , H ₂ , Ar, mixtures

Instrumentation

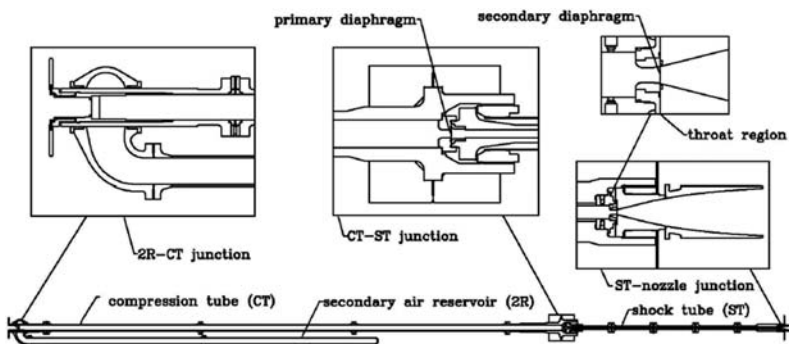
- Data acquisition system: 48 channels
- Temperature: coaxial thermocouples
- Shock tube equipment: accelerometer, LVDT, pressure transducers
- Visualisation: Schlieren, shadowgraphs, interferograms, holographic interferometry

References

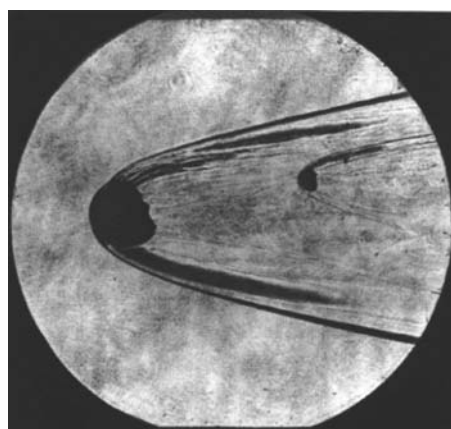
Adams, P. H., "Enthalpy Effects on Hypervelocity Boundary Layers," Caltech PhD thesis, California Institute of Technology, 1997.

Hornung, H., "Performance Data of the New Free-piston Shock Tunnel at GALCIT," 1992.

Laurence, S. J., "Proximal Bodies in Hypersonic Flow," Caltech PhD thesis, California Institute of Technology, 2006.



Schematic of the T5 hypersonic shock tunnel



Shadowgraph of a broken spherical projectile
in the light gas gun modification

Information Contacts

Joseph E. Shepherd

Tel: (626) 395-3283; Fax: (626) 449-2677;

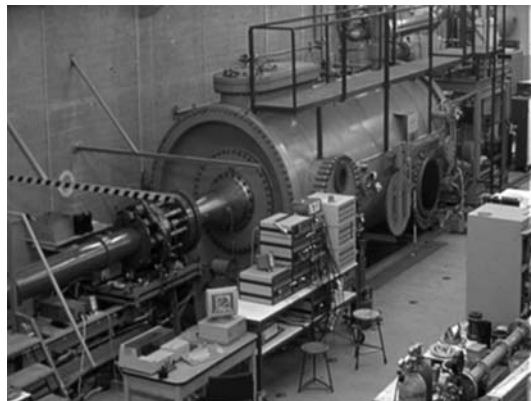
jeshep@caltech.edu

Hans G. Hornung

Tel: (626) 395-4551

hans@caltech.edu

TH2 HYPERSONIC SHOCK TUNNEL



Name: Hypersonic Shock Tunnel TH2

Mission: Study the flow field around typical reentry bodies or hypersonic space planes

Location: RWTH, Aachen, Germany

Type of tunnel: Shock tunnel

Nozzle exit diameter	Ø 586 mm	Running time	2–6 ms
Mach number	6–12	Reservoir pressure	30–800 bar
Temperature range	1200–7400 K	Velocity	1.5–4.8 km/s
Reservoir enthalpy	1.3–14 MJ/kg	Working gases	Air, CO ₂

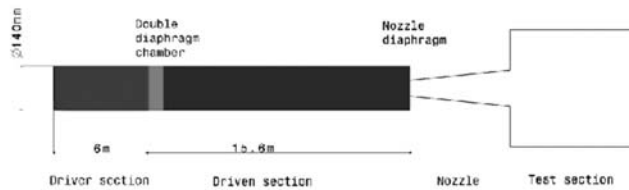
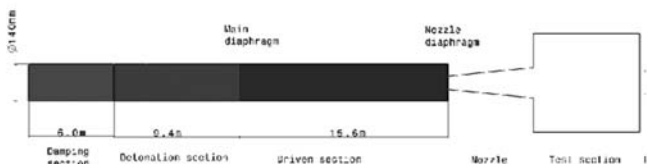
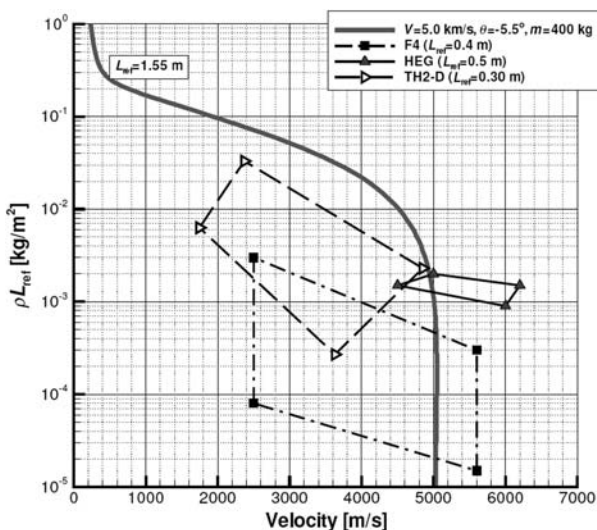
Instrumentation

- Pressure: miniaturized pressure transducers
- Force: 6 component force and moment balance
- Temperature: Coaxial thermocouples, thin film gauges, fast infrared thermography
- Visualization: Time resolved Schlieren

Reference

Olivier, H., and Grönig, H., "The Aachen Shock Tunnel TH2," 2005.

www.swl.rwth-aachen.de

Conventional Driver Mode**Detonation Driver Mode****TH2 schematic view****Binary scaling performance of TH2****Information Contact**

Univ.-Prof. Dr.-Ing. Olivier, Herbert
 Head of the Shock Wave Laboratory
 Tel.: +49 241 80 24606
 olivier@swl.rwth-aachen.de

X2 SUPER ORBITAL EXPANSION TUBE



Mission: Recreate hyper velocity planetary entry test flows, and high Mach number scramjet test flows

Location: The University of Queensland, Brisbane, Australia

Type of tunnel: Expansion tube impulse facility

Tube exit diameter	Ø 85 mm (without nozzle) Ø 202 mm (with contoured nozzle)
Test gases	Various
Maximum stagnation enthalpy	>100 MJ/kg
Maximum total pressure	Gigapascals
Maximum velocity	~15 km/s
Maximum Mach number	>20
Test time	10–200 μ s

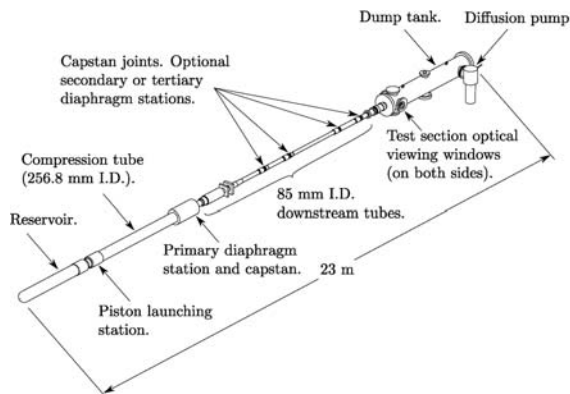
Instrumentation

- Pressure: PCB/Kulite pressure gauges, static and Pitot pressure measurements.
- Temperature: thin film heat flux gauges.

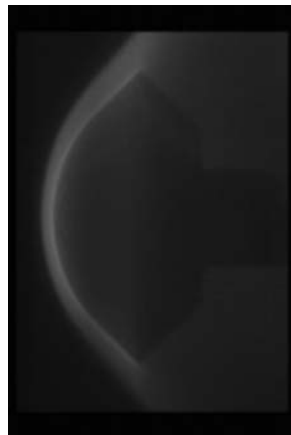
- Visualization: spectro-radiometry, high speed video (up to 1MHz), holographic interferometry (single wavelength, simultaneous two wavelength, and near resonant).

Reference

Centre for Hypersonics, The University of Queensland.



Schematic of X2, 2010 configuration

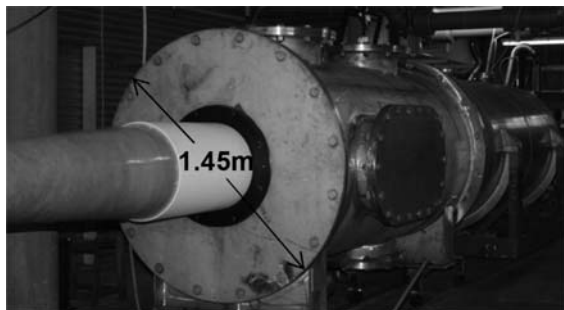


Filtered luminosity photograph of the flow over the Muses-C/Hayabusa sample return capsule

Information Contact

Prof. Richard Morgan, Director, Centre for Hypersonics,
The University of Queensland, Brisbane, QLD 4072, Australia.
Tel: +61 (0)7 3365 3592
r.morgan@uq.edu.au

X3 SUPER ORBITAL EXPANSION TUBE



X3 test section with filament-wound Mach 10 contour nozzle

Mission: Recreate hyper velocity planetary entry test flows, and high Mach number scramjet test flows

Location: The University of Queensland, Brisbane, Australia

Type of tunnel: Expansion tube impulse facility

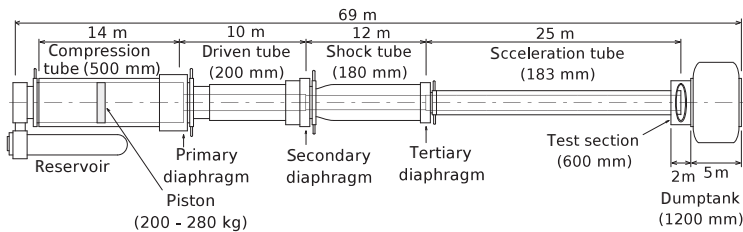
Tube exit diameter	Ø 183 mm (without nozzle) Ø 440 mm (with contoured nozzle)
Test gases	Various
Maximum stagnation enthalpy	>100 MJ/kg
Maximum total pressure	Gigapascals
Maximum velocity	~15 km/s
Maximum Mach number	>20
Test time	50–500 μ s

Instrumentation

- Pressure: PCB/Kulite pressure gauges, static and Pitot pressure measurements.
- Temperature: thin film heat flux gauges.
- Visualization: spectro-radiometry, high speed video (up to 1 MHz), holographic interferometry (single wavelength, simultaneous two wavelength, and near resonant).

Reference

Centre for Hypersonics, The University of Queensland.



Schematic of X3, 2010 configuration



Blunt waverider in X3 (Ne-H₂ at 9.25 km/s)

Information Contact

Prof. Richard Morgan, Director, Centre for Hypersonics,
The University of Queensland,
Brisbane, QLD 4072, Australia.

Tel: +61 (0)7 3365 3592

r.morgan@uq.edu.au

NASA Ames AERODYNAMIC HEATING FACILITY (AHF)



Stagnation point test of PICA thermal protection material in the AHF facility

Mission: The Aerodynamic Heating Facility is designed to match heating rates of Earth or planetary hypersonic entry to enable the selection, validation and qualification of thermal protection systems (TPS) and materials.

Location: NASA Ames Research Center, Moffett Field, CA, United States

Type of tunnel: Huels and constricted arc heater facility

Test gas	Air, N ₂	Test duration (min)	≤ 30	
Nozzle exit (mm)	Conical ($\theta/2 = 8^\circ$), Ø 178, 305, 457, 610, 762, 914	Test article type	Stagnation point	Wedge
Input power (MW)	20	Test article size (mm)	<Ø 350	660 × 660
Bulk enthalpy (MJ/kg)	2–33	Surface pressure (kPa)	0.5–45	0.1
Flow rates (kg/s)	0.05–0.7	Heating rate (kW/m²)[*]	90–9000	0.6–250

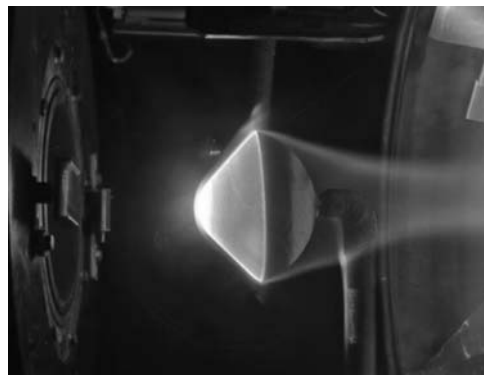
*Cold wall fully catalytic surface on a 102-mm Ø sphere

Instrumentation

- Hot wall temperature: thermocouples, IR pyrometry and radiometry
- Pressure: Pitot/static
- Cold wall heat flux: calorimetric probes of Gardon and slug types and null-point calorimetry
- Optical diagnostics: optical emission spectroscopy (OES), laser induced fluorescence (LIF)

References

- Grinstead, J. H., Harris, C. L., Yeung, D., Scott, G. P., Porter, B. J., Graube, P., and Greenberg, R. B., "Next-generation Laser-induced Fluorescence Diagnostic Systems for NASA Arc Jet Facilities," *47th AIAA Aerospace Sciences Meeting Including The New Horizons Forum and Aerospace Exposition*, January 2009, Orlando, FL, AIAA 2009-1521.
- Terrazas-Salinas, I., et al., "Test Planning Guide for NASA Ames Research Center Arc Jet Complex and Range Complex," Document A029-9701-XM3 Rev.C., April 2009.



Full-scale SPRITE capsule geometry at
simulated entry conditions



AHF stagnation point test samples, calorimetric
and pitot probes

Information Contact

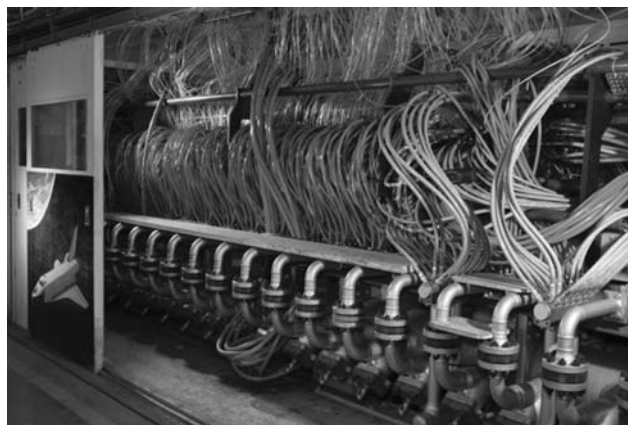
Ernest Fretter

Tel: +1 (650) 604-6166

ernest.f.fretter@nasa.gov

<http://thermo-physics.arc.nasa.gov/>

NASA Ames INTERACTION HEATING FACILITY (IHF)



The segmented arc heater in the IHF

Mission: The Interaction Heating Facility is designed to study aerodynamic heating in the thermal environment arising from the interaction of an energetic flow field during a hypersonic entry into a planetary atmosphere.

Location: NASA Ames Research Center, Moffett Field, CA, United States

Type of tunnel: Constricted arc heater facility

Test gas	Air	Test duration (min)	≤ 60	
Nozzle exit (mm)	Conical ($\theta/2 = 10^\circ$), Ø 152, 330, 533, 762 & 1041	Semielliptical, 203 × 813	Test article type	Stagnation point Wedge/Flat plate
Input power (MW)	60		Test article size (mm)	Ø 380 610 × 610
Bulk enthalpy (MJ/kg)	2 to 28		Surface pressure (kPa)	1–155 0.01–2
Flow rates (kg/s)	0.03 to 1.7		Heating rate (kW/m ²)*	250–20,000 60–4000

*Cold wall fully catalytic to a 102 mm Ø sphere (stagnation)

Instrumentation

- Hot wall temperature: thermocouples, IR pyrometry and radiometry
- Pressure: Pitot/static

- Cold wall heat flux: calorimetric probes with copper gauges (Gardon, Slug and Null Point types)
- Optical diagnostics: optical emission spectroscopy (OES), laser induced fluorescence (LIF), photogrammetric ablation rate

References

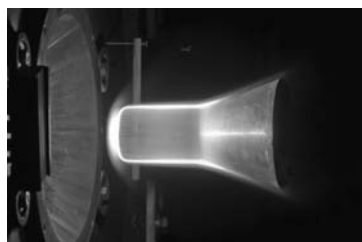
Stewart, D. A., Gökçen, T., and Chen, Y.-K., "Characterization of Hypersonic Flows in the AHF and IHF NASA Ames Arc-Jet Facilities," *41st AIAA Thermophysics Conference*, June 2009, San Antonio, TX, AIAA 2009-4237.

Terrazas-Salinas, I., et al., "Test Planning Guide for NASA Ames Research Center Arc Jet Complex and Range Complex," Document A029-9701-XM3 Rev.C., April 2009.

Winter, M. W., Raiche, G. A., Terrazas-Salinas, I., Frank, C. L. H., White, B., and Taunk, J. S., "Measurements of Radiation Heat Flux to a Probe Surface in the NASA Ames IHF Arc Jet Facility," *43rd AIAA Thermophysics Conference*, June 2012, New Orleans, LA, AIAA 2012-3189.



Large-scale panel/pylon test in IHF



UHTC ceramic tests in IHF

Information Contact

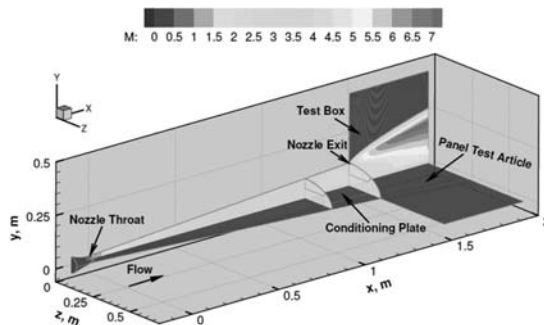
Ernest Fretter

Tel: +1 (650) 604-6166

ernest.f.fretter@nasa.gov

<http://thermo-physics.arc.nasa.gov/>

NASA Ames PANEL TEST FACILITY (PTF)



Computed PTF nozzle flow and flowfield over the calibration plate at 0° deflection

Mission: The Panel Test Facility is designed to enable testing spacecraft heat shield material samples in a high enthalpy, moderate shear boundary layer flow field. A modified version is available for higher shear and pressure conditions (TPTF).

Location: NASA Ames Research Center, Moffett Field CA 94035-1000, USA

Type of tunnel: Constricted arc heater facility

Test gas	Air
Nozzle type	Semielliptical
Nozzle exit (mm)	102 × 432 (PTF: 38 × 170)
Input power (MW)	20
Bulk enthalpy (MJ/kg)	4.6–32
Shear stress (Pa)- est.	5–30 (PTF: 80–270)
Test duration (min)	≤30
Test article type	Flat plate, –5 to +8°
Test article size (mm)	406 × 406 (PTF: 103 × 103)
Surface pressure (kPa)	0.05–5 (PTF: 1–30)
Heating rate (kW/m²)	20–500 (PTF: 80–2000)

Instrumentation

- Hot wall temperature: thermocouples, IR thermography, radiometry
- Pressure: Pitot/static
- Cold wall heat flux: copper gauges
- Optical emission spectroscopy (OES)

References

- Gökçen, T., Alunni, I. A., and Skokova, K. A., "Computational Simulations of Panel Test Facility Flow: Compression-Pad Arc-Jet Tests," *42nd AIAA Thermophysics Conference*, June 2011, Honolulu, HI, AIAA 2011-3635.
- Balboni, J. A., Gökçen, T., Frank, C. L. H., Taunk, J. S., Noyes, E., and Schickele, D., "Calibration of the Truncated Panel Test Arc-Jet Facility," *41st AIAA Thermophysics Conference*, June 2009, San Antonio, TX, AIAA 2009-4090.
- Terrazas-Salinas, I., et. al., "Test Planning Guide for NASA Ames Research Center Arc Jet Complex and Range Complex," Document A029-9701-XM3 Rev.C., April 2009.



Side view of a PTF run



MER TIRS cover test (left) Body flap test in PTF (right)

Information Contact

Ernest Fretter

Tel:+1 (650) 604-6166, ernest.f.fretter@nasa.gov
<http://thermo-physics.arc.nasa.gov/>

NASA TURBULENT FLOW DUCT (TFD)



View of the TFD test section

Mission: The Turbulent Flow Duct is designed to produce high enthalpy supersonic turbulent flow over the surface of a wall-mounted panel in the constant-area section of a duct.

Location: NASA Ames Research Center, Moffett Field CA 94035-1000, USA

Type of tunnel: Huels (Linde) arc heater facility

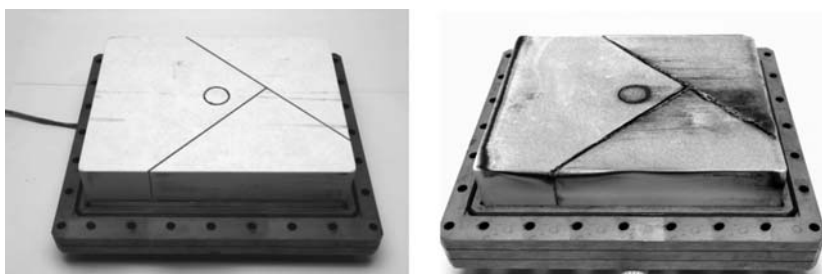
Test gas	Air, N ₂	Test duration (min)	≤ 30
Nozzle exit (mm)	51 × 229	Test article type	Flat plate
Input power (MW)	12	Test article size (mm)	203 × 254 or 203 × 508
Bulk enthalpy (MJ/kg)	3–9.5	Surface pressure (kPa)	2–15.2
Shear stress (Pa) – estimate	50–720	Heating rate (kW/m²)	23–681

Instrumentation

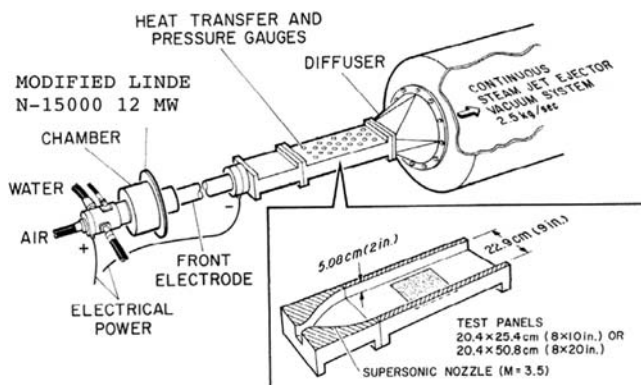
- Hot wall temperature: thermocouples, IR thermography and radiometry
- Pressure: static
- Cold wall heat flux: Gardon gauges

References

- Alunni, A. L., Olson, M. W., Gökçen, T., and Skokova, K. A., "Comparisons of Surface Roughness in Laminar and Turbulent Environments for Orion Thermal Protection System," *42nd AIAA Thermophysics Conference*, June 2011, Honolulu, HI, AIAA 2011-3776.
- Covington, M. A., and Vojvodich, N. S., "Turbulent Flow Studies in Two Arc-Heated Duct Facilities," *Journal of Spacecraft and Rockets*, Vol. 9, No. 6, June 1972, pp. 441–447.
- Terrazas-Salinas, I., et al., "Test Planning Guide for NASA Ames Research Center Arc Jet Complex and Range Complex," Document A029-9701-XM3 Rev.C, April 2009.



TFD test model prior to (left) and after testing (right)



Schematic of the TDF facility

Information Contact

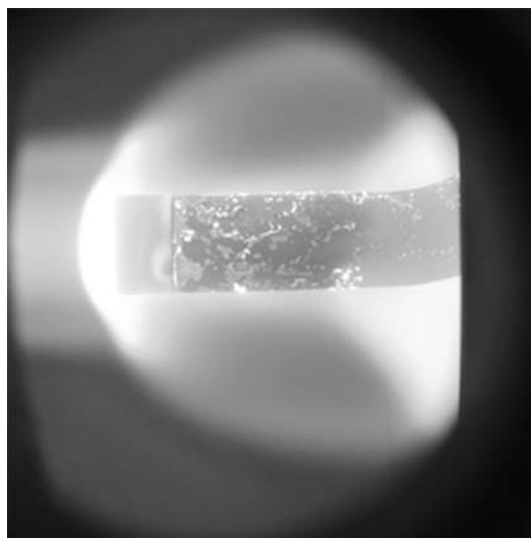
Ernest Fretter

Tel: +1 (650) 604-6166

ernest.f.fretter@nasa.gov

<http://thermo-physics.arc.nasa.gov>

NASA Langley Hypersonic Materials Environmental Test System (HYMETS)



Thermal protection material during HYMETS test in air plasma

Mission: Thermal protection materials testing under simulated hypersonics heating rates

Location: NASA Langley Research Center, Hampton, VA, United States

Type of tunnel: Segmented-constrictor-dielectric-arc-heater

Test gas	Air, N ₂ , O ₂ -N ₂ , CO ₂ , Ar
Nozzle exit (mm)	Conical, Ø 63.5
Input power (kW)	400
Bulk enthalpy	10–35 MJ/kg
Mach number	3.5
Test article type	Stagnation point
Test article size (mm)	Ø 33
Surface pressure (kPa)	2–4
Heating rate (kW/m²)	up to 3000

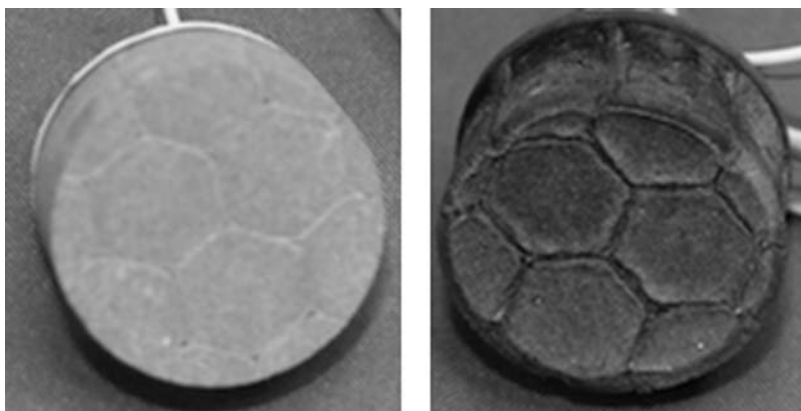
Instrumentation

- Hot wall temperature: thermocouples, IR pyrometry and radiometry
- Pressure: Pitot/static
- Cold wall heat flux: calorimetric probes with copper and quartz gauges
- Optical diagnostics: optical emission spectroscopy (OES), laser induced fluorescence (LIF)

References

Danehy, P. M., Hires, D. V., Johansen, C. T., Bathel, B. F., Jones, S. B., Gragg, J. G., and Splinter, S. C., "Quantitative Spectral Radiance Measurements in the HYMETS Arc Jet," *50th AIAA Aerospace Sciences Meeting including the New Horizons Forum and Aerospace Exposition*, Nashville, TN, USA, January, 2012, AIAA 2012-0856.

Szalai, C. E., Beck, R. A. S., Gasch, M. J., Alunni, A. I., Chavez-Garcia, J., Splinter, S. C., Gragg, J. G., and Brewer, A., "Thermal Protection System Aerothermal Screening Tests in the HYMETS Facility," *42nd AIAA Thermophysics Conference*, Honolulu, HI, USA, June, 2011, AIAA 2011-3493.



Pre-test photographs of Avcoat TPS specimens: virgin (left) and CO₂-tested (right)

Information Contact

Splinter C. Scott
Tel: +1 (757) 864-9602
scott.c.splinter@nasa.gov

DLR ARC-HEATED WIND TUNNEL 2 (L2K)



The L2K facility at DLR Koeln

Mission: The L2K enables the simulation of Earth and Mars atmospheres for the characterization of heat shield materials and qualification of hot structures and high temperature sensors. Atmospheres with dust particles typical for Mars entry can also be added to the flow.

Location: German Aerospace Center (DLR), Koeln, Germany

Type of tunnel: Huels type arc heater plasma generator

Test gas	Air, N ₂ , CO ₂ /N ₂	Test duration (min)	up to 120		
Nozzle exit (mm)	Conical ($\theta/2 = 12^\circ$), Ø 14, 20, 25, 29	Test article type	Stag. pt.	Flat plate	
Input power (MW)	1	Test article size (mm)	Ø up to 100	150 × 250 × 50	
Bulk enthalpy (MJ/kg)	4–20	Surface pressure (kPa)	up to 16	–*	
Flow rates (g/s)	5–75	Heating rate (kW/m²)	2000	–*	

*Data not available

Instrumentation

- Hot wall temperature: thermocouples, IR pyrometry and IR thermography
- Pressure: Pitot/static
- Cold wall heat flux: calorimetric sensors
- Flow optical diagnostics: laser induced fluorescence (LIF)

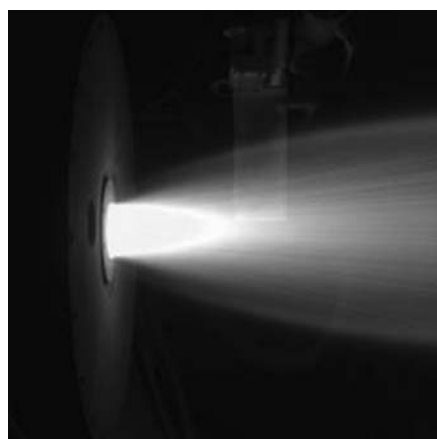
References

Esser, B., and Gühan, A., "Flow Field Characteristics of DLR's Arc Heated Facilities L2K and L3K," *3rd European Symposium on Aerothermodynamics for Space Vehicles*, ESA SP 426, November 1998, ESTEC, Noordwijk, The Netherlands.

Gühan, A., Esser, B., and Koch, U., "Mars Entry Simulation in the Arc Heated Facility L2K," *4th European Symposium on Aerothermodynamics for Space Vehicles*, ESA SP 487, October 2001, CIRA, Capua, Italy.



L2K material testing in Martian atmosphere

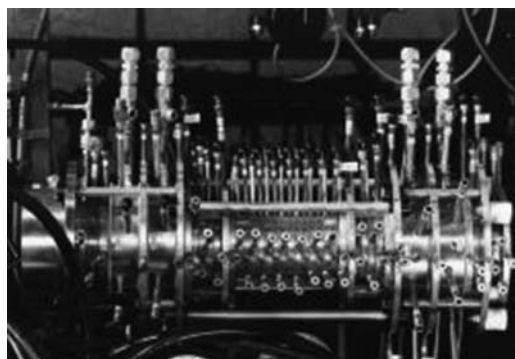


Particle loaded flow in the L2K facility

Information Contact

Dr.-Ing. Ali Gühan
Tel.: +49 2203 601-2363
ali.guelhan@dlr.de
http://www.dlr.de/as/en/desktopdefault.aspx/tabcid-194/407_read-5449/

DLR ARC-HEATED WIND TUNNEL 3 (L3K)



The segmented arc of the L3K facility at DLR Koeln

Mission: The L3K is a European asset for qualification of thermal protection systems, hot structures and high-temperature sensors. It is also used to study gas/surface interaction in atmospheric reentry conditions.

Location: German Aerospace Center (DLR), Koeln, Germany

Type of tunnel: Segmented arc heater plasma wind tunnel

Test gas	Air, N ₂ , CO ₂ /N ₂	Test duration (min)	up to 120	
Nozzle exit (mm)	Conical ($\theta/2 = 12^\circ$), Ø 14, 29	Test article type	Stag. pt.	Flat plate
Input power (MW)	6	Test article size (mm)	Ø up to 100	150 × 250 × 50
Bulk enthalpy (MJ/kg)	up to 25	Surface pressure (kPa)	up to 35	–
Flow rates (g/s)	10–100	Heating rate (kW/m²)	4000	–

Instrumentation

- Hot wall temperature: thermocouples, IR pyrometry and IR thermography
- Pressure: Pitot/static
- Cold wall heat flux: calorimetric sensors
- Flow optical diagnostics: laser induced fluorescence (LIF)

References

- Böhrk, H., Ditter, C., Weihs, H., Thiele, T., and, Gühan, A., "Thermal Testing of the Sharp Leading Edge of SHEFEX II," *18th AIAA/3AF International Space Planes and Hypersonic Systems and Technologies Conference*, Tours, France, September 2012, AIAA 2012-5919.
- Esser, B., and Gühan, A., "Flow Field Characteristics of DLR's Arc Heated Facilities L2K and L3K," *3rd European Symposium on Aerothermodynamics for Space Vehicles*, ESA SP 426, November 1998, ESTEC, Noordwijk, The Netherlands.



Infrared thermography picture of an ablative material tested in flat plate configuration



Sharp leading edge structure testing

Information Contact

Dr.-Ing. Ali Gühan
Tel: +49 2203 601-2363
ali.guelhan@dlr.de

CIRA PLASMA WIND TUNNEL SCIROCCO



Aerial view of the SCIROCCO facility complex at CIRA

Mission: SCIROCCO is the largest and most powerful plasma wind tunnel in the world. Its primary function is to provide capabilities for large and real scale thermal protection systems and hot structures.

Location: Centro Italiano Ricerche Aerospaziali (CIRA), Capua, Italy

Type of tunnel: Segmented constricted arc heater plasma wind tunnel

Test gas	Air, Ar	Test duration (min)	≤ 30
Nozzle exit (mm)	$\varnothing 1950, 1350, 1150, 900, (187)$	Test article type	Various types in stag. pt. and flap configurations
Input power (MW)	70	Test article size (mm)	$\leq \varnothing 600$
Bulk enthalpy (MJ/kg)	2.5–45	Total pressure (kPa)	1–17.5
Flow rates (kg/s)	0.1–3.5	Heating rate (kW/m^2)	≤ 3000 on $\varnothing 100$ mm $\leq 20,000$ on $\varnothing 75$ mm

Instrumentation

- Hot wall: thermocouples, IR pyrometry and IR thermography
- Pressure: Pitot/static
- Cold wall heat flux: calorimetric sensors
- Flow optical diagnostics: optical emission spectroscopy (OES)

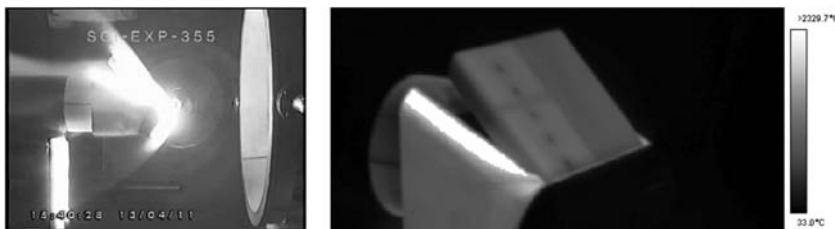
References

Cipullo, A., De Filippis, F., and Zeni, L., "Temperature Measurements of the Air Plasma Flow Using Optical Emission Spectroscopy," *Journal of Thermophysics and Heat Transfer*, Vol. 25, No. 3, 2011, pp. 354–360.

Di Clemente, M., Rufolo, G., Ianiro, A., and Cardone, G., "Hypersonic Test Analysis by Means of Aerothermal Coupling Methodology and Infrared Thermography," *AIAA Journal*, Early Edition, 2013, pp. 1–15.

Information Contact

Eduardo Trifoni



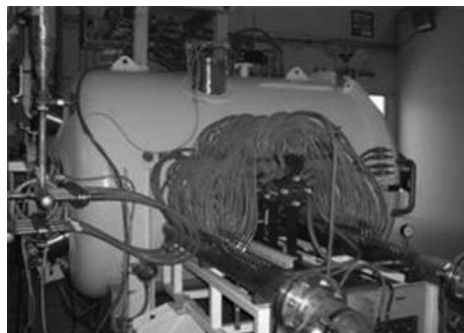
Photograph and infrared thermography map of the EXPERT C/SiC flap test model in SCIROCCO

Tel: +39 0823-623740

e.trifoni@cira.it

<http://www.cira.it/en/impianti-en/pwt-plasma-wind-tunnel>

CIRA PLASMA WIND TUNNEL GHIBLI



The arc-heated of the GHIBLI facility at CIRA

Mission: GHIBLI is an hypersonic high enthalpy arc-heated continuous facility for the development of experiments on small size models (up to 80 mm diameter). It allows one to perform tests for material sample characterization and selection, as well as CFD codes validation.

Location: Centro Italiano Ricerche Aerospaziali (CIRA), Capua, Italy

Type of tunnel: Segmented constricted arc-heater plasma wind tunnel

Test gas	N ₂ , Ar	Test duration (min)	≤30
Nozzle exit (mm)	150	Test article type	Stagnation point
Input power (MW)	2	Test article size (mm)	≤Ø100
Bulk enthalpy (MJ/kg)	10–30	Total pressure (kPa)	1–15
Flow rates (g/s)	1–55	Heating rate (kW/m²)	≤3000 on Ø100 mm

Instrumentation

- Hot wall: thermocouples, IR pyrometry and IR thermography
- Pressure: Pitot/static
- Cold wall heat flux: calorimetric sensors
- Flow optical diagnostics: optical emission spectroscopy (OES)

References

Purpura, C., De Filippis, F., Graps, E., Trifoni, E., and Savino, R., "The Ghibli Plasma Wind Tunnel: Description of the New CIRA-PWT Facility," *57th International Astronautical Congress*, October 2006, Valencia, Spain.

Trifoni, Purpura, Martucci, Graps, Schettino, Battista, Passaro, Baccarella, Cristofolini, Neretti, "MHD Experiment at CIRA GHIBLI Plasma Wind Tunnel," *7th European Symposium on Aerothermodynamics for Space Vehicles*, 2011, Bruges, Belgium.



Probe models (top) and test run (bottom) photographs of an MHD experiment in the GHIBLI PWT

Information Contact

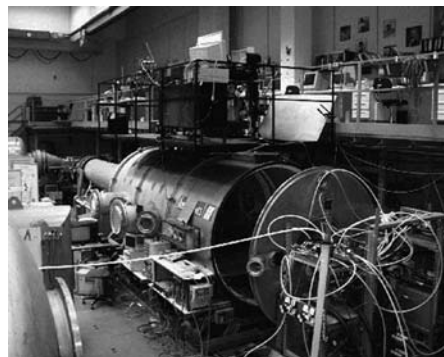
Eduardo Trifoni

Tel: +39 0823-623740

e.trifoni@cira.it

<http://www.cira.it/en/impianti-en/galleria-ipersonica-ghibli>

IRS PLASMA WIND TUNNELS (PWK1, 2, 4)



Overview of the PWK1 facility at IRS

Mission: PWKs at IRK are designed to qualify and perform basic research on TPS materials, verify numerical models, develop and qualify diagnostic methods and develop and qualify flight experiments.

Location: Institute of Space Systems (IRS), Stuttgart University, Stuttgart, Germany

Type of tunnel: Thermal (RB3) or magnetoplasmadynamic (RD5 and RD7) driven generators

	RB3	RD5	RD7
Test gas	N ₂ , N ₂ /O ₂ , N ₂ /CO ₂	N ₂ , Ar, N ₂ /O ₂ , Ar/O ₂ , N ₂ /CH ₄ , N ₂ /CO ₂	
Test article type		Stagnation point	
Input power (MW)		0.1–6 (6 units)	
Test duration (min)		≤120	
Flow rates (g/s)	≤10	0.3–50	
Bulk enthalpy (MJ/kg)	≤20	≤150	
Nozzle exit (mm)	Ø = 75	Ø = 125	Ø = 340
Test article size (mm)	≤100	Ø ≤ 100	Ø ≤ 400
Surface pressure (kPa)	≤10	≤7	
Heating rate (MW/m²)	≤10	≤14	

Instrumentation

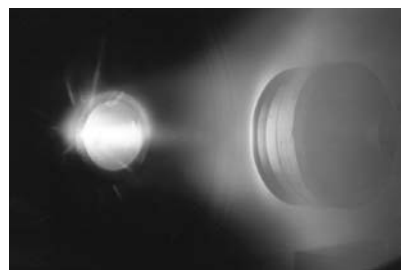
- Hot wall temperature: thermocouples, IR pyrometry and IR radiometry
- Pressure: Pitot/static

- Cold wall heat flux: slug and calorimetric sensors, hot wall heat flux, NISI
- Flow optical diagnostics: laser induced fluorescence (LIF), emission and absorption spectroscopy.

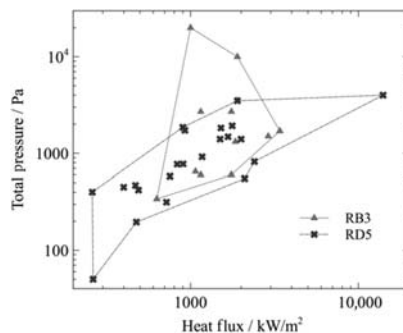
References

Herdrich, G., Knapp, A., Loehle, S., Petkow, D., and Fasoulas, S., "Ground Testing Facilities and Modeling Tools: Research Examples," *In 27th AIAA Aerodynamic Measurement Technology and Ground Testing Conference*, July 2010, Chicago, IL, AIAA 2010-4339.

Herdrich, G., Fertig, M., and Löhle, S., "Experimental Simulation of High Enthalpy Planetary Entries," *The Open Plasma Physics Journal*, Vol. 2, No. 15, 2009, pp. 150–164, ISSN: 1876-5343, doi: 10.2174/1876534300902010150, September 2009.



Heat shield material testing at 10 MW/m² PWK1 (RD7)



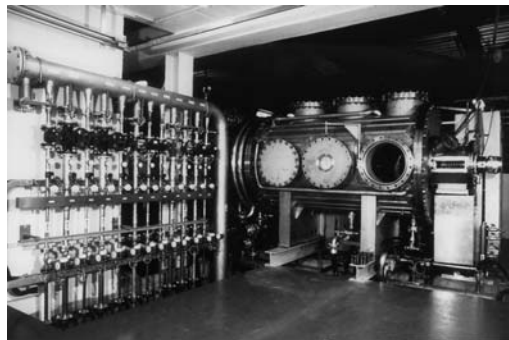
Envelopes of PWK1, 2 and 4

Information Contacts

Priv. Doz. Dr. G. Herdrich
herdrich@irs.uni-stuttgart.de

Dr. S. Löhle
loehle@irs.uni-stuttgart.de
IRS Website: <http://www.irs.uni-stuttgart.de>

VKI INDUCTIVELY COUPLED PLASMA WIND TUNNEL (PLASMATRON)



Mission: Ground testing for TPS materials for entry into a variety of planetary atmospheres. Characterization of Gas-Surface Interactions, investigation on Catalysis, Oxidation and Ablation.

Location: Aeronautics/Aerospace Department, von Karman Institute for Fluid Dynamics, Belgium

Type of tunnel: Inductively coupled plasma wind tunnel

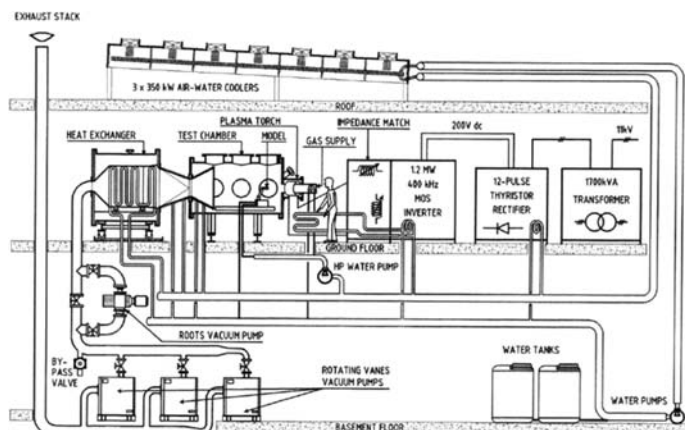
Test gas	Ar, Air, N ₂ , CO ₂	Test duration (min)	≤ 90
ICP Torch exit (mm)	Ø: 160, 80, 35	Test article type	Stag. point Flat plate
Input power (MW)	1.2	Test article size (mm)	Ø up to 120 150 × 60 × 25
Jet enthalpy (MJ/kg)	≤ 50	Surface pressure (kPa)	≤ 85 ≤ 85
Flow rates (g/s)	6–30	Heating rate (MW/m²)	≤ 16 ≤ 1.5

Instrumentation

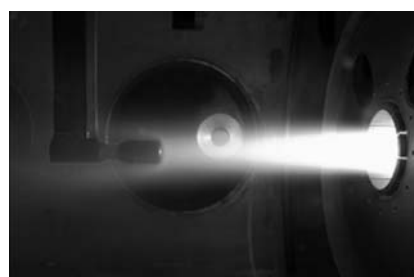
- Hot wall temperature: thermocouples, IR pyrometry and IR thermography
- Pressure: Pitot/static
- Cold wall heat flux: slug, water-cooled calorimeter and Gardon Gauge sensors
- Flow optical diagnostics: High Speed Camera, Optical Emission Spectroscopy

References

- Bottin, B., Chazot, O., Carbonaro, M., Vander Haegen, V., and Paris, S., "The VKI Plasmatron Characteristics and Performance," *Measurement Techniques for High Enthalpy and Plasma Flows*, NATO-RTO-EN 8, 1999.
- Chazot, O., "Hypersonic Stagnation Point Aerothermodynamic in Plasmatron Facilities," *Collection of Works on Hypersonic Entry and Cruise Vehicles*, Stanford and NASA Ames Research center, edited by Von Karman Institute 2009, ISBN-13 978-2-930389-87-7.
- Panerai, F., and Chazot O., "Characterization of Gas/Surface Interactions for Ceramic Matrix Composites in High Enthalpy, Low Pressure Air Flow," *Materials Chemistry and Physics*, Vol. 134, No. 2–3, 2012, pp. 597–607.



VKI Plasmatron facility (sketch)



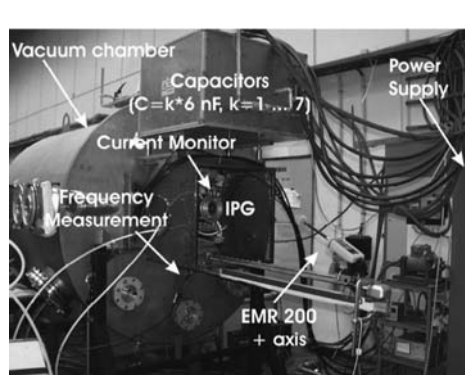
Heat flux measurement in the VKI Plasmatron facility using a copper calorimetric probe

Information Contact

Prof. O. Chazot

chazot@vki.ac.be

VKI Website: <https://www.vki.ac.be/>



Photograph of the PWK3 facility

Mission: PWK 3 at IRS is designed to qualify and perform basic research on TPS materials, verify numerical models, develop and qualify diagnostic methods and develop and qualify flight experiments.

Location: Institute of Space Systems (IRS), Stuttgart University, Stuttgart, Germany

Type of tunnel: Inductively coupled plasma wind tunnel

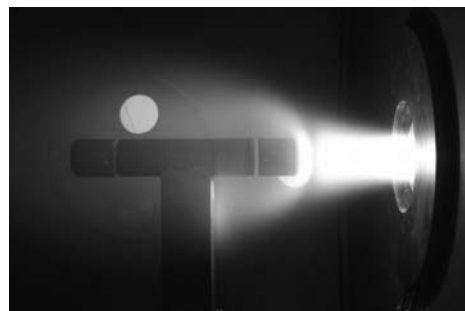
Test gas	Ar, Air, N ₂ , O ₂ , CO ₂	Test duration (min)	≤ 45
ICP Torch exit (mm)	80	Test article type	Stagnation point
Input power (MW)	375 kW	Test article size (mm)	≤ 100
Jet enthalpy (MJ/kg)	Up to 80	Surface pressure (kPa)	≤ 100
Flow rates (g/s)	Up to 20	Heating rate (MW/m²)	≤ 10

Instrumentation

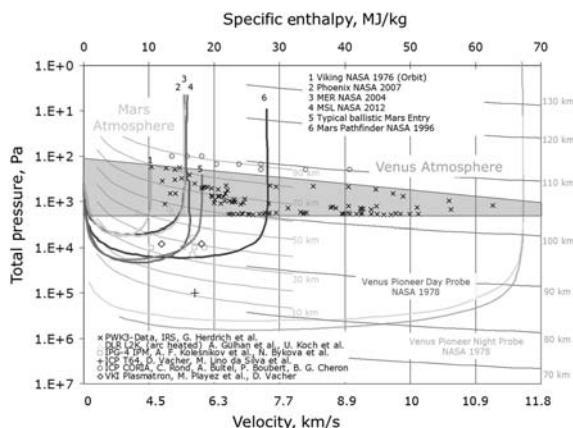
- Hot wall temperature: thermocouples, IR pyrometry and IR radiometry
- Pressure: Pitot/static
- Cold wall heat flux: slug and calorimetric sensors
- Flow optical diagnostics: laser induced fluorescence (LIF), emission and absorption spectroscopy.

References

- Herdrich, G., Marynowski, T., Dropmann, M., and Fasoulas, S., "Mars and Venus Entry Simulation Capabilities of IRS Plasma Wind Tunnel PWK3," *Applied Physics Research*, Vol. 4, No. 1, 2012, p. 146.
- Löhle, S., Lein, S., Eichhorn, Ch., Herdrich, G., and Winter, M., "Spectroscopic Investigation of an Inductively Heated CO₂ Plasma for Mars Entry Simulation," *Journal of Technical Physics, Quarterly*, Vol. L, No. 3, 2010, pp. 233–246.



Probe testing in PWK 3



Operating envelope of PWK 3 facility

Information Contacts

Dr. G. Herdrich
 herdrich@irs.uni-stuttgart.de

Dr. S. Löhle
 loehle@irs.uni-stuttgart.de
 IRS website
<http://www.irs.uni-stuttgart.de>

IPM INDUCTION PLASMA GENERATOR (IPG-3 AND IPG-4)



Photograph of the IPG3 facility

Mission: Development, diagnostics and applications of low-temperature plasmas for simulation of re-entry heating. Thermochemical testing of thermal protection materials in high-enthalpy gas flows.

Location: Institute for Problems in Mechanics of Russian Academy of Sciences, Moscow, Russia

Type of tunnel: Inductively coupled plasma wind tunnel

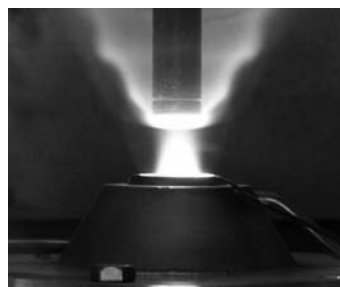
	IPG-3	IPG-4		IPG-3	IPG-4
Test gas	Ar, Air, N ₂ , O ₂ , CO ₂		Test duration (min)	≤45	
ICP Torch exit (mm)	150–200	80	Test article type	Stagnation point	
Input power (MW)	1.0	0.1	Test article size (mm)	20–300	20–150
Jet enthalpy (MJ/kg)	≤50	≤50	Surface pressure, kPa	1.5–100	1.5–100
Flow rates (g/s)	≤15	≤6	Heating rate (MW/m²)	0.2–6	0.2–12.8

Instrumentation

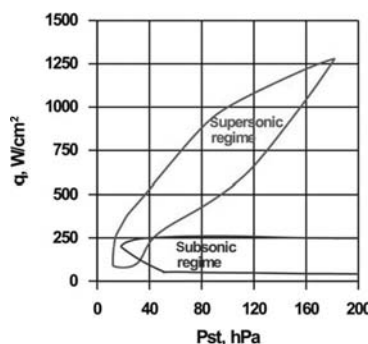
- Hot wall temperature: pyrometry and thermography
- Pressure: Pitot/static
- Cold wall heat flux: water-cooled calorimeter
- Flow optical diagnostics: Optical Emission Spectroscopy

References

- Gordeev, A. N., "Overview of Characteristics and Experiments in IPM Plasmatrons," In *Measurement Techniques for High Enthalpy and Plasma Flows*, NATO-RTO-EN 8, 1999.
- Kolesnikov, A. F., "The Aerothermodynamic Simulation in Sub- and Supersonic High-Enthalpy Jets: Experiment and Theory," *Second European Symposium on Aerothermodynamics for Space Vehicles*, ESTEC, Noordwijk, Netherlands, 1994, Proceedings, pp. 583–588.
- Kolesnikov, A. F., Pershin, I. S., Vasil'evskii, S. A., and Yakushin, M. I., "Study of Quartz Surface Catalicity in Dissociated Carbon Dioxide Subsonic Flows," *Journal of Spacecraft and Rockets*, Vol. 37, No. 5, 2000, pp. 573–579.



Supersonic testing in IPG-4



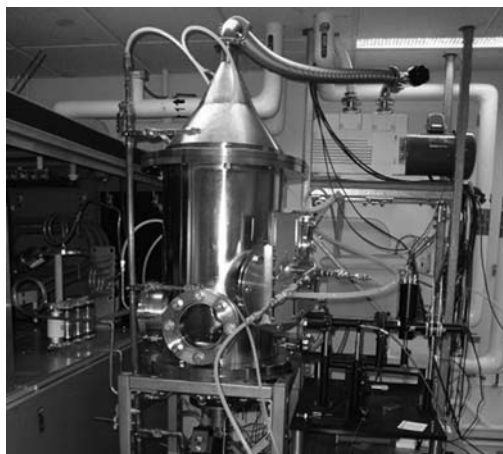
Operating envelope of IPG-4 facility

Information Contacts

Dr. A. F. Kolesnikov
koles@ipmnet.ru

Dr. A. N. Gordeev
a_gord@mail.ru
IPM website: <http://www.ipmnet.ru/>

UVM 30 kW INDUCTIVELY COUPLED PLASMA TORCH FACILITY



Photograph of the UVM ICP torch

Mission: Ground testing for advanced aerospace materials. Spectroscopic diagnostics in boundary layer over thermal protection material to quantify gas-surface interaction rates.

Location: Plasma Test and Diagnostics Laboratory, Mechanical Engineering, University of Vermont, Vermont, USA

Type of tunnel: Inductively coupled plasma torch facility

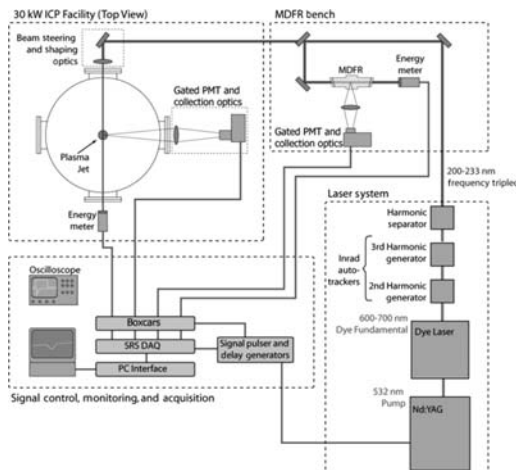
Test gases (& mixtures)	Ar, Air, N ₂ , O ₂ , CO ₂	Test duration (min)	>60
ICP Torch exit (mm)	Ø: 36	Test article type	Stag. point
Input power (kW)	30	Test article size (mm)	18, 25, 35
Jet enthalpy (MJ/kg)	≤50	Surface pressure (kPa)	≤25
Flow rates (g/s)	6–30	Heating rate (MW/m²)	≤1.5

Instrumentation

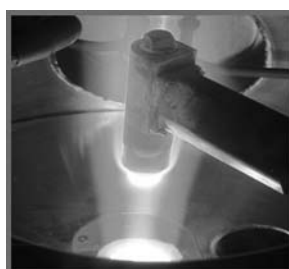
- Hot wall temperature: thermocouples, IR pyrometry
- Pressure: Pitot/static
- Cold wall heat flux: slug calorimeter, gardon gage
- Flow optical diagnostics: Optical Emission Spectroscopy, Laser Induced Fluorescence (& PLIF), IR diode laser absorption.

References

- Meyers, J. M., Owens, W. P., and Fletcher, D. G., "Surface Catalyzed Reaction Efficiencies in Air Plasmas Using Laser Induced Fluorescence Measurements," AIAA 2013-3140.
- Owens, W. P., Uhl, J., Dougherty, M., Lutz, A., Meyers, J., and Fletcher, D. G., "Development of a 30 kW Inductively Coupled Plasma Torch Facility for Aerospace Material Testing," AIAA 2010-4322.
- Owens, W. P., Meyers, J. M., and Fletcher, D. G., "Surface Catalysis and Oxidation of Flexible Thermal Protection Materials in Air Plasma," AIAA 2013-3141.



LIF diagnostic setup for the UVM ICP torch



Ablative material test in the UVM ICP torch facility

Information Contact

Prof. D. G. Fletcher
 dfletche@uvm.edu
 Website: <http://www.uvm.edu>

INDEX

Note: Page numbers followed by *f* or *t* (indicating figures or tables).

- Abel equation, 362
Abel-inversion, 353, 362, 363*f*
Ablation, 245
Absorption spectroscopy, 373
 broadening mechanisms, 375–377
 cavity-enhanced methods, 389–390
 CRDS, 389–390
 hardware using for absorption, 390
 rotational temperature, 379–384
 sample absorption measurement, 385*f*
 species concentrations, 384–386
 strengths and weaknesses, 390–391
 tomography, 388–389
 translational temperature, 377–379
 velocimetry, 386–388
 vibrational temperature, 384
Absorption theory, 373
 spectral irradiance of light, 374
 spectral overlap integral, 375
 two-level energy diagram, 374*f*
Acceleration tube, 337
AE measurements. *See* Atmospheric Explorer measurements
Aeroassisted Orbital Transfer Vehicle (AOTV), 103
Aerodynamic Heating Facility (AHF), 494–495
Aerothermodynamic ground testing, 330
 binary scaling, 331
 Damköhler number, 331
 ground testing strategies, 333
 high-enthalpy facilities, 334–338
 LHTS methodology, 332
 plasma wind tunnels, 338–339
 TPS testing in plasma wind tunnel in LHTS conditions, 333*f*
Aerothermodynamics, 6, 103, 329.
 See also Computational fluid dynamics (CFD)
 DAC for MGS analysis, 78
 DS2V DSMC code, 76
AHF. *See* Aerodynamic Heating Facility
Air–carbon surface chemistry, 297
 atomic mass fractions of oxygen and nitrogen, 299
CO production, 303
Park model, 300, 302
product mass fractions, 303*f*
reactions and rates for Zhukov and Abe model, 301*t*
SRE model, 297
wedge flow field computed with DPLR, 298*f*
Amorphous silica (a-SiO₂), 267, 269
 annealing simulations, 271
 structural features, 271
 total correlation function, 270
Anti-Stokes Raman scattering, 418
AOTV. *See* Aeroassisted Orbital Transfer Vehicle
Arcjet facility, 338, 339*f*
Arrhenius equation, 35
Atmospheric Explorer measurements (AE measurements), 187
Background Oriented Schlieren (BOS), 446–447
Balanced ratiometric method, 383–384
Ballute, 81
Beer–Lambert law, 373
BGK approximation. *See* Bhatnagar–Gross–Krook approximation
Bhatnagar–Gross–Krook approximation (BGK approximation), 4
Bird's No Time Counter (Bird's NTC), 48
Bird's NTC. *See* Bird's No Time Counter
BL model. *See* Borgnakke–Larsen model
Blow down wind tunnel, 334, 335*f*
Blunt body configurations, 75, 78
 DS2V DSMC code, 76
 measured and computed spectra comparison for Stardust, 77*f*
 mole fraction profiles, 77*f*
 temperature profiles along Stardust SRC stagnation streamline, 76*f*

- Boltzmann distribution law, 344
 Boltzmann equation, 3, 10, 45
 Chapman–Enskog approach, 15–21
 generalized, 10–14
 numerical solutions, 14
 distribution function, 14, 15*f*
 macroscopic parameters, 16*f*
 macroscopic variables
 comparison, 18*f*
 VDFs, 14, 17*f*
 state kinetic transport coefficients study, 21–22
 Boltzmann fraction (f_B), 394
 Boltzmann plot, 365
 Borgnakke–Larsen model (BL model), 55, 56, 59
 Born–Oppenheimer approximation, 108
 BOS. *See* Background Oriented Schlieren
 Boundary-layer diffusion and chemistry, 309–310
 Bound–bound emission processes, 354
 Bound–free absorption cross section, 164–165
 Bound–free transitions, 164
 Bow Shock Ultraviolet flight experiments, 182
 Bow-Shock Ultra-Violet-2 (BSUV-2), 72
 Broadening mechanisms, 375
 Doppler broadening, 376
 multi-component gas mixture, 375
 spectral line shape, 377*f*
 BSUV-2. *See* Bow-Shock Ultra-Violet-2
 Calspan–University of Buffalo Research Center (CUBRC), 82, 378
 Carbon dioxide (CO₂), 244, 364
 Carbon monoxide (CO), 244, 303
 Carbuncle, 216
 CARS. *See* Coherent anti-Stokes Raman spectroscopy
 Cavity ring-down spectroscopy (CRDS), 389–390
 Cavity-enhanced absorption (CEA), 390
 Cavity-enhanced absorption spectroscopy (CEAS), 390
 Cavity-enhanced methods, 389–390
 CCD cameras. *See* Charge coupled device cameras
 CCM. *See* Computational chemistry model
 CDF. *See* Cumulative distribution function
 CEA. *See* Cavity-enhanced absorption
 CEAS. *See* Cavity-enhanced absorption spectroscopy
 Centro Italiano Ricerche Aerospaziali (CIRA), 508
 GHIBLI, plasma wind tunnel, 510–511
 SCIROCCO, plasma wind tunnel, 508–509
 Cercignani–Lampis–Lord model (CLL model), 65, 66
 CFD. *See* Computational fluid dynamics; Continuum fluid dynamics
 Chapman–Enskog approach, 14, 15
 approximation, 3
 distribution function
 evolution, 16, 17
 first-order, 20
 zeroth-order, 18
 macroscopic equations, 19
 macroscopic parameters, 18–19
 transport coefficients, 20
 Chapman–Enskog distribution, 46
 velocity distribution function, 84
 CHAR. *See* CHarring Ablator Response
 Charge coupled device cameras (CCD cameras), 351, 424, 446
 Charged species, 64, 74, 94
 CHarring Ablator Response (CHAR), 309
 Chemical reactions, 59
 dissociation incubation distance, 60*f*
 DSMC results, 60
 GCE model, 61
 nitric oxide formation
 reaction cross-sections for, 61*f*
 vibrational energy distribution function of products in, 63*f*
 vibrational energy distribution function of reactants in, 62*f*
 CIRA. *See* Centro Italiano Ricerche Aerospaziali
 CLL model. *See* Cercignani–Lampis–Lord model

- Coarse-grained model, 150. *See also* Heavy particle rate coefficients
shock tube heated flows, 152, 154
bin number convergence study, 153f
dissociation dynamics, 153
theory, 151
energy grouping, 151
population reconstruction, 151–152
solution of master equation, 152
- Coherent anti-Stokes Raman spectroscopy (CARS), 346, 431
advantages and disadvantages, 438–439
dual-pump, 432
energy level diagram, 432f
in gas flows, 444
mole fraction and nonequilibrium temperature measurement, 439–442
nonlinear process, 433
nonthermalized population distributions measurement, 442–443
theory, 433–436
ultrafast, 437
- Coherent measurement approach, 346
- Collision broadening, 361
- Collisional excitation processes, 141
- Computational chemistry, 310–311
- Computational chemistry model (CCM), 291–293
- Computational fluid dynamics (CFD), 103, 241. *See also* Implicit time integration; Low-dissipation numerical flux; Thermal protection system (TPS); Upwind numerical flux functions
Da role in, 6
shock wave prediction, 51
tightly coupled, 308–309
- Continuous wave lasers (CW lasers), 348
- Continuum fluid dynamics (CFD), 162
- Coupled catalysis models, 294
CO loss efficiencies, 296
O-atom loss efficiency, 295
reactions and rates for mars entry catalysis, 294t
- Coupled vibration-dissociation vibration (CVDV), 259
- Coupling procedures, 87
continuum and particle boundary cells, 89
hybrid, 88f
- CRDS. *See* Cavity ring-down spectroscopy
- Crystalline quartz surfaces, 268–269
- CUBRC. *See* Calspan-University of Buffalo Research Center
- Cumulative distribution function (CDF), 148
- CVDV. *See* Coupled vibration-dissociation vibration
- CW lasers. *See* Continuous wave lasers
- Damköhler number (*Da*), 6–7, 36, 331
- Data-parallel line-relaxation method (DPLR method), 225–226, 241, 258–259
- CFD code, 293, 309
- finite-rate model, 299
- finite-rate surface chemistry framework, 308
- GMRes, 226–227
- high-Reynolds number flows, 226
SCEBD model, 309
wedge flow field computation, 298f
- Decoupled implicit method, 227
- Degenerate four-wave mixing (DFWM), 432, 447–448
- Density functional theory (DFT), 266, 315
- DFT. *See* Density functional theory
- DFWM. *See* Degenerate four-wave mixing
- DG finite element method.
See Discontinuous Galerkin finite element method
- Diode lasers, 348, 349, 382, 391
absorption measurement, 386f
semiconductor, 390
single-mode, 375
tunable, 388, 390
- Dirac delta-function formalism, 3–4
- Direct reaction rate coefficients, 141
- Direct simulation Monte Carlo method (DSMC method), 4–5, 46, 73, 160.
See also Hybrid DSMC-continuum methods

- Direct simulation Monte Carlo method
(Continued)
- analysis of hypersonic flows, 67
 - Earth's atmosphere, 72–78
 - hypersonic laboratory experiments, 68–72
 - planetary atmospheres, 78–79
 - basic algorithm, 48
 - steps in iteration, 49
 - vector and parallel computers, 50
 - for hypersonic flows, 47
 - Knudsen number profiles in Earth's atmosphere, 47*f*
 - physical models, 50
 - charged species, 64
 - chemical reactions, 59–63
 - elastic momentum exchange, 50–54
 - gas–surface interaction, 65–67
 - radiation, 64–65
 - rotational energy exchange, 54–57
 - vibrational energy exchange, 57–59
- Discontinuous Galerkin finite element method (DG finite element method), 206
- Dissociated states, 131
- DLR arc-heated wind tunnel 2 (L2K), 504–505
- DLR arc-heated wind tunnel 3 (L3K), 506–507
- DLSODA, 27
- Doppler broadening, 350–352, 361, 364, 376, 381, 397, 422
- Doppler effect, 395, 408
- Doppler shift, 351, 376, 387, 422, 425, 426
- absorption profiles, 409–410
 - DLAS, 387*f*
 - Rayleigh scattering, 423
 - spectral shift of Rayleigh, 421
 - velocimetry, 386–387
- Doppler-based velocimetry
- Doppler effect, 408
 - fluorescence-based, 410
 - two-component velocity measurement, 410*f*
 - velocity component measurements, 409
- Double-cone flow, 227, 231
- flow conditions, 228
 - flux evaluation schemes, 229
- hypersonic, 228*f*
- variation of recirculation zone size, 230*f*
- DPLR method. *See* Data-parallel line-relaxation method
- DS2V code, 70
- DSMC code, 76
- DSMC method. *See* Direct simulation Monte Carlo method
- Earth's atmosphere, DSMC analyses of flight in, 72. *See also* Planetary atmospheres, DSMC analyses of flight in
- blunt body configurations, 75, 78
 - DS2V DSMC code, 76
 - measured and computed spectra comparison for Stardust, 77*f*
 - mole fraction profiles, 77*f*
 - temperature profiles along Stardust SRC stagnation streamline, 76*f*
 - slender body configurations, 72
 - NO emission as function of altitude for BSUV-2 hypersonic flight, 74*f*
 - normalized NO spectra, 74*f*
 - peak plasma density as function of axial location, 75*f*
 - plasma density as function of radial distance, 75*f*
 - radiative emission calculation, 73
- EAST facility. *See* Electric Arc Shock Tube facility
- EBK quantization condition.
- See* Einstein–Brillouin–Keller quantization condition
- Eigensystem
- for chemically reacting mixture of perfect gases, 212
 - derivation, 214
 - high-enthalpy flows, 212
 - vector of conserved variables and flux vector, 213
- for gas with arbitrary equation of state, 208
- diagonal matrix of eigenvalues, 210
 - eigenvector matrices of intermediate Jacobian, 211
 - intermediate diagonalized matrix, 211

- modified Steger–Warming approach, 212
primitive variables, 209
- Einstein coefficients, 166, 168, 354–355, 396
- Einstein–Brillouin–Keller quantization condition (EBK quantization condition), 124, 125
- Elastic momentum exchange, 50. *See also* Rotational energy exchange; Vibrational energy exchange
- argon
profiles of normalized density through Mach 9 normal shock wave, 52 f
reciprocal shock thickness for normal shock waves, 52 f
- electron–nitrogen molecule collision cross sections, 54 f
- electron–oxygen atom collision cross sections, 54 f
- helium
VDF in front Mach 25 normal shock, 53 f
VDF in middle of Mach 25 normal shock, 53 f
VHS model, 51
- Electric Arc Shock Tube facility (EAST facility), 163, 369 f , 429, 472–473
- Electric field models, 35–36
- Electromagnetic discharge (EM discharge), 338
- Electron Spin Resonance (ESR), 273
- Electron temperature, 162, 175 f
in DSMC, 178
spatially homogeneous, 36
- Electron-beam fluorescence, 447
- Electron-multiplying charged-coupled device camera (EMCCD), 424
- Eley–Rideal reactions (ER reactions), 253
- EM. *See* Empirical model
- EM discharge. *See* Electromagnetic discharge
- EMCCD. *See* Electron-multiplying charged-coupled device camera
- Emission random number database (ERND), 171
- Emission spectroscopy, 352, 353
application examples, 367–372
- data analysis, 362
atomic emission lines, 363
simulation codes, 366–367
temperature determination methods, 364–366
disadvantage, 361–362
- Empirical model (EM), 285, 291
for catalytic O-atom recombination, 285–289
reactions and rates, 286 f
- Endo-atmospheric radiation, 182
bulk *vs.* NO translational and internal temperatures, 185 f
forward viewing radiometer intensities, 183 f
NO translational temperature, 184
spectra as function of altitude, 183 f
T-V relaxation rates, chemistry models, and temperatures effect, 187 f
- Energy accommodation, 311
finite-rate modeling formulation, 311
material microstructure, 312–313
NO-titrated nitrogen discharge flow, 312
- Energy grouping, 151
- Equilibrium constants, 254
activity-based, 255, 256
attempt frequency, 257
concentration-based, 257
Gibbs formation energy, 256
TST, 257, 258
- ER reactions. *See* Eley–Rideal reactions
- ER-recombination, 277–278
- ERND. *See* Emission random number database
- Escape factor, 173–174
distribution of atomic N, 182 f
for strongest atomic O transition, 181
- ESR. *See* Electron Spin Resonance
- Euler–MacLaurin summation formula, 129
- Expansion tube/tunnel, 337–338
- F4 hypersonic arc-jet wind tunnel, 474–475
- Fabry–Perot etalon, 424
- FBC. *See* Flux Boundary Condition
- Femtosecond Laser Electronic Excitation Tagging (FLEET), 412
- Femtosecond lasers, 350
- Fermi's golden rule, 13

- FHO model. *See* Forced harmonic oscillator model
- Field of view (FOV), 182
- FIN-S code. *See* Fully-Implicit Navier–Stokes code
- Finite fringe interferograms, 445
- Finite-rate formulation
- equilibrium constants, 254–258
 - forward reaction rates, 253t
 - species production rates, 251–254
 - surface reaction formulation, reaction fluxes, 251–254
 - system definitions, 248–251
 - thermodynamic data, 254–258
- Finite-rate models, 310–311
- Finite-volume approach
- (FV approach), 170
- Finite-volume–photon Monte Carlo method (FV-PMC method), 170, 171, 180
- Finite-rate surface chemistry model, 245
- in aerothermal heating simulations, 247
 - finite-rate formulation
 - equilibrium constants, 254–258
 - forward reaction rates, 253t
 - species production rates, 251–254
 - surface reaction formulation, reaction fluxes, 251–254
 - system definitions, 248–251
 - thermodynamic data, 254–258
- incorporation into CFD code
- DPLR, 258–259
 - surface boundary conditions, 259–265
 - SRE, 246
- FLEET. *See* Femtosecond Laser Electronic Excitation Tagging
- Flow-tagging velocimetry
- fluorescence-based, 411
 - multilaser methods, 413–416
 - single-laser methods, 411–413
- Fluid transport equations
- BGK approximation, 4
 - Boltzmann equation, 3–4
 - Damköhler number, 6–7
 - DSMC method, 4–5
 - FHO theory, 7–8
 - Knudsen number, 2
 - Navier–Stokes equations, 3
- QCT, 8
- WCU equation, 9
- Fluorescence lifetime, 396, 404–405
- Flux Boundary Condition (FBC), 271
- Flux evaluation schemes, 229
- Flux-based coupling method, 88
- Force Field. *See* Potential Energy Surface (PES)
- Forced harmonic oscillator model (FHO model), 7–8, 58, 59
- FOV. *See* Field of view
- Franck–Condon principle, 360
- Franck–Condon factor, 166
- Free piston driver tube, 337
- Free-bound transitions, 164
- Free-free transitions, 164
- Full width half maximum (FWHM), 350, 361
- Fully-Implicit Navier–Stokes code (FIN-S code), 309
- FV approach. *See* Finite-volume approach
- FV-PMC method. *See*
- Finite-volume–photon Monte Carlo method
- FWHM. *See* Full width half maximum
- Gas–surface interactions (GSI), 65, 241, 244, 267, 274, 329
- CLL model, 65
- computed scattering distributions from DSMC simulation, 66f
 - distributions of argon scattering from platinum, 66f
- ER-recombination, 277–278
- finite-rate catalytic model, 275
- finite-rate catalytic model formation for O-atom recombination, 280–285
- high Knudsen number conditions, 67
 - molecular dynamics simulations, 276
 - molecular oxygen formation, 277–278
 - O-atom adsorption, 276
 - O₂ replacement/ER-recombination, 278–280
 - at silica surface defects, 274t
 - velocity profiles for hypersonic flow, 67f
- Gas–surface interface. *See* Gas–surface interactions (GSI)

- Gas-surface model, 160, 190
 quantum chemical descriptions of, 266–267
- Gaunt factor, 165
- GCE model. *See* Generalized Collision Energy model
- Generalized Boltzmann equation, 10
 collision kernel, 13
 conservation equations, 12–13
 distribution function evolution, 11–12
 Maxwell–Boltzmann distribution, 11
 WCU equation numerical solution, 14
- Generalized Collision Energy model (GCE model), 61, 62
- Generalized Method of Residuals (GMRes), 226–227
- GHIBLI plasma wind tunnel, 510–511
- Gladstone-Dale equation, 445
- Global dissociation rate coefficient, 147
- GMRes. *See* Generalized Method of Residuals
- Gradient-length Knudsen number, 83, 84
- Grotian diagrams, 355
- GSI. *See* Gas-surface interactions
- Hamilton’s equations, 124
- HARA. *See* High-temperature Aerothermodynamic RAdiation
- Harten–Lax–van Leer scheme (HLL scheme), 229
- Harten–Lax–van Leer–Contact scheme (HLLC scheme), 229
- Hartree Fock approximation, 109
- Heavy particle rate coefficients, 103
 collisional calculations to state-to-state
 rate coefficients
 classical mechanical treatment of
 collision, 123–133
 quantum mechanical theory, 119–123
 quasi-classical trajectory calculations,
 results of, 133–139
- computational methods, 106
- energy surface calculation, 107
 analytical representation of potential
 energy surface for N₃, 119^f
- Cartesian coordinates of atoms, 108
- fitting parameters, 117
- functional forms, 116
- Jacobi coordinates, 109
- MOLPRO code, 110
- N₃ PES, 111
- potential energy curves for N₂, 114^f, 115^f
- RHF UCCSD(T) calculations, 112, 113
- “spectator” diatom, 118
- time-dependent Schrödinger equation, 107, 108
- nonequilibrium gas characterization, 105
- phenomenological rate coefficients from master equation model, 139
 energy transfer and dissociation kinetics, 144–150
 kinetic processes, 140–142
- 2-T model, 104
- HEG. *See* High enthalpy shock tunnel Göttingen
- HFFGAF. *See* Hypervelocity free flight aerodynamic facility
- HIEST. *See* High enthalpy shock tunnel
- High enthalpy shock tunnel (HIEST), 480–481
- High enthalpy shock tunnel Göttingen (HEG), 476, 477^f, 481^f
- High Resolution Transmission (HITRAN), 375
- High-enthalpy facilities, 334
 ballistic range, 335
 blow down wind tunnel, 334, 335^f
 expansion tube/tunnel, 337–338
 free piston driver tube, 337
 hot shot tunnel, 335
 shock tube, 335–336
 shock tunnel, 336, 337^f
- High-enthalpy flows, 212
- High-Mach number hypersonic flows, 217
- High-temperature Aerothermodynamic RAdiation (HARA), 162
- Highly Oriented Pyrolytic Graphite (HOPG), 311
- HITRAN. *See* High Resolution Transmission
- HLL scheme. *See* Harten–Lax–van Leer scheme
- HLLC scheme. *See* Harten–Lax–van Leer–Contact scheme

- Honl–London factor, 359, 360
- HOPG. *See* Highly Oriented Pyrolytic Graphite
- Hot shot tunnel, 335
- Hybrid DSMC-continuum methods, 79
- challenges, 93
 - coupling procedures, 87
 - continuum and particle boundary cells, 89
 - hybrid, 88^f
- hybrid codes and application, 89
- comparison of rotational energy distribution functions, 91^f
 - comparison of velocity distribution functions, 91^f
 - interface location and variation of mean free path, 90^f
- MPC method, 89, 90, 93
- surface coefficient of heat flux, 92
- surface heat transfer along planetary probe, 92^f
- hybrid particle-continuum framework, 82–87
- multi-scale hypersonic flows
- over blunted body with regions, 80^f
 - examples of, 79
 - geometry and variation in mean free path, 83^f
 - heat transfer predictions, 80^f
 - hypersonic viscous interaction flows, 82
 - variation of gradient-length Knudsen number for flow, 81^f
- Hybrid particle-continuum framework, 82
- continuum breakdown, 83
- comparison of probability density functions, 86^f, 87^f
 - comparison of translational temperature prediction of hybrid method, 85, 86^f
 - development, 84
 - gradient-length Knudsen number, 83, 84
- HyMETS. *See* Hypersonic Materials Environmental Test System
- Hypersonic flows, 1, 174.
- See also* Radiation models
- endo-atmospheric radiation, 182
- bulk *vs.* NO translational and internal temperatures, 185^f
- forward viewing radiometer intensities, 183^f
- NO translational temperature, 184
- spectra as function of altitude, 183^f
- T-V relaxation rates, chemistry models, and temperatures effect, 187^f
- high-Mach number, 217
- spacecraft glow, 187, 189^f, 193
- AE measurements, 187
 - angle of attack, 193
 - experimental measurements of normal shock flow fields, 188^t
 - experimental measurements of radiation from normal shocks, 189^t
 - gas–surface model, 190
 - radiation dependency, 191
 - SKIRT, 192
- Stardust, 175
- comparison of distributions, 175^f
 - comparison of heat fluxes, 176^f
 - comparison of QSS, 180^f
 - divergence of radiative heat flux, 181^f
 - DSMC-PMC coupled simulations, 178
 - escape factor, 181, 182^f
 - radiative transport, 179
 - stagnation-point convective heat flux and radiative heat flux comparison, 177^f
- Hypersonic laboratory experiments
- code validation exercise, 69
 - contours of Mach number, 71^f, 72^f
 - drag coefficient
 - for capsule at angle of attack, 73^f
 - for cone at angle of attack, 71^f - DSMC and measured data, 69^f
 - heat flux
 - along surface of double cone testing, 70^f
 - coefficient on planetary probe, 69^f
- MONACO DSMC code, 68

- pitching moment
for capsule at angle of attack, 73f
for cone at angle of attack, 72f
planetary probe geometry, 68
pressure along surface of double cone
testing, 70f
- Hypersonic Materials Environmental Test System (HyMETS), 402, 403f, 502–503
- Hypersonic non-equilibrium flows, 343. *See also* Molecular-based optical measurement techniques
Boltzmann distribution law, 344
coherent measurement approach, 346
flowfield and radiation modeling, 162
effect of non-local VUV radiation on, 171
escape factor, 173
non-local escape factor, 174
rate equation, 172
nonequilibrium effects, 347
spectroscopic measurement techniques, 346
- Hypersonic propulsion system, 438
- Hypersonic viscous interaction flows, 82
- Hypervelocity free flight aerodynamic facility (HFFGAF), 478–479
- IAD. *See* Inflatable aerodynamic decelerator
- icACPF method. *See* internally contracted Average-Coupled-Pair-Functional method
- icMRCI method. *See* internally contracted Multi-Reference-Configuration-Interaction method
- ICOS. *See* Integrated cavity output spectroscopy
- ICP. *See* Inductively coupled plasma
- Ideal gas law, 384, 431
- IHF. *See* Interaction Heating Facility
- Impact parameter, 129
- Implicit time integration, 224
decoupled implicit method, 227
- DPLR method, 225
GMRes, 226–227
- high-Reynolds number flows, 226
semi-implicit approach, 224
- Incoherent measurement techniques, 346
- Inductively coupled plasma (ICP), 243, 338–339
- Infinite fringe interferograms, 445
- Inflatable aerodynamic decelerator (IAD), 81
- Infrared (IR), 348
- Institute of Space Systems (IRS), 512, 516
PWK 1, 2, 4, 512–513
PWK 3, 516–517
- Integrated cavity output spectroscopy (ICOS), 390
- Interaction Heating Facility (IHF), 496–497
- Interferogram, 425, 444
- Interferometry, 444
fluid mechanical applications, 445
nonequilibrium hypersonic flows, 445–446
path-averaged measurement technique, 445
- internally contracted
Average-Coupled-Pair-Functional method (icACPF method), 112
- internally contracted
Multi-Reference-Configuration-Interaction method (icMRCI method), 112
- Inverse pre-dissociation, 371
- Inverse square law, 346
- IPM induction plasma generator, 518–519
- IR. *See* Infrared
- IRS. *See* Institute of Space Systems
- Jacobi coordinates, 109
- Japan aerospace Exploration Agency (JAXA), 163, 480
- JF-10 oxygen-hydrogen detonation-driven high-enthalpy shock wind tunnel, 482–483
- KAIST. *See* Korea Advanced Institute of Science and Technology
- Knudsen number (Kn), 2, 45, 46
- Korea Advanced Institute of Science and Technology (KAIST), 163

- Laboratory of high-temperature gas dynamics (LHD), 482
- Landau–Teller equation, 104
model, 28, 259
- Langley Optimized Radiative Nonequilibrium code (LORAN code), 162, 178
- Langmuir–Hinshelwood reactions (LH reactions), 253
- Large Energy National Shock facility (LENS facility), 69, 82 XX, 484–485
- Large Energy Shock Tunnel facility (LENS I facility), 378, 379^f
- Laser Enhanced Ionization (LEI), 413
- Laser induced fluorescence (LIF), 345, 391, 444, 494, 497, 513, 516
advantages and limitations of, 416–417
for atom, 392
Boltzmann fraction, 394
Doppler-based velocimetry, 408–410
flow-tagging velocimetry, 411–416
linear, steady state solution, 394–395
multilevel fluorescence modeling, 396–397
nonsteady state solution, 395–396
pressure, 408
rotational temperature, 398–400
single-photon fluorescence two-level model, 392^f
species concentration, 402–408
translational temperature, 397–398
two-photon LIF process, 393
vibrational temperature, 401–402
- Laser system, 348
- Laser-induced thermal acoustics (LITA), 448
- Left-hand side (LHS), 168
- LEI. *See* Laser Enhanced Ionization
- LENS facility. *See* Large Energy National Shock facility
- LEO. *See* Low earth orbit
- LH reactions. *See* Langmuir–Hinshelwood reactions
- LHD. *See* Laboratory of high-temperature gas dynamics
- LHS. *See* Left-hand side
- LHTS. *See* Local Heat Transfer Simulation
- LIF. *See* Laser induced fluorescence
- Line strength factor, 166
- LITA. *See* Laser-induced thermal acoustics
- Local Heat Transfer Simulation (LHTS), 331
- Local thermodynamic equilibrium (LTE), 332, 352
- LORAN code. *See* Langley Optimized Radiative Nonequilibrium code
- Low earth orbit (LEO), 160
- Low-dissipation numerical flux, 219.
See also Upwind numerical flux functions
- higher than second-order accuracy, 223
positivity preserving schemes, 222
practical implementation, 222–223
secondary conservation, 220
1-D Euler equations, 220
convective fluxes for mass and momentum, 221
Courant–Friedrichs–Lowy number restriction, 222
- LTE. *See* Local thermodynamic equilibrium
- Macroscopic nonequilibrium transport equations, 32. *See also* Fluid transport equations
- Arrhenius equation, 35
- Debye length, 32–33
- electric field models, 35–36
- ideal plasma, 32
- reactive collisions, 34–35
- thermochemical nonequilibrium flow, 33–34
- total radiation heat flux, 34
- Macroscopic transport equations coupled to master equation, 22–23.
See also Fluid transport equations
- inviscid fluid transport equations, 29–30
- numerical solutions, 28–29, 30–32
methodology, 26–28
- simplifications in transport equations, 23–26
- Mars Global Surveyor (MGS), 78
- Martian atmosphere, 294
density reconstruction, 78

- entry surface chemistry, 294
CO loss efficiencies, 296
O-atom loss efficiency, 295
reactions and rates for mars entry
catalysis, 294
- L2Kmaterial testing, 505f
- Master equation model, phenomenological
rate coefficients from, 139
assumptions, 142–143
energy transfer and dissociation
kinetics, 144
ab initio relaxation time, 145f
dynamics of relaxation, 150
global dissociation rate coefficient,
147, 148f, 149f
normalized population distribution
function, 146f
thermal relaxation studies, 145f
- kinetic processes, 140
collisional excitation processes, 141
translational partition
functions, 142
- Material particles, 9
- Maxwell–Boltzmann distribution, 148
- MCHF method. *See* Multi-configuration
Hartree–Fock method
- MD. *See* Molecular dynamics
- MGS. *See* Mars Global Surveyor
- Microscopic dissociation rate
coefficient, 123
- Microscopic reversibility, 121
- Modified Fastie–Ebert design, 182
- Modified Steger–Warming
approach, 212
- Modular Particle-Continuum method
(MPC method), 89, 90
- Molecular dynamics (MD), 48, 266
- Molecular oxygen formation, 277–278
- Molecular-based measurement
techniques, 444
- BOS, 446–447
- DFWM, 447–448
- electron-beam fluorescence, 447
- interferometry, 444–446
- LITA, 448
- optical measurement techniques, 345
diode lasers, 349
equipment, 348
- pulse burst laser technology, 350
pulsed lasers, 349
- spectroscopic measurement
techniques, 351
- MOLPRO code, 110
- MONACO DSMC code, 68
- Monotone Upwind Schemes for
Conservation Laws approach
(MUSCL approach), 26–27, 215
- Motion modes for diatomic gas molecules, 6
- MPC method. *See* Modular
Particle-Continuum method
- Multi-configuration Hartree–Fock method
(MCHF method), 112
- Multi-scale hypersonic flows
over blunted body with regions, 80f
examples, 79
geometry and variation in mean free
path, 83f
heat transfer predictions, 80f
hypersonic viscous interaction flows, 82
variation of gradient-length Knudsen
number for flow, 81f
- Multilaser methods, 413. *See also*
Single-laser methods
- NO₂–NO flow tagging velocimetry, 414
- single-shot measurement precision, 416
- streamwise velocity profiles on flat
plate, 415f
- tagging process, 413
- Multiline technique, 379
- Multirotational-line temperature
methods, 400
- MUSCL approach. *See* Monotone Upwind
Schemes for Conservation Laws
approach
- National Aeronautics and Space
Administration (NASA), 241
- Ames database, 140
- Ames Research Center
AHF, 494–495
IHF, 496–497
PTF, 498–499
TFD, 500–501
- National Institute of Standards and
Technology (NIST), 355
- Natural broadening, 375

- Navier–Stokes equations, 3, 51, 53, 82
 NEQAIR code. *See* Nonequilibrium Air Radiation code
 NIST. *See* National Institute of Standards and Technology
 Nitric oxide (NO), 402
 Nitrogen (N_2), 23, 435
 - anharmonic-oscillator behavior, 25
 - density, 24
 - expression for vibrational heat flux, 24
 - kinetics of particle exchanges, 24–25
 - mass conservation of species, 26
 - master equation methodology, 26
 - vibrational population distribution, 29*f*
 V-T and V-V excitation and de-excitation rates, 25
 Non-gray equilibrium radiation models, 161
 Non-local escape factor, 174
 Nonequilibrium Air Radiation code (NEQAIR code), 73, 77, 162–163, 174, 179, 193
 - NASA nonequilibrium radiation code, 73, 77
 Nonequilibrium gas
 - characterization, 105
 - escape factor and, 181
 - transport equations, 9
 Number, pressure, and temperature dynamics (NPT dynamics), 270
 Number, volume, and temperature dynamics (NVT dynamics), 269
 O-atom adsorption, 276
 O-atom recombination
 - CCM and EM rates comparison for, 291–293
 - EM for catalytic, 285–289
 finite-rate catalytic model formation, 280, 281, 285
 - O-atom loss efficiency, 284*f*
 - pre-exponential factors, 282
 - reaction-specific production rates, 283
 - relative structure energies within catalytic cycle, 281*f*
 ODE. *See* Ordinary differential equation
 OES. *See* Optical emission spectroscopy
 OF. *See* Optical fiber
 One-dimension (1-D), 162
 - tangent slab approximation, 169–170
 One-particle basis set, 109
 One-temperature model (OT model), 29
 “Onion peeling” method, 362
 Optical emission spectroscopy (OES), 345, 352, 497, 498, 508
 - application examples, 367–372
 - atoms and molecules emission, 353
 - Franck-Condon principle, 360
 - Grotian diagrams, 355
 - molecular potential, 356, 357*f*, 358
 - RKR potential, 359
 - single emission lines, 354
 - spontaneous emission, 354*f*
 - codes for simulation of plasma radiation, 368*t*
 - data analysis, 362–367
 - line shape of emission lines and line broadening, 361
 - spatial resolution, 361–362
 Optical fiber (OF), 425
 Orbital Re-entry Experiment entry (OREX entry), 246
 Ordinary differential equation (ODE), 28
 OREX entry. *See* Orbital Re-entry Experiment entry
 OT model. *See* One-temperature model
 Oxygen-silica system, 241, 310
 Panel Test Facility (PTF), 498–499
 Park model, 300
 - carbon monoxide production, 303
 - CN production, 302
 - effective loss efficiencies, 302
 - reactions and rates for, 300*t*
 Particle-image velocimetry (PIV), 446
 PDF. *See* Probability density function
 Peroxyl defect, 273
 PES. *See* Potential energy surface
 Phenolic ablator in air with pyrolysis, 303–308
 Phenolic impregnated carbon ablator (PICA), 303
 Photomultiplier tubes (PMTs), 351, 424, 426

- Photon Monte Carlo approaches
(PMC approaches), 160, 170
electron impact continuum
transitions, 180
ray tracing scheme, 170–171
- PICA. *See* Phenolic impregnated
carbon ablator
- Picosecond-duration lasers, 350
- PIV. *See* Particle-image velocimetry
- Planar laser induced fluorescence (PLIF),
66, 349, 391, 417
- Planck's formula, 353
- Planetary atmospheres, DSMC analyses of
flight in, 78–79
- Plasma wind tunnels, 338–339
- Plasmatron facilities, 338, 339f
- PLIF. *See* Planar laser induced fluorescence
- PMC approaches. *See* Photon Monte
Carlo approaches
- PMTs. *See* Photomultiplier tubes
- Post-collision vibrational quantum
number, 58
- Potential energy hyper-surface, 109
- Potential energy surface (PES), 105–106,
107, 266
analytical representation, 109f, 119f
Cartesian coordinates of atoms, 108
fitting parameters, 117
functional forms, 116
Jacobi coordinates, 109
MOLPRO code, 110
 N_3 PES, 111
potential energy curves for N_2 ,
114f, 115f
RHF UCCSD(T) calculations, 112, 113
“spectator” diatom, 118
time-dependent Schrödinger equation,
107, 108
- Predissociated states, 131, 141–142
- Primitive variables, 209
- Probability density function (PDF),
148–149
- PTF. *See* Panel Test Facility
- Pulse burst laser technology, 350
- Pulsed lasers, 349, 395
availability, 416
excitation, 426
Q-switch, 437
- Pyrolysis, 259
chemistry, 244
phenolic ablator in air with,
303–308
steady-state, 242, 262
- QCT method. *See* Quasi-classical trajectory
method
- QK model. *See* Quantum Kinetic model
- QSS. *See* Quasi-steady-state
- Quantum chemical descriptions of
gas–surface systems, 266–267
- Quantum Kinetic model
(QK model), 63
- Quantum mechanical theory, 119
basis functions, 122
microscopic dissociation rate
coefficient, 123
microscopic reversibility, 121
uncoupled representation, 120
- Quasi-bound states, 131
- Quasi-classical molecular dynamic
calculations, 8
- Quasi-classical trajectory method
(QCT method), 60–61, 106
calculation results, 133–139
state-to-state rate coefficients for
 N_2+N pairs, 135
- Quasi-steady-state (QSS), 160, 173
assumption for NEQAIR and
LORAN, 162
distribution, 147
using Maxwellian *vs.* DSMC
derived distribution
functions, 180f
theory, 160
- Quenching rate constant, 393
- Radiant intensity, 419
- Radiating states, populations
determination in, 167, 169
baseline excitation/de-excitation
processes, 167
- QSS condition, 168
- Radiation, 64–65
atomic species, 163, 166
bound-free absorption cross section,
164–165

- Radiation (*Continued*)
 normalized emission and absorption coefficients, 164
 transition mechanisms, 164
- diatomic species, 166–167
- history, 161
 electron temperature, 162
 NEQAIR and HARA codes, 163
- models, 161
 in ultraviolet spectral region, 163–174
- Radiative intensity, 169
- Radiative transfer equation (RTE), 162, 163
- Radiative transport, 169
 one-dimensional tangent slab approximation, 169–170
 photon Monte Carlo ray tracing scheme, 170–171
- Radiative trapping, 417
- Radio Attenuation Measurement experiments (RAM experiments), 74
 peak plasma density as function of axial location, 75*f*
 plasma density as function of radial distance, 75*f*
- Raman active vibrations, 421
- Raman Excitation and Laser-Induced Electronic Fluorescence (RELIEF), 413
- Raman inactive vibrations, 421
- Raman scattering, 418. *See also* Coherent anti-Stokes Raman spectroscopy (CARS)
 advantages and disadvantages of, 422
 rotational and vibrational temperature measurements, 427–430
 species concentration measurement, 430–431
 theory of spontaneous, 418–422
 translational temperature, velocity, and density measurements, 422–427
- RANS turbulence model. *See* Reynolds-averaged Navier–Stokes turbulence model
- Rarefied gas flows, 2–3
- Ratio thermometry technique, 379
- Rayleigh scattering, 345, 418
 advantages and disadvantages of, 422
 rotational and vibrational temperature measurements, 427–430
 species concentration measurement, 430–431
 theory of spontaneous, 418–422
 translational temperature, velocity, and density measurements, 422–427
- ReaxFF potential, 266
- ReaxFF_{SiO} potential, 268
- RELIEF. *See* Raman Excitation and Laser-Induced Electronic Fluorescence
- Resonant states, 131
- Reynolds-averaged Navier–Stokes turbulence model (RANS turbulence model), 206
- RHF approximation. *See* Spin-restricted Hartree–Fock approximation
- “Ring-down time”, 389–390
- RKR potential. *See* Rydberg–Klein–Rees potential
- Roe approximate Riemann solver, 26
- Roe variables, 208
- Rotational energy exchange, 54. *See also* Elastic momentum exchange; Vibrational energy exchange
- BL model, 55–56
- Boltzmann distribution, 55
- distribution functions, 57*f*
 profiles of density and rotational temperature, 56*f*
- Rotational temperature, 379
- absorption spectroscopy
 absorption features, 380, 382
 balanced ratiometric method, 383–384
 comparison of direct and WMS absorption, 383*t*
 diode lasers, 382
 high-resolution line shapes, 381
 LIF, 398–400
 Rayleigh and Raman scattering, 427–430
- RTE. *See* Radiative transfer equation
- Rydberg formula, 355
- Rydberg–Klein–Rees potential (RKR potential), 359

- S-AS. *See* Stokes to anti-Stokes
- Sample Return Capsule (SRC), 76
measured and computed spectra
comparison, 77*f*
mole fraction profiles, 77*f*
temperature profiles, 76*f*
- SCEBD. *See* Self-consistent effective binary diffusion
- SCIROCCO plasma wind tunnel, 508–509
- Self-consistent effective binary diffusion (SCEBD), 259, 309
- Semi-classical procedure, 132
- Semi-implicit approach, 224
- Shock layer, 1
gas, 5, 103
population distribution, 31*f*
radiative VSL calculations, 161
- Shock tube, 335–336, 367, 429
experiments for gas mixtures, 105
facility, 336*f*
piston-driven, 337*f*
- Shock tunnel, 336, 337*f*
- Silica
O-atom recombination
CCM and EM rates comparison for, 291–293
EM for catalytic on, 285–289
finite-rate catalytic model formation for, 280–285
- oxides, 241
- polymorphs, 267
- surfaces, 267–268
active chemical sites on, 271–274
amorphous silica surfaces, 269–271
crystalline quartz surfaces, 268–269
- Silicon carbide (SiC), 244
- Silicon monoxide (SiO), 244
- Simulation codes, 366–367
- Single-laser methods, 411. *See also*
Multilaser methods
FLEET, 412–413
indirect excitation scheme, 412
single-line excitation of NO fluorescence, 412*f*
- SKIRT. *See* Spacecraft Kinetic Infrared Test
- Slender body configurations, 72
NO emission as function of altitude for
BSUV-2 hypersonic flight, 74*f*
- normalized NO spectra, 74*f*
- peak plasma density as function of axial location, 75*f*
- plasma density as function of radial distance, 75*f*
- radiative emission calculation, 73
- SMILE code, 70, 76
- Space Technology Mission Directorate (STMD), 106
- Spacecraft glow, 187, 189*f*
AE measurements, 187
angle of attack, 193
comparison of altitude dependence, 191*f*
- experimental measurements
of normal shock flow fields, 188*t*
of radiation from normal shocks, 189*t*
- gas-surface model, 190
- Spacecraft Kinetic Infrared Test (SKIRT), 192
- SPARADIAN. *See* Structured Package for RADIation ANalysis
- Spatial resolution, 361–362
- Species concentration, LIF, 402
bi-directional beam LIF, 405–406
combined LIF/Rayleigh/Raman, 406–408
- nonquantitative flow visualization, 402–403
- pre-dissociation LIF, 404
- saturated LIF, 403–404
- short-pulse LIF, 404–405
- Specified reaction efficiency (SRE), 246, 290
catalysis models, 289–290
- Spin-restricted Hartree–Fock approximation (RHF approximation), 112
- Spontaneous Raman scattering, 418
- Spontaneous Rayleigh scattering, 418
- Spontaneous spectral emission coefficient, 163
- SRC. *See* Sample Return Capsule
- SRE. *See* Specified reaction efficiency
- SSEB equation. *See* Steady-state energy balance equation
- Stanton number, 28*f*

- Stardust, 175
 comparison
 of distributions, 175/*f*
 of heat fluxes, 176/*f*
 of QSS, 180/*f*
 divergence of radiative heat flux, 181/*f*
 DSMC-PMC coupled simulations, 178
 escape factor, 181, 182/*f*
 radiative transport, 179
 stagnation-point convective heat flux
 and radiative heat flux
 comparison, 177/*f*
 State kinetic transport coefficients, 21–22
 State-based coupling, 88
 State-to-state kinetic models
 (STS kinetic models), 7
 State-to-state rate coefficients, collisional
 calculations to
 classical mechanical treatment of
 collision, 123, 133
 DSMC flow calculations, 130
 EBK quantization condition, 125
 Euler–MacLaurin summation
 formula, 129
 Hamilton’s equations, 124
 Monte-Carlo method, 128
 1-D problem, 126
 rotation angle as function of
 time, 127/*f*
 unnormalized relative translational
 energy distributions, 131/*f*, 132/*f*
 quantum mechanical theory, 119
 basis functions, 122
 microscopic dissociation rate
 coefficient, 123
 microscopic reversibility, 121
 uncoupled representation, 120
 quasi-classical trajectory calculation
 results, 133
 dissociation rate coefficients, 136
 molar rate coefficients, 136/*f*, 137/*f*
 potential energy curves for N₂, 134/*f*
 thermal rate coefficients for N₂
 dissociation, 138/*f*, 139/*f*
 translation energy, 135
 Steady-state energy balance equation
 (SSEB equation), 261
 Steger–Warming formulation, 207
 STMD. *See* Space Technology Mission Directorate
 Stokes Raman scattering, 418
 Stokes to anti-Stokes (S-AS), 428
 Strang splitting, 27
 Structured Package for RADiation
 ANalysis (SPARADIAN), 163
 STS kinetic models. *See* State-to-state
 kinetic models
 Super orbital expansion tube
 X2, 490–491
 X3, 492–493
 Supercatalytic boundary condition, 245
 Surface boundary conditions, 259
 gas-phase species masses, 263
 mass balance, 260
 molar production, 259
 SSEB equation, 261
 sublimation reaction rates, 265
 surface-phase concentration, 264
 total production of gaseous species, 262
 Surface catalytic chemistry, 244
 Surface chemistry. *See also* Finite-rate
 surface chemistry model
 ablation, 245
 advanced diagnostics for plasma
 facilities, 314–315
 boundary-layer diffusion and chemistry,
 309–310
 chemical and thermal relaxation, 243
 computational chemistry, 265, 310, 311
 active chemical sites on silica surfaces,
 271–274
 gas–surface interactions, 274–280
 quantum chemical descriptions of
 gas–surface systems, 266–267
 silica surfaces, 267–271
 surface energies for α -quartz
 surfaces, 269/*f*
 computational examples, 285
 air–carbon surface chemistry, 297–302
 CCM and EM rates comparison for
 O-atom recombination, 291–293
 coupled catalysis models, 294–296
 EM for catalytic O-atom
 recombination, 285–289
 phenolic ablator in air with pyrolysis,
 303–308

- relationship to SRE catalysis models, 289–290
consistency between experimental analyses and CFD simulations, 313–314
energy accommodation, 311–313
finite-rate models, 310, 311
materials response computations, 308–309
net heat flux, 242
nonequilibrium boundary layer, 243
pyrolysis chemistry, 244
surface catalytic chemistry, 244
tightly coupled CFD, 308–309
Surface coefficient of heat flux, 92
Surface reaction model, 304
- T5 hypervelocity shock tunnel facility, 486–487
TALIF. *See* Two-photon laser-induced fluorescence
Tangent-slab approximation (TS approximation), 160
Taylor series, 419
TCE model. *See* Total Collision Energy model
Tcheremissine’s method, 3
Temperature determination methods, 364
band shapes, 366
Boltzmann plot, 365
effects of plasma state, 365*f*
Stark broadening factors, 364
Temperature jump, 2
TFD. *See* Turbulent Flow Duct
TH2 hypersonic shock tunnel, 488–489
Thermal nonequilibrium, 6
Thermal protection system (TPS), 103, 241, 329, 367, 494
effect of finite-rate processes, 231
simulation, 231
surface species mass fluxes and temperature distribution, 232*f*
temperature distribution in nose region of sphere-cone, 232*f*
translational–rotational temperature distribution, 233
Thermal radiation, 8
- Thermal rate coefficient, 133, 148
Three-dimension (3-D), 170
Euler equations, 208
flows, 70
Time-dependent Schrödinger equation, 107, 108
Tomography, 388–389
Total Collision Energy model (TCE model), 59
TPS. *See* Thermal protection system
Transition mechanisms, 164
Transition state theory (TST), 257
Translational partition functions, 142
Translational temperature, 377
absorption spectroscopy
Doppler width contribution, 379
LENS, 378
LIF, 397–398
Rayleigh and Raman scattering, 422–427
TS approximation. *See* Tangent-slab approximation
TST. *See* Transition state theory
TT model. *See* Two-temperature model
Turbulent Flow Duct (TFD), 500–501
Two-photon laser-induced fluorescence (TALIF), 371
Two-temperature model (TT model), 29
- Ultra-high temperature ceramic (UHTC), 241
Ultrafast lasers, 350
Ultraviolet (UV), 348
Uncoupled representation, 120
Uniform semi-classical method, 132
Unnormalized relative translational energy distributions
linear energy axis, 131*f*
logarithmic energy axis, 132*f*
Upwind numerical flux functions, 206.
See also Low-dissipation numerical flux
Eigensystem
for chemically reacting mixture of perfect gases, 212–214
for gas with arbitrary equation of state, 208–212

- Upwind numerical flux functions
(Continued)
- higher-order, added dissipation, and limiting, 214, 217
 - carbuncle, 216
 - minmod function, 215
 - MUSCL, 215
 - implementation on unstructured grids, 217
 - high-Mach number hypersonic flows, 217
 - standard weighted least-squares approach, 219
 - stencil, 218f
 - Steger–Warming formulation, 207
- UV. *See* Ultraviolet
- UVM 30 kW inductively coupled plasma torch facility, 520–521
- Vacuum ultra-violet (VUV), 159
- Variable Hard Sphere (VHS), 51
- Variable Soft Sphere (VSS), 51
- VCSEL. *See* Vertical cavity surface-emitting laser
- VDF. *See* Velocity distribution function; Vibrational distribution function
- Velocimetry
- DLAS velocimetry measurements, 387
 - Doppler-shift based, 386
 - VCSEL, 388
- Velocity distribution function (VDF), 14, 17f, 45
- Velocity slip, 2
- Vertical cavity surface-emitting laser (VCSEL), 388
- VFD model. *See* Vibrationally Favored Dissociation model
- VHS. *See* Variable Hard Sphere
- Vibrational distribution function (VDF), 443
- Vibrational energy exchange, 57. *See also* Elastic momentum exchange; Rotational energy exchange
- average probability, 57
 - FHO model, 58, 59
 - post-collision vibrational quantum number, 58
- profiles of relative population in fourth vibrational state, 59f
- Vibrational nonequilibrium, 439–440
- Vibrational temperature
- absorption spectroscopy, 384
 - LIF, 401–402
 - Rayleigh and Raman scattering, 427–430
- Vibrationally Favored Dissociation model (VFD model), 60
- Vibrational–translational processes (VT processes), 7
- Vibration–translation transfer (V–T transfer), 7
- Vibration–vibration transfer (V–V transfer), 7
- Viscous shock layer (VSL), 162
- VKI inductively coupled plasma wind tunnel (PLASMATRON), 514–515
- Voigt function, 376
- VSL. *See* Viscous shock layer
- VSS. *See* Variable Soft Sphere
- VT processes. *See* Vibrational–translational processes
- V–T transfer. *See* Vibration–translation transfer
- VUV. *See* Vacuum ultra-violet
- V–V transfer. *See* Vibration–vibration transfer
- Wall Damköhler number (Da_w), 332
- Wang–Chang–Uhlenbeck equation (WCU equation), 9
- Wavelength modulation spectroscopy (WMS), 382
- WCU equation. *See* Wang–Chang–Uhlenbeck equation
- Weighted essentially nonoscillatory methods (WENO methods), 206
- WENO methods. *See* Weighted essentially nonoscillatory methods
- Width of resonance, 132
- WMS. *See* Wavelength modulation spectroscopy
- Zeldovich exchange reaction, 60

SUPPORTING MATERIALS

A complete listing of titles in the Progress in Astronautics and Aeronautics series is available from AIAA's electronic library, Aerospace Research Central (ARC) at arc.aiaa.org. Visit ARC frequently to stay abreast of product changes, corrections, special offers, and new publications.

AIAA is committed to devoting resources to the education of both practicing and future aerospace professionals. In 1996, the AIAA Foundation was founded. Its programs enhance scientific literacy and advance the arts and sciences of aerospace. For more information, please visit www.aiaafoundation.org.

